Meet the man who invented the gravitational-wave detector *p. 532*

The flood at the dawn of China *pp. 538 & 579*

Watching flows in a battery *pp. 543 & 566*

Science

$15
5 AUGUST 2016
sciencemag.org

AAAS

FOLLOW THE SUN

Circadian rhythms regulate growth in sunflower plants
pp. 541 & 587

CONTENTS

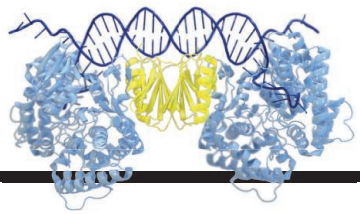

556 & 557
The CRISPR-Cas defense system

5 AUGUST 2016 • VOLUME 353 • ISSUE 6299

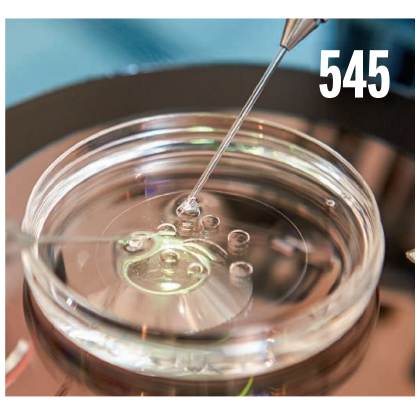

PHOTO (TOP LEFT): © KEN RICHARDSON

Published by AAAS

575
Electron chirality

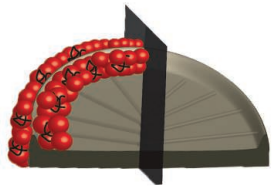

590
Mineral templating in coccoliths

RESEARCH

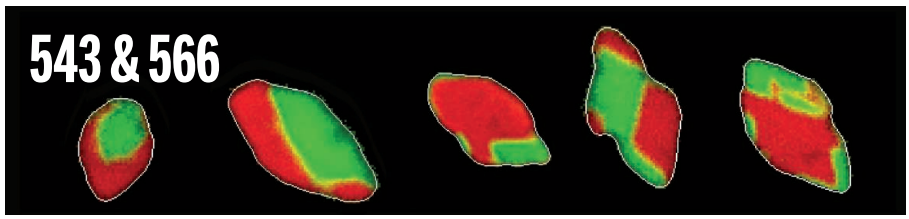

IN BRIEF

REVIEW

RESEARCH ARTICLES

REPORTS

DEPARTMENTS

ON THE COVER

Sunflower head just before floral maturation, with the Sun setting behind it. Whereas mature sunflowers always face east, young sunflower plants track the Sun from east to west during the day and then reorient overnight to face east in anticipation of dawn. Both heliotropic growth patterns are mediated by the circadian clock and enhance pollinator visits and plant yield. See pages 541 and 587.
Photo: Stephen Coleman/Alamy

SCIENCE (ISSN 0036-8075) is published weekly on Friday, except the last week in December, by the American Association for the Advancement of Science, 1200 New York Avenue, NW, Washington, DC 20005. Periodicals mail postage (publication No. 484460) paid at Washington, DC, and additional mailing offices. Domestic individual membership and subscription (51 issues): $165 ($74 allocated to subscription). Domestic institutional subscription (51 issues): $1522; Foreign postage extra: Mexico, Caribbean (surface mail) $55; other countries (air assist delivery) $89. First class, airmail, student, and emeritus rates on request. Canadian rates with GST available upon request, GST #1254 88122. Publications Mail Agreement Number 1069624. **Printed in the U.S.A.**
Change of address: Allow 4 weeks, giving old and new addresses and 8-digit account number. **Postmaster:** Send change of address to AAAS, P.O. Box 96178, Washington, DC 20090–6178. **Single-copy sales:** $15.00 current issue, $20.00 back issue prepaid includes surface postage; bulk rates on request. *Science* is indexed in the *Reader's Guide to Periodical Literature* and in several specialized indexes.

Published by AAAS

Science
AAAS
1200 New York Avenue, NW, Washington, DC 20005
Clarendon House, Clarendon Road, Cambridge, UK CB2 8FH

SUBSCRIPTION SERVICES For change of address, missing issues, new orders and renewals, and payment questions: 866-434-AAAS (2227) or 202-326-6417, FAX 202-842-1065. Mailing addresses: AAAS, P.O. Box 96178, Washington, DC 20090-6178 or AAAS Member Services, 1200 New York Avenue, NW, Washington, DC 20005

INSTITUTIONAL SITE LICENSES 202-326-6730 **REPRINTS:** Author Inquiries 800-635-7181 **COMMERCIAL INQUIRIES** 803-359-4578 **PERMISSIONS** 202-326-6765, permissions@aaas.org **AAAS Member Services** 202-326-6417 or http://membercentral.aaas.org/discounts

INFORMATION FOR AUTHORS See pages 624 and 625 of the 5 February 2016 issue or access www.sciencemag.org/authors/science-information-authors

EDITORIAL

JIFfy Pop

Editor-in-Chief, Science *Journals*
Email: jberg@aaas.org

Tools for judging the impact of publications are critical for scientific leaders, librarians, and individual investigators. An important, but certainly imperfect, measure of impact is the number of times that a paper is cited over time. Citation numbers for individual papers can be aggregated to develop indices that are used to evaluate the content of journals or productivity over the course of a career. Although these indices are convenient, it is important to examine them critically to avoid their misuse.

A case in point is the journal impact factor (JIF), defined as the average number of times that articles published in a journal over the past 2 years are cited in a given year. JIF was developed as a metric to evaluate journals for, as an example, library resource allocation. As described recently, JIF values are based on broad and skewed distributions of citations.* I have extended these observations in my new *Science* blog, *Sciencehound* (http://blogs.sciencemag.org/sciencehound/). In my first post, I develop a mathematical function that captures the key features of the citation distributions. Subsequent posts will examine how these distributions can be used to address statistical questions regarding papers from journals with different JIF values. This analytical framework enables one to quantitatively assess the utility and, most importantly, the limitations of the use of JIFs.

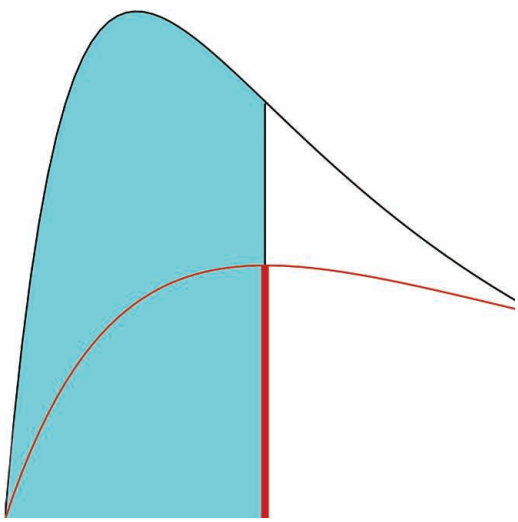

"...how should one's publications be judged?"

As an example, take *Science*, with an impact factor for 2015 of 34.7. What is the probability that a randomly chosen paper from *Science* will have more citations than a paper randomly chosen from another journal with a JIF of 30? Modeling (to be discussed in *Sciencehound*) suggests a probability of 53%, barely different from chance. What about journals with JIFs of 20, 10, or 5? These probabilities are estimated to be 62%, 80%, and 91%, respectively. Even with a spread of 30 in the average number of citations per paper, the probability for concluding that a paper from one journal will have more citations than a paper from another does not reach the usual criterion of a *P* value below 0.05 used to judge statistical significance.

Despite this lack of discriminating power, JIFs are sometimes (ab)used to judge individual papers or scientists in some institutions around the world. The presumption is that comparison of the JIF of the journal in which a given paper appears with that from other journals or against some other standard provides substantial insight about the impact of that paper. Given the analysis of the citation distributions, this presumption is clearly invalid as a matter of mathematical fact. Thus, JIFs should not be a component of key decision processes such as faculty recruitment or promotion. This concern is independent of other criticisms regarding the robustness of JIFs, such as those noted in the San Francisco Declaration on Research Assessment,† of which the American Association for the Advancement of Science (the publisher of *Science*) is a signatory.

If using JIFs to assess faculty is excluded, how should one's publications be judged? If a numerical metric is desired, the number of citations for a paper can be useful. This is a more direct measure of impact, particularly if factors such as the time since publication and comparative citation data from other papers in the same field are taken into consideration. More subjective measures can also be very important. Opinions about the impact of particular papers or a body of work rendered by qualified scientists in the same or similar fields have traditionally played an important role, and this should continue, ideally with appropriate consideration of potential sources of conscious or unconscious bias from these referees. Who knows? Perhaps those charged with making these important decisions should read the papers themselves, assuming that their area of expertise is close enough to the field under consideration.

–Jeremy Berg

*www.biorxiv.org/content/biorxiv/early/2016/07/05/062109.full.pdf. †www.ascb.org/files/SFDeclarationFINAL.pdf

10.1126/science.aah6493

IMAGES: (INSET) JEREMY BERG; (TOP RIGHT) TERRY CLARK

> “It’s not science fiction.”
>
> **Moncef Slaoui, chair of Galvani Bioelectronics**, to STAT.
> The company, formed this week by GlaxoSmithKline and Verily Life Sciences (owned by Google’s parent company, Alphabet), aims to make implantable devices that will fight diseases by targeting the body’s electrical signals.

IN BRIEF

Human activity in Brazil’s Cerrado is responsible for a record number of brush fires in 2016 so far.

Brazil in flames

Brazil is on fire this year, and it has nothing to do with the Olympics. Satellites detected more than 46,000 wildfires in the country during the first 7 months of 2016—an increase of 60% compared with the same period last year, and the largest number since 2004, according to the Brazilian National Institute for Space Research (INPE). Most of the fires are burning in occupied areas of the Amazon and the Cerrado, Brazil’s great central savanna. “Humans are to blame,” says Alberto Setzer, the head of INPE’s Fire Monitoring Program in São José dos Campos. Climatologists predict this could be the driest winter ever in the region, which is likely to make things worse in the coming months. But “there is no climate anomaly so far—only a human anomaly,” Setzer says. “For some reason, people are using more fire this year than before.” A drop in funding for fire surveillance, fueled by the country’s economic crisis, may contribute to the problem, he adds. Fire numbers are going up even as deforestation rates remain stable, suggesting the flames are being used to clear agricultural fields and pastures more than to take down new forest, says Paulo Artaxo, a researcher at the University of São Paulo, São Paulo, in Brazil. “We are going to need new policies to deal with that.” Setzer notes, however, that fire is often used as a first step to clean up forest swaths targeted for deforestation, so continued monitoring and surveillance is essential.

AROUND THE WORLD

Ax falls on Russian science

MOSCOW | Russia’s scientific community is reeling from news that the government plans to fire some 10,000 researchers over the next 3 years. Most layoffs would be from Russian Academy of Sciences (RAS) institutes, the online news site Gazeta.ru revealed this week. The staff cuts, representing about 17% of RAS’s workforce, are the latest move in a controversial effort to overhaul the academy that also includes merging dozens of institutes. Last month, more than 150 Russian scientists said in an open letter to President Vladimir Putin that the reforms are eroding science’s image in Russia; they warned of disastrous consequences for the nation, including a brain drain of young scientists and an “upsurge in activities of bureaucrats and impostors.” The mergers are “a completely unnatural way of development,” says Mikhail Sadovsky, a physicist at RAS’s Institute of Electrophysics in Ekaterinburg. Internal education ministry documents obtained by Gazeta.ru acknowledge that layoffs will erode productivity; the

education ministry told Gazeta.ru that it does not plan to fire scientists, although it does not dispute the documents' authenticity. A spokesperson for the Kremlin says the government gives the scientists' concerns "great attention" but that it sees "positive results" from the ongoing reforms and will let them play out. http://scim.ag/RASupset

NEWSMAKERS

New NIMH head selected

Nearly a year after losing its director to Google, the U.S. National Institute of Mental Health last week selected a new head. Neuroscientist and psychiatrist **Joshua Gordon** has split his career between working with patients with mental illness and with mice designed to mimic that illness. He spent the last 12 years at Columbia University Medical Center and has developed mouse models that mirror aspects of anxiety and schizophrenia. Many expect him to embrace a similar approach to that of his predecessor, Tom Insel, who was known for emphasizing the basic biology underlying psychiatric illness. "I think this very much continues in that tradition," says Eric Morrow, a developmental neurobiologist and psychiatrist at Brown University. "The field has to bridge some pretty big gaps," he says. "So it's fantastic to have somebody who ... understands broadly how to go from gene to behavior." http://scim.ag/GordonNIMH

FINDINGS

Evolution of female orgasms

Surveys suggest only one-third of women are regularly fully aroused during intercourse, which may be due in part to poor partner performance, psychological issues, or physiological shortfalls. But last week, evolutionary biologists offered another explanation in the *Journal of Experimental Zoology Part B: Molecular and Developmental Evolution*. Female orgasm, they argued, is an evolutionary holdover from an ancient system, seen in some other mammals, in which intercourse stimulated hormonal surges that drive ovulation. In humans and other primates, the ovulatory cycle—in which cells destined to become eggs mature, escape from the ovary, and travel down the reproductive tract—has become spontaneous, generally on a set schedule that requires neither an environmental trigger nor a male. But the hormonal changes accompanying intercourse persist and fuel the orgasms that make sex more enjoyable—and because those hormonal surges no longer confer a biological advantage, orgasms during intercourse may be lost in some women, the biologists hypothesize. But other researchers remain unconvinced, noting that a lot of questions remain and more data are needed to confirm the theory. http://scim.ag/_femaleorgasm

ILLUSTRATION: JULIUS T. CSOTONYI

The hadrosaur (likely *Hadrosaurus foulkii*; its cousin, *Rhinorex*, is shown here) may have developed the disease after a predator's attack.

Dino fossils show signs of septic arthritis

Some 70 million years ago, a dinosaur lived alongside a shallow sea covering what is now New Jersey, and it had a real pain in the arm. Scientists examining the fossil arm bones of a hadrosaur have determined that the dinosaur likely suffered from septic arthritis, a bone disease that develops when an injury is followed by infection. Paleopathologists have previously spotted signs of traumas from cancer to combat in dinosaur bones, offering a unique—if painful—window into the animals' daily lives. But the new paper, published this week in *Royal Society Open Science*, offers the first diagnosis of septic arthritis in a dinosaur. Diagnosis through fossils can be especially difficult, as it requires looking inside the bones—and slicing these particular bones open was out of the question, as they are both historically and scientifically valuable, being among the earliest dinosaur fossils ever discovered in the United States, says lead author Jennifer Anné of the University of Manchester in the United Kingdom. Instead, Anné and her team used x-ray microtomography, a non-invasive technique, to peer inside the fossils. Only septic arthritis, they determined, could cause both the internal bone density loss and reactive bone growth they observed. The extent of the bone growth does suggest that the dinosaur likely survived the injury, which could have started out as a cut, a broken bone, or perhaps an attack from a crocodilian. "It's a hard-knock life for any wild animal," Anné says.

Melting a Cold War legacy

Thanks to climate change, Greenland may be forced to revisit a clandestine chapter of its past. Model predictions suggest that the island's melting ice could release waste entombed at Camp Century, a Cold War military site carved into the ice in the 1950s by the U.S. Army Corps of Engineers to conduct scientific research—and to test a secret (ultimately unsuccessful) system of storing and launching ballistic missiles. When the camp closed, sewage, diesel fuel, PCBs, and radiological waste were left behind; it was thought they would stay buried under the ice and snow. But if greenhouse gas emissions follow business-as-usual projections, melting at Camp Century could outpace snow accumulation within the next 75 years, finds a study published this week in *Geophysical Research Letters*. Once exposed, it's unclear who would be responsible for cleaning up the waste, the researchers write: It may represent a new type of conflict triggered by global warming. http://scim.ag/CampCent

Corrected 8 August 2016; see full text.

IN DEPTH

Venezuela's Urumaco formation is famed for its supersized creatures, including crocodiles (left) up to 11 meters long.

PALEONTOLOGY

Venezuela's woes hamper access to fossil trove

Only the most daring researchers now risk a trip to premier site in the American tropics

By **Lizzie Wade**

Edwin Cadena was organizing his field gear in a hotel in Caracas in April 2015 when three armed men burst into the lobby. The paleontologist was preparing to go fossil hunting in northwestern Venezuela's Urumaco formation, a site replete with bones of weird supersized creatures. Many experts call it the best fossil deposit in the American tropics. "They took almost everything—the computers, the cameras, the GPS, all the major equipment," says Cadena, who works at Yachay Tech in Urcuquí, Ecuador. "Oh no," he thought: "What are we going to do?"

As Venezuela spirals deeper into economic and political chaos, its people are suffering from shortages of essential goods and rising crime. The environment is hostile for science as well, but with a string of recent finds that are reshaping views on the geographic and ecological evolution of the Americas over the last 20 million years, Urumaco holds a powerful allure. "It's too good not to do anything," says Carlos Jaramillo, a paleontologist at the Smithsonian Tropical Research Institute in Panama City. "These are very tough times, but those fossils need to be studied."

The Urumaco formation lies in the heart of an anomalous tropical desert created by fierce coastal winds and a dearth of rivers. It's part of a vast inland basin where, beginning 30 million years ago, the jostling of the Caribbean and South American plates caused rapid subsidence, allowing sediments to accumulate rapidly. "You can see smaller fractions of time than in any other place in the tropics," says Jaramillo, who started working in Urumaco 14 years ago. Unlike in the Amazon or the jungles of Central America, the fossils are not covered by dense vegetation.

Fossils preserved in the sediments offer a glimpse of a strange lost world from the Neogene period, which stretched from 23 million to 2.5 million years ago. "Almost every creature there is really, really gigantic," Cadena says, including turtles with 3-meter shells, 11-meter crocodiles, and a 500-kilogram rodent, the largest ever discovered. The Neogene was a turbulent time for South America: The Andes were shooting up in a rapid growth spurt, the Amazon and the Orinoco rivers were shifting into their current positions, and sea level changes were remaking the coastlines. The fossils provide an ecological record of those convulsions.

Petroleum geologists first unearthed fossils at Urumaco in the 1950s; academic interest in the site has exploded only recently. In 2013, for example, Orangel Aguilera, a Venezuelan paleontologist now at Fluminense Federal University in Rio de Janeiro, Brazil, used fossil catfish from the formation to trace shifts in the Orinoco River. The presence of many freshwater species showed that the river, which now flows westward through Venezuela and empties into the Atlantic near Guyana, once ran north into the Caribbean Sea, then changed course between 2 million and 3 million years ago. He suspects that the river was steered westward by the late rise of one section of the Andes.

Urumaco's fossils could also be key to determining when the Panama isthmus formed. Scientists have long believed that the thin strip of land trailing from North America collided with South America about 3.5 million years ago, connecting the continents for the first time. More recently, Jaramillo and others argued for a much ear-

Land of the long-lost giants

Urumaco lies in the heart of a tropical desert, which means there is little vegetation to hide fossils.

CREDITS: (PHOTO) JORGE CARRILLO BRICEÑO; (MAP) A. CUADRA/*SCIENCE*

Corrected 8 August 2016; see full text.

lier date, between 15 million and 13 million years ago, based in part on fossils found during the Panama Canal expansion (*Science*, 10 April 2015, p. 226).

At Urumaco, Luis Quiroz, a Colombian doctoral student at the University of Saskatchewan in Saskatoon, Canada, has found evidence that the later date may be correct. He studies trace fossils left by animals burrowing into beaches and coastal mudflats. The species he has identified live in nutrient-rich seawater, which Quiroz believes repeatedly submerged Urumaco during the early Neogene. The finding points not only to wildly fluctuating sea levels, but also to a source of nutrients, which most likely came from Pacific waters flowing into the Caribbean—dealing a blow to the idea of an earlier land bridge.

Just as its star is rising, Urumaco is becoming a destination for only the most daring scientists. "The last 2 years have been particularly challenging ... it's truly putting in danger the possibility of doing fieldwork there," says Marcelo Sánchez-Villagra, a paleobiologist at the University of Zürich in Switzerland who grew up in Venezuela. He plans to go to Urumaco in December, but has stopped bringing students.

Meanwhile, fewer paleontologists remain nearby, in Venezuela. Before moving to Brazil, Aguilera worked at Francisco de Miranda University in Coro, just a 35-minute drive from Urumaco. When the school's budget was slashed, the administration forced him to retire. Now, he says, he's lucky to get back to Urumaco once a year. Geologist Mauricio Bermúdez held on until 2015 at the Central University of Venezuela, Caracas, studying the Orinoco River's ancient route. One day, on his way home from work, his bus was hijacked. Passengers were robbed and held hostage for 7 hours. Days after the ordeal, Bermúdez fled to Colombia with his family. "Many of the professors we work with ... they are already gone," Jaramillo says, who hasn't been back to Urumaco for 5 years. "It's a massive migration of the educated people from Venezuela." A local paleontologist maintains the collections and the museum in Urumaco, but he lost his government salary during the political upheavals. And as foreign researchers grow reluctant to travel to Venezuela, collaborations that might help Venezuelan scientists continue their work are dwindling.

But the Urumaco fossils are so important to the story of South America that Cadena and a few intrepid colleagues vow to keep coming back. Even after his equipment was stolen in Caracas, Cadena continued to Urumaco and unearthed a key fragment of a fossil he had long been hunting for. He's heading back for more fieldwork in September. This time, he won't tarry in Caracas. ■

PHOTO: BERND THISSEN/PICTURE-ALLIANCE/DPA/AP IMAGES

BIOMEDICINE

Antiaging trial using young blood stirs concerns

Company plans to charge volunteers $8000 each for plasma transfusions from young donors

By **Jocelyn Kaiser**

It was one of the most mind-bending scientific reports in 2014: Injecting old mice with the plasma portion of blood from young mice seemed to improve the elderly rodents' memory and ability to learn. Inspired by such findings, a startup company has now launched the first clinical trial in the United States to test the antiaging benefits of young blood in relatively healthy people. But there's a big caveat: It's a pay-to-participate trial, a type that has raised ethical concerns, most recently in the stem cell field.

A clinical trial will test whether blood's plasma (yellow) has antiaging properties.

The firm's cofounder and trial principal investigator is a 31-year-old physician named Jesse Karmazin. His company, Ambrosia, in Monterey, California, plans to charge participants $8000 for lab tests and a one-time treatment with young plasma. Volunteers don't have to be sick or even particularly aged—the trial is open to anyone 35 and older. Karmazin notes that the study passed ethical review and argues that it's not that unusual to charge people to participate in clinical trials.

But for some ethicists and researchers, the trial raises red flags, both for its cost to participants and for a design that they contend is unlikely to deliver much science. "There's just no clinical evidence [that the treatment will be beneficial] and you're basically abusing people's trust and the public excitement around this," says neuroscientist Tony Wyss-Coray of Stanford University in Palo Alto, California, who led the 2014 young plasma study in mice.

Decades ago, so-called parabiosis studies, in which the circulation of old and young animals was connected, suggested that young blood can rejuvenate aging mice. A recent revival of the unusual approach has shown beneficial effects on muscle, the heart, brain, and other tissues, and some researchers are scrutinizing young blood for specific factors that explain these observations. The 2014 study, however, suggested that repeated injections of plasma from young animals were an easy alternative to parabiosis.

Wyss-Coray has since started a company, Alkahest, that, with Stanford, has launched a study of young plasma in 18 people with Alzheimer's disease, evaluating its safety and monitoring whether the treatment relieves any cognitive problems or other symptoms. The company covers the participants' costs. Wyss-Coray expects results by the end of this year. (Another trial at a research hospital in South Korea is examining whether cord blood or plasma can prevent frailty in the elderly.)

In Ambrosia's trial, 600 people ages 35 and older would receive plasma from a donor under age 25, according to the description registered on ClinicalTrials.gov, the federal website intended to track human trials and their results. Karmazin says each person will receive roughly 1.5 liters over 2 days. Before the infusions and 1 month after, their blood will be tested for more than 100 biomarkers that may vary with age, from hemoglobin level to inflammation markers. The $8000 fee—not mentioned on ClinicalTrials.gov—will cover costs such as plasma from a blood bank, lab tests, the ethics review, insurance, and an administrative fee, Karmazin says. "It adds up fairly quickly."

Karmazin became interested in aging as an undergraduate. In medical school at Stanford, where he rotated through labs focused on stem cells and aging, he took note

of the young plasma mouse study and other parabiosis research. While at Stanford, he says, he and colleagues began combing through hospital and blood bank donor records and found a preliminary association between transfusions of young blood and shorter hospital stays and lower mortality. Karmazin was also intrigued by the story of a Russian physician named Alexander Bogdanov who in the 1920s gave himself infusions of young human blood that he claimed boosted his energy level and bestowed a more youthful appearance. There is "overwhelming data" suggesting that young plasma will be beneficial to people, Karmazin says.

Last year, he co-founded a company called xVitality Sciences that aimed to offer plasma treatments at clinics overseas. The venture didn't pan out—Karmazin left, and the company is now apparently defunct. Karmazin then started Ambrosia with Craig Wright, a former chief scientific officer at a vaccine company, who now runs a clinic in Monterey. Ambrosia's study, which was reviewed by a commercial ethics board used by some for-profit stem cell clinics, doesn't need approval by the U.S. Food and Drug Administration, the pair says, because plasma transfusions are a well-established, standard treatment. Karmazin says he and Wright have now heard from about 20 prospective participants and have enrolled three, all elderly. Wright will likely transfuse plasma into the first person in late August.

To bioethicist Leigh Turner of the University of Minnesota, Twin Cities, the study brings to mind a growing number of scientifically dubious trials registered on ClinicalTrials.gov by private for-profit stem cell clinics. A trial's presence in the database confers "undeserved legitimacy," he says.

The scientific design of the trial is drawing concerns as well. "I don't see how it will be in any way informative or convincing," says aging biologist Matt Kaeberlein of the University of Washington, Seattle. The participants won't necessarily be elderly, making it hard to see any effects, and there are no well-accepted biomarkers of aging in blood, he says. "If you're interested in science," Wyss-Coray adds, why doesn't such a large trial include a placebo arm? Karmazin says he can't expect people to pay knowing they may get a placebo. With physiological measurements taken before and after treatment, each person will serve as their own control, he explains.

Karmazin says he's filling a void, suggesting that most companies wouldn't be interested in developing human plasma as an antiaging treatment. "It's this extremely abundant therapeutic that's just sitting in blood banks," he insists. ■

U.S. RESEARCH MANAGEMENT

NSF tries two-step review, drawing praise—and darts

Brief preliminary proposals can't do justice to innovative research, scientists complain

By **Jeffrey Mervis**

As if getting a grant weren't hard enough already, the National Science Foundation (NSF) now requires thousands of conservation and environmental biologists to survive two rounds of peer review. The change, part of an experiment aimed at easing the strain on agency staff and outside reviewers, includes a first step in which three-quarters of applications are rejected.

NSF says that the two-stage process, which it launched 4 years ago as a pilot project in two divisions within its biology directorate, has resulted in a more manageable workload and fuller consideration of the highest quality proposals. Some scientists, however, aren't happy about the new procedures. They warn that the changes, notably a dramatically shorter initial application and only one chance a year to file applications rather than the previous two deadlines, could result in NSF funding less innovative research.

"You run out of room to describe anything that may be controversial or a little edgy," says Peter Wainwright, president of the Society for Integrative and Comparative Biology and a professor at the University of California, Davis. "I suspect there are types of projects that don't get to the full proposal stage because it's just too hard to write them up in the allowable space. It's a whole new ballgame."

Last month, a congressional watchdog agency singled out the NSF project for praise and urged other major research agencies to be more aggressive in streamlining procedures that affect academic research. The study, released 22 July by the Government Accountability Office (GAO), was prompted by mounting concern that the the U.S. government's system for funding academic science is being stretched to the breaking point.

One reason is that scientists, with money tight, are submitting more grant applications. That creates more work for their universities, for the agencies that manage the grantsmaking process, and for the scientists who serve as reviewers. Ironically, the budget squeeze has also contributed to increased federal oversight to ensure those scarce dollars aren't being wasted.

The GAO report, which surveys a variety of approaches to the problem at four major research agencies, makes clear there are no simple solutions. And NSF's pilot project may seem counterintuitive: How could adding a second round of review actually reduce the burden on program officers and reviewers?

The answer lies in what NSF officials call binding preliminary proposals. Starting in 2012, scientists applying to core programs in the divisions of environmental biology (DEB) and integrative organismal systems could

Shaking up the system

Applications rose and overall success rates dropped after the National Science Foundation's division of integrative and organismal systems required preliminary proposals. Applications that reached the full-proposal round faced better odds than in the past.

	2008	2009	2010	2011	2012	2013	2014	2015
Number of preliminary proposals					1824	1963	1973	1996
Percentage invited to submit full proposal					30%	22%	23%	24%
Number of full proposals	1364	1498	1379	1351	532	497	446	441
Number of awards	255	296	193	250	158	163	156	150
Percentage of full proposals funded					30%	33%	35%	34%
Overall success rate	19%	20%	14%	19%	9%	8%	8%	8%

DATA: NATIONAL SCIENCE FOUNDATION/DIVISION OF INTEGRATIVE AND ORGANISMAL SYSTEMS

no longer submit the agency's standard 15-page application. Instead, they write a four-page preliminary proposal that is stripped of many details about methodology, budgets, references, and collaborators. It is reviewed by three scientists rather than the usual five. (The slimmer proposals don't require so-called ad hoc reviewers with special expertise, NSF decided.) And program officers typically invite only about one-fourth of preliminary applications to proceed to the second round, where a review panel vets a full proposal. About one-quarter of the full proposals are ultimately funded (see table, p. 528).

Other federal agencies also use preliminary proposals, GAO notes. But they've been less effective at reducing workloads because the initial assessment isn't binding or because the agencies filter out a far lower percentage of preliminary proposals. Other variations that GAO cites offer even less relief: The National Institutes of Health, for example, simply allows applicants to hold off submitting some details of their application until after a proposal has received a favorable score from reviewers and is assured of moving forward.

At NSF, the pilot has been a godsend to overworked program officers, says Alan Tessier, DEB's deputy director in Arlington, Virginia. He admits that an overall success rate of less than 8% is not a happy situation. But the new procedures have helped ease the stress created by a decade of rising application numbers, which peaked in 2010 and created what Tessier calls an "unsustainable" situation. For instance, "instead of asking 12,000 people to be ad hoc reviewers, it's now more like 2000," he says. (Recruiting qualified reviewers is a chronic problem at NSF.) In addition, the second panel has far fewer proposals to vet, meaning the final reviewers can spend more time discussing higher quality proposals.

"We were prepared to pull the plug [on the pilot] after the first year if we were really causing damage," Tessier says, "but that doesn't seem to be the case." An outside evaluation, including interviews with affected scientists, is due to be completed early next year. NSF will then decide whether to make the changes permanent and, perhaps, whether the system should be extended to other directorates.

Wainwright hopes that won't happen. "Of course there's a lot of frustration because success rates are so low," he says. "And we understand that's not something NSF can control. However, I predict that a community survey would find that most scientists would like NSF to take a third approach [to reducing workload], something that doesn't require such short and binding preliminary proposals and annual deadlines. That's a very tough world to live in." ■

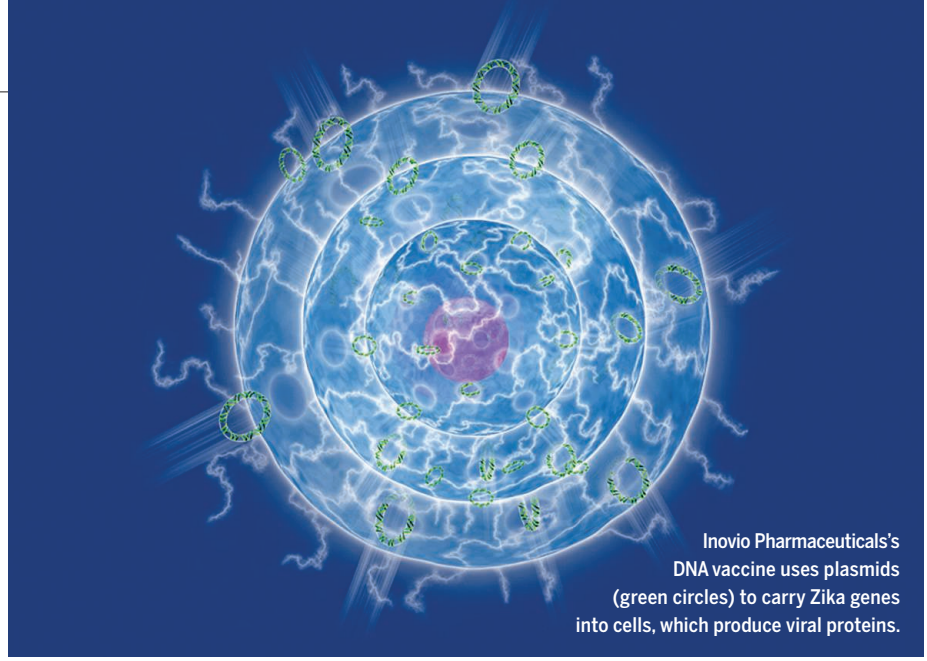

Inovio Pharmaceuticals's DNA vaccine uses plasmids (green circles) to carry Zika genes into cells, which produce viral proteins.

IMAGE: INOVIO PHARMACEUTICALS

INFECTIOUS DISEASE

Zika vaccine has a good shot

Modest immune responses outwit virus in monkey studies, but trials will be complex

By **Jon Cohen**

When it comes to making vaccines, not all viruses are created equal: Some, like HIV, notoriously find ways to outmuscle the immune responses raised by a vaccine. This week, new studies in monkeys put Zika virus squarely in the wimp corner, welcome news as the first human vaccine trial against it begins.

A vaccine is sorely needed. The virus has blasted through Latin America, leaving severe birth defects and other maladies in its wake. Just this week, Florida health officials confirmed the first cases of local transmission in the United States; until now, all cases here involved people who had traveled to affected countries. These Florida cases were mainly infected by mosquitoes within a 2.5-square-kilometer area of northern Miami.

Since Brazilian health officials first reported local transmission of Zika virus in May 2015, researchers have been scrambling to develop a vaccine. The monkey studies, published online this week in *Science*, suggest that outwitting Zika virus should present few obstacles. A research team from the Beth Israel Deaconess Medical Center in Boston and the Walter Reed Army Institute of Research in Silver Spring, Maryland, vaccinated 16 monkeys with three experimental vaccines and then "challenged" them with injections of Zika virus. As a control, they challenged 12 unvaccinated monkeys. None of the vaccinated monkeys became infected, whereas the Zika virus rose to high levels in the blood of all of the control animals. "The protection was striking, and it certainly raises optimism about development of a Zika virus vaccine for humans," says Dan Barouch, an immunologist at Beth Israel who co-led the studies.

The group tested three different approaches. One is a traditional vaccine that uses a whole, killed Zika virus. The second contains DNA from Zika woven into a small, harmless circle of DNA called a plasmid; once in cells, this DNA produces Zika proteins that spark an immune response against them. The third strategy stitched Zika genes into adenoviruses, which act as Trojan horses and infect cells to trigger immune responses.

Barouch stresses that his group's data do not predict which vaccine will work best in humans. "The goal of the study was not to have a cook-off of different vaccine modalities," he says. Instead, a key aim was to identify which components of the immune response correlated with protection against the virus to help guide human trials. Specifically, the monkey studies showed that even low levels of antibodies directed toward the Zika virus completely protected the animals.

On 26 July, Inovio Pharmaceuticals, a small company based in Plymouth Meeting, Pennsylvania, began the first human trials of a Zika vaccine. The biotech's DNA vaccine is

being tested in a phase I study on 40 healthy people for safety and its ability to trigger immune responses. Others are in the works. The National Institute of Allergy and Infectious Diseases (NIAID) in Rockville, Maryland, is collaborating with the Walter Reed group, the Butantan Institute in São Paulo, Brazil, and the pharmaceutical company Sanofi Pasteur in Swiftwater, Pennsylvania, to develop three other Zika vaccines, including one that also uses Zika DNA alone and will likely enter human studies within the next few weeks.

NIAID Director Anthony Fauci says the monkey results are "encouraging" and add to other evidence that "strongly suggest we'll get an effective vaccine." But determining whether any Zika vaccine works in humans may present tricky challenges. Researchers hope to fast track vaccines that pass muster in phase I studies and go straight into efficacy trials in a few thousand people in regions of Latin America where the virus has spread rapidly. If all goes well, those prevention trials could start as early as the beginning of 2017 and determine within a year whether the vaccines protect people.

But Neil Ferguson, a mathematical modeler at Imperial College London, thinks the epidemic is racing so fast through Latin America that many people may have been exposed and become immune by the time efficacy trials begin, leading to a drop in transmission rates that, in turn, make it far more difficult to see the benefit of a vaccine. A similar drop hampered some vaccine trials during the Ebola epidemic in West Africa. Ferguson, who led a team that recently modeled the spread of Zika in Latin America (*Science*, 22 July, p. 353), says the virus has already peaked in Brazil and Colombia and that infected people will likely develop lifelong immunity. "My gut instinct is the way the epidemic is moving, by the end of next year there'll be very little Zika left there."

Ferguson suggests that instead of setting up vaccine trials in one place, researchers could run sequential trials in different populations. "We need to be ready to restart trials when new outbreaks are seen," he says.

Fauci, however, expects to see large numbers of new Zika infections in South America for several years. It's now winter in much of the continent, which explains why cases have precipitously dropped, he says, and he doubts that the level of so-called "herd immunity" in the population will significantly lower the spread of the virus there next summer when mosquito populations swell. "The second wave I'd assume is going to be less robust, but there's still going to be enough infections to get an answer from vaccine trials," Fauci says. "Unlike Ebola, Zika is not going to disappear." ■

SCIENCE DIPLOMACY

Synchrotron aims to bridge divides in the Middle East

Light source in Jordan is just about ready to start shining

By **Erik Stokstad**, *in Manchester, U.K.*

A beleaguered experiment in science diplomacy is on the threshold of success. Last week, an $80 million synchrotron lab in Allan, Jordan, announced its first call for research that will be conducted on two beamlines of high-energy particles that are expected to switch on this autumn. Full-fledged studies should start early next year at the Synchrotron-light for Experimental Science and Applications in the Middle East (SESAME).

"The news is that it's working, against the odds," says Chris Llewellyn Smith, a physicist at the University of Oxford in the United Kingdom and president of the SESAME Council. The project was behind schedule because of political complications—visa problems for scientists (*Science*, 15 December 2006, p. 1668), for example, and sanctions against Iran, a partner—and a freak snowstorm that collapsed the main building's roof in 2013. Now, "we are in the final stage," Eliezer Rabinovici, a theoretical physicist at the Hebrew University of Jerusalem, said at a 27 July press conference here at the EuroScience Open Forum. "To see dreams become reality, this is a very special moment."

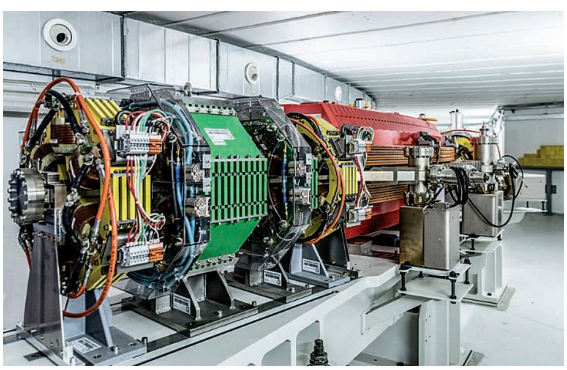

As final touches are put on the SESAME synchrotron and its storage ring (above), work with lower power sources is already underway.

A synchrotron is an important tool for many fields, as it creates intense beams of light that are used to probe biological samples or materials. There are about 60 synchrotrons in the world; SESAME is the first to come online in the Middle East. Projects envisioned for the synchrotron include analyzing breast cancer tissue samples, studying Red Sea corals and soil pollution, and probing the Dead Sea Scrolls and other archaeological remains. A focus on applied sciences relevant to the region helped SESAME scientists secure funding from their governments, says Alessandro Treves, a neuroscientist at the International School for Advanced Studies in Trieste, Italy, who has followed the initiative. "It was the key to make it successful."

SESAME was founded in 1999 as a partnership of many Middle Eastern countries. Germany donated a big-ticket component: the injector that sends particles into the main storage ring. The initiative has attracted about $30 million in donations from outside the region, including $11 million from the European Union, supplementing the construction costs financed primarily by Israel, Jordan, and Turkey. Iran has pledged $5 million, but sanctions have delayed its contributions. SESAME's operating costs are expected to be paid for by its members: Bahrain, Cyprus, Egypt, Iran, Israel, Jordan, Pakistan, the Palestinian National Authority, and Turkey.

Smith says the facility is on track for commissioning in December. Two beamlines will be ready this year—for x-ray and absorption and fluorescence, and infrared spectromicroscopy—and two more will be built by 2018 for materials science and macromolecular crystallography. Gihan Kamel, SESAME's infrared beamline scientist, says researchers have already begun working at the facility, by hooking up detectors and microscopes to lower power sources at the facility. Once the synchrotron fires up, the resolution and brightness will increase dramatically.

In the conflict-riven Middle East, security is a worry. "There are severe concerns," Rabinovici says. SESAME is building a guest house for visiting researchers inside its perimeter fence. Still, Rabinovici hopes the scientific oasis will help ease regional tensions. "We are offering light at the end of one tunnel." ■

PHOTO: © 2016 CERN

Christian Bréchot is hoping for a renewal of his contract so he can continue reforms he began in 2014.

PHOTO: SEBA/ZUMA PRESS/NEWSCOM

FRANCE

Dispute over president's age tears Pasteur Institute apart

Center's board of directors was sent home after denying Christian Bréchot, who's almost 65, a second term

By **Tania Rabesandratana**

Is 65 too old to stay at the helm of a major research center? That question is sowing division at the Pasteur Institute in Paris, *Science* has learned, and has plunged the 128-year-old institute, home to 1200 scientists and the place where HIV was first isolated, into a leadership crisis. At the center is Christian Bréchot, a physician and viral hepatitis specialist whose first 4-year term as Pasteur president will end on 1 October 2017.

Bréchot, who previously led INSERM, the French biomedical research agency, aspires to a second term, but he will turn 65 in July 2017. Under the governing statutes of the foundation that runs the Paris center, that disqualifies him for the renewal, Pasteur's 21-strong board of directors has concluded. Angered by the board's refusal to change the rules, Pasteur's General Meeting, a parliament-style governing body, dissolved the board in June. Now, Bréchot's future is in limbo.

Bréchot's supporters say that the age limit is outdated and that the institute needs him to finish reforms set in motion in 2014. "If we have to find another director, it may crush the momentum," says Pasteur structural biologist and General Meeting member Félix Rey. Bréchot's reforms include efforts to help Pasteur and its sister institutes around the world share and analyze data, as well as a plan to update the Paris lab's forays into fields such as bioinformatics and electron microscopy, Rey says. Bréchot says he also tried to make Pasteur's salaries and career prospects more attractive to top researchers.

Louis Pasteur himself headed the institute he founded until his death at 72 in 1895. But today, Article 12 of the statutes of the Pasteur Foundation says that "at the time of his or her nomination or of the renewal of his or her mandate, the president must not have reached the age of 65." In May, after the board signaled in a statement that it would enforce Article 12, several Pasteur scientists sent letters expressing their support for Bréchot and urging the board to raise the age limit. Among them was a note signed by the heads of the Paris institute's 11 research departments that praised Bréchot for his "leadership, vision, dynamism and full commitment."

The board, which includes six Pasteur scientists, would not budge. Changing Article 12 would be a lengthy affair that requires government involvement and could lead to a complete review of the foundation's statutes to align them with those of other French foundations, says board chair Rose-Marie Van Lerberghe. That could damage Pasteur, she adds: For example, Bréchot earns a sizable salary but typical foundation statutes require an unpaid president, which would make it difficult to recruit a top candidate. Changing the statutes could also mean that the institute loses favorable fiscal provisions. A 3 June email to Pasteur staff explaining the board's viewpoint included a legal review by an expert in French foundation law to back up the decision.

The explanation didn't satisfy Pasteur's General Meeting, which provides checks and balances for the board and president. It includes elected representatives of staff, directors of Pasteur Institutes abroad, appointed members from universities and government bodies, as well as other outside members. On 21 June, 60 out of 101 General Meeting members rejected the board's annual report, in a secret ballot—a show of dissent that automatically triggered the board's dissolution. (Of the meeting's 36 staff representatives, 32 had already signed a letter of support to Bréchot on 9 May.)

The General Meeting did not aim to create mayhem, says Antoine Talarmin, head of the Pasteur Institute of Guadeloupe in Point-à-Pitre and a General Meeting member, but it wanted to send a strong statement supporting a second term for Bréchot and express its mistrust of the board. "Pasteurians will not be pushed around," Talarmin says. "It is ridiculous that this issue has taken on such proportions at a time when many politicians think it is time to raise the legal age of retirement."

Some suspected that the board was using the age limit as an excuse to get rid of Bréchot, Talarmin says. Not true, says Van Lerberghe, who points out that she was part of the search committee that picked Bréchot, worked well with him, supported his plans, and sought ways to retain him. "But the law is the law, even when it's just about a 3-month difference," she says.

Bréchot, however, does have detractors. One researcher who's also a General Meeting member says it's time for Bréchot to move on. He is "arrogant" and has created a climate of fear among staff, says this scientist, who asked not to be named: "He will never have my vote to stay." Bréchot says you can't be loved by everyone if you're reforming an institute and admits that the situation is tense. "A few people think I've manipulated [scientists on] campus or solicited the letters of support myself," he says. "But this discussion goes beyond me as a person."

Bréchot's supporters hope that the next board will change Article 12, but Van Lerberghe warns that this won't be easy. Until a new board is formed in October, the outgoing members and Bréchot can only conduct routine business. Meanwhile, Pasteur's research goes on as usual, Bréchot says. There have been other crises in Pasteur's long history, Rey adds. "I'm very confident. We have always emerged stronger from them." ■

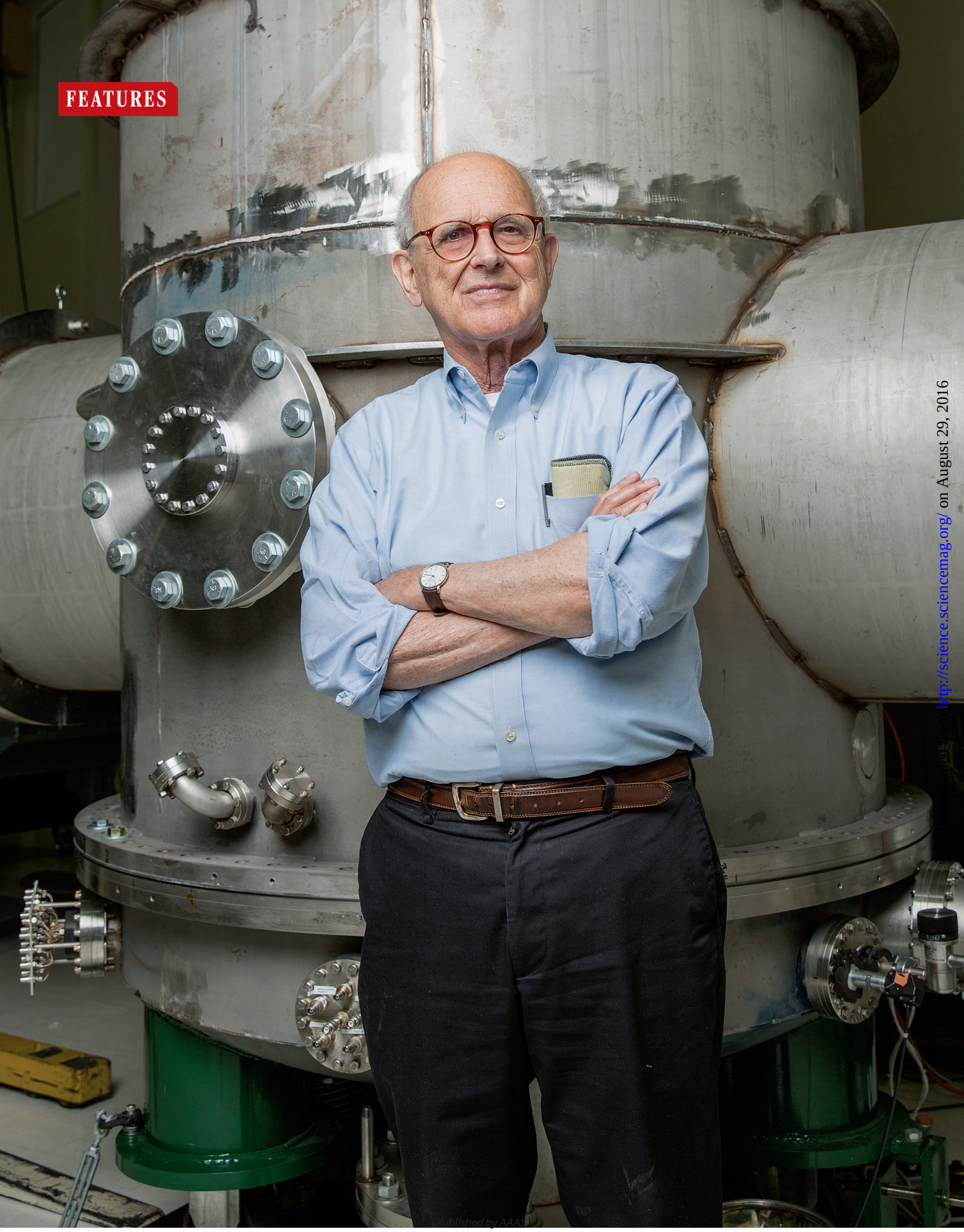

THE STORYTELLER

With Rainer Weiss, gravitational wave hunter and likely Nobel laureate, there's the story—and there's the subtext

By **Adrian Cho**

Nearly 50 years ago, Rainer Weiss dreamed up a way to detect gravitational waves—infinitesimal ripples in spacetime predicted by Einstein's theory of gravity, general relativity. Last September, that dream came true as 1000 physicists working with the Laser Interferometer Gravitational-Wave Observatory (LIGO), two huge detectors in Livingston, Louisiana, and Hanford, Washington, sensed a pulse of waves radiated by two massive black holes as they spiraled into each other a billion light-years away. The discovery makes Weiss, a physicist at the Massachusetts Institute of Technology (MIT) in Cambridge, a sure bet to win a Nobel Prize, his peers say.

Weiss, 83, acknowledges the prospect with some apprehension. "It will fuck me up for a year," he predicts as he nimbly steers his silver Volkswagen Beetle ragtop through Cambridge traffic. "That's what it did to John Mather." The line is vintage "Rai," his friends will tell you: blunt, irreverent, funny, and impatient with anything that gets in the way of his work.

By any measure, Weiss has led an extraordinary life. Born in 1932 in Berlin, he and his family fled the Nazis. He grew up in New York City, on Manhattan's Upper West Side, a street-smart kid with a gift for tinkering who built and sold his own high fidelity (hi-fi) systems. As an MIT undergrad, Weiss flunked out, and he later struggled to get tenure there. Still, he established himself as a leading physicist and worked for more than 40 years on LIGO, one of the most audacious experiments ever attempted. He works on it even now. "He's the best person I know with a soldering iron," says David Shoemaker, a LIGO physicist at MIT.

Shoemaker adds that Weiss's foremost quality is empathy. A college dropout, Shoemaker credits Weiss with getting him into graduate school at MIT without an undergraduate degree. "He sought ways to bring out the best in me," Shoemaker says. "He also took a rather irregular path, and I think because of that and just his nature, he is really interested in helping people."

Weiss is also known for speaking his mind. "He is absolutely 100% committed to honesty, both in his physics and in life," says Peter Saulson, a LIGO physicist at Syracuse University in New York, who worked with Weiss at MIT in the 1980s. Dirk Muehlner, a retired physicist in Alamo, California, and one of Weiss's early graduate students, shares that sentiment. "He's totally honest. There's no bullshitting for Rai. There's no performance."

> ***"People say, 'I failed out of college! My life is over!' Well, it's not over."***

Yet getting a fix on Weiss isn't easy. An inveterate storyteller, he has clearly told his tales many times, smoothing the edges and burnishing the details. As he conjures up his past, little clues—loose threads, differing versions—suggest he's not quite an open book. In fact, for Weiss, storytelling itself seems to serve some more subtle purpose.

In his modest office at MIT, on the second floor of a brick building resembling an old warehouse, Weiss settles behind a small wooden desk with a gaping hole in the top. Before the advent of flat-panel displays, Weiss took a saw to the desk so that he could tilt back bulky computer monitors. In a staccato New York accent, he tells his tale.

RAINER WEISS WAS BORN of a tryst between Frederick Weiss, a neurologist and scion of a wealthy German-Jewish family, and Gertrude Loesner, a stage and radio actress. While Gertrude was pregnant, Frederick, an ardent Communist, got into trouble by testifying in court against an incompetent Nazi doctor. The Nazis abducted him, and Gertrude's family had to pull strings to get him released. The couple, who wed in 1933, soon fled to Prague, then in Czechoslovakia, where Weiss's sister was born in 1937. Weiss says he was a happy, headstrong child. "I was probably an egotistical little bastard," he says.

The family soon had to flee again, when U.K. Prime Minister Neville Chamberlain signed an accord ceding parts of Czechoslovakia to Germany. They heard the news on the night of 30 September 1938, while on vacation in the Tatra Mountains in Slovakia. As Chamberlain's address blared from the hotel's massive radio, 6-year-old Rainer stared in fascination at the glowing array of vacuum tubes inside the cabinet. The hotel emptied overnight as people fled to Prague.

The family immigrated to New York City in January 1939, 2 months before Hitler's Wehrmacht rolled into Prague. "It was a miracle," Weiss says. Unable to pass the medical board exams because of the language barrier, Frederick set up a practice as a counselor and eventually became a noted psychoanalyst. Gertrude worked in department stores, as a housekeeper, and at odd jobs. It was an un-

PHOTO: © KEN RICHARDSON

Rainer Weiss at the LIGO testbed at MIT in Cambridge. He conceived the detector concept in 1972.

happy household. "My father was a dictator in the true German sense," Weiss says. "He suppressed my mother." Both parents blamed Hitler for their marriage, he says.

Weiss says he grew up in an environment of benign neglect. "My parents were singularly uninterested in me," he says. "My father was too self-centered and too busy with his own practice to pay a lot of attention to me, and my mother was probably deflected more by my sister." He attended the prestigious Columbia Grammar and Preparatory School on a scholarship—"My mother went over and pleaded for them to take me," Weiss says—but he sometimes cut classes, and teachers compared him unfavorably with his older schoolmate Murray Gell-Mann, who went on to win the Nobel Prize in Physics in 1969.

As a teenager, Weiss developed two passions: classical music and electronics. Snapping up army surplus parts, he repaired radios out of his bedroom. He even made a deal with the local toughs: If they left him alone as he lugged radios to and from the subway, he'd fix theirs for free. "They would steal things and I would have to fix them," he says. "It wasn't a good deal."

Weiss's sister, playwright Sybille Pearson, confirms that Weiss spent as much time as possible out of the unhappy home. But, as the only son, he was still something of a prince in his family, she says. For example, whenever the family moved to a new apartment, Weiss got the biggest bedroom to himself, she recalls. "He was adored."

Nor was he a laggard at school, Pearson says. "He was bright and interested in everything and very smart." Michael Wallach, Weiss's classmate at Columbia Grammar, agrees. "Rai's scientific abilities were widely recognized at school," says Wallach, a psychologist retired from Duke University in Durham, North Carolina, although he adds that Weiss really was a street-smart kid and once broke his leg in some sort of a tangle.

If Weiss did cut classes, it wasn't to hang out on the corner, says his son, Benjamin Weiss, a historian and curator at Boston's Museum of Fine Arts. "He was going to piano recitals at Town Hall." At the same time, Benjamin speculates, Weiss was drawn to tinkering partly as a reaction to his family's cerebral atmosphere. "This is a German-refugee kid with very self-consciously cultured parents, and he's rebelling against them by doing things with his hands," Benjamin says. "But he's surely not rejecting doing things with his head."

IF WEISS SKIPPED CHEERFULLY through his youth, he stumbled in early adulthood. He applied to MIT to study electrical engineering so that he could solve a problem in hi-fi—how to suppress the hiss made by the shellac records of the day. But electrical engineering courses disappointed him, as they focused more on power plants than on hi-fi. So Weiss switched to physics—the major that had, he says, the fewest requirements.

Then, in his junior year, Weiss flunked out of school entirely. He fell for a woman he met on a ferry from Nantucket to Boston. "She

The long road to LIGO

By **Adrian Cho**

The quest to build the Laser Interferometer Gravitational-Wave Observatory (LIGO) was a story of ingenuity and persistence—and a decades-long scientific soap opera. In 1972, Rainer Weiss, a physicist at the Massachusetts Institute of Technology (MIT) in Cambridge, described how a device called an interferometer could detect ripples in spacetime. But LIGO, two giant interferometers in Livingston, Louisiana, and Hanford, Washington, didn't take data until 2002. It finally scored a discovery on 14 September 2015, after a 5-year, $205 million upgrade.

The idea for LIGO gathered steam only after Kip Thorne, a theorist at the California Institute of Technology (Caltech) in Pasadena, took an interest, Weiss says. In the summer of 1975, the two attended a NASA workshop in Washington, D.C. Thorne had forgotten to book a hotel room, so Weiss took him in and the two talked all night. Thorne had doubted Weiss's scheme and had even suggested in a textbook that it couldn't work. Now, Weiss says, Thorne "flipped completely, saying what was in his book was wrong and becoming an advocate."

Thorne saw LIGO as an opportunity for Caltech, and in 1979 he brought in Ronald Drever, a physicist at the United Kingdom's University of Glasgow, who was working on an interferometer of his own. Thorne had asked Weiss to apply for the Caltech job, Weiss says, but Weiss's record was too thin. "I sent him my CV," he says, "and he calls me up and says, 'Well, I got it, but it's not all here. There must be some pages missing.'"

Weiss expected to work with Drever. However, Drever "wanted nothing to do with me," Weiss says. "And it was not just me. He was going to come to America and build something by himself." (Drever is in poor health and cannot give his side.) So for several years, Drever, Thorne, and Weiss all ran the nascent project together as a "troika," building separate prototypes at MIT and Caltech until 1987, when the National Science Foundation (NSF) demanded that they combine their efforts under one director.

That director was Rochus "Robbie" Vogt, who had been provost of Caltech. He and Drever tangled, and Vogt kicked Drever out in 1992, changing the locks on his office. Still, Vogt advocated effectively for the project with Congress, and under his guidance the team wrote "a damn good proposal" for the twin LIGO instruments, says Michael Zucker, a LIGO physicist at Caltech. But Vogt didn't see LIGO through to completion. "He envisioned a very small elite group pulling this whole thing off," Zucker says. "That was misreading the environment." In 1994, Caltech replaced Vogt with Barry Barish, a particle physicist and veteran of several big projects, who expanded the organization. "He put the project together in a way that was solidly run, and a lot of the personal squabbles stopped," Weiss says. Only then did NSF approve $300 million for construction.

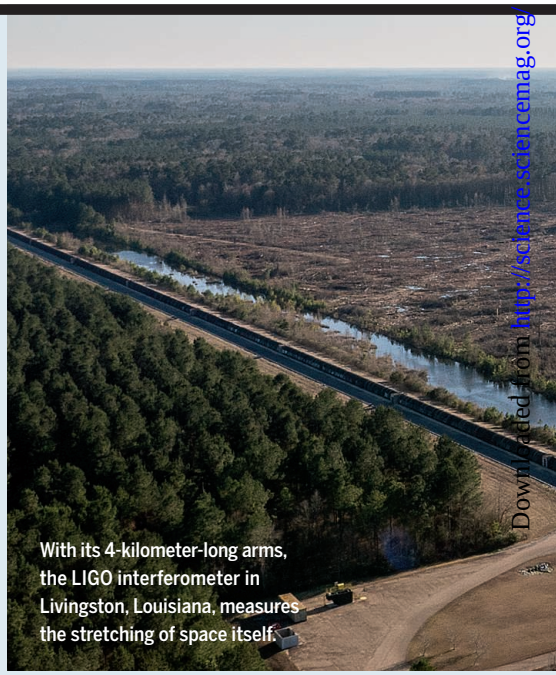

With its 4-kilometer-long arms, the LIGO interferometer in Livingston, Louisiana, measures the stretching of space itself.

taught me about folk dancing and playing the piano," he says. Weiss followed her when she moved to Evanston, Illinois, abandoning his classes in midterm. But the affair fizzled. "I fell in love and went crazy," he says, "and of course she couldn't stand to be around a crazy man." Weiss returned to MIT hoping to take his finals only to find he'd flunked out.

Weiss says he was unfazed. "People say, 'I failed out of college! My life is over!' Well, it's not over. It depends on what you do with it." He took a job as a technician in MIT's legendary Building 20, a temporary structure erected during the war, working for Jerrold Zacharias, who studied beams of atoms and molecules with light and microwaves and developed the first commercial atomic clock. Under Zacharias's tutelage, Weiss finished his bachelor's degree in 1955 and earned his Ph.D. in 1962.

Other physicists say Zacharias's approach to research—using high-precision measurements to probe fundamental physics—inspired Weiss's. But Weiss says he owes Zacharias a larger personal debt. "He got me back into school, then he got me into graduate school, all with a very bad record," he says. "I think that extends all the way up to tenure." A photograph of Zacharias hangs on Weiss's office wall.

After a postdoc at Princeton University developing experimental tests of gravity under physicist Robert Dicke, Weiss returned to MIT in 1964. As a junior faculty member, he says, he published little and didn't worry about advancing his career. MIT's Shoemaker says Weiss probably got tenure only for his teaching—and wouldn't get it today. Bernard Burke, an emeritus physicist at MIT, agrees that early on Weiss was a "happy gadgeteer" who "wasn't likely to get tenure unless he did something that did something." But, Burke says, Weiss soon turned things around.

Burke suggested that Weiss turn his attention from gravity to measurements of so-called cosmic microwave background (CMB) radiation, an all-pervading fuzz of radio waves that had been discovered in 1965 and that had been tentatively identified as the afterglow of the big bang, stretched to longer, cooler wavelengths by the unrelenting expansion of the universe.

In the late 1960s that connection remained tenuous, however. Radiation from the big bang should have a "thermal spectrum" with a lopsided peak indicating the radiation's temperature. At long wavelengths, several groups had observed a climbing spectrum consistent with a temperature of 3°C above absolute zero. But in 1968, rocket measurements found high amounts of shorter wavelength radiation that clashed with a thermal spectrum and threatened the big bang hypothesis.

To probe the matter, Weiss and his graduate student Muehlner built a device that would fly on a weather balloon and measure the microwave spectrum to shorter wavelengths. In 1973, after three flights and a rebuild, they had solid data that fit a thermal spectrum and for the first time revealed

PHOTO: © ATMOSPHERE AERIAL

Meanwhile, Weiss couldn't convince MIT to take a larger role in the project. Once, Weiss recalls, Marcel Bardon, director of NSF's physics division, came to MIT to urge John Deutch, MIT's dean of sciences from 1982 to 1985, to invest more in LIGO. After hearing Bardon's plea, Deutch asked for a piece of paper, Weiss says. "He takes out a pen, scrawls a big zero on it, and shoves it under Bardon's nose," he says. Deutch says, "I don't remember the drama of writing on a piece of paper," and notes that other MIT administrators and physicists also opposed LIGO.

Through it all, Weiss continued to work on LIGO, even more so after he retired from MIT in 2001. "No scientific puzzle is too minor or beneath him," says Nergis Mavalvala, a LIGO physicist at MIT. In recent years Weiss has led an effort to chase down and explain leaks in the enormous, 8-kilometer-long vacuum systems that contain the LIGO interferometers.

Over the years, Weiss suffered his share of frustration, says his son, Benjamin Weiss, a curator at Boston's Museum of Fine Arts. "We used to hear about Drever and Vogt around the dinner table," he says. But Weiss seems to have avoided bitterness, perhaps because of the way he dealt with disappointment. "Honestly, he worked more," Benjamin says. After dinner—and a spell at the piano—Weiss would sit at the dining table with a legal pad, working after others were in bed. By all accounts he still does. ■

the telltale peak. "It completely destroyed the rocket result," Burke says. "Among those interested in the microwave background, [Weiss] was suddenly one of their stars."

Robert Birgeneau, chancellor emeritus at the University of California, Berkeley, who was at MIT from 1975 to 2000, says that Weiss's work won respect within the MIT physics department, too. "He liked to have the affectation of going to a working-class bar and stuff like that," Birgeneau says. But "people looked up to him broadly at MIT. They respected his passion and his courage in going after really important physics."

The CMB study not only secured tenure for Weiss, but also propelled him to a leading role in the broader scientific community. In 1976, NASA began work on its Cosmic Background Explorer (COBE) satellite, and the project's scientific working group elected Weiss chair. Launched in 1989, COBE measured the spectrum of the microwaves with exquisite precision, proving beyond doubt that the CMB has a thermal spectrum. It also sensed tiny 1-part-in-100,000 variations in the CMB's temperature from point to point on the sky—traces of infinitesimal quantum fluctuations in the newborn universe that are essential to the standard model of cosmology. In 2006, Americans John Mather and George Smoot shared the Nobel Prize in Physics for, respectively, measuring the spectrum and detecting the fluctuations.

Some physicists say Weiss should have shared that award. "It was a near miss," Syracuse's Saulson says. Nevertheless, Weiss's contributions to COBE show he excelled in a role for which he says he's badly suited: leader of a large scientific effort. "He's a good collaborator," says Mather, who works at NASA's Goddard Space Flight Center in Greenbelt, Maryland. "He's also good at deciding who should do what and making sure that people get the credit they deserve."

LONG BEFORE COBE, during his wayward untenured days, Weiss hatched the idea that would become LIGO. In the late 1960s, the MIT physics department asked him to teach a graduate course on general relativity. "I couldn't tell them that I didn't know any general relativity," he says. So, striving to stay one step ahead of his students, Weiss focused on experimental tests of gravity.

Weiss's students asked him to discuss experiments in which Joseph Weber, an engineer at the University of Maryland, College Park, was trying to detect gravitational waves using aluminum cylinders the size of a footlocker. General relativity states that massive objects—such as two black holes—spiraling together should radiate ripples in spacetime. Weber argued that those ripples—gravitational waves—would stretch his cylinders and make them vibrate like tuning forks. In 1969, he would claim a discovery of the waves, which others couldn't reproduce.

Weiss couldn't grasp Weber's method, so he invented his own, based on an L-shaped device called an interferometer. It splits a laser beam and sends the two beams down perpendicular "arms." The beams reflect off mirrors and race back to the beam splitter. If the arms are precisely the same length, the light waves return in sync and recombine so that light flows back toward the laser. But if the arms differ by a sliver of the light's wavelength, then the out-of-kilter overlap sends some light leaking out a perpendicular "dark port." Weiss realized that output could reveal a passing gravitational wave, which generally would stretch the arms by different amounts. He let the class chew on the idea in homework and wrote a 23-page report in the quarterly newsletter of MIT's Research Laboratory of Electronics. LIGO sprouted from that document.

Weiss insists the concept of an interferometric detector was already "floating around." But others say he was the first to spell out that the detector would have to be kilometers long and to describe how to deal with the various types of noise—from seismic vibrations to the pinging of individual photons on the mirrors—that could drown out the elusive waves.

Making the experiment a reality required mind-boggling technological feats. The twin LIGO interferometers have arms 4 kilometers long. To detect a gravitational wave, physicists must compare the arms' lengths to within 1/10,000 the width of a proton. Approval to build the $300 million project did not come until 1994, 22 years later (see sidebar, p. 534).

In the meantime, Weiss became a fixture in Building 20, identifiable by the corncob pipes he smoked until he suffered a mild heart attack in 1995. He would work until 2 a.m., says Nergis Mavalvala, a LIGO physicist at MIT who was Weiss's graduate student from 1990 to 1997, and would stay even later to help a student. When Mavalvala failed her qualifying exams, Weiss had her attend "reform school" in his office every Saturday for weeks. "He didn't give a damn about the exams," Mavalvala says. "But he knew that I had to get past them."

Weiss earned a reputation for lending nontraditional students a helping hand. In 1983, Lyman Page, who had been out of school for 5 years and had spent 2 years sailing around the world, walked into Weiss's lab and asked whether he could work for him. "He said 'I can't pay you, but you can work in the lab,'" Page says. "So I worked as a carpenter during the day and in the lab at night." Page, now a cosmologist at

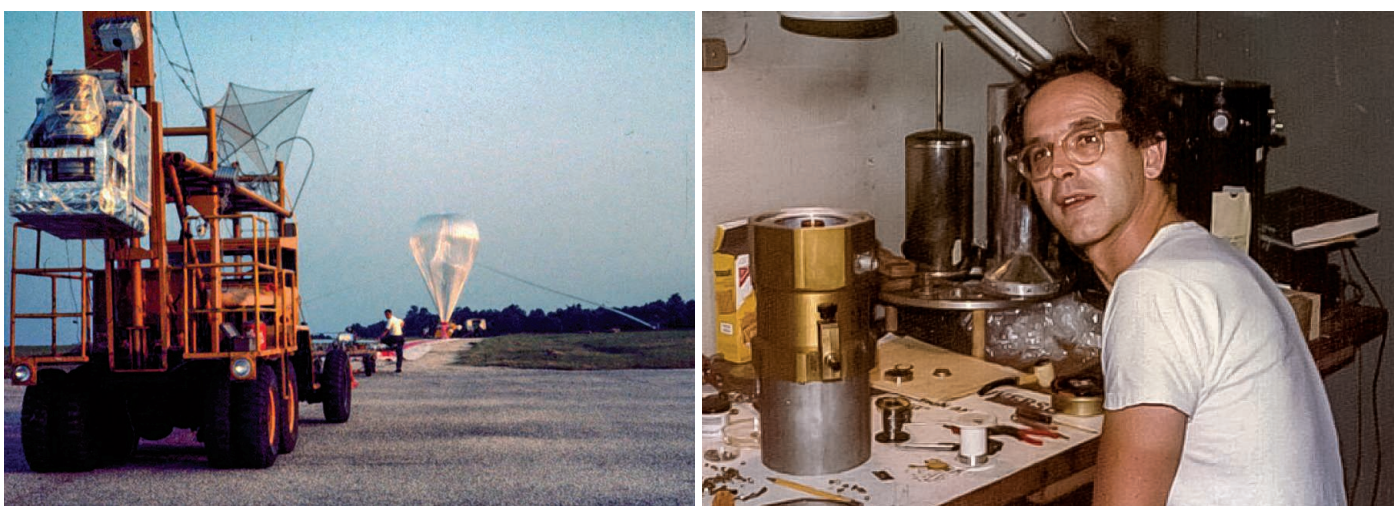

In the 1970s, Rainer Weiss made his name studying the cosmic microwave background with balloons (left). But even then he was working on prototype interferometers (right).

PHOTOS: MASSACHUSETTS INSTITUTE OF TECHNOLOGY

Princeton, credits Weiss for giving him a chance that others did not.

A functioning workaholic, Weiss enjoyed a full life outside the lab, too. In 1959, he married Rebecca Young, a recently graduated biology student working at the Harvard University Herbaria. The two frequented the same diner, says Rebecca, a retired children's librarian. "One evening he asked me to pass the salt and we started having this big conversation about photosynthesis," she says. "After we had been married for years it occurred to me that he never puts salt on anything."

Rebecca says she was often a "physics widow," especially in the 1960s and 70s, when Weiss would travel to Palestine, Texas, to launch his balloon experiments. Still, she says, he was a devoted husband and father. Even when he was away "there was always a lifeline," she says. On Sundays Weiss would take his children to the lab, says Sarah Weiss, the couple's daughter, now an ethnomusicologist at Yale-NUS College in Singapore. "I never felt that I didn't have the access that I needed or hoped for," she says.

Through it all, Weiss has had music. "Music is a big factor in his life," Rebecca says. Weiss says he started playing the piano at 20, when the woman he failed to win started teaching him. He plays for an hour every evening, favoring classical composers such as Mozart, Beethoven, and Schubert, on a Steinway baby grand in the living room of the couple's two-story Victorian in Newton, Massachusetts. "He goes in there at 8 o'clock and he shuts all the doors," Rebecca says. "He thinks I can't hear him."

Weiss insists that even after 63 years of practice, he isn't very good. "My technique sucks," he says. "You will recognize the piece I play, but you won't be satisfied."

NOW, Weiss's tranquil life seems sure to be upended, as physicists expect him to share the Nobel Prize, if not this year, then the next. Since the LIGO team announced their discovery in February, he and LIGO cofounders Kip Thorne of the California Institute of Technology (Caltech) in Pasadena and Ronald Drever, retired from Caltech, have already won several prizes: the Special Breakthrough Award, the Gruber Cosmology Prize, the Shaw Prize in Astronomy, and the Kavli Prize in Astrophysics. "To tell you the truth, these prizes give me the willies," says Weiss, who adds that he plans to use 90% of the award money to help graduate students.

Weiss's humility, expressed in the many stories in which he is never the hero, is striking. "He's a very modest person," his friend Wallach says. "That's part of his charm." But Weiss's compulsive storytelling also seems to serve some deeper purpose, as becomes clear in what he calls "this famous story": how he fell in love and flunked out of college.

LIGO has spotted just the type of source Rainer Weiss had hoped to see: black holes spiraling together.

The conversation circles back to the incident a couple times. At first, it seems simple enough. Weiss falls in love, comes on too strong, and scares the girl away. On the second pass, however, Weiss says that he wasn't more of a lover than the woman could handle, but less than she wanted. "I had made a goddess out of her, and you don't touch a goddess," he says. "She wanted something more." But that version soon fades, too. Asked whether he was popular as a young man, Weiss responds, "I wasn't unpopular. I didn't have any trouble getting girls." When it came to love, Weiss says, "I had the experience."

Wallach remembers it all differently. When Weiss was in his early 20s he fell in love with his piano teacher, a woman in her 30s. Wallach recalls that Weiss spent most of his time at his teacher's house. "She was, not surprisingly, very taken with him and wanted to marry him," Wallach says. Too young to marry, Weiss broke it off, he says.

Weiss's sister questions how much any of it had to do with his failing out of college. "At that age that's rebellion," Pearson says. "And from the family we came from, what's the way to do it? You drop out of school."

The specifics of the decades-old affair matter far less than the way Weiss tells the story. He revels in changing the details, revealing a little more each time. But he never explains exactly what happened, how he really felt, or why he tells the story in the first place. Perhaps that is the point.

LIGO, Weiss's brainchild, proved beyond a reasonable doubt the existence of black holes, the intense gravitational fields left by stars that collapse to infinitesimal points. Within a certain distance of that point—beyond the event horizon—gravity grows so strong that nothing can escape, not even light. In telling his tales, Weiss seems to create his own personal event horizon, a charming screen of words and anecdotes behind which he conceals his deeper self. For all his storytelling, Weiss remains a deeply private person.

At the couple's house, Rebecca explains how, tinkering as always, Weiss has rigged a computer monitor to magnify his sheet music to compensate for his weakening sight. At her insistence, Weiss shows how the system works. In the living room stands his aging Steinway baby grand, the gloss finish worn to matte, the wood showing through at the corners, the top piled with sheet music. A flat-panel screen on makeshift gimbaled mount displays the enlarged music—a Beethoven sonata?—the 16th notes running up and down like staircases. The keyboard beckons.

"No," Weiss says. "I won't play." ■

PHOTO: © MATT WEBER

ANTHROPOLOGY

Emperor Yu's Great Flood

Geological data provide support for a legendary flood in China ~4000 years ago

By **David R. Montgomery**

We know of the legendary Emperor Yu through the story of China's Great Flood, a tale already ancient when first recorded around 1000 BCE (*1*). On page 579 of this issue, Wu *et al*. offer a provocative new explanation for this story. They present evidence for an enormous landslide dam break 1922 ± 28 BCE (*2*) that coincided with the major cultural transition from the Late Neolithic to the Early Bronze Age in China and that also helps explain curious details of Yu's story.

According to folk tradition, the story of Yu's Great Flood is an oral history of real disaster, handed down for a millennium before entering written records. However, in the absence of geological evidence for such a flood, some scholars have argued that the story is either a historicized version of an older myth or propaganda to justify the centralized power of imperial rule (*1*, *3*).

In contrast to the hero of another well-known flood story, Yu is not heralded for surviving a great deluge sent by an angry god. Rather, the story tells of how he directed efforts to dredge and channel rivers to drain the floodwaters (*3*). It casts this

Earth and Space Sciences, University of Washington, Seattle, WA 98195, USA. Email: bigdirt@uw.edu

IMAGE: WILLIAM STURGIS BIGELOW COLLECTION

Battling the Great Flood. Emperor Yu's fantastical achievements include defeating the dragon that stirred up the Great Flood and ridding the floodwaters of serpents and dragons that drove off settlers.

triumph of human ingenuity as bringing order to the land so that fields could be planted, thereby setting the stage for the lowland agriculture that fueled the blossoming of Chinese civilization. A telling aspect of the story—that it took Yu and his followers decades to control the floodwaters—makes sense in light of the geological evidence that Wu *et al*. present.

Wu *et al*. report that an ancient landslide dammed the Yellow River in the Jishi Gorge on the edge of the Tibetan Plateau. Through mapping and dating lake sediments impounded behind the dam and also distinctive sediments deposited downstream, the authors show that an enormous flood surged down the river when the dam broke. They find that this flood coincided with the social disruption of a major cultural transition and suggest that it breached the river's natural levees. The timing of the flood, Wu *et al*. report, coincides with an avulsion that redirected the Yellow River to carve a new course across the North China Plain about 2000 BCE (*2*). It would have taken considerable time for a large river to adjust to such a change, and the associated sustained flooding would fall in the right time and place to account for Yu's story—including the long time it took to control the floodwaters.

This support for the historicity of Yu's flood is part of a broader pattern, another piece in long-standing debates over stories of epic deluges. These stories have been particularly contentious in the Western world. After all, attempts to explain the biblical story of Noah's Flood not only shaped the early development of geology but later fueled discoveries refuting the biblically inspired idea that a global flood laid down the world's sedimentary rocks in the first place (*4*). But how many of these ancient stories might actually record regional flood disasters?

A century ago, the Scottish anthropologist James Frazer detected a pattern in flood stories from around the world (*5*). In case after case across cultures, stories of great floods evoked descriptions of local natural events. A rising sea was the cause of floods in stories from Pacific islands prone to huge earthquake-generated waves (tsunamis). Many Native American stories along the Cascadia subduction zone, from Northern California to British Columbia, also describe floods coming from the sea (*6*). They tell of ancient fights between Thunderbird and Whale so violent that they caused the ground to shake and triggered huge waves, killing scores and lodging canoes in treetops. Indeed, stories from across the tsunami-prone Pacific—from Indonesia to Chile—tell of surprise floods from the sea.

In contrast, stories from regions with formerly more extensive glaciers, such as Scandinavia, Tibet, and North America, evoke failure of glacial dams as the cause of great floods (*4*). Another recurring theme is lowland flooding. For example, Ryan and Pitman have argued that the story of Noah's Flood describes how a rising Mediterranean Sea spilled into a low-lying freshwater valley to create the Black Sea (*7*). Another potential explanation for Noah's Flood updates the idea of levee failures inundating low-lying terrain along the Tigris and Euphrates rivers (*4*), in light of catastrophic flooding during Cyclone Nargis in 2008, when more than 130,000 people were killed in Myanmar's Irrawaddy delta (*8*). It increasingly seems that fundamental elements of the global tapestry of great flood stories mirror the geography of tsunamis, glacial outburst floods, and catastrophic lowland flooding.

> ***"Great floods occupy a central place in some of the world's oldest stories."***

Great floods occupy a central place in some of the world's oldest stories. And Emperor Yu's flood now stands as another such story potentially rooted in geological events. Time and again, natural disasters like great floods, earthquakes, and volcanic eruptions inspired tales passed down through generations and civilizations to become legends (*4*, *9*). How many other ancient stories of intriguing disasters might just have more than a grain of truth to them? ■

REFERENCES

1. S. Allan, *The Shape of the Turtle: Myth, Art, and Cosmos in Early China* (State Univ. of New York Press, Albany, 1991).
2. Q. Wu *et al*., *Science* **353**, 579 (2016).
3. M. E. Lewis, *The Flood Myths of Early China* (State Univ. of New York Press, Albany, 2006).
4. D. R. Montgomery, *The Rocks Don't Lie: A Geologist Investigates Noah's Flood* (Norton, New York, 2012).
5. J. G. Frazer, *Folk-Lore in the Old Testament* (Macmillan, London, 1918).
6. R. S. Ludwin *et al*., *Seismol. Res. Lett.* **76**, 140 (2005).
7. W. Ryan, W. Pitman, *Noah's Flood: The New Scientific Discoveries About the Event That Changed History* (Simon & Schuster, New York, 1998).
8. H. M. Fritz *et al*., *Nat. Geosci.* **2**, 448 (2009).
9. D. B. Vitaliano, *Legends of the Earth: Their Geological Origins* (Indiana Univ. Press, Bloomington, 1973).

10.1126/science.aah4040

PHYSICS

Bringing order to the expanding fermion zoo

Crystallographic classification provides an inventory of the electron-like particles that emerge in a lattice world

By **Carlo Beenakker**

We observe space as a continuum, but we might entertain the thought that there is an underlying lattice and that space is actually a crystal. Which particles would inhabit such a lattice world? This question was first raised by Werner Heisenberg in 1930 in an attempt to remove the infinities that plagued the continuum quantum mechanics. His *Gitterwelt* (lattice world) hosted electrons that could morph into protons, photons that were not massless, and more peculiarities that compelled him to abandon "this completely crazy idea" (*1*, *2*). Heisenberg's motivation to put electrons on a lattice came from solid-state physics, which in the 1930s was just developing as a field of research and which has now become a playground for "crazy ideas" from particle physics. In this spirit, on page 558 of this issue Bradlyn *et al*. (*3*) use concepts borrowed from crystallography to classify the electronic excitations of the lattice world, and then use that to identify possible candidates of materials where they become a reality as (nonfundamental) quasiparticles.

The idea that electrons on a lattice might turn into altogether different quasiparticles was forcefully demonstrated in graphene: An electron moving on the two-dimensional honeycomb lattice of carbon atoms loses its mass. In the language of particle physics, the electron is said to have been transformed from a massive Dirac fermion into a massless Weyl fermion. If the lattice

Instituut-Lorentz, Leiden University, 2300 RA Leiden, Netherlands. Email: beenakker@lorentz.leidenuniv.nl

is superconducting, then the electron may lose its charge, becoming a neutral Majorana fermion. These three types of fermions exhaust the options for a spin-½ particle in continuous space, but lattices offer more possibilities. Recent additions (*4*–*10*) to the fermion family go by the names of nodal-line fermions, nexus fermions, hourglass fermions, double-Dirac fermions, and tilted fermions—each one of the particles is stabilized by a different lattice symmetry and characterized by a different energy-momentum relationship.

To bring order into this zoo of lattice fermions, Bradlyn *et al*. turned to the symmetry classification of crystals: A table that groups all known crystal structures (more than half a million) into one of 230 "space groups," depending on their translational, rotational, and reflection symmetry. The proof that there are no more and no less than 230 distinct ways to combine these symmetries in three-dimensional space (in two dimensions, there are only 17 ways) was a tour de force of 19th-century crystallography. Weyl fermions appear in any space group without inversion symmetry, but only a few space groups (a total of 16, to be precise) have the right combination of symmetries to stabilize the lattice fermions.

"To bring order into this zoo of lattice fermions, Bradlyn* et al. *turned to the symmetry classification of crystals..."

A symmetry operation that is particularly effective at preventing the opening of an excitation gap (*11*) is the combination of a translation by a fraction of the unit cell with a rotation or reflection, resulting in a screw-rotation or a glide-reflection symmetry (the technical term is "nonsymmorphic" symmetry). Bradlyn *et al*. show that this can transform the spin-½ Weyl fermion into a spin-1 quasiparticle. It remains a fermion—the requirement that particles with integer spin are bosons applies only to fundamental particles. Whereas a spin-½ particle is represented by a two-component wave function (its magnetic moment can be −½ or +½), for spin-1 we need three components (magnetic moment −1, 0, and +1). Two components produce a linear crossing of energy bands, and the third component intersects it with a nearly flat band (see the figure). Such a three-band crossing point was observed in a zinc-blende crystal (*12*), accompanied by a massless excitation (a "Kane fermion"), but fine-tuning to a critical point of the phase diagram was required in order to avoid a gap opening. The gapless spectrum of a spin-1 Weyl fermion is enforced by lattice symmetry, without any fine-tuning of parameters.

Because the lattice symmetries are broken when the crystal terminates, surfaces can locally destabilize the lattice fermions. Topology comes to the rescue, protecting some of the quasiparticles with a conserved quantity called the Chern number C. In a magnetic field, C counts the difference between the number of left-moving and right-moving states relative to the magnetic field direction. The excess number of left- or right-movers cannot terminate at a boundary; it must continue as a gapless surface state called a "Fermi arc." The spin-½ Weyl fermions have $C = 1$, producing a single Fermi arc; the new spin-1 variety has $C = 2$, with two Fermi arcs. Under such circumstances, an unusual magnetoresistance is expected from the imbalance of left-movers and right-movers, by analogy with the "chiral anomaly" of Weyl fermions (*13*).

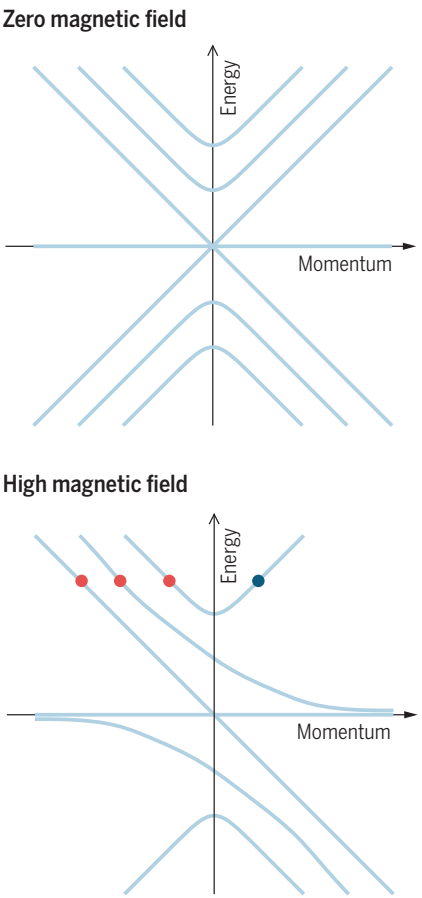

Classifying fermion behavior. Energy-momentum relation of a spin-1 Weyl fermion, in (**Top**) zero magnetic field and (**Bottom**) a high field parallel to the momentum. The flat band at zero energy appears when the lattice augments the spin from ½ to 1. The slope of the curves gives the direction of motion. At a given energy in (bottom), there are $n_L = 3$ left-movers (red dots) and $n_R = 1$ right-mover (blue dot), indicating a Chern number $C = n_L - n_R = 2$. In contrast, $C = 1$ for spin-½ Weyl fermions.

There is no shortage of crystals in which these phenomena might be observed, at least based on numerical calculations of the band structure. Bradlyn *et al*. suggest half a dozen hosts for the spin-1 Weyl fermion, and experiments to detect it with spectroscopy are under way. For detection by transport experiments one would like to have the Fermi level at or close to the band crossing point (the Weyl point). In graphene this alignment of the Fermi level and the Weyl point is ensured by charge neutrality, but that is a special property of the two-dimensional carbon lattice that does not carry over to three dimensions. Fortunately, the band structure calculations indicate that in the most promising materials the Fermi level is only a few tenths of an electron volt from the Weyl point, so that signatures of the singularity should be readily observable in electrical conduction measurements.

Stepping back from the lattice world, we might ask ourselves the question, why not discretize time as well as space and put space-time on a lattice? A reflection in the temporal direction corresponds to time reversal; with this additional symmetry operation, the 230 space groups expand to a total of 1651 so-called magnetic space groups. With all those additional space groups considered, the fermion zoo therefore has the scope to expand quite a bit further. ■

REFERENCES AND NOTES

1. W. Heisenberg, correspondence cited and discussed in (*2*).
2. B. Carazza, H. Kragh, *Am. J. Phys.* **63**, 595 (1995).
3. B. Bradlyn *et al.*, *Science* **353**, aaf5073 (2016).
4. A. A. Burkov, M. D. Hook, L. Balents, *Phys. Rev. B* **84**, 235126 (2011).
5. T. T. Heikkilä, G. E. Volovik, *New J. Phys.* **17**, 093019 (2015).
6. G. Chang *et al.*, https://arxiv.org/abs/1605.06831 (2016).
7. Z. Wang, A. Alexandradinata, R. J. Cava, B. A. Bernevig, *Nature* **532**, 189 (2016).
8. B. J. Wieder, Y. Kim, A. M. Rappe, C. L. Kane, *Phys. Rev. Lett.* **116**, 186402 (2016).
9. A. A. Soluyanov *et al.*, *Nature* **527**, 495 (2015).
10. L. Muechler, A. Alexandradinata, T. Neupert, R. Car, http://arxiv.org/abs/1604.01398 (2016).
11. S. M. Young, C. L. Kane, *Phys. Rev. Lett.* **115**, 126803 (2015).
12. M. Orlita *et al.*, *Nature Phys.* **10**, 233 (2014).
13. H. B. Nielsen, M. Ninomiya, *Phys. Lett.* B **130**, 389 (1983).

ACKNOWLEDGMENTS

I thank C. Kane and T. Neupert for insightful comments and a European Research Commission Synergy grant 319360 QC-LAB for support.

10.1126/science.aag2865

GRAPHIC: N. CARY/*SCIENCE*

PLANT SCIENCE

How do sunflowers follow the Sun—and to what end?

Solar tracking may provide sunflowers with an unexpected evolutionary benefit

By **Winslow R. Briggs**

A field of domesticated sunflowers (*Helianthus annuus*) fully in bloom is a striking sight. The large and showy flowering heads face east, positioned toward the rising Sun. Before floral development, however, elongating vegetative stems move their apices steadily from facing east in the morning to facing west in the afternoon, following the Sun—a process known as solar tracking or heliotropism (*1*). During the night, the shoots reorient their apices to face east again at sunrise (see the figure). As flower development is initiated, solar tracking diminishes and finally ceases, with the developing flowering heads at rest and facing east. On page 587 of this issue, Atamian *et al.* (*2*) provide mechanistic insights into this tracking phenomenon and postulate an evolutionary link to pollination.

Although a fair amount is known about the solar-tracking process in the sunflower (*1, 3, 4*), many questions persist. What are the biological advantages of solar tracking? Not all plants do it. Is tracking the consequence of differential growth between irradiated and shaded sides of the stem (phototropism)? Or, is there a reversible osmotic component leading to complementary cell-turgor changes on the east versus the west side of the stem? The former mechanism involves the light-induced lateral transport of the plant growth hormone auxin to the shaded side of an irradiated elongating organ (*5, 6*). This transport leads to compensatory growth changes (*7*) and differential expression of auxin-induced genes (*8*). The latter mechanism involves light-activated reversible ion movements, leading to water gain or loss (and cell swelling or shrinking) as required by the movement needed to keep a solar-tracking organ aligned to face the Sun. This process prevails in many species that have solar-tracking mature leaves. A specialized organ at the base of leaf petioles (a pulvinus) usually provides this osmotic motor (*3*). It is, of course, possible that both mechanisms play a role in the sunflower solar-tracking response. Both mechanisms include nocturnal reorientation (*3*).

When Atamian *et al.* either tethered sunflower stems (immature, nonflowering plants) to prevent movement, or rotated plants at dusk so that they faced west at dawn, they noted a loss in photosynthetic productivity in the absence of tracking. Hence, a photosynthetic advantage is clearly gained by solar tracking under their conditions. Growth measurements of solar-tracking plants in the field indicated more rapid growth shifting from the west to the east side of stems during the day and back to the west side at night. Simultaneous monitoring of tracking also showed that as growth diminished, tracking diminished, and when growth ceased, tracking ceased. Solar tracking is indeed driven by irreversible differential growth. Because the elongation that drives solar tracking is irreversible, any contribution by a reversible osmotic process is essentially ruled out.

There are several other intriguing questions: Is a circadian rhythm involved? That is, do changes in plant metabolism, physiology, and/or behavior that fluctuate between day and night regulate heliotropism? Night reorientation suggests as much. However, as Atamian *et al.* point out, reversal of the end-of-day stem curvature in darkness could be a one-time hourglass phenomenon that is preloaded by signals from the preceding day. The authors observed that stem movement—including nocturnal reorientation—persists through several diurnal cycles under constant light before damping out. They also found that the tracking response is seriously perturbed under day-night cycles lasting 30 hours instead of 24. These are classic tests for circadian function (*9*). The authors also detected diurnal oscillations in the expression of genes encoding well-known components of circadian circuitry of other systems. However, there was no difference in these oscillations between illuminated and shaded sides of sunflower's elongating stem tissue. By contrast, there were dramatic changes in the expression of auxin-induced genes between the two sides, both during tracking and during nocturnal reorientation. The results are fully consistent with the involvement of a diurnally alternating auxin differential

Stem orientation

Phototropically driven auxin movement promotes growth of the shaded side over the illuminated side of the stem, causing curvature that keeps the shoot tracking the Sun westward. As the Sun passes the zenith, the shaded side becomes the east side, continuing to drive curvature westward. At night, intrinsic circadian signals cause auxin to reaccumulate on the west side, driving the direction of shoot growth back east.

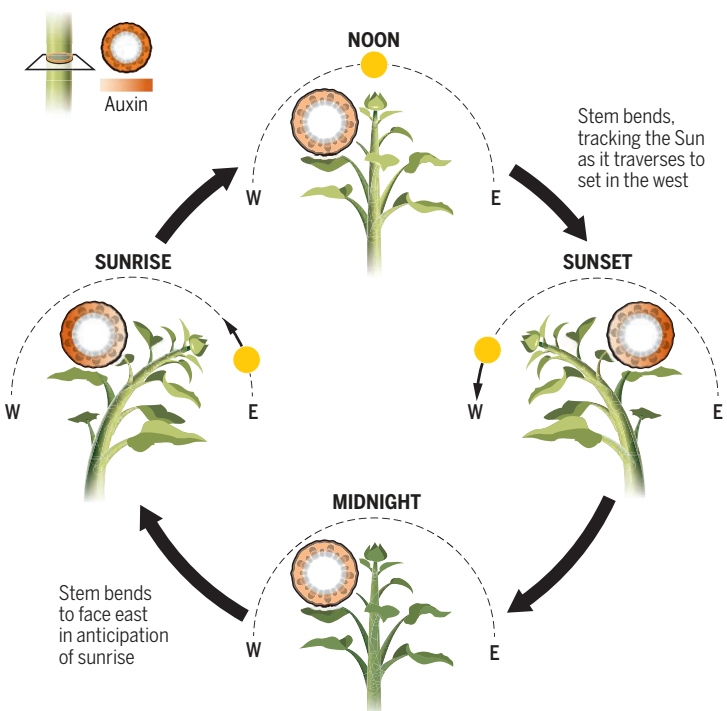

GRAPHIC: V. ALTOUNIAN/*SCIENCE*

Department of Plant Biology, Carnegie Institution for Science, Stanford, CA 94305, USA. Email: briggs@stanford.edu

(*8*)—auxin moving to the east side of the stem during the day and returning to the west side at night to dominate growth. Nighttime reversal of the auxin gradient, then, occurs in response to intrinsic circadian cues.

How do mature flowering heads acquire their eastward orientation? Atamian *et al.* investigated whether the phototropic sensitivity of growing vegetative sunflower plants is gated—more sensitive at some times of day than at others. Indeed, sunflower seedlings responded more strongly to unilateral light in the morning than in the afternoon. Thus, if the seedling response persists in older plants, as tracking declines, east-oriented phototropism will be stronger, overall, than west-oriented, inevitably leaving the shoots facing eastward when growth and tracking cease.

Why do sunflower heads terminate their existence facing the rising Sun? What was the selective pressure leading to this end? Atamian *et al.* found that heads facing the morning Sun warmed up more rapidly than heads deliberately turned away from it. During the morning hours, the heads facing the Sun were visited by more pollinating insects than those facing away from the Sun. If heads facing away from the Sun were artificially heated to a temperature to match heads in the normal orientation, the difference in pollinator visits diminished substantially. The positive effect of tracking on potential pollination may be part of the story, although other factors could be at play. In any case, it is clear that to encourage pollinator visits, warmer heads prevail.

One morning many years ago, I passed a field of the sunflower relative *Rudbeckia hirta* (black-eyed Susan). Every flowering head was facing the morning Sun. In my naïvety, I photographed the field with the intention of rephotographing it in the late afternoon to document solar tracking. However, on my return, every flowering head was still facing east. This was my first encounter with what at the time seemed like bizarre plant behavior. Atamian *et al.* have gone far in elucidating the origin and physiological mechanisms underlying this fascinating chapter of natural history. ■

REFERENCES

1. J. P. Vandenbrink *et al.*, *Plant Biol.* **224**, 26 (2014).
2. H. S. Atamian *et al.*, *Science* **353**, 587 (2016).
3. D. Koller, *The Restless Plant* (Harvard Univ. Press, 2011).
4. U. Kutschera, W. R. Briggs, *Ann. Bot.* **117**, 1 (2016).
5. F. W. Went, *Rec. Trav. Bot. Néerl.* **25**, 1 (1928).
6. W. R. Briggs, *Science* **126**, 210 (1957).
7. M. Lino, W. R. Briggs, *Plant Cell Environ.* **7**, 97 (1984).
8. C. A. Esmon *et al.*, *Proc. Natl. Acad. Sci. U.S.A.* **103**, 236 (1999).
9. M. Merrow, M. Brunner, T. Roenneberg, *Nature* **399**, 584 (2011).

10.1126/science.aah4439

BIOTECHNOLOGY

Benefits of selective feeding

Microbes engineered to digest unusual nutrients outcompete contaminants in chemicals production

By **Rebecca M. Lennen**

Industrial processes using microbial cells allow the conversion of renewable-carbon feedstocks into a complex range of chemical products at comparatively low temperatures and pressures (*1*). In contrast, traditional chemical manufacturing relies mainly on energy-intensive conversions of petroleum-derived carbon feedstocks. However, record-low oil prices are making it difficult for biotechnology processes to compete with traditional manufacturing, particularly for low-cost bulk products such as biofuels and commodity chemicals. On page 583 of this issue, Shaw *et al.* (*2*), report a cost-effective technology to control contamination in nonsterilized process equipment (see the figure). This technology has the potential to greatly lower the cost of producing fermentation-derived chemicals with microbial processes.

> ***"...the engineered organisms outcompete common contaminant species..."***

Fermentation has been used to preserve food since the dawn of human civilization. It likely arose fortuitously when stored foods were contaminated with microbes in the environment. The microbes involved, such as brewers' yeast (*Saccharomyces cerevisiae*) and lactic acid bacteria, naturally outcompete other organisms by secreting ethanol or organic acids that retard the growth of other organisms.

These same microbes are now used in the industrial production of both food and chemicals. In the modern fuel ethanol industry in Brazil, for example, fermentors operate with nonsterilized raw feedstocks and are inoculated with indigenous yeasts that are recycled in subsequent batches (*3*). Ethanol excretion gives *S. cerevisiae* a strong competitive advantage, but the ethanol industry is nevertheless plagued by large contamination events and low-level contamination (*4*). These bacterial infections reduce ethanol yields (*5*). Use of chlorine dioxide and biocidal additives has gained popularity, but many manufacturers still add antibiotics to control infections, further exacerbating the contamination cycle by speeding up the evolution of antibiotic-resistant strains.

Beyond ethanol production, the impact of contamination is likely to be greater. To minimize capital costs production of fuels and bulk chemicals from algae or cyanobacteria would require cultivation in large open reservoirs (*6*), but these organisms typically have little to no competitive advantage under the growth conditions used. Bulk and specialty products can also be produced with highly engineered organisms that are often physiologically defective relative to wild organisms, making it even more important to maintain pure cultures. Media and fermentation vessels used in these processes are typically partially or fully sterilized, increasing the operating costs. Antibiotic usage imposes additional costs and is untenable for products used in food or pharmaceuticals.

Shaw *et al.* now present a technology for preventing contamination in fermentation processes through metabolic engineering of the production organism. They introduce a pathway into the organism that enables it to digest a xenobiotic nutrient (a nutrient not naturally produced or degraded by the organism). In doing so, the authors give the production organism a competitive advantage because environmental contaminants do not possess the degradation pathway required for using the xenobiotic nutrient. The xenobiotic nutrients—in particular, the phosphorus source sodium phosphite—appear to be cost-competitive supplements relative to either the cost of typical antibiotics used in ethanol fermentations or the use of steam sterilization.

Industrial-scale feasibility remains to be demonstrated, but the authors show convincingly that the engineered organisms outcompete common contaminant species both in defined media and in complex feedstocks supplemented with the xenobiotic nutrient. Complex biomass-derived feedstocks often contain suffiecient biotic nutrients to fully support microbial growth. Shaw *et al.* therefore fractionated corn kernels to obtain a starch fraction with a reduced phosphate content, low enough to give the engineered organism—*Yarrowia lipolytica,* an oil-accumulating yeast engineered to use

The Novo Nordisk Foundation Center for Biosustainability, Technical University of Denmark, 2970 Hørsholm, Denmark. Email: rlen@biosustain.dtu.dk

phosphite—a selective advantage. Use of other complex fermentation substrates will require careful matching between the levels of biotic components (such as ammonia or phosphate) present and the xenobiotic supplement.

Wider adoption of the technology will likely require engineering of a wider range of xenobiotic nutrient utilization pathways. Suitable enzymes could be found in microorganisms from environments rich in atypical substrates; further xenobiotic nutrients, such as alternative sulfur sources, could also be identified. If multiple distinct enzymes are found that catalyze separate steps in a degradation pathway, they can be expressed together in the same organism to reconstitute a full pathway for complete degradation. Once a minimally functional pathway has been found, it can be optimized through adaptive laboratory evolution. Shaw *et al.* use this approach to dramatically improve growth on melamine and cyanamide as nitrogen sources and on phosphite as a phosphorus source.

The genes encoding the enzymes for xenobiotic nutrient utilization originate naturally and exist in the environment. New contaminating microorganisms are thus likely to evolve, much like microbes evolve antibiotic resistance or weeds evolve herbicide resistance (*7*). A parallel arms race will likely ensue, with the need to rotate use of xenobiotic nutrients. This should not cause the same level of concern as the evolution of antibiotic resistance, which has direct implications on human health, but further studies are warranted. A full life-cycle analysis will also be needed because compounds such as melamine, associated with food contamination crises, must not be present when recycling fermentation wastes for animal feed.

Despite these challenges, Shaw *et al.*'s report illustrates the possibilities offered by the combination of genomics, synthetic biology, and evolutionary engineering. The former facilitates the discovery of new enzyme functions, whereas advances in gene synthesis and DNA assembly enable novel biochemical pathways to be rapidly engineered in the host strain. Evolutionary engineering can then be used to improve pathway activities and fluxes. The biochemical creativity enabled by these three technologies will help to overcome economic hurdles for biobased chemical production via fermentation. ■

REFERENCES

1. J. W. Lee *et al.*, *Nat. Chem. Biol.* **8**, 536 (2012).
2. A. J. Shaw *et al.*, *Science* **353**, 583 (2016).
3. B. E. Della-Bianca *et al.*, *Appl. Microbiol. Biotechnol.* **97**, 979 (2013).
4. O. Y. Costa *et al.*, *J. Ind. Microbiol. Biotechnol.* **42**, 73 (2015).
5. U.S. Food and Drug Administration, Report of FY 2010 Nationwide Survey of Distillers Products for Antibiotic Residues, www.fda.gov/AnimalVeterinary/Products/AnimalFoodFeeds/Contaminants/ucm300126.htm.
6. U.S. Department of Energy (DOE), *National Algal Biofuels Technology Roadmap* (DOE, 2010).
7. M. R. Behrens *et al.*, *Science* **316**, 1185 (2007).

10.1126/science.aah4106

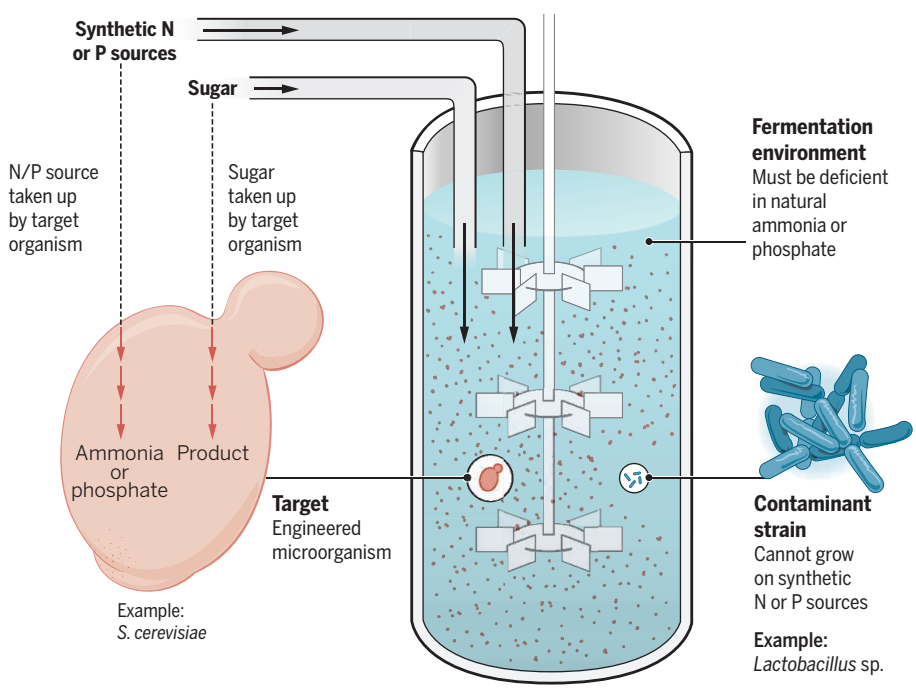

Contamination control. Shaw *et al.* use synthetic nitrogen or phosphorus sources to control contamination in industrial fermentation. They metabolically engineered pathways for digesting these synthetic sources into their target organisms. The latter have a competitive advantage over contaminating organisms when availability of natural nitrogen or phosphorus sources, such as ammonia or phosphate, is restricted.

GRAPHIC: K. SUTLIFF/*SCIENCE*

ANALYTICAL METHODS

A nanoview of battery operation

Single cathode particles for lithium-ion batteries are analyzed during cycling

By **Steen B. Schougaard**[1,2]

The redox-active materials in lithium-ion batteries have relatively poor electronic and ionic conduction and may experience stress from charge-discharge volume changes, so their formulation into structures with nano-sized features is highly desirable. On page 566 of this issue, Lim *et al.* (*1*) characterize individual nanoparticles of the positive electrode material $LiFePO_4$ during charging and discharging. This "in operando" technique ensures that all particles experience the same voltage. The current and lithium concentration are then inferred for individual particles via the change in Fe oxidation state measured during the transformation from $LiFePO_4$ to $FePO_4$ and back.

Lithium-ion batteries are moving into new large-scale applications like mass storage of renewable energy and electric cars, with their performance constituting a source of both great frustration and hope. Since its discovery by Goodenough and co-workers as a lithium battery cathode (*2*), $LiFePO_4$ has fascinated physicists, engineers, and chemists alike. Its performance is surprising in that phosphates are generally poor conductors. Additionally, it separates into lithium-rich $LiFePO_4$ and lithium-poor $FePO_4$ phases when partially delithiated, which would suggest that reaction kinetics are sluggish. Yet, once conductively coated with carbon (*3*), $LiFePO_4$ has an unusually good performance at high charge and discharge rates, capable of delivering >50% of its capacity within 2 min for thousands of cycles (*4*).

This high performance has been associated experimentally with the intermittent formation of a solid-solution phase (*5*). The mechanism at more practical battery

[1]*Département de chimie, Université du Québec à Montréal, Montréal, PQ H3C 3P8, Canada.* [2]*Temporary address: Department of Energy Conversion and Storage, Technical University of Denmark, Denmark.*
Email: schougaard.steen@uqam.ca

rates is less well understood. Lim *et al.* fill an important gap by providing maps of single-particle current densities at charge-discharge times between 0.5 and 3 hours. Their time-resolved high-resolution maps provide unusual insight into the kinetics of the charge-and-discharge process, showing "domains" within the particle that have widely different rate performance. Why these domains form is unclear; the authors suggest inhomogeneous strain and variations in carbon coating as possible origins. Inside the domains, the time-resolved quantification made possible by the x-ray absorption technique shows that the kinetics, expressed electrochemically as the exchange current, is highly dependent on the local concentration of lithium. Surprisingly, the peak performance occurs at compositions closer to $Li_{0.25}FePO_4$ than $Li_{0.5}FePO_4$.

The state-of-the-art methodology presented by Lim *et al.* has several important applications. First, the particle-to-particle variation is readily observed. This information is crucial in materials design and production, especially given that electrochemical techniques often provide only average particle populations. For example, it has been difficult to determine if a reduction to half performance was more correctly described by 50% of the particles performing at the zero level, or 100% performing at the 50% level.

Second, single-particle data provide opportunities to improve battery design (see the figure). Commercial battery electrodes are based on a porous mixture of carbon particles, active material, and binder. This composite provides structural stability and adhesion to the current collector, as well as efficient paths for electron transport. Filling the porous structure with electrolyte enables ionic transport. The composite structure is more efficient at providing ionic and electronic charge transport to the electrode bulk than a monolith of the active material, but it still sets severe limitations. The combination of the opposite flows of ionic and electronic transport along with the highly complex local electrode structure yields a highly heterogeneous reaction environment. Determining if performance is limited by the particles within the electrode structure or by the electrode structure itself is a challenge.

Attempts to overcome this situation include Newman-type modeling (*6*). Varying degrees of sophistication can be used to express the transport in the different regions of the heterogeneous composite with effective bulk values taken from a homogeneous, fictitious material. Based on the response of the full electrode, it should in principle be possible to obtain the single-particle response, because the voltage loss caused by electrode transport can be calculated. However, at a practical level, the interdependence between the effective transport and the reaction at the local particle, combined with a large number of variables that require fitting, makes solving this inverse problem difficult. The high-resolution particle-level current-voltage-composition maps provided by Lim *et al.* greatly simplify this task. The effect of transport in the electrode structure should be more readily available from Newman-type modeling, thereby limiting the need for trial-and-error electrode optimization (*7*).

Third, the redox mechanism of $LiFePO_4$ is remarkably rich in complexity, as shown by the state-of-the-art time- and space-resolved reaction maps of Lim *et al.* As such, these data provide an exciting opportunity for testing existing theories and developing new physical-chemical models, including ones based on quantum-level calculation. This approach has practical implications. $LiFePO_4$ has found widespread use for high-power operation and is comparably safe under overcharge conditions, but its operational potential of ~3.4 V versus Li^+/Li yields an energy density insufficient for many applications. Moreover, only precious few other structures support the topotactic insertion reaction.

Insertion reactions, where the inorganic framework remains relatively unchanged while lithium ions enter and leave the structure in response to the addition or removal of electrons, is likely to remain in vogue. This is because it can provide the ~99.995% charge-discharge reaction yields required for 80% capacity retention after 4000 cycles. What is needed is a thorough understanding of the operational mechanism of $LiFePO_4$ so that its virtues can be designed into new materials with higher energy density, with the goal of providing cheap, reliable, and safe energy storage for solar and wind power, as well as for the electric car. ■

REFERENCES

1. J. Lim *et al.*, *Science* **353**, 566 (2016).
2. A. K. Padhi *et al.*, *J. Electrochem. Soc.* **144**, 1188 (1997).
3. N. Ravet *et al.*, in *The Electrochemical Society and The Electrochemical Society of Japan, Meeting Abstracts* (Honolulu, HI, 1999), vol. 99–2.
4. K. Zaghib *et al.*, *J. Power Sources* **216**, 192 (2012).
5. H. Liu *et al.*, *Science* **344**, 1252817 (2014).
6. J. Newman *et al.*, *Electrochemical Systems* (Wiley, 2004).
7. D. Y. W. Yu *et al.*, *J. Electrochem. Soc.* **153**, A835 (2006).

10.1126/science.aah4124

Battery building blocks

The work of Lim *et al.* provides quantitative images of how a cathode particle for lithium batteries works at the nanoscale, which affects real battery operation.

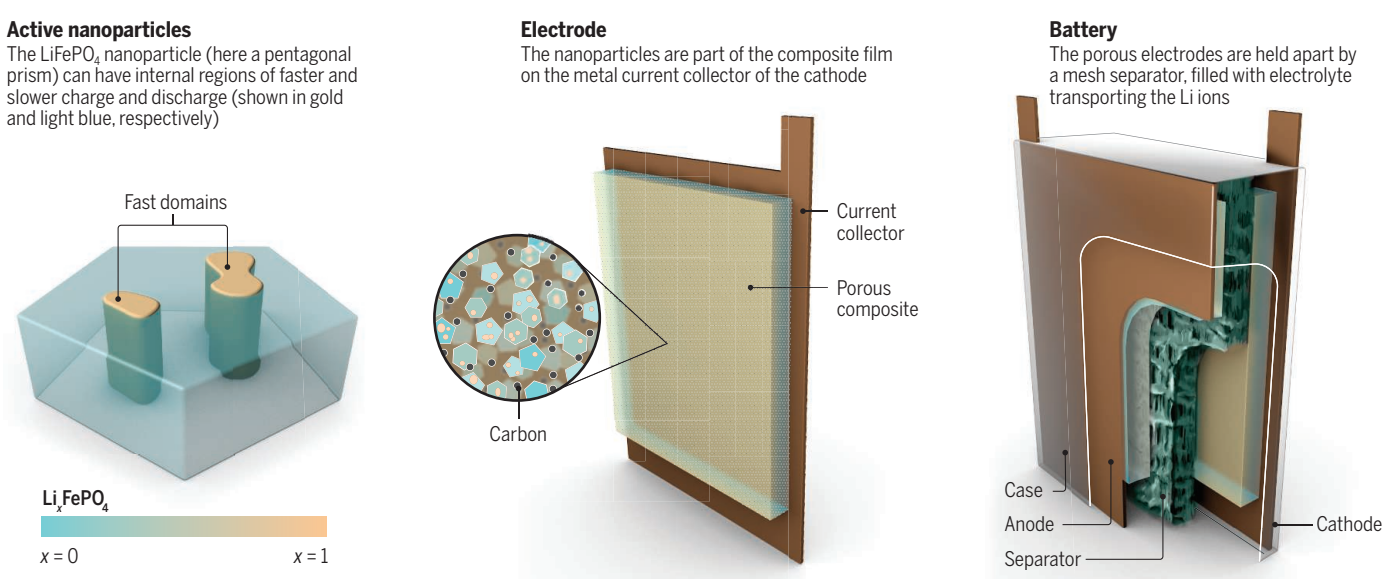

GRAPHIC: C. BICKEL/*SCIENCE*

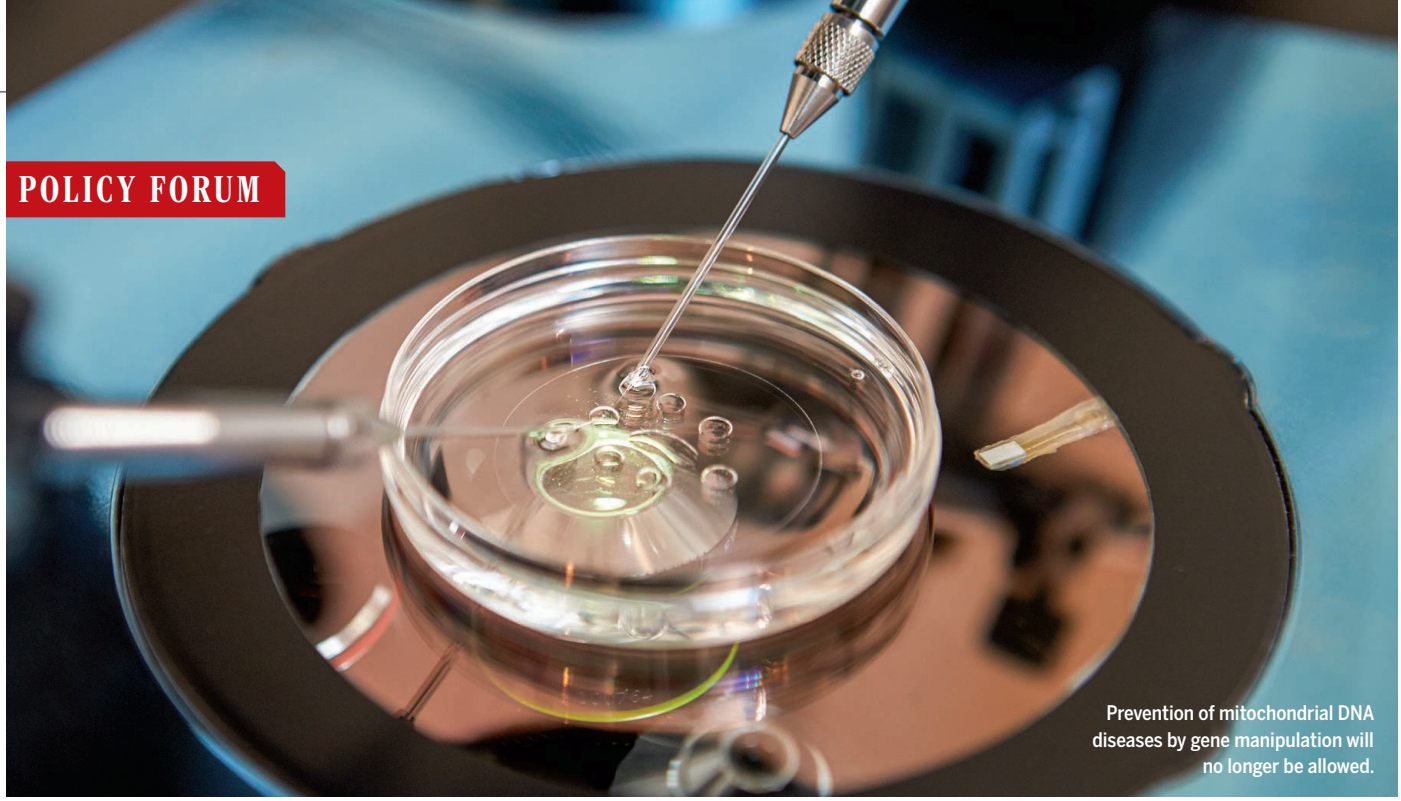

Prevention of mitochondrial DNA diseases by gene manipulation will no longer be allowed.

PHOTO: MONKEYBUSINESSIMAGES/ISTOCKPHOTO

SCIENCE AND REGULATION

The FDA is prohibited from going germline

Full stop: U.S. Congress precludes human germline modification

By **I. Glenn Cohen**[1] *and* **Eli Y. Adashi**[2]

A potentially renewable provision of the *Consolidated Appropriation Act of 2016* forestalling the prospect of human germline modification was signed into law on 18 December 2015 (*1*). The provision, also known as a rider (an amendment extraneous to the main purpose of the bill to which it is attached), stipulates that "none of the funds made available by this Act [to the FDA] may be used to review or approve an application for an exemption for investigational use of a drug or biological product… in which a human embryo is intentionally created or modified to include a heritable genetic modification" (*1*). Destined to expire at the conclusion of this fiscal year (30 September 2016), the rider has since been incorporated yet again into the House and Senate appropriation bills for the fiscal year ending 30 September 2017 (*2*, *3*). Subject to ongoing annual renewal, this congressionally legislated ban undermines ongoing conversations on the possibility of human germline modification, its likely distant time horizon notwithstanding (*4*). Also affected are ongoing efforts of the FDA to review the prevention of mitochondrial DNA diseases through germline modification of human zygotes or oocytes at risk (*5*).

A draft version of the *Agriculture, Rural Development, Food and Drug Administration, and Related Agencies Appropriations Act of 2016* in the House contained the rider, whereas the Senate version did not (*6*, *7*). The final version of the merged House and Senate bills, the *Consolidated Appropriations Act of 2016* (H.R. 2029), inclusive of the rider, contained last-minute additions, stipulating that germline-modifying Investigational New Drug (IND) applications "shall be deemed to have not been received by the Secretary [of Health and Human Services]" (*1*, *8*). Indispensable to the intent of the rider, the added language precludes the unintended consequence of forbidding the FDA from responding to (and blocking) an IND application, which would have allowed such applications to be approved automatically within 30 days of submission.

As a practical matter, it might have been hard for the rider to have succeeded as a stand-alone bill. The rider might never have been voted out of committee, given that it lacked the urgency of a "must-pass" bill and might have been the subject of opposing arguments and hostile amendments. A presidential veto, a real possibility in the case of a stand-alone bill, is far less likely in the context of a rider to an omnibus bill (in the absence of line-item veto authority), because the failure of the omnibus bill could cause a government shutdown. The omnibus bill containing the rider was the year-end $1.8 trillion *Consolidated Appropriations Act of 2016* without which the federal government would not have been funded for the duration of fiscal year 2016 (*1*).

Congressional concerns regarding germline editing have been articulated in a report (H. Rept. 114-205) accompanying the House appropriation bill (*9*). In one passage of the report, the committee states that "… researchers do not yet fully understand all the possible side effects of editing the genes of a human embryo" (*9*). The report goes on to note that "editing of the human germline may involve serious and unquantifiable safety and ethical issues" (*9*). Similar concerns were expressed during a congressional hearing on "The Science and Ethics of Genetically Engineered Human DNA" before the House Subcommittee on Research and Technology (*10*). In his opening state-

[1]*Professor of Law, Harvard Law School, Director, Petrie-Flom Center for Health Law Policy, Biotechnology, and Bioethics, Harvard University, Cambridge, MA 02138, USA.* [2]*Professor of Medical Science, The Warren Alpert Medical School, Brown University, Providence, RI 02903, USA. Email: eli_adashi@brown.edu*

ment, Chair Lamar S. Smith (R–TX) noted that "a recent report from China, where teams of researchers have begun to experiment with engineering DNA in human embryos, is alarming" (*10*). Chair Smith went on to say that "most of the scientific community members have been clear: the science and ethics of this new technology must be resolved in order to prevent dangerous abuses and unintended consequences" (*10*). Finally, Chair Smith offered that a recent *Science* article authored by prominent thought leaders "recommended a moratorium on further research, while creating public forums for scientists, ethicists and policy makers to discuss the attendant ethical, social, and legal implications of genome modification" (*10*, *11*).

IMPLICATIONS OF THE RIDER

Editing the genome of a human embryo for research purposes and without intrauterine transfer remains permissible, even though it is ineligible for public funding (*12*). By contrast, editing the genome of a human embryo in the clinical realm followed by intrauterine transfer is precluded (*1*). Thus, editing the genome of a human embryo for the prevention of rare incurable Mendelian disorders will not be undertaken (*4*). Also affected will be efforts to secure "savior siblings" through editing of the genome of a human embryo when in vitro fertilization fails to secure tissue-matched embryos for intrauterine transfer (*4*). Finally, the rider appears to preclude the prevention of mitochondrial DNA diseases by mitochondrial replacement due to attendant "heritable genetic modification" (*1*, *5*). The FDA could have sidestepped the "heritable genetic modification" constraint on mitochondrial replacement by accepting the "male-only" embryo transfer recommendation of the Institute of Medicine (*5*). However, the FDA has resolved to forgo consideration of mitochondrial replacement during this fiscal year (*13*).

The enactment of the FDA rider adds yet another layer to a complex regulatory and statutory web concerned with human embryo research in general and human germline modification in particular. In 1996, the Dickey-Wicker Amendment, a statutory ban on federal funding of human embryo research, was enacted (*12*). The amendment proved instrumental in precluding the derivation of human embryonic stem cells. In reaffirming a 30-year policy, National Institutes of Health Director Francis S. Collins recently stated that the Recombinant DNA Advisory Committee (RAC) "…will not at present entertain proposals for germline alteration," which all but stamps out the possibility of federally funded germline modification trials (*14*). Viewed collectively, the aforementioned constraints have had a chilling effect on studies of early human development, despite decades of unprecedented progress in other areas of the life sciences. With this rider, legislators have now extended the ban on therapeutic germline modification to any corporate entity that might apply to the FDA for permission to proceed with clinical trials (e.g., for testing of cell and gene therapy products). Never before have lawmakers relied on the FDA to constrain the prospect of therapeutic germline modification. In so doing, lawmakers have drawn new lines in the sand only a few weeks after the conclusion of the International Summit on Human Gene Editing led by the National Academies (*4*). Lawmakers have also altered the context of an ongoing Consensus Study of the National Academy of Medicine on the *Scientific, Medical, and Ethical Considerations of Human Gene Editing* (*15*). A recently released report, *Mitochondrial Replacement Techniques: Ethical, Social, and Policy Considerations*, has also been affected in that its recommendations have been placed on hold by the FDA (*5*, *12*). Viewed in this light, this latest congressional intervention appears premature, if not unhelpful, in that the germline modification debate is barely getting under way.

> ***"…this latest congressional intervention appears premature, if not unhelpful, in that the germline modification debate is barely getting under way."***

FUTURE OF THE RIDER

Whether or not the rider will be repealed in the future remains to be seen. If history is any guide, imminent congressional policy reversal is unlikely. Riders pertaining to the reproductive arena have shown themselves to evolve into the "new normal" the modification of which is viewed as a litmus test on the campaign trail (*16*). What is more, riders such as the Dickey-Wicker Amendment have displayed remarkable longevity across several administrations and variable congressional constellations (*17*). With little comfort to be derived from the apparent lack of congressional efforts to strike the rider in the course of its legislative advancement, the prospects for a change in the status quo any time soon must be viewed as guarded. Absent such course correction, the United States is ceding its leadership in this arena to other nations. Whether or not successful human germline modification in nations other than the United States might lead to a reversal of congressional policy at some point in time remains to be seen. ■

REFERENCES AND NOTES

1. Consolidated Appropriations Act, 2016, Public Law no. 114-113 (2015); www.congress.gov/bill/114th-congress/house-bill/2029/text.
2. U.S. Congress, House Committee on Appropriations, Bill for Agriculture, Rural Development, Food and Drug Administration, and Related Agencies for the fiscal year ending September 30, 2017, 114th Cong. 2d sess., 2016; www.appropriations.house.gov/uploadedfiles/bills-114hr-fc-ap-fy2017-ap00-agriculture.pdf.
3. U.S. Congress, Senate Committee on Appropriations, Bill for Agriculture, Rural Development, Food and Drug Administration, and Related Agencies for the fiscal year ending September 30, 2017, S.2956, 114th Cong. 2d sess., 2016; http://bit.ly/FDAfunding.
4. The National Academies of Sciences, Engineering, and Medicine, "On human gene editing: International summit statement" (National Academies, Washington, DC, 2015).
5. National Academies of Sciences, Engineering, and Medicine, *Mitochondrial Replacement Techniques: Ethical, Social, and Policy Considerations* (National Academies, Washington, DC, 2016).
6. H.R.3049—Agriculture, Rural Development, Food and Drug Administration, and Related Agencies Appropriations Act, 2016, H.R.3049, 114th Cong., 2015; https://www.congress.gov/bill/114th-congress/house-bill/3049.
7. S.1800—Agriculture, Rural Development, Food and Drug Administration, and Related Agencies Appropriations Act, 2016, 114th Cong., 2015) https://www.congress.gov/bill/114th-congress/senate-bill/1800.
8. H.R.2029—Consolidated Appropriations Act, 2016, 114th Cong., 2015; https://www.congress.gov/bill/114th-congress/house-bill/2029.
9. U.S. Congress, House Committee on Appropriations, Report together with minority views (to accompany H.R.3049) (2015); https://www.congress.gov/114/crpt/hrpt205/CRPT-114hrpt205.pdf.
10. U.S. Congress, House Committee on Science, Space, and Technology, Subcommittee on Research and Technology, Statement of Chairman Lamar Smith (R–Texas), "The science and ethics of genetically engineered human DNA" (2015); http://bit.ly/HouseSciCtte.
11. D. Baltimore *et al.*, *Science* **348**, 36(2015).
12. The Balanced Budget Downpayment Act of 1996 Public 104-99 (1996); https://www.gpo.gov/fdsys/pkg/PLAW-104publ99/content-detail.html.
13. Z. Brennan, Expert Committee: "FDA should allow mitochondrial replacement trials under certain conditions" (Regulatory Affairs Professionals Society, Rockville, MD, 2016); http://bit.ly/RegulatoryProfessionalsonFDA.
14. National Institutes of Health, The NIH Director, Statement on NIH funding of research using gene-editing technologies in human embryos (2015); www.nih.gov/about/director/04292015_statement_gene_editing_technologies.htm.
15. National Academies of Sciences, Engineering, and Medicine, *Project: Scientific, Medical, and Ethical Considerations of Human Gene Editing* (National Academies, Washington, DC, 2016).
16. E.Y. Adashi, I. G. Cohen, JAMA Forum: Reproductive Freedom and the 2012 Presidential Election (2012); http://bit.ly/JAMANews.
17. S. Rodriguez *et al.*, *Am. J. Bioeth.* **11**, 20 (2011).

ACKNOWLEDGMENTS

I.G.C. is supported by the Greenwall Foundation Faculty Scholar in Bioethics Award.

10.1126/science.aag2960

NUCLEAR ENERGY

China-U.S. cooperation to advance nuclear power

Mass-manufacturing and coordinated approvals are key

By **Junji Cao[1], Armond Cohen[2], James Hansen[3]*, Richard Lester[4], Per Peterson[5], Hongjie Xu[6]**

With China having the largest fossil fuel CO_2 emissions today and the United States being higher in per capita emissions (see related energy consumption in the first figure), these countries have a strong mutual interest in stabilizing climate and reducing air pollution. Yet even Germany, despite sizable subsidies of renewable energies, gets only a small fraction of energy from them (see the first figure). Historically the fastest growth of low-carbon power occurred during scale-up of national nuclear power programs (see the second figure). Some studies project that a doubling to quadrupling of nuclear energy output is required in the next few decades, along with a large expansion of renewable energy, in order to achieve deep cuts in fossil fuel use while meeting the growing global demand for affordable, reliable energy (*1*–*4*). In light of this large-scale energy and emissions picture, climate and nuclear energy experts from China and the United States convened (see Acknowledgments) to consider the potential of increased cooperation in developing advanced nuclear technologies.

Barriers to expansion of nuclear energy include high construction costs relative to coal and gas; a long time to build conventional large nuclear plants (about 4 to 7 years in Asia versus 1 or 2 years for coal-fired plants); and public concern about reactor safety, waste disposal, and potential for weapons use. Innovative nuclear technologies can help address some of these issues. A large reduction of cost and construction time, essential to accelerate deployment rates, likely requires mass manufacturing, analogous to ship and airplane construction. Such an approach lends itself to product-type licensing, which avoids the long delay and costs associated with case-by-case approval. Passive safety features are available that allow reactor shutdown and cooling without external power or operator intervention. Other innovative designs use fuel more efficiently and produce less nuclear waste, can directly supply energy to industrial processes that currently rely on fossil fuels, can be ordered in a range of scales to suit a variety of needs and geographies, and can reduce or eliminate cooling-water requirements. Some of these developments could be deployed on a large scale by 2030–2050, a time when deep reductions in global carbon emissions will be needed, even as much of the world's current nuclear fleets are approaching the end of useful life.

U.S.-China cooperation to accelerate nuclear energy innovation has potential to deliver benefits to both countries and the world. Test sites at U.S. Department of Energy laboratories are needed to perform experiments in existing test reactors and to build and demonstrate advanced designs. China's growing demand for electricity, even though slowing, and its need to displace large amounts of existing coal-fired capacity provide the large market for nuclear reactors that is needed to drive down unit costs.

Innovative concepts are emerging in both countries. Recent reactor development in the United States is entrepreneurially driven, in a departure from the traditional model in which nuclear innovation flowed outward from government. Technologies under development include small modular light-water, molten salt, gas-cooled, and liquid-metal–cooled reactors. China has recently made major investments in several nuclear innovation projects, including high-temperature gas reactors, thorium-fueled molten salt reactors, sodium-cooled fast reactors, and accelerator-driven subcritical systems.

Current China-U.S. cooperation includes collaboration between a U.S. company (TerraPower) and the China National Nuclear Corporation to demonstrate traveling-wave reactor technology, as well as the cooperation of Oak Ridge National Laboratory, U.S. universities, and the Shanghai Institute of Applied Physics to develop molten salt reactor technologies, including near-term options for fluoride salt–cooled, solid-fuel, high-temperature reactors. Molten salt technology, which has large potential but remains immature, provides a particularly large opportunity for U.S.-China cooperation.

Development of large floating nuclear plants—constructed in shipyards before being towed and anchored 10 to 20 km off-

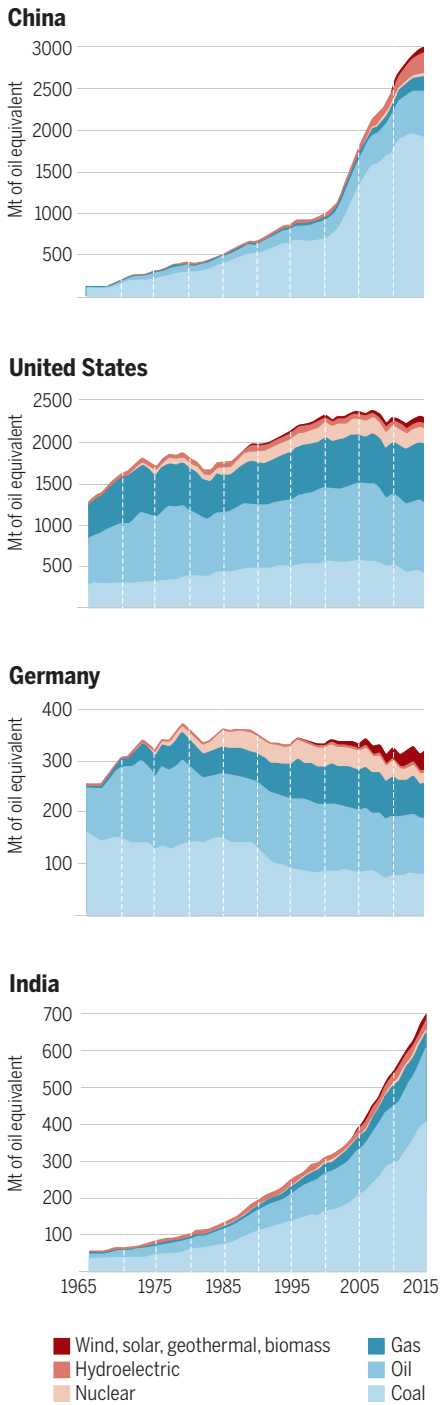

Energy consumption in four nations. Data source (*6*). See supplementary materials.

[1]*Key Lab of Aerosol Chemistry and Physics, SKLLQG, Institute of Earth Environment, Xi'an 710061, China,* [2]*Clean Air Task Force, Boston, MA 02108, USA.* [3]*Earth Institute, Columbia University, New York, NY 10025, USA.* [4]*Massachusetts Institute of Technology, Cambridge, MA 02139, USA.* [5]*University of California, Berkeley, CA 94720, USA.* [6]*Shanghai Institute of Applied Physics, Shanghai 21203, China. *Email: jimehansen@gmail.com*

shore—has promise to reduce cost, speed deployment, reduce tsunami and earthquake risk, and enhance security. Recent studies show that gigawatt-scale plants can be deployed on robust floating platforms using technology developed for deep-water drilling in the severe weather conditions of the North Sea (*5*). Such power plants could be constructed more rapidly than conventional reactors. China's shipyards already build most of the world's large deep-water platforms and could be adapted to the large floating reactor application.

Further suggestions to accelerate progress include (i) test sites for prototype projects providing access to innovators from China, the United States, and other countries; (ii) joint development of open-source architecture for major advanced plant subsystems—such as a standards-based specification for reactor modules of all types that would address general safety criteria, fuel lifetime, transportability, and so on, as well as open-source codes for advanced reactors; (iii) joint programs to develop, demonstrate, and license advanced non–light-water reactors; (iv) agreement on a regulatory approach that encourages technical innovation in safety assurance, as opposed to detailed prescriptive specifications, also "stage gates" of approval rather than a single review that can require hundreds of millions of dollars in preparation. Jointly funded projects would be governed by the regulations of the host country.

However, obstacles to broader Sino-U.S. nuclear cooperation must be overcome. Obstacles and benefits are both illustrated by recent developments in light-water reactor technology. China-U.S. cooperation was instrumental in development and demonstration of the U.S.-invented AP1000, an 1150-MWe advanced light-water reactor with passive safety features now being deployed in both countries.

As counterpoint, recent charges brought by U.S. authorities under nuclear export control laws—claiming that light-water reactor design information was illegally transferred to Chinese nuclear organizations—is a reminder of the competing strategic economic and security interests of the two countries and the fact that Chinese and U.S. nuclear firms are commercial competitors.

Collaboration in next-generation technologies requires government and industry in both countries to balance interests in cooperation and competition. Joint projects may require participating commercial firms to decide on the intellectual property they are willing to transfer. Regulators in the two countries may choose to align safety standards, which would expand market opportunities for suppliers in both countries, or promulgate their own regulatory criteria, which might benefit their own suppliers by creating barriers to suppliers from the other country but limit their available market.

One barrier our U.S. authors recommend for review is U.S. policy requiring specific authorization for exports of civilian reactor technologies to China, in contrast to general authorization allowed for exports to Japan, South Korea, France, and the United Kingdom. The protracted review process makes cooperation between U.S. and Chinese industry difficult and slow and impedes joint efforts to improve key areas for civil reactor technologies, such as passive safety.

Efforts to overcome obstacles to expanded U.S.-China cooperation in the development of advanced nuclear power technologies are justified by the large potential benefits. Each country has a major stake in the other's success in reducing its carbon emissions, and each has a major stake in the achievement of enhanced nuclear safety in the other country and the rest of the world. In light of this potential, a review of U.S. export policy for civilian reactor technology is warranted with the goal of differentiating and managing U.S.-Chinese commercial intellectual property exchanges, while also creating a stronger mutual foundation for coordinating U.S. and Chinese support for vital international nuclear nonproliferation and security objectives.

Climate science reveals that the world is approaching limits on fossil fuel emissions, if climate is to be stabilized. Future workshops will include climate and nuclear experts from countries such as Indonesia and India, which—with the third greatest CO_2 emissions and population projected to pass China's in 2021 (*6*)—has rapidly growing energy needs that are fossil fuel–dependent (see the first figure). ■

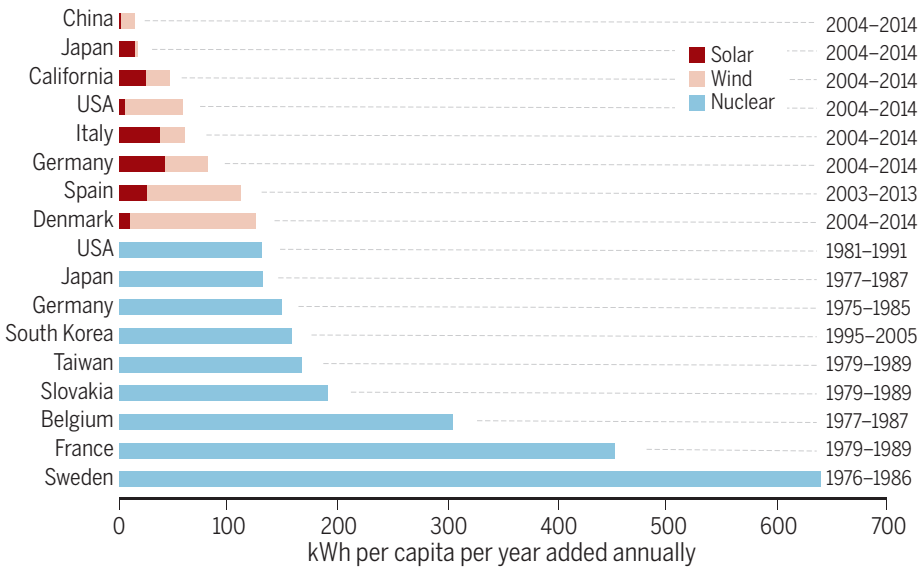

Average annual increase of carbon-free electricity per capita during decade of peak scale-up. Energy data from (*6*) except California renewables data from (*7*). Population data from (*8*). See supplementary materials.

REFERENCES AND NOTES

1. Intergovernmental Panel on Climate Change, *Climate Change 2014: Mitigation of Climate Change*, O. Edenhofer *et al.*, Eds. (Cambridge Univ. Press, New York, 2014).
2. International Energy Agency, *World Energy Outlook 2014* (IEA, Paris, 2014), p. 396.
3. Joint Global Change Research Institute, Pacific Northwest National Laboratory, presentation to Implications of Paris, First Workshop, College Park, MD, 4 May 2016 (JGCRI, College Park, MD, 2016); http://bit.ly/JCRI-Paris.
4. Deep Decarbonization Pathways Project, *Pathways to Deep Decarbonization 2015 Report* (Sustainable Development Solutions Network, Institute for Sustainable Development and International Relations, Paris, 2015); http://bit.ly/DDPP-2015.
5. J. Buongiorno, J. Jurewicz, M. Golay, N. Todreas, *Nucl. Technol.* **194**, 1 (2016).
6. BP, BP Statistical Review of World Energy 2015 (BP, London, ed. 64, 2015).
7. California Energy Almanac, http://energyalmanac.ca.gov.
8. U.S. Census Bureau, http://bit.ly/IntlPrograms.

ACKNOWLEDGMENTS

Our essay draws upon discussions at the Workshop on Advanced Nuclear Energy to Address Climate Change and Air Pollution, 17 to 20 December 2015, Wanning, Hainan, China. The Chinese Academy of Sciences funded local workshop costs. Travel costs of a majority of non-Chinese participants were paid by the U.S. nonprofit Climate Science, Awareness and Solutions, Inc., with funding from Gary L. Russell. P.P.'s research group receives funding from the U.S. Department of Energy and the Shanghai Institute of Applied Physics to work on advanced molten salt reactor technologies.

SUPPLEMENTARY MATERIALS

www.sciencemag.org/content/353/6299/547/suppl/DC1

10.1126/science.aaf7131

NUCLEAR WEAPONRY

Bombs away?

A journalist probes the morality of nuclear weapons in the 21st century

By **Alex Wellerstein**

In 2012, three activists, including Megan Rice, an 82-year old Catholic nun (shown), infiltrated the Y-12 National Security Complex, prompting criticism of the federal government's efforts to safeguard nuclear materials.

PHOTO: AP PHOTO/KNOXVILLE NEWS SENTINEL/MICHAEL PATRICK

After the atomic bombs were dropped on Japan, American scientists and statesmen opined dramatically about the importance of understanding the moral implications of nuclear weapons. Their immense power, their sense of increased collective risk, their potentialities for collateral damage, and their inability to be adequately defended against implied that these were weapons that fell outside the normal moralistic conventions of war.

Dan Zak, a reporter for *The Washington Post*, has written a provocative book that attempts, through a variety of lenses, to restore the big moral questions of the nuclear age. *Almighty* is a collection of stories and characters, organized around the break-in and vandalism at the Y-12 nuclear site in Oak Ridge, Tennessee, in 2012. One of the three antinuclear activists, Megan Rice, was an 82-year-old nun and former missionary, a fact that dominated headlines about the event.

How could a site that was proudly proclaimed the "Fort Knox of uranium" have been infiltrated by a group of elderly Catholic "peaceniks"? Y-12's vaunted security was, in fact, a house of cards. The security contractor took in billions of dollars but cut corners. At the time of the break-in, 10% of the site's surveillance cameras were on the fritz, and the thousands of false alarms per day had conditioned the staff to ignore the few actual ones.

Zak's subject is not really Y-12, even though it serves as the rhetorical fulcrum of his narrative. It is morality and the broad costs and risks associated with nuclear weapons. The book is about the passions that drive people to take strong, potentially self-destructive stands in the name of something they believe in. And this is where things get messy.

For peaceniks, nuclear weapons have the power to destroy millions of lives, and therefore they are an unpardonable abomination. (The Y-12 activists in question are frequently quoted referring to them as the antichrist, which sums up their position well enough.) Many would also note that, although the future nuclear holocaust is, as of yet, hypothetical, the bombings of Hiroshima and Nagasaki represent the "original sin" of the nuclear age. Last, they would point to the immense costs (fiscal, environmental, and human) of the development of these armaments.

Those who favor the bomb argue that the atomic bombings of Japan were no sin: They saved lives. Moreover, modern nuclear weapons are "used every day," the official line goes, because their very existence maintains the peace. As for the costs, those in favor tend to see it as money well spent. They credit nuclear weapons with the dramatic decrease in great-power wars from the mid-20th century onward and the subsequent dramatic drops in both battle and civilian deaths from war.

Do nuclear weapons threaten the world, or do they protect it from such threats? Both may in fact be true. Rational people disagree on the degrees of risk inherent, on the roles of the bombing in World War II, on whether nuclear deterrence actually works, and on whether the costs have been worth the security gained. That risk and security may be inherently intertwined is perhaps the key paradox of the nuclear age.

The amount of time that has passed since the invention of nuclear weapons is less than a century and thus a very small unit of human history to try to generalize about. Yet the debate seems to have become even more polarized than it was during the Cold War.

Both the vehemently antinuclear and the vehemently pronuclear positions are, to be frank, unpalatable to this reader. The antinuclear activists profiled by Zak come off as extremists and kooks. Their vision of the world is one of philosophical ideals, far from the realities of international or domestic order. They appear to be relics of a past age, arrogant in their moral certainties, uncompromising in the way that people who do not have to grapple with the practical consequences of serious decisions can be. Their argument that the world would somehow become rapidly safer, or more moral, were the United States to unilaterally disarm is frankly unconvincing.

Those in favor of nuclear weapons likewise come off in a decidedly unfavorable light. Zak deftly chronicles the disturbing ways in which the military, Congress, and the federal government established and advanced the nuclear program. The story is replete with scandals, spills, pork-barrel politics, meaningless performance reviews coupled to millions of dollars in bonuses, soaring cost overruns, and appalling levels of both corporate and government irresponsibility.

Apparently it required an incredible $53,000 of taxpayer dollars to clean up the small amount of graffiti, spilled blood, and chipped concrete following the break-in at the Y-12 site. This alone is as devastating an indictment of the government-owned, contractor-operated model as I have ever seen.

Our early 21st-century public conversations on nuclear weapons have been dominated by all-or-nothing approaches. It is hard to come away with much faith in the current system, or much hope that it will be meaningfully reformed without radical changes, but Zak's book, in a roundabout way, nudges us toward a new conversation about the morality of security that is not dominated only by the extremes.

Almighty
Courage, Resistance, and Existential Peril in the Nuclear Age
Dan Zak
Blue Rider Press, 2016. 402 pp.

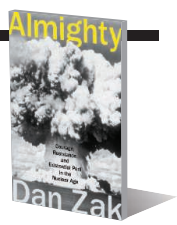

The reviewer is at the College of Arts and Letters, Stevens Institute of Technology, Hoboken, NJ 07030, USA. Email: wellerstein@gmail.com

10.1126/science.aag1183

DATA SCIENCE

Facts versus fallacy

A statistics-driven treatise teaches readers how to spot lies, half-truths, and outright deception

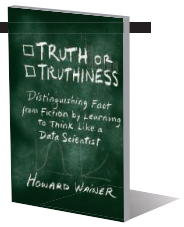

Truth or Truthiness
Distinguishing Fact from Fiction by Learning to Think Like a Data Scientist
Howard Wainer
Cambridge University Press, 2016. 228 pp.

By **Christopher J. Phillips**

Charles Dickens opened his 1854 novel *Hard Times* with the memorable figure of Thomas Gradgrind admonishing a schoolmaster to "teach these boys and girls nothing but Facts. Facts alone are wanted in life" (*1*). Proselytizing "men of facts and calculations" were ripe for Dickensian satire in the mid-19th century, thanks, in part, to the mathematical sciences, which had been established as powerful, even definitive, ways of knowing about the world.

Since antiquity, mathematics had been an exemplar of certain knowledge. Reasoning like a mathematician meant reasoning reliably from assumptions to conclusions. Geometry, for example, was taught for centuries as a model for reasoning in general.

Howard Wainer's new book, *Truth or Truthiness: Distinguishing Fact from Fiction by Learning to Think Like a Data Scientist*, suggests that geometry's role in the search for truth has been replaced by data science. That is, replaced by a "complex mixture of ideas and methods drawn from many related fields," especially statistics, that can be used to evaluate and make inferences from numerical data. There's a bit of an irony here, given that statistics and probability were long considered sciences of uncertainty, as distinguished from geometry's eternal truths. Nevertheless, at a time when PolitiFact's "Truth-O-Meter" provides an essential guide to politicians' stump speeches, Wainer's book is welcome indeed. It is perhaps especially relevant in a divisive election year, when evidence, truth, and expertise seem under assault and yet desperately needed.

Truth or Truthiness consists of a series of short, lively chapters that discuss how data scientists would approach various contemporary quandaries. Wainer groups the chapters under the headings of "thinking like a data scientist," "communicating like a data scientist," and "applying the tools of data science to education." His chosen examples are thoughtful and touch on relevant and engaging problems, especially in medicine and education. (Wainer is currently with the National Board of Medical Examiners and spent more than two decades with the Educational Testing Service.)

Aside from brief case studies, Wainer's book also functions as a popularization of the work of his colleagues (primarily Paul Holland and Don Rubin), an homage to well-designed data displays (from college acceptance letters to inside-out plots of baseball statistics), and a repository for his favorite quotations (with sources ranging from Blanche DuBois to the Roman philosopher Seneca).

"Truthiness," a term coined by Stephen Colbert in 2005, is defined as "truth that comes from the gut, not books."

Books like this face the inevitable problem of how to spread the gospel of data analysis to neophytes without reading like an introductory statistics textbook. There is certainly little here that will be new to professional statisticians; at the other end of the spectrum, readers who have never taken a statistics course will find few details about how to actually use most of the tools Wainer mentions. Rather, it seems that he's writing more to convince policy-makers that data science provides reliable ways to approach complex questions. Even when the data are incomplete, we don't have to settle for "truthiness," he argues.

Wainer spent 5 years on a school board, and often the book reads as if he's writing to fellow board members: people who have basic statistical knowledge, who are often faced with incomplete data, and who are ultimately responsible for making and justifying difficult decisions. His examples form a convincing argument that no matter how intractable a problem seems, careful use of data can help sort things out.

Wainer is also intent on debunking the belief that more data is always better: "the mindless gathering of truckloads of data," he writes, "is mooted by the gathering of even a small amount of thoughtfully collected evidence."

The book is a fun read unless you happen to be a policy-maker who leans to the right politically. The only examples Wainer provides of people with such "an excessive dimness of mind" that they won't ever be capable of "connecting the dots of evidence" are congressional Republicans. This is a shame, because his ultimate message is that whatever one's political background might be, policy decisions require careful analysis of available evidence.

Of course, sometimes issues are inherently political. Good, reliable evidence is important to many of the debates that Wainer wades into—the value of teacher tenure, the measurement of surgical outcomes, the achievement gap in public schools, the possible seismic effects of fracking—but these are also issues that unavoidably engage humanistic debates about rights, priorities, and values.

Wainer's point, though, is that for the questions where evidence does exist, we should know what to do with it. He plausibly suggests that data science provides a good toolbox for that task. Policy-makers and the electorate would do well to follow his advice.

The reviewer is at the Department of History, Carnegie Mellon University, 240 Baker Hall, 5000 Forbes Avenue, Pittsburgh, PA 15213, USA. E-mail: cjp1@cmu.edu

REFERENCES

1. Charles Dickens, *Hard Times: For These Times* (London, Bradbury and Evans, 1854).

10.1126/science.aag2776

Edited by **Jennifer Sills**

Deciphering P *values: Beware false certainty*

IN HIS POLICY Forum "Aligning statistical and scientific reasoning" (*3* June, p. 1180), S. N. Goodman discussed a recent statement by the American Statistical Association highlighting the persistent misapplication of the *P* value and its meaning in the scientific community (*1*). Statistical misinterpretations in science also undermine the development of robust evidenced-based policy and management [e.g., (*2*, *3*)].

Findings of nonsignificance, in the absence of context, may lead to a false certainty that no impact occurs (*4*, *5*). In the field of ecology, false certainty that a human activity (e.g., release of nutrients, heavy metals, or novel compounds) has no effect on species could lead to planning decisions that cause adverse species interactions (*6*) False certainty that a recently arrived invader is "safe" and unlikely to cause harm could lead to the degradation of ecosystems (*3*, *7*).

Goodman suggests that scientists combine the use of *P* values with context to establish more robust thresholds. The appropriate use and reporting of a priori and post hoc power analyses will provide relevant context to a *P* value (*2*, *3*, *5*, *6*). Editors should require authors to provide such context. Nonsignificant tests should be clearly identified as inconclusive; they cannot shed light on impact or effect where power is unduly low (*8*). Moreover, nonsignificant findings should be published only when accompanied by associated analyses of power, particularly for small effect size or small sample sizes (*5*). We must communicate clearly to policy-makers that the absence of evidence of impact is not equivalent to the absence of impact.

Chad L. Hewitt,[1] Marnie L. Campbell,[1] Alisha Dahlstrom Davidson,[2]

[1]University of Waikato, Hamilton, 3240, New Zealand. [2]Wayne State University, Detroit, MI 48202, USA.

*Corresponding author. Email: chewitt@waikato.ac.nz

REFERENCES

1. R. L. Wasserstein, N. A. Lazar, *Am. Stat.* 10.1080/00031305.2016.1154108 (2016).
2. B. D Mapstone, *Ecol. Appl.* **5**, 401 (1995).
3. A. D. Davidson, C. L. Hewitt, *Biol. Inv.* **16**, 1165 (2014).
4. T. Page, *Ecol. Law. Q.* **7**, 207 (1978).
5. P. G. Fairweather, *Mar. Freshw. Res.* **42**, 555 (1991).
6. J. Weinberg *et al.*, *Mar. Biol.* **93**, 305 (1986).
7. D. Simberloff *et al.*, *Nature* **475**, 36 (2011).
8. J. Hayes, *Ecotoxicol. Environ. Safety* **14**, 73 (1987).

10.1126/science.aag3065

One or two replications of a study result cannot definitively support or reject a hypothesis.

Deciphering P *values: Defining significance*

IN HIS POLICY Forum "Aligning statistical and scientific reasoning" (*3* June, p. 1180), S. N. Goodman cautions against using *P* values to determine statistical significance in the absence of context, but he does not adequately define significance level, *P* value, and hypothesis.

Significance level is decided before the test; it is the confidence the researcher deems necessary to reject the null hypothesis. The *P* value emerges from the test and (along with other evidence, as Goodman rightly notes) serves as a tool to make and interpret the statistical decision.

A well-stated hypothesis describes a state of nature. It is either true or not true, not subject to probability. The phrase "probability the hypothesis is true" is meaningless. One can only say, "likelihood that the observed data came from a population characterized by the hypothesis."

Statistical inference was the 20th century's greatest contribution to epistemology. But all it means is that if one rejects a hypothesis at the 90% level, and if one were to repeat the test on 100 independent samples, then one would expect the same result approximately 90 times. Thus one or two replications, even conducted by different researchers, would not lead to firm knowledge.

Fred Phillips

Yuan Ze University, Zhongli District, Taoyuan City, 32003, Taiwan and Stony Brook University, New York, NY 11794, USA.
Email: fred.phillips@stonybrook.edu

10.1126/science.aah4157

Expanding protected areas is not enough

THE CONVENTION ON Biological Diversity (CBD) Aichi Target 11 calls for a substantial expansion in terrestrial and marine protected areas by 2020, but the change may not be sufficient to meet its intended conservation goals. Although protected areas can be effective conservation tools (*1*), many fail to halt species decline (*2*).

All global and local conservation decisions must be underpinned by comprehensive and strategic evaluation of the tangible benefits of protected areas for species conservation. Such an evaluation system must be targeted, institutionally embedded, and scientifically credible (with controls, counterfactuals, replication, and standard methods). It will

require a large initial investment and incur ongoing costs, but the longer we wait to implement it, the more information we will irretrievably lose. The Strategy for Resource Mobilization of the CBD can help to create financial pathways toward this goal.

With better data, we can determine the effectiveness of protected areas and make better decisions (*3*). In the meantime, the conservation community should demand that biodiversity, not proxies such as area, be explicitly embedded into the realization of Target 11 beyond 2020.

Aliénor L. M. Chauvenet[1]* and Megan Barnes[1,2]

[1]ARC Centre of Excellence for Environmental Decisions, University of Queensland, St. Lucia, QLD 4072, Australia. [2]School of Natural Resources and Environmental Management, University of Hawaii at Manoa, Honolulu, HI 96822, USA.

*Corresponding author. Email: a.chauvenet@uq.edu.au

REFERENCES

1. M. Hoffmann *et al.*, *Science* **330**, 1503 (2010).
2. J. Geldmann *et al.*, *Biol. Cons.* **161**, 230 (2013).
3. P. J. Ferraro, S. K. Pattanayak, *PLOS Biol.* **4**, e105 (2006).

10.1126/science.aah3762

TECHNICAL COMMENT ABSTRACTS

Comment on "Open-ocean fish reveal an omnidirectional solution to camouflage in polarized environments"

Thomas W. Cronin, Yakir Luc Gagnon, Sönke Johnsen, N. Justin Marshall, Nicholas W. Roberts

Brady *et al.* (Reports, 20 November 2015, p. 965) claimed that the silvery sides of certain fish are cryptic when viewed by animals with polarization sensitivity, which they termed "polarocrypsis." After examining their evidence, we find this claim to be unsupported due to (i) pseudoreplication, (ii) confounding polarization contrast with intensity contrast, and (iii) measurements taken at very shallow depths.

Full text at http://dx.doi.org/10.1126/science.aaf4481

Response to Comment on "Open-ocean fish reveal an omnidirectional solution to camouflage in polarized environments"

Parrish Brady, Alex Gilerson, George Kattawar, Jim Sullivan, Mike Twardowski, Heidi Dierssen, Molly Cummings

Cronin *et al.* take issue with our evidence for polarocryptic carangid fish based on concerns of pseudoreplication, our contrast metric, and habitat. We clarify (i) the importance of camouflage in near-surface open-ocean environments and (ii) the use of a Stokes contrast metric and further (iii) conduct individual-based statistics on our data set to confirm the reported polarocrypsis patterns.

Full text at http://dx.doi.org/10.1126/science.aaf4481

ERRATA

Erratum for the Research Article "The TopoVIB-Like protein family is required for meiotic DNA double-strand break formation"

by T. Robert *et al.*, *Science* **352**, aaf9649 (2016). Published online 6 May 2016; 10.1126/science.aaf9649

Erratum for the Report "Network of epistatic interactions within a yeast snoRNA"

by O. Puchta *et al.*, *Science* **352**, aaf9112 (2016). Published online 6 May 2016; 10.1126/science.aaf9112

TECHNICAL COMMENT

CAMOUFLAGE

Comment on "Open-ocean fish reveal an omnidirectional solution to camouflage in polarized environments"

Thomas W. Cronin,[1]*† Yakir Luc Gagnon,[2] Sönke Johnsen,[3] N. Justin Marshall,[2] Nicholas W. Roberts[4]

Brady *et al*. (Reports, 20 November 2015, p. 965) claimed that the silvery sides of certain fish are cryptic when viewed by animals with polarization sensitivity, which they termed "polarocrypsis." After examining their evidence, we find this claim to be unsupported due to (i) pseudoreplication, (ii) confounding polarization contrast with intensity contrast, and (iii) measurements taken at very shallow depths.

It has long been hypothesized that a major function of polarization vision is to heighten the visibility of objects in scattering media, such as water. A Report by Brady *et al.* (*1*) concludes that marine silvery fish have evolved to reduce their visibility to such vision, an adaptation the authors call "polarocrypsis." We have a number of concerns about this study but focus here on three equally important critical ones.

First, the statistics throughout much of (*1*) are confounded by high levels of pseudoreplication. As one example, figure 2A in (*1*) reports an N of 1183 for bigeye scad (*Selar crumenophthalmus*), but the supplementary materials show that these are 1183 photos taken of only five individual fish (leading to P values as low as 10^{-24}). By using an N value of 1183, the authors are not testing whether the bigeye scad, or even a population of it, shows "polarocrypsis" but whether this group of five individual fish do (*2*, *3*). Although these few fish may possibly be representative of the species, multiple measurements on a single animal are not statistically independent and cannot be treated as such. The situation is similar or worse for the other examined species. The 200 photos of the lookdown (*Selene vomer*) were from six fish, the 77 photos of the ballyhoo were from two fish, and the 42 and 33 photos of the bar jack, and almaco jack were from one fish each. To support the conclusions of the Report, we argue that the correct values of N for each species should be 5, 6, 2, 1, and 1. Following this argument, few if any of the results would prove significant if the correct number of degrees of freedom were used, because the effect sizes in figures 2 and 3 in (*1*) are typically quite small relative to the variances.

Second, the metric W_s used to assess contrast, termed "Stokes contrast" in (*1*), includes intensity information as well as polarization information and is thus inappropriate for judging the contrast of the polarization component of the signal. From the supplementary materials for (*1*)

$$W_s = \frac{\sqrt{(I_o - I_b)^2 + \frac{1}{2}(Q_o - Q_b)^2 + \frac{1}{2}(U_o - U_b)^2}}{I_b}$$

where I, Q, and U are the first three Stokes parameters, I being the intensity, and Q and U comprising the linear polarization information. Although polarization-sensitive animals do likely combine intensity and polarization information in their visual processing (*4*), including intensity information in the contrast metric makes it difficult to assess whether the results are driven by the presence of "polarocrypsis," as the authors state, or by intensity contrast. Critically, the data shown in figures S4 to S6 in (*1*) paint a more complex and revealing picture than what is shown in (*1*) (see our Fig. 1). Again using bigeye scad as an example, figure S4A from (*1*), which considers only intensity, shows the pattern seen in the main text's figure 2 that displays Stokes contrast, where the fish have a lower contrast than the mirror. However, figures S5A and S6A from (*1*), which examine the purely polarization measures Q and U respectively, show the opposite pattern: The fish have a greater contrast than the mirror. Because Q and U are the actual polarization parameters, this suggests that the pattern seen in figure 2A of the main text is driven by intensity contrast, not polarization contrast. So, even if the results were significant, which we argue against in the above text, they show that bigeye scad are actually more visible to polarization vision than the mirror, rather than less visible. In addition, the effect sizes using any of the forms of contrast are small, and the average intensity contrast of the bigeye scad is high—0.352 (table S3 from Brady *et al.*). The minimum contrast threshold of aquatic species in bright-light conditions is typically ~0.02 (*4*). Therefore, based on well-established equations of contrast attenuation (*5*) and the clarity of oceanic water, the scad would be visible at distances on the order of 20 m. Thus, crypsis relative to polarization vision, if it existed, would be irrelevant because the fish are already highly visible due to their brightness contrast alone.

Third, although the silvery species examined were marine fishes that occupy a range of depths,

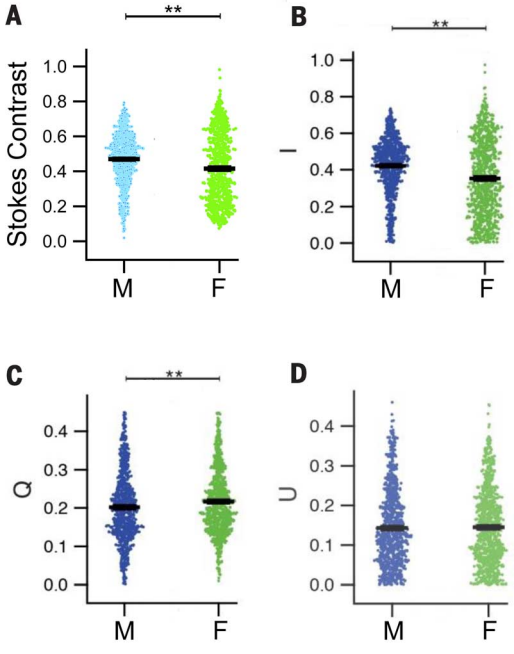

Fig. 1. A compilation of figures adapted from Brady *et al*. We do not include the diffuse mirror results for clarity. (**A**) Figure 2A from (*1*), which shows that the Stokes contrast W_s is less for the bigeye scad (F) than for the mirror (M). (**B**) Figure S4A from (*1*), which shows that the intensity contrast of the bigeye scad is also less than that of the mirror. (**C** and **D**) Figures S5A and S6A, which show that contrasts based on Q and U, the actual polarization parameters, are greater for the bigeye scad than for the mirror (7% and 2% greater based on tables S4 and S5). Together, (B) to (D) suggest that the pattern shown in figure 2A of Brady *et al*. is driven by intensity contrast rather than polarization contrast. $^{**}P << 0.01$, based on the statistics used in (*1*).

[1]Department of Biological Sciences, University of Maryland, Baltimore, MD 21250, USA. [2]Queensland Brain Institute, University of Queensland, Brisbane St Lucia, QLD 4072, Australia. [3]Biology Department, Duke University, Durham, NC 27708, USA. [4]School of Biological Sciences, University of Bristol, Bristol, BS8 1TQ, UK.
*Corresponding author. Email: cronin@umbc.edu †Authors are listed in alphabetical order.

the work in (*1*) was done at depths of only two to four meters below the surface. Denton's pioneering work showed that the silvery sides of fish could indeed serve as excellent camouflage (*6*), but only in a simple and vertically symmetric light field. The light field in near-surface oceanic waters is anything but simple, being heavily influenced by the lensing of direct sunlight by waves, and thus varying rapidly over small temporal and spatial scales (*7*, *8*). In addition, unless the sun is near the zenith, the light field near the surface is far from symmetric, even under windless and waveless conditions (*9*). All this may explain why the intensity contrasts of the measured fish and mirrors were relatively high (*10*), as well as why the data have a very large range. Again, as mentioned above, any sort of crypsis relative to polarization vision is irrelevant in situations where the animals are easily seen using visual systems lacking any polarization sensitivity.

Thus, in conclusion, although we recognize that there may be circumstances where open-ocean fish face evolutionary pressures due to exposure to predation enhanced by polarization vision, we feel that the evidence presented by Brady *et al.* does not support the conclusion that open-ocean fish have evolved to become cryptic to animals with polarization sensitivity.

REFERENCES AND NOTES

1. P. C. Brady *et al.*, *Science* **350**, 965–969 (2015).
2. S. H. Hurlbert, *Ecol. Monogr.* **54**, 187–211 (1984).
3. S. H. Hurlbert, *J. Comp. Psychol.* **123**, 434–443 (2009).
4. T. W. Cronin, S. Johnsen, N. J. Marshall, E. J. Warrant, *Visual Ecology* (Princeton Press, 2014).
5. S. Q. Duntley, "The Visibility of Submerged Objects: Final Report to Office of Naval Research" (Office of Naval Research, 1952).
6. E. J. Denton, *Philos. Trans. R. Soc. London B Biol. Sci.* **258**, 285–313 (1970).
7. M. Darecki, D. Stramski, M. Sokolski, *J. Geophys. Res.* **116**, C00H09 (2011).
8. J. Dera, D. Stramski, *Oceanologia* **23**, 15–42 (1986).
9. S. Johnsen, E. Gassmann, R. A. Reynolds, D. Stramski, C. Mobley, *Limnol. Oceanogr.* **59**, 1839–1852 (2014).
10. S. Sabbah, S. M. Gray, C. W. Hawryshyn, *Limnol. Oceanogr.* **57**, 1025–1041 (2012).

ACKNOWLEDGMENTS

T.W.C., N.W.R., and N.J.M. are supported by the Air Force Office of Scientific Research, grant numbers FA9550-12-1-032 and FA8655-12-2112. N.J.M. is also supported by the Australian Research Council.

9 February 2016; accepted 20 June 2016
10.1126/science.aaf4481

TECHNICAL RESPONSE

CAMOUFLAGE

Response to Comment on "Open-ocean fish reveal an omnidirectional solution to camouflage in polarized environments"

Parrish Brady,[1] Alex Gilerson,[2] George Kattawar,[3] Jim Sullivan,[4] Mike Twardowski,[4] Heidi Dierssen,[5] Molly Cummings[1]*

Cronin *et al*. take issue with our evidence for polarocryptic carangid fish based on concerns of pseudoreplication, our contrast metric, and habitat. We clarify (i) the importance of camouflage in near-surface open ocean environments and (ii) the use of a Stokes contrast metric and further (iii) conduct individual-based statistics on our data set to confirm the reported polarocrypsis patterns.

In Brady *et al*. (*1*), we comprehensively measured the camouflage performance of live fish in one of the most dynamic optical environments on our planet (the near-surface epipelagic zone) by collecting polarization and intensity (or more appropriately, radiance) measurements from an unprecedented number of biologically relevant viewing angles. Cronin *et al*. have raised concerns about these inaugural field measures regarding the choice of habitat, employment of our Stokes contrast measure, and the possibility of pseudoreplication (*2*). We welcome the opportunity to answer these queries and hope that we provide greater clarification in the process.

First, we conducted our measurements at near surface depths (<4 m) because this represents an important ecological zone for predation in the ocean (*3*) and a region where camouflage for predators and prey is extremely challenging, given the dynamic variation in light polarization (*1*, *4*) and radiance (*5*). In deeper environments, the light field is more homogenous and the background polarization is much lower, making the physics of crypsis simpler. Our interests were in identifying camouflage processes in more complicated background light environments (e.g., with asymmetric background light fields), and our unprecedented approach provided the ability to evaluate crypsis performance in a comprehensive predator viewing space.

Reflective camouflage strategies had been previously proposed for ocean regions with homogenous light [mirrors (*6*)] or randomly scattering backgrounds [diffuse reflectors (*7*)], yet no reflective strategy had yet been formulated for the complex and dynamic optical fields of the near-surface pelagic environment. Using a specular mirror and silvery diffuse reflector as references, we found that fish matched the background light field better than either of these reflective surfaces. Using our automated platform, we collected measurements from a variety of viewing angles to evaluate whether fish minimize their contrast from viewing angles associated with predation more than other viewing angles. We found that in this heavy-predation zone, native open-ocean fish showed significantly lower contrast to the background at ecologically relevant predator pursuit viewing angles. We further identified the physiological mechanisms that afforded the enhancement in camouflage via microscopy and histology in the laboratory.

Second, we used a measure of camouflage that accounted for the visual sensitivities of many fish living in near-surface environments. Polarization sensitivity has been documented in six different families of fish, so we selected a measure of contrast that included both polarization and intensity components of the light field. Although behavior (*8*) and laboratory (*9*) studies have documented behavioral responses to polarization, the exact weighting of this sensory information relative to intensity components is not yet known in any vertebrate. Hence, we employed a conservative approach to evaluating the light field using Stokes contrast that includes both polarization and intensity, an approach that is similar to using Euclidian distance to evaluate conspicuousness with color and brightness quantities (*10*). In addition, we also report results for each component of the Stokes vector [*I*, *Q*, and *U*; for definitions, see (*1*)]. We found that fish

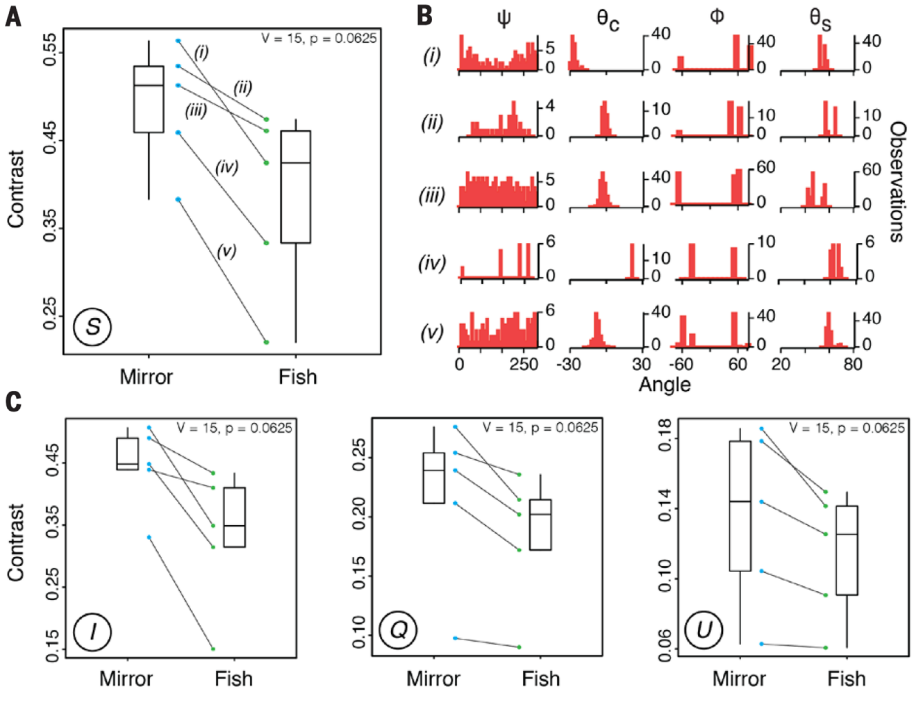

Fig. 1. Box plots of the contrast averages for five live carangid fish (from Brady *et al*.) with the largest series of measurements in chase angle conditions. (**A**) Stokes contrast averages between individual fish (labeled *i* to *v*) and mirror along with (**B**) histograms for specific angular parameters of the measurements pooled for each fish and mirror average shown in (A). We show in (**C**) the results for each linear Stokes elements *I*, *Q*, and *U*.

[1]Department of Integrative Biology, University of Texas, Austin, TX 78712, USA. [2]Optical Remote Sensing Laboratory, City College of New York–CUNY, New York, NY 10031, USA. [3]Department of Physics and Astronomy and Institute for Quantum Science and Engineering, Texas A&M University, College Station, TX 77843-4242, USA. [4]Harbor Branch Oceanographic Institute, Florida Atlantic University, Ft. Pierce, FL 34946, USA. [5]Department of Marine Sciences, University of Connecticut Avery Point, 1080 Shennecossett Road, Groton, CT 06340-6048, USA.
*Corresponding author. Email: mcummings@austin.utexas.edu

minimize contrast across each of these components for predator pursuit angles. Our results suggest that fish have evolved a means to minimize contrast in this complex environment with predators that have either simple (intensity only) or complex (polarization and intensity) visual sensitivities.

Finally, we address the pseudoreplication concern of Cronin *et al*. The issue of pseudoreplication involves careful attention to relevant number of sampling units. In our study (*1*), we collected angular viewing measurement series from 11 open-ocean carangid fish [5 bigeye scad (*Selar crumenophthalmus*), 6 lookdown (*Selene vomer*)], and we extensively analyzed the data set from a number of different "sampling unit" scales—from all angles [figure 2 in (*1*)], from discrete bins of viewing angles [figure. 3 in (*1*)], and from individual viewing angles [figure 4 and figure S3 in (*1*)], with each viewing condition representing a unique optical backdrop due to the angular dependence of intensity and polarization. Inspired by Cronin *et al*., we now also evaluate the data set at the level of individual fish (see Fig. 1). When we calculate an average contrast from each of these 11 fish across all of their angular measurements, we find significant reduction in Stokes contrast relative to mirrors (Wilcoxon signed rank test at all angles: $N = 11$, $V = 55$, $P = 0.054$; chase angles: $V = 56$, $P = 0.042$). Furthermore, when we limit our examination to the five carangid fish with sufficiently large range of viewing angle measurements (ranging from 15 to 160 measurements in chase angles), we still find the same pattern of a reduction in Stokes contrast, as well as in each of the Stokes contrast elements (see Fig. 1). This individual-based analysis reveals the same pattern of improved fish crypsis (reduction in contrast) at ecologically relevant viewing angles as all of our different levels of angular comparisons from Brady *et al*. 2015 [see figures 2 to 4 and figures S3 to S6 in (*1*)], highlighting that our results are robust under a variety of statistical approaches.

Given the angular dependence of crypsis in the open ocean, we contend that it is vitally important to consider all levels of measurement sampling and direct specific attention to the unique viewing configurations that are relevant for the species of interest. Pooling all our angular measurements for each individual fish informs the reader that this is a consistent finding within these species, whereas our different angular analyses inform the reader of exactly which viewing angles carangid fish perform exceptionally well at camouflage and for which viewing angles they do not. We hope that these measurements will inspire others to investigate the complexity of any environment and incorporate angle-specific structure into their measurements to gain a more accurate picture as to how animals interact and survive within their unique optical worlds.

REFERENCES AND NOTES

1. P. C. Brady *et al*., *Science* **350**, 965–969 (2015).
2. T. W. Cronin, Y. L. Gagnon, S. Johnsen, N. J. Marshall, N. W. Roberts, *Science* **353**, 552 (2016).
3. J. K. Parrish, *Environ. Biol. Fishes* **34**, 257–263 (1992).
4. P. C. Brady, K. A. Travis, T. Maginnis, M. E. Cummings, *Proc. Natl. Acad. Sci. U.S.A.* **110**, 9764–9769 (2013).
5. S. Johnsen, E. Gassmann, R. A. Reynolds, D. Stramski, C. Mobley, *Limnol. Oceanogr.* **59**, 1839–1852 (2014).
6. E. J. Denton, *Philos. Trans. R. Soc. London B Biol. Sci.* **258**, 285–313 (1970).
7. N. W. Pankhurst, J. N. Lythgoe, *J. Fish Biol.* **21**, 279–296 (1982).
8. G. M. Calabrese, P. C. Brady, V. Gruev, M. E. Cummings, *Proc. Natl. Acad. Sci. U.S.A.* **111**, 13397–13402 (2014).
9. M. Kamermans, C. Hawryshyn, *Philos. Trans. R. Soc. London B Biol. Sci.* **366**, 742–756 (2011).
10. M. E. Maan, M. E. Cummings, *Am. Nat.* **179**, E1–E14 (2012).

ACKNOWLEDGMENTS

This research was supported by an Office of Naval Research Multi-University Research Initiative grant (N000140911054) to M.C., H.D., J.S., A.G., and G.K. and NSF-OCE (1130793) to M.C. and G.K..

15 March 2016; accepted 20 June 2016
10.1126/science.aaf5018

RESEARCH

Exotic fermions in solid-state systems

Bradlyn et al., *p. 558*

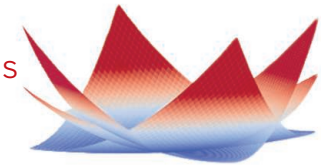

IN *SCIENCE* JOURNALS

Edited by **Caroline Ash**

Delays in asylum processing harm employment prospects and subsequent integration.

SOCIAL SCIENCES

Asylum delay reduces employment

The current refugee crisis calls for better understanding of how refugees integrate into life in a host country. A key element of integration is finding paid work. Hainmueller *et al.* found consistently that refugees across categories and origins who had to wait an additional year for the host government's asylum decision subsequently had difficulty finding employment. This finding is consistent with a pattern in which refugees whose asylum applications are slow become psychologically discouraged. Thus, speeding up asylum processing would appear to be a sensible policy for unlocking the economic potential of vulnerable people. —NTK

Sci. Adv. 10.1126.sciadv.1600432 (2016).

SHAPE-MEMORY ALLOYS

Bend it, shape it, remember it

Shape-memory alloys have the useful property of returning to their original shape after being greatly deformed. This process depends on the collective behavior of many small mineral grains in the metal. Using three-dimensional x-ray diffraction, Sedmák *et al*. tracked over 15,000 grains in a nickel-titanium shape-memory alloy as it moved through this transformation, thus linking microscopic changes to the bulk deformation. —BG

Science, this issue p. 559

ARCHAEOLOGY

Flood control initiates Chinese civilization

Around four millennia ago, Emperor Yu the Great succeeded in controlling a huge flood in the Yellow River basin. This is considered to have led to the establishment of the Xia dynasty and the start of Chinese civilization. However, the dates of the events and the links between them have remained uncertain and controversial. Using stratigraphic data and radiocarbon dating, Wu *et al*. verify that the flood occurred and place the start of the Xia dynasty at about 1900 BC, thus reconciling the historical and archaeological chronologies (see the Perspective by Montgomery). —AMS

Science, this issue p. 579; see also p. 538

Flood control marked the start of the Xia dynasty.

MOLECULAR IMAGING

Spatial organization inside the nucleus

In eukaryotic cells, DNA is packaged into a complex macromolecular structure called chromatin. Wang *et al.* have developed an imaging method to map the position of multiple regions on individual chromosomes, and the results confirm that chromatin is organized into large contact domains called TADS (topologically associating domains). Unexpectedly, though, folding deviates from the classical fractal-globule model at large length scales. —VV

Science, this issue p. 598

PREGNANCY

A monofilament stitch in time

Cervical cerclage, a procedure that uses a suture to reinforce the cervical opening, is frequently used to reduce the risk of preterm delivery. A clinical study by Kindinger *et al*. shows that using a braided suture for cerclage is associated with a higher risk of preterm birth and intrauterine death than using a monofilament suture. The braided suture is more conducive to bacterial colonization, which results in vaginal dysbiosis and inflammation, helping to explain the clinical findings. —YN

Sci. Transl. Med. **8**, 350ra102 (2016).

Published by AAAS

INFECTIOUS DISEASE

Setting the stage for HIV vaccines

Some HIV-infected individuals produce broadly neutralizing antibodies that can target multiple HIV strains. Moody *et al.* found that broadly neutralizing antibody production is associated with a higher frequently of autoantibodies, fewer regulatory T cells, and more circulating memory T follicular helper cells. Vaccine protocols that can mimic these immune perturbations may therefore promote better immune responses to HIV. —ACC

Sci. Immunol. 10.1126/sciimmunol.aag0851 (2016).

BIOMINERALIZATION

Recognition before nucleation

Some algae have evolved a remarkable ability to grow ornate crystalline structures called coccoliths. These structures consist of an organic base plate and complex calcium carbonate minerals spreading outward. Gal *et al*. found that the algae control site-specific mineralization, not by interactions between the base plate and the growing mineral edge, but by directing large amounts of calcium to the base plate. Recognition between two organic constituents determines when and where crystal nucleation will take place. —NW

Science, this issue p. 590

AXONAL DEGENERATION

Axonal pathology and necroptosis in ALS

Necroptosis, a non–caspase-dependent form of cell death, can be reduced in disease states by inhibiting a kinase called RIPK1. Until now, no human mutations have been linked to necroptosis. Ito *et al*. show that loss of optineurin, which is encoded by a gene that has been implicated in the human neurodegenerative disorder ALS (amyotrophic lateral sclerosis), results in sensitivity to necroptosis and axonal degeneration. When RIPK1-kinase dependent signaling is disrupted in mice that lack optineurin, necroptosis is inhibited and axonal pathology is reversed. —SMH

Science, this issue p. 603

GRAPHENE

Teasing out chirality in graphene

A chiral elementary particle has its spin pointing in either the same or the opposite direction as its momentum. In graphene, electrons have an analogous chirality, but observing it in electrical transport experiments is tricky. To do this, Wallbank *et al*. studied how electrons tunnel between two slightly misaligned graphene sheets separated by a layer of insulating hexagonal boron nitride. The chiral nature of the electrons imposed restrictions on the tunneling, which made it possible to discern the signatures of chirality in the data. —JS

Science, this issue p. 575

CATALYSIS

Membranes to make benzene from methane

Methane gas is expensive to ship. It is usually converted into carbon monoxide and hydrogen and then liquefied. This is economically feasible only on very large scales. Hence, methane produced in small amounts at remote locations is either burned or not extracted. A promising alternative is conversion to benzene and hydrogen with molybdenum-zeolite catalysts. Unfortunately, these catalysts deactivate because of carbon buildup; plus, hydrogen has to be removed to drive the reaction forward. Morejudo *et al*. address both of these problems with a solid-state $BaZrO_3$ membrane reactor that electrochemically removes hydrogen and supplies oxygen to suppress carbon buildup. —PDS

Science, this issue p. 563

IN OTHER JOURNALS

Edited by **Kristen Mueller** *and* **Jesse Smith**

Resistance of *Shigella* bacteria to antibiotics is a growing problem.

INFECTIOUS DISEASES

How antibiotic resistance spreads

Shigella bacteria cause diarrheal illnesses in about 125 million people each year, particularly in developing countries. Antibiotics are widely used to prevent complications and reduce spreading of the disease, but resistance to the antibiotic ciprofloxacin is an increasing problem. The *et al.* report whole-genome sequencing of 60 ciprofloxacin-resistant *S. sonnei* bacteria from Vietnam, Bhutan, Thailand, Cambodia, Australia, and Ireland. They show that the bacteria all belong to the same lineage, one that probably originated in South Asia. This lineage emerged in a single clonal event and has since spread widely across Asia and beyond. —JFU

PLOS Med. 10.1371/journal.pmed.1002055 (2016).

NEUROIMMUNOLOGY

Neural inputs shape gut immunity

Immune cells called innate lymphoid cells (ILCs) are important peacekeepers in the gut. For instance, they help prevent microbial contents from leaking through the intestinal epithelial barrier. Ibiza *et al*. now report that, at least in mice, ILCs carry out this function with the aid of neural inputs. They found that ILCs express an enzyme on their surface called RET that responds to proteins secreted by glial cells in the gut. Mice engineered to lack RET expression in ILCs secreted less interleukin-22, a protein that promotes gut epithelial integrity, and fared worse in an experimental colitis model or when infected with the enteric pathogen *Citrobacter rodentium*. Thus, a multitissue defense unit helps defend the complex microenvironment of the gut. —KLM

Nature **535**, 440 (2016).

ROCK MECHANICS

Printing out the pores

The diversity of three-dimensional (3D) printing applications now includes fabricating porous rocks. The organization of pore space in rocks strongly influences

PHOTO: SCIENCE SOURCE

ALSO IN *SCIENCE* JOURNALS

Edited by **Caroline Ash**

CRISPR EVOLUTION

The CRISPR-Cas evolutionary mix

Prokaryotes are under a constant barrage of viruses and parasitic DNA. Many bacteria have adaptive immune systems called CRISPR-Cas that protect them from this onslaught. Although the underlying mechanism of CRISPR-Cas–based immunity is similar among prokaryote species, there are many variants. Mohanraju *et al*. review the common themes and the many differences in the basic structure and function of the CRISPR loci and associated effector Cas proteins. Abudayyeh *et al*. present an interesting version of a class 2 CRISPR-Cas single effector that appears to target single-stranded RNA viruses of bacteria and that could be valuably exploited for a range of biotechnological tools. —GR and LMZ

Science, this issue p. 556, p. 557

NANOMATERIALS

Long-life excimer-like structures

Metal quantum clusters have ideal properties for medical applications such as imaging. The challenge is to prolong their transient properties for the fabrication of useful devices. Santiago-Gonzalez *et al*. arranged gold clusters in a supramolecular lattice held together by hydrogen bonding and showed that this material can be used for imaging of fibroblast cells. In the superstructure, the gold molecules can come together in the excited state as excimers and then dissociate to emit radiation. Because they are within a lattice, this behavior shows long-term stability. Furthermore, the lattice superstructure scavenges reactive oxygen species and reduces cell damage. —MSL

Science, this issue p. 571

BIOENGINEERING

Xenobiotics to the rescue

Contaminating microorganisms can be highly detrimental to the large-scale fermentation of complex low-cost feedstocks, such as sugarcane or dry-milled corn for biofuels or other industrial purposes. The challenge is that foreign organisms have to be inhibited without using antibiotics because of concerns about spreading antibiotic resistance. Shaw *et al*. engineered bacteria and yeast to use rare compounds as sources of nutrients (see the Perspective by Lennen). Engineering the common biocatalyst *Escherichia coli,* for example, to consume melamine as a nitrogen source allowed it to outcompete contaminating organisms. Similarly, engineering yeast to use cyanamide for nitrogen or phosphite for phosphorus also improved competitive fitness. —NW

Science, this issue p. 583; see also p. 542

TOPOLOGICAL MATTER

Classifying the crystalline fermionic zoo

Elementary particles must obey the rules and symmetries of free space, unless, it turns out, they reside in a periodic crystal lattice. This periodicity can enhance variety among the resident fermionic species. Bradlyn *et al*. classify fermionic quasiparticles in a class of materials called semimetals and examine their topological properties (see the Perspective by Beenakker). In addition to the well-characterized Dirac, Majorana, and Weyl fermions, which can "live" in free space, crystal-space group symmetries allow other types of fermions to exist. Calculations indicate that these fermion types occur near the Fermi levels of known crystals, which bodes well for their experimental observation. —JS

Science, this issue p. 558; see also p. 539

ANALYTICAL METHODS

Watching batteries fail

Rechargeable batteries lose capacity in part because of physical changes in the electrodes caused by electrochemical cycling. Lim *et al*. track the reaction dynamics of an electrode material, $LiFePO_4$, by measuring the relative concentrations of Fe(II) and Fe(III) in it by means of high-resolution x-ray absorption spectrometry (see the Perspective by Schougaard). The exchange current density is then mapped for Li^+ insertion and removal. At fast cycling rates, solid solutions form as Li^+ is removed and inserted. However, at slow cycling rates, nanoscale phase separation occurs within battery particles, which eventually shortens battery life. —MSL

Science, this issue p. 566; see also p. 543

PLANT SCIENCE

Searching for the Sun

The growth of immature sunflower plants tracks the Sun's movement. The young plants lean westward as the day progresses but reorient to the east each night. As the flowers mature and open, they settle into a stable east-facing orientation. Atamian *et al*. show how circadian rhythms regulate the east-west elongation of cells in the young plants' stems (see the Perspective by Briggs). They show that eastward-oriented flowers are warmer than westward-oriented flowers, and this warmth attracts pollinators. Auxin signaling pathways in the stem coordinate to fix the eastward orientation of the mature plant. —PJH

Science, this issue p. 587; see also p. 541

NEUROSCIENCE

From channel mutation to neuropathy

A child with progressive early-onset motor neuropathy has revealed the molecular key to this profound disability. Kahle *et al*. discovered a point mutation in the gene encoding the K^+-Cl^- transporter KCC3 in the patient's peripheral nervous system. The mutated transporter could not be inhibited by phosphorylation and remained constitutively active. Mice expressing KCC3 with the same mutation showed increased transporter activity and impaired locomotor function. —NRG

Sci. Signal. **9**, ra77 (2016).

STRUCTURAL BIOLOGY

Insights into proteasome inhibition

Proteasomes are large protein complexes that degrade and remove proteins to maintain proper cellular physiology and growth. Proteasomes are a validated target for anticancer therapy, but drug design has been hampered by poor understanding of how inhibitors interact with the active site. Schrader *et al*. succeeded in crystallizing various proteasome-inhibitor complexes. They subsequently obtained crystal structures for the native human proteasome and eight different inhibitor complexes at resolutions between 1.9 and 2.1 Å. The inhibitors sampled include drugs that are approved or in trial for cancer treatment. —VV

Science, this issue p. 594

their strength and fluid flow through them. Head and Vanorio constructed virtual 3D images of rocks by using x-ray tomography, which they followed with a series of pore microgeometry modifications and 3D printing of samples. Measurements of fluid flow through the samples brings deeper understanding to how processes such as mineral precipitation and compaction clog up the pore network. This technique helps reverse-engineer how rocks get their pore structure and offers a method for measuring flow properties through delicate samples. —BG

Geophys. Res. Lett. 10.1002/2016GL069334 (2016).

CANCER BIOLOGY

For metastasis, accessibility matters

Each year, over 200,000 people die of small cell lung cancer (SCLC). These tumors grow aggressively, and most patients are diagnosed after metastasis has already occurred. Denny *et al*. explored potential mechanisms driving metastasis of SCLC by studying a mouse model of the human disease. They conclude that primary tumor cells acquire a propensity to metastasize at least in part through large-scale remodeling of their chromatin state. The experiments revealed a large increase in chromatin accessibility in liver metastases compared with primary SCLC cells. This change correlated with increased expression of a transcription factor called NFIB, and binding sites for NFIB were enriched in the open regions of chromatin. Conceivably, these regions could help pinpoint genes required for metastasis. —PAK

Cell **166**, 328 (2016).

POLYMER CHEMISTRY

Reactive crystals have the edge

A recently reported strategy for making two-dimensional polymer crystals uses a rigid monomer with three photoreactive anthracene arms that polymerize through cycloaddition. Like the end groups of a linear polymer, the reactive anthracene edge groups should only be along the rim of the hexaprismatic crystals that form, and not on the faces. Zhao *et al*. show that this is indeed the case by decorating the edges of these two-dimensional crystals with a dye. A maleic anhydride derivatized with a BODIPY (boron-dipyrromethene) dye reacts with the crystals through a Diels-Alder reaction. The dye, which fluoresces in a wavelength range outside of that of the self-fluorescence of the crystal, is observed only on the edges. —PDS

J. Am. Chem. Soc. 10.1021/jacs.6b05456 (2016).

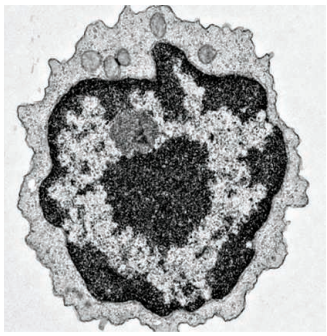

When activated, T lymphocytes increase their mitochondria, in both size and number.

METABOLISM

Activated T cells' mitochondria adapt

Proliferation of mitochondria provides not only a way for cells to increase the metabolic function of existing organelles but also an opportunity to adjust the mitochondria for specialized functions. Ron-Harel *et al*. quantified proteomic changes in the mitochondria of activated mouse CD4$^+$ T cells. To support rapid proliferation of the activated cells, new mitochondria showed an increased abundance of enzymes that participate in folate-mediated one-carbon metabolism. Blocking this pathway by depleting the mitochondrial serine hydroxymethyltransferase enzyme inhibited T cell proliferation and survival. Such remodeling of mitochondrial function, along with replication, may be an important step in how cells adapt to physiological or pathological stimuli. —LBR

Cell Metab. 10.1016/j.cmet.2016.06.007 (2016).

Oak tree in Big Sur, California affected by sudden oak death fungus

INVASIVE SPECIES

Tree pests and pathogens in North America

Global trade continually introduces alien species of insects and pathogens throughout the world, often with serious ecological and economic consequences. Lovett *et al*. analyzed information about the past 150 years of invading forest tree pests in the United States, documenting their means of arrival and their impacts on U.S. trees and forest ecosystems. They estimate that invasive insects continue to arrive in the United States at a rate of 2.5 species annually; of these, about 10% are the particularly damaging wood-boring insects. Pests typically arrive on live plants and in wooden packaging material. Policies for combating such invasions should include cleaning shipments before export and inspections, surveillance, quarantine, and eradication efforts upon entry. —AMS

Ecol. Appl. **26**, 1437 (2016).

REVIEW SUMMARY

CRISPR EVOLUTION

Diverse evolutionary roots and mechanistic variations of the CRISPR-Cas systems

Prarthana Mohanraju, Kira S. Makarova, Bernd Zetsche, Feng Zhang, Eugene V. Koonin, John van der Oost*

BACKGROUND: Prokaryotes have evolved multiple systems to combat invaders such as viruses and plasmids. Examples of such defense systems include receptor masking, restriction-modification (R-M) systems, DNA interference (Argonaute), bacteriophage exclusion (BREX or PGL), and abortive infection, all of which act in an innate, nonspecific manner. In addition, prokaryotes have evolved adaptive, heritable immune systems: clustered regularly interspaced palindromic repeats (CRISPR) and the CRISPR-associated proteins (CRISPR-Cas). Adaptive immunity is conferred by the integration of DNA sequences from an invading element into the CRISPR array (adaptation), which is transcribed into long pre-CRISPR RNAs (pre-crRNAs) and processed into short crRNAs (expression), which guide Cas proteins to specifically degrade the cognate DNA on subsequent exposures (interference).

ADVANCES: A plethora of distinct CRISPR-Cas systems are represented in genomes of most archaea and almost half of the bacteria. The latest CRISPR-Cas classification scheme delineates two classes that are each subdivided into three types. Integration of biochemistry and molecular genetics has contributed substantially to revealing many of the unique features of the variant CRISPR-Cas types. Additionally, structural analysis and single-molecule studies have further advanced our understanding of the molecular basis of CRISPR-Cas functionality. Recent progress includes relevant steps in the adaptation stage, when fragments of foreign DNA are processed and incorporated as new spacers into the CRISPR array. In addition, three novel CRISPR-Cas types (IV, V, and VI) have been identified, and in particular, the type V interference complexes have been experimentally characterized. Moreover, the ability to easily program sequence-specific DNA targeting and cleavage by CRISPR-Cas components, as demonstrated for Cas9 and Cpf1, allows for the application of CRISPR-Cas components as highly effective tools for genetic engineering and gene regulation in a wide range of eukaryotes and prokaryotes. The pressing issue of off-target cleavage by the Cas9 nuclease is being actively addressed using structure-guided engineering.

OUTLOOK: Although our understanding of the CRISPR-Cas system has increased tremendously over the past few years, much remains to be revealed. The continuing discovery of CRISPR-Cas variants will provide direct tests of the recently proposed modular scenario for the evolution of CRISPR-Cas systems. The recent discovery and characterization of new CRISPR-Cas types with previously unknown features implies that our current knowledge has relatively limited power for predicting the functional details of distantly related CRISPR-Cas variants. Hence, newly discovered CRISPR-Cas systems need to be dissected thoroughly to gain insight into their biological roles, to unravel their molecular mechanisms, and to harness their potential for biotechnology. Key outstanding questions regarding CRISPR-Cas biology include the ecological roles of microbial adaptive immunity, the high rates of CRISPR-Cas horizontal transfer, and the coevolution of CRISPR-Cas and phage-encoded anti-CRISPR proteins. Relatively little is known about the regulation of CRISPR-Cas expression, and about the roles of CRISPR-Cas in processes other than defense. With respect to the CRISPR-Cas mechanism, details illuminating the connection between the adaptation stage and the interference stage in primed spacer acquisition remain elusive. A key aspect of CRISPR-Cas that is poorly understood at present is self/nonself discrimination. The discrimination mechanisms seem to differ substantially among CRISPR variants. Recent comparison of class 2 type effector complexes (Cas9/Cpf1) has revealed overall architectural similarities as well as structural and mechanistic differences, as had previously been found for the distinct types of class 1 effector complexes (Cascade/Cmr). These variations may translate into complementary biotechnological applications. As well as innovative tools for basic research, CRISPR-associated effector complexes will be instrumental for developing the next generation of antiviral prophylactics and therapeutics. For applications in human gene therapy, improved methods for efficient and safe delivery of Cas9/Cpf1 and their guide RNAs to cells and tissues are still needed. Further insight into the basic details of CRISPR-Cas structure, functions, and biology—and characterization of new Cas effector proteins in particular—is crucial for optimizing and further expanding the diverse applications of CRISPR-Cas systems. ■

ON OUR WEBSITE

Read the full article at http://dx.doi.org/10.1126/science.aad5147

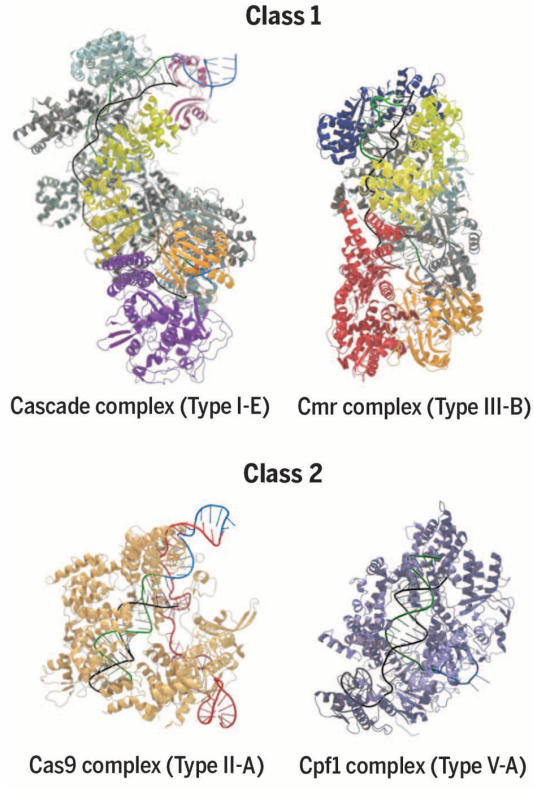

Evolution of CRISPR-Cas systems resulted in incredible structural and functional diversity. Class 1 CRISPR-Cas systems are considered to be the evolutionary ancestral systems. The class 2 systems have evolved from class 1 systems via the insertion of transposable elements encoding various nucleases, and are now being used as tools for genome editing.

The list of author affiliations is available in the full article online.
*Corresponding author. Email: john.vanderoost@wur.nl
Cite this article as P. Mohanraju *et al.*, *Science* 353, aad5147 (2016). DOI: 10.1126/science.aad5147

REVIEW

CRISPR EVOLUTION

Diverse evolutionary roots and mechanistic variations of the CRISPR-Cas systems

Prarthana Mohanraju,[1] Kira S. Makarova,[2] Bernd Zetsche,[3] Feng Zhang,[3] Eugene V. Koonin,[2] John van der Oost[1]*

Adaptive immunity had been long thought of as an exclusive feature of animals. However, the discovery of the CRISPR-Cas defense system, present in almost half of prokaryotic genomes, proves otherwise. Because of the everlasting parasite-host arms race, CRISPR-Cas has rapidly evolved through horizontal transfer of complete loci or individual modules, resulting in extreme structural and functional diversity. CRISPR-Cas systems are divided into two distinct classes that each consist of three types and multiple subtypes. We discuss recent advances in CRISPR-Cas research that reveal elaborate molecular mechanisms and provide for a plausible scenario of CRISPR-Cas evolution. We also briefly describe the latest developments of a wide range of CRISPR-based applications.

Bacteria and archaea suffer constant predation by viruses, which are extremely abundant in almost all environments (*1*). Accordingly, bacteria and archaea have evolved a wide range of antivirus defense mechanisms (*2*). Because viruses generally have high rates of mutation and recombination, they have the potential to rapidly escape these prokaryotic defense systems. Thus, the hosts' defenses must also adjust and evolve rapidly, leading to an ongoing virus-host arms race. Protective systems provide innate immunity at all stages of the parasite's infection cycle via receptor masking, restriction-modification (R-M) systems, DNA interference [prokaryotic Argonaute proteins protect the host against mobile genetic elements (MGEs) through DNA-guided DNA interference], bacteriophage exclusion (BREX systems allow phage adsorption but block phage DNA replication; PGL systems have been hypothesized to modify the phage progeny DNA to inhibit their growth upon reinfection), and abortive infection (*2*–*8*).

The innate immunity strategies are complemented by an adaptive immune function of the systems of prokaryotic clustered regularly interspaced short palindromic repeats (CRISPR) and the associated Cas proteins (*9*, *10*). Diverse variants of the CRISPR-Cas systems are present in the examined genomes of most archaea and almost half of the bacteria (*2*). Here, we discuss insights into the evolution and functionality of class 1 and class 2 CRISPR-Cas systems. This progress has enabled the development of sophisticated tools for genetic engineering in molecular biology, biotechnology, and molecular medicine.

CRISPR-Cas defense

The CRISPR-Cas systems provide protection against MGEs—in particular, viruses and plasmids—by sequence-specific targeting of foreign DNA or RNA (*9*, *11*–*15*). A CRISPR-*cas* locus generally consists of an operon of CRISPR-associated (*cas*) genes and a CRISPR array composed of a series of direct repeats interspaced by variable DNA sequences (known as spacers) (Fig. 1A). The repeat sequences and lengths as well as the number of repeats in CRISPR arrays vary broadly, but all arrays possess the characteristic arrangement of alternating repeat and spacer sequences. The spacers are key elements of adaptive immunity, as they store the "memory" of an organism's encounters with specific MGEs acquired as a result of a previous unsuccessful infection (*16*–*19*). This memory enables the recognition and neutralization of the invaders upon subsequent infections (*9*).

CRISPR-mediated adaptive immunity involves three steps: adaptation, expression, and interference (*14*, *20*–*23*) (Fig. 1B). During the adaptation step, fragments of foreign DNA (known as protospacers) from invading elements are processed and incorporated as new spacers into the CRISPR array. The expression step involves the transcription of the CRISPR array, which is followed by processing of the precursor transcript into mature CRISPR RNAs (crRNAs). The crRNAs are assembled with one or more Cas proteins into CRISPR ribonucleoprotein (crRNP) complexes. The interference step involves crRNA-directed cleavage of invading cognate virus or plasmid nucleic acids by Cas nucleases within the crRNP complex (*14*, *20*, *24*). The multifaceted and modular architecture of the CRISPR-Cas systems also allows it to play nondefense roles, such as biofilm formation, cell differentiation, and pathogenicity (*25*–*27*).

CRISPR-Cas diversity, classification, and evolution

The rapid evolution of highly diverse CRISPR-Cas systems is thought to be driven by the continuous arms race with the invading MGEs (*28*, *29*). The latest classification scheme for CRISPR-Cas systems, which takes into account the repertoire of *cas* genes and the sequence similarity between Cas proteins and the locus architecture, includes two classes that are currently subdivided into six types and 19 subtypes (*30*, *31*). The key feature of the organization and evolution of the CRISPR-Cas loci is their pronounced modularity. The module responsible for the adaptation step is largely uniform among the diverse CRISPR-Cas systems and consists of the *cas1* and *cas2* genes, both of which are essential for the acquisition of spacers. In many CRISPR-Cas variants, the adaptation module also includes the *cas4* gene. By contrast, the CRISPR-Cas effector module, which is involved in the maturation of the crRNAs as well as in target recognition and cleavage, shows a far greater versatility (Fig. 2A) (*30*).

The two classes of CRISPR-Cas systems differ fundamentally with respect to the organization of the effector module (*30*). Class 1 systems (including types I, III, and IV) are present in bacteria and archaea, and encompass effector complexes composed of four to seven Cas protein subunits in an uneven stoichiometry [e.g., the CRISPR-associated complex for antiviral defense (Cascade) of type I systems, and the Csm/Cmr complexes of type III systems]. Most of the subunits of the class 1 effector complexes—in particular, Cas5, Cas6, and Cas7—contain variants of the RNA-binding RRM (RNA recognition motif) domain (*32*, *33*). Although the sequence similarity between the individual subunits of type I and type III effector complexes is generally low, the complexes share strikingly similar overall architectures that suggest a common origin (*31*, *32*, *34*, *35*). The ancestral CRISPR-Cas effector complex most likely resembled the extant type III complexes, as indicated by the presence of the archetypal type III protein, the large Cas10 subunit, which appears to be an active enzyme of the DNA polymerase–nucleotide cyclase superfamily, unlike its inactive type I counterpart (Cas8) (*31*–*33*).

In the less common class 2 CRISPR-Cas systems (types II, V, and VI), which are almost completely restricted to bacteria, the effector complex is represented by a single multidomain protein (*30*). The best-characterized class 2 effector is Cas9 (type II), the RNA-dependent endonuclease that contains two unrelated nuclease domains, HNH and RuvC, that are responsible for the cleavage of the target and the displaced strand, respectively, in the crRNA–target DNA complex (*36*). The type II loci also encode a trans-acting CRISPR RNA (tracrRNA) that evolved from the corresponding CRISPR

[1]Laboratory of Microbiology, Department of Agrotechnology and Food Sciences, Wageningen University, 6703 HB Wageningen, Netherlands. [2]National Center for Biotechnology Information, National Library of Medicine, Bethesda, MD 20894, USA. [3]Broad Institute of MIT and Harvard, Cambridge, MA 02142, USA.
*Corresponding author. Email: john.vanderoost@wur.nl

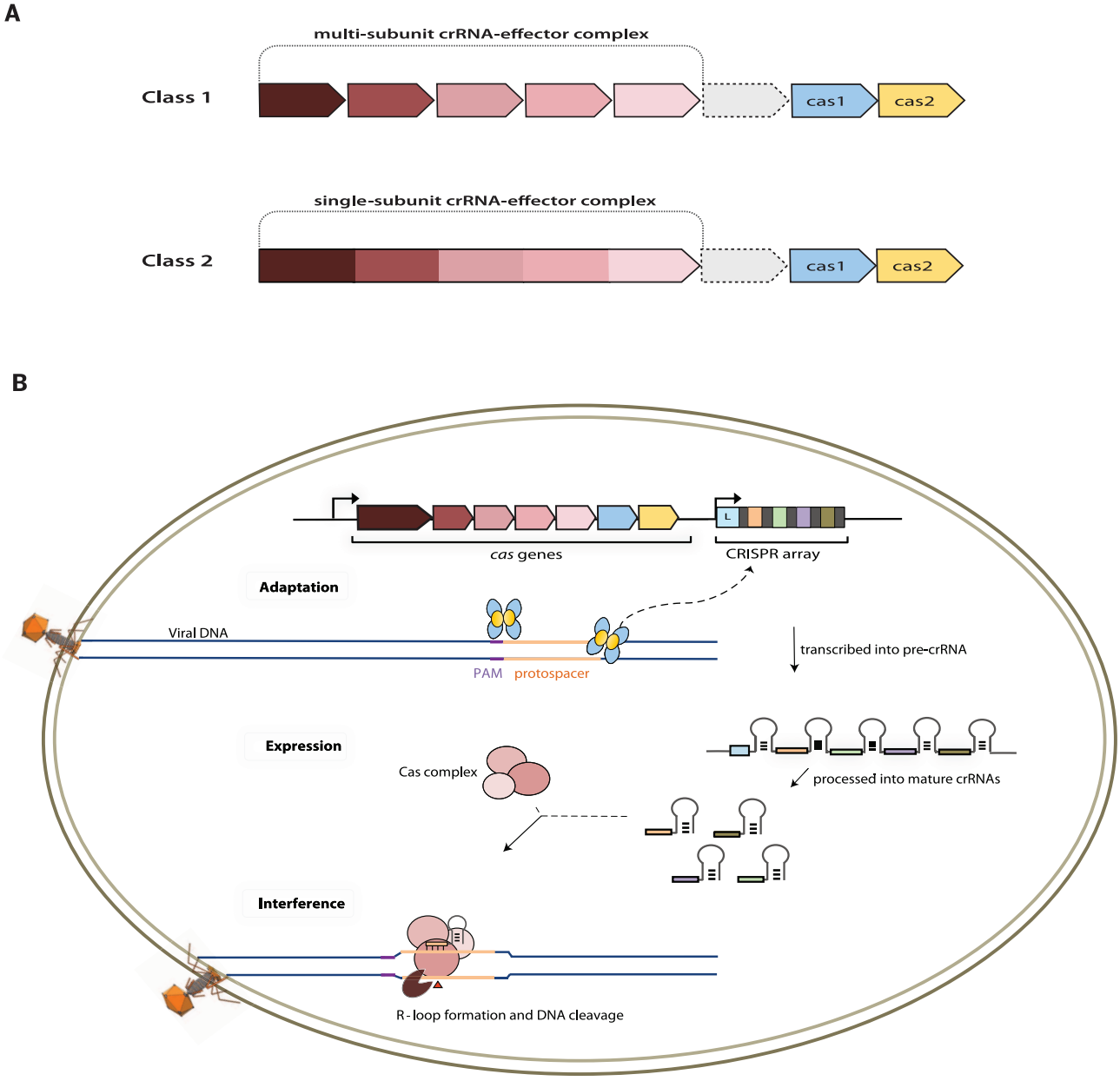

Fig. 1. Overview of the CRISPR-Cas systems. (**A**) Architecture of class 1 (multiprotein effector complexes) and class 2 (single-protein effector complexes) CRISPR-Cas systems. (**B**) CRISPR-Cas adaptive immunity is mediated by CRISPR RNAs (crRNAs) and Cas proteins, which form multicomponent CRISPR ribonucleoprotein (crRNP) complexes. The first stage is adaptation, which occurs upon entry of an invading mobile genetic element (in this case, a viral genome). Cas1 (blue) and Cas2 (yellow) proteins select and process the invading DNA, and thereafter, a protospacer (orange) is integrated as a new spacer at the leader end of the CRISPR array [repeat sequences (gray) that separate similar-sized, invader-derived spacers (multiple colors)]. During the second stage, expression, the CRISPR locus is transcribed and the pre-crRNA is processed into mature crRNA guides by Cas (e.g., Cas6) or non-Cas proteins (e.g., RNase III). During the final interference stage, the Cas-crRNA complex scans invading DNA for a complementary nucleic acid target, after which the target is degraded by a Cas nuclease.

repeat and is essential for pre-crRNA processing and target recognition in type II systems (*37*, *38*). The prototype type V effector Cpf1 (subtype V-A) contains only one nuclease domain (RuvC-like) that is identifiable by sequence analysis (*39*). However, analysis of the recently solved structure of Cpf1 complexed with the crRNA and target DNA has revealed a second nuclease domain, the fold of which is unrelated to HNH or any other known nucleases. In analogy to the HNH domain in Cas9, the novel nuclease domain in Cpf1 is inserted into the RuvC domain, and it is responsible for cleavage of the target strand (*40*).

Screening of microbial genomes and metagenomes for undiscovered class 2 systems (*31*) has resulted in the identification of three novel CRISPR-Cas variants. These include subtypes V-B and V-C, which resemble Cpf1 in that their predicted effector proteins contain a single, RuvC-like nuclease domain. Cleavage of target DNA by the type V-B effector, denoted C2c1, has been experimentally demonstrated (*31*). Type VI is unique in that its effector protein contains two conserved HEPN domains that possess ribonuclease (RNase) activity (Fig. 2A).

Recent comparative genomic analyses of variant CRISPR-Cas systems (Fig. 2B) (*31*) have revealed a strong modular evolution with multiple combinations of adaptation modules and

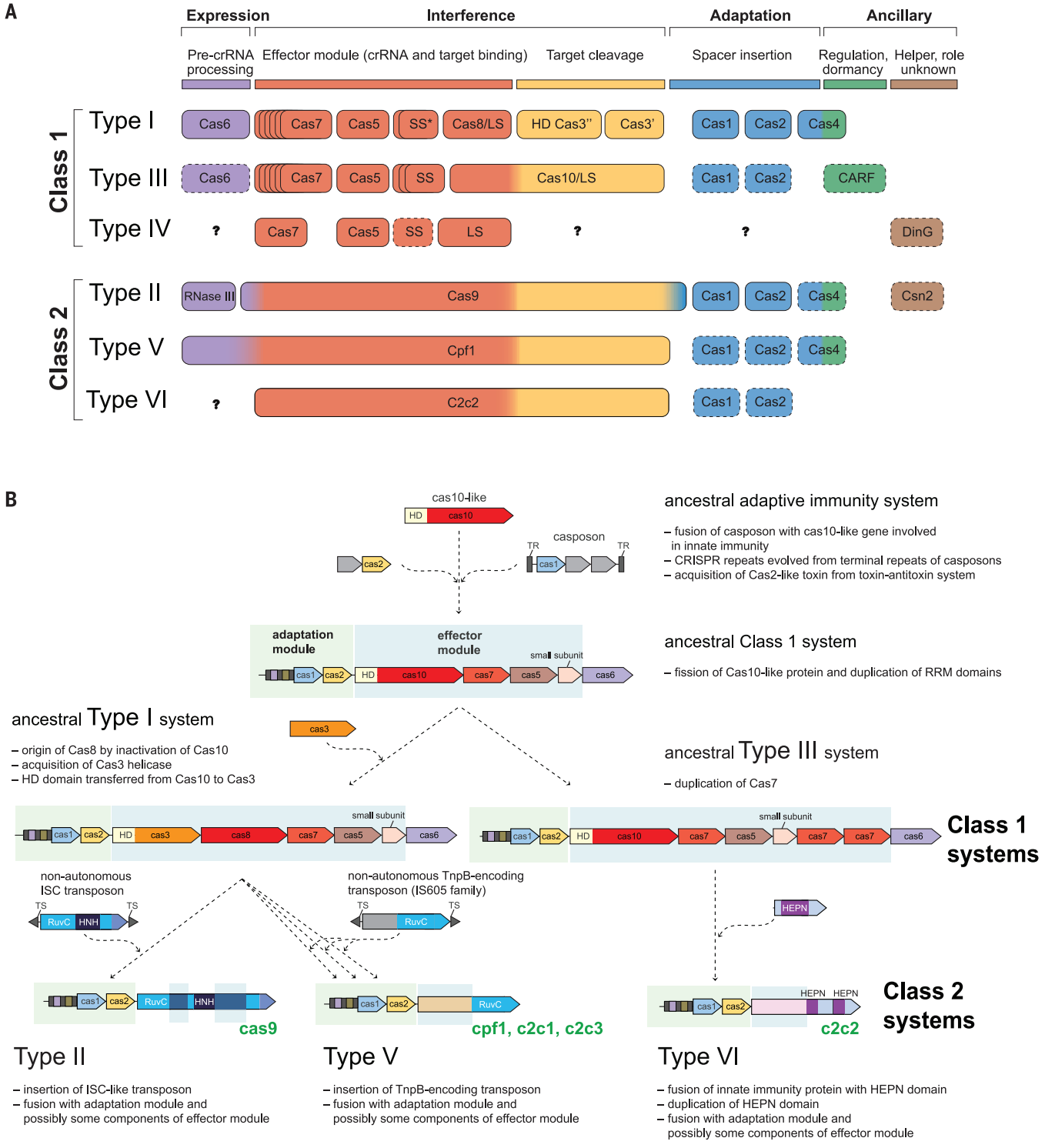

Fig. 2. CRISPR diversity and evolution. (**A**) Modular organization of the CRISPR-Cas systems. LS, large subunit; SS, small subunit. A putative small subunit that might be fused to the large subunit in several type I subtypes is indicated by an asterisk. Cas3 is shown as fusion of two distinct genes encoding the helicase Cas3′ and the nuclease HD Cas3″; in some type I systems, these domains are encoded by separate genes. Functionally dispensable components are indicated by dashed outlines. Cas6 is shown with a thin solid outline for type I because it is dispensable in some systems, and by a dashed line for type III because most systems lack this gene and use the Cas6 provided in trans by other CRISPR-Cas loci. The two colors for Cas4 and C2c2 and three colors for Cas9 and Cpf1 reflect the contributions of these proteins to different stages of the CRISPR-Cas response (see text). The question marks indicate currently unknown components. [Modified with permission from (*30*)] (**B**) Evolutionary scenario for the CRISPR-Cas systems. TR, terminal repeats; TS, terminal sequences; HD, HD-family endonuclease; HNH, HNH-family endonuclease; RuvC, RuvC-family endonuclease; HEPN, putative endoribonuclease of HEPN superfamily. Genes and portions of genes shown in gray denote sequences that are thought to have been encoded in the respective mobile elements but were eliminated in the course of evolution of CRISPR-Cas systems. [Modified with permission from (*31*)]

effector modules, as well as a pivotal contribution of mobile genetic elements to the origin and diversification of the CRISPR-Cas systems. The ancestral prokaryotic adaptive immune system could have emerged via the insertion of a casposon (a recently discovered distinct class of self-synthesizing transposons that appear to encode a Cas1 homolog) next to an innate immunity locus (probably consisting of genes encoding a Cas10 nuclease and possibly one or more RNA binding proteins). Apart from providing the Cas1 nuclease/integrase that is required for recombination during spacer acquisition (*41*–*43*), the casposon may also have contributed the prototype CRISPR repeat unit that could have evolved from one of the inverted terminal repeats of the casposon (*44*). An additional toxin-antitoxin module that inserted either in the ancestral casposon or in the evolving adaptive immunity locus probably provided the *cas2* gene, thus completing the adaptation module. The Cas10 nuclease and one or more additional proteins with an RRM fold (the ultimate origin of which could be a polymerase or cyclase that gave rise to Cas10) of the hybrid locus could have subsequently evolved to become the ancestral CRISPR-Cas effector module (*31*–*33*, *44*).

The widespread occurrence of class 1 systems in archaea and bacteria, together with the proliferation of the ancient RRM domain in class 1 effector proteins, strongly suggests that the ancestral CRISPR-Cas belonged to class 1. Most likely, the multiple class 2 variants then evolved via several independent replacements of the class 1 effector locus with nuclease genes that were derived from distinct MGEs (Fig. 2B). In particular, type V effector variants (Cpf1) seem to have evolved from different families of the TnpB transposase genes that are widespread in transposons (*31*), whereas the type II effector (Cas9) may have evolved from IscB, a protein with two nuclease domains that belongs to a recently identified distinct transposon family (*45*). Notably, class 2 CRISPR-Cas systems, in their entirety, appear to have been derived from different MGEs: Cas1 from a casposon, Cas2 from a toxin-antitoxin module, and the different effector proteins (such as Cas9 and Cpf1) from respective transposable elements (*31*).

CRISPR adaptation

The spacers of a CRISPR array represent a chronological archive of previous invader encounters. The captured spacer sequences are integrated into the CRISPR loci after exposure to MGEs, at the leader end of the array that contains the start site of CRISPR transcription (*9*, *14*, *46*). Analysis of invader target sequences (also called protospacers) has revealed a short motif directly adjacent to the target sequence, called the protospacer adjacent motif (PAM) (*47*). This PAM motif allows self/nonself discrimination by the host in two ways: (i) because its presence in alien targets is required for nonself interference, and (ii) because its absence in the host's CRISPR array avoids self-targeting (*48*). In class 1–type I and class 2–type II systems, the PAM is not only involved in interference, but also plays a role in spacer selection during the adaptation stage, implying the acquisition of functional spacers only (*49*, *50*). The PAM is a short [2 to 7 nucleotides (nt)], partially redundant sequence that in itself cannot preclude incorporation of spacers from the host DNA because of the low information content of the motif. The short PAM appears to be the result of an evolutionary trade-off between efficient incorporation of spacers from nonself DNA and preventing an autoimmune reaction.

Although host chromosomal fragments can be incorporated as new CRISPR spacers, detection of such events obviously implies that this did not result in a lethal phenotype, either due to a modified PAM and/or to an inactivated CRISPR-Cas effector module (*51*). Indeed, in the absence of the effector module, elevated frequencies of self-spacer acquisition occur in *Escherichia coli* (*52*). Similarly, *Streptococcus thermophilus* with a catalytically inactive Cas9 results in a major increase of spacers derived from the host genome (*53*). In addition, there is a strong preference for the integration of plasmid over chromosomal spacer sequences (*52*, *54*, *55*), with plasmid sequences incorporated more frequently than host DNA by two to three orders of magnitude (*56*). Spacer acquisition in *E. coli* requires active replication of the protospacer-containing DNA (*56*). Thus, small, fast-replicating plasmid genomes are a much better source of spacers than the large host DNA, and such findings are consistent with acquisition of spacers from an infecting virus genome in the archaeon *Sulfolobus islandicus* requiring its active replication (*57*). In *E. coli*, the CRISPR-Cas system derives the spacers primarily from products of RecBCD-catalyzed DNA degradation that are formed during the repair of double-stranded breaks associated with stalled replication forks (*58*). Other possible sources of substrates for CRISPR adaptation include DNA fragments generated either by other defense systems, such as restriction-modification systems (*59*), or by the CRISPR-Cas system itself (*49*).

Cas1 and Cas2 play crucial roles in spacer acquisition in all CRISPR-Cas systems (*50*, *52*). In addition, these proteins can function in trans, provided that the repeats involved are sufficiently similar in size and structure. Accordingly, *cas1* and *cas2* genes are missing in many active CRISPR-Cas loci—in particular, of type III as well as types IV and VI (*30*). Overexpression of Cas1 and Cas2 from the *E. coli* type I-E system has been shown to be sufficient for the extension of the CRISPR array (*52*). Mutations in the active site of Cas1 abolish spacer integration in *E. coli* (*52*), whereas the nuclease activity of Cas2 is dispensable (*55*). In *E. coli*, a central Cas2 dimer and two flanking Cas1 dimers form a complex that binds and processes PAM-containing DNA fragments (Fig. 3A) (*55*, *60*), after which the newly generated spacers can be integrated into a CRISPR array via a recombination mechanism akin to that of retroviral integrases and transposases (*61*) (Fig. 3B).

In several type III CRISPR-Cas systems, Cas1 is fused to reverse transcriptase (*20*), and it was recently shown that these systems are capable of acquisition of RNA spacers by direct incorporation of an RNA segment into the CRISPR array followed by reverse transcription and replacement of the RNA strand by DNA (*62*). Although the biological function of this process remains to be elucidated, these findings demonstrate remarkable versatility of adaptation pathways.

Spacer acquisition (adaptation) in type I systems proceeds along two distinct paths: (i) naïve acquisition, which occurs during an initial infection, and (ii) primed acquisition, when the CRISPR contains a previously integrated spacer that is complementary to the invading DNA (*63*). According to the proposed model, naïve spacer adaptation involves five steps (Fig. 3B):

1) Fragmentation of (mainly) invasive nucleic acids by non-Cas systems [e.g., by RecBCD after stalling a replication fork, or by restriction enzymes (restriction-modification systems) (*56*, *59*)] or by CRISPR-associated nucleases (*49*). Although this step may be non-essential, it probably enhances the efficiency of the overall process and its specificity toward invading DNA.

2) Selection of DNA fragments for (proto) spacers by scanning for potential PAMs (after partial target unwinding) by one of the four Cas1 subunits of the Cas1-Cas2 complex (*64*).

3) Measuring of the selected protospacer generating fragments of the correct size with 3′ hydroxyl groups by Cas1 nuclease.

4) Nicking of both strands of the leader-proximal repeat of the CRISPR array at the 5′ ends through a direct nucleophilic attack by the generated 3′ OH groups, resulting in covalent links of each of the strands of the newly selected spacer to the single-stranded repeat ends.

5) Second-strand synthesis and ligation of the repeat flanks by a non-Cas repair system (*46*, *61*).

Primed spacer adaptation so far has been demonstrated only in type I systems (*50*, *65*, *66*). This priming mechanism constitutes a positive feedback loop that facilitates the acquisition of new spacers from formerly encountered genetic elements (*67*). Priming can occur even with spacers that contain several mismatches, making them incompetent as guides for targeting the cognate foreign DNA (*67*). Based on PAM selection, functional spacers are preferentially acquired during naïve adaptation. This initial acquisition event triggers a rapid priming response after subsequent infections. Priming appears to be a major pathway of CRISPR adaptation, at least for some type I systems (*65*). Primed adaptation strongly depends on the spacer sequence (*68*), and the acquisition efficiency is highest in close proximity to the priming site. In addition, the orientation of newly inserted spacers indicates a strand bias, which is consistent with the involvement of single-stranded adaption intermediates (*69*). According to one proposed model (*70*), replication forks in the invader's DNA are blocked by the Cascade complex bound to the priming crRNA, enabling the RecG helicase and the Cas3 helicase/nuclease

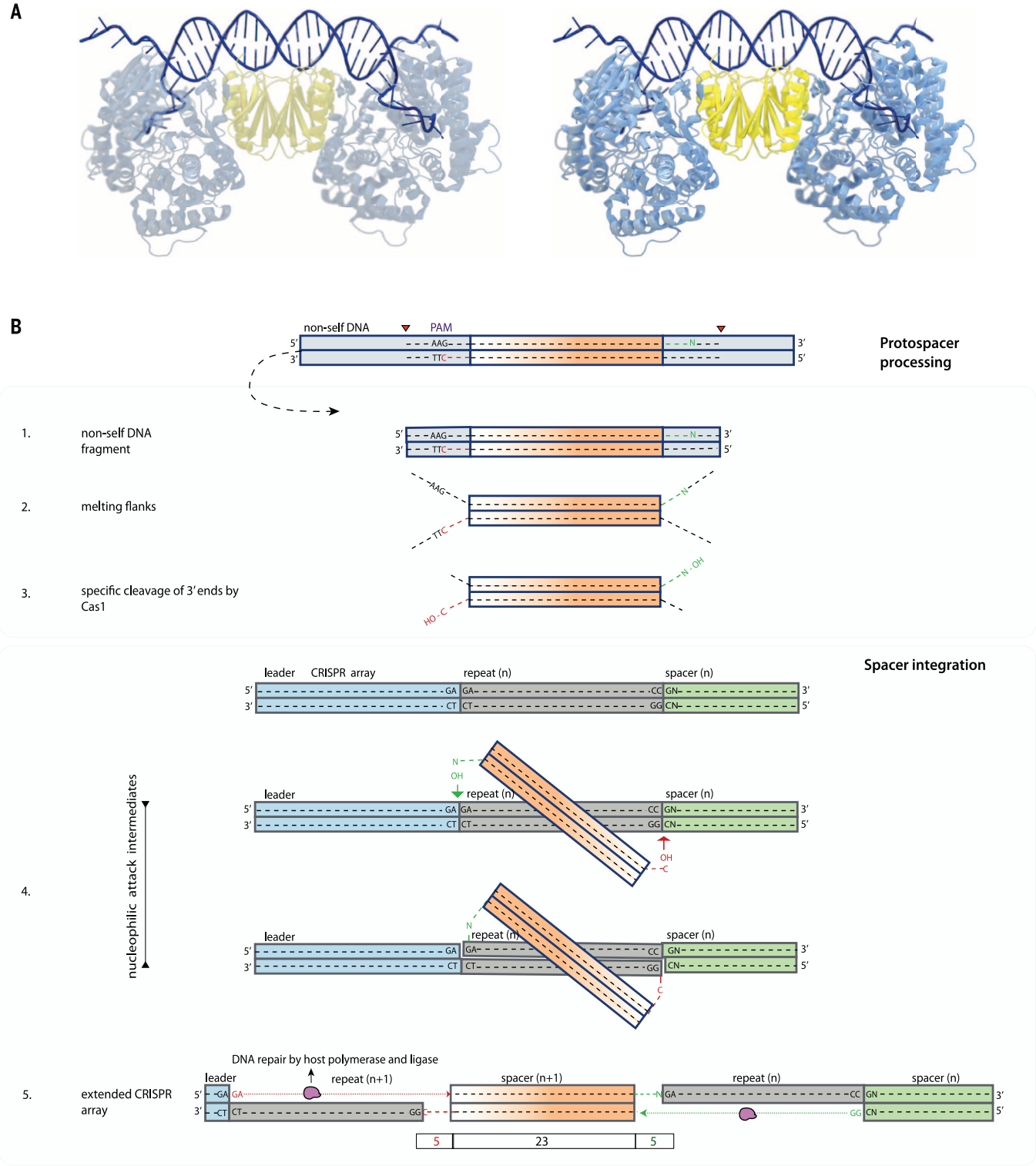

Fig. 3. Spacer acquisition. (**A**) Crystal structure of the complex of Cas1-Cas2 bound to the dual-forked DNA (PDB accession 5DQZ). The target DNA is shown in dark blue; the Cas1 and Cas2 dimers of the complex are indicated in blue and yellow, respectively. (**B**) Model explaining the capture of new DNA sequences from invading nucleic acid and the subsequent DNA integration into the host CRISPR array. The numbers on the left correspond to the order of events as described in the text. The dashed lines indicate nucleotides; the nucleotides C and N on the two sides of the protospacer are shown in red and green to clarify the orientation.

proteins to attack the DNA. The ends at the collapsed forks then could be targeted by RecBCD, which provides DNA fragments for new spacer generation (*70*). Given that the use of crRNA for priming has much less strict sequence requirements than direct targeting of the invading DNA, priming is a powerful strategy that might have evolved in the course of the host-parasite arms race to reduce the escape by viral mutants, to

provide robust resistance against invading DNA, and to enhance self/nonself discrimination. Naïve as well as primed adaptation in the subtype I-F system of *Pseudomonas aeruginosa* CRISPR-Cas require both the adaptation and the effector module (*69*).

In the type II-A system, the Cas9-tracrRNA complex and Csn2 are involved in spacer acquisition along with the Cas1-Cas2 complex (*53*, *71*); the involvement of Cas9 in adaptation is likely to be a general feature of type II systems. Although the key residues of Cas9 involved in PAM recognition are dispensable for spacer acquisition, they are essential for the incorporation of new spacers with the correct PAM sequence (*71*). The involvement of Cas9 in PAM recognition and protospacer selection (*71*) suggests that in type II systems Cas1 may have lost this role. Similarly, Cas4 that is present in subtypes IA-D and II-B has been proposed to be involved in the CRISPR adaptation process, and this prediction has been validated experimentally for type I-B (*65*). Cas4 is absent in the subtype II-C system of *Campylobacter jejuni*. Nonetheless, a conserved Cas4-like protein found in *Campylobacter* bacteriophages can activate spacer acquisition to use host DNA as an effective decoy to bacteriophage DNA. Bacteria that acquire self-spacers and escape phage infection must either overcome CRISPR-mediated autoimmunity by loss of the interference functions, leaving them susceptible to foreign DNA invasions, or tolerate changes in gene regulation (*72*). Furthermore, in subtypes I-U and V-B, Cas4 is fused to Cas1, which implies cooperation between these proteins during adaptation. In type I-F systems, Cas2 is fused to Cas3 (*19*), which suggests a dual role for Cas3 (*20*): involvement in adaptation as well as in interference. These findings support the coupling between the adaptation and interference stages of CRISPR-Cas defense during priming.

Biogenesis of crRNAs

The short mature crRNAs contain spacer sequences, which are the guides that are responsible for the specificity of CRISPR-Cas immunity (*12*). They associate with one or more Cas proteins to form effector complexes that target invading MGEs through crRNA:target sequence–specific recognition. The CRISPR arrays are transcribed as long precursors, known as pre-crRNA, that may contain secondary structured elements (hairpins) in those cases where the CRISPR contains palindromic repeats. The processing of the pre-crRNA typically yields 30- to 65-nt mature crRNAs that consist of a single spacer flanked by a partial repeat at either one or both ends (*12*, *73*).

The pathways of crRNA biogenesis differ among the different CRISPR-Cas types. In class 1 systems, the Cas6 protein is critical for the primary processing of pre-crRNA. Cas6 is a metal-independent endoribonuclease that recognizes and cleaves a single phosphodiester bond in the repeat sequences of a pre-crRNA transcript (*12*, *74*, *75*). Members of the Cas6 family contain two RRM-type RNA-binding domains. The primary cleavage by Cas6 results in crRNAs containing a repeat-derived 5′ "handle" of 8 nt with a 5′ hydroxyl group, followed by the complete spacer sequence and a repeat-derived 3′ handle of variable size that in some subtypes forms a hairpin structure with either a 3′-phosphate or a cyclic 2′,3′-phosphate (*12*, *74*, *76*). The Cas6 family proteins show considerable structural variation that might reflect the cleavage specificity (*73*, *77*, *78*).

In type I-E and I-F systems, the Cas6 ribonuclease is a single-turnover enzyme that remains attached to the crRNA cleavage product. In these cases, Cas6 is a subunit of a multisubunit Cascade complex (*12*, *79*) (Fig. 4A). In the type I-F systems, the crRNP complex consists of the crRNA, Cas6f, and Csy1, Csy2, and Csy3 proteins (*80*–*82*). In other systems (subtypes I-A, I-B, I-D, and III-A to III-D), Cas6 is not associated with the crRNA-processing complex. The absence of a Cas6 subunit in the complex correlates with the lack of a hairpin structure of the 3′ handle and a variable 3′ end. The absence of a *cas6* gene in type I-C is complemented by another double RRM-fold subunit, Cas5d, which has adopted the role of the endoribonuclease that in other subtypes is carried out by Cas6 (*83*). Some systems coexisting in the same species have been demonstrated to share the same set of guides; examples include type III-A (Csm) and type III-B (Cmr) of *Thermus thermophilus* (*84*) and type III-B (Cmr), type I-A (Csa), and type I-G (Cst) of *Pyrococcus furiosus* (*85*). Given that the type III loci usually lack *cas6* genes, a single stand-alone Cas6 nuclease is likely to be responsible for the supply of crRNAs to the type III complexes in *T. thermophilus* (*84*). In *P. furiosus*, Cas6 nuclease of type I generates the crRNAs from all CRISPR loci for the different coexisting complexes (*85*). Cas6-based processing of pre-crRNA in type III systems is typically followed by a sequence-unspecific trimming at the 3′ end (by RNases yet to be identified) to yield mature crRNAs with a defined 8-nt 5′ end and a variable 3′ end (*34*, *86*, *87*).

Type II systems use a unique mechanism for crRNA biogenesis whereby processing depends on Cas9, a host RNase III, and a tracrRNA that forms base pairs with the repeats of the pre-crRNA (*36*, *37*, *73*) (Fig. 4B). The cleaved crRNA-tracrRNA hybrid is bound and stabilized by Cas9, triggering a conformational change toward a state compatible with target scanning, recognition, and interference (*36*, *37*, *88*). Trimming of the 5′ end of the crRNA probably occurs by a non-Cas RNase. The absence of type II systems in archaea is consistent with the absence of RNase III genes in most archaeal genomes (*89*). In the type II-C system of *Neisseria meningitidis*, short intermediate crRNA guides are transcribed from multiple promoters embedded within the repeats of the CRISPR array, implying that the system does not require RNase III (*90*) (Fig. 4C). Expression of tracrRNA has also been demonstrated for the subtype V-B system, suggestive of a crRNA processing pathway analogous to that in type II. By contrast, in subtype V-A and type VI systems, no tracrRNA is coexpressed with the pre-crRNA (*31*, *39*). Class 2 CRISPR-Cas systems lacking tracrRNA can be expected to function using novel mechanisms of crRNA biogenesis, including processing by other host RNases or by the effector proteins themselves.

A third variant of guide maturation has recently been described for the Cpf1 effector complex, a class 2 system that (unlike Cas9) does not associate with a tracrRNA. It has been demonstrated that Cpf1 has an intrinsic RNase activity that allows for the primary processing of the pre-crRNA to crRNA guides with a 5′ hairpin (*91*). The biosynthesis of crRNAs by Cpf1 system is metal-, sequence-, and structure-dependent (*91*). Secondary processing of CRISPR guides probably occurs via a non-Cas RNase; maturation of Cas9-associated guides occurs by trimming at the 5′ end (Fig. 4B), whereas in Cpf1 the 3′ flanks of the crRNA are removed.

Target interference

Selection of CRISPR-Cas targets is a stepwise process that relies on recognition of a nonself sequence, a complementary spacer of which is stored in the CRISPR locus. In most cases, with the exception of the RNA-targeting type III systems, cognate protospacer sequences flanked by a PAM sequence are recognized by a CRISPR ribonucleoprotein (crRNP) complex [type I Cascade, type II Cas9, type V Cpf1 (Fig. 5)] and specifically degraded (*12*, *14*, *39*). In addition, selection of an appropriate target sequence depends on a so-called seed sequence on the guide (*79*, *92*). The seed is a sequence of seven or eight base pairs in close proximity to the PAM. Matching PAM and seed sequences are crucial for target interference (*79*, *92*, *93*) and act as a quality control step that is required for the complete displacement of the noncomplementary strand of the target DNA by the crRNA guide, the so-called R-loop conformation. Downstream of the seed region, mismatches between spacer and protospacer are tolerated to some extent (see below) (*92*).

In type I systems, the Cascade RNP complex scans DNA for complementary target sites, initially by identifying an appropriate PAM motif, followed by partial melting and base pairing by the guide's seed sequence, and eventually by formation of a complete R-loop structure (*76*, *94*). Upon reaching a PAM-proximal mismatch, the R-loop propagation stalls and the interference is aborted (*95*). When base pairing between guide and protospacer is complete, the R-loop structure appears to be locked in a state to license DNA degradation by the Cas3 nuclease/helicase (*12*, *19*, *95*).

Single-molecule experiments with *E. coli* Cascade demonstrate that crRNA-guided Cascade exhibits two distinct binding modes for matching and mismatched targets, which trigger either interference (matching target) or primed spacer acquisition (mismatched target). Unlike the interference of matching targets, mismatched targets are recognized with low fidelity, as indicated by a short-lived binding. The latter association is PAM- and seed-independent and can involve base pairing by any part of the crRNA spacer. In this case, the Cascade complex does not adopt a

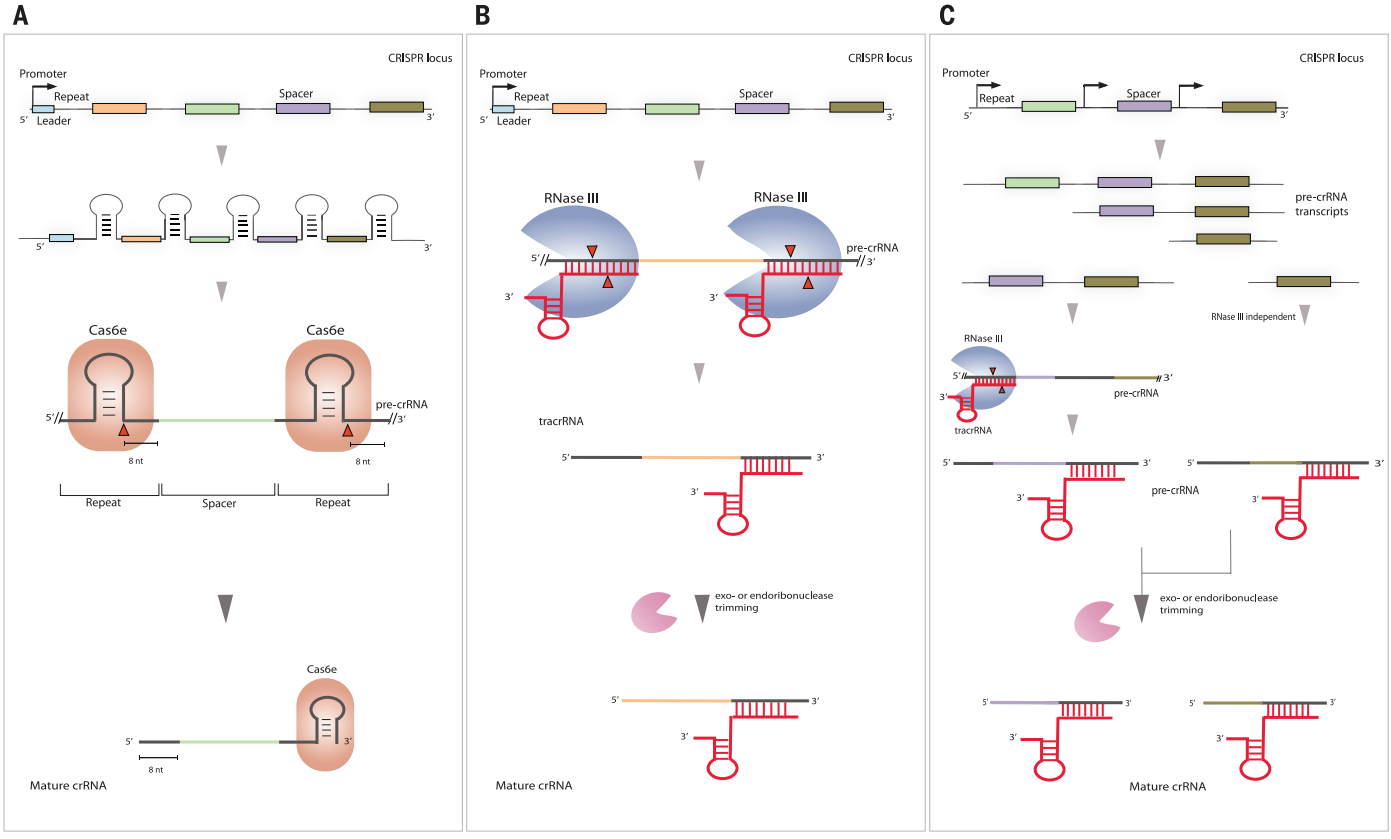

Fig. 4. Guide expression and processing. (**A**) Generation of CRISPR RNA (crRNA) guides in type I and type III CRISPR-Cas systems. Primary processing of the pre-crRNA is catalyzed by Cas6, which typically results in a crRNA with a 5′ handle of 8 nt, a central spacer sequence, and (in some subtypes) a longer 3′ handle. Shown here is the guide processing (red triangles) for subtype I-E by Cas6e. The occasional secondary processing of the 3′ end of crRNA is catalyzed by one or more unknown RNases. (**B**) In type II-A CRISPR-Cas systems, the repeat sequences of the pre-crRNA hybridize with complementary sequences of transactivating CRISPR RNA (tracrRNA). The double-stranded RNA is cleaved by RNase III (red triangles); further trimming of the 5′ end of the spacer is carried out by unknown RNase(s) (pink). (**C**) CRISPR with transcriptional start site (TSS) in repeats, as observed in type II-B CRISPR-Cas systems.

conformation that allows docking of Cas3 (*96*), precluding DNA interference. Instead, this Cascade-target complex primes the formation of a spacer acquisition complex that consists of Cas3 and Cas1-Cas2, and generates DNA fragments that are integrated as new spacers in the CRISPR array (*94*). These dual roles of Cascade allow for efficient degradation of bona fide targets and priming the acquisition of new spacers from mismatched targets (e.g., from viral escape mutants) as an update of the CRISPR memory (*96*).

Although type III systems are structurally related to the type I system (Fig. 5) (*34*, *35*, *60*, *97*–*101*), they show some substantial mechanistic variations. Initial analyses indicated that Csm (III-A) complexes target DNA (*13*), whereas Cmr (III-B) complexes target RNA (*11*, *102*, *103*). However, it has recently been demonstrated that both type III complexes are transcription-dependent DNA nucleases (*84*, *104*); that is, they initially recognize their target through specific interaction of the crRNA guide with a complementary nascent mRNA, after which cleavage of the flanking DNA sequences occurs (*105*–*110*). Robust interference by these systems relies on the concerted cleavage of the transcript RNA and the transcribed DNA. The Cas7-like backbone subunits (Csm3, Cmr4) are responsible for the RNase activity, typically resulting in cleavage of the target RNA at 6-nt intervals (*84*, *99*, *103*, *104*, *111*–*113*). Binding of the Cmr complex to its complementary RNA target induces a conformational change (*35*, *99*) that results in activation of the Cas10 DNA-cleaving subunit (Csm1/Cmr2) (*106*, *107*, *109*). Disruption of the RNase active sites (in Csm3/Cmr4), at least in some cases, does not hamper the activation of the DNA nuclease activity of the complexes (*104*, *106*). Exonucleolytic cleavage of single-stranded DNA and RNA by recombinant *Staphylococcus epidermidis* Csm1 (Cas10) and by *Thermotoga maritima* and *P. furiosus* Cmr2 has been demonstrated in vitro (*106*, *107*, *114*). In the *S. epidermidis* system, a Csx1 ortholog (Csm6) provides an auxiliary RNA-targeting activity that operates in conjunction with the RNA- and DNA-targeting endonuclease activities of the Csm effector complex (*115*–*117*); in the *P. furiosus* Cmr system, Csx1 appears not to be an essential component (*104*). The relative contribution of the different nuclease subunits appears to vary in the different type III systems and under different conditions, and awaits further characterization.

Another unique feature of type III systems concerns the mechanism of self/nonself discrimination. Genetic analyses have revealed that type III systems do not use the PAM-based "nonself-activation" mechanism of type I (Cascade), type II (Cas9), and type V (Cpf1). The mechanism used by the *S. epidermidis* Csm system apparently involves crRNA- or protein-based recognition of the repeats in the CRISPR locus, resulting in "self-inactivation" (*118*, *119*). However, the DNA cleavage activity of the *P. furiosus* Cmr complex was recently reported to require the presence of a short sequence adjacent to the target sequence within the activating target RNA (i.e., an RNA PAM) (*107*). Additional analysis is required to reveal whether the reported motifs are typical features that distinguish the two subtypes.

Class 2 systems require only a single protein for interference. In type II, the crRNP complex involved in target recognition and degradation consists of Cas9 bound to the crRNA guide base-paired with the tracrRNA (*37*). The crystal structures of Cas9 reveal two distinct lobes that are involved in target recognition and nuclease activity (Fig. 5). The positively charged groove at the interface of the two lobes accommodates the crRNA-DNA heteroduplex (*120*, *121*). A major step in Cas9 activation is the reorientation of the structural lobes upon crRNA/tracrRNA loading, which results in the formation of a central channel that accommodates the target DNA (*120*). Binding and cleavage of the target DNA by the Cas9-crRNA

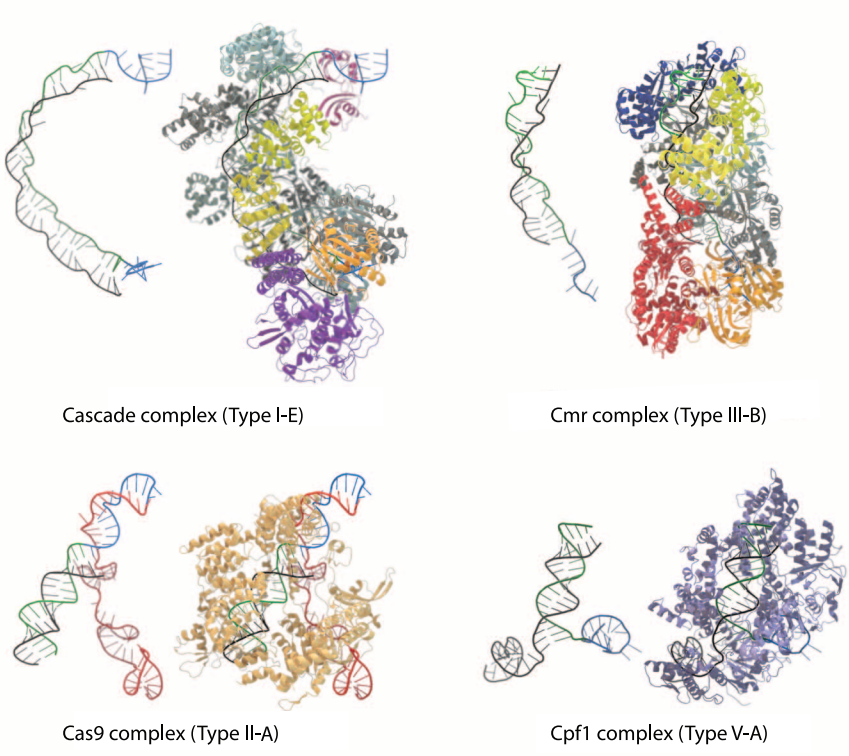

Fig. 5. CRISPR RNP complexes. Crystal structures of the CRISPR ribonucleoprotein (crRNP) complexes responsible for target interference. Shown are the type I-E Cascade complex (PDB accession 4QYZ) and type III-B Cmr complex (PDB accession 3X1L) from class 1, and the type II-A Cas9 complex (PDB accession 4OO8) and type V-A Cpf1 complex (PDB accession 5B43) from class 2. Colors of nucleic acid fragments are the same as in Fig. 6.

effector complex depend on the recognition of an appropriate PAM located at the 3′ end of the protospacer (*93*), which serves as a licensing element in subsequent DNA strand displacement and R-loop formation. The PAM motif resides in a base-paired DNA duplex. Sequence-specific PAM readout by Arg^{1333} and Arg^{1335} in Cas9 positions the DNA duplex such that the +1 phosphate group of the target strand interacts with the phosphate lock loop (*122*). This promotes local duplex melting, allowing the Cas9-RNA complex to probe the identity of the nucleotides immediately upstream of the PAM. Base pairing between a 12-nt seed sequence of the guide RNA and the target DNA strand (*93*) drives further stepwise destabilization of the target DNA duplex and directional formation of the guide RNA–target DNA heteroduplex (*122*). This R-loop triggers a conformational change of the two nuclease domains (HNH and RuvC) of Cas9, which adopt an active state that allows for the completion of interference by cleavage of both target strands (*121*, *123*). Cas9 generates a blunt-end double-strand break, typically located 3 nt from the 3′ end of the protospacer (*14*, *124*). Recently, however, PAM-independent single-stranded targeting by *N. meningitidis* Cas9 has been described (*125*).

Similar to type II, the effector modules of type V systems consist of a large multidomain protein complex (Cpf1 and C2c1 in subtypes V-A and V-B, respectively). Like Cas9, these proteins encompass a RuvC-like nuclease domain and an arginine-rich bridging helix. However, in contrast to Cas9, the RuvC-like domain of Cpf1 and C2c1 is more compact and the HNH domain is missing (Fig. 6). Subtype V-B systems resemble type II with respect to the requirement for a tracrRNA, both for processing and for interference. In contrast, Cpf1-crRNA (type V-A) complexes are single RNA-guided endonucleases that cleave target DNA molecules in the absence of a tracrRNA (*39*). A model is proposed for a stepwise cleavage of the target DNA by Cpf1 (i.e., initial RuvC-dependent cleavage of the displaced strand, followed by cleavage of the target strand by the novel nuclease domain) (*40*). The observation that inactivation of the RuvC domain prevents cleavage of both strands of the target DNA (*39*, *91*) suggests that the novel nuclease is allosterically activated by the RuvC cleavage event. Although allosteric control has also been demonstrated in interference by Cas9 (*123*), details appear to differ (*40*). Both Cpf1 and C2c1 from different bacteria efficiently cleave target DNA containing a well-defined T-rich PAM at the 5′ end of the protospacer (5′-PAM) (*31*, *39*), in contrast to the more variable, G-rich 3′-PAM sequence of Cas9 (*126*). Structural analysis has shown that Cpf1 recognizes its PAM through a combination of base and shape readout, in which several PAM-interacting amino acid residues that are conserved in the Cpf1 family are involved (*40*). Another unique feature of the Cpf1 endonuclease is the generation of staggered double-stranded DNA breaks with 4- or 5-nt 5′ overhangs (*39*); in the Cpf1 structure, the unique nuclease domain is positioned so as to cleave the target strand outside the heteroduplex, as opposed to the HNH domain of Cas9, in which the active site contacts the target within the heteroduplex (*40*) (Fig. 6).

The type VI systems contain a unique effector protein (C2c2) with two HEPN domains. The *Leptotrichia shahii* C2c2 protein provides efficient interference against the RNA phage MS2. C2c2 is guided by a single crRNA and can be programmed to cleave ssRNA targets carrying complementary protospacers (*127*) (Fig. 6). Spacers with a G immediately flanking the 3′ end of the protospacer are less fit relative to all other nucleotides at this position, which suggests that the 3′ protospacer flanking site (PFS) affects the efficacy of C2c2-mediated targeting (*128*) (Fig. 6). Remarkably, once primed with the cognate target RNA, the C2c2 protein turns into a sequence-nonspecific RNase that causes a toxic effect in bacteria (*127*). Thus, the defense strategy of type VI systems appears to couple adaptive immunity with programmed cell death or dormancy induction.

Phages are constantly evolving multiple tactics to avoid, circumvent, or subvert prokaryotic defense mechanisms (*8*). Phages can evade CRISPR interference through single-nucleotide substitution in the protospacer region or in the conserved protospacer-adjacent motif (*47*). Additionally, *P. aeruginosa* phages encode several proteins affecting the activity of type I-E and I-F systems (*128*). Diverse sequences of these proteins and mechanisms of action, coupled with the strong selection imposed by different antiviral systems, suggest an abundance of anti-CRISPR proteins yet to be discovered. Strikingly, some bacteriophages themselves encode a CRISPR-Cas system that in this case functions as an antidefense device targeting an antiphage island of the bacterial host and thus enabling productive infection (*129*). Together, these findings emphasize the complexity of the virus-host arms race in which CRISPR-Cas systems are involved and suggest that many important aspects of this race remain to be characterized.

Very recently, an unexpected claim has been published on the existence of a CRISPR-like defense system in a giant mimivirus infecting unicellular eukaryotes (amoeba) (*130*). This system, named "mimivirus virophage resistance element" (MIMIVIRE), has been proposed to protect certain mimivirus strains from the Zamilon virophage, a small virus that parasitizes on mimiviruses. However, the MIMIVIRE locus lacks CRISPR-like repeats or a Cas1 homolog and encodes only very distant, generic homologs of two Cas proteins (a helicase and a nuclease that belong to the same protein superfamilies as Cas3 and Cas4, respectively, but lack any specific relationship with these Cas proteins). Thus, any analogy between this putative eukaryotic giant virus defense system and CRISPR-Cas should be perceived with caution.

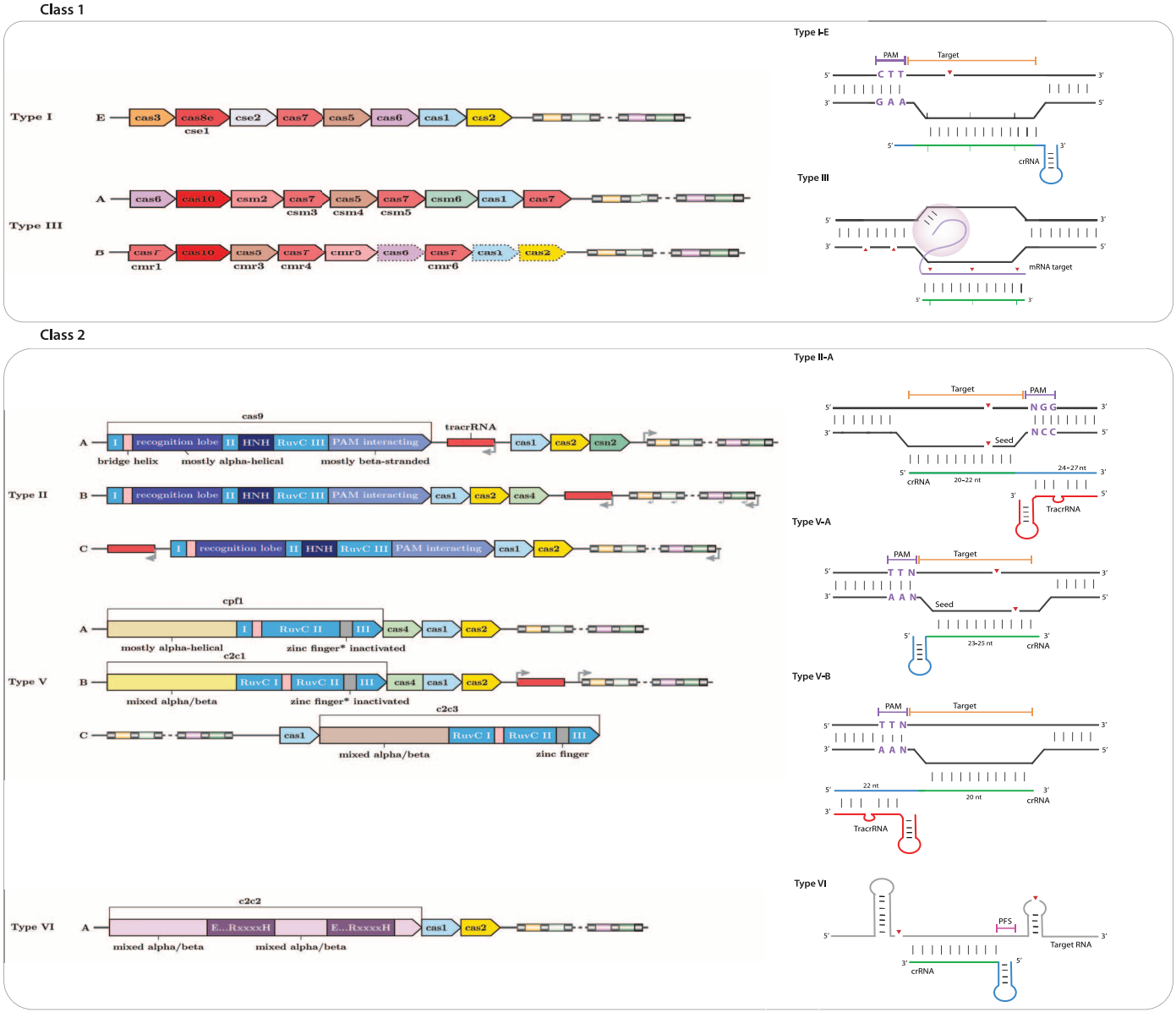

Fig. 6. Target interference. Genomic loci architecture of the components of class 1 and class 2 CRISPR-Cas systems and schematic representation of target interference for the different subtypes. The double-stranded DNA (target) is shown in black, the target RNA in gray, the CRISPR RNA (crRNA) repeat in blue, the spacer region of the crRNA in green, and the transactivating CRISPR RNA (tracrRNA) in red.

Genome editing applications

The molecular features of CRISPR-Cas systems, particularly class 2 systems with single-protein effectors, have made them attractive starting points for researchers interested in developing programmable genome editing tools. In 2013, the first reports of harnessing Cas9 for multiplex gene editing in human cells appeared (*131*–*134*). These studies have demonstrated that Cas9 could efficiently create indels at precise locations and that by supplying exogenous repair templates, insertion of a new sequence at target sites could be achieved via homologous recombination. A "dead" Cas9 (dCas9) variant with inactivating mutations in the HNH and RuvC domains binds DNA without cutting, providing a programmable platform for recruiting different functional moieties to target sites. The dCas9 has been used for transcriptional activation and repression (*135*–*138*), localizing fluorescent protein labels (*139*), and recruiting histone-modifying enzymes (*140*, *141*). Other applications of Cas9 include building gene circuits (*142*–*144*), creating new antimicrobials (*145*) and antivirals (*146*–*148*), and large-scale gain- and loss-of-function screening (*149*–*152*).

The genome editing toolbox has been expanding through the discovery of novel class 2 effector proteins, such as Cpf1 (*39*). The Cpf1 nuclease possesses on-target efficiencies in human cells that are comparable with that of Cas9. Besides, Cpf1 is also highly specific in its targeting, as minimal or no off-target cleavage has been detected (*153*, *154*). Cpf1 does not require a tracrRNA, further simplifying the system for genome editing applications. In addition, it generates sticky ends, which could potentially increase the efficiency of insertion of new DNA sequences relative to the blunt ends created by Cas9 (*39*).

Central to the success of any Cas-based genome editing tool is the specificity of the enzyme, and many approaches to increase specificity have been reported. For example, "double-nicking," which uses dimers of two Cas9 variants, each mutated to create a nick in one strand of the DNA, improves specificity by requiring two target matches to create the double-strand break (*155*, *156*). Another tactic is to control the amount of Cas9 in the cell via an inducible system that expresses a low level

of Cas9 (*157*, *158*). Shortening the region of complementarity in the guide RNA also reduces off-target cleavage (*159*). Finally, structure-guided engineering has been used to mutate specific residues in Cas9, to weaken the interaction with the nontarget strand or to decrease nonspecific interactions with the target DNA site, favoring cleavage at sites that are perfectly complementary to the guide RNA and reducing off-target effects to undetectable levels at many sites (*160*, *161*).

A major outstanding challenge for realizing the full potential of Cas-based genome editing, including its use as a therapeutic, is efficient and tissue-specific delivery. Some progress has been made in this area, including the use of a smaller Cas9 ortholog (*162*), which is more amenable to packaging into viral vectors. Other approaches are also being pursued, including nonviral methods for delivery of DNA or mRNA by nanoparticles (*163*) and electroporation (*164*), or direct delivery of Cas9 protein (*165*). Additionally, the long-term effects of Cas9 expression in heterologous eukaryotic cells remain unexplored. Finally, the potential for editing the human genome as well as the possibility of using Cas-based gene drives for ecosystem engineering (*166*) raise ethical concerns that must be fully considered.

Outlook

The intensive research over the past few years on structural and functional features of variant CRISPR-Cas systems has revealed that they encompass many homologous components and share common mechanistic principles but also show enormous variability. A key aspect of this variability is module shuffling, which involves frequent recombination of adaptation and effector modules coming from different types of CRISPR-Cas within the same locus. Apart from major differences in the architectures of the effector complexes, functional diversity of CRISPR-Cas includes versatile mechanisms of crRNA guide processing, self/nonself discrimination, and target cleavage. The versatility of class 2 systems in particular, where distinct subtypes apparently evolved via independent recombination of adaptation modules with widely different effectors, is notable, given the potential of these systems as genome editing tools. The in-depth analysis of a few well-characterized CRISPR systems has revealed key structural and mechanistic features. However, the continuing discovery of novel CRISPR-Cas variants and new molecular mechanisms implies that our current insights have limited power for predicting functional details of distantly related variants. Hence, such new CRISPR-Cas systems need to be meticulously analyzed to understand the biology of prokaryotic adaptive immunity and harness its potential for biotechnology. In this Review, we could not cover in any detail several fascinating aspects of CRISPR-Cas biology, such as coevolution of immune systems with viruses, the interplay between CRISPR-Cas activity and horizontal gene transfer, or nonimmune functions of CRISPR-Cas. The complexity and extreme variability of the CRISPR-Cas systems ensure that researchers in this field will have much to do for many years to come.

REFERENCES AND NOTES

1. E. V. Koonin, V. V. Dolja, A virocentric perspective on the evolution of life. *Curr. Opin. Virol.* **3**, 546–557 (2013). doi: 10.1016/j.coviro.2013.06.008; pmid: 23850169
2. K. S. Makarova, Y. I. Wolf, E. V. Koonin, Comparative genomics of defense systems in archaea and bacteria. *Nucleic Acids Res.* **41**, 4360–4377 (2013). doi: 10.1093/nar/gkt157; pmid: 23470997
3. M. R. Tock, D. T. Dryden, The biology of restriction and anti-restriction. *Curr. Opin. Microbiol.* **8**, 466–472 (2005). doi: 10.1016/j.mib.2005.06.003; pmid: 15979932
4. D. C. Swarts *et al*., DNA-guided DNA interference by a prokaryotic Argonaute. *Nature* **507**, 258–261 (2014). doi: 10.1038/nature12971; pmid: 24531762
5. T. Goldfarb *et al*., BREX is a novel phage resistance system widespread in microbial genomes. *EMBO J.* **34**, 169–183 (2015). doi: 10.15252/embj.201489455; pmid: 25452498
6. K. S. Makarova, Y. I. Wolf, S. Snir, E. V. Koonin, Defense islands in bacterial and archaeal genomes and prediction of novel defense systems. *J. Bacteriol.* **193**, 6039–6056 (2011). doi: 10.1128/JB.05535-11; pmid: 21908672
7. M. C. Chopin, A. Chopin, E. Bidnenko, Phage abortive infection in lactococci: Variations on a theme. *Curr. Opin. Microbiol.* **8**, 473–479 (2005). doi: 10.1016/j.mib.2005.06.006; pmid: 15979388
8. J. E. Samson, A. H. Magadán, M. Sabri, S. Moineau, Revenge of the phages: Defeating bacterial defences. *Nat. Rev. Microbiol.* **11**, 675–687 (2013). doi: 10.1038/nrmicro3096; pmid: 23979432
9. R. Barrangou *et al*., CRISPR provides acquired resistance against viruses in prokaryotes. *Science* **315**, 1709–1712 (2007). doi: 10.1126/science.1138140; pmid: 17379808
10. R. Jansen, J. D. Embden, W. Gaastra, L. M. Schouls, Identification of genes that are associated with DNA repeats in prokaryotes. *Mol. Microbiol.* **43**, 1565–1575 (2002). doi: 10.1046/j.1365-2958.2002.02839.x; pmid: 11952905
11. C. R. Hale *et al*., RNA-guided RNA cleavage by a CRISPR RNA-Cas protein complex. *Cell* **139**, 945–956 (2009). doi: 10.1016/j.cell.2009.07.040; pmid: 19945378
12. S. J. Brouns *et al*., Small CRISPR RNAs guide antiviral defense in prokaryotes. *Science* **321**, 960–964 (2008). doi: 10.1126/science.1159689; pmid: 18703739
13. L. A. Marraffini, E. J. Sontheimer, CRISPR interference limits horizontal gene transfer in staphylococci by targeting DNA. *Science* **322**, 1843–1845 (2008). doi: 10.1126/science.1165771; pmid: 19095942
14. J. E. Garneau *et al*., The CRISPR/Cas bacterial immune system cleaves bacteriophage and plasmid DNA. *Nature* **468**, 67–71 (2010). doi: 10.1038/nature09523; pmid: 21048762
15. M. P. Terns, R. M. Terns, CRISPR-based adaptive immune systems. *Curr. Opin. Microbiol.* **14**, 321–327 (2011). doi: 10.1016/j.mib.2011.03.005; pmid: 21531607
16. F. J. Mojica, C. Díez-Villaseñor, J. García-Martínez, E. Soria, Intervening sequences of regularly spaced prokaryotic repeats derive from foreign genetic elements. *J. Mol. Evol.* **60**, 174–182 (2005). doi: 10.1007/s00239-004-0046-3; pmid: 15791728
17. A. Bolotin, B. Quinquis, A. Sorokin, S. D. Ehrlich, Clustered regularly interspaced short palindrome repeats (CRISPRs) have spacers of extrachromosomal origin. *Microbiology* **151**, 2551–2561 (2005). doi: 10.1099/mic.0.28048-0; pmid: 16079334
18. C. Pourcel, G. Salvignol, G. Vergnaud, CRISPR elements in *Yersinia pestis* acquire new repeats by preferential uptake of bacteriophage DNA, and provide additional tools for evolutionary studies. *Microbiology* **151**, 653–663 (2005). doi: 10.1099/mic.0.27437-0; pmid: 15758212
19. K. S. Makarova, N. V. Grishin, S. A. Shabalina, Y. I. Wolf, E. V. Koonin, A putative RNA-interference-based immune system in prokaryotes: Computational analysis of the predicted enzymatic machinery, functional analogies with eukaryotic RNAi, and hypothetical mechanisms of action. *Biol. Direct* **1**, 7 (2006). doi: 10.1186/1745-6150-1-7; pmid: 16545108
20. J. van der Oost, M. M. Jore, E. R. Westra, M. Lundgren, S. J. Brouns, CRISPR-based adaptive and heritable immunity in prokaryotes. *Trends Biochem. Sci.* **34**, 401–407 (2009). doi: 10.1016/j.tibs.2009.05.002; pmid: 19646880
21. B. Wiedenheft, S. H. Sternberg, J. A. Doudna, RNA-guided genetic silencing systems in bacteria and archaea. *Nature* **482**, 331–338 (2012). doi: 10.1038/nature10886; pmid: 22337052
22. R. Barrangou, L. A. Marraffini, CRISPR-Cas systems: Prokaryotes upgrade to adaptive immunity. *Mol. Cell* **54**, 234–244 (2014). doi: 10.1016/j.molcel.2014.03.011; pmid: 24766887
23. L. A. Marraffini, CRISPR-Cas immunity in prokaryotes. *Nature* **526**, 55–61 (2015). doi: 10.1038/nature15386; pmid: 26432244
24. G. Gasiunas, T. Sinkunas, V. Siksnys, Molecular mechanisms of CRISPR-mediated microbial immunity. *Cell. Mol. Life Sci.* **71**, 449–465 (2014). doi: 10.1007/s00018-013-1438-6; pmid: 23959171
25. E. R. Westra, A. Buckling, P. C. Fineran, CRISPR-Cas systems: Beyond adaptive immunity. *Nat. Rev. Microbiol.* **12**, 317–326 (2014). doi: 10.1038/nrmicro3241; pmid: 24704746
26. T. R. Sampson, D. S. Weiss, CRISPR-Cas systems: New players in gene regulation and bacterial physiology. *Front. Cell Infect. Microbiol.* **4**, 37 (2014). doi: 10.3389/fcimb.2014.00037; pmid: 24772391
27. R. Louwen, R. H. Staals, H. P. Endtz, P. van Baarlen, J. van der Oost, The role of CRISPR-Cas systems in virulence of pathogenic bacteria. *Microbiol. Mol. Biol. Rev.* **78**, 74–88 (2014). doi: 10.1128/MMBR.00039-13; pmid: 24600041
28. N. Takeuchi, Y. I. Wolf, K. S. Makarova, E. V. Koonin, Nature and intensity of selection pressure on CRISPR-associated genes. *J. Bacteriol.* **194**, 1216–1225 (2012). doi: 10.1128/JB.06521-11; pmid: 22178975
29. E. V. Koonin, Y. I. Wolf, Evolution of the CRISPR-Cas adaptive immunity systems in prokaryotes: Models and observations on virus-host coevolution. *Mol. Biosyst.* **11**, 20–27 (2015). doi: 10.1039/C4MB00438H; pmid: 25238531
30. K. S. Makarova *et al*., An updated evolutionary classification of CRISPR-Cas systems. *Nat. Rev. Microbiol.* **13**, 722–736 (2015). doi: 10.1038/nrmicro3569; pmid: 26411297
31. S. Shmakov *et al*., Discovery and functional characterization of diverse class 2 CRISPR-Cas systems. *Mol. Cell* **60**, 385–397 (2015). doi: 10.1016/j.molcel.2015.10.008; pmid: 26593719
32. K. S. Makarova, L. Aravind, Y. I. Wolf, E. V. Koonin, Unification of Cas protein families and a simple scenario for the origin and evolution of CRISPR-Cas systems. *Biol. Direct* **6**, 38 (2011). doi: 10.1186/1745-6150-6-38; pmid: 21756346
33. K. S. Makarova, Y. I. Wolf, E. V. Koonin, The basic building blocks and evolution of CRISPR-CAS systems. *Biochem. Soc. Trans.* **41**, 1392–1400 (2013). doi: 10.1042/BST20130038; pmid: 24256226
34. C. Rouillon *et al*., Structure of the CRISPR interference complex CSM reveals key similarities with cascade. *Mol. Cell* **52**, 124–134 (2013). doi: 10.1016/j.molcel.2013.08.020; pmid: 24119402
35. M. Spilman *et al*., Structure of an RNA silencing complex of the CRISPR-Cas immune system. *Mol. Cell* **52**, 146–152 (2013). doi: 10.1016/j.molcel.2013.09.008; pmid: 24119404
36. M. Jinek *et al*., A programmable dual-RNA-guided DNA endonuclease in adaptive bacterial immunity. *Science* **337**, 816–821 (2012). doi: 10.1126/science.1225829; pmid: 22745249
37. E. Deltcheva *et al*., CRISPR RNA maturation by trans-encoded small RNA and host factor RNase III. *Nature* **471**, 602–607 (2011). doi: 10.1038/nature09886; pmid: 21455174
38. K. Chylinski, K. S. Makarova, E. Charpentier, E. V. Koonin, Classification and evolution of type II CRISPR-Cas systems. *Nucleic Acids Res.* **42**, 6091–6105 (2014). doi: 10.1093/nar/gku241; pmid: 24728998
39. B. Zetsche *et al*., Cpf1 is a single RNA-guided endonuclease of a class 2 CRISPR-Cas system. *Cell* **163**, 759–771 (2015). doi: 10.1016/j.cell.2015.09.038; pmid: 26422227
40. T. Yamano *et al*., Crystal structure of Cpf1 in complex with guide RNA and target DNA. *Cell* **165**, 949–962 (2016). doi: 10.1016/j.cell.2016.04.003; pmid: 24884953
41. M. Krupovic, K. S. Makarova, P. Forterre, D. Prangishvili, E. V. Koonin, Casposons: A new superfamily of self-synthesizing DNA transposons at the origin of prokaryotic CRISPR-Cas immunity. *BMC Biol.* **12**, 36 (2014). pmid: 24884953
42. A. B. Hickman, F. Dyda, The casposon-encoded Cas1 protein from *Aciduliprofundum boonei* is a DNA integrase that generates target site duplications. *Nucleic Acids Res.* **43**, 10576–10587 (2015). doi: 10.1093/nar/gkv1180; pmid: 26573596
43. M. Krupovic, S. Shmakov, K. S. Makarova, P. Forterre, E. V. Koonin, Recent mobility of casposons, self-synthesizing

transposons at the origin of the CRISPR-Cas immunity. *Genome Biol. Evol.* **8**, 375–386 (2016). doi: 10.1093/gbe/evw006; pmid: 26764427
44. E. V. Koonin, M. Krupovic, Evolution of adaptive immunity from transposable elements combined with innate immune systems. *Nat. Rev. Genet.* **16**, 184–192 (2015). doi: 10.1038/nrg3859; pmid: 25488578
45. V. V. Kapitonov, K. S. Makarova, E. V. Koonin, ISC, a novel group of bacterial and archaeal DNA transposons that encode Cas9 homologs. *J. Bacteriol.* **198**, 797–807 (2016). pmid: 26712934
46. G. Amitai, R. Sorek, CRISPR-Cas adaptation: Insights into the mechanism of action. *Nat. Rev. Microbiol.* **14**, 67–76 (2016). doi: 10.1038/nrmicro.2015.14; pmid: 26751509
47. H. Deveau *et al*., Phage response to CRISPR-encoded resistance in *Streptococcus thermophilus*. *J. Bacteriol.* **190**, 1390–1400 (2008). doi: 10.1128/JB.01412-07; pmid: 18065545
48. F. J. Mojica, C. Díez-Villaseñor, J. García-Martínez, C. Almendros, Short motif sequences determine the targets of the prokaryotic CRISPR defence system. *Microbiology* **155**, 733–740 (2009). doi: 10.1099/mic.0.023960-0; pmid: 19246744
49. D. C. Swarts, C. Mosterd, M. W. van Passel, S. J. Brouns, CRISPR interference directs strand specific spacer acquisition. *PLOS ONE* **7**, e35888 (2012). doi: 10.1371/journal.pone.0035888; pmid: 22558257
50. K. A. Datsenko *et al*., Molecular memory of prior infections activates the CRISPR/Cas adaptive bacterial immunity system. *Nat. Commun.* **3**, 945 (2012). doi: 10.1038/ncomms1937; pmid: 22781758
51. A. Stern, L. Keren, O. Wurtzel, G. Amitai, R. Sorek, Self-targeting by CRISPR: Gene regulation or autoimmunity? *Trends Genet.* **26**, 335–340 (2010). doi: 10.1016/j.tig.2010.05.008; pmid: 20598393
52. I. Yosef, M. G. Goren, U. Qimron, Proteins and DNA elements essential for the CRISPR adaptation process in *Escherichia coli*. *Nucleic Acids Res.* **40**, 5569–5576 (2012). doi: 10.1093/nar/gks216; pmid: 22402487
53. Y. Wei, R. M. Terns, M. P. Terns, Cas9 function and host genome sampling in type II-A CRISPR-Cas adaptation. *Genes Dev.* **29**, 356–361 (2015). doi: 10.1101/gad.257550.114; pmid: 25691466
54. C. Díez-Villaseñor, N. M. Guzmán, C. Almendros, J. García-Martínez, F. J. Mojica, CRISPR-spacer integration reporter plasmids reveal distinct genuine acquisition specificities among CRISPR-Cas I-E variants of *Escherichia coli*. *RNA Biol.* **10**, 792–802 (2013). doi: 10.4161/rna.24023; pmid: 23445770
55. J. K. Nuñez *et al*., Cas1-Cas2 complex formation mediates spacer acquisition during CRISPR-Cas adaptive immunity. *Nat. Struct. Mol. Biol.* **21**, 528–534 (2014). doi: 10.1038/nsmb.2820; pmid: 24793649
56. A. Levy *et al*., CRISPR adaptation biases explain preference for acquisition of foreign DNA. *Nature* **520**, 505–510 (2015). doi: 10.1038/nature14302; pmid: 25874675
57. S. Erdmann, S. Le Moine Bauer, R. A. Garrett, Inter-viral conflicts that exploit host CRISPR immune systems of *Sulfolobus*. *Mol. Microbiol.* **91**, 900–917 (2014). doi: 10.1111/mmi.12503; pmid: 24433295
58. D. B. Wigley, RecBCD: The supercar of DNA repair. *Cell* **131**, 651–653 (2007). doi: 10.1016/j.cell.2007.11.004; pmid: 18022359
59. M. E. Dupuis, M. Villion, A. H. Magadán, S. Moineau, CRISPR-Cas and restriction-modification systems are compatible and increase phage resistance. *Nat. Commun.* **4**, 2087 (2013). doi: 10.1038/ncomms3087; pmid: 23820428
60. J. Wang *et al*., Structural and mechanistic basis of PAM-dependent spacer acquisition in CRISPR-Cas systems. *Cell* **163**, 840–853 (2015). doi: 10.1016/j.cell.2015.10.008; pmid: 26478180
61. J. K. Nuñez, A. S. Lee, A. Engelman, J. A. Doudna, Integrase-mediated spacer acquisition during CRISPR-Cas adaptive immunity. *Nature* **519**, 193–198 (2015). doi: 10.1038/nature14237; pmid: 25707795
62. S. Silas *et al*., Direct CRISPR spacer acquisition from RNA by a natural reverse transcriptase-Cas1 fusion protein. *Science* **351**, aad4234 (2016). doi: 10.1126/science.aad4234; pmid: 26917774
63. P. C. Fineran, E. Charpentier, Memory of viral infections by CRISPR-Cas adaptive immune systems: Acquisition of new information. *Virology* **434**, 202–209 (2012). doi: 10.1016/j.virol.2012.10.003; pmid: 23123013
64. Z. Arslan, V. Hermanns, R. Wurm, R. Wagner, Ü. Pul, Detection and characterization of spacer integration intermediates in type I-E CRISPR-Cas system. *Nucleic Acids Res.* **42**, 7884–7893 (2014). doi: 10.1093/nar/gku510; pmid: 24920831
65. M. Li, R. Wang, D. Zhao, H. Xiang, Adaptation of the *Haloarcula hispanica* CRISPR-Cas system to a purified virus strictly requires a priming process. *Nucleic Acids Res.* **42**, 2483–2492 (2014). doi: 10.1093/nar/gkt1154; pmid: 24265226
66. C. Richter *et al*., Priming in the type I-F CRISPR-Cas system triggers strand-independent spacer acquisition, bi-directionally from the primed protospacer. *Nucleic Acids Res.* **42**, 8516–8526 (2014). doi: 10.1093/nar/gku527; pmid: 24990370
67. P. C. Fineran *et al*., Degenerate target sites mediate rapid primed CRISPR adaptation. *Proc. Natl. Acad. Sci. U.S.A.* **111**, E1629–E1638 (2014). doi: 10.1073/pnas.1400071111; pmid: 24711427
68. C. Xue *et al*., CRISPR interference and priming varies with individual spacer sequences. *Nucleic Acids Res.* **43**, 10831–10847 (2015). doi: 10.1093/nar/gkv1259; pmid: 26586800
69. D. Vorontsova *et al*., Foreign DNA acquisition by the I-F CRISPR-Cas system requires all components of the interference machinery. *Nucleic Acids Res.* **43**, 10848–10860 (2015). doi: 10.1093/nar/gkv1261; pmid: 26586803
70. I. Ivančić-Baće, S. D. Cass, S. J. Wearne, E. L. Bolt, Different genome stability proteins underpin primed and naïve adaptation in *E. coli* CRISPR-Cas immunity. *Nucleic Acids Res.* **43**, 10821–10830 (2015). doi: 10.1093/nar/gkv1213; pmid: 26578567
71. R. Heler *et al*., Cas9 specifies functional viral targets during CRISPR-Cas adaptation. *Nature* **519**, 199–202 (2015). doi: 10.1038/nature14245; pmid: 25707807
72. S. P. Hooton, I. F. Connerton, *Campylobacter jejuni* acquire new host-derived CRISPR spacers when in association with bacteriophages harboring a CRISPR-like Cas4 protein. *Front. Microbiol.* **5**, 744 (2014). pmid: 25601859
73. E. Charpentier, H. Richter, J. van der Oost, M. F. White, Biogenesis pathways of RNA guides in archaeal and bacterial CRISPR-Cas adaptive immunity. *FEMS Microbiol. Rev.* **39**, 428–441 (2015). doi: 10.1093/femsre/fuv023; pmid: 25994611
74. J. Carte, R. Wang, H. Li, R. M. Terns, M. P. Terns, Cas6 is an endoribonuclease that generates guide RNAs for invader defense in prokaryotes. *Genes Dev.* **22**, 3489–3496 (2008). doi: 10.1101/gad.1742908; pmid: 19141480
75. L. A. Marraffini, E. J. Sontheimer, CRISPR interference: RNA-directed adaptive immunity in bacteria and archaea. *Nat. Rev. Genet.* **11**, 181–190 (2010). doi: 10.1038/nrg2749; pmid: 20125085
76. M. M. Jore *et al*., Structural basis for CRISPR RNA-guided DNA recognition by Cascade. *Nat. Struct. Mol. Biol.* **18**, 529–536 (2011). doi: 10.1038/nsmb.2019; pmid: 21460843
77. J. Reeks, J. H. Naismith, M. F. White, CRISPR interference: A structural perspective. *Biochem. J.* **453**, 155–166 (2013). doi: 10.1042/BJ20130316; pmid: 23805973
78. O. Niewoehner, M. Jinek, J. A. Doudna, Evolution of CRISPR RNA recognition and processing by Cas6 endonucleases. *Nucleic Acids Res.* **42**, 1341–1353 (2014). doi: 10.1093/nar/gkt922; pmid: 24150936
79. B. Wiedenheft *et al*., RNA-guided complex from a bacterial immune system enhances target recognition through seed sequence interactions. *Proc. Natl. Acad. Sci. U.S.A.* **108**, 10092–10097 (2011). doi: 10.1073/pnas.1102716108; pmid: 21536913
80. M. F. Rollins, J. T. Schuman, K. Paulus, H. S. Bukhari, B. Wiedenheft, Mechanism of foreign DNA recognition by a CRISPR RNA-guided surveillance complex from *Pseudomonas aeruginosa*. *Nucleic Acids Res.* **43**, 2216–2222 (2015). doi: 10.1093/nar/gkv094; pmid: 25662606
81. B. Wiedenheft *et al*., Structures of the RNA-guided surveillance complex from a bacterial immune system. *Nature* **477**, 486–489 (2011). doi: 10.1038/nature10402; pmid: 21938068
82. R. E. Haurwitz, M. Jinek, B. Wiedenheft, K. Zhou, J. A. Doudna, Sequence- and structure-specific RNA processing by a CRISPR endonuclease. *Science* **329**, 1355–1358 (2010). doi: 10.1126/science.1192272; pmid: 20829488
83. K. H. Nam *et al*., Cas5d protein processes pre-crRNA and assembles into a cascade-like interference complex in subtype I-C/Dvulg CRISPR-Cas system. *Structure* **20**, 1574–1584 (2012). doi: 10.1016/j.str.2012.06.016; pmid: 22841292
84. R. H. Staals *et al*., RNA targeting by the type III-A CRISPR-Cas Csm complex of *Thermus thermophilus*. *Mol. Cell* **56**, 518–530 (2014). doi: 10.1016/j.molcel.2014.10.005; pmid: 25457165
85. S. Majumdar *et al*., Three CRISPR-Cas immune effector complexes coexist in *Pyrococcus furiosus*. *RNA* **21**, 1147–1158 (2015). doi: 10.1261/rna.049130.114; pmid: 25904135
86. J. Zhang *et al*., Structure and mechanism of the CMR complex for CRISPR-mediated antiviral immunity. *Mol. Cell* **45**, 303–313 (2012). doi: 10.1016/j.molcel.2011.12.013; pmid: 22227115
87. A. Hatoum-Aslan, P. Samai, I. Maniv, W. Jiang, L. A. Marraffini, A ruler protein in a complex for antiviral defense determines the length of small interfering CRISPR RNAs. *J. Biol. Chem.* **288**, 27888–27897 (2013). doi: 10.1074/jbc.M113.499244; pmid: 23935102
88. G. Gasiunas, R. Barrangou, P. Horvath, V. Siksnys, Cas9-crRNA ribonucleoprotein complex mediates specific DNA cleavage for adaptive immunity in bacteria. *Proc. Natl. Acad. Sci. U.S.A.* **109**, E2579–E2586 (2012). doi: 10.1073/pnas.1208507109; pmid: 22949671
89. R. A. Garrett *et al*., CRISPR-Cas adaptive immune systems of the sulfolobales: Unravelling their complexity and diversity. *Life* **5**, 783–817 (2015). doi: 10.3390/life5010783; pmid: 25764276
90. Y. Zhang *et al*., Processing-independent CRISPR RNAs limit natural transformation in *Neisseria meningitidis*. *Mol. Cell* **50**, 488–503 (2013). doi: 10.1016/j.molcel.2013.05.001; pmid: 23706818
91. I. Fonfara, H. Richter, M. Bratovič, A. Le Rhun, E. Charpentier, The CRISPR-associated DNA-cleaving enzyme Cpf1 also processes precursor CRISPR RNA. *Nature* **532**, 517–521 (2016). doi: 10.1038/nature17945; pmid: 27096362
92. E. Semenova *et al*., Interference by clustered regularly interspaced short palindromic repeat (CRISPR) RNA is governed by a seed sequence. *Proc. Natl. Acad. Sci. U.S.A.* **108**, 10098–10103 (2011). doi: 10.1073/pnas.1104144108; pmid: 21646539
93. S. H. Sternberg, S. Redding, M. Jinek, E. C. Greene, J. A. Doudna, DNA interrogation by the CRISPR RNA-guided endonuclease Cas9. *Nature* **507**, 62–67 (2014). doi: 10.1038/nature13011; pmid: 24476820
94. S. Redding *et al*., Surveillance and processing of foreign DNA by the *Escherichia coli* CRISPR-Cas system. *Cell* **163**, 854–865 (2015). doi: 10.1016/j.cell.2015.10.003; pmid: 26522594
95. M. Rutkauskas *et al*., Directional R-loop formation by the CRISPR-Cas surveillance complex cascade provides efficient off-target site rejection. *Cell Rep.* **10**, 1534–1543 (2015). pmid: 25753419
96. T. R. Blosser *et al*., Two distinct DNA binding modes guide dual roles of a CRISPR-Cas protein complex. *Mol. Cell* **58**, 60–70 (2015). doi: 10.1016/j.molcel.2015.01.028; pmid: 25752578
97. R. N. Jackson *et al*., Crystal structure of the CRISPR RNA-guided surveillance complex from *Escherichia coli*. *Science* **345**, 1473–1479 (2014). doi: 10.1126/science.1256328; pmid: 25103409
98. S. Mulepati, A. Héroux, S. Bailey, Crystal structure of a CRISPR RNA-guided surveillance complex bound to a ssDNA target. *Science* **345**, 1479–1484 (2014). doi: 10.1126/science.1256996; pmid: 25123481
99. D. W. Taylor *et al*., Structures of the CRISPR-Cmr complex reveal mode of RNA target positioning. *Science* **348**, 581–585 (2015). doi: 10.1126/science.aaa4535; pmid: 25837515
100. T. Osawa, H. Inanaga, C. Sato, T. Numata, Crystal structure of the CRISPR-Cas RNA silencing Cmr complex bound to a target analog. *Mol. Cell* **58**, 418–430 (2015). doi: 10.1016/j.molcel.2015.03.018; pmid: 25921071
101. R. N. Jackson, B. Wiedenheft, A conserved structural chassis for mounting versatile CRISPR RNA-guided immune responses. *Mol. Cell* **58**, 722–728 (2015). doi: 10.1016/j.molcel.2015.05.023; pmid: 26028539
102. Z. Zebec, A. Manica, J. Zhang, M. F. White, C. Schleper, CRISPR-mediated targeted mRNA degradation in the archaeon *Sulfolobus solfataricus*. *Nucleic Acids Res.* **42**, 5280–5288 (2014). doi: 10.1093/nar/gku161; pmid: 24603867
103. R. H. Staals *et al*., Structure and activity of the RNA-targeting type III-B CRISPR-Cas complex of *Thermus thermophilus*. *Mol. Cell* **52**, 135–145 (2013). doi: 10.1016/j.molcel.2013.09.013; pmid: 24119403
104. G. Tamulaitis *et al*., Programmable RNA shredding by the type III-A CRISPR-Cas system of *Streptococcus thermophilus*.

Mol. Cell **56**, 506–517 (2014). doi: 10.1016/j.molcel.2014.09.027; pmid: 25458845
105. W. Peng, M. Feng, X. Feng, Y. X. Liang, Q. She, An archaeal CRISPR type III-B system exhibiting distinctive RNA targeting features and mediating dual RNA and DNA interference. *Nucleic Acids Res.* **43**, 406–417 (2015). doi: 10.1093/nar/gku1302; pmid: 25505143
106. M. A. Estrella, F. T. Kuo, S. Bailey, RNA-activated DNA cleavage by the type III-B CRISPR-Cas effector complex. *Genes Dev.* **30**, 460–470 (2016). doi: 10.1101/gad.273722.115; pmid: 26848046
107. J. R. Elmore *et al*., Bipartite recognition of target RNAs activates DNA cleavage by the type III-B CRISPR-Cas system. *Genes Dev.* **30**, 447–459 (2016). doi: 10.1101/gad.272153.115; pmid: 26848045
108. L. Deng, R. A. Garrett, S. A. Shah, X. Peng, Q. She, A novel interference mechanism by a type IIIB CRISPR-Cmr module in *Sulfolobus*. *Mol. Microbiol.* **87**, 1088–1099 (2013). doi: 10.1111/mmi.12152; pmid: 23320564
109. P. Samai *et al*., Co-transcriptional DNA and RNA cleavage during type III CRISPR-Cas immunity. *Cell* **161**, 1164–1174 (2015). doi: 10.1016/j.cell.2015.04.027; pmid: 25959775
110. G. W. Goldberg, W. Jiang, D. Bikard, L. A. Marraffini, Conditional tolerance of temperate phages via transcription-dependent CRISPR-Cas targeting. *Nature* **514**, 633–637 (2014). doi: 10.1038/nature13637; pmid: 25174707
111. C. R. Hale, A. Cocozaki, H. Li, R. M. Terns, M. P. Terns, Target RNA capture and cleavage by the Cmr type III-B CRISPR-Cas effector complex. *Genes Dev.* **28**, 2432–2443 (2014). doi: 10.1101/gad.250712.114; pmid: 25367038
112. C. Benda *et al*., Structural model of a CRISPR RNA-silencing complex reveals the RNA-target cleavage activity in Cmr4. *Mol. Cell* **56**, 43–54 (2014). doi: 10.1016/j.molcel.2014.09.002; pmid: 25280103
113. N. F. Ramia *et al*., Essential structural and functional roles of the Cmr4 subunit in RNA cleavage by the Cmr CRISPR-Cas complex. *Cell Rep.* **9**, 1610–1617 (2014). doi: 10.1016/j.celrep.2014.11.007; pmid: 25482566
114. N. F. Ramia, L. Tang, A. I. Cocozaki, H. Li, *Staphylococcus epidermidis* Csm1 is a 3′-5′ exonuclease. *Nucleic Acids Res.* **42**, 1129–1138 (2014). doi: 10.1093/nar/gkt914; pmid: 24121684
115. N. F. Sheppard, C. V. Glover 3rd, R. M. Terns, M. P. Terns, The CRISPR-associated Csx1 protein of *Pyrococcus furiosus* is an adenosine-specific endoribonuclease. *RNA* **22**, 216–224 (2016). doi: 10.1261/rna.039842.113; pmid: 26647461
116. W. Jiang, P. Samai, L. A. Marraffini, Degradation of phage transcripts by CRISPR-associated RNases enables type III CRISPR-Cas immunity. *Cell* **164**, 710–721 (2016). doi: 10.1016/j.cell.2015.12.053; pmid: 26853474
117. O. Niewoehner, M. Jinek, Structural basis for the endoribonuclease activity of the type III-A CRISPR-associated protein Csm6. *RNA* **22**, 318–329 (2016). doi: 10.1261/rna.054098.115; pmid: 26763118
118. L. A. Marraffini, E. J. Sontheimer, Self versus non-self discrimination during CRISPR RNA-directed immunity. *Nature* **463**, 568–571 (2010). doi: 10.1038/nature08703; pmid: 20072129
119. J. van der Oost, E. R. Westra, R. N. Jackson, B. Wiedenheft, Unravelling the structural and mechanistic basis of CRISPR-Cas systems. *Nat. Rev. Microbiol.* **12**, 479–492 (2014). doi: 10.1038/nrmicro3279; pmid: 24909109
120. M. Jinek *et al*., Structures of Cas9 endonucleases reveal RNA-mediated conformational activation. *Science* **343**, 1247997 (2014). doi: 10.1126/science.1247997; pmid: 24505130
121. H. Nishimasu *et al*., Crystal structure of Cas9 in complex with guide RNA and target DNA. *Cell* **156**, 935–949 (2014). doi: 10.1016/j.cell.2014.02.001; pmid: 24529477
122. C. Anders, O. Niewoehner, A. Duerst, M. Jinek, Structural basis of PAM-dependent target DNA recognition by the Cas9 endonuclease. *Nature* **513**, 569–573 (2014). doi: 10.1038/nature13579; pmid: 25079318
123. S. H. Sternberg, B. LaFrance, M. Kaplan, J. A. Doudna, Conformational control of DNA target cleavage by CRISPR-Cas9. *Nature* **527**, 110–113 (2015). doi: 10.1038/nature15544; pmid: 26524520
124. A. H. Magadán, M. È. Dupuis, M. Villion, S. Moineau, Cleavage of phage DNA by the *Streptococcus thermophilus* CRISPR3-Cas system. *PLOS ONE* **7**, e40913 (2012). doi: 10.1371/journal.pone.0040913; pmid: 22911717
125. Y. Zhang, R. Rajan, H. S. Seifert, A. Mondragón, E. J. Sontheimer, DNase H activity of *Neisseria meningitidis* Cas9. *Mol. Cell* **60**, 242–255 (2015). doi: 10.1016/j.molcel.2015.09.020; pmid: 26474066
126. P. D. Hsu, E. S. Lander, F. Zhang, Development and applications of CRISPR-Cas9 for genome engineering. *Cell* **157**, 1262–1278 (2014). doi: 10.1016/j.cell.2014.05.010; pmid: 24906146
127. O. O. Abudayyeh *et al*., C2c2 is a single-component programmable RNA-guided RNA-targeting CRISPR effector. *Science* **353**, aaf5573 (2016).
128. J. Bondy-Denomy *et al*., Multiple mechanisms for CRISPR-Cas inhibition by anti-CRISPR proteins. *Nature* **526**, 136–139 (2015). doi: 10.1038/nature15254; pmid: 26416740
129. K. D. Seed, D. W. Lazinski, S. B. Calderwood, A. Camilli, A bacteriophage encodes its own CRISPR/Cas adaptive response to evade host innate immunity. *Nature* **494**, 489–491 (2013). doi: 10.1038/nature11927; pmid: 23446421
130. A. Levasseur *et al*., MIMIVIRE is a defence system in mimivirus that confers resistance to virophage. *Nature* **531**, 249–252 (2016). doi: 10.1038/nature17146; pmid: 26934229
131. L. Cong *et al*., Multiplex genome engineering using CRISPR/Cas systems. *Science* **339**, 819–823 (2013). doi: 10.1126/science.1231143; pmid: 23287718
132. P. Mali *et al*., RNA-guided human genome engineering via Cas9. *Science* **339**, 823–826 (2013). doi: 10.1126/science.1232033; pmid: 23287722
133. M. Jinek *et al*., RNA-programmed genome editing in human cells. *eLife* **2**, e00471 (2013). doi: 10.7554/eLife.00471; pmid: 23386978
134. S. W. Cho, S. Kim, J. M. Kim, J. S. Kim, Targeted genome engineering in human cells with the Cas9 RNA-guided endonuclease. *Nat. Biotechnol.* **31**, 230–232 (2013). doi: 10.1038/nbt.2507; pmid: 23360966
135. L. S. Qi *et al*., Repurposing CRISPR as an RNA-guided platform for sequence-specific control of gene expression. *Cell* **152**, 1173–1183 (2013). doi: 10.1016/j.cell.2013.02.022; pmid: 23452860
136. D. Bikard *et al*., Programmable repression and activation of bacterial gene expression using an engineered CRISPR-Cas system. *Nucleic Acids Res.* **41**, 7429–7437 (2013). doi: 10.1093/nar/gkt520; pmid: 23761437
137. S. Konermann *et al*., Optical control of mammalian endogenous transcription and epigenetic states. *Nature* **500**, 472–476 (2013). pmid: 23877069
138. L. A. Gilbert *et al*., CRISPR-mediated modular RNA-guided regulation of transcription in eukaryotes. *Cell* **154**, 442–451 (2013). doi: 10.1016/j.cell.2013.06.044; pmid: 23849981
139. B. Chen *et al*., Dynamic imaging of genomic loci in living human cells by an optimized CRISPR/Cas system. *Cell* **155**, 1479–1491 (2013). doi: 10.1016/j.cell.2013.12.001; pmid: 24360272
140. I. B. Hilton *et al*., Epigenome editing by a CRISPR-Cas9-based acetyltransferase activates genes from promoters and enhancers. *Nat. Biotechnol.* **33**, 510–517 (2015). doi: 10.1038/nbt.3199; pmid: 25849900
141. N. A. Kearns *et al*., Functional annotation of native enhancers with a Cas9-histone demethylase fusion. *Nat. Methods* **12**, 401–403 (2015). doi: 10.1038/nmeth.3325; pmid: 25775043
142. S. Kiani *et al*., CRISPR transcriptional repression devices and layered circuits in mammalian cells. *Nat. Methods* **11**, 723–726 (2014). doi: 10.1038/nmeth.2969; pmid: 24797424
143. Y. Liu *et al*., Synthesizing AND gate genetic circuits based on CRISPR-Cas9 for identification of bladder cancer cells. *Nat. Commun.* **5**, 5393 (2014). doi: 10.1038/ncomms6393; pmid: 25373919
144. L. Nissim, S. D. Perli, A. Fridkin, P. Perez-Pinera, T. K. Lu, Multiplexed and programmable regulation of gene networks with an integrated RNA and CRISPR/Cas toolkit in human cells. *Mol. Cell* **54**, 698–710 (2014). doi: 10.1016/j.molcel.2014.04.022; pmid: 24837679
145. D. Bikard *et al*., Exploiting CRISPR-Cas nucleases to produce sequence-specific antimicrobials. *Nat. Biotechnol.* **32**, 1146–1150 (2014). doi: 10.1038/nbt.3043; pmid: 25282355
146. H. Ebina, N. Misawa, Y. Kanemura, Y. Koyanagi, Harnessing the CRISPR/Cas9 system to disrupt latent HIV-1 provirus. *Sci. Rep.* **3**, 2510 (2013). doi: 10.1038/srep02510; pmid: 23974631
147. V. Ramanan *et al*., CRISPR/Cas9 cleavage of viral DNA efficiently suppresses hepatitis B virus. *Sci. Rep.* **5**, 10833 (2015). doi: 10.1038/srep10833; pmid: 26035283
148. W. Hu *et al*., RNA-directed gene editing specifically eradicates latent and prevents new HIV-1 infection. *Proc. Natl. Acad. Sci. U.S.A.* **111**, 11461–11466 (2014). doi: 10.1073/pnas.1405186111; pmid: 25049410
149. O. Shalem *et al*., Genome-scale CRISPR-Cas9 knockout screening in human cells. *Science* **343**, 84–87 (2014). doi: 10.1126/science.1247005; pmid: 24336571
150. T. Wang, J. J. Wei, D. M. Sabatini, E. S. Lander, Genetic screens in human cells using the CRISPR-Cas9 system. *Science* **343**, 80–84 (2014). doi: 10.1126/science.1246981; pmid: 24336569
151. S. Konermann *et al*., Genome-scale transcriptional activation by an engineered CRISPR-Cas9 complex. *Nature* **517**, 583–588 (2015). doi: 10.1038/nature14136; pmid: 25494202
152. L. A. Gilbert *et al*., Genome-scale CRISPR-mediated control of gene repression and activation. *Cell* **159**, 647–661 (2014). doi: 10.1016/j.cell.2014.09.029; pmid: 25307932
153. B. P. Kleinstiver *et al*., Genome-wide specificities of CRISPR-Cas Cpf1 nucleases in human cells. *Nat. Biotechnol.* 10.1038/nbt.3620 (2016). doi: 10.1038/nbt.3620; pmid: 27347757
154. D. Kim *et al*., Genome-wide analysis reveals specificities of Cpf1 endonucleases in human cells. *Nat. Biotechnol.* 10.1038/nbt.3609 (2016). doi: 10.1038/nbt.3609; pmid: 27272384
155. P. Mali, K. M. Esvelt, G. M. Church, Cas9 as a versatile tool for engineering biology. *Nat. Methods* **10**, 957–963 (2013). doi: 10.1038/nmeth.2649; pmid: 24076990
156. F. A. Ran *et al*., Double nicking by RNA-guided CRISPR Cas9 for enhanced genome editing specificity. *Cell* **154**, 1380–1389 (2013). doi: 10.1016/j.cell.2013.08.021; pmid: 23992846
157. B. Zetsche, S. E. Volz, F. Zhang, A split-Cas9 architecture for inducible genome editing and transcription modulation. *Nat. Biotechnol.* **33**, 139–142 (2015). doi: 10.1038/nbt.3149; pmid: 25643054
158. K. M. Davis, V. Pattanayak, D. B. Thompson, J. A. Zuris, D. R. Liu, Small molecule-triggered Cas9 protein with improved genome-editing specificity. *Nat. Chem. Biol.* **11**, 316–318 (2015). doi: 10.1038/nchembio.1793; pmid: 25848930
159. Y. Fu, J. D. Sander, D. Reyon, V. M. Cascio, J. K. Joung, Improving CRISPR-Cas nuclease specificity using truncated guide RNAs. *Nat. Biotechnol.* **32**, 279–284 (2014). doi: 10.1038/nbt.2808; pmid: 24463574
160. I. M. Slaymaker *et al*., Rationally engineered Cas9 nucleases with improved specificity. *Science* **351**, 84–88 (2016). doi: 10.1126/science.aad5227; pmid: 26628643
161. B. P. Kleinstiver *et al*., High-fidelity CRISPR-Cas9 nucleases with no detectable genome-wide off-target effects. *Nature* **529**, 490–495 (2016). doi: 10.1038/nature16526; pmid: 26735016
162. F. A. Ran *et al*., In vivo genome editing using *Staphylococcus aureus* Cas9. *Nature* **520**, 186–191 (2015). doi: 10.1038/nature14299; pmid: 25830891
163. R. J. Platt *et al*., CRISPR-Cas9 knockin mice for genome editing and cancer modeling. *Cell* **159**, 440–455 (2014). doi: 10.1016/j.cell.2014.09.014; pmid: 25263330
164. W. Qin *et al*., Efficient CRISPR/Cas9-mediated genome editing in mice by zygote electroporation of nuclease. *Genetics* **200**, 423–430 (2015). doi: 10.1534/genetics.115.176594; pmid: 25819794
165. D. S. D'Astolfo *et al*., Efficient intracellular delivery of native proteins. *Cell* **161**, 674–690 (2015). doi: 10.1016/j.cell.2015.03.028; pmid: 25910214
166. K. M. Esvelt, A. L. Smidler, F. Catteruccia, G. M. Church, Concerning RNA-guided gene drives for the alteration of wild populations. *eLife* **3**, e03401 (2014). doi: 10.7554/eLife.03401; pmid: 25035423

ACKNOWLEDGMENTS

E.V.K. and K.S.M. are supported by the intramural program of the U.S. Department of Health and Human Services (to the National Library of Medicine). J.v.d.O. and P.M. are supported by the NWO/TOP grant 714.015.001. F.Z. is a New York Stem Cell Foundation–Robertson Investigator. F.Z. is supported by the NIH through NIMH (5DP1-MH100706 and 1R01-MH110049) and NIDDK (5R01DK097768-03), the New York Stem Cell, Simons, Paul G. Allen Family, and Vallee Foundations, and D. R. Cheng, T. Harriman, and R. Metcalfe. F.Z. is a founder of Editas Medicine and scientific advisor for Editas Medicine and Horizon Discovery.

SUPPLEMENTARY MATERIALS

www.sciencemag.org/content/353/6299/aad5147/suppl/DC1
Movie S1

10.1126/science.aad5147

RESEARCH ARTICLE SUMMARY

CRISPR EVOLUTION

C2c2 is a single-component programmable RNA-guided RNA-targeting CRISPR effector

Omar O. Abudayyeh, Jonathan S. Gootenberg, Silvana Konermann, Julia Joung, Ian M. Slaymaker, David B. T. Cox, Sergey Shmakov, Kira S. Makarova, Ekaterina Semenova, Leonid Minakhin, Konstantin Severinov, Aviv Regev, Eric S. Lander, Eugene V. Koonin,* Feng Zhang*

INTRODUCTION: Almost all archaea and about half of bacteria possess clustered regularly interspaced short palindromic repeat (CRISPR)–CRISPR-associated genes (Cas) adaptive immune systems, which protect microbes against viruses and other foreign DNA. All functionally characterized CRISPR systems have been reported to target DNA, with some multicomponent type III systems also targeting RNA. The putative class 2 type VI system, which has not been functionally characterized, encompasses the single-effector protein C2c2, which contains two Higher Eukaryotes and Prokaryotes Nucleotide-binding (HEPN) domains commonly associated with ribonucleases (RNases), suggesting RNA-guided RNA-targeting function.

RATIONALE: Existing studies have only established a role for RNA interference, in addition to DNA interference, in the multicomponent type III-A and III-B systems. We investigated the possibility of C2c2-mediated RNA inference by heterologously expressing C2c2 locus from *Leptotrichia shahii* (LshC2c2) in the model system *Escherichia coli*. The ability of LshC2c2 to protect against MS2 single-stranded RNA (ssRNA) phage infection was assessed by using every possible spacer sequence against the phage genome. We next developed protocols to reconstitute purified recombinant LshC2c2 protein and test its biochemical activity when incubated with its mature CRISPR RNA (crRNA) and target ssRNA. We systematically evaluated the parameters necessary for cleavage. Last, to demonstrate the potential utility of the LshC2c2 complex for RNA targeting in living bacterial cells, we guided it to knockdown red fluorescent protein (RFP) mRNA in vivo.

RESULTS: This work demonstrates the RNA-guided RNase activity of the putative type VI CRISPR-effector LshC2c2. Heterologously expressed C2c2 can protect *E. coli* from MS2 phage, and by screening against the MS2 genome, we identified a H (non-G) protospacer flanking site (PFS) following the RNA target site, which was confirmed by targeting a complementary sequence in the β-lactamase transcript followed by a degenerate nucleotide sequence. Using purified LshC2c2 protein, we demonstrate that C2c2 and crRNA are sufficient in vitro to achieve RNA-guided, PFS-dependent RNA cleavage. This cleavage preferentially occurs at uracil residues in ssRNA regions and depends on conserved catalytic residues in the two HEPN domains. Mutation of these residues yields a catalytically inactive RNA-binding protein. The secondary structure of the crRNA direct repeat (DR) stem is required for LshC2c2 activity, and mutations in the 3′ region of the DR eliminate cleavage activity. Targeting is also sensitive to multiple or consecutive mismatches in the spacer:protospacer duplex. C2c2 targeting of RFP mRNA in vivo results in reduced fluorescence. The knockdown of the RFP mRNA by C2c2 slowed *E. coli* growth, and in agreement with this finding, in vitro cleavage of the target RNA results in "collateral," nonspecific cleavage of other RNAs present in the reaction mix.

ON OUR WEBSITE

Read the full article at http://dx.doi.org/10.1126/science.aaf5573

CONCLUSION: LshC2c2 is a RNA-guided RNase which requires the activity of its two HEPN domains, suggesting previously unidentified mechanisms of RNA targeting and degradation by CRISPR systems. Promiscuous RNase activity of C2c2 after activation by the target slows bacterial growth and suggests that C2c2 could protect bacteria from virus spread via programmed cell death and dormancy induction. A single-effector RNA targeting system has the potential to serve as a general chassis for molecular tools for visualizing, degrading, or binding RNA in a programmable, multiplexed fashion. ■

The list of author affiliations is available in the full article online.
*Corresponding author. Email: zhang@broadinstitute.org (F.Z.); koonin@ncbi.nlm.nih.gov (E.V.K.)
Cite this article as O. O. Abudayyeh *et al.*, *Science* **353**, aaf5573 (2016). DOI: 10.1126/science.aaf5573

C2c2 is an RNA-guided RNase that provides protection against RNA phage. CRISPR-C2c2 from *L. shahii* can be reconstituted in *E. coli* to mediate RNA-guided interference of the RNA phage MS2. Biochemical characterization of C2c2 reveals crRNA-guided RNA cleavage facilitated by the two HEPN nuclease domains. Binding of the target RNA by C2c2-crRNA also activates a nonspecific RNase activity, which may lead to promiscuous cleavage of RNAs without complementarity to the crRNA guide sequence.

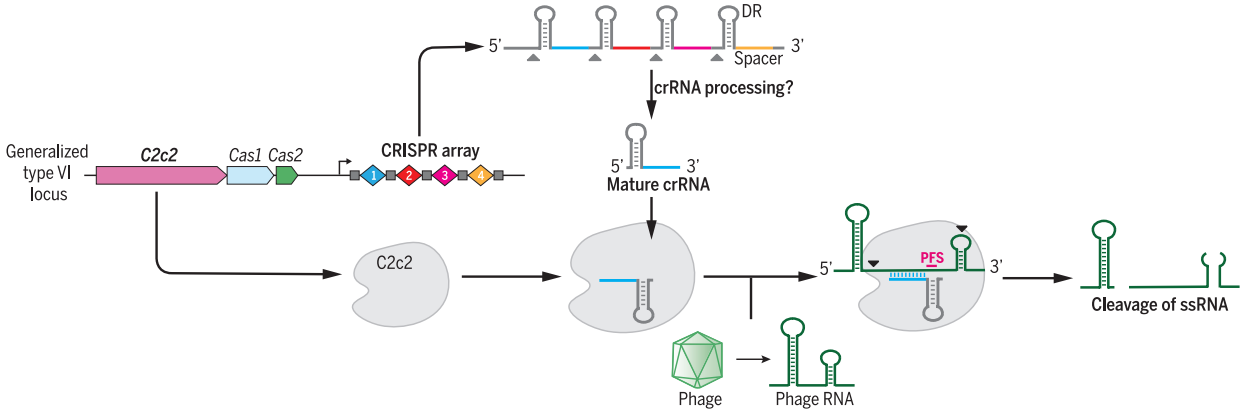

RESEARCH ARTICLE

CRISPR EVOLUTION

C2c2 is a single-component programmable RNA-guided RNA-targeting CRISPR effector

Omar O. Abudayyeh,[1,2,3,4]* Jonathan S. Gootenberg,[2,3,4,5]* Silvana Konermann,[2,3,4]* Julia Joung,[2,3,4] Ian M. Slaymaker,[2,3,4] David B. T. Cox,[1,2,3,4,6] Sergey Shmakov,[7,8] Kira S. Makarova,[8] Ekaterina Semenova,[9] Leonid Minakhin,[9] Konstantin Severinov,[7,9,10] Aviv Regev,[2,6] Eric S. Lander,[2,5,6] Eugene V. Koonin,[8]† Feng Zhang[1,2,3,4]†

The clustered regularly interspaced short palindromic repeat (CRISPR)–CRISPR-associated genes (Cas) adaptive immune system defends microbes against foreign genetic elements via DNA or RNA-DNA interference. We characterize the class 2 type VI CRISPR-Cas effector C2c2 and demonstrate its RNA-guided ribonuclease function. C2c2 from the bacterium *Leptotrichia shahii* provides interference against RNA phage. In vitro biochemical analysis shows that C2c2 is guided by a single CRISPR RNA and can be programmed to cleave single-stranded RNA targets carrying complementary protospacers. In bacteria, C2c2 can be programmed to knock down specific mRNAs. Cleavage is mediated by catalytic residues in the two conserved Higher Eukaryotes and Prokaryotes Nucleotide-binding (HEPN) domains, mutations of which generate catalytically inactive RNA-binding proteins. These results broaden our understanding of CRISPR-Cas systems and suggest that C2c2 can be used to develop new RNA-targeting tools.

Almost all archaea and about half of bacteria possess clustered regularly interspaced short palindromic repeats (CRISPRs) and CRISPR-associated genes (CRISPR-Cas)–adaptive immune systems (*1*, *2*), which protect microbes from viruses and other invading DNA through three steps: (i) adaptation—insertion of foreign nucleic acid segments (spacers) into the CRISPR array in between pairs of direct repeats (DRs); (ii) transcription and processing of the CRISPR array to produce mature CRISPR RNAs (crRNAs); and (iii) interference, by which Cas enzymes are guided by the crRNAs to target and cleave cognate sequences in the respective invader genomes (*3*–*5*). All CRISPR-Cas systems characterized to date follow these three steps, although the mechanistic implementation and proteins involved in these processes display extensive diversity.

[1]Department of Health Sciences and Technology, Massachusetts Institute of Technology, Cambridge, MA 02139, USA. [2]Broad Institute of MIT and Harvard, Cambridge, MA 02142, USA. [3]McGovern Institute for Brain Research at MIT, Cambridge, MA 02139, USA. [4]Departments of Brain and Cognitive Science and Biological Engineering, Massachusetts Institute of Technology, Cambridge, MA 02139, USA. [5]Department of Systems Biology, Harvard Medical School, Boston, MA 02115, USA. [6]Department of Biology, Massachusetts Institute of Technology, Cambridge, MA 02139, USA. [7]Skolkovo Institute of Science and Technology, Skolkovo, 143025, Russia. [8]National Center for Biotechnology Information, National Library of Medicine, National Institutes of Health, Bethesda, MD 20894, USA. [9]Waksman Institute for Microbiology, Rutgers, The State University of New Jersey, Piscataway, NJ 08854, USA. [10]Institute of Molecular Genetics, Russian Academy of Sciences, Moscow, 123182, Russia.
*These authors contributed equally to this work. †**Corresponding author. Email: zhang@broadinstitute.org (F.Z.); koonin@ncbi.nlm.nih.gov (E.V.K.)**

The CRISPR-Cas systems are broadly divided into two classes on the basis of the architecture of the interference module: Class 1 systems rely on multisubunit protein complexes, whereas class 2 systems use single-effector proteins (*1*). Within these two classes, types and subtypes are delineated according to the presence of distinct signature genes, protein sequence conservation, and organization of the respective genomic loci. Class 1 systems include type I, in which interference is achieved through assembly of multiple Cas proteins into the Cascade complex, and type III systems, which rely on either the Csm (type III-A/D) or Cmr (Type III-B/C) effector complexes, which are distantly related to the Cascade complex (*1*, *6*–*11*).

Class 2 CRISPR systems comprise type II systems, characterized by the single-component effector protein Cas9 (*12*–*17*), which contains RuvC and HNH nuclease domains, and type V systems, which use single RuvC domain–containing effectors such as Cpf1 (*18*), C2c1, and C2c3 (*19*). All functionally characterized systems, to date, have been reported to target DNA, and only the multicomponent type III-A and III-B systems additionally target RNA (*7*, *20*–*25*). However, the putative class 2 type VI system is characterized by the presence of the single-effector protein C2c2, which lacks homology to any known DNA nuclease domain but contains two Higher Eukaryotes and Prokaryotes Nucleotide-binding (HEPN) domains (*19*). Given that all functionally characterized HEPN domains are ribonucleases (RNases) (*26*), there is a possibility that C2c2 functions solely as an RNA-guided RNA-targeting CRISPR effector.

HEPN domains are also found in other Cas proteins. Csm6, a component of type III-A systems, and the homologous protein Csx1, in type III-B systems, each contain a single HEPN domain and have been biochemically characterized as single-stranded RNA (ssRNA)–specific endoribonucleases (endoRNases) (*21*, *27*, *28*). In addition, type III systems contain complexes of other Cas enzymes that bind and cleave ssRNA through acidic residues associated with RNA-recognition motif (RRM) domains. These complexes (Cas10-Csm in type III-A and Cmr in type III-B) carry out RNA-guided cotranscriptional cleavage of mRNA in concert with DNA target cleavage (*22*, *29*, *30*). In contrast, the roles of Csm6 and Csx1, which cleave their targets with little specificity, are less clear, although in some cases, RNA cleavage by Csm6 apparently serves as a second line of defense when DNA-targeting fails (*21*). Additionally, Csm6 and Csx1 have to dimerize to form a composite active site (*27*, *28*, *31*), but C2c2 contains two HEPN domains, which suggests that it functions as a monomeric endoRNase.

As is common with class 2 systems, type VI systems are simply organized. In particular, the type VI locus in *Leptotrichia shahii* contains Cas1, Cas2, C2c2, and a CRISPR array, which is expressed and processed into mature crRNAs (*19*). In all CRISPR-Cas systems characterized to date, Cas1 and Cas2 are exclusively involved in spacer acquisition (*32*–*37*), which suggests that C2c2 is the sole effector protein that uses a crRNA guide to achieve interference, likely targeting RNA.

Reconstitution of the *L. shahii* C2c2 locus in *Escherichia coli* confers RNA-guided immunity

We explored whether LshC2c2 could confer immunity to MS2 (*25*), a lytic ssRNA phage without DNA intermediates in its life cycle that infects *E. coli*. We constructed a low-copy plasmid carrying the entire LshC2c2 locus (pLshC2c2) so as to allow for heterologous reconstitution in *E. coli* (fig. S1A). Because expressed mature crRNAs from the LshC2c2 locus have a maximum spacer length of 28 nucleotides (nt) (fig. S1A) (*19*), we tiled all possible 28-nt target sites in the MS2 phage genome (Fig. 1A). This resulted in a library of 3473 spacer sequences (along with 588 nontargeting guides designed to have a Levenshtein distance of ≥8 with respect to the MS2 and *E. coli* genomes), which we inserted between pLshC2c2 DRs. After transformation in of this construct into *E. coli*, we infected cells with varying dilutions of MS2 (10^{-1}, 10^{-3}, and 10^{-5}) and analyzed surviving cells to determine the spacer sequences carried by cells that survived the infection. Cells carrying spacers that confer robust interference against MS2 are expected to proliferate faster than those that lack such sequences. After growth for 16 hours, we identified a number of spacers that were consistently enriched across three independent infection replicas in both the 10^{-1} and 10^{-3} dilution conditions, suggesting that they enabled interference against MS2. Specifically, 152 and 144 spacers showed >0.8 $\log_2$-fold enrichment in all three replicates for the 10^{-1} and

10^{-3} phage dilutions, respectively; of these two groups of top enriched spacers, 75 are shared (Fig. 1B; fig. S2, A to G; and table S1). Additionally, no nontargeting guides were found to be consistently enriched among the three 10^{-1}, 10^{-3}, or 10^{-5} phage replicates (fig. S2, D and G). We also analyzed the flanking regions of protospacers on the MS2 genome corresponding to the enriched spacers and found that spacers with a G immediately flanking the 3′ end of the protospacer were less fit relative to all other nucleotides at this position (A, U, or C), suggesting that the 3′ protospacer-flanking site (PFS) affects the efficacy of C2c2-mediated targeting (Fig. 1C and figs. S2, E and F, and S3). Although the PFS is adjacent to the protospacer target, we chose not to use the commonly used protospacer-adjacent motif (PAM) nomenclature because it has come to connote a sequence used in self versus nonself differentiation (*38*), which is irrelevant in a RNA-targeting system. It is worth noting that the avoidance of G by C2c2 echoes the absence of PAMs observed for other RNA-targeting CRISPR systems and effector proteins (*20*, *22*, *24*, *25*, *39*, *40*).

That only ~5% of crRNAs are enriched may reflect other factors influencing interference activity, such as accessibility of the target site that might be affected by RNA-binding proteins or secondary structure. In agreement with this hypothesis, the enriched spacers tend to cluster into regions of strong interference, where they are closer to each other than one would expect by random chance (fig. S3, F and G).

To validate the interference activity of the enriched spacers, we individually cloned four top-enriched spacers into pLshC2c2 CRISPR arrays and observed a 3- to 4-$\log_{10}$ reduction in plaque formation, which is consistent with the level of enrichment observed in the screen (Fig. 1B and fig. S4). We cloned 16 guides targeting distinct regions of the MS2 *mat* gene (four guides per possible single-nucleotide PFS). All 16 crRNAs mediated MS2 interference, although higher levels of resistance were observed for the C, A, and U PFS-targeting guides (Fig. 1, D and E, and fig. S5), indicating that C2c2 can be effectively retargeted in a crRNA-dependent fashion to sites within the MS2 genome.

To further validate the observed PFS preference with an alternate approach, we designed a protospacer site in the pUC19 plasmid at the 5′ end of the β-lactamase mRNA, which encodes ampicillin resistance in *E. coli*, flanked by five randomized nucleotides at the 3′ end. Significant depletion and enrichment was observed for the LshC2c2 locus (****P < 0.0001) as compared with the pACYC184 controls (fig. S6A). Analysis of the depleted PFS sequences confirmed the presence of a PFS preference of H (fig. S6B).

C2c2 is a single-effector endoRNase mediating ssRNA cleavage with a single crRNA guide

We purified the LshC2c2 protein (fig. S7) and assayed its ability to cleave an in vitro–transcribed 173-nt ssRNA target (Fig. 2A and fig. S8) containing

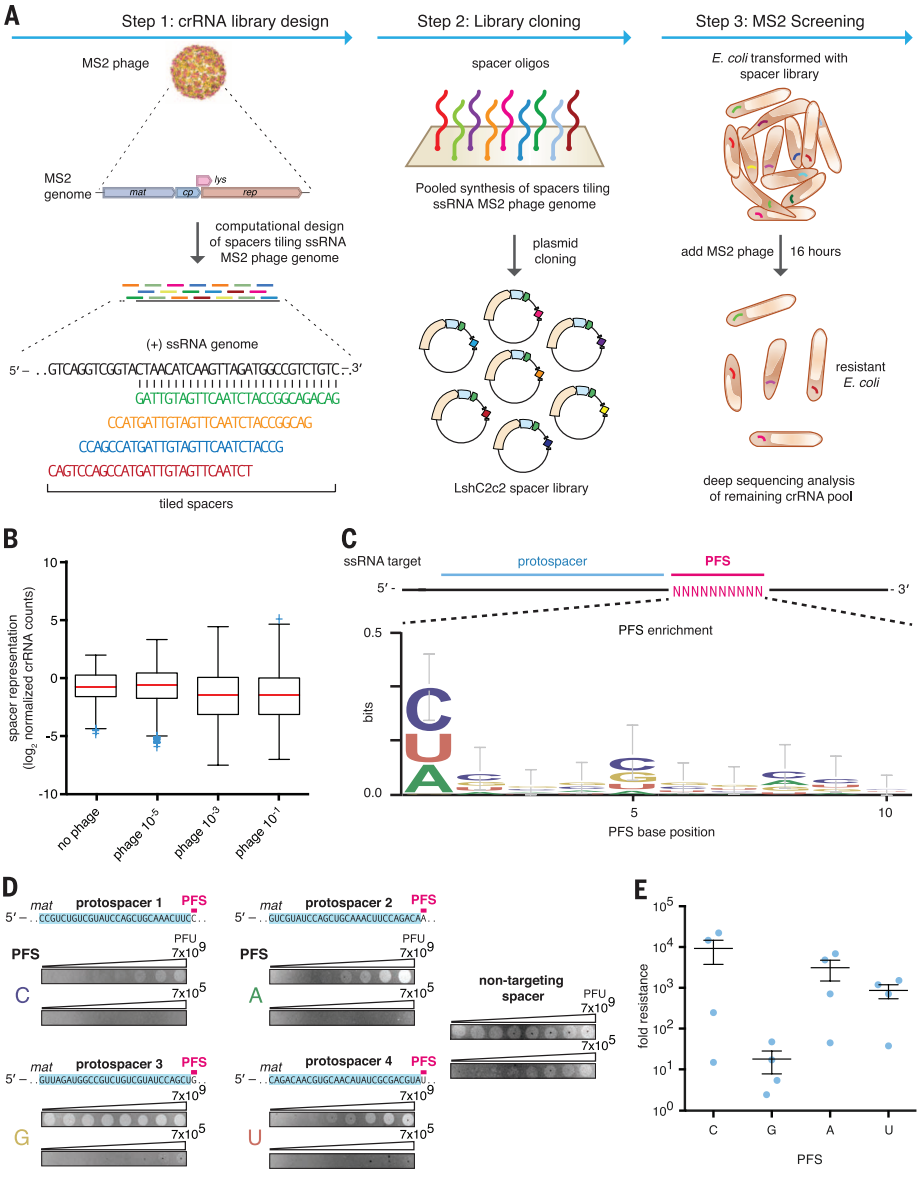

Fig. 1. Heterologous expression of the *L. shahii* C2c2 locus mediates robust interference of RNA phage in *E. coli*. (**A**) Schematic for the MS2 bacteriophage interference screen. A library consisting of spacers targeting all possible sequences in the MS2 RNA genome was cloned into the LshC2c2 CRISPR array. Cells transformed with the MS2-targeting spacer library were then treated with phage and plated, and surviving cells were harvested. The frequency of spacers was compared with an untreated control (no phage), and enriched spacers from the phage-treated condition were used for the generation of PFS preference logos. (**B**) Box plot showing the distribution of normalized crRNA frequencies for the phage-treated conditions and control screen (no phage) biological replicates (n = 3). The box extends from the first to third quartile, with whiskers denoting 1.5 times the interquartile range. The mean is indicated by the red horizontal bar. The 10^{-1} and 10^{-3} phage dilution distributions are significantly different than each of the control replicates [****P < 0.0001 by means of analysis of variance (ANOVA) with multiple hypothesis correction]. (**C**) Sequence logo generated from sequences flanking the 3′ end of protospacers corresponding to enriched spacers in the 10^{-3} phage dilution condition, revealing the presence of a 3′ H PFS (not G). (**D**) Plaque assay used to validate the functional importance of the H PFS in MS2 interference. All protospacers flanked by non-G PFSs exhibited robust phage interference. Spacer were designed to target the MS2 *mat* gene, and their sequences are shown above the plaque images; the spacer used in the nontargeting control is not complementary to any sequence in either the *E. coli* or MS2 genome. Phage spots were applied as series of half-log dilutions. (**E**) Quantitation of MS2 plaque assay validating the H (non-G) PFS preference. Four MS2-targeting spacers were designed for each PFS. Each point on the scatter plot represents the average of three biological replicates and corresponds to a single spacer. Bars indicate the mean of four spacers for each PFS and standard error (SEM).

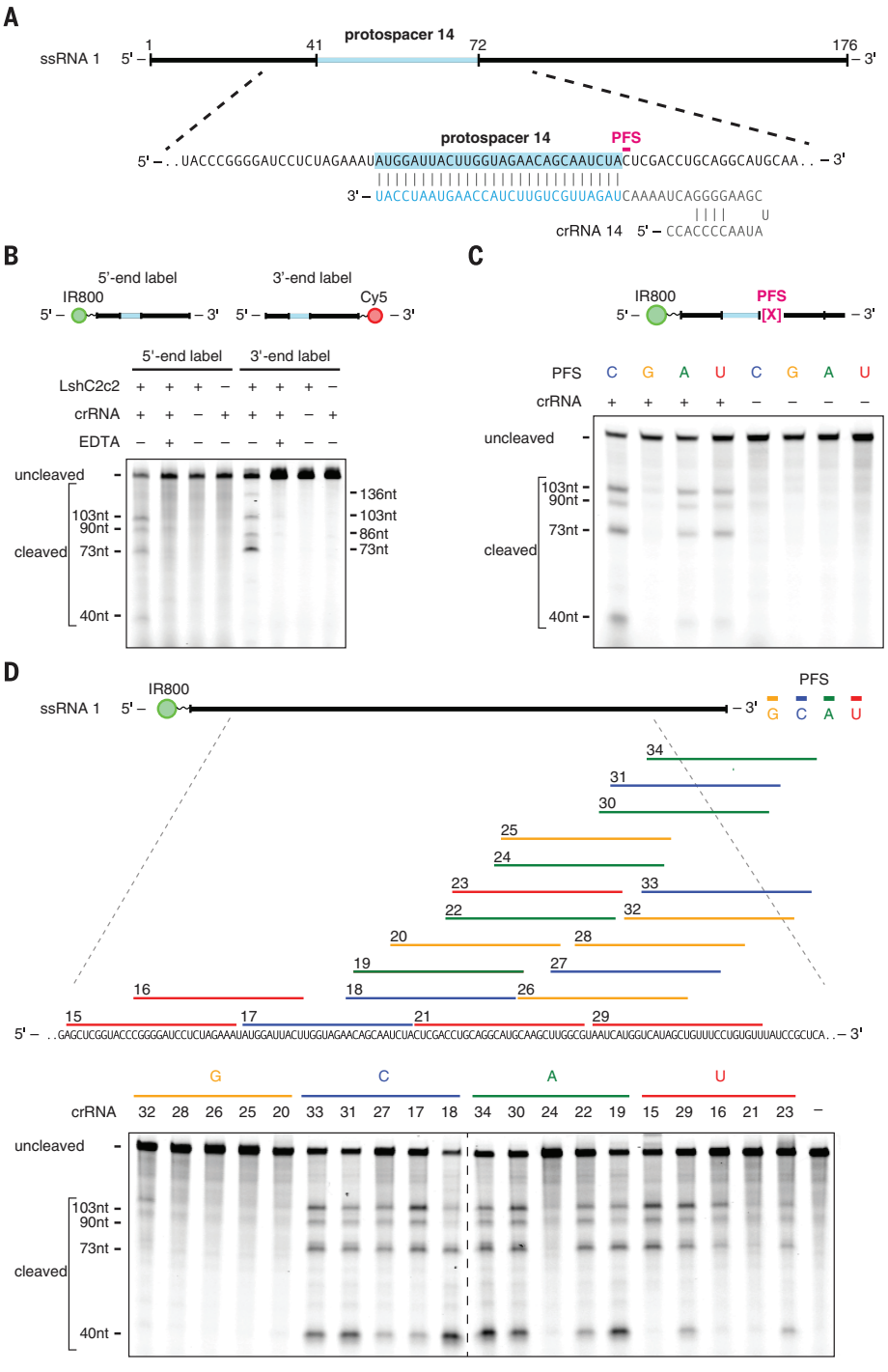

Fig. 2. LshC2c2 and crRNA mediate RNA-guided ssRNA cleavage. (**A**) Schematic of the ssRNA substrate being targeted by the crRNA. The protospacer region is highlighted in blue, and the PFS is indicated by the magenta bar. (**B**) A denaturing gel demonstrating crRNA-mediated ssRNA cleavage by LshC2c2 after 1 hour of incubation. The ssRNA target is either 5′ labeled with IRDye 800 or 3′ labeled with Cy5. Cleavage requires the presence of the crRNA and is abolished by addition of EDTA. Four cleavage sites are observed. Reported band lengths are matched from RNA sequencing. (**C**) A denaturing gel demonstrating the requirement for an H PFS (not G) after 3 hours of incubation. Four ssRNA substrates that are identical except for the PFS (indicated by the magenta "X" in the schematic) were used for the in vitro cleavage reactions. ssRNA cleavage activity is dependent on the nucleotide immediately 3′ of the target site. Reported band lengths are matched from RNA sequencing. (**D**) Schematic showing five protospacers for each PFS on the ssRNA target (top). Denaturing gel showing crRNA-guided ssRNA cleavage activity after 1 hour of incubation. crRNAs correspond to protospacer numbering. Reported band lengths are matched from RNA sequencing.

a C PFS (ssRNA target 1 with protospacer 14). Mature LshC2c2 crRNAs contain a 28-nt DR and a 28-nt spacer (fig. S1A) (*19*). We therefore generated an in vitro–transcribed crRNA with a 28-nt spacer complementary to protospacer 14 on ssRNA target 1. LshC2c2 efficiently cleaved ssRNA in a Mg^{2+}- and crRNA-dependent manner (Fig. 2B and fig. S9). We then annealed complementary RNA oligos to regions flanking the crRNA target site. This partially double-stranded RNA (dsRNA) substrate was not cleaved by LshC2c2, which suggests that it is specific for ssRNA (fig. S10, A and B).

We tested the sequence constraints of RNA cleavage by LshC2c2 with additional crRNAs complementary to ssRNA target 1 in which protospacer 14 is preceded by each PFS variant. The results of this experiment confirmed the preference for C, A, and U PFSs, with little cleavage activity detected for the G PFS target (Fig. 2C). Additionally, we designed five crRNAs for each possible PFS (20 total) across the ssRNA target 1 and evaluated cleavage activity for LshC2c2 paired with each of these crRNAs. As expected, we observed less cleavage activity for G PFS–targeting crRNAs as compared with other crRNAs tested (Fig. 2D).

We then generated a dsDNA plasmid library with protospacer 14 flanked by seven random nucleotides so as to account for any PFS preference. When incubated with LshC2c2 protein and a crRNA complementary to protospacer 14, no cleavage of the dsDNA plasmid library was observed (fig. S10C). We also did not observe cleavage when targeting a ssDNA version of ssRNA target 1 (fig. S10D). To rule out cotranscriptional DNA cleavage, which has been observed in type III CRISPR-Cas systems (*22*), we recapitulated the *E. coli* RNA polymerase cotranscriptional cleavage assay (fig. S11A) (*22*), expressing ssRNA target 1 from a DNA substrate. This assay involving purified LshC2c2 and crRNA targeting ssRNA target 1 did not show any DNA cleavage (fig. S11B). Together, these results indicate that C2c2 cleaves specific ssRNA sites directed by the target complementarity encoded in the crRNA, with a H PFS preference.

C2c2 cleavage depends on local target sequence and secondary structure

Given that C2c2 did not efficiently cleave dsRNA substrates and that ssRNA can form complex secondary structures, we reasoned that cleavage by C2c2 might be affected by secondary structure of the ssRNA target. Indeed, after tiling ssRNA target 1 with different crRNAs (Fig. 2D), we observed the same cleavage pattern regardless of the crRNA position along the target RNA. This observation suggests that the crRNA-dependent cleavage pattern was determined by features of the target sequence rather than the distance from the binding site. We hypothesized that the LshC2c2-crRNA complex binds the target and cleaves exposed regions of ssRNA within the secondary structure elements, with potential preference for certain nucleotides.

In agreement with this hypothesis, cleavage of three ssRNA targets with different sequences

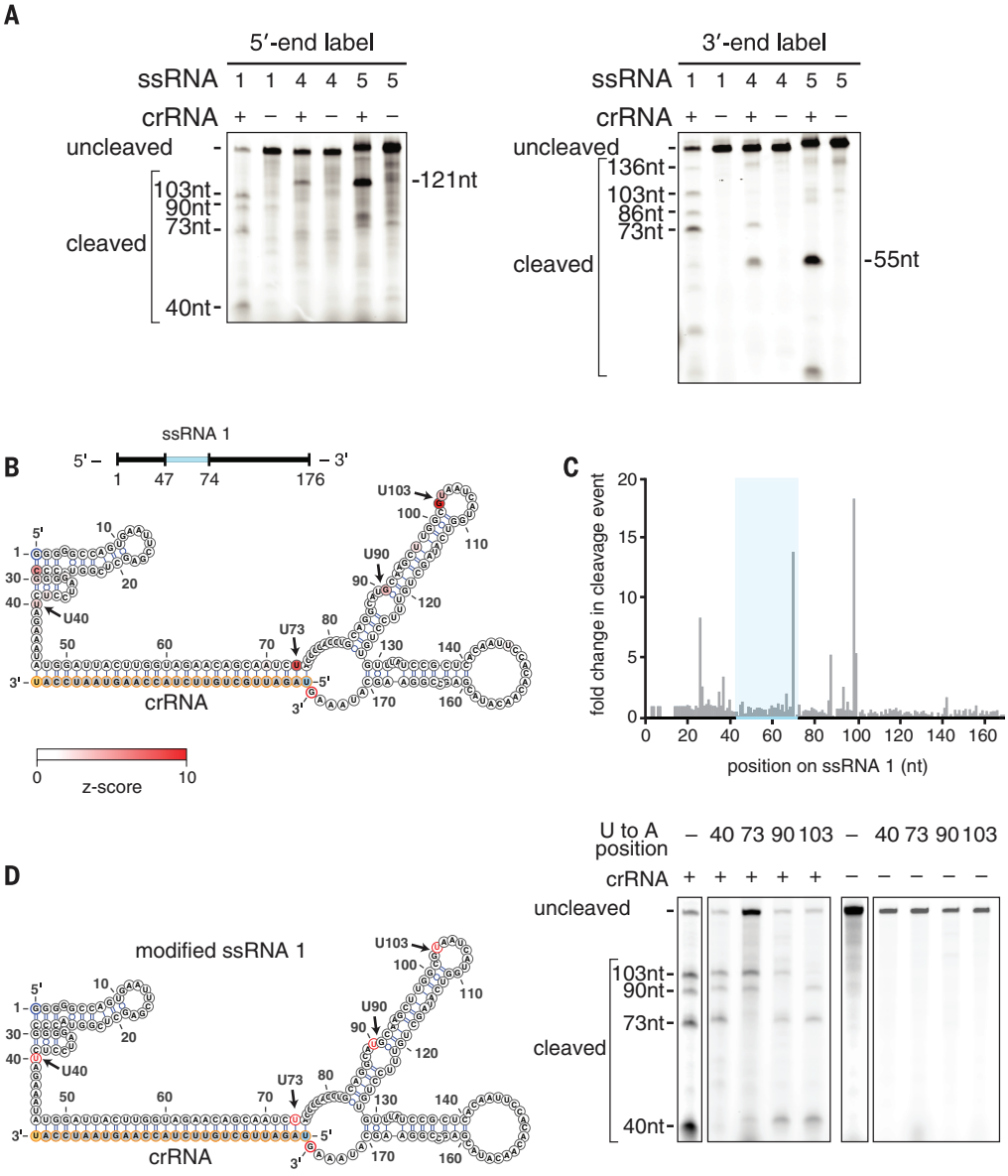

Fig. 3. C2c2 cleavage sites are determined by secondary structure and sequence of the target RNA. (**A**) Denaturing gel showing C2c2-crRNA–mediated cleavage after 3 hours of incubation of three nonhomopolymeric ssRNA targets (1, 4, 5; black, blue, and green, respectively, in Fig. 3, B and C, and fig. S12, A to D) that share the same protospacer but are flanked by different sequences. Despite identical protospacers, different flanking sequences resulted in different cleavage patterns. Reported band lengths are matched from RNA sequencing. (**B**) The cleavage sites of nonhomopolymer ssRNA target 1 were mapped with RNA-sequencing of the cleavage products. The frequency of cleavage at each base is colored according to the *z*-score and shown on the predicted crRNA-ssRNA cofold secondary structure. Fragments used to generate the frequency analysis contained the complete 5′ end. The 5′ and 3′ end of the ssRNA target are indicated by blue and red outlines, on the ssRNA and secondary structure, respectively. The 5′ and 3′ end of the spacer (outlined in yellow) is indicated by the blue and orange residues highlighted, respectively. The crRNA nucleotides are highlighted in orange. (**C**) Plot of the frequencies of cleavage sites for each position of ssRNA target 1 for all reads that begin at the 5′ end. The protospacer is indicated by the blue highlighted region. (**D**) Schematic of a modified ssRNA 1 target showing sites (red) of single U-to-A flips (left). Denaturing gel showing C2c2-crRNA–mediated cleavage of each of these single nucleotide variants after 3 hours of incubation (right). Reported band lengths are matched from RNA sequencing.

flanking identical 28-nt protospacers resulted in three distinct patterns of cleavage (Fig. 3A). RNA-sequencing of the cleavage products for the three targets revealed that cleavage sites mainly localized to uracil-rich regions of ssRNA or ssRNA-dsRNA junctions within the in silico–predicted cofolds of the target sequence with the crRNA (Fig. 3, B and C, and fig. S12, A to D). To test whether the LshC2c2-crRNA complex prefers cleavage at uracils, we analyzed the cleavage efficiencies of homopolymeric RNA targets (a 28-nt protospacer extended with 120 As or Us regularly interspaced by single bases of G or C to enable oligo synthesis) and found that LshC2c2 preferentially cleaved the uracil target compared with adenine (fig. S12, E and F). We then tested cleavage of a modified version of ssRNA 4 that had its main site of cleavage, a loop, replaced with each of the four possible homopolymers and found that cleavage only occurred at the uracil homopolymer loop (fig. S12G). To further test whether cleavage was occurring at uracil residues, we mutated single-uracil residues in ssRNA 1 that showed cleavage in the RNA-sequencing (Fig. 3B) to adenines. This experiment showed that by mutating each uracil residue, we could modulate the presence of a single cleavage band, which is consistent with LshC2c2 cleaving at uracil residues in ssRNA regions (Fig. 3D).

The HEPN domains of C2c2 mediate RNA-guided ssRNA-cleavage

Bioinformatic analysis of C2c2 has suggested that the HEPN domains are likely to be responsible for the observed catalytic activity (*19*). Each of the two HEPN domains of C2c2 contains a dyad of conserved arginine and histidine residues (Fig. 4A), which is in agreement with the catalytic mechanism of the HEPN endoRNAse (*26*–*28*). We mutated each of these putative catalytic residues separately to alanine (R597A, H602A, R1278A, H1283A) in the LshC2c2 locus plasmids and assayed for MS2 interference. None of the four mutant plasmids were able to protect *E. coli* from phage infection (Fig. 4B and fig. S13). (Single-letter abbreviations for the amino acid residues are as follows: A, Ala; C, Cys; D, Asp; E, Glu; F, Phe; G, Gly; H, His; I, Ile; K, Lys; L, Leu; M, Met; N, Asn; P, Pro; Q, Gln; R, Arg; S, Ser; T, Thr; V, Val; W, Trp; and Y, Tyr. In the mutants, other amino acids were substituted at certain locations; for example, R597A indicates that arginine at position 597 was replaced by alanine.)

We purified the four single-point mutant proteins and assayed their ability to cleave 5′ end–labeled ssRNA target 1 (Fig. 4C). In agreement with our in vivo results, all four mutations abolished cleavage activity. The inability of either of the two wild-type HEPN domains to compensate for inactivation of the other implies cooperation between the two domains. These results agree with observations that several bacterial and eukaryotic single-HEPN proteins function as dimers (*27*, *28*, *41*).

Catalytically inactive variants of Cas9 retain target DNA binding, allowing for the creation of programmable DNA-binding proteins (*12*, *13*). Electrophoretic mobility shift assays (EMSAs) on both the wild-type (Fig. 4D) and R1278A mutant LshC2c2 (Fig. 4E) in complex with crRNA showed the wild-type LshC2c2 complex binding strongly [dissociation constant (K_d) ~ 46 nM] (fig. S14A) and specifically to 5′ end–labeled ssRNA target 10 but not to the 5′ end–labeled nontarget ssRNA (the reverse complement of ssRNA target 10). The R1278A mutant C2c2 complex showed even stronger (K_d ~ 7 nM) (fig. S14B) specific binding, indicating that this HEPN mutation results in a catalytically inactive, RNA-programmable, RNA-binding protein. The LshC2c2 protein or crRNA alone showed reduced levels of target affinity, as expected (fig. S14, C to E). Additionally, no specific binding of LshC2c2-crRNA complex to ssDNA was observed (fig. S15).

These results demonstrate that C2c2 cleaves RNA via a catalytic mechanism distinct from other known CRISPR-associated RNases. In particular, the type III Csm and Cmr multiprotein complexes rely on acidic residues of RRM domains for catalysis, whereas C2c2 achieves RNA cleavage through the conserved basic residues of its two HEPN domains.

Sequence and structural requirements of C2c2 crRNA

Similar to the type V-A (Cpf1) systems (*18*), the LshC2c2 crRNA contains a single stem loop in the DR, suggesting that the secondary structure of the crRNA could facilitate interaction with LshC2c2. We thus investigated the length requirements of the spacer sequence for ssRNA cleavage and found that LshC2c2 requires spacers of at least 22 nt length to efficiently cleave ssRNA target 1 (fig. S16A). The stem-loop structure of the crRNA is also critical for ssRNA cleavage because DR truncations that disturbed the stem loop abrogated target cleavage (fig. S16B). Thus, a DR longer than 24 nt is required to maintain the stem loop necessary for LshC2c2 to mediate ssRNA cleavage.

Single-base-pair inversions in the stem that preserved the stem structure did not affect the activity of the LshC2c2 complex. In contrast, inverting all four G-C pairs in the stem eliminated the cleavage, despite maintaining the duplex structure (fig. S17A). Other perturbations, such as those that introduced kinks and reduced or increased base-pairing in the stem, also eliminated or drastically suppressed cleavage. This suggests that the crRNA stem length is important for complex formation and activity (fig. S17A). We also found that loop deletions eliminated cleavage, whereas insertions and substitutions mostly maintained some level of cleavage activity (fig. S17B). In contrast, nearly all substitutions or deletions in the region 3′ to the DR prevented cleavage by LshC2c2 (fig. S18). Together, these results demonstrate that LshC2c2 recognizes structural characteristics of its cognate crRNA but is amenable to loop insertions and most tested base substitutions outside of the 3′ DR region.

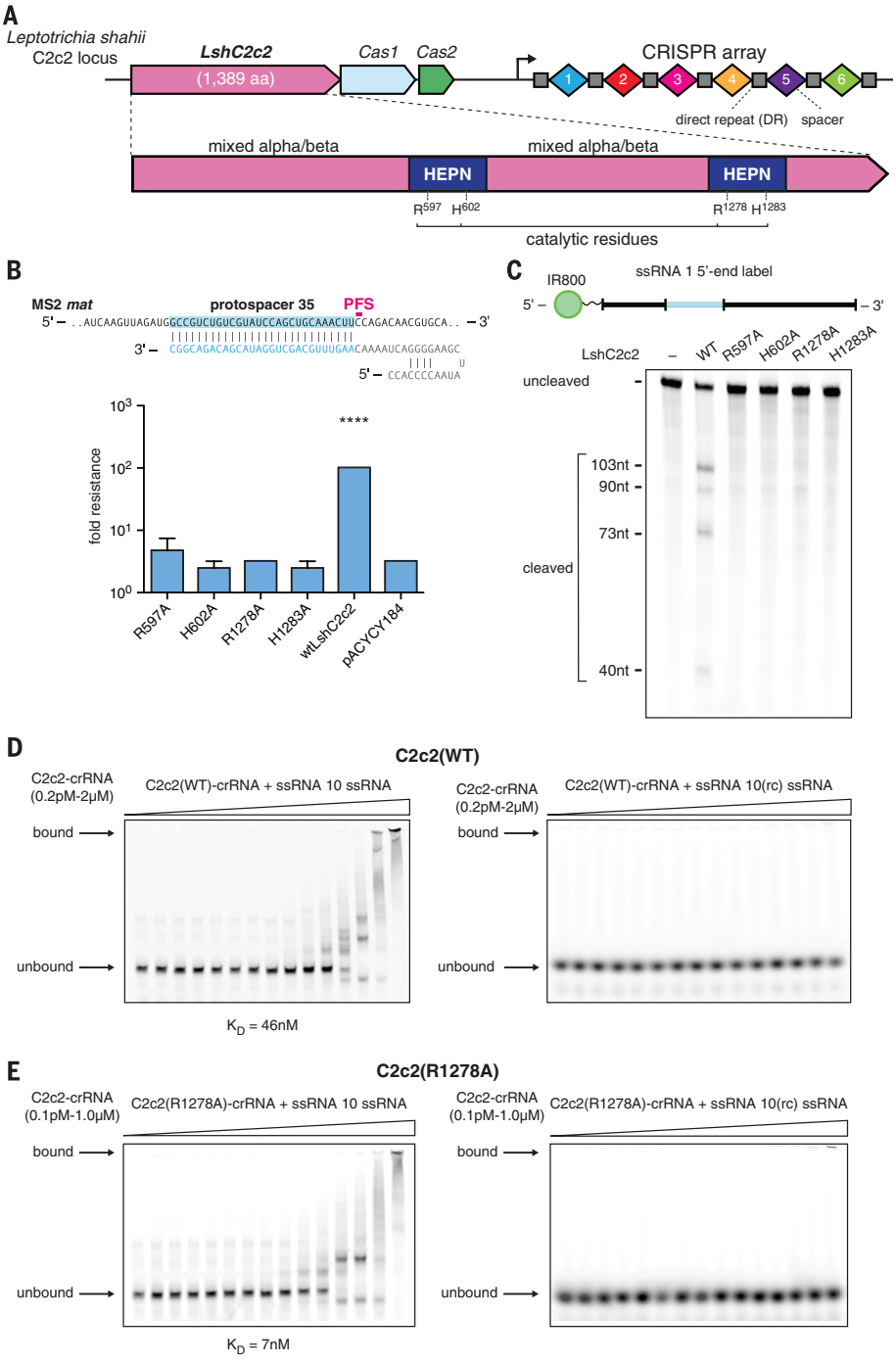

Fig. 4. The two HEPN domains of C2c2 are necessary for crRNA-guided ssRNA cleavage but not for binding. (**A**) Schematic of the *LshC2c2* locus and the domain organization of the LshC2c2 protein, showing conserved residues in HEPN domains (dark blue). (**B**) Quantification of MS2 plaque assay with HEPN catalytic residue mutants. For each mutant, the same crRNA targeting protospacer 35 was used. (n = 3 biological replicates, ****P < 0.0001 compared with pACYC184 by Student's t test. Bars represent mean ± SEM). (**C**) Denaturing gel showing conserved residues of the HEPN motif, indicated as catalytic residues in (A), are necessary for crRNA-guided ssRNA target 1 cleavage after 3 hours of incubation. Reported band lengths are matched from RNA sequencing. (**D**) Electrophoretic mobility shift assay (EMSA) evaluating affinity of the wild-type LshC2c2-crRNA complex against a targeted (left) and a nontargeted (right) ssRNA substrate. The nontargeted ssRNA substrate is the reverse-complement of the targeted ssRNA 10. EDTA is supplemented to reaction condition in order to reduce any cleavage activity. (**E**) Electrophoretic mobility shift assay with LshC2c2(R1278A)-crRNA complex against on-target ssRNA 10 and nontargeting ssRNA [same substrate sequences as in (D)].

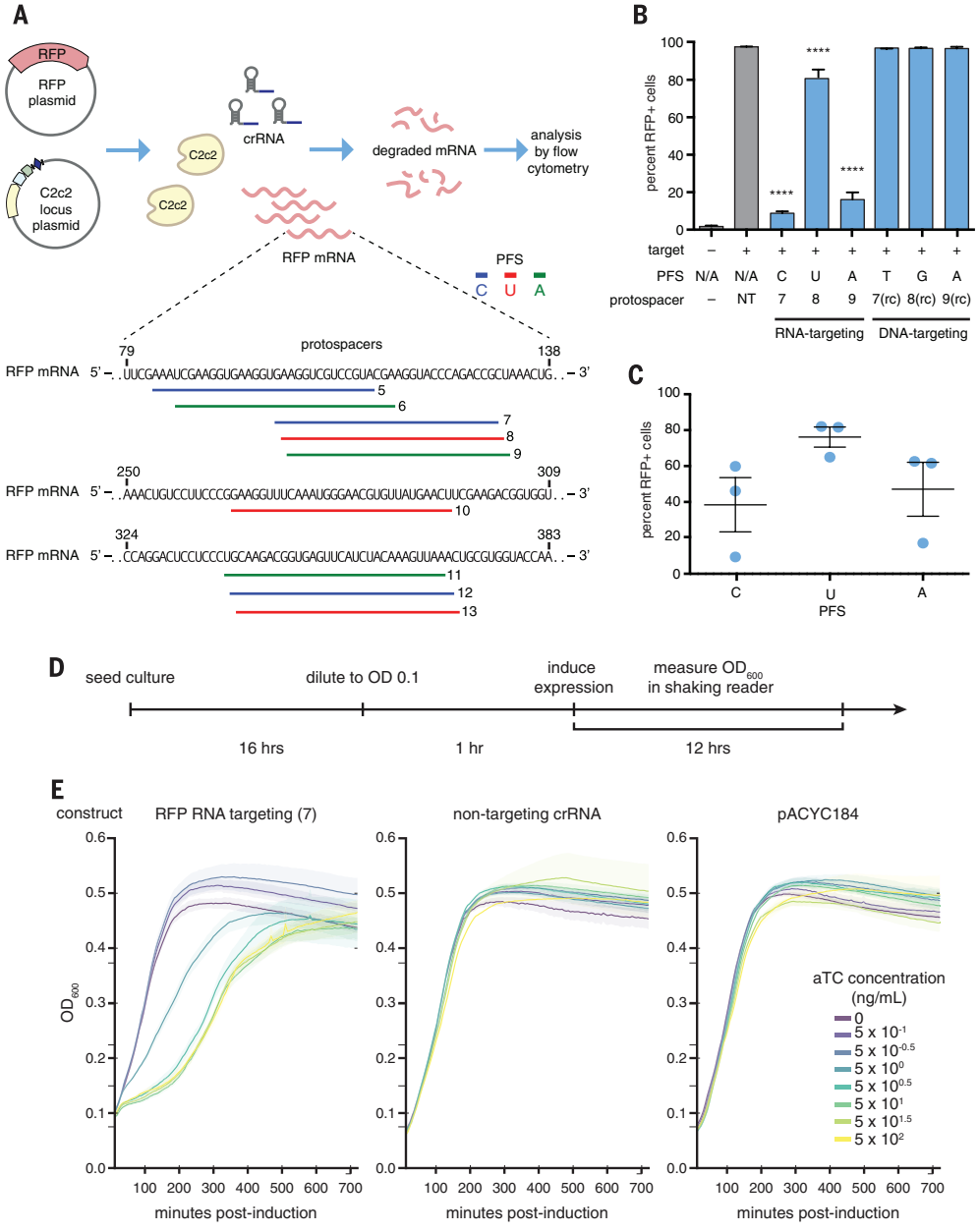

Fig. 5. RFP mRNA knockdown by retargeting LshC2c2. (**A**) Schematic showing crRNA-guided knockdown of RFP in *E. coli* heterologously expressing the LshC2c2 locus. Three RFP-targeting spacers were selected for each non-G PFS, and each protospacer on the RFP mRNA is numbered. (**B**) RFP mRNA-targeting spacers effected RFP knockdown, whereas DNA-targeting spacers (targeting the noncoding strand of the RFP gene on the expression plasmid, indicated as "rc" spacers) did not affect RFP expression. (n = 3 biological replicates, ****P < 0.0001 compared with nontargeting guide by means of ANOVA with multiple hypothesis correction. Bars represent mean ± SEM). (**C**) Quantification of RFP knockdown in *E. coli*. Three spacers each targeting C, U, or A PFS-flanking protospacers [nine spacers, numbered 5 to 13 as indicated in (A)] in the RFP mRNA were introduced, and RFP expression was measured with flow cytometry. Each point on the scatter plot represents the average of three biological replicates and corresponds to a single spacer. Bars indicate the mean of three spacers for each PFS, and errors bars are shown as the SEM. (**D**) Timeline of *E. coli* growth assay. (**E**) Effect of RFP mRNA targeting on the growth rate of *E. coli* transformed with an inducible RFP expression plasmid as well as the LshC2c2 locus with nontargeting, RNA targeting (spacer complementary to the RFP mRNA or RFP gene coding strand), and pACYC control plasmid at different anhydrotetracycline (aTc) concentrations.

These results have implications for the future application of C2c2-based tools that require guide engineering for recruitment of effectors or modulation of activity (*42*–*44*).

C2c2 cleavage is sensitive to double mismatches in the crRNA-target duplex

We tested the sensitivity of the LshC2c2 system to single mismatches between the crRNA guide and target RNA by mutating single bases across the spacer to the respective complementary bases (for example, A to U). We then quantified plaque formation with these mismatched spacers in the MS2 infection assay and found that C2c2 was fully tolerant to single mismatches across the spacer because such mismatched spacers interfered with phage propagation with similar efficiency as fully matched spacers (figs. S19A and S20). However, when we introduced consecutive double substitutions in the spacer, we found a ~3-$\log_{10}$–fold reduction in the protection for mismatches in the center, but not at the 5′ or 3′ end, of the crRNA (figs. S19B and S20). This observation suggests the presence of a mismatch-sensitive "seed region" in the center of the crRNA-target duplex.

We generated a set of in vitro–transcribed crRNAs with mismatches similarly positioned across the spacer region. When incubated with LshC2c2 protein, all single mismatched crRNA supported cleavage (fig. S19C), which is in agreement with our in vivo findings. When tested with a set of consecutive and nonconsecutive double-mutant crRNAs, LshC2c2 was unable to cleave the target RNA if the mismatches were positioned in the center, but not at the 5′ or 3′ end of the crRNA (figs. S19D and S21A), further supporting the existence of a central seed region. Additionally, no cleavage activity was observed with crRNAs containing consecutive triple mismatches in the seed region (fig. S21B).

C2c2 can be reprogrammed to mediate specific mRNA knockdown in vivo

Given the ability of C2c2 to cleave target ssRNA in a crRNA sequence–specific manner, we tested whether LshC2c2 could be reprogrammed to degrade selected nonphage ssRNA targets, and particularly mRNAs, in vivo. We cotransformed *E. coli* with a plasmid encoding LshC2c2 and a crRNA targeting the mRNA of red fluorescent protein (RFP) as well as a compatible plasmid expressing RFP (Fig. 5A). For optical density (OD)–matched samples, we observed an ~20 to 92% decrease in RFP-positive cells for crRNAs

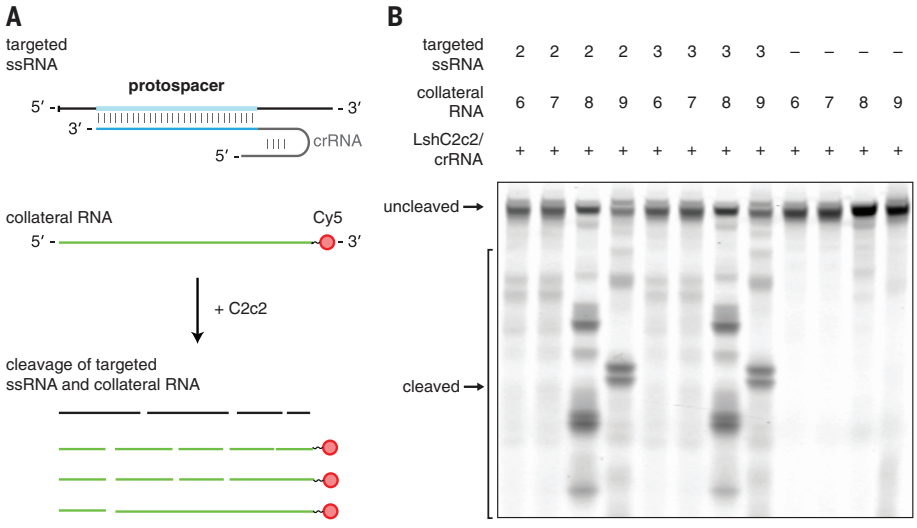

Fig. 6. crRNA-guided ssRNA cleavage activates nonspecific RNase activity of LshC2c2. (**A**) Schematic of the biochemical assay used to detect crRNA-binding–activated nonspecific RNase activity on non-crRNA–targeted collateral RNA molecules. The reaction consists of C2c2 protein, unlabeled crRNA, unlabeled target ssRNA, and a second ssRNA with 3′ fluorescent labeling and is incubated for 3 hours. C2c2-crRNA mediates cleavage of the unlabeled target ssRNA as well as the 3′ end–labeled collateral RNA, which has no complementarity to the crRNA. (**B**) Denaturing gel showing nonspecific RNase activity against nontargeted ssRNA substrates in the presence of target RNA after 3 hours of incubation. The nontargeted ssRNA substrate is not cleaved in the absence of the crRNA-targeted ssRNA substrate.

targeting protospacers flanked by C, A, or U PFSs (Fig. 5, B and C). As a control, we tested crRNAs containing reverse complements (targeting the dsDNA plasmid) of the top performing RFP mRNA-targeting spacers. As expected, we observed no decrease in RFP fluorescence by these crRNAs (Fig. 5B). We also confirmed that mutation of the catalytic arginine residues in either HEPN domain to alanine precluded RFP knockdown (fig. S22). Thus, C2c2 is capable of general retargeting to arbitrary ssRNA substrates, governed exclusively by predictable nucleic-acid interactions.

When we examined the growth of cells carrying the RFP-targeting spacer with the greatest level of RFP knockdown, we noted that the growth rate of these bacteria was substantially reduced (Fig. 5A, spacer 7). We investigated whether the effect on growth was mediated by the RFP mRNA–targeting activity of LshC2c2 by introducing an inducible-RFP plasmid and an RFP-targeting LshC2c2 locus into *E. coli*. Upon induction of RFP transcription, cells with RFP knockdown showed substantial growth suppression not observed in nontargeting controls (Fig. 5, D and E). This growth restriction was dependent on the level of the RFP mRNA, as controlled by the concentration of the inducer anhydrotetracycline. In contrast, in the absence of RFP transcription, we did not observe any growth restriction, nor did we observe any transcription-dependent DNA-targeting in our biochemical experiment (fig. S11). These results indicate that RNA-targeting is likely the primary driver of this growth restriction phenotype. We therefore surmised that in addition to the cleavage of the target RNA, C2c2 CRISPR systems might prevent virus reproduction also via nonspecific cleavage of cellular mRNAs, causing programmed cell death (PCD) or dormancy (*45*, *46*).

C2c2 cleaves collateral RNA in addition to crRNA-targeted ssRNA

Cas9 and Cpf1 cleave DNA within the crRNA-target heteroduplex at defined positions, reverting to an inactive state after cleavage. In contrast, C2c2 cleaves the target RNA outside of the crRNA binding site at varying distances depending on the flanking sequence, presumably within exposed ssRNA loop regions (Fig. 3, B and C, and fig. S12, A to D). This observed flexibility with respect to the cleavage distance led us to test whether cleavage of other, nontarget ssRNAs also occurs upon C2c2 target-binding and activation. Under this model, the C2c2-crRNA complex, once activated by binding to its target RNA, cleaves the target RNA as well as other RNAs nonspecifically. We carried out in vitro cleavage reactions that included, in addition to LshC2c2 protein, crRNA and its target RNA, one of four unrelated RNA molecules without any complementarity to the crRNA guide (Fig. 6A). These experiments showed that whereas the LshC2c2-crRNA complex did not mediate cleavage of any of the four collateral RNAs in the absence of the target RNA, all four were efficiently degraded in the presence of the target RNA (Fig. 6B and fig. S23A). Furthermore, R597A and R1278A HEPN mutants were unable to cleave collateral RNA (fig. S23B).

To further investigate the collateral cleavage and growth restriction in vivo, we hypothesized that if a PFS preference screen for LshC2c2 was performed in a transcribed region on the transformed plasmid, then we should be able to detect the PFS preference due to growth restriction induced by RNA-targeting. We designed a protospacer site flanked by five randomized nucleotides at the 3′ end in either a nontranscribed region or in a region transcribed from the *lac* promoter (fig. S24A). The analysis of the depleted and enriched PFS sequences identified a H PFS only in the assay with the transcribed sequence but no discernable motif in the nontranscribed sequence (fig. S24, B and C).

These results suggest a HEPN-dependent mechanism by which C2c2 in a complex with crRNA is activated upon binding to target RNA and subsequently cleaves nonspecifically other available ssRNA targets. Such promiscuous RNA cleavage could cause cellular toxicity, resulting in the observed growth rate inhibition. These findings imply that in addition to their likely role in direct suppression of RNA viruses, type VI CRISPR-Cas systems could function as mediators of a distinct variety of PCD or dormancy induction that is specifically triggered by cognate invader genomes (Fig. 7). Under this scenario, dormancy would slow the infection and supply additional time for adaptive immunity. Such a mechanism agrees with the previously proposed coupling of adaptive immunity and PCD during the CRISPR-Cas defensive response (*47*).

Conclusions

The class 2 type VI effector protein C2c2 is a RNA-guided RNase that can be efficiently programmed to degrade any ssRNA by specifying a 28-nt sequence on the crRNA (fig. S10). C2c2 cleaves RNA through conserved basic residues within its two HEPN domains, in contrast to the catalytic mechanisms of other known RNases found in CRISPR-Cas systems (*25*, *48*). Alanine substitution of any of the four predicted HEPN domain catalytic residues converted C2c2 into an inactive programmable RNA-binding protein (dC2c2, analogous to dCas9). Many different spacer sequences work well in our assays, although further screening will likely define properties and rules governing optimal function.

These results suggest a broad range of biotechnology applications and research questions (*49*–*51*). For example, the ability of dC2c2 to bind to specified sequences could be used to (i) bring effector modules to specific transcripts in order to modulate their function or translation, which could be used for large-scale screening, construction of synthetic regulatory circuits, and other purposes; (ii) fluorescently tag specific RNAs in order to visualize their trafficking and/or localization; (iii) alter RNA localization through domains with affinity for specific subcellular compartments; and (iv) capture specific transcripts (through direct pull-down of dC2c2) in order to enrich for proximal molecular partners, including RNAs and proteins.

Active C2c2 also has many potential applications, such as targeting a specific transcript for destruction, as performed here with RFP.

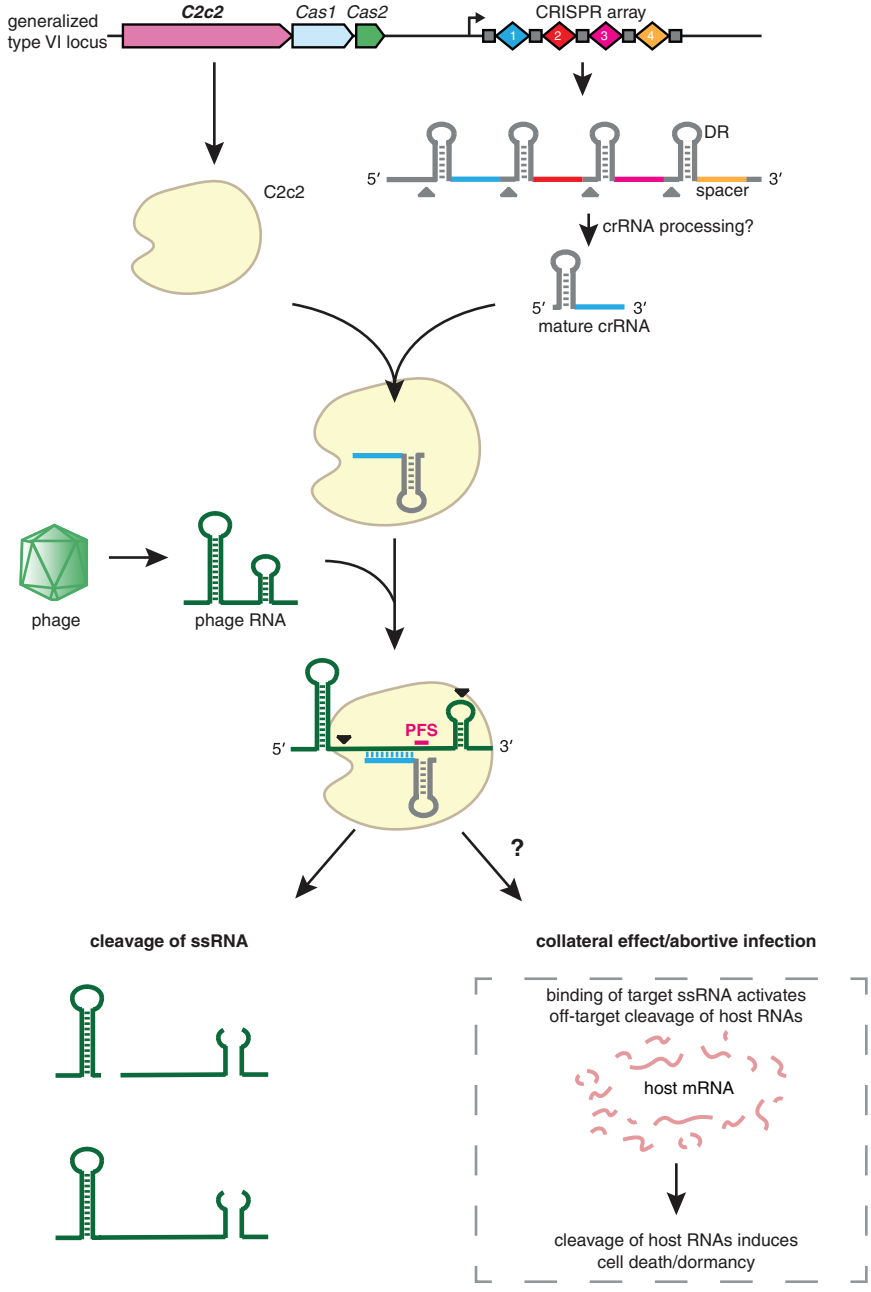

Fig. 7. C2c2 as a putative RNA-targeting prokaryotic immune system. The C2c2-crRNA complex recognizes target RNA via base pairing with the cognate protospacer and cleaves the target RNA. In addition, binding of the target RNA by C2c2-crRNA activates a nonspecific RNase activity, which may lead to promiscuous cleavage of RNAs without complementarity to the crRNA guide sequence. Through this nonspecific RNase activity, C2c2 may also cause abortive infection via programmed cell death or dormancy induction.

In addition, C2c2, once primed by the cognate target, can cleave other (noncomplementary) RNA molecules in vitro and inhibit cell growth in vivo. Biologically, this promiscuous RNase activity might reflect a PCD/dormancy–based protection mechanism of the type VI CRISPR-Cas systems (Fig. 7). Technologically, it might be used to trigger PCD or dormancy in specific cells, such as cancer cells expressing a particular transcript, neurons of a given class, or cells infected by a specific pathogen.

Further experimental study is required to elucidate the mechanisms by which the C2c2 system acquires spacers and the classes of pathogens against which it protects bacteria. The presence of the conserved CRISPR adaptation module consisting of typical Cas1 and Cas2 proteins in the LshC2c2 locus suggests that it is capable of spacer acquisition. Although C2c2 systems lack reverse transcriptases, which mediate acquisition of RNA spacers in some type III systems (*52*), it is possible that additional host or viral factors could support RNA spacer acquisition. Additionally or alternatively, type VI systems could acquire DNA spacers similar to other CRISPR-Cas variants but then target transcripts of the respective DNA genomes, eliciting PCD and abortive infection (Fig. 7).

The CRISPR-C2c2 system represent a distinct evolutionary path among class 2 CRISPR-Cas systems. It is likely that other, broadly analogous class 2 RNA-targeting immune systems exist, and further characterization of the diverse members of class 2 systems will provide a deeper understanding of bacterial immunity and provide a rich starting point for the development of programmable molecular tools for in vivo RNA manipulation.

Materials and methods

Expanded materials and methods, including computational analysis, can be found in supplementary materials and methods.

Bacterial phage interference

The C2c2 CRISPR locus was amplified from DNA from *Leptotrichia shahii DSM 19757* (ATCC, Manassas, VA) and cloned for heterologous expression in *E. coli*. For screens, a library of all possible spacers targeting the MS2 genome were cloned into the spacer array; for individual spacers, single specific spacers were cloned into the array. Interference screens were performed in liquid culture and plated; surviving colonies were harvested for DNA and spacer representation was determined by next-generation sequencing. Individual spacers were tested by spotting on top agar.

β–lactamase and transcribed/non-transcribed PFS preference screens

Sequences with randomized nucleotides adjacent to protospacer 1 were cloned into pUC19 in corresponding regions. Libraries were screened by co-transformation with LshC2c2 locus plasmid or pACYC184 plasmid control, harvesting of the surviving colonies, and next-generation sequencing of the resulting regions.

RFP-targeting assay

Cells containing an RFP expressing plasmid were transformed with an LshC2c2 locus plasmid with corresponding spacers, grown overnight, and analyzed for RFP fluorescence by flow cytometry. The growth effects of LshC2c2 activity were quantified by titrating inducible RFP levels with dilutions of anhydrotetracycline inducer and then measuring OD_{600}.

in vitro nuclease and electrophoretic mobility shift assays

LshC2c2 protein and HEPN mutants were purified for use in in vitro reactions; RNA were synthesized via in vitro transcription. For nuclease assays, protein was co-incubated with crRNA and either 3′ or 5′-labeled targets and analyzed via denaturing gel electrophoresis and imaging or by next-generation sequencing. For electrophoretic mobility shift assays, protein and nucleic

acid were co-incubated and then resolved by gel electrophoresis and imaging.

REFERENCES AND NOTES

1. K. S. Makarova *et al*., An updated evolutionary classification of CRISPR-Cas systems. *Nat. Rev. Microbiol.* **13**, 722–736 (2015). doi: 10.1038/nrmicro3569; pmid: 26411297
2. K. S. Makarova *et al*., Evolution and classification of the CRISPR-Cas systems. *Nat. Rev. Microbiol.* **9**, 467–477 (2011). doi: 10.1038/nrmicro2577; pmid: 21552286
3. A. V. Wright, J. K. Nuñez, J. A. Doudna, Biology and applications of CRISPR systems: Harnessing nature's toolbox for genome engineering. *Cell* **164**, 29–44 (2016). doi: 10.1016/j.cell.2015.12.035; pmid: 26771484
4. L. A. Marraffini, CRISPR-Cas immunity in prokaryotes. *Nature* **526**, 55–61 (2015). doi: 10.1038/nature15386; pmid: 26432244
5. J. van der Oost, M. M. Jore, E. R. Westra, M. Lundgren, S. J. Brouns, CRISPR-based adaptive and heritable immunity in prokaryotes. *Trends Biochem. Sci.* **34**, 401–407 (2009). doi: 10.1016/j.tibs.2009.05.002; pmid: 19646880
6. S. J. Brouns *et al*., Small CRISPR RNAs guide antiviral defense in prokaryotes. *Science* **321**, 960–964 (2008). doi: 10.1126/science.1159689; pmid: 18703739
7. C. R. Hale *et al*., RNA-guided RNA cleavage by a CRISPR RNA-Cas protein complex. *Cell* **139**, 945–956 (2009). doi: 10.1016/j.cell.2009.07.040; pmid: 19945378
8. R. N. Jackson *et al*., Crystal structure of the CRISPR RNA-guided surveillance complex from *Escherichia coli*. *Science* **345**, 1473–1479 (2014). doi: 10.1126/science.1256328; pmid: 25103409
9. L. A. Marraffini, E. J. Sontheimer, CRISPR interference limits horizontal gene transfer in staphylococci by targeting DNA. *Science* **322**, 1843–1845 (2008). doi: 10.1126/science.1165771; pmid: 19095942
10. S. Mulepati, A. Héroux, S. Bailey, Crystal structure of a CRISPR RNA-guided surveillance complex bound to a ssDNA target. *Science* **345**, 1479–1484 (2014). doi: 10.1126/science.1256996; pmid: 25123481
11. T. Sinkunas *et al*., In vitro reconstitution of Cascade-mediated CRISPR immunity in Streptococcus thermophilus. *EMBO J.* **32**, 385–394 (2013). doi: 10.1038/emboj.2012.352; pmid: 23334296
12. G. Gasiunas, R. Barrangou, P. Horvath, V. Siksnys, Cas9-crRNA ribonucleoprotein complex mediates specific DNA cleavage for adaptive immunity in bacteria. *Proc. Natl. Acad. Sci. U.S.A.* **109**, E2579–E2586 (2012). doi: 10.1073/pnas.1208507109; pmid: 22949671
13. M. Jinek *et al*., A programmable dual-RNA-guided DNA endonuclease in adaptive bacterial immunity. *Science* **337**, 816–821 (2012). doi: 10.1126/science.1225829; pmid: 22745249
14. E. Deltcheva *et al*., CRISPR RNA maturation by trans-encoded small RNA and host factor RNase III. *Nature* **471**, 602–607 (2011). doi: 10.1038/nature09886; pmid: 21455174
15. R. Sapranauskas *et al*., The Streptococcus thermophilus CRISPR/Cas system provides immunity in *Escherichia coli*. *Nucleic Acids Res.* **39**, 9275–9282 (2011). doi: 10.1093/nar/gkr606; pmid: 21813460
16. J. E. Garneau *et al*., The CRISPR/Cas bacterial immune system cleaves bacteriophage and plasmid DNA. *Nature* **468**, 67–71 (2010). doi: 10.1038/nature09523; pmid: 21048762
17. R. Barrangou *et al*., CRISPR provides acquired resistance against viruses in prokaryotes. *Science* **315**, 1709–1712 (2007). doi: 10.1126/science.1138140; pmid: 17379808
18. B. Zetsche *et al*., Cpf1 is a single RNA-guided endonuclease of a class 2 CRISPR-Cas system. *Cell* **163**, 759–771 (2015). doi: 10.1016/j.cell.2015.09.038; pmid: 26422227
19. S. Shmakov *et al*., Discovery and functional characterization of diverse class 2 CRISPR-Cas systems. *Mol. Cell* **60**, 385–397 (2015). doi: 10.1016/j.molcel.2015.10.008; pmid: 26593719
20. C. R. Hale *et al*., Essential features and rational design of CRISPR RNAs that function with the Cas RAMP module complex to cleave RNAs. *Mol. Cell* **45**, 292–302 (2012). doi: 10.1016/j.molcel.2011.10.023; pmid: 22227116
21. W. Jiang, P. Samai, L. A. Marraffini, Degradation of phage transcripts by CRISPR-associated RNases enables type III CRISPR-Cas immunity. *Cell* **164**, 710–721 (2016). doi: 10.1016/j.cell.2015.12.053; pmid: 26853474
22. P. Samai *et al*., Co-transcriptional DNA and RNA cleavage during type III CRISPR-Cas immunity. *Cell* **161**, 1164–1174 (2015). doi: 10.1016/j.cell.2015.04.027; pmid: 25959775
23. R. H. Staals *et al*., Structure and activity of the RNA-targeting type III-B CRISPR-Cas complex of *Thermus thermophilus*. *Mol. Cell* **52**, 135–145 (2013). doi: 10.1016/j.molcel.2013.09.013; pmid: 24119403
24. R. H. Staals *et al*., RNA targeting by the type III-A CRISPR-Cas Csm complex of *Thermus thermophilus*. *Mol. Cell* **56**, 518–530 (2014). doi: 10.1016/j.molcel.2014.10.005; pmid: 25457165
25. G. Tamulaitis *et al*., Programmable RNA shredding by the type III-A CRISPR-Cas system of *Streptococcus thermophilus*. *Mol. Cell* **56**, 506–517 (2014). doi: 10.1016/j.molcel.2014.09.027; pmid: 25458845
26. V. Anantharaman, K. S. Makarova, A. M. Burroughs, E. V. Koonin, L. Aravind, Comprehensive analysis of the HEPN superfamily: Identification of novel roles in intra-genomic conflicts, defense, pathogenesis and RNA processing. *Biol. Direct* **8**, 15 (2013). doi: 10.1186/1745-6150-8-15; pmid: 23768067
27. O. Niewoehner, M. Jinek, Structural basis for the endoribonuclease activity of the type III-A CRISPR-associated protein Csm6. *RNA* **22**, 318–329 (2016). doi: 10.1261/rna.054098.115; pmid: 26763118
28. N. F. Sheppard, C. V. Glover 3rd, R. M. Terns, M. P. Terns, The CRISPR-associated Csx1 protein of *Pyrococcus furiosus* is an adenosine-specific endoribonuclease. *RNA* **22**, 216–224 (2016). doi: 10.1261/rna.039842.113; pmid: 26647461
29. G. W. Goldberg, W. Jiang, D. Bikard, L. A. Marraffini, Conditional tolerance of temperate phages via transcription-dependent CRISPR-Cas targeting. *Nature* **514**, 633–637 (2014). doi: 10.1038/nature13637; pmid: 25174707
30. L. Deng, R. A. Garrett, S. A. Shah, X. Peng, Q. She, A novel interference mechanism by a type IIIB CRISPR-Cmr module in Sulfolobus. *Mol. Microbiol.* **87**, 1088–1099 (2013). doi: 10.1111/mmi.12152; pmid: 23320564
31. Y. K. Kim, Y. G. Kim, B. H. Oh, Crystal structure and nucleic acid-binding activity of the CRISPR-associated protein Csx1 of *Pyrococcus furiosus*. *Proteins* **81**, 261–270 (2013). doi: 10.1002/prot.24183; pmid: 22987782
32. J. K. Nuñez, A. S. Lee, A. Engelman, J. A. Doudna, Integrase-mediated spacer acquisition during CRISPR-Cas adaptive immunity. *Nature* **519**, 193–198 (2015). doi: 10.1038/nature14237; pmid: 25707795
33. R. Heler *et al*., Cas9 specifies functional viral targets during CRISPR-Cas adaptation. *Nature* **519**, 199–202 (2015). doi: 10.1038/nature14245; pmid: 25707807
34. J. K. Nuñez *et al*., Cas1-Cas2 complex formation mediates spacer acquisition during CRISPR-Cas adaptive immunity. *Nat. Struct. Mol. Biol.* **21**, 528–534 (2014). doi: 10.1038/nsmb.2820; pmid: 24793649
35. C. Díez-Villaseñor, N. M. Guzmán, C. Almendros, J. García-Martínez, F. J. Mojica, CRISPR-spacer integration reporter plasmids reveal distinct genuine acquisition specificities among CRISPR-Cas I-E variants of *Escherichia coli*. *RNA Biol.* **10**, 792–802 (2013). doi: 10.4161/rna.24023; pmid: 23445770
36. I. Yosef, M. G. Goren, U. Qimron, Proteins and DNA elements essential for the CRISPR adaptation process in *Escherichia coli*. *Nucleic Acids Res.* **40**, 5569–5576 (2012). doi: 10.1093/nar/gks216; pmid: 22402487
37. K. A. Datsenko *et al*., Molecular memory of prior infections activates the CRISPR/Cas adaptive bacterial immunity system. *Nat. Commun.* **3**, 945 (2012). doi: 10.1038/ncomms1937; pmid: 22781758
38. L. A. Marraffini, E. J. Sontheimer, Self versus non-self discrimination during CRISPR RNA-directed immunity. *Nature* **463**, 568–571 (2010). doi: 10.1038/nature08703; pmid: 20072129
39. C. R. Hale, A. Cocozaki, H. Li, R. M. Terns, M. P. Terns, Target RNA capture and cleavage by the Cmr type III-B CRISPR-Cas effector complex. *Genes Dev.* **28**, 2432–2443 (2014). doi: 10.1101/gad.250712.114; pmid: 25367038
40. J. Zhang *et al*., Structure and mechanism of the CMR complex for CRISPR-mediated antiviral immunity. *Mol. Cell* **45**, 303–313 (2012). doi: 10.1016/j.molcel.2011.12.013; pmid: 22227115
41. G. Kozlov *et al*., Structural basis of defects in the sacsin HEPN domain responsible for autosomal recessive spastic ataxia of Charlevoix-Saguenay (ARSACS). *J. Biol. Chem.* **286**, 20407–20412 (2011). doi: 10.1074/jbc.M111.232884; pmid: 21507954
42. S. Kiani *et al*., Cas9 gRNA engineering for genome editing, activation and repression. *Nat. Methods* **12**, 1051–1054 (2015). doi: 10.1038/nmeth.3580; pmid: 26344044
43. S. Konermann *et al*., Genome-scale transcriptional activation by an engineered CRISPR-Cas9 complex. *Nature* **517**, 583–588 (2015). doi: 10.1038/nature14136; pmid: 25494202
44. J. E. Dahlman *et al*., Orthogonal gene knockout and activation with a catalytically active Cas9 nuclease. *Nat. Biotechnol.* **33**, 1159–1161 (2015). doi: 10.1038/nbt.3390; pmid: 26436575
45. K. S. Makarova, Y. I. Wolf, E. V. Koonin, Comprehensive comparative-genomic analysis of type 2 toxin-antitoxin systems and related mobile stress response systems in prokaryotes. *Biol. Direct* **4**, 19 (2009). doi: 10.1186/1745-6150-4-19; pmid: 19493340
46. F. Hayes, L. Van Melderen, Toxins-antitoxins: Diversity, evolution and function. *Crit. Rev. Biochem. Mol. Biol.* **46**, 386–408 (2011). doi: 10.3109/10409238.2011.600437 pmid: 21819231
47. K. S. Makarova, V. Anantharaman, L. Aravind, E. V. Koonin, Live virus-free or die: Coupling of antivirus immunity and programmed suicide or dormancy in prokaryotes. *Biol. Direct* **7**, 40 (2012). doi: 10.1186/1745-6150-7-40; pmid: 23151069
48. C. Benda *et al*., Structural model of a CRISPR RNA-silencing complex reveals the RNA-target cleavage activity in Cmr4. *Mol. Cell* **56**, 43–54 (2014). doi: 10.1016/j.molcel.2014.09.002; pmid: 25280103
49. Z. Abil, H. Zhao, Engineering reprogrammable RNA-binding proteins for study and manipulation of the transcriptome. *Mol. Biosyst.* **11**, 2658–2665 (2015). doi: 10.1039/C5MB00289C; pmid: 26166256
50. J. P. Mackay, J. Font, D. J. Segal, The prospects for designer single-stranded RNA-binding proteins. *Nat. Struct. Mol. Biol.* **18**, 256–261 (2011). doi: 10.1038/nsmb.2005; pmid: 21358629

ACKNOWLEDGMENTS

We thank P. Boutz, J. Doench, P. Sharp, and B. Zetsche for helpful discussions and insights; R. Belliveau for overall research support; J. Francis and D. O'Connell for generous MiSeq instrument access; D. Daniels and C. Garvie for providing bacterial incubation space for protein purification; R. Macrae for critical reading of the manuscript; and the entire Zhang laboratory for support and advice. We thank N. Ranu for generously providing plasmid pRFP and D. Daniels for providing 6-His-MBP-TEV. O.O.A. is supported by a Paul and Daisy Soros Fellowship, a Friends of the McGovern Institute Fellowship, and the Poitras Center for Affective Disorders. J.S.G. is supported by a U.S. Department of Energy (DOE) Computational Science Graduate Fellowship. S.S. is supported by the graduate program of Skoltech Data-Intensive Biomedicine and Biotechnology Center for Research, Education, and Innovation. I.M.S. is supported by the Simons Center for the Social Brain. D.B.T.C. is supported by award T32GM007753 from the National Institute of General Medical Sciences. K.S.M., E.V.K., and, in part, S.S. are supported by the intramural program of the U.S. Department of Health and Human Services (to the National Library of Medicine). K.S. is supported by NIH grant GM10407, Russian Science Foundation grant 14-14-00988, and Skoltech. F.Z. is a New York Stem Cell Foundation Robertson Investigator. F.Z. is supported by the NIH through the National Institute of Mental Health (5DP1-MH100706 and 1R01-MH110049), NSF, the New York Stem Cell, Simons, Paul G. Allen Family, and Vallee Foundations; and J. Poitras, P. Poitras, R. Metcalfe, and D. Cheng. A.R. is a member of the scientific advisory board for Syros Pharmaceuticals and Thermo Fisher. O.O.A., J.S.G., J.J., E.V.K., S.K., E.S.L., K.S.M., L.M., E.S., K.S., S.S., and F.Z. are inventors on provisional patent application 62/181,675 applied for by the Broad Institute, MIT, Harvard, NIH, Skoltech, and Rutgers that covers the C2c2 proteins described in this paper. Deep sequencing data are available at Sequence Read Archive under BioProject accession no. PRJNA318890. The authors plan to make the reagents widely available to the academic community through Addgene subject to a materials transfer agreement and to provide software tools via the Zhang laboratory website (www.genome-engineering.org) and GitHub (https://github.com/fengzhanglab).

SUPPLEMENTARY MATERIALS

www.sciencemag.org/content/353/6299/aaf5573/suppl/DC1
Materials and Methods
Tables S1 to S5
Figs. S1 to S24
References (*51*–*55*)

2 March 2016; accepted 25 May 2016
Published online 2 June 2016
10.1126/science.aaf5573

RESEARCH ARTICLE SUMMARY

TOPOLOGICAL MATTER

Beyond Dirac and Weyl fermions: Unconventional quasiparticles in conventional crystals

Barry Bradlyn,* Jennifer Cano,* Zhijun Wang,* M. G. Vergniory, C. Felser, R. J. Cava, B. Andrei Bernevig†

INTRODUCTION: Condensed-matter systems have recently become a fertile ground for the discovery of fermionic particles and phenomena predicted in high-energy physics; examples include Majorana fermions, as well as Dirac and Weyl semimetals. However, fermions in condensed-matter systems are not constrained by Poincare symmetry. Instead, they must only respect the crystal symmetry of one of the 230 space groups. Hence, there is the potential to find and classify free fermionic excitations in solid-state systems that have no high-energy counterparts.

RATIONALE: The guiding principle of our classification is to find irreducible representations of the little group of lattice symmetries at high-symmetry points in the Brillouin zone (BZ) for each of the 230 space groups (SGs), the dimension of which corresponds to the number of bands that meet at the high-symmetry point. Because we are interested in systems with spin-orbit coupling, we considered only the double-valued representations, where a 2π rotation gives a minus sign. Furthermore, we considered systems with time-reversal symmetry that squares to –1. For each unconventional representation, we computed the low-energy $\mathbf{k} \cdot \mathbf{p}$ Hamiltonian near the band crossings by writing down all terms allowed by the crystal symmetry. This allows us to further differentiate the band crossings by the degeneracy along lines and planes that emanate from the high-symmetry point, and also to compute topological invariants. For point degeneracies, we computed the monopole charge of the band-crossing; for line nodes, we computed the Berry phase of loops encircling the nodes.

RESULTS: We found that three space groups exhibit symmetry-protected three-band crossings. In two cases, this results in a threefold degenerate point node, whereas the third case results in a line node away from the high-symmetry point. These crossings are required to have a nonzero Chern number and hence display surface Fermi arcs. However, upon applying a magnetic field, they have an unusual Landau level structure, which distinguishes them from single and double Weyl points. Under the action of spatial symmetries, these fermions transform as spin-1 particles, as a consequence of the interplay between nonsymmorphic space group symmetries and spin. Additionally, we found that six space groups can host sixfold degeneracies. Two of these consist of two threefold degeneracies with opposite chirality, forced to be degenerate by the combination of time reversal and inversion symmetry, and can be described as "sixfold Dirac points." The other four are distinct.

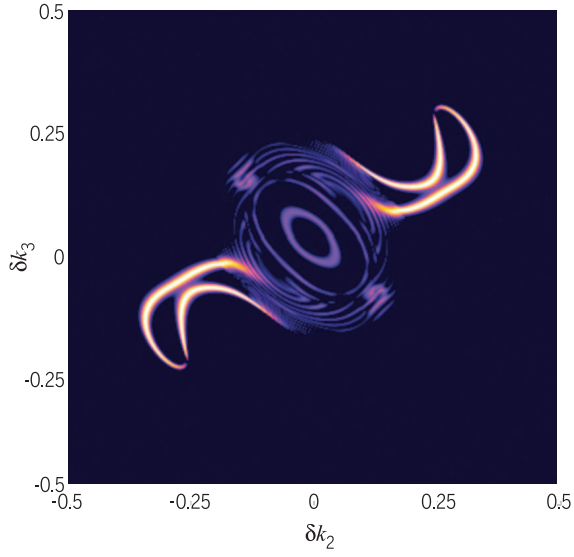

Fermi arcs from a threefold degeneracy. Shown is the surface density of states as a function of momentum for a crystal in SG 214 with bulk threefold degeneracies that project to (0.25, 0.25) and (−0.25, −0.25). Two Fermi arcs emanate from these points, indicating that their monopole charge is 2. The arcs then merge with the surface projection of bulk states near the origin.

Furthermore, seven space groups can host eightfold degeneracies. In two cases, the eightfold degeneracies are required; all bands come in groups of eight that cross at a particular point in the BZ. These two cases also exhibit fourfold degenerate line nodes, from which other semimetals can be derived: By adding strain or a magnetic field, these line nodes split into Weyl, Dirac, or line node semimetals. For all the three-, six-, and eight-band crossings, nonsymmorphic symmetries play a crucial role in protecting the band crossing.

ON OUR WEBSITE

Read the full article at http://dx.doi.org/10.1126/science.aaf5037

Last, we found that seven space groups may host fourfold degenerate "spin-3/2" fermions at high symmetry points. Like their spin-1 counterparts, these quasiparticles host Fermi surfaces with nonzero Chern number. Unlike the other cases we considered, however, these fermions can be stabilized by both symmorphic and nonsymmorphic symmetries. Three space groups that host these excitations also host unconventional fermions at other points in the BZ.

We propose nearly 40 candidate materials that realize each type of fermion near the Fermi level, as verified with ab initio calculations. Seventeen of these have been previously synthesized in single-crystal form, whereas others have been reported in powder form.

CONCLUSION: We have analyzed all types of fermions that can occur in spin-orbit coupled crystals with time-reversal symmetry and explored their topological properties. We found that there are several distinct types of such unconventional excitations, which are differentiated by their degeneracies at and along high-symmetry points, lines, and surfaces. We found natural generalizations of Weyl points: three- and four-band crossings described by a simple $\mathbf{k} \cdot \mathbf{S}$ Hamiltonian, where S_i is the set of spin generators in either the spin-1 or spin-3/2 representations. These points carry a Chern number and, consequently, can exhibit Fermi arc surface states. We also found excitations with six- and eightfold degeneracies. These higher-band crossings create a tunable platform to realize topological semimetals by applying an external magnetic field or strain to the fourfold degenerate line nodes. Last, we propose realizations for each species of fermion in known materials, many of which are known to exist in single-crystal form. ■

The list of author affiliations is available in the full article online.
*These authors contributed equally to this work.
†Corresponding author. Email: bernevig@princeton.edu
Cite this article as B. Bradlyn *et al.*, *Science* **353**, aaf5037 (2016). DOI: 10.1126/science.aaf5037

RESEARCH ARTICLE

TOPOLOGICAL MATTER

Beyond Dirac and Weyl fermions: Unconventional quasiparticles in conventional crystals

Barry Bradlyn,[1]* Jennifer Cano,[1]* Zhijun Wang,[2]* M. G. Vergniory,[3] C. Felser,[4] R. J. Cava,[5] B. Andrei Bernevig[2]†

In quantum field theory, we learn that fermions come in three varieties: Majorana, Weyl, and Dirac. Here, we show that in solid-state systems this classification is incomplete, and we find several additional types of crystal symmetry–protected free fermionic excitations. We exhaustively classify linear and quadratic three-, six-, and eight-band crossings stabilized by space group symmetries in solid-state systems with spin-orbit coupling and time-reversal symmetry. Several distinct types of fermions arise, differentiated by their degeneracies at and along high-symmetry points, lines, and surfaces. Some notable consequences of these fermions are the presence of Fermi arcs in non-Weyl systems and the existence of Dirac lines. Ab initio calculations identify a number of materials that realize these exotic fermions close to the Fermi level.

Condensed-matter systems have recently become a fertile ground for the discovery of fermionic particles and phenomena predicted in high-energy physics. Starting with graphene and its Dirac fermions (*1*), continuing to Majorana fermions in superconducting heterostructures (*2*–*7*), and most recently, with the discovery of Weyl (*8*–*16*) and Dirac (*17*–*22*) semimetals, solid-state physics has proven to abound in analogs of relativistic free fermions. There is, however, a fundamental difference between electrons in a solid and those at high energy: For relativistic fermions, the constraints imposed by Poincaré symmetry greatly limit the types of particles that may occur. The situation in condensed-matter physics is less constrained; only certain subgroups of Poincaré symmetry—the 230 space groups (SGs) that exist in three-dimensional (3D) lattices—need be respected. There is the potential, then, to find free fermionic excitations in solid-state systems that have no high-energy analogs.

Here, we theoretically identify and classify these exotic fermions, propose experiments to demonstrate their topological character, and point out a large number of different classes of candidate materials in which these fermions appear close to the Fermi level. We consider materials with time-reversal (TR) symmetry and spin-orbit coupling. We found that three of the SGs host half-integer angular momentum fermionic excitations with threefold degeneracies, stabilized by nonsymmorphic symmetries. The existence of threefold (and higher) degeneracies has long been known from a band theory perspective (*23*–*27*). Our purpose is to elucidate their topological nature. Here, we show that all of the threefold degeneracies either carry a Chern number ±2 or sit at the critical point separating the two Chern numbers. In two closely related SGs, the combination of TR and inversion results in sixfold degeneracies that consist of a threefold degeneracy and its time-reversed partner, a "sixfold Dirac point." There are two other types of sixfold degeneracies, both of which are distinct from free spin-5/2 particles. We also discuss eightfold degeneracies, which were recently introduced in (*28*). Here, we prove that there exists a finer classification of the eightfold degenerate fermions. Last, we show that for the threefold, as well as for a class of fourfold degeneracies, the low-energy Hamiltonian is of the form $\mathbf{k}\cdot\mathbf{S}$, where $\mathbf{S}$ is the vector of spin-1 or -3/2 matrices. This provides a natural generalization of the recently discovered Weyl fermion Hamiltonian, $\mathbf{k}\cdot\sigma$ (*26*, *29*, *43*, *44*, *53*, *60*, *63*, *66*, *67*).

We enumerate all possible three-, six-, and eightfold degenerate fermions in the subsequent sections. We include a symmetry analysis for each degeneracy type; an exhaustive search of the 230 SGs (*23*) guarantees that the list is complete. For each type of fermion, we investigated the low-energy $\mathbf{k}\cdot\mathbf{p}$ Hamiltonian allowed by the SG symmetries (*23*, *29*–*31*). This determines which degeneracies carry nontrivial Berry curvature or host exotic symmetry-enforced degeneracies along high-symmetry lines or planes in the Brillouin zone (BZ) (*32*–*34*). We explore the role these features play in transport and surface properties. Last, using ab initio techniques, we predict existing material realizations for each distinct type of fermion, where they appear close to the Fermi level.

SGs with three-, six-, and eight-band crossings

The guiding principle of our classification is to find irreducible representations (irreps) of the (little) group of lattice symmetries at high-symmetry points in the BZ for each of the 230 SGs; the dimension of

Table 1. Summary of the fermion types identified in this paper in solid-state systems. La indicates the type of lattice (cP, cubic primitive; cB, cubic body-centered; and tP, tetragonal primitive), d indicates the maximum degeneracy at the relevant k point in the presence of TR symmetry. Group generators are defined in (*35*).

SG	La	k	d	Generators
198	cP	R	6	$\{C_{3,111}^{-}\|010\},\{C_{2x}\|\frac{1}{2}\frac{3}{2}0\},\{C_{2y}\|0\frac{3}{2}\frac{1}{2}\}$
199	cB	P	3	$\{C_{3,111}^{-}\|101\},\left\{C_{2x}\|\bar{\frac{1}{2}}\frac{1}{2}0\right\},\left\{C_{2y}\|0\frac{1}{2}\bar{\frac{1}{2}}\right\}$
205	cP	R	6	$\{C_{3,111}^{-}\|010\},\{C_{2x}\|\frac{1}{2}\frac{3}{2}0\},\{C_{2y}\|0\frac{3}{2}\frac{1}{2}\},\{I\|000\}$
206	cB	P	6	$\{C_{3,111}^{-}\|101\},\left\{C_{2x}\|\bar{\frac{1}{2}}\frac{1}{2}0\right\},\left\{C_{2y}\|0\frac{1}{2}\bar{\frac{1}{2}}\right\}$
212	cP	R	6	$\{C_{2x}\|\frac{1}{2}\frac{1}{2}0\},\{C_{2y}\|0\frac{1}{2}\frac{1}{2}\},\{C_{3,111}^{-}\|000\},\{C_{2,1\bar{1}0}\|\frac{1}{4}\frac{1}{4}\frac{1}{4}\}$
213	cP	R	6	$\{C_{2x}\|\frac{1}{2}\frac{1}{2}0\},\{C_{2y}\|0\frac{1}{2}\frac{1}{2}\},\{C_{3,111}^{-}\|000\},\{C_{2,1\bar{1}0}\|\frac{3}{4}\frac{3}{4}\frac{3}{4}\}$
214	cB	P	3	$\{C_{3,111}^{-}\|101\},\left\{C_{2x}\|\bar{\frac{1}{2}}\frac{1}{2}0\right\},\left\{C_{2y}\|0\frac{1}{2}\bar{\frac{1}{2}}\right\}$
220	cB	P	3	$\{C_{3,\bar{1}11}\|0\frac{1}{2}\frac{1}{2}\},\{C_{2y}\|0\frac{1}{2}\frac{1}{2}\},\{C_{2x}\|\frac{3}{2}\frac{3}{2}0\},\{IC_{4x}^{-}\|\frac{1}{2}11\}$
230	cB	P	6	$\{C_{3,\bar{1}\bar{1}1}\|0\frac{1}{2}\frac{1}{2}\},\{C_{2y}\|0\frac{1}{2}\frac{1}{2}\},\{C_{2x}\|\frac{3}{2}\frac{3}{2}0\},\{IC_{4x}^{-}\|\frac{1}{2}11\}$
130	tP	A	8	$\{C_{4z}\|000\},\{\sigma_{\bar{x}y}\|00\frac{1}{2}\},\{I\|\frac{1}{2}\frac{1}{2}\frac{1}{2}\}$
135	tP	A	8	$\{C_{4z}\|\frac{1}{2}\frac{1}{2}\frac{1}{2}\},\{\sigma_{\bar{x}y}\|00\frac{1}{2}\},\{I\|000\}$
218	cP	R	8	$\{C_{2x}\|001\},\{C_{2y}\|000\},\{C_{3,111}^{-}\|001\}\{\sigma_{\bar{x}y}\|\frac{1}{2}\frac{1}{2}\frac{1}{2}\}$
220	cB	H	8	$\{C_{2x}\|\frac{1}{2}\frac{1}{2}0\},\{C_{2y}\|0\frac{1}{2}\frac{3}{2}\},\{C_{3,111}^{-}\|001\}\{\sigma_{\bar{x}y}\|\frac{1}{2}\frac{1}{2}\frac{1}{2}\}$
222	cP	R	8	$\{C_{4z}^{-}\|000\},\{C_{2x}\|000\},\{C_{3,111}^{-}\|010\}\{I\|\frac{1}{2}\frac{1}{2}\frac{1}{2}\}$
223	cP	R	8	$\{C_{4z}^{-}\|\frac{1}{2}\frac{1}{2}\frac{1}{2}\},\{C_{2x}\|000\},\{C_{3,111}^{-}\|010\}\{I\|000\}$
230	cB	H	8	$\{C_{4z}\|0\frac{1}{2}0\},\{C_{2y}\|1\frac{1}{2}\frac{1}{2}\},\{C_{3,111}\|111\}\{I\|000\}$

[1]Princeton Center for Theoretical Science, Princeton University, Princeton, NJ 08544, USA. [2]Department of Physics, Princeton University, Princeton, NJ 08544, USA. [3]Donostia International Physics Center, P. Manuel de Lardizabal 4, 20018 Donostia-San Sebastián, Spain. [4]Max Planck Institute for Chemical Physics of Solids, 01187 Dresden, Germany. [5]Department of Chemistry, Princeton University, Princeton, NJ 08544, USA.
*These authors contributed equally to this work. †Corresponding author. Email: bernevig@princeton.edu

these representations corresponds to the number of bands that meet at the high-symmetry point and is one of the characteristics of the fermion type. Because we are interested in fermions with spin-orbit coupling, we consider only the double-valued representations; TR symmetry is an antiunitary that squares to –1. The results of our search are summarized in Table 1. All the SGs include nonsymmorphic generators, and all representations are projective; these are in fact necessary ingredients for the three-, six-, and eightfold degenerate irreps (*35*).

We found that SGs 199, 214, and 220 may host a 3D representation at the *P* point in the BZ [the high-symmetry points are defined in (*35*)]. These SGs have a body-centered cubic Bravais lattice, and the *P* point is a TR noninvariant point at a corner of the BZ (that is, $P \neq -P$). All three of these systems host a complementary threefold degeneracy at $-P$ because of TR symmetry; Kramers's theorem requires this to be the case. SG 214 is distinct in that the threefold degeneracy at $-P$ persists even if TR symmetry is broken, because the *P* and $-P$ points are related by a twofold screw rotation in the full-symmetry group.

In the presence of TR symmetry, six SGs can host sixfold degeneracies. In all cases, these arise as threefold degeneracies that are doubled by the presence of TR symmetry. Four of these—SGs 198, 205, 212, and 213—correspond to simple-cubic Bravais lattice, and the sixfold degeneracy occurs at the TR invariant *R* point at the corner of the BZ. The other two sixfold degeneracies occur in SGs 206 and 230 at the *P* point. Although this point is not TR invariant, these SGs are inversion symmetric, and hence all degeneracies are doubled.

Last, in agreement with previous work (*28*), we found that seven SGs may host eightfold degeneracies. However, as shown below, the resulting fermions fall into distinct classes. Two of these, SGs 130 and 135, have a tetragonal Bravais lattice; these are special in that they require eightfold degeneracies at the TR invariant *A* point. In addition, SGs 222, 223, and 230 may host eightfold degeneracies. SGs 222 and 223 are simple-cubic, and an eightfold fermion can occur at the *R* point in the BZ; for SG 230, it occurs at the TR invariant *H* point.

There are two more SGs that can host eightfold degeneracies, SG 218 and SG 220. These differ from the others in that they lack inversion symmetry. Energy bands away from high-symmetry points need no longer come in pairs. SG 218 has a simple cubic Bravais lattice, and an eightfold degeneracy may occur at the *R* point. In SG 220, the degeneracy may occur at the *H* point.

Low-energy effective models

For each of the band crossings in Table 1, we computed a low-energy expansion of the most general Hamiltonian consistent with the symmetries of the little group near the degeneracy point, $\mathbf{k}_0$, in terms of $\delta\mathbf{k} \equiv \mathbf{k} - \mathbf{k}_0$. Full details of the constructions are in (*35*). Representative plots of the band dispersion along high-symmetry lines are shown in Figs. 1 to 3, where higher-order terms have been included for the sake of clarity.

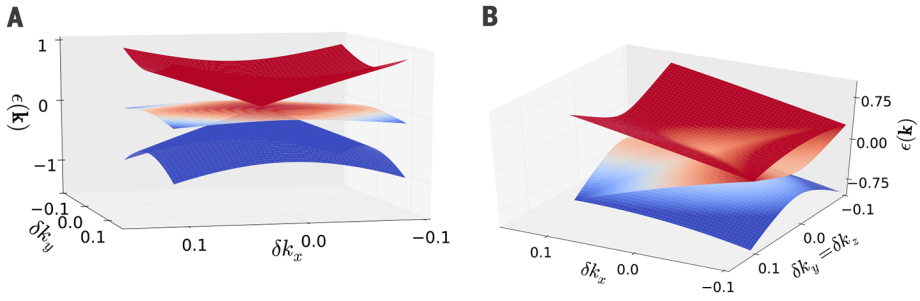

Fig. 1. Energy dispersion near a threefold degeneracy at the *P* point. (**A** and **B**) Shown are threefold degenerate points in (A) SGs 199 and 214 and (B) SG 220. In the latter case, pairs of bands remain degenerate in energy along the high-symmetry lines $|\delta k_x| = |\delta k_y| = |\delta k_z|$.

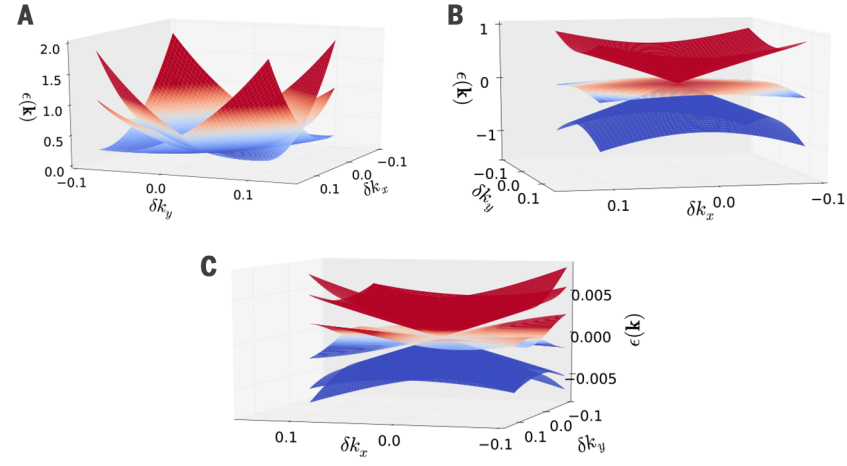

Fig. 2. Energy dispersion near a sixfold degeneracy. (**A** to **C**) Six-band crossings in (A) SG 205; (B) SG 206 and 230; and (C) SGs 198, 212, and 213. In SGs 198, 212, and 213, bands become degenerate in pairs along the faces $\delta k_i = 0$ of the BZ. In SGs 205, 206, and 230, all bands are twofold degenerate owing to inversion symmetry.

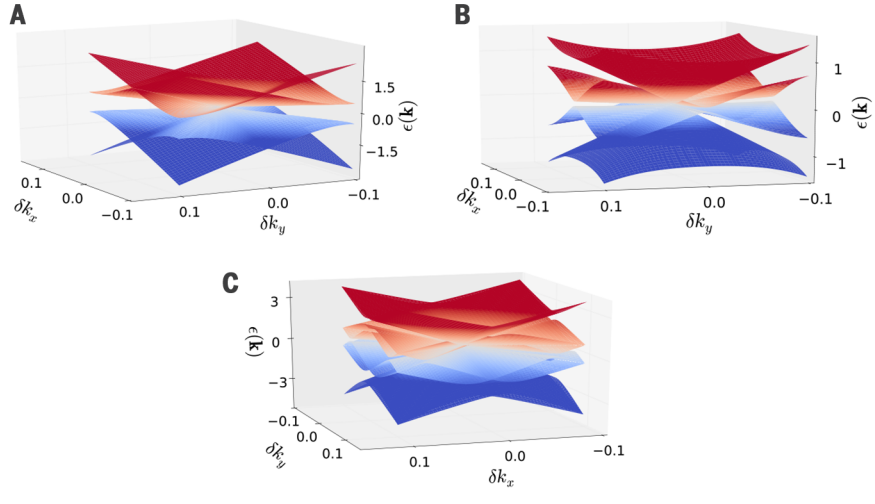

Fig. 3. Energy dispersion near an eightfold degeneracy. (**A** to **C**) Eightfold degenerate points in (A) SGs 130 and 135; (B) SGs 222, 223, and 230; and (C) SGs 218 and 220. (A) and (B) show pairwise degeneracy owing to inversion symmetry. In addition, in (A), two degenerate bands form fourfold degenerate line nodes along the edges of the BZ. In (C), the eightfold degeneracy splits into four nondegenerate and two doubly degenerate pairs of bands along the high-symmetry $|\delta k_x| = |\delta k_y| = |\delta k_z|$ lines.

We began by analyzing the threefold degeneracy points. The linearized $\mathbf{k}\cdot\mathbf{p}$ Hamiltonian for SGs 199 and 214 takes the form

$$H_{199}(\phi,\delta\mathbf{k})=\begin{pmatrix}0 & e^{i\phi}\delta k_x & e^{-i\phi}\delta k_y\\ e^{-i\phi}\delta k_x & 0 & e^{i\phi}\delta k_z\\ e^{i\phi}\delta k_y & e^{-i\phi}\delta k_z & 0\end{pmatrix} \quad (1)$$

where ϕ is a real parameter; without loss of generality, we set the zero of energy at zero throughout and omit an overall energy scale. The bands are nondegenerate away from $\delta\mathbf{k}=0$, unless $\phi=n\pi/3$ for integer n, in which case bands become degenerate along the lines $|\delta k_x|=|\delta k_y|=|\delta k_z|$. Although the locations of these degeneracies in $(\delta\mathbf{k},\phi)$ change in the presence of higher-order terms, they identify two topologically distinct phases. First, for $\pi/3<\phi<2\pi/3$, the $\delta\mathbf{k}\neq 0$ Hamiltonian is adiabatically connected to the one with $\phi=\pi/2$ for sufficiently small $|\delta\mathbf{k}|>0$. At this value of ϕ, the Hamiltonian takes the form

$$H_{199}(\pi/2,\delta\mathbf{k})=\delta\mathbf{k}\cdot\mathbf{S} \quad (2)$$

where the matrices S_i are the generators of the rotation group $SO(3)$ in the spin-1 representation. This shows that our threefold fermion is a fermionic spin-1 generalization of an ordinary Weyl fermion. The translation phases of the nonsymmorphic little-group symmetries have effectively converted a half-integer spin representation into an integer-spin representation. The three bands $\psi_\pm$, ψ_0 of the Hamiltonian have energies $\varepsilon_\pm=\pm|\delta\mathbf{k}|$, $\varepsilon_0=0$. Furthermore, the Chern numbers of each of these bands evaluated over any closed surface enclosing the degeneracy point are $v_\pm=\mp 2$ and $v_0=0$. These Berry fluxes characterize the entire phase $\pi/3<\phi<2\pi/3$.

At $\phi=n\pi/3$, the $v=0$ band becomes degenerate, with both $\psi_\pm$ bands at different points in momentum space; these degeneracies transport Berry curvature between ψ_+ and ψ_-. The formation of line nodes at the transition is an artifact of linearization: When higher-order terms are included in the Hamiltonian, the line nodes break up into sets of four single Weyl nodes, which carry Berry curvature away from the degeneracy point. The properties of all the phases for the other values of ϕ can be derived from those for $\pi/3<\phi<2\pi/3$; all regions feature bands with Chern number ± 2 (*35*). Thus, this three-band crossing has the topological character of a double Weyl point (*36*), but the dispersion of a single Weyl point; this behavior is facilitated by the trivial ($v=0$) band passing through the gapless point (Fig. 1A, energy spectrum).

Having identified a fermion with a spin-1 $\mathbf{k}\cdot\mathbf{S}$ Hamiltonian, it is natural to ask whether there exist similar particles for higher values of angular momentum j. Our fermion classification rules out the possibility of $j\geq 2$ because these would either have degeneracy greater than eight, which we have ruled out via an exhaustive search, or would have appeared on our list. In (*35*), we present a full classification of $j=3/2$ fermions, which we found can be stabilized by either symmorphic or nonsymmorphic symmetries; we found seven SGs that can host this excitation. Three of these overlap with groups mentioned earlier: SGs 212 and 213 can host spin-3/2 fermions at the Γ point, and SG 214 can host a spin-3/2 fermion at the Γ and H points.

The threefold degeneracy in SG 220 is distinct from that in SGs 199 and 214. The linear-order $\mathbf{k}\cdot\mathbf{p}$ Hamiltonian reads

$$H_{220}(\delta\mathbf{k})=H_{199}[0,(\delta k_y,\delta k_x,-\delta k_z)] \quad (3)$$

This threefold degeneracy sits at a critical point in the phase diagram for SG 199 described in the previous paragraph. Consequently, pairs of two bands are degenerate along the lines $|\delta k_x|=|\delta k_y|=|\delta k_z|$ (Fig. 1B). Mirror and threefold rotation symmetry dictate that—unlike for SGs 199 and 214 discussed above—these line nodes persist to all orders in the $\mathbf{k}\cdot\mathbf{p}$ expansion (*35*). The line nodes are characterized by the holonomy of the wavefunction (Berry phase), around any loop encircling the line, given by $w=-1$.

Next, we consider the sixfold band degeneracies. We start with SGs 205, 206, and 230, in which TR symmetry $\mathcal{T}$ times inversion I forces all bands to be twofold degenerate (Fig. 2, A and B). In SGs 206 and 230, the $\mathbf{k}\cdot\mathbf{p}$ Hamiltonian can be written as

$$H_{206}=H_{199}\oplus H_{199}^{*} \quad (4)$$

Thanks to $\mathcal{T}I$, there is no abelian Berry curvature (Chern number) associated with these degeneracies. Instead, we can consider the non-Abelian $SU(2)$-valued holonomy [Wilson loop (*37*, *38*)] of the wavefunction in each twofold degenerate pair of bands. Evaluated along C_2 symmetric loops, the eigenvalues of the $SU(2)$ holonomy matrix wind twice—and in opposite directions—around the unit circle as a function of position in the BZ (*35*). As gauge-invariant quantities, these eigenvalues are in-principle measurable (*39*, *40*), hence their winding provides a meaninful topological classification.

Unlike the previous cases, SG 205 contains inversion symmetry in the little group of the R point. This forces the effective Hamiltonian to be quadratic in $\delta\mathbf{k}$. However, it is still related to H_{199} by

$$H_{205}(\delta\mathbf{k})=H_{199}(\delta k')\oplus H_{199}^{*}(\delta k')+F(\delta\mathbf{k})\oplus F(\delta\mathbf{k})$$

where $F(\delta\mathbf{k})$ is a diagonal matrix whose entries are $E_1\delta k_x^2+E_2\delta k_y^2+E_3\delta k_z^2$ and all cyclic permutations of δk_i. Because of its quadratic coordinate dependence, $H_{205}(\delta\mathbf{k})$ has only bands of zero net Berry flux, and Wilson loop eigenvalues do not wind.

We conclude our analysis of the three- and sixfold fermions with SGs 198, 212, and 213. Unlike the other six-band systems, these lack inversion symmetry, and so host six bands with distinct energies. The linearized $\mathbf{k}\cdot\mathbf{p}$ Hamiltonians may be written as

$$H_{198}(\delta\mathbf{k})=\begin{pmatrix}H_{199}(\phi,\delta\mathbf{k}) & bH_{199}(0,\delta\mathbf{k})\\ b^{*}H_{199}(0,\delta\mathbf{k}) & -H_{199}^{*}(\phi,\delta\mathbf{k})\end{pmatrix},$$

$$H_{212,213}(\delta\mathbf{k})=\begin{pmatrix}H_{199}(\pi/2,\delta\mathbf{k}) & bH_{199}(0,\delta\mathbf{k})\\ b^{*}H_{199}(0,\delta\mathbf{k}) & -H_{199}^{*}(\pi/2,\delta\mathbf{k})\end{pmatrix} \quad (5)$$

where $\delta\mathbf{k}'=(\delta k_z,\delta k_x,-\delta k_y)$, and b is an arbitrary parameter. The six eigenstates of these Hamiltonians have distinct energies except along the faces of the BZ, where the spectrum degenerates into pairs related by the composition of a nonsymmorphic C_2 rotation and time reversal; this degeneracy is shown in Fig. 2C. Because this symmetry is antiunitary and squares to -1, these degeneracies are stable to higher-order terms in $\mathbf{k}\cdot\mathbf{p}$.

Next, we examine the eightfold fermions. In SGs 130 and 135, $\mathcal{T}I$ symmetry mandates doubly degenerate bands. Close to the A point, the linearized $\mathbf{k}\cdot\mathbf{p}$ Hamiltonian reads

$$\begin{aligned}H_{130}=H_{135}=\delta k_z(&a\sigma_2\sigma_3\sigma_3+b\sigma_2\sigma_3\sigma_2\\&+c\sigma_2\sigma_3\sigma_1)+\delta k_x(-d\sigma_1\sigma_3\sigma_0\\&+e\sigma_1\sigma_2\sigma_3+f\sigma_1\sigma_2\sigma_2+g\sigma_1\sigma_2\sigma_1)\\&+\delta k_y(-d\sigma_3\sigma_3\sigma_0+e\sigma_3\sigma_2\sigma_3\\&+f\sigma_3\sigma_2\sigma_2+g\sigma_3\sigma_2\sigma_1)\end{aligned} \quad (6)$$

where a, b, ... g are real-valued parameters. This Hamiltonian has fourfold degenerate line nodes along lines $\delta k_i=\delta k_j=0$ with $i\neq j$; $i,j\in\{x,y,z\}$, which follow the BZ edges (Fig. 3A). This is seen by noting that the matrices multiplying any given δk_i are part of a Clifford

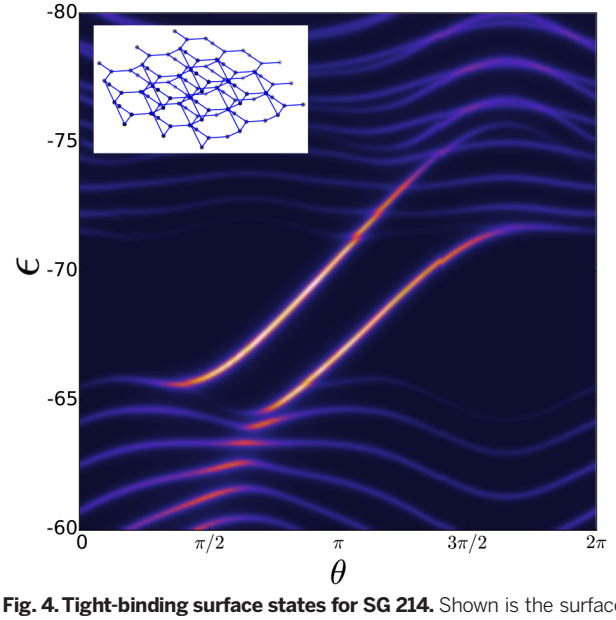

Fig. 4. Tight-binding surface states for SG 214. Shown is the surface density of states for a surface in the $\bar{1}11$ direction, calculated by using the open-source PythTB package (*70*). The x axis gives the angle around a circle $\delta k(\theta)=0.05[g_2\cos(\theta)+g_3\sin(\theta)]$ surrounding the surface projection of the P point, and the y axis is energy. Here, $g_2=2\pi(1,0,1)$ and $g_3=2\pi(1,1,0)$ are the surface reciprocal lattice vectors. Two chiral Fermi arcs can be clearly seen traversing the bulk gap. (Inset) The atoms in nine unit cells with lines to indicate the nonzero hopping amplitudes. Each unit cell consists of four atoms with three p orbitals per atom. Only p orbitals with intersite spin-orbit coupling are included.

algebra. These lines are generally protected by composites of time reversal and nonsymmorphic mirror symmetry. Thanks to $\mathcal{T}I$ symmetry, abelian Berry phase of these line nodes vanishes. However, they can be characterized by the two (–1) eigenvalues of the $SU(2)$ Wilson loop encircling them.

Similarly, for SGs 222, 223, and 230, we have

$$\begin{aligned} H_{222}=H_{223}=&\delta k_z(a\sigma_3\sigma_1\sigma_3+b\sigma_1\sigma_1\sigma_1+c\sigma_1\sigma_1\sigma_2)\\ &-\delta k_x\left(\frac{a}{2}\sigma_1\sigma_1\sigma_3+\frac{a\sqrt{3}}{2}\sigma_1\sigma_2\sigma_0\right.\\ &\left.+b\sigma_3\sigma_1\sigma_1+c\sigma_3\sigma_1\sigma_2\right)\\ &+\delta k_y\left(\frac{a}{2}\sigma_2\sigma_1\sigma_0+\frac{a\sqrt{3}}{2}\sigma_2\sigma_2\sigma_3\right.\\ &\left.+b\sigma_0\sigma_1\sigma_2+c\sigma_0\sigma_1\sigma_1\right) \end{aligned} \quad (7)$$

and a similar expression holds for H_{230} after a permutation of every δk. Besides the $\mathcal{T}I$ double degeneracy of all bands, there are no additional degeneracies (Fig. 3B).

Last, we examine the eightfold degeneracy in SGs 218 and 220. Because both of these cases lack $\mathcal{T}I$, they have eight nondegenerate bands away from the high-symmetry point. However, there is a degeneracy along high-symmetry lines emanating from it. Along lines $|\delta k_x| = |\delta k_y| = |\delta k_z|$, the eightfold degeneracy splits into four singly degenerate bands and two pairs of doubly degenerate bands. In addition, along lines where two of the δk_i are zero, and along lines where $\delta k_i = \delta k_j$, $\delta k_k = 0$, there are four pairs of doubly degenerate bands. Unlike SGs 198, 212, and 213 above, however, there are no additional degeneracies along high-symmetry planes. The spectrum is shown in Fig. 3C. The $\mathbf{k}\cdot\mathbf{p}$ Hamiltonian is given in (*35*).

Experimental signatures

We now consider how to experimentally detect the topological character of the new fermions. We start with the threefold degeneracy in SGs 199 and 214. Because the degeneracy at the P point carries net Berry flux $|v| = 2$, the surface spectrum will host two Fermi arcs that emerge from the surface projection of the P point (*13*), similar to those that appear from double Weyl points (*36*). In the presence of TR, an additional threefold degeneracy exists at the $-P$ point at the same energy; its surface projection will be the origin for two more Fermi arcs. Furthermore, because the monopole charge is invariant under the action of time reversal, materials in this symmetry group will always exhibit Fermi arcs. Whether these arcs are masked by other spurious Fermi pockets depends on the details of the band structure; the arcs will nevertheless always exist. These four Fermi arcs must terminate on the surface projection of four Weyl points (or two double Weyl points), which must exist elsewhere in the BZ. These can be identified with the Weyl points that drive the topological phase transition between Chern number $v = \pm 2$: At the phase transition, two Weyl fermions emerge from the threefold degeneracy to carry away the Fermi arcs of the $v = +2$ phase, whereas two other Weyl points emerge as the endpoints of the Fermi arcs for the $v = -2$ phase. We have verified this with a toy tight-binding model for SG 214. In the surface density of states for a surface in the $\bar{1}11$ direction in the first surface BZ (Fig. 4), a pair of Fermi arcs is visible, emanating from the surface projections of the P point. Breaking TR symmetry with an external Zeeman field will split each threefold

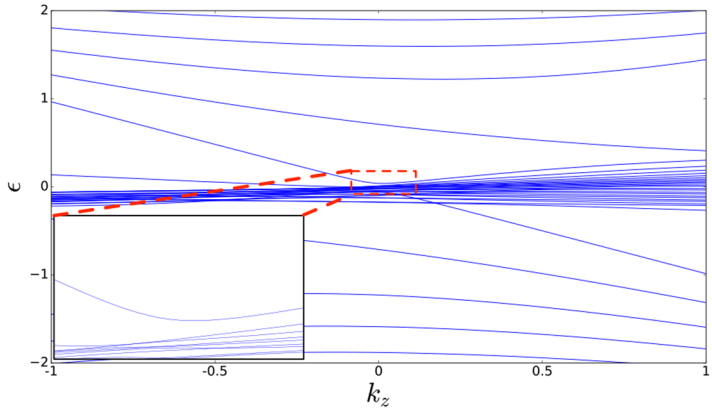

Fig. 5. Landau level spectrum of the threefold degenerate fermion. The spectrum is shown as a function of δk_z with magnetic field along the z direction. The two chiral modes are distinguished by being monotonic until they reach an avoided crossing (inset) with the family of bands near zero energy. Because of the avoided crossing, both chiral modes have a spectral flow that goes through $k_z \to \pm\infty$.

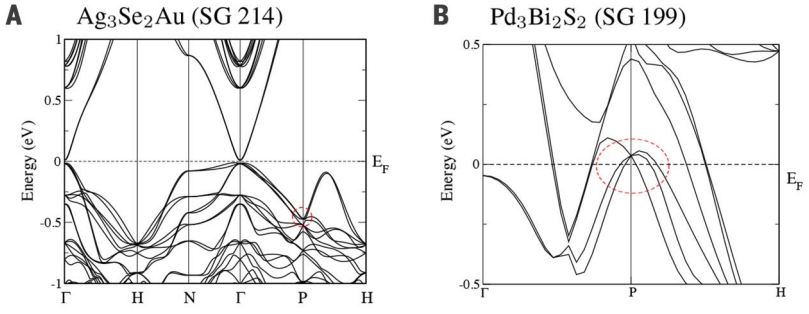

Fig. 6. Materials exhibiting threefold fermions near the Fermi level. (**A** and **B**) The band structures of (A) Ag_3Se_2Au (SG 214), where the threefold band crossing is 0.5 eV below the Fermi level, and (B) $Pd_3Bi_2S_2$ (SG 199), where the threefold crossing is almost exactly at the Fermi level.

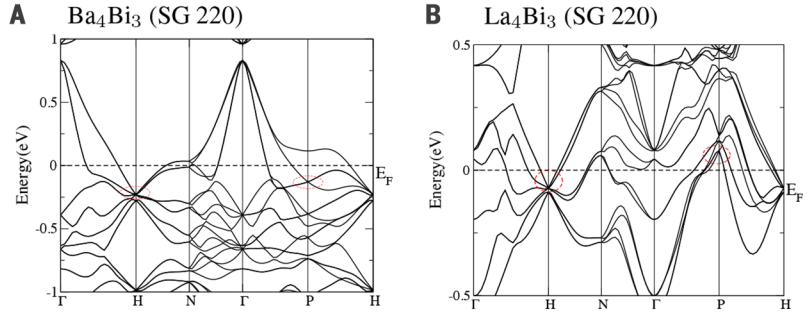

Fig. 7. Compounds in SG 220 display three- and eightfold fermions near the Fermi level. (**A** and **B**) The band structures of (A) Ba_4Bi_3 and (B) La_4Bi_3, both in SG 220. Both materials exhibit both a threefold fermion at the P point and an eightfold fermion at the H point. The threefold crossings split into a doubly degenerate line node and a single band along the cuts of the BZ shown in the figure; hence, the band crossings appear to be only twofold degenerate. Similarly, the eightfold crossing splits into four doubly degenerate line nodes and hence appears as a fourfold crossing. The band crossings are within 0.25 eV of the Fermi level.

degeneracy into a number of Weyl points (*35*); generically, these will be a mix of type I and type II Weyl fermions (*41*). In SG 199, this will destroy the exact degeneracy between the *P* and –*P* points, but the degeneracy will persist in SG 214 for perturbations invariant under $C_{2,1\bar{1}0}$.

In addition to Fermi arc surface states, the threefold fermions will exhibit anomalous negative magnetoresistance and a chiral anomaly distinct from that of either a single or double Weyl point. For weak magnetic fields, semiclassical considerations (*42*) suggest that the magnetoresistance in SGs 199 and 214 match that of a double Weyl point (*36*), although the density of states corresponds to a linear dispersion. At large magnetic fields, the Landau level spectrum for the threefold fermions displays two chiral modes; unlike the case of an ordinary (single or double) Weyl point, the spectral flow of these chiral modes does not pass through zero momentum but instead flows to $k_z \rightarrow \pm\infty$, assisted by the presence of the nearly flat trivial band. We show the numerically computed Landau level spectrum in Fig. 5 and the analytical derivation of the spectrum at the exactly solvable $\phi = \pi/2$ point in (*35*).

Because the rest of the fermion types we identified here do not host net Berry curvature, there is no guarantee of topologically protected surface states in the strictest sense. However, the nontrivial Berry phase associated with the line node in SG 220 implies the presence of a "Fermi drum" surface state (*33*, *43*), although this will not be robust to breaking of the crystal symmetry in the bulk. Also, despite the name, these states need not be flat—or even nearly flat—in energy. Similarly, the non-abelian Berry phase associated to the Dirac lines in SG 130 and 135 suggests the existence of pairs of drumhead states. And in the presence of an external magnetic field (or strain perturbation), these Dirac lines may be split to yield any of the usual gapless topological phases: Weyl, Dirac, and line node semimetals. This opens up the possibility of tuning topological Dirac semimetals in these materials with a Zeeman field, similar to the recent progress made with field-created Weyl semimetals in half-Heusler materials (*8*, *12*). Last, all of the fermion types are also detectable via angle-resolved photoemission spectroscopy (ARPES) [for example, similar experimental results in (*44*)] and through quantum oscillation experiments.

Material realizations

We propose candidate materials (*45*, *46*) that realize each of the types of fermions identified here near the Fermi level. In (*35*), we provide many more examples that require doping to bring the Fermi level to the band crossing but that, in the cases in which the fermions are below the Fermi level, are still observable in ARPES experiments. We have computed the band structure of each candidate (Figs. 6 to 9) to confirm that the desired band crossings exist and are relatively close to the Fermi level. We performed electronic structure calculations within density-functional theory (DFT) as implemented in the Vienna ab initio simulation package (*47*) and used the core-electron projector-augmented-wave basis in the generalized-gradient method (*48*). Spin-orbital coupling (SOC) is accounted for self-consistently. Unless otherwise noted, the materials we propose to host these fermions have been synthesized as single crystals.

We begin with an exotic three-band fermion in SG 199, in the material $Pd_3Bi_2S_2$, which exists in single-crystal form (*49*). The band crossing at the *P* point is only 0.1 eV above the Fermi level, and its position could be further tuned with doping (Fig. 6B).

Next, we consider the exotic three-band fermion in SG 214 in Ag_3Se_2Au, which can be grown as a single crystal (*50*). As shown in Fig. 6A, although the spin-1 Weyl point is located 0.5 eV below the Fermi level, there are fourfold degeneracies at the Γ and *H* points located only 0.02 eV below the Fermi level, and there are no other bands in the vicinity; this remarkable material exhibits a $\mathbf{k} \cdot \mathbf{S}$ type spin-3/2 Hamiltonian close to the Γ and *H* points.

SGs 220 and 230 can host these types of fermions at both the *P* and *H* points. In SG 220, we found threefold and eightfold fermions in Ba_4Bi_3 (*51*) and La_4Bi_3 (Fig. 7, A and B) (*52*) . In the latter case, the band crossings are <0.1 eV from the Fermi level. These materials are parts of the families of compounds A_4Pn_3 and R_4Pn_3 [A, Ca, Sr, Ba, and Eu; R, rare-earth element (La, Ce); Pn (pnictogen), As, Sb, and Bi], which are also potential candidates.

MgPt (*53*) is a near ideal example of a six-band fermion in SG 198; As shown in Fig. 8A, the band crossing is ~0.3 eV above the Fermi level and isolated from other bands. More examples can be found in the families of PdAsS (*54*) and K_3BiTe_3 (Fig. 8, B and C) (*55*). These band crossings are ~0.7 eV below and 0.5 eV above the Fermi level, respectively. Similar fermions can be found closer to the Fermi level in the compounds Li_2Pd_3B (SG 212) (*56*) and Mg_3Ru_2 (*57*), shown in Fig. 8, D and E.

The quadratic six-band fermions in SG 205 can be found in $PdSb_2$ (*58*), as shown in Fig. 8F, as well as in the similar compounds FeS_2 and PtP_2.

The eight-band fermions required to exist in SG 130 sit almost exactly at the Fermi level in $CuBi_2O_4$ and are isolated from all other bands

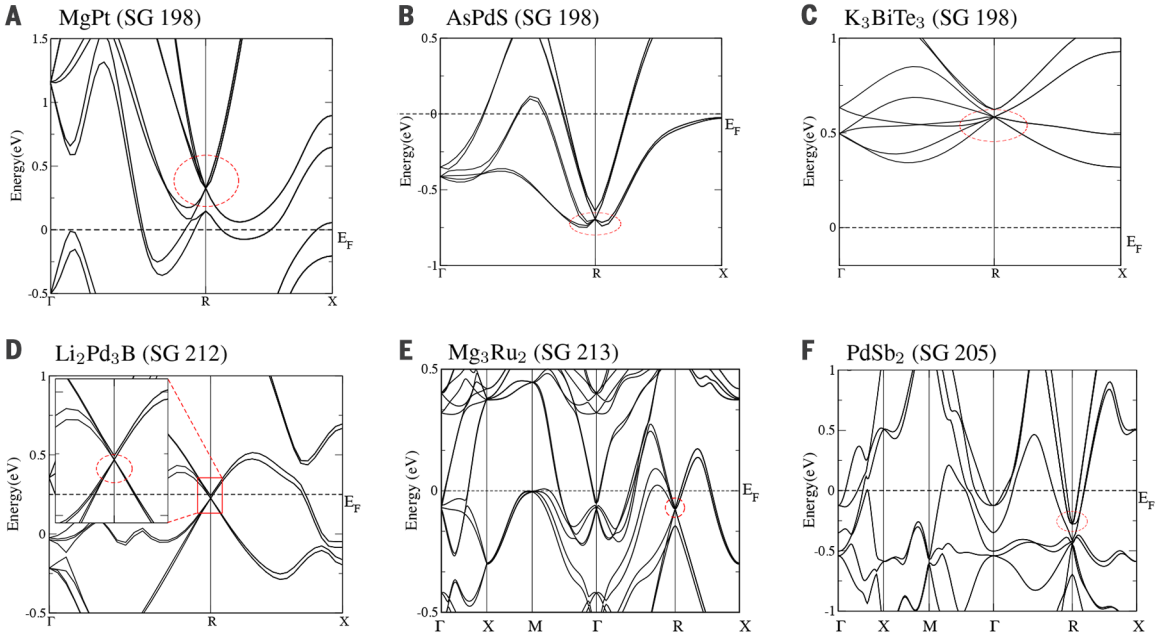

Fig. 8. Sixfold fermions at the *R* point. (**A** to **F**) The band structures of the representative compounds (A) MgPt, (B) AsPdS, and (C) K_3BiTe_3 in SG 198 and (D) Li_2Pd_3B (SG 212), (E) Mg_3Ru_2 (SG 213), and (F) $PdSb_2$ (SG 205). Because SG 205 contains inversion symmetry, all bands are doubly degenerate.

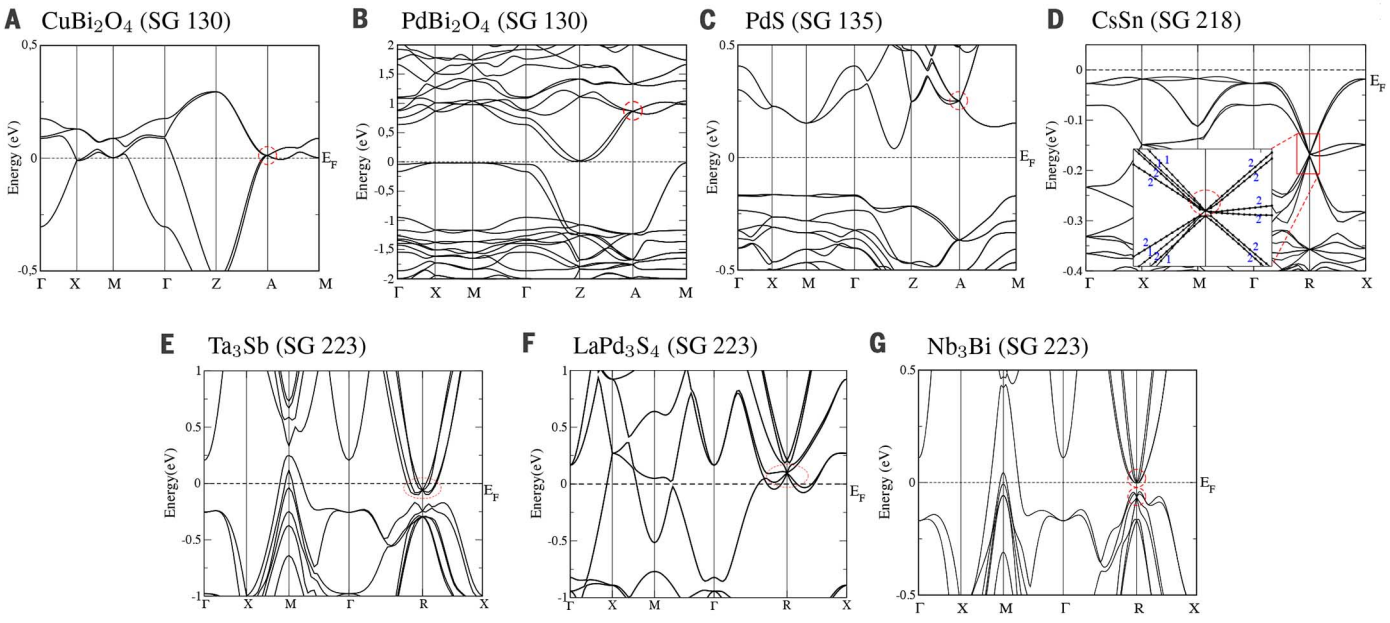

Fig. 9. Eightfold fermions at the *A* and *R* points. Eightfold fermions are visible at the *A* point in (**A**) $CuBi_2O_4$ (SG 130), (**B**) $PdBi_2O_4$ (SG 130), and (**C**) PdS (SG 135) and at the *R* point in (**D**) CsSn (SG 218), (**E**) Ta_3Sb (SG 223), (**F**) $LaPd_3S_4$ (SG 223), and (**G**) Nb_3Bi (SG 223). Because (A) to (C) and (D) to (G) have inversion symmetry (in addition to TR symmetry), all bands are doubly degenerate. In addition, in (A) to (C), the fourfold degenerate line nodes are visible along the *A*-*M* line, as described in the main text. [(D), inset] The eight-band crossing splits into four doubly degenerate lines along *R*-*X* and into four nondegenerate and two pairs of double degenerate bands along Γ-*R*.

(Fig. 9A). This material has a filling of 180 = 8*22 + 4 electrons per unit cell, and hence it could be a realizable example of a filling enforced semimetal (*59*) above its Neèl temperature, if not for interaction effects, which appear to make the material insulating (*60*). Other bismuth oxides in this SG may be more promising candidates for eight-fold fermions; $PdBi_2O_4$ (*61*), which exists in single-crystal form, is shown in Fig. 9B, and two predicted compounds are shown in (*35*)

Eight-band fermions are also required to exist in SG 135. One example is shown in Fig. 9C in PdS, sitting 0.25 eV above the Fermi level. This material is naturally insulating but could be potentially doped. It has been observed in polycrystalline form (*62*).

The eight-band fermions predicted to occur in SG 218 should exist in CsSn (*63*) and CsSi (*64*) and, more generally, in the class *AB* for A = K, Rb, Cs and B = Si, Ge, Sn; the band structure of CsSn shows its distinct splitting into four twofold degenerate bands in the $k_x = k_z$ direction away from the *R* point in Fig. 9D. There is a similar eight-band fermion at the *H* point in SG 220, which is shown in Fig. 7 for Ba_4Bi_3 (*51*) and La_4Bi_3 (*65*).

The eight-band fermions predicted to occur in SG 223 are exhibited in the candidates X_3Y, where X is either Nb or Ta and Y is any group A-IV or A-V element in the β-tungsten structure A15, as well as in the family MPd_3S_4, where M is any rare-earth metal. The band structures for Ta3Sb (powder) (*66*) and $LaPd_3S_4$ (*67*) show the eight-band crossing within nearly 0.1 eV of Fermi level (Fig. 9, E and F). Nb_3Bi (powder) (*68*), which has two eightfold fermions within 0.1 eV of the Fermi level, is shown in Fig. 9G. It is possible that other materials that host these types of fermions near the Fermi level may be identified through an exhaustive database search of filling-enforced semimetals.

Outlook

Here, we have analyzed all possible exotic fermion types that can occur in spin-orbit coupled crystals with TR symmetry going beyond the Majorana-Weyl-Dirac classification. By virtue of their band topology, these fermions can play host to interesting surface states, magnetotransport properties, and ARPES signatures. Growth of many of the material candidates mentioned above—including AsPdS, La_3PbI_3, La_4Bi_3, $LaPd_3S_4$, and Ta_3Sb—may be possible and, if successful, should yield fruitful results in ARPES and magnetotransport experiments.

As we have emphasized throughout, nonsymmorphic crystal symmetries were essential for stabilizing these fermions; it is the presence of half-lattice translations that allow spin-1/2 electrons to transform under integer spin representations of the rotation group, yielding threefold and sixfold degeneracies. The types of fermions we identified here also provide an explicit realization of the nonsymmorphic insulating filling bounds derived recently in (*59*, *69*), as follows. Thanks to the presence of TR symmetry, we know that our threefold fermions must occur in connection with an additional nondegenerate band, so that all bands have Kramers partners at TR invariant momenta; this suggests that the minimal band connectivity in these SGs is four, which is consistent with the filling bounds. Similarly, the sixfold fermions arise from doubling a threefold degeneracy, each of which comes along with an aforementioned additional nondegenerate band. We thus expect—and indeed confirm—that the minimal insulating filling is eight in these cases. Last, as noted in (*28*), the eightfold degenerate fermions saturate the filling bound for those SGs.

Looking ahead, there are several open questions that deserve future attention. First, gapping these degeneracies by breaking the symmetries that protect them can lead to distinct symmetry-protected topological phases, with new classes of 2D gapless surface modes. Furthermore, our symmetry analysis can be extended to crystals with magnetic order, and hence with interactions. This requires an investigation of representations of the 1191 remaining magnetic SGs.

Materials and methods

For all 230 space groups, we identified unconventional excitations by identifying the allowed little-group representations at each high-symmetry point in the Brillouin zone. Next, we used $\mathbf{k} \cdot \mathbf{p}$ perturbation theory to derive the most general symmetry-allowed low-energy Hamiltonian for each fermion type; we computed topological invariants from eigenvectors obtained by diagonalizing these Hamiltonians. We did our ab initio electronic structure within DFT as implemented in the Vienna ab initio simulation package (*37*) and used the core-electron projector-augmented-wave basis in the generalized-gradient method (*49*). SOC is accounted for self-consistently.

REFERENCES AND NOTES

1. A. H. Castro Neto, F. Guinea, N. M. R. Peres, K. S. Novoselov, A. K. Geim, The electronic properties of graphene. *Rev. Mod. Phys.* **81**, 109–162 (2009). doi: 10.1103/RevModPhys.81.109
2. L. Fu, C. L. Kane, Superconducting proximity effect and majorana fermions at the surface of a topological insulator. *Phys. Rev. Lett.* **100**, 096407 (2008). doi: 10.1103/PhysRevLett.100.096407; pmid: 18352737
3. R. M. Lutchyn, J. D. Sau, S. Das Sarma, Majorana fermions and a topological phase transition in semiconductor-superconductor heterostructures. *Phys. Rev. Lett.* **105**, 077001 (2010). doi: 10.1103/PhysRevLett.105.077001; pmid: 20868069
4. V. Mourik *et al*., Signatures of Majorana fermions in hybrid superconductor-semiconductor nanowire devices. *Science* **336**, 1003–1007 (2012). doi: 10.1126/science.1222360; pmid: 22499805
5. S. Nadj-Perge *et al*., Observation of Majorana fermions in ferromagnetic atomic chains on a superconductor. *Science* **346**, 602–607 (2014). doi: 10.1126/science.1259327; pmid: 25278507
6. Y. Oreg, G. Refael, F. von Oppen, Helical liquids and Majorana bound states in quantum wires. *Phys. Rev. Lett.* **105**, 177002 (2010). doi: 10.1103/PhysRevLett.105.177002; pmid: 21231073
7. N. Read, D. Green, Paired states of fermions in two dimensions with breaking of parity and time-reversal symmetries and the fractional quantum hall effect. *Phys. Rev. B* **61**, 10267–10297 (2000). doi: 10.1103/PhysRevB.61.10267
8. M. Hirschberger *et al*., The chiral anomaly and thermopower of Weyl fermions in the half-Heusler GdPtBi. *Nature Mater.* 10.1038/NMAT4684 (2016). pmid: 27348578
9. S.-M. Huang *et al*., A Weyl fermion semimetal with surface Fermi arcs in the transition metal monopnictide TaAs class. *Nat. Commun.* **6**, 7373 (2015). doi: 10.1038/ncomms8373; pmid: 26067579
10. B. Q. Lv *et al*., Experimental discovery of Weyl semimetal TaAs. *Phys. Rev. X* **5**, 031013 (2015). doi: 10.1103/PhysRevX.5.031013
11. B. Q. Lv *et al*., Observation of Weyl nodes in TaAs. *Nat. Phys.* **11**, 724–727 (2015). doi: 10.1038/nphys3426
12. C. Shekhar *et al*., Observation of chiral magneto-transport in RPtBi topological Heusler compounds; https://arxiv.org/abs/1604.01641 (2016).
13. X. Wan, A. M. Turner, A. Vishwanath, S. Y. Savrasov, Topological semimetal and Fermi-arc surface states in the electronic structure of pyrochlore iridates. *Phys. Rev. B* **83**, 205101 (2011). doi: 10.1103/PhysRevB.83.205101
14. H. Weng, C. Fang, Z. Fang, B. A. Bernevig, X. Dai, Weyl semimetal phase in noncentrosymmetric transition-metal monophosphides. *Phys. Rev. X* **5**, 011029 (2015). doi: 10.1103/PhysRevX.5.011029
15. S.-Y. Xu *et al*., Discovery of a Weyl fermion state with Fermi arcs in niobium arsenide. *Nat. Phys.* **11**, 748–754 (2015). doi: 10.1038/nphys3437
16. S.-Y. Xu *et al*., Discovery of a Weyl fermion semimetal and topological Fermi arcs. *Science* **349**, 613–617 (2015). doi: 10.1126/science.aaa9297; pmid: 26184916
17. Z. K. Liu *et al*., A stable three-dimensional topological Dirac semimetal Cd3As2. *Nat. Mater.* **13**, 677–681 (2014). doi: 10.1038/nmat3990; pmid: 24859642
18. Z. K. Liu *et al*., Discovery of a three-dimensional topological Dirac semimetal, Na3Bi. *Science* **343**, 864–867 (2014). doi: 10.1126/science.1245085; pmid: 24436183
19. J. A. Steinberg *et al*., Bulk Dirac points in distorted spinels. *Phys. Rev. Lett.* **112**, 036403 (2014). doi: 10.1103/PhysRevLett.112.036403; pmid: 24484151
20. Z. Wang *et al*., Dirac semimetal and topological phase transitions in $\boldsymbol{A}_3$Bi ($\boldsymbol{A}$ = Na, K, Rb). *Phys. Rev. B* **85**, 195320 (2012). doi: 10.1103/PhysRevB.85.195320
21. J. Xiong *et al*., Evidence for the chiral anomaly in the Dirac semimetal Na_3Bi. *Science* **350**, 413–416 (2015). doi: 10.1126/science.aac6089; pmid: 26338798
22. S. M. Young *et al*., Dirac semimetal in three dimensions. *Phys. Rev. Lett.* **108**, 140405 (2012). doi: 10.1103/PhysRevLett.108.140405; pmid: 22540776
23. C. J. Bradley, A. P. Cracknell, *The Mathematical Theory of Symmetry in Solids* (Clarendon, 1972).
24. A. Casher, A. Glück, Y. Gur, *The Irreducible Representations of Space Groups* (Benjamin, 1969).
25. D. K. Faddeyev, *Tables of the Principal Unitary Representations of Fedorov Groups: The Mathematical Tables Series*, vol. 34 (Elsevier, 2014).
26. O. V. Kovalev, *Irreducible Representations of the Space Groups* (Routledge, 1965).
27. S. C. Miller, W. F. Love, *Tables of Irreducible Representations of Space Groups and Co-representations of Magnetic Space Groups* (Pruett Press, 1967).
28. B. J. Wieder, Y. Kim, A. M. Rappe, C. L. Kane, Double Dirac semimetals in three dimensions. *Phys. Rev. Lett.* **116**, 186402 (2016). doi: 10.1103/PhysRevLett.116.186402; pmid: 27203335
29. M. I. Aroyo, A. Kirov, C. Capillas, J. M. Perez-Mato, H. Wondratschek, Bilbao Crystallographic Server. II. Representations of crystallographic point groups and space groups. *Acta Crystallogr. A* **62**, 115–128 (2006). doi: 10.1107/S0108767305040286; pmid: 16489249
30. M. I. Aroyo *et al*., Bilbao Crystallographic Server: I. Databases and crystallographic computing programs. *Z. Kristallogr.* **221**, 15–27 (2009). doi: 10.1524/zkri.2006.221.1.15
31. M. I. Aroyo *et al*., *Bulg. Chem. Commun.* **43**, 183 (2011).
32. G. Bian *et al*., Drumhead surface states and topological nodal-line fermions in $TlTaSe_2$. *Phys. Rev. B* **93**, 121113 (2016). doi: 10.1103/PhysRevB.93.121113
33. Y.-H. Chan, C.-K. Chiu, M. Y. Chou, A. P. Schnyder, Ca_3P_2 and other topological semi-metals with line nodes and drumhead surface states. *Phys. Rev. B* **93**, 205132 (2016). doi: 10.1103/PhysRevB.93.205132
34. C.-K. Chiu, A. P. Schnyder, Classification of reflection-symmetry-protected topological semimetals and nodal superconductors. *Phys. Rev. B* **90**, 205136 (2014). doi: 10.1103/PhysRevB.90.205136
35. Additional analyses are available as supplementary materials on *Science* Online.
36. C. Fang, M. J. Gilbert, X. Dai, B. A. Bernevig, Multi-Weyl topological semimetals stabilized by point group symmetry. *Phys. Rev. Lett.* **108**, 266802 (2012). doi: 10.1103/PhysRevLett.108.266802; pmid: 23005002
37. A. Alexandradinata, X. Dai, B. A. Bernevig, Wilson-loop characterization of inversion-symmetric topological insulators. *Phys. Rev. B* **89**, 155114 (2014). doi: 10.1103/PhysRevB.89.155114
38. A. Alexandradinata, Z. Wang, B. A. Bernevig, Topological insulators from group cohomology. *Phys. Rev. X* **6**, 021008 (2016). doi: 10.1103/PhysRevX.6.021008
39. F. Grusdt, D. Abanin, E. Demler, Measuring Z_2 topological invariants in optical lattices using interferometry. *Phys. Rev. A* **89**, 043621 (2014). doi: 10.1103/PhysRevA.89.043621
40. T. Li *et al*., Bloch state tomography using Wilson lines. *Science* **352**, 1094–1097 (2016). doi: 10.1126/science.aad5812; pmid: 27230376
41. A. A. Soluyanov *et al*., Type-II Weyl semimetals. *Nature* **527**, 495–498 (2015). doi: 10.1038/nature15768; pmid: 26607545
42. D. T. Son, B. Z. Spivak, Chiral anomaly and classical negative magnetoresistance of Weyl metals. *Phys. Rev. B* **88**, 104412 (2013). doi: 10.1103/PhysRevB.88.104412
43. A. A. Burkov, M. D. Hook, L. Balents, Topological nodal semimetals. *Phys. Rev. B* **84**, 235126 (2011). doi: 10.1103/PhysRevB.84.235126
44. L. M. Schoop *et al*., Dirac cone protected by non-symmorphic symmetry and three-dimensional Dirac line node in ZrSiS. *Nat. Commun.* **7**, 11696 (2016). doi: 10.1038/ncomms11696; pmid: 27241624
45. Fachinformationszentrum (FIZ) Karlsruhe, Inorganic Crystal Structure Database (FIZ, 2016); www.fiz-karlsruhe.de/de/leistungen/kristallographie/icsd.html.
46. A. Jain *et al*., The Materials Project: A materials genome approach to accelerating materials innovation. *APL Materials* **1**, 011002 (2013). doi: 10.1063/1.4812323
47. G. Kresse, J. Hafner, *Ab initio* molecular dynamics for open-shell transition metals. *Phys. Rev. B Condens. Matter* **48**, 13115–13118 (1993). doi: 10.1103/PhysRevB.48.13115; pmid: 10007687
48. J. P. Perdew, K. Burke, M. Ernzerhof, Generalized gradient approximation made simple. *Phys. Rev. Lett.* **77**, 3865–3868 (1996). doi: 10.1103/PhysRevLett.77.3865; pmid: 10062328
49. R. Weihrich *et al*., Structure, ordering, and bonding of half antiperovskites: $PbNi_{3/2}S$ and $BiPd_{3/2}S$. *Progr. Sol. State Chem.* **35**, 309–327 (2007). doi: 10.1016/j.progsolidstchem.2007.01.011
50. L. Bindi, C. Cipriani, Structural and physical properties of fischesserite, a rare gold–silver selenide from the De Lamar Mine, Owyhee County, Idaho, USA. *Can. Mineral.* **42**, 1733–1737 (2004). doi: 10.2113/gscanmin.42.6.1733
51. B. Li, A.-V. Mudring, J. D. Corbett, Valence compounds versus metals. Synthesis, characterization, and electronic structures of cubic Ae_4Pn_3 phases in the systems Ae = Ca, Sr, Ba, Eu; Pn = As, Sb, Bi. *Inorg. Chem.* **42**, 6940–6945 (2003). doi: 10.1021/ic0301472; pmid: 14552646
52. F. Hulliger, H. R. Ott, Superconductivity of lanthanum pnictides. *J. Less Common Met.* **55**, 103–113 (1977). doi: 10.1016/0022-5088(77)90266-1
53. H. H. Stadelmaier, W. K. Hardy, Ternare kohlenstofflegierungen von palladium und platin mit magnesium, aluminium, zink, gallium, germanium, kadmium, indium, zinn, quecksilber, thallium und blei. *Z. Metallk.* **52**, 391–396 (1961).
54. F. Hulliger, New compounds with cobaltite structure. *Nature* **198**, 382–383 (1963). doi: 10.1038/198382b0
55. B. Eisenmann, R. Zagler, Crystal structure of tripotassium tritellurobismutate (iii), k3bite3. *Z. Kristallogr.* **197**, 257–258 (1991).
56. U. Eibenstein, W. Jung, Li_2Pd_3B and Li_2Pt_3B: Ternary lithium borides of palladium and platinum with boron in octahedral coordination. *J. Solid State Chem.* **133**, 21–24 (1997). doi: 10.1006/jssc.1997.7310
57. R. Pöttgen, V. Hlukhyy, A. Baranov, Y. Grin, Crystal structure and chemical bonding of Mg_3Ru_2. *Inorg. Chem.* **47**, 6051–6055 (2008). doi: 10.1021/ic800387a; pmid: 18549193
58. S. Furuseth, K. Selte, A. Kjekshus, Redetermined crystal structures of $PdAs_2$, $PdSb_2$, PtP_2, $PtAs_2$, $PtSb_2$, alpha-$PtBi_2$, and $AuSb_2$. *Acta Chem. Scand.* **19**, 735–741 (1967). doi: 10.3891/acta.chem.scand.19-0735
59. H. C. Po, H. Watanabe, M. P. Zaletel, A. Vishwanath, Filling-enforced quantum band insulators in spin-orbit coupled crystals. *Science Advances* **2**, e1501782 (2016). doi: 10.1126/sciadv.1501782; pmid: 27152352
60. G. Sharma *et al*., Electronic structure, photovoltage, and photocatalytic hydrogen evolution with p-$CuBi_2O_4$ nanocrystals. *J. Mat. Chem. A* **4**, 2936–2942 (2016). doi: 10.1039/C5TA07040F
61. P. Conflant, J.-C. Boivin, D. Thomas, Etude structurale du conducteur anionique $Bi_{0,765}Sr_{0,235}O_{1,383}$. *J. Solid State Chem.* **35**, 192–199 (1980). doi: 10.1016/0022-4596(80)90493-4
62. G. Kliche, J. Köhler, W. Bauhofer, Röntgenographische, elektrische und spektroskopische untersuchungen an den palladiumchalkogeniden pds1-xsex/roentgenographic, electrical and spectroscopic investigations of the palladium chalcogenides $PdS_{1-x}Se_x$. *Z. Naturforsch. B* **47**, 383–388 (1992). doi: 10.1515/znb-1992-0314
63. C. Hoch, C. Röhr, Alkalimetall-stannid-silicate und -germanate: 'Doppelsalze' mit dem zintl-anion $[Sn4]^{4-}$. *Z. Anorg. Allg. Chem.* **628**, 1541–1547 (2002). doi: 10.1002/1521-3749(200207)628:7<1541::AID-ZAAC1541>3.0.CO;2-J
64. H. G. von Schnering *et al*., Refinement of the crystal structures of the tetrahedrotetrasilicides K_4Si_4, Rb_4Si_4 and Cs_4Si_4. *Z. Kristallogr., New Cryst. Struct.* **220**, 525–527 (2005). doi: 10.1524/ncrs.2005.220.4.525
65. D. Hohnke, E. Parthé, The anti-Th_3P_4 structure type for rare earth germanides, antimonides and bismuthides. *Acta Crystallogr.* **21**, 435–437 (1966). doi: 10.1107/S0365110X66003098
66. S. Furuseth *et al*., On the arsenides and antimonides of tantalum. *Acta Chem. Scand.* **19**, 95–106 (1965). doi: 10.3891/acta.chem.scand.19-0095
67. D. A. Keszler, J. A. Ibers, M. H. Mueller, Preparation, characterization, and physical properties of the series MPd_3S_4 (M = rare earth). *J. Chem. Soc. Dalton Trans.* **11**, 2369–2373 (1985). doi: 10.1039/DT9850002369
68. D. H. Killpatrick, Pressure-temperature phase diagrams for Nb_3In and Nb_3Bi. *J. Phys. Chem. Solids* **25**, 1213–1216 (1964). doi: 10.1016/0022-3697(64)90018-6
69. H. Watanabe, H. C. Po, A. Vishwanath, M. Zaletel, Filling constraints for spin-orbit coupled insulators in symmorphic and nonsymmorphic crystals. *Proc. Natl. Acad. Sci. U.S.A.* **112**, 14551–14556 (2015). doi: 10.1073/pnas.1514665112; pmid: 26604304
70. S. Coh, D. Vanderbilt, Python Tight Binding (PythTB) (2013); www.physics.rutgers.edu/pythtb

ACKNOWLEDGMENTS

The authors thank A. Alexandradinata, T. Neupert, A. Soluyanov, and A. Yazdani for helpful discussions. M.G.V. acknowledges the Fellow Gipuzkoa Program through Fondo Europeo de Desarrollo Regional Una Manera de hacer Europa and the FIS2013-48286-C2-1-P national project of the Spanish Ministerio de Economía y Competitividad. B.A.B. acknowledges the support of the Army Research Office (ARO) Multidisciplinary University Research Initiative (MURI) on topological insulators, grant W911-NF-12-1-0461, ONR-N00014-11-1-0635, NSF CAREER DMR-0952428, NSF–Materials Research Science and Engineering Center (MRSEC) DMR-1005438, the Packard Foundation. and a Keck grant. R.J.C. similarly acknowledges the support of the ARO MURI and the NSF MRSEC grants. The authors declare no competing interest.

SUPPLEMENTARY MATERIALS

www.sciencemag.org/content/353/2699/aaf5037/suppl/DC1
Supplementary text
Figs. S1 to S9
Tables S1 to S3
References (*71*–*94*)

18 February 2016; accepted 5 July 2016
Published online 21 July 2016
10.1126/science.aaf5037

REPORTS

SHAPE-MEMORY ALLOYS

Grain-resolved analysis of localized deformation in nickel-titanium wire under tensile load

P. Sedmák,[1,2] J. Pilch,[1] L. Heller,[1] J. Kopeček,[1] J. Wright,[3] P. Sedlák,[4] M. Frost,[4] P. Šittner[1]*

The stress-induced martensitic transformation in tensioned nickel-titanium shape-memory alloys proceeds by propagation of macroscopic fronts of localized deformation. We used three-dimensional synchrotron x-ray diffraction to image at micrometer-scale resolution the grain-resolved elastic strains and stresses in austenite around one such front in a prestrained nickel-titanium wire. We found that the local stresses in austenite grains are modified ahead of the nose cone–shaped buried interface where the martensitic transformation begins. Elevated shear stresses at the cone interface explain why the martensitic transformation proceeds in a localized manner. We established the crossover from stresses in individual grains to a continuum macroscopic internal stress field in the wire and rationalized the experimentally observed internal stress field and the topology of the macroscopic front by means of finite element simulations of the localized deformation.

NiTi-based shape-memory alloys (SMAs) are used in a wide variety of engineering applications (*1*), which exploit their distinctive thermomechanical functional properties related to the martensitic transformation (*2*). Theoretically, a cubic-to-monoclinic martensitic transformation in NiTi could deliver millions of mechanical or thermomechanical loading cycles at strains of several percent and stresses of hundreds of megapascals (*3*). In practice, the structural fatigue performance of NiTi (*3*–*9*) is reduced by issues related to the crystallography of martensitic transformation, specifically, the atomic-level strain incompatibility at the habit plane (*8*), inclusions (*4*), surface oxides (*5*), and insufficient resistance to dislocation slip (*6*). Recent work on microstructure manipulation, precipitation strengthening, and thin films (*7*–*9*) provides new hope for making fatigue-resistant NiTi SMAs. Despite progress, the tendency for superelastic NiTi bars, wires, tubes, and sheets to deform in a localized manner (*10*–*27*) implies macroscopic strain compatibility issues, which reduces fatigue performance under cyclic tensile loading. Because we wanted to better understand the strain localization in order to eventually suppress it, we used three-dimensional x-ray diffraction microscopy (3D-XRD) and digital image correlation (DIC) to analyze the martensite band front (MBF) propagating in a NiTi wire loaded in tension, and we simulated the localized deformation with a macroscopic SMA model implemented in finite element (FE) software.

The 3D-XRD methods (*28*–*34*) were developed over the past 15 years at synchrotron x-ray sources for the purpose of in situ grain-resolved crystallographic analysis of polycrystalline materials, enabling measurement of grain sizes, shapes, defects, phases, orientations, and internal stresses. A major difference between 3D-XRD and other strain tomography methods (*35*, *36*) is that 3D-XRD captures the full tensorial strains and stresses on a grain-by-grain basis. We show that for materials with appropriate grain sizes, the pixelated stress field determined by 3D-XRD can be homogenized to give the continuum stress field, so that for each material point, we were able to obtain the local discontinuous stress state as well as the macroscopic stress state.

Tensile deformation localized in propagating macroscopic fronts is not unique to NiTi; it has

[1]Institute of Physics, Czech Academy of Sciences, Na Slovance 1992/2, 1822 Prague, Czech Republic. [2]Faculty of Nuclear Sciences and Physical Engineering, Czech Technical University in Prague, Trojanova 13, 12000 Prague, Czech Republic. [3]European Synchrotron Radiation Facility, 71 Avenue des Martyrs, 38043 Grenoble, France. [4]Institute of Thermomechanics, Czech Academy of Sciences, Dolejškova 1402/5, 18200 Prague, Czech Republic.
*Corresponding author. Email: sittner@fzu.cz

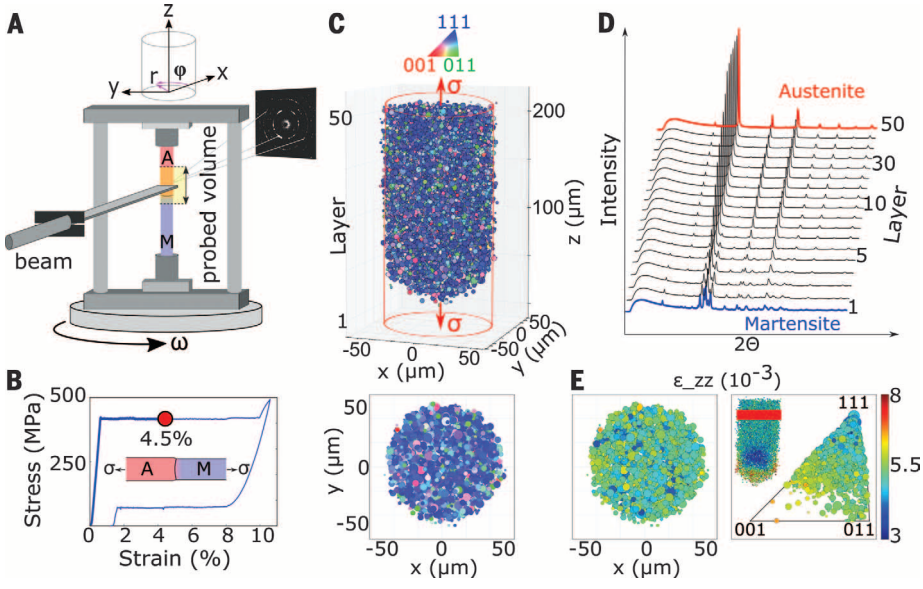

Fig. 1. In situ 3D-XRD experiment. (**A**) Polycrystalline NiTi wire was mounted onto a load frame installed on the beamline and (**B**) deformed to 4.5% strain to create a MBF in its center (*r*, radius; φ, azimuth; A, austenite; M, martensite). The prestrained wire was illuminated by a monochromatic synchrotron x-ray beam, and the diffracted beams originating from individual grains in the irradiated volume were recorded by the 2D detector while the wire was rotated around the vertical *z* axis. By moving the wire along the *z* direction and repeating the ω rotation, horizontal layers 1 to 50 in the probed volume were scanned. (**C**) The spotty diffraction patterns associated with each ω angle and *z* position were analyzed to obtain information about the position, size, orientation, and strain of the austenite crystal lattice with respect to the *z* axis for ~15,000 austenite grains in the probed volume. Elastic strain and stress tensors in all austenite grains were calculated from the grain-resolved diffraction data. (**D**) Diffraction spots from all grains in each horizontal layer were integrated into a single 1D pattern (2Θ, diffraction angle). Rietveld fit analysis of the 1D patterns provided information about lattice parameters and phase fractions within each layer. (**E**) The spatial and/or orientation dependence of selected strain or stress components in selected layers cut through the complete data set is presented using 2D diagrams in figs. S5 to S9 (*29*); an example is shown here (ε_{zz}, axial elastic strain).

long been known to engineers studying plastic flow in mild steels. In the case of NiTi, it has been described as a Lüders-like deformation and has been thoroughly studied over the past 20 years (*10*–*26*). Shaw (*10*) characterized the localized deformation of NiTi sheets experimentally and modeled it assuming a trilinear constitutive response with softening. Šittner *et al.* (*13*) explained why NiTi exhibits localized deformation in tension but other SMA materials do not, based on the crystallography of the cubic-to-monoclinic transformation, the anisotropy, and the texture of NiTi. Iadicola and Shaw (*14*) described the roles of strain rate and heat exchange between the transforming sample and the surrounding environment and simulated internal stresses associated with the propagating MBF in a wire. In contrast to sheets or wires, MBFs in NiTi tubes tend to form helical bands in tension but deform homogeneously in combined tension-torsion (*15*, *16*). Detailed information on the macroscopic appearance and kinetics of the localized deformation has been obtained from in situ infrared camera observations of the latent heat generated and absorbed by the phase transformation within the propagating MBFs (*14*, *18*, *22*) and, later, by digital image correlation (DIC) analysis of the surface strains (*19*–*23*). Last, the recent implementation of the DIC method inside the scanning electron microscope (SEM-DIC), combined with electron back-scattered diffraction (EBSD) (*24*, *25*), has revealed details of the strain localization on the level of individual grains. Because most of the experimental methods rely on surface observations, in spite of a large number of publications, uncertainties persist concerning the topology of MBFs within the bulk of NiTi wires. Looking at a wire surface, the MBF appears to be broad and perpendicular to the wire axis (*20*), whereas in sheets (*10*), the MBFs are typically planar, sharp, and inclined ~55° to the loading axis. The inclination angle of 55° minimizes the strain incompatibility at the macroscopic interface (*17*) between the elastically strained austenite (~1%) and the already transformed martensite band (~10%).

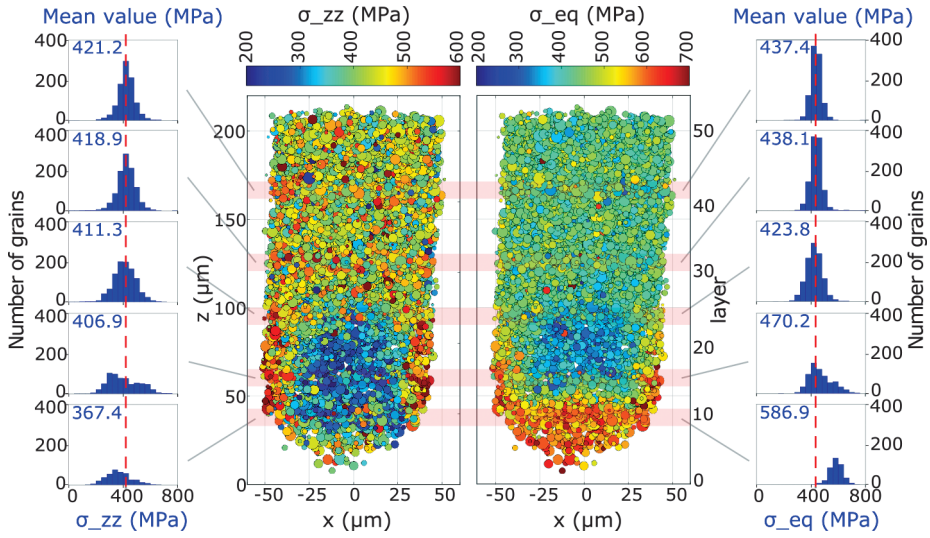

Fig. 2. Grain-resolved internal stresses in austenite, evaluated by the 3D-XRD method. The two central panels show the axial stress component σ_{zz} and the von Mises equivalent stress σ_{eq} in grains in a 20-μm vertical layer cut through the complete data set; detailed information is presented in figs. S6 to S11 (*29*). The histograms show the results of the statistical analyses for the denoted horizontal layers (10-μm discs); means are noted in blue and indicated with red dashed lines.

Our 3D-XRD experiment was performed on electropulse-treated NiTi wire (Fort Wayne Metals #1; Ti with 50.8 atomic % Ni; diameter, 0.1 mm). Commercial superelastic NiTi wires have a nanograined partially recrystallized microstructure that yields continuous Debye-Scherrer rings on the 2D detector. To resolve diffraction spots from individual grains and apply the 3D-XRD method to measure strain tensors, we needed a wire with fewer grains in the cross section (fig. S3) (*29*). This was achieved with an electropulse-treated wire (*29*) with an austenite grain size of 5.9 μm, equiaxed grains, and a <111> drawing texture (fig. S4A) (*29*). Although the tensile stress-strain response of the electropulsed wire was different from that of a straight annealed wire, it still showed localized superelasticity through nucleation and propagation of MBFs (fig. S1B) (*29*). The wire was prestrained in the load frame to create the MBF, and the 3D-XRD experiment was performed and analyzed as shown in Fig. 1. The key experimental result is the data on the spatial distribution of strains and stresses in ~15,000 austenite grains in a 200-μm-long segment of the tensioned wire (Fig. 2 and figs. S5 to S11) (*29*). The complete 3D-XRD data set gives for each austenite grain in this segment its center-of-mass position, size, austenite lattice orientation, and six independent components of the elastic strain tensor, from which we computed the stress tensor (*29*). We observed a buried macroscopic interface separating the pristine austenite from the martensite band. The interface was not flat but had the shape of a nose cone pointing toward the martensite band (Fig. 2). The inclination of the cone surface to the *z* axis was ~55°, the same inclination angle as observed for planar MBFs in tensioned NiTi sheets (*10*, *17*, *23*) or tubes (*15*, *19*, *22*).

The elastic strains and stresses in individual grains of the tensioned polycrystal varied from grain to grain in real space, as well as in orientation space, without correlations between grain position, size, and orientation (fig. S4D) (*29*). Although gradients of internal stress surely exist within the grains, these were not resolved by our experiment. The grain-resolved strains and stresses were obtained by diffraction averaging of the lattice spacings within the elastically strained grains. Although the local stress states in grains were multiaxial, statistical analysis (*29*) revealed that a homogenized macroscopic internal stress state far from the front was uniaxially tensile; the mean axial stress component σ_{zz} = 424 MPa corresponded to the applied tensile stress of 420 MPa, and other stress components were close to zero (fig. S5B) (*29*). We determined a certain minimum constitutive volume (~3000 μm^3 or ~45 grains for the microstructure of our wire) for which the macroscopic stress tensor could be meaningfully defined (*29*).

The internal stress states of grains changed substantially within the MBF (Fig. 2 and figs. S6 to S10) (*29*). Because the conditions for the onset of martensitic transformation in grains cannot be estimated from single stress components, we calculated the principal strains and stresses (fig. S9) (*29*) and then used the von Mises equivalent stress σ_{eq} (Fig. 2) or maximum shear stress (fig. S10) (*29*) to estimate the level of shear stress that triggered the martensitic transformation in grains. The tensile principal strain ε_1 remained aligned with the wire axis in all grains, except those on the cone interface, where deviations up to 25° from the loading direction (figs. S9 and S10) (*29*) were observed. As the tensile principal stress σ_1 decreased and the principal stresses σ_2 and σ_3 became compressive ahead of the cone, the hydrostatic stress changed from tensile to compressive and maximum shear stresses increased in the grains within the MBF (figs. S9 and S10) (*29*). The tensor imaging visualization of stress states in austenite grains in fig. S10 (*29*) offers compact information on the sharp spatial variation of grain-resolved stress states and maximum shear stresses. The density of spheres (grains) at the cone interface is diluted because the partially transformed grains at the interface were not resolved. The persisting grains that were just about to transform exhibited the largest equivalent strains and equivalent stresses of the whole data set (figs. S7 to S11) (*29*).

Using the lattice parameters of B2 austenite (a = 3.015 Å) and B19′ martensite (a = 2.883Å, b = 4.166 Å, c = 4.633 Å, γ = 96.5°), the orientation of

the parent austenite lattice, and the stress state in each grain, we estimated the most energetically favorable microstructure of martensite, which starts to form in grains on the cone interface, and calculated the resolved shear stress that initiates its nucleation. Applying the nonlinear theory of martensitic transformations specified for the particular case of cubic (B2)–to–monoclinic (B19′) martensitic transformation (*29*, *37*–*41*), we calculated all martensitic microstructures that have a compatible habit plane with austenite (the solution was 192 martensitic laminates formed of two lattice correspondence variants in a twin configuration, so-called habit plane variants or HPVs). We determined the maximum resolved shear stresses over all possible HPVs in each grain (fig. S11). The obtained distribution qualitatively agrees with that of the von Mises equivalent stress σ_{eq} (Fig. 2) and maximum shear stress (fig. S10) (*29*). Because the stress states in grains on the cone interface are very different from uniaxial tension (fig. S10) (*29*), the predicted HPVs and transformation strains are different from those that would be predicted for uniaxial tensile stresses in grains. The martensite-variant microstructures and strains in grains within the martensitic band are thus likely to be different from what is commonly assumed in the literature (*13*, *24*, *25*, *27*).

The gradual change in stress states in austenite grains as they enter the propagating MBF (fig. S10) (*29*) plays key role in the localized deformation. The applied stress of 420 MPa under which the MBF propagated in the tensile test (Fig. 1B) is far below the mean equivalent stress of 587 MPa in grains at the cone interface (Fig. 2). The martensitic transformation is thus preferentially triggered by the elevated shear stresses in grains on the cone interface. It is only because of this gradual change in stress states that the resolved shear stresses in HPV transformation systems in all grains on the cone interface (fig. S10) (*29*) simultaneously approached the critical resolved shear stresses, regardless of grain orientation, and thus that those grains transformed collectively at constant applied force. This mesoscopic coordination is necessary for the macroscopic interface to propagate through the grain microstructure of the wire. The elevated equivalent stress in transforming grains also explains why dislocation slip couples with the martensitic transformation at applied stress levels that are much lower than the yield stress for the dislocation slip in NiTi (*6*).

Because the redistribution of local stresses in grains within the MBF has a macroscopic origin, we need to understand the macroscopic internal stress field in the wire. We homogenized and interpolated the grain-resolved stresses (*29*) to evaluate it experimentally (Fig. 3A). In addition, we simulated the localized deformation of the wire by using the continuum-based macroscopic SMA model (*42*) implemented in FE software (*29*). The constitutive strain-softening response in tension adopted in the model (red curve in fig. S12) (*29*) is essential for capturing the strain localization phenomenon in the FE simulation (*14*). As a result of the softening, the material deformation is not homogeneous, but a front of localized transformation forms and moves along the wire at constant tensile force, giving rise to the simulated macroscopic force-elongation curve (blue curve in fig. S12) (*29*), which is similar to the curve that we measured experimentally (fig. S1B). The FE simulation predicted heterogeneous internal stress, axial elastic strain, and phase fraction fields within the MBF (Fig. 3B), in reasonable agreement with the corresponding fields obtained from the 3D-XRD experiment (Fig. 3A). We suspect that similar internal stress gradients may exist during propagation of true Lüders bands in tensioned round bars of mild steel or even at the onset of necking during tensile deformation of a ductile wire, although dedicated experiments are still needed to confirm this supposition.

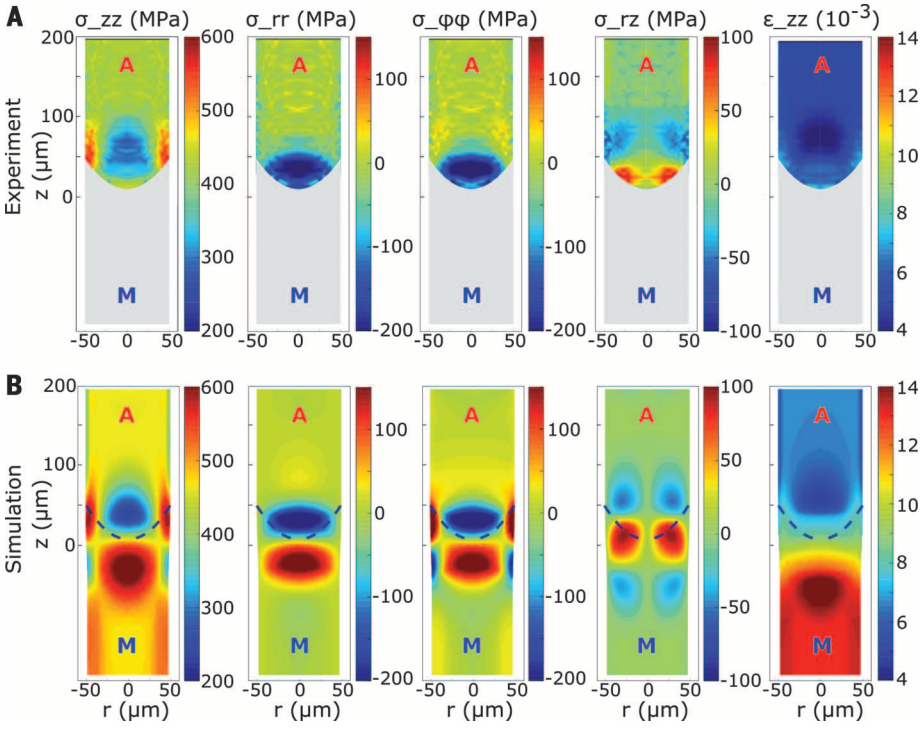

Fig. 3. Comparison of the experimentally determined and FE-simulated macroscopic internal stress field and axial elastic strain in tensioned NiTi wire. (**A**) Experimental results and (**B**) simulation results, shown in cylindrical coordinates (axial stress, σ_{zz}; radial stress, σ_{rr}; hoop stress, $\sigma_{\varphi\varphi}$; shear stress, σ_{rz}; axial elastic strain, ε_{zz}). Two plots are stitched in mirror symmetry to create a wire-like image of the fields. The experimentally determined macroscopic elastic strain and stress fields were obtained by homogenization and interpolation of grain-resolved stresses (*29*). The experimentally determined macroscopic nose-cone-shaped interface (dashed line) was inserted into the plots of the simulation results at the proper location to facilitate comparison.

The MBF in a wire is a complex object (Fig. 4) consisting of a nose cone–shaped macroscopic interface surrounded by gradients in stress, strain, and phase fraction that move collectively toward the pristine austenite under constant external force during the tensile superelastic deformation. The key feature is the macroscopic internal stress field (σ_{eq} in Fig. 4), which raised the shear stress in all grains on the cone interface to critical values (Fig. 2 and fig. S11) so that they started to transform in a highly coordinated manner. Because the 3D-XRD experiment only provided data for the austenite and the DIC experiment only for the total strain field on the surface (*29*), without the FE simulation, we would not know how the stresses, strains, and phase fractions associated with the propagating MBF are distributed below the cone toward the martensite band (Figs. 3B and 4). The model predictions for the martensite band (Fig. 3B) remain to be verified by future experiments.

Based on the available experimental evidence and the FE simulation, we conclude that there is a phase fraction gradient below the cone interface (Fig. 4) that is wider than the sharp interfaces observed in thin NiTi sheets (*24*). The sharp interface inclined 55° to the load axis in sheets can fulfill the strain compatibility condition without any considerable additional elastic deformation. In other words, under the assumption of volume conservation, the grains lying along a 55°-inclined macroscopic interface in a sheet may deform to large tensile strains, with minimum constraints exerted by the adjoining portion of the elastically strained austenite. The situation is different in bulk 3D objects such as wires and square bars, where such a strain-compatible sharp macroscopic interface cannot form because of the macroscopic constraints. As a result, the cone interface in a wire is also inclined ~55° to the load axis, but wider gradients of phase fraction, strain, and stress are necessary to maintain the

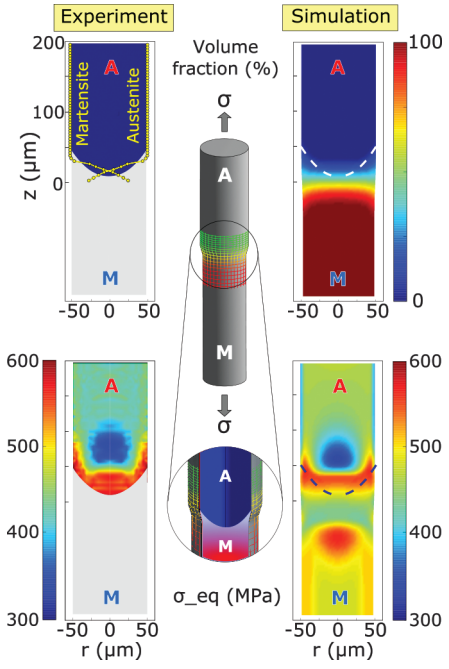

Fig. 4. The MBF propagates as a rigid macroscopic object in tensioned NiTi wire at constant force. Key features include (i) strain gradients observable by DIC on the wire surface (*29*), (ii) the buried nose cone–shaped interface, (iii) phase fraction gradients, and (iv) the internal stress field revealed by the 3D-XRD experiment and FE simulation with the SMA model.

macroscopic strain compatibility at the cone interface (*29*). On the basis of this and supplementary experiments with cyclic deformation (fig. S13) (*29*), we conclude that the strain localization causes degradation of the tensile fatigue performance of superelastic NiTi wires because it promotes accumulation of the surface damage.

Our analysis of the localized deformation of NiTi wire in tension through the combination of 3D-XRD stress tomography, DIC evaluation of total strains on the wire surface (*29*), and FE simulation of internal stress gradients offers new insights into the mechanics of localized deformation of NiTi, even though this subject has been widely studied. This progress is mainly due to the 3D-XRD results: In the context of conventional strain tomography methods for mapping bulk internal stresses in polycrystals (*35, 36*), we have shown that the application of the 3D-XRD method in the configuration described here (a large number of small grains) enables the evaluation of internal strain and stress tensor fields (*29*) in bulk polycrystalline engineering materials, with exceptionally high resolution in position (~1 μm), strain (~1×10^{-4}), and stress (~20 MPa). Both conventional methods and 3D-XRD evaluate the crystal lattice strain to calculate stresses, but the macroscopic internal stress field is derived differently. Conventional methods need many grains in the gauge volume where the stress state is being determined so that a suitably oriented lattice diffracts in the right direction (i.e., a subset of suitably oriented grains in the volume). In contrast, with the 3D-XRD method, full tensorial stress states are determined for all grains, and these are post-homogenized to evaluate the macroscopic internal stress field. The grains thus serve as oriented voxels for the 3D-XRD stress tomography method, and the spatial resolution depends on the grain size. In this way, the usual limitations for conventional strain tomography with high-energy x-rays, in which poor spatial resolution along the pencil beam direction and artifacts at free surfaces or buried interfaces complicate the evaluation of internal stress fields, can be avoided. A key advantage of the 3D-XRD approach is that the grain-resolved stress states are directly calculated from lattice strains by using well-defined anisotropic elastic constants. In contrast, conventional methods need at least three different measurement orientations for the same gauge volume (*43*), which creates problems for sample rotations and scanning; preserving the size and shape of the gauge volume and selecting reflections and elastic constants for an anisotropic textured polycrystalline aggregate is not straightforward either. It is thus a challenging task (*36, 43*) to derive a macroscopic internal stress tensor field that is not in contradiction with continuum deformation. We have shown that these problems are overcome by 3D-XRD if grains are large enough to measure spotty 2D diffraction patterns but small enough to achieve high spatial resolution. Thanks to recent advances in 3D-XRD data analysis, the method is now ready to tackle a wide range of unsolved problems associated with sharp gradients of microstructure, phase composition, and/or stress in engineering materials, for which only theoretical predictions are available (e.g., internal stresses in necking, welding, surface processing, and layered structures).

REFERENCES AND NOTES

1. J. Mohd Jani, L. Leary, A. Subic, M. A. Gibson, *Mater. Des.* **56**, 1078–1113 (2014).
2. K. Otsuka, X. Ren, *Prog. Mater. Sci.* **50**, 511–678 (2005).
3. S. W. Robertson, A. R. Pelton, R. O. Ritchie, *Int. Mater. Rev.* **57**, 1–37 (2012).
4. S. W. Robertson *et al.*, *J. Mech. Behav. Biomed. Mater.* **51**, 119–131 (2015).
5. J. Racek *et al.*, *Shape Mem. Superelasticity* **1**, 204–230 (2015).
6. P. Sedmák, P. Šittner, J. Pilch, C. Curfs, *Acta Mater.* **94**, 257–270 (2015).
7. C. Chluba *et al.*, *Science* **348**, 1004–1007 (2015).
8. R. D. James, *Science* **348**, 968–969 (2015).
9. D. Dye, *Nat. Mater.* **14**, 760–761 (2015).
10. J. A. Shaw, *Int. J. Plast.* **16**, 541–562 (2000).
11. Y. Liu, Y. Liu, J. Van Humbeeck, *Acta Mater.* **47**, 199–209 (1998).
12. G. Tan, Y. Liu, P. Sittner, M. Saunders, *Scr. Mater.* **50**, 193–198 (2004).
13. P. Šittner, Y. Liu, V. Novak, *J. Mech. Phys. Solids* **53**, 1719–1746 (2005).
14. M. A. Iadicola, J. A. Shaw, *Int. J. Plast.* **20**, 577–605 (2004).
15. Q. P. Sun, Z. Q. Li, *Int. J. Solids Struct.* **39**, 3797–3809 (2002).
16. L. Dong, Q. P. Sun, *Int. J. Solids Struct.* **49**, 1063–1076 (2012).
17. L. Dong, R. H. Zhou, X. L. Wang, G. K. Hu, Q. P. Sun, *Int. J. Solids Struct.* **80**, 445–455 (2016).
18. E. A. Pieczyska, S. P. Gadaj, W. K. Nowacki, H. Tobushi, *Exp. Mech.* **46**, 531–542 (2006).
19. B. J. Reedlunn, Ch. B. Churchill, E. E. Nelson, J. A. Shaw, S. H. Daly, *J. Mech. Phys. Solids* **63**, 506–537 (2014).
20. C. Elibol, M. F. X. Wagner, *Mater. Sci. Eng. A* **621**, 76–81 (2015).
21. N. J. Bechle, S. Kyriakides, *Int. J. Solids Struct.* **51**, 967–980 (2014).
22. D. Favier *et al.*, *Acta Mater.* **55**, 5310–5322 (2007).
23. Y. Xiao, P. Zeng, L. Lei, *Smart Mater. Struct.* **25**, 017002 (2016).
24. M. Kimiecik, J. W. Jones, S. Daly, *Mater. Lett.* **95**, 25–29 (2013).
25. M. Kimiecik, J. Wayne Jones, S. Daly, *Acta Mater.* **94**, 214–223 (2015).
26. S. C. Mao *et al.*, *Acta Mater.* **58**, 3357–3366 (2010).
27. Y. Liu, *Acta Mater.* **95**, 411–427 (2015).
28. H. F. Poulsen, *Three-Dimensional X-Ray Diffraction Microscopy: Mapping Polycrystals and Their Dynamics* (Springer, 2004).
29. Materials and methods are available as supplementary materials on *Science* Online.
30. J. Oddershede *et al.*, *J. Appl. Cryst.* **43**, 539–549 (2010).
31. J. Oddershede *et al.*, *Mater. Charact.* **62**, 651–660 (2011).
32. B. Jakobsen *et al.*, *Science* **312**, 889–892 (2006).
33. S. E. Offerman *et al.*, *Nucl. Instrum. Methods Phys. Res. B* **246**, 194–200 (2006).
34. E. Jimenez-Melero *et al.*, *Acta Mater.* **55**, 6713–6723 (2007).
35. W. R. B. Lionheart, P. J. Withers, *Inverse Probl.* **31**, 045005 (2015).
36. M. Korsunsky *et al.*, *Acta Mater.* **54**, 2101–2108 (2006).
37. K. F. Hane, T. W. Shield, *Acta Mater.* **47**, 2603–2617 (1999).
38. J. M. Ball, R. D. James, *Z. Angew. Math. Mech.* **76**, 389–392 (1996).
39. A. G. Khachaturyan, *Theory of Structural Transformations in Solids* (Wiley, 1983).
40. K. Bhattacharya, *Microstructure of Martensite* (Oxford Univ. Press, 2003).
41. M. S. Wechsler, D. S. Lieberman, T. A. Read, *Trans. AIME J. Metals* **197**, 1503–1515 (1953).
42. P. Sedlák, M. Frost, B. Benešová, T. Ben Zineb, P. Šittner, *Int. J. Plast.* **39**, 132–151 (2012).
43. B. Malard *et al.*, *Acta Mater.* **60**, 1378–1394 (2012).

ACKNOWLEDGMENTS

We acknowledge support from the Czech Science Foundation (research projects P107/12/0800, P108/12/P111, and GA14-15264S) and the Czech Technical University Student Grant Competition (SGS16/249/OHK4/3T/14). We thank the European Synchrotron Radiation Facility for the provision of synchrotron beam time and a Ph.D. grant to P. Sedmák; the Ministry of Education, Youth and Sports of the Czech Republic for the support of the SAFMAT (Centre for Analysis of Functional Materials) project LM2015088 and European Spallation Source project LM2015048; the company TESCAN (J. Dluhoš) for assistance with the 3D EBSD analysis; and L. Kadeřávek for assistance with graphical works. Data and additional visualization tools are available at http://ofm.fzu.cz/localized%20deformation%20of%20NiTi%20in%20tension.

SUPPLEMENTARY MATERIALS

www.sciencemag.org/content/353/6299/559/suppl/DC1
Materials and Methods
Supplementary Text
Figs. S1 to S13
References (*44–62*)
Movies S1 to S5

10 November 2015; accepted 14 July 2016
10.1126/science.aad6700

CATALYSIS

Direct conversion of methane to aromatics in a catalytic co-ionic membrane reactor

S. H. Morejudo,[1,2] R. Zanón,[3] S. Escolástico,[3] I. Yuste-Tirados,[1] H. Malerød-Fjeld,[1] P. K. Vestre,[1] W. G. Coors,[1] A. Martínez,[3] T. Norby,[2] J. M. Serra,[3]* C. Kjølseth[1]*

Nonoxidative methane dehydroaromatization (MDA: $6CH_4 \leftrightarrow C_6H_6 + 9H_2$) using shape-selective Mo/zeolite catalysts is a key technology for exploitation of stranded natural gas reserves by direct conversion into transportable liquids. However, this reaction faces two major issues: The one-pass conversion is limited by thermodynamics, and the catalyst deactivates quickly through kinetically favored formation of coke. We show that integration of an electrochemical $BaZrO_3$-based membrane exhibiting both proton and oxide ion conductivity into an MDA reactor gives rise to high aromatic yields and improved catalyst stability. These effects originate from the simultaneous extraction of hydrogen and distributed injection of oxide ions along the reactor length. Further, we demonstrate that the electrochemical co-ionic membrane reactor enables high carbon efficiencies (up to 80%) that improve the technoeconomic process viability.

Natural gas constitutes a large and relatively clean fraction of fossil hydrocarbon resources, but the high capital cost of multistage industrial conversion via synthesis gas (i.e., syngas, a mixture of H_2 and CO) leaves much of it stranded. Nonoxidative methane (CH_4) dehydroaromatization (MDA) is a promising catalytic route that directly converts natural gas into valued petrochemicals such as benzene. The MDA reaction is conventionally run at ~700°C in the presence of bifunctional catalysts comprising carbided molybdenum nanoclusters dispersed in acidic shape-selective zeolites such as ZSM-5 and MCM-22 (*1*). The process suffers from two major hurdles that challenge its further development and industrial implementation: The per-pass conversion is limited by thermodynamics, and the catalyst activity rapidly drops with time on stream because of the accumulation of polyaromatic-type coke on the external zeolite surface that impedes the access to internal active sites (*2*, *3*).

Attempts to overcome thermodynamic limitations by selective removal of the coproduct H_2 from the reactor using, for instance, Pd-type (*4*) or ceramic ($La_{5.5}W_{0.6}Mo_{0.4}O_{11.25-\delta}$) (*5*) membranes were limited by enhanced coke formation that accelerated catalyst decay. Strategies based on fine-tuning the zeolite acidity and porosity and cofeeding small amounts of CO_2, CO, H_2, and H_2O with CH_4 were applied to stabilize the catalyst by restraining the production of coke, but with limited success (*2*, *6*, *7*).

Recently, a direct nonoxidative CH_4 conversion path on single-iron sites embedded in a silica matrix with negligible coke formation and high stability has been reported (*8*). However, this reaction requires very harsh conditions (950°C) and produces ethylene (rather than liquids) as the major product, with selectivity of ~55%.

Here we present an approach to circumvent the current limitations of the MDA reaction by integrating an ion-conducting membrane into the reactor. We report an innovative catalytic membrane reactor (CMR) for intensification of the MDA process that resulted in high and prolonged aromatic yields. In addition, a high-purity H_2 stream is produced during CMR operation. The CMR is driven by a tailored co-ionic membrane that enables fast and accurate simultaneous control of H_2 extraction and injection of oxygen species along the catalyst bed (Fig. 1A). The concerted action of both functions leads to marked gains in aromatics yield and catalyst stability and, consequently, in the viability of MDA technology.

The electrolyte of the membrane is based on acceptor-doped $BaZrO_3$, which takes up protons from steam and exhibits high proton (H^+) and minor oxide ion (O^{2-}) conductivity at elevated temperatures (*9*). Applications of protonic conductivity have shown promising results (*10*–*12*), but, as shown here, the co-ionic transport property of the material—more specifically, the conduction

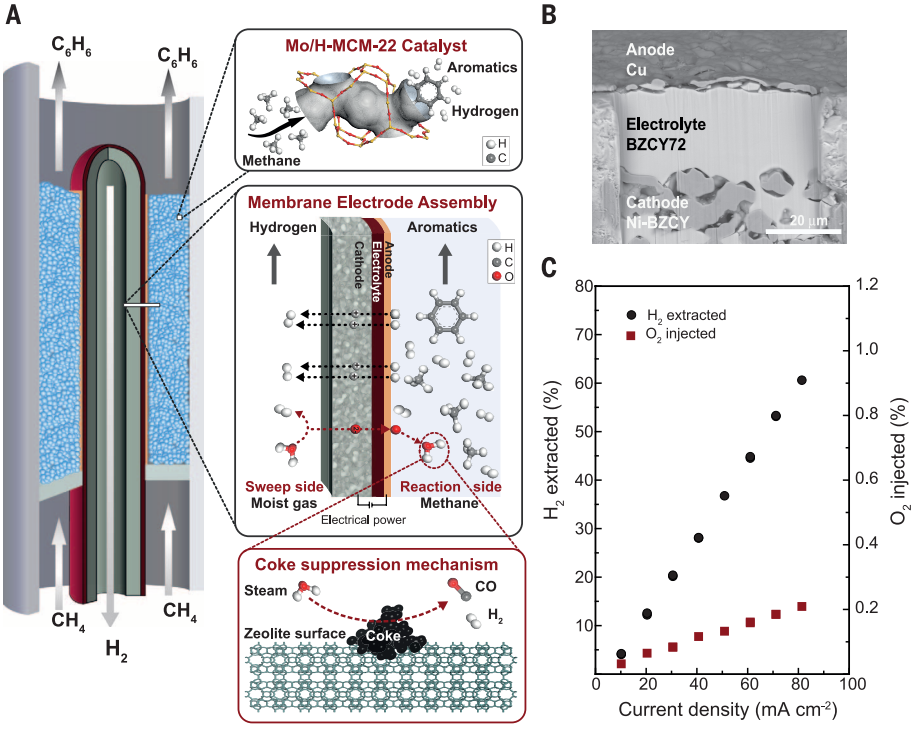

Fig. 1. Current-controlled co-ionic membrane reactor. (**A**) CH_4 is converted to benzene and hydrogen via a Mo/zeolite catalyst. H_2 is transported as protons to the sweep side. Oxide ions are transported to the reaction medium to react with H_2 and form steam as an intermediate before reacting with coke to form CO and H_2. (**B**) Scanning electron microscopy image of the membrane electrode assembly (focused ion beam section). Cathode porosity formed upon reduction of NiO can be observed beneath the dense electrolyte. (**C**) Percentage of H_2 extracted and O_2 injected versus current density at 700°C. The anode is swept with a 10/90 mixture of H_2/CH_4 and the cathode with a 3/5/92 mixture of $H_2O/H_2/Ar$.

ratio of protons and oxide ions—allowed the successful implementation into the MDA process. The tubular membrane consists of a dense 25-μm-thick $BaZr_{0.7}Ce_{0.2}Y_{0.1}O_{3-\delta}$ (BZCY72) electrolyte film on a porous BZCY72-Ni support, which also acted as a cathode (*11*). The metallic Ni had sufficient catalytic activity for H_2 evolution and reduction of steam (Fig. 1B). A Cu-based anode was applied on the electrolyte film facing the catalyst; it activates the electrochemical oxidation of H_2 into protons while preventing secondary conversion of hydrocarbons into coke, as typically reported for Ni- or Pt-based electrodes (*13*). As the current density was increased, both hydrogen extraction and oxygen injection increased proportionally, so that the amount of O_2 injected was ~0.3% that of extracted H_2 (Fig. 1C).

Figure 2 shows the results of MDA experiments, comparing our CMR with a fixed-bed reactor (FBR) under otherwise similar conditions using 6Mo/MCM-22 as a catalyst. The catalyst behavior in the FBR is fully representative of the state of the art at standard MDA conditions: The aromatics yield initially increased during the induction period, reached a maximum of ~10%, and rapidly fell as the reaction progressed. In contrast, by applying an electrical current to the CMR ("on" mode), the aromatics yield continued to increase beyond the induction period and attained a maximum of ~12%, after which the catalyst activity started to decline (Fig. 2A). An almost-instant catalytic response (for conversion, see fig. S2) (*14*) to on-off switching, as well as to changes in the intensity of the imposed electrical current, allowed us to accurately tune the catalytic performance of our CMR system. Interestingly, the yield enhancement observed upon current application occurred while maintaining the characteristic high selectivity to aromatics [particularly to benzene, >85% on a coke-free basis (Fig. 2B)] of the shape-selective 6Mo/MCM-22 catalyst. However, CMR operation produced some CO, albeit in relatively low selectivity (see below). The most notable result in Fig. 2A is the improved stability of the catalyst in the CMR, with an average decay rate about one order of magnitude lower than that observed in the conventional FBR. Although the aromatics yield decreased to ~1.5% in the FBR after 45 hours of reaction, it remained as high as ~9% in the CMR, translating into a twofold increase in the cumulative yield (Fig. 2C). The high stability exhibited by the catalyst in the CMR arose from a decreased tendency to form coke, which became more evident at longer reaction times (Fig. 2C).

Thermodynamic calculations predict that in situ H_2 extraction increases CH_4 conversion and shifts selectivity toward heavier aromatics (and, ultimately, coke) at the cost of benzene and C_2 hydrocarbons (fig. S3) (*14*), as experimentally demonstrated with H_2 permselective membranes (*15*, *16*). Although thermodynamics thus accounts for the increase in CH_4 conversion, the high benzene selectivity and improved catalyst stability during the galvanic operation in our CMR cannot be anticipated by considering merely those effects related to H_2 extraction.

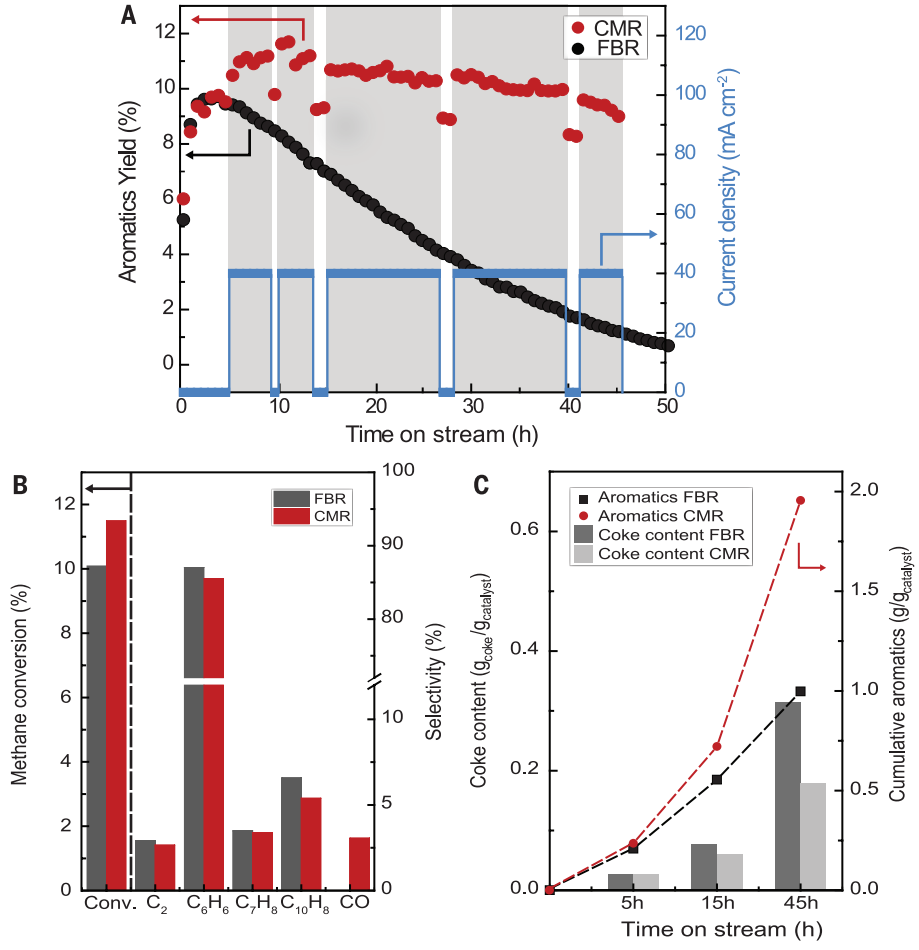

Fig. 2. FBR and co-ionic CMR performance in MDA using a 6Mo/MCM-22 catalyst. (**A**) Aromatics yield versus time. Gray-shaded areas indicate when hydrogen is extracted. (**B**) CH_4 conversion and selectivity to main products after 5 hours (FBR) and 9 hours (CMR). (**C**) Coke deposition in 6Mo/MCM-22 and cumulative aromatics production in grams per gram of catalyst. Reaction conditions: 710°C, 1500 ml g^{-1} $hour^{-1}$, 1 bar, and current density of 40 mA cm^{-2}.

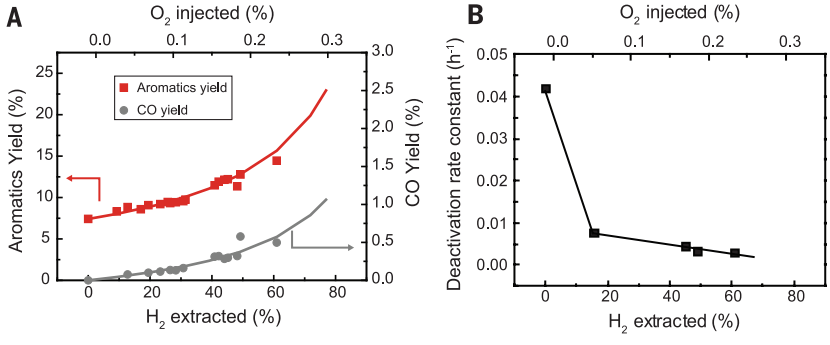

Fig. 3. Effect of co-ionic membrane reactor. (**A**) Aromatics and CO yield as a function of H_2 extracted and O_2 injected at 700°C and 1 bar. (**B**) Deactivation rate constant, assuming first-order catalyst decay, as a function of H_2 extracted and O_2 injected.

[1]CoorsTek Membrane Sciences, Forskningsparken, Gaustadalléen 21, NO-0349 Oslo, Norway. [2]Department of Chemistry, University of Oslo, FERMiO, Gaustadalléen 21, NO-0349 Oslo, Norway. [3]Instituto de Tecnología Química, Universitat Politècnica de València–Consejo Superior de Investigaciones Científicas, Avenida de los Naranjos, s/n 46022 Valencia, Spain.
***Corresponding author. Email: jmserra@itq.upv.es (J.M.S.); ckjolseth@coorstek.com (C.K.)**

The BZCY72 membrane enables the concomitant transport of oxide ions toward the reaction medium, where they rapidly oxidize the produced H_2 to steam at the electrode (*17*). Thus, we investigated the isolated effect of steam on the performance of the 6Mo/MCM-22 catalyst in the FBR by cofeeding 0.25 to 0.9 mole % steam together with CH_4, corresponding to steam concentrations within the range achieved by the O_2 injection in our CMR. Whereas the observed decrease in both conversion and aromatics selectivity (fig. S4) (*14*) is thermodynamically consistent (*18*), postreaction characterization of the spent catalysts by thermogravimetry and temperature-programmed oxidation analyses showed that the improved stability achieved in the CMR could be ascribed to the inhibition of coke formation by the in situ–generated steam (fig. S5) (*14*). The steam-promoted coke suppression during MDA has also been reported for oxygen-permeable membrane reactors (*19*) and probably occurs by a mechanism that involves scavenging of reactive carbon from the catalyst surface via steam reforming (*20*), which accounts for the observed formation of CO (Fig. 2B). The superior stability achieved in our CMR compared with the FBR experiment with an equivalent steam concentration (0.25 mole %) indicates that the controlled and distributed oxygen injection is more effective in improving the catalyst stability than the external addition of steam.

Additionally, the x-ray absorption near-edge structure analysis at the Mo K-edge and x-ray photoelectron spectroscopy Mo 3d spectral signals (fig. S5) (*14*) did not reveal appreciable changes in Mo speciation during CMR operation, with respect to the FBR fed with pure CH_4. Conversely, a higher average Mo oxidation state is inferred for the catalyst used in the FBR experiment cofed with 0.9 mole % steam, which might imply a certain loss of active molybdenum carbide species by reoxidation (*20*). The crystalline structure of the zeolite host remained almost intact upon contact with the in situ–generated steam under MDA conditions (fig. S5) (*14*). Thus, the distributed O_2 injection allowed by the BZCY72 membrane effectively suppressed coke production while preserving the structural integrity of the zeolite and active Mo-carbide sites.

In situ extraction of H_2 with the CMR should shift the equilibrium of aromatics formation, which would have major consequences for process industrialization. In Fig. 3A, the experimentally obtained yield of aromatics is plotted as a function of the magnitude of both H_2 extracted and equivalent O_2 injected. High H_2 extraction rates (>60%) with respect to the H_2 produced in the MDA reaction were achieved by using the electrochemical cell reactor. By increasing the magnitude of the imposed co-ionic current, the aromatic yield rose and surpassed the theoretical equilibrium yield (12.3%) at H_2 extraction rates exceeding 50%. As expected from the coke-suppression mechanism operating in the CMR, CO formation was negligible when no current was imposed and rose parallel to the aromatics yield with increasing co-ionic currents (Fig. 3A). These results show that the galvanic current drove the transport of atomic oxide ions. This oxide ion supplies reduced coke production and decreased the catalyst degradation rate by a factor of 6 with respect to the FBR, even at low extraction rates (18%), and then continued to decrease smoothly at higher currents (Fig. 3B).

To assess the practical implications of the described CMR, we performed process simulations using Aspen tools (*21*). Figure 4A schematizes a complete gas-to-liquid process based on our MDA reactor architecture and includes recycling of the reactant CH_4 stream. In this process, the critical parameter for maximizing the per-pass conversion is the H_2 concentration in the recycle loop. By including a methanation stage, CO and H_2 are converted to CH_4 and steam, generating a typical H_2 concentration of 5% at the reactor inlet (fig. S7) (*14*). Experimental CMR results under recycle operating conditions (5% H_2 cofeed) resulted in aromatics yields of about 6.5%, with near-zero degradation rates (Fig. 4B). In Fig. 4C, the process performance metrics for different extraction rates (50 to 80%) are compared with (i) a plant based on a conventional MDA reactor, implementing downstream gas fractioning with polymeric membranes (FBR-PolyM) (*22*), and (ii) a plant based on a CMR with Pd membranes (Pd-CMR) (*4*). Carbon efficiency is superior for our CMR system, improving steeply with increasing extraction rates. At rates exceeding 80%, the carbon efficiency is similar to that exhibited by large and optimized Fischer-Tropsch (FT) plants (*23*). The difference between both processes relies on plant size and complexity. Although the traditional FT process requires multiple steps, including syngas production, the MDA co-ionic CMR produces aromatics directly. This feature allows for modularity and flexibility to adapt to the size of the natural gas field, in contrast to FT plants that become uneconomic at small to medium scales (1 to 10 metric tons hour^{-1}).

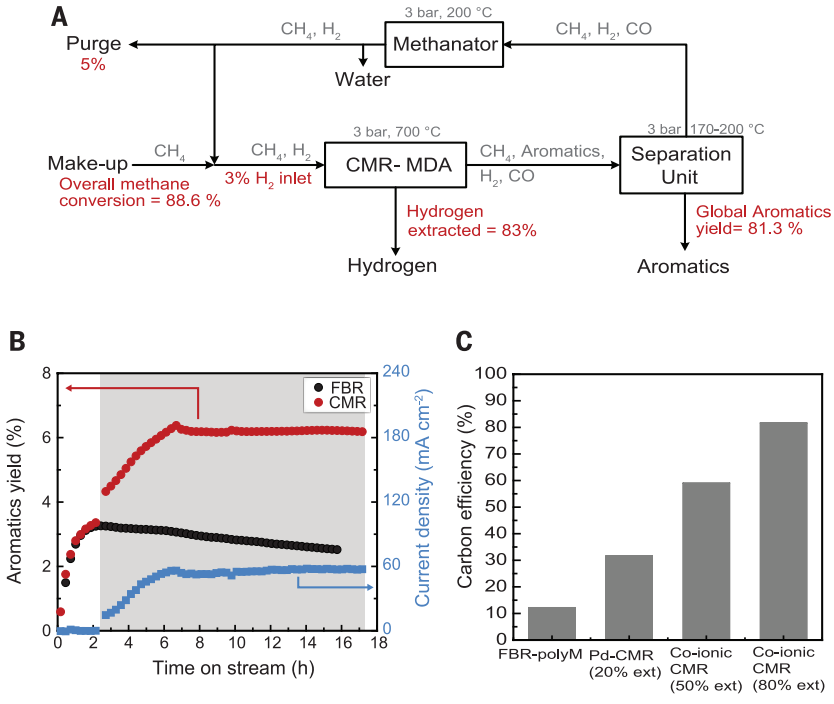

Fig. 4. Synloop process for MDA using co-ionic CMR. (**A**) Process flow diagram. (**B**) Aromatics yield versus time on stream at the following conditions: 700°C, 3000 ml g^{-1} hour^{-1}, 3 bar, and 5% H_2 cofeeding. The gray-shaded area indicates when H_2 is extracted. (**C**) Carbon efficiency of a synloop process using co-ionic CMR for different H_2 extractions (50 to 80%) compared with plants based on Pd-CMR (*4*) and FBR with external H_2 removal (polymer membrane) (*20*).

REFERENCES AND NOTES

1. J. Gao *et al.*, *Science* **348**, 686–690 (2015).
2. Y. Xu, X. Bao, L. Lin, *J. Catal.* **216**, 386–395 (2003).
3. C. H. L. Tempelman, E. J. M. Hensen, *Appl. Catal. B* **176–177**, 731–739 (2015).
4. S. Natesakhawat *et al.*, *Catal. Sci. Technol.* **5**, 5023–5036 (2015).
5. J. Xue *et al.*, *ACS Catal.* **6**, 2448–2451 (2016).
6. J. J. Spivey, G. Hutchings, *Chem. Soc. Rev.* **43**, 792–803 (2014).
7. Z. R. Ismagilov, E. V. Matus, L. T. Tsikoza, *Energy Environ. Sci.* **1**, 526–541 (2008).
8. X. Guo *et al.*, *Science* **344**, 616–619 (2014).
9. K. D. Kreuer, *Solid State Ion.* **125**, 285–302 (1999).
10. C. Duan *et al.*, *Science* **349**, 1321–1326 (2015).
11. V. Kyriakou *et al.*, *Appl. Catal. B* **186**, 1–9 (2016).
12. E. Vasileiou *et al.*, *Top. Catal.* **58**, 1193–1201 (2015).
13. Y. Chen *et al.*, *Nano Energy* **10**, 1–9 (2014).
14. Materials and methods are detailed in the supplementary materials on *Science* Online.
15. A. K. Kinage, R. Ohnishi, M. Ichikawa, *Catal. Lett.* **88**, 199–202 (2003).
16. Z. Liu, L. Li, E. Iglesia, *Catal. Lett.* **82**, 175–180 (2002).

17. A. Atkinson *et al.*, *Nat. Mater.* **3**, 17–27 (2004).
18. P. Moghimpour Bijani, M. Sohrabi, S. Sahebdelfar, *Chem. Eng. Technol.* **35**, 1825–1832 (2012).
19. Z. Cao *et al.*, *Angew. Chem. Int. Ed.* **52**, 13794–13797 (2013).
20. S. Liu, R. Ohnishi, M. Ichikawa, *J. Catal.* **220**, 57–65 (2003).
21. Chemical process simulation and optimization were performed using ASPEN PLUS v8.0 software.
22. Y. Shudo, T. Ohkubo, Y. Hideshima, T. Akiyama, *Int. J. Hydrogen Energy* **34**, 4500–4508 (2009).
23. National Energy Technology Laboratory, "Analysis of natural gas-to liquid transportation fuels via Fischer-Tropsch" (U.S. Department of Energy, DOE/NETL-2013/1597, 2013).

ACKNOWLEDGMENTS

This work was supported by the Research Council of Norway (grants 195912, 210418, 210765, and 219194) and the Spanish government (grants SEV-2012-0267 and ENE2014-57651). We thank the ALBA Synchrotron Light Laboratory for beam time provision. C.K. and P.K.V. have applied for a patent based on this work (PCT/EP2014/071697). Experimental data are available online at ftp://itqrepositorio.itq.upv.es/pub/.

SUPPLEMENTARY MATERIALS

www.sciencemag.org/content/353/6299/563/suppl/DC1
Materials and Methods
Figs. S1 to S9
Tables S1 and S2
References (*24*–*27*)

12 May 2016; accepted 12 July 2016
10.1126/science.aag0274

ANALYTICAL METHODS

Origin and hysteresis of lithium compositional spatiodynamics within battery primary particles

Jongwoo Lim,[1,2]* Yiyang Li,[1]* Daan Hein Alsem,[3] Hongyun So,[4] Sang Chul Lee,[1] Peng Bai,[5] Daniel A. Cogswell,[5] Xuzhao Liu,[1] Norman Jin,[1] Young-sang Yu,[6] Norman J. Salmon,[3] David A. Shapiro,[6] Martin Z. Bazant,[1,5,7,8] Tolek Tyliszczak,[6] William C. Chueh[1,2]†

The kinetics and uniformity of ion insertion reactions at the solid-liquid interface govern the rate capability and lifetime, respectively, of electrochemical devices such as Li-ion batteries. Using an operando x-ray microscopy platform that maps the dynamics of the Li composition and insertion rate in Li_xFePO_4, we found that nanoscale spatial variations in rate and in composition control the lithiation pathway at the subparticle length scale. Specifically, spatial variations in the insertion rate constant lead to the formation of nonuniform domains, and the composition dependence of the rate constant amplifies nonuniformities during delithiation but suppresses them during lithiation, and moreover stabilizes the solid solution during lithiation. This coupling of lithium composition and surface reaction rates controls the kinetics and uniformity during electrochemical ion insertion.

The insertion of a guest ion into the host crystal is the fundamental reaction underpinning insertion electrochemistry and has been applied to store energy (*1*), tune catalysts (*2*), and switch optoelectronic properties (*3*). In Li-ion batteries, for example, Li ions from the liquid electrolyte insert into solid host particles in the electrode. Nanoscale intraparticle electrochemical inhomogeneities in phase and in composition are responsible for mechanical strain and fracture, which decrease the reversibility of the reaction (*4*). Moreover, these nonuniformities make it difficult to correlate current-voltage measurements to microscopic ion insertion mechanisms. Simultaneously quantifying nonuniform nanoscale reaction kinetics and the underlying material composition at the solid-liquid interface holds the key to improving device performance.

A model material for investigating ion insertion reactions is Li_xFePO_4 ($0 < x < 1$), which separates into two phases at equilibrium (*5*). Recent studies using in situ x-ray diffraction revealed a continuous distribution of lattice constants at high rates of (de)lithiation (*6*–*9*). This finding supports the hypothesis that phase separation is suppressed during (de)lithiation and is replaced by a solid-solution crystallographic insertion pathway (*10*), consistent with theoretical predictions (*11*, *12*). Precise quantification of the Li composition (x) is difficult because the change in lattice constant convolves information from both Li composition and mechanical strain (*8*). Whereas heterogeneous current distributions between particles have been studied (*7*, *13*, *14*), there exists little understanding of how compositional nonuniformities evolve within individual particles. Diffuse interfaces have been proposed from diffraction patterns (*7*), but it is unclear where they occur or how they develop over time. Even less understood is the effect of interfacial reactivity on the single-particle lithiation pathway, which has been explored using models (*11*, *15*) but has not been probed experimentally.

In Li_xFePO_4, an insertion reaction changes x as well as the valence of Fe (*13*). Thus, tracking the spatial and temporal evolution of the Fe oxidation state reveals both the composition and the nanoscale insertion rate. Scanning electrochemical microscopy provides quantitative current-voltage measurement but is insensitive to the Li composition (*16*). Redox-sensitive liquid microscopy techniques such as transmission hard x-ray microscopy (*17*–*19*), fluorescence soft x-ray microscopy (*20*), and transmission electron microscopy (TEM) (*21*) have been used to track Li transport with single-particle sensitivity (*7*, *20*, *21*), or within agglomerates (*17*, *19*) in insertion electrodes. However, tracking the spatial evolution of lithiation within the same particles under multiple electrochemical conditions in liquid has not been realized because of insufficient spatial and temporal resolution, beam-induced damage, and/or low absorption contrast. Additionally, although three-dimensional x-ray microscopies have revealed important insights on the morphology, strain, and dislocation of single particles (*22*–*24*), quantitative measurement of the local insertion rate remains elusive.

We developed synchrotron-based liquid scanning transmission x-ray microscopy (STXM) to probe the spatiotemporal evolution of the Li composition and insertion rate within primary particles (Fig. 1A). Using a microfluidic electrochemical cell, we imaged the Li composition of ~30 single-crystalline, carbon-coated Li_xFePO_4 particles (Fig. 1, B and C) as they delithiated (charged) and lithiated (discharged) in an organic liquid electrolyte. This platelet particle morphology has been used in fundamental studies of Li_xFePO_4 (*20*, *25*–*27*). The particles' [010] crystallographic axis, which is the fast Li diffusion direction (*28*), lies parallel to the soft x-ray beam. We used operando STXM to track the change in the Fe oxidation state that accompanies lithiation at the Advanced Light Source STXM beam line 11.0.2.2 and at 5.3.2.1 (*29*). By raster-scanning Li_xFePO_4 platelet particles (~1 μm wide and 150 nm thick, specific capacity ~150 mAh g^{-1}; figs. S1 to S3) with a 50-nm x-ray probe, we acquired the nanoscale x-ray absorption spectra at the Fe L_3 edge (Fig. 1D), from which the local Li composition (x) can be quantified (*13*). Spectral analysis confirmed that the composition of solid-solution and phase-separating Li_xFePO_4 could

[1]Department of Materials Science and Engineering, Stanford University, Stanford, CA 94305, USA. [2]Stanford Institute for Materials & Energy Sciences, SLAC National Accelerator Laboratory, Menlo Park, CA 94025, USA. [3]Hummingbird Scientific, Lacey, WA 98516, USA. [4]Department of Aeronautics and Astronautics, Stanford University, Stanford, CA 94305, USA. [5]Department of Chemical Engineering, Massachusetts Institute of Technology, Cambridge, MA 02139, USA. [6]Advanced Light Source, Lawrence Berkeley National Laboratory, Berkeley, CA 94720, USA. [7]Department of Mathematics, Massachusetts Institute of Technology, Cambridge, MA 02139, USA. [8]SUNCAT Interfacial Science and Catalysis, Stanford University, Stanford, CA 94305, USA. *These authors contributed equally to this work. **†Corresponding author. Email: wchueh@stanford.edu**

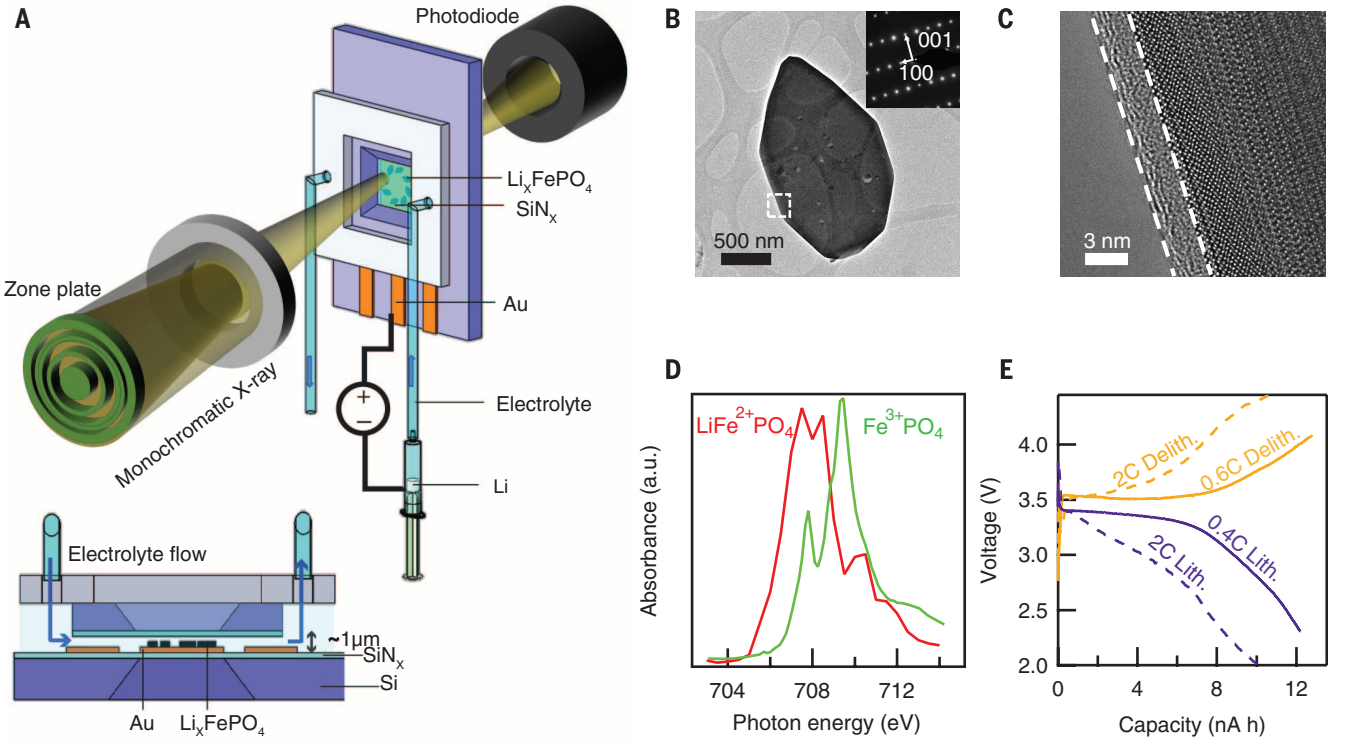

Fig. 1. Liquid STXM nanoimaging platform. (**A**) Schematic of the operando liquid imaging platform. The Li_xFePO_4/Au working electrode is placed in the sandwiched SiN_x stack, and the Li foil counter/reference electrode is placed in a syringe outside of the chamber, connected ionically via the electrolyte tube and electronically via a potentiostat. The inset shows a cross-sectional view of the cell. (**B**) Bright-field TEM and electron diffraction of a typical $LiFePO_4$ platelet particle. (**C**) High-resolution TEM of the carbon coating (outlined) of a $LiFePO_4$ particle. (**D**) Typical x-ray absorption spectra of $LiFePO_4$ and $FePO_4$ particles in liquid. (**E**) Electrochemical cycling of Li_xFePO_4 particles in the microfluidic liquid cell.

be determined through a linear combination fit of the end-member states (figs. S4 to S6), consistent with previous work (*13*, *20*, *30*).

In our setup, the battery particles are housed in a multimodal microfluidic electrochemical cell (Hummingbird Scientific), also used for liquid TEM (*21*, *31*). The liquid electrochemical cell consists of two sandwiched Si membrane chips, with 75-nm-thick SiN_x windows and fluoropolymer O-rings for imaging and sealing, respectively. The electrolyte (1.0 M $LiClO_4$ in tetraethylene glycol dimethyl ether) flows from the liquid inlet to the outlet, passing through the ~1-μm gap between the chips (Fig. 1A). The thin spacing minimizes attenuation of soft x-rays, and the flow of electrolyte minimizes interaction between the sample and the beam. The working electrode consists of a single layer of Li_xFePO_4 platelet particles dispersed on a 1.2 mm × 1.7 mm Au current collector (fig. S7), which was evaporated on one of the SiN_x membranes. By using a single layer of particles with an electrode porosity of >90%, we minimize tortuosity and transport losses at the electrode level. Low active material loading in this dilute electrode yields current density on the order of 0.1 μA cm^{-2} when normalized against the projected area of the current collector. This is approximately three orders of magnitude less than typical porous electrodes. Finite element analysis confirms that the electrolyte salt concentration and potential do not deviate from open-circuit values by more than 0.04 M and 2 mV, respectively, in the chip during cycling at 0.2C [where C indicates the rate to fully (de)lithiate the particles in 1 hour] and do not deviate by more than 0.2 M and 15 mV at 2C (fig. S8). The microfluidic cell has negligible capacitance or stray reactions (fig. S9) and uses a Li foil counter electrode (Fig. 1A). As a result, we observed the expected voltage plateau at ~3.4 V (Fig. 1E) and stable capacity (fig. S10) over multiple cycles, despite a low active material loading. At low rates, the electrochemical profile of the microfluidic cell was similar to that of a Li_xFePO_4 electrode cycled in a coin cell (fig. S3). At high rates, the profile deviated somewhat from that of coin cells. We hypothesize that these deviations arise from delamination of certain particles at higher rates; our analyses were conducted on particles that are not delaminated.

Figure 2A shows operando spectroimaging of a typical particle undergoing multiple delithiation and lithiation cycles. The particles successfully (de)lithiated electrochemically even after repeated exposure to the x-ray beam, reflecting the low x-ray dose (fig. S11) and high electrochemical fidelity. We tracked several particles (de)lithiating at 0.2C, 0.3C, 0.6C, and 2C (Fig. 2, A to C). The Li composition averaged over each particle (determined spectroscopically) corresponded to the mean composition of the electrode (determined electrochemically) (fig. S12). This implies that nearly all particles are active, consistent with previous reports on this particle morphology (*20*). We computed the single-particle C rate (Fig. 2, A to C) and confirmed that increasing the global current increases the rate of (de)lithiation of individual particles. When lithiated at a high rate of 2C, the operando Li composition maps (Fig. 2B and movie S1) show that the particles intercalated uniformly. In other words, there was little variation in composition across each particle, and the composition changed continuously over time from $x = 0$ to $x = 1$, as also quantified using line cuts (Fig. 3A). We interpret this as a solid-solution behavior. X-ray diffraction of the (020) reflection reveals strong diffraction intensity between the peaks for the Li-rich and the Li-poor phases, which suggests that phase separation along [010]—the direction parallel to the x-ray beam—is unlikely to explain the spatially uniform Li composition (fig. S13). This finding is consistent with the high elastic strain energy penalty of phase separation in that direction for our particle size (*15*, *32*).

We also conducted an ex situ experiment by mapping the Li composition in half-delithiated particles cycled at 1C and subsequently relaxed for ~12 hours (Fig. 2D). These particles displayed sharp phase boundaries between Li-rich and Li-poor regions. The phase boundaries follow the facets of the particle, consistent with an elastically driven process. The line cuts of x within a

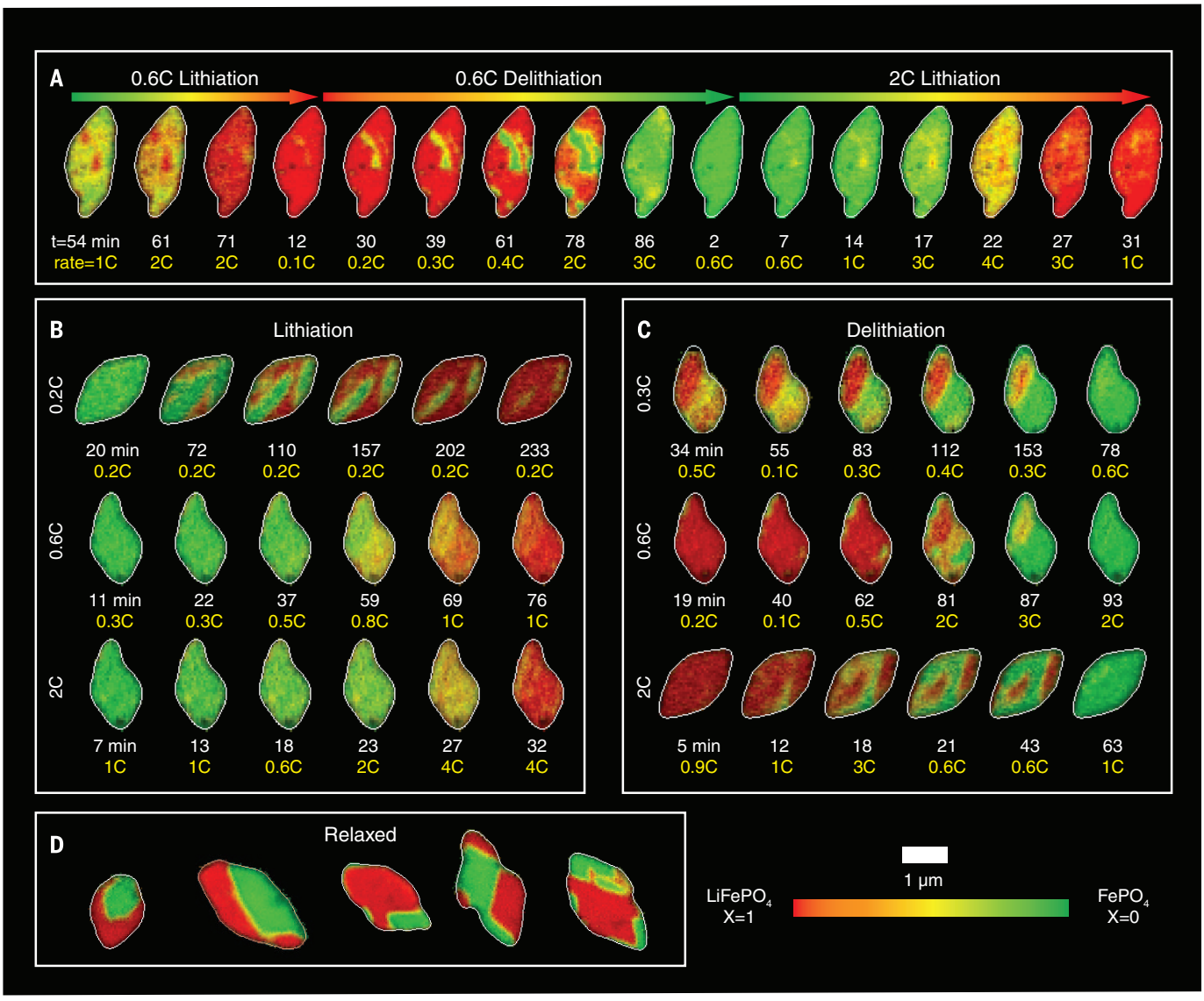

Fig. 2. Representative operando frames of Li insertion and extraction. (**A**) Operando Li composition frames of a single particle over multiple lithiation and delithiation cycles. The hue represents the Li composition (green, x = 0; red, x = 1). (**B** and **C**) Representative frames of different particles taken at various lithiation and delithiation rates, respectively. (**D**) Ex situ frames of Li composition for relaxed particles, showing the equilibrium distribution of Li within particles. Because the particle loading on the electrode is low, each acquired image typically contains a single particle, and this figure assembles multiple images together. Numbers below each frame indicate the time in minutes (white) and the C rate (yellow; see supplementary text for calculation protocol). t = 0 is defined as the starting time of the (de)lithiation cycle.

relaxed particle (Fig. 3B) clearly show that the Li composition is binary, where $x \approx 0$ or $x \approx 1$ for nearly every pixel. These observations, similar to previous ex situ studies (*25*, *26*) and theoretical calculations (*15*, *27*), confirm that phase separation under the influence of elastic strain dominates the equilibrium Li distribution.

A surprising observation for intermediate C rates (0.2C to 0.6C) during lithiation, and for all rates during delithiation, is that regions of fast Li ion (de)insertion and slow (de)insertion are visible (Fig. 2, B and C, and movie S2). Fast regions (de)lithiated preferentially while the remainder of the particle lagged behind. We term these regions "domains" because their Li composition is not binary, but rather varies continuously during cycling, as evident in the line cuts (Fig. 3A). This is a visualization of the compositionally nonuniform solid-solution pathway, where there exist many solid-solution domains in a single particle. At rates of 0.6C and higher, the electrochemical domains are largely circular or ellipsoidal, without being oriented with respect to the facets. At rates of 0.2C and 0.3C, the domain shapes contain both faceted and ellipsoidal features.

In contrast to standard phase-separation models that incorporate moving phase boundaries (*5*), intercalation waves (*33*), or domino cascades (*34*), we observed that the size of the fast domains (*35*) did not grow substantially in size. Rather, lithiation was accompanied by continuous change of the Li composition within each domain, with two or more concurrent solid-solution processes (Fig. 3C). Our results show that the presence of Li-rich and Li-poor regions within a single particle does not necessarily lead to moving phase boundaries. The slow growth of these domains can be explained because gradient energies, as modeled by Cahn-Hilliard–based reaction kinetics (*36*), slightly favor the (de)insertion of Li at domain boundaries (*11*).

We quantified the local current density within individual particles, calculated by evaluating the pixelwise difference in x between sequential frames (*35*). Because Li_xFePO_4 is a one-dimensional Li conductor (*28*), a change in x is attributed to ion insertion at the solid-liquid interface perpendicular to the ion conduction channels. Figure 3D maps the current density of several particles and shows domains of higher current density

relative to the rest of the particle. The same domains are fast under both lithiation and delithiation, thus confirming that the domain structures do not arise from random nucleation sites or spinodal decomposition. We rule out spatial variations in solid Li diffusion in the [010] direction as the origin of domain structures; the characteristic solid Li diffusion time in Li_xFePO_4 along the 150-nm-thick [010] direction is ~1 ms for x = 0 and ~10 ms for x = 1 (*28*), which are both much faster than total (de)lithiation times of 0.5 to 5 hours. We conclude that spatial variations in the insertion reaction kinetics at the solid-liquid interface give rise to these domain structures. The surfaces of the fast domains are more reactive for all Li compositions (fig. S16). We use "heterogeneity" to describe spatial variations in reaction rates, and "nonuniformity" to describe spatial variations in composition. Possible origins for these reaction heterogeneities include inhomogeneous strain (*24*), variations in carbon coating, and surface defects induced by cycling (*18*).

We quantified the degree of intraparticle composition uniformity by analyzing the standard deviation of x in each particle at every recorded frame (Fig. 3E and fig. S14). Our statistical analysis confirms that higher cycling rates reduce the variations in composition within a particle, resulting in more uniform intercalation (higher uniformity coefficient). Moreover, delithiation is substantially less uniform than lithiation. The statistical analysis and direct imaging of the same particle under different cycling rates show that Li_xFePO_4 exhibits (i) fully lithiated and delithiated regions (i.e., phase separation) when relaxed for an extended period of time, (ii) compositionally nonuniform solid solution (i.e., domains) at intermediate rates, and (iii) domain-free, compositionally uniform solid solution at high rates (summarized in Fig. 3F). In other words, the difference in the Li composition between Li-rich and Li-poor domains diminishes at higher rates of cycling, where the high applied overpotential stabilizes the uniform compositions for the same reasons that solid solution is stable with faster cycling (*6*, *8*, *9*, *11*, *15*). Consistent with this physical picture, restarting delithiation on a relaxed, phase-separated particle brings the particle into a solid solution, and a solid-solution particle phase separates over time when it is idle (fig. S15).

To understand the intrinsic ion insertion rate constant as a function of the Li composition, we identified a set of actively (de)intercalating pixels with approximately uniform composition in each particle at low cycling rates, and then spectroscopically measured the current density for that set of pixels. The chosen set of pixels lies within a single domain and intercalates uniformly. Because there is a disagreement regarding the quantitative relationship of current and overpotential between Butler-Volmer and Marcus kinetics (*37*), we limit our analysis to overpotentials of <120 mV. In this regime, the reaction models converge, and we used a linear relationship between current and voltage to extract the exchange current density (j_0) and quantify the reaction kinetics (*35*) (figs. S16 to S18).

By measuring the nanoscale j_0 at the subparticle level, our results show that the reaction rate depends strongly on x, the local Li composition (Fig. 4A): j_0 is low for Li-poor and Li-rich end members, likely because of low concentrations of Li ions and vacancies, respectively (*36*, *38*, *39*). We found that the magnitude of j_0 varies nonmonotonically with Li composition

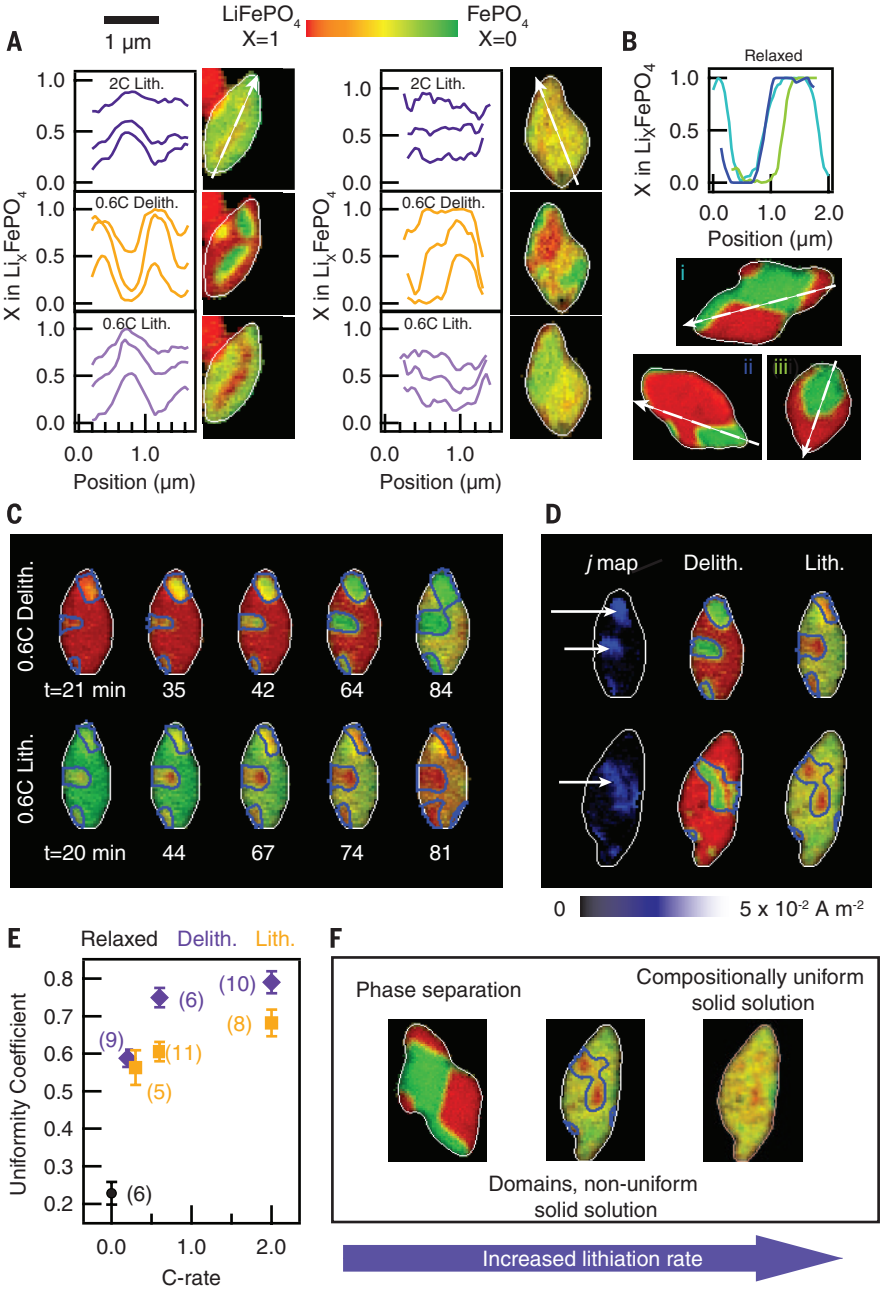

Fig. 3. Identification of domains in Li composition. (**A**) Line cuts of Li composition (x) of the same particles under different cycling conditions. The same pixels in a particle were sampled. (**B**) Line cuts of the relaxed, phase-separated particles. (**C**) The fast domains, outlined in blue, do not substantially grow in size. (**D**) Current density quantification reveals regions of higher insertion kinetics, calculated from delithiation. The same fast domains are present in both charge and discharge. (**E**) The uniformity coefficient increases with cycling rate and is consistently higher for lithiation than for delithiation. This was calculated from the standard deviation of x in each frame of a particle, where higher standard deviation indicates lower uniformity (see fig. S14). A coefficient of 0 indicates a binary distribution in the phase separation limit, whereas a coefficient of 1 indicates the uniform solid-solution limit. The value in parentheses indicates the number of particles analyzed under that condition. (**F**) Scheme of the insertion pathway as a function of the lithiation rate.

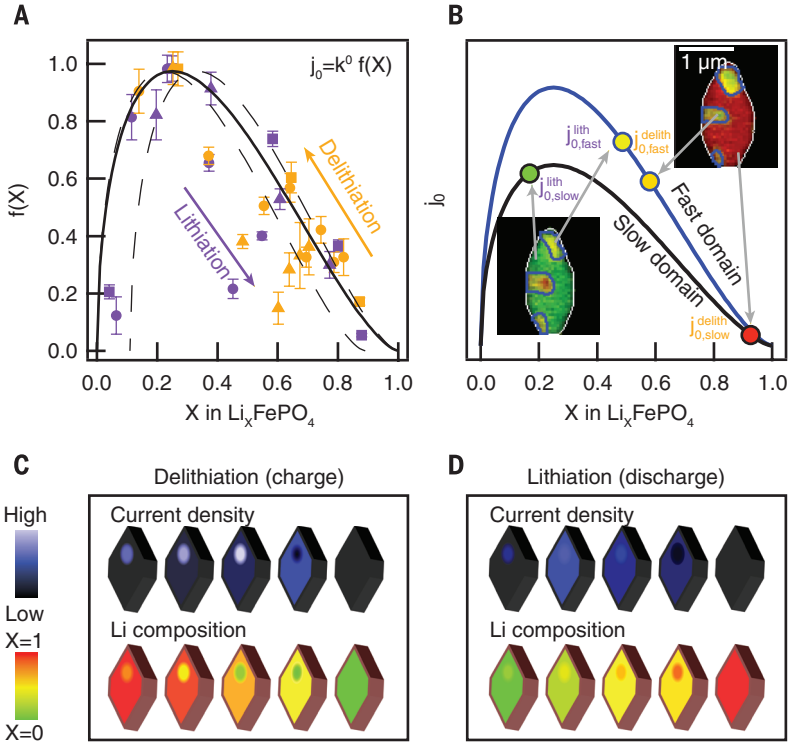

Fig. 4. Quantifying the insertion kinetics and exchange current density. (**A**) The measured exchange current density (j_0) varies nonmonotonically with the Li composition x. Solid line is a guide to the eye; k^0 is ~1 × 10^{-2} A m^{-2}. See supplementary text for error calculation. Each marker in each color represents a different particle. The dashed lines show the shifted j_0-x curve due to uncertainty arising from the fact that the specific capacity of the particles is less than the theoretical capacity. (**B**) Because the skewed j_0 peaks at $x \approx 0.25$, the value of j_0 for the fast domains is several times that of j_0 for the slow domains during delithiation, but the two quantities are comparable during lithiation. (**C**) During delithiation from $x = 1$ to $x = 0$, the fast domains have lower x, which amplifies the difference in current density between the two domains. (**D**) Upon lithiation from $x = 0$ to $x = 1$, the fast domains have higher x, reducing the difference in the current density.

and peaks at a composition of ~$Li_{0.25}FePO_4$. For the particles measured, j_0 peaks between 6×10^{-3} and 1×10^{-2} A m^{-2}. This composition-dependent j_0 reflects the defect chemistry of Li_xFePO_4 (*38*), whereby x modulates not only bulk thermodynamics and transport but also the surface kinetics of ion insertion. The skewed j_0-x relationship is in contrast to Newman's model (*39*), which is symmetric about $x = 0.5$. A skewed j_0-x curve was first proposed by Bazant using a general phase-field theory of chemical kinetics based on nonequilibrium thermodynamics (*36*). Following Bai, Cogswell, and Bazant (*11*, *15*), we conducted a linear stability analysis of the model and confirmed that such a skewed j_0-x curve is a necessary condition to suppress phase separation above a critical lithiation current (fig. S19). In contrast, the theory predicts that the solid-solution pathway is linearly unstable for a j_0 curve symmetric about $x = 0.5$ for all lithiation rates, although diffuse interfaces or quasi–solid solutions may still form.

The strong spatial and compositional dependence of j_0 within individual particles explains why domains persist more during delithiation than during lithiation. If the shape of the j_0-x curve is invariant between domains within a particle (fig. S16), the fast domains must consistently exhibit a higher j_0 for any x (Fig. 4B). During delithiation from $x = 1$, the rate accelerates from $x = 1$ to $x \approx 0.25$ (Fig. 4B). This positive feedback amplifies the difference in the reaction rate between slow and fast domains: The value of j_0 for the fast domain (which has a lower x) is much larger than for the slow domain (Fig. 4C). On the other hand, during lithiation from $x = 0$, the fast domain initially accelerates from $x = 0$ to $x \approx 0.25$ but decelerates once it passes $x \approx 0.25$, when j_0 starts to decrease with greater x. Because x is higher for the faster domain, this negative feedback diminishes the difference in reaction rate between the two domains (Fig. 4D). The acceleration regime during delithiation is larger than during lithiation by a factor of ~3 and quantitatively explains why delithiation is less uniform than lithiation. Thus, whereas high rates of lithiation yield nearly uniform compositions and current densities, similar rates of delithiation are highly nonuniform (Fig. 2C and Fig. 3, A and E). This skewed relationship may also describe some of the observed asymmetries in the voltage profile between charge and discharge. Other factors, such as an asymmetric charge transfer coefficient (*13*), may also contribute to the observed hysteresis.

Our results show that spatial heterogeneities in reaction rates account for the compositionally nonuniform solid-solution domains during (de)lithiation of Li_xFePO_4, and that the skewed j_0-x relationship amplifies reaction heterogeneities during delithiation but suppresses them during lithiation, consistent with theoretical predictions (*11*, *15*, *36*). These results highlight the crucial role of surface reaction rate in lithiation, with implications for electrode engineering and battery management. Higher rates of lithiation suppress compositional nonuniformities within particles and minimize mechanical stress, and have been shown to improve cyclability (*4*). However, the same statement is not true for delithiation, where reaction heterogeneities manifest as compositional nonuniformities. Beyond batteries, our work highlights the importance of composition in ion insertion kinetics, which affects a broad class of electrochemical materials.

REFERENCES AND NOTES

1. M. S. Whittingham, *Chem. Rev.* **114**, 11414–11443 (2014).
2. H. Wang *et al.*, *Proc. Natl. Acad. Sci. U.S.A.* **110**, 19701–19706 (2013).
3. A. Llordés, G. Garcia, J. Gazquez, D. J. Milliron, *Nature* **500**, 323–326 (2013).
4. W. H. Woodford, W. C. Carter, Y.-M. Chiang, *Energy Environ. Sci.* **5**, 8014–8024 (2012).
5. A. K. Padhi, K. S. Nanjundaswamy, J. B. Goodenough, *J. Electrochem. Soc.* **144**, 1188–1194 (1997).
6. X. Zhang *et al.*, *Nano Lett.* **14**, 2279–2285 (2014).
7. X. Zhang *et al.*, *Nat. Commun.* **6**, 8333 (2015).
8. H. Liu *et al.*, *Science* **344**, 1252817 (2014).
9. M. Hess, T. Sasaki, C. Villevieille, P. Novák, *Nat. Commun.* **6**, 8169 (2015).
10. J. Niu *et al.*, *Nano Lett.* **14**, 4005–4010 (2014).
11. P. Bai, D. A. Cogswell, M. Z. Bazant, *Nano Lett.* **11**, 4890–4896 (2011).
12. R. Malik, F. Zhou, G. Ceder, *Nat. Mater.* **10**, 587–590 (2011).
13. Y. Li *et al.*, *Nat. Mater.* **13**, 1149–1156 (2014).
14. W. Dreyer *et al.*, *Nat. Mater.* **9**, 448–453 (2010).
15. D. A. Cogswell, M. Z. Bazant, *ACS Nano* **6**, 2215–2225 (2012).
16. Y. Takahashi *et al.*, *Nat. Commun.* **5**, 5450 (2014).
17. J. Wang, Y. C. Chen-Wiegart, J. Wang, *Nat. Commun.* **5**, 4570 (2014).
18. Y.-S. Yu *et al.*, *Adv. Energy Mater.* **5**, 1402040 (2014).
19. J. Nelson Weker, Y. Li, R. Shanmugam, W. Lai, W. C. Chueh, *ChemElectroChem* **2**, 1576–1581 (2015).
20. Y. Li *et al.*, *Adv. Funct. Mater.* **25**, 3677–3687 (2015).
21. M. E. Holtz *et al.*, *Nano Lett.* **14**, 1453–1459 (2014).
22. M. Ebner, F. Marone, M. Stampanoni, V. Wood, *Science* **342**, 716–720 (2013).
23. J. N. Weker *et al.*, *Energy Environ. Sci.* **7**, 2771–2777 (2014).
24. A. Ulvestad *et al.*, *Science* **348**, 1344–1347 (2015).
25. D. A. Shapiro *et al.*, *Nat. Photonics* **8**, 765–769 (2014).
26. U. Boesenberg *et al.*, *Chem. Mater.* **25**, 1664–1672 (2013).
27. D. A. Cogswell, M. Z. Bazant, *Nano Lett.* **13**, 3036–3041 (2013).
28. D. Morgan, A. Van der Ven, G. Ceder, *Electrochem. Solid-State Lett.* **7**, A30–A32 (2004).
29. H. Bluhm *et al.*, *J. Electron Spectrosc. Relat. Phenom.* **150**, 86–104 (2006).
30. X. Liu *et al.*, *J. Am. Chem. Soc.* **134**, 13708–13715 (2012).
31. M. Gu *et al.*, *Nano Lett.* **13**, 6106–6112 (2013).
32. A. Abdellahi, O. Akyildiz, R. Malik, K. Thornton, G. Ceder, *J. Mater. Chem. A* **2**, 15437–15447 (2014).
33. G. K. Singh, G. Ceder, M. Z. Bazant, *Electrochim. Acta* **53**, 7599–7613 (2008).
34. C. Delmas, M. Maccario, L. Croguennec, F. Le Cras, F. Weill, *Nat. Mater.* **7**, 665–671 (2008).
35. See supplementary materials on *Science* Online.
36. M. Z. Bazant, *Acc. Chem. Res.* **46**, 1144–1160 (2013).
37. P. Bai, M. Z. Bazant, *Nat. Commun.* **5**, 3585 (2014).

38. J. Maier, R. Amin, *J. Electrochem. Soc.* **155**, A339–A344 (2008).
39. K. E. Thomas, R. M. Darling, J. Newman, *Advances in Lithium-Ion Batteries* (Kluwer Academic/Plenum, 2002).

ACKNOWLEDGMENTS

The x-ray component of this work was supported by the U.S. Department of Energy (DOE), Office of Basic Energy Sciences, Division of Materials Sciences and Engineering (contract DE-AC02-76SF00515). The battery component of this work was supported by the Ford-Stanford Alliance. The Advanced Light Source is supported by the DOE Office of Basic Energy Sciences under contract DE-AC02-05CH11231. N.J.S. and D.H.A. acknowledge support from the DOE Office of Basic Energy Sciences SBIR program under awards DE-SC-0007691 and DE-SC-0009573. Beam line 5.3.2.1 at the Advanced Light Source was funded through a donation by the King Abdullah University of Science and Technology. Also supported by a NSF Graduate Research Fellowship under grant DGE-114747 (Y.L.) and by the Global Climate and Energy Project at Stanford University and the DOE Office of Basic Energy Sciences through the SUNCAT Center for Interface Science and Catalysis (M.Z.B.). N.J.S. and D.H.A. are employed by Hummingbird Scientific, which designed and manufactured the microfluidic liquid cell used in these experiments. Part of this work was conducted the Stanford Nano Shared Facilities and the Stanford Nanofabrication Facility. We thank J. Nelson Weker, A. Wise, H. W. Shiu, M. Farmand, D. Kilcoyne, S. Fakra, Y. S. Hsieh, and A. Kammers for insightful discussions and assistance with the experiment.

The raw data for this experiment are available as part of the supplementary materials.

SUPPLEMENTARY MATERIALS

www.sciencemag.org/content/353/6299/566/suppl/DC1
Materials and Methods
Supplementary Text
Figs. S1 to S19
Movies S1 and S2
References (*40*–*49*)
Archive of Image Data

24 November 2015; accepted 8 July 2016
10.1126/science.aaf4914

NANOMATERIALS

Permanent excimer superstructures by supramolecular networking of metal quantum clusters

Beatriz Santiago-Gonzalez,[1]* Angelo Monguzzi,[1]*† Jon Mikel Azpiroz,[2,3] Mirko Prato,[4] Silvia Erratico,[5] Marcello Campione,[6] Roberto Lorenzi,[1] Jacopo Pedrini,[1] Carlo Santambrogio,[7] Yvan Torrente,[5] Filippo De Angelis,[2,4] Francesco Meinardi,[1]† Sergio Brovelli[1]†

Excimers are evanescent quasi-particles that typically form during collisional intermolecular interactions and exist exclusively for their excited-state lifetime. We exploited the distinctive structure of metal quantum clusters to fabricate permanent excimer-like colloidal superstructures made of ground-state noninteracting gold cores, held together by a network of hydrogen bonds between their capping ligands. This previously unknown aggregation state of matter, studied through spectroscopic experiments and ab initio calculations, conveys the photophysics of excimers into stable nanoparticles, which overcome the intrinsic limitation of excimers in single-particle applications—that is, their nearly zero formation probability in ultra-diluted solutions. In vitro experiments demonstrate the suitability of the superstructures as nonresonant intracellular probes and further reveal their ability to scavenge reactive oxygen species, which enhances their potential as anticytotoxic agents for biomedical applications.

Metal quantum clusters are functional nanoscale materials with potential for use in sensing (*1*), bio imaging (*2*), optoelectronics (*3*), and nanomedicine (*4*). With "magic" sizes dictated by the valence of the metal constituents (*5*) and dimensions approaching the Fermi wavelength of the electron, these few-atom structures bridge the gap between atoms and colloidal nanoparticles. As a result, metal quantum clusters combine a molecule-like electronic structure with quantum confinement effects that confer them with size- and shape-tunable optical properties, ultralarge surface-to-volume ratios, and unmatched flexibility for tailoring their physical properties through surface functionalization. Specifically, ligand-to-metal electron transfer (LM-ET) in metal quantum clusters with electron-rich capping agents (*6*–*8*) leads to strongly Stokes-shifted emission, which is beneficial for photon management (*9*) and bio imaging (*1*) applications. On the other hand, suppression of LM-ET results in intrinsic luminescence, with energy determined by the quantum mechanical combination of single-atom electronic orbitals (*10*, *11*). Fundamentally, the key common feature of "intrinsic emitting" metal quantum clusters is their capping with bulky molecules (*12*–*15*) or their encapsulation in supramolecular vesicles (*14*, *16*, *17*), imposing large distances between the metal cores. The use of short ligands, even in the absence of LM-ET, has led instead to a variety of optical behaviors (*18*–*21*). This points to a role of intercluster interactions in the photophysics of metal quantum clusters and suggests a supramolecular strategy for tuning their optical properties through controlled formation of aggregate species, similarly to what is achieved with organic chromophores.

In molecular physics, aggregate species are typically divided into two main categories based on the type of interaction that leads to their formation: Molecular dimers arise from ground-state interactions between individual moieties (monomers) (*22*), whereas excimers are evanescent quasi-particles existing exclusively in the excited state and formed through the aggregation of an excited monomer and a ground-state monomer. When excimers return to the ground state, their constituent monomers dissociate (*22*). As a result, dimers are capable of ground-state absorption, whereas excimers exhibit the absorption spectrum of the monomers and long-lived Stokes-shifted emission from lower-lying intermolecular states. Molecular excimers are typically formed through collisional interactions between monomers in concentrated solutions, and their formation probability drops to zero upon dilution (*23*). The excimer motif is, therefore, intrinsically prevented from being used for the fabrication of stable, self-standing emitters for single-particle applications.

In this work, we overcame this limitation by demonstrating a previously unknown aggregation state of matter that conveys the photophysics of excimers into individual particles that can find application as nonresonant emitters in cellular imaging and integrated photonic nanotechnologies. Specifically, we used Au_n (gold quantum clusters consisting of n atoms) as building blocks for fabricating permanent excimer-like colloidal superstructures (Au-pXs) held together by a network of hydrogen bonds between their capping ligands. As a result of repulsive forces between the metal cores, in the ground state, the networked Au_n behave as independent chromophores, whereas on photoexcitation, they form bimolecular excimers with largely Stokes-shifted emission (~1 eV). In contrast, encapsulation of Au_n in bulky vesicles hinders the excimeric interaction, resulting in the photophysics of isolated clusters. Last, we used Au-pXs for in vitro imaging

[1]Dipartimento di Scienza dei Materiali, Università degli Studi Milano-Bicocca, Via R. Cozzi 55, 20125 Milano, Italy. [2]Computational Laboratory for Hybrid and Organic Photovoltaics, National Research Council–Institute of Molecular Science and Technologies (CNR-ISTM), Via Elce di Sotto 8, 06123 Perugia, Italy. [3]Kimika Fakultatea, Euskal Herriko Unibertsitatea (UPV/EHU), and Donostia International Physics Center, 20080 Donostia, Euskadi, Spain. [4]Istituto Italiano di Tecnologia, Via Morego 30, 16163 Genova, Italy. [5]Dipartimento di Fisiopatologia Medico-Chirurgica e dei Trapianti, Università degli Studi di Milano, Fondazione IRCCS (Istituto di Ricovero e Cura a Carattere Scientifico) Cá Granda Ospedale Maggiore Policlinico, Centro Dino Ferrari, Via Francesco Sforza 35, 20122 Milano, Italy. [6]Dipartimento di Scienze dell'Ambiente e del Territorio e di Scienze della Terra, Università degli Studi Milano-Bicocca, Piazza della Scienza, 20125 Milano, Italy. [7]Dipartimento di Biotecnologie e Bioscienze, Università degli Studi Milano-Bicocca, Piazza della Scienza, 2 20126 Milano, Italy.
*These authors contributed equally to this work. **†Corresponding author. Email: angelo.monguzzi@mater.unimib.it (A.M.); meinardi@mater.unimib.it (F.M.); sergio.brovelli@unimib.it (S.B.)**

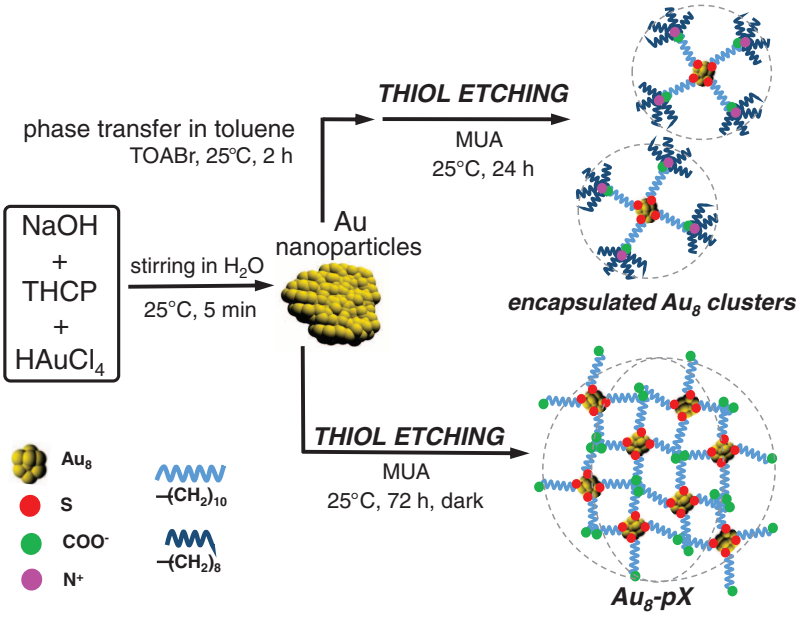

Fig. 1. Synthesis of encapsulated and networked gold quantum clusters. The diagram illustrates the protocols for synthesizing encapsulated Au_8 and networked superstructures (Au-pXs) by thiol-induced etching of gold nanoparticles. Au-pXs are obtained by networking of MUA-capped clusters. Phase transfer using TOABr in toluene leads instead to isolated clusters. THCP, tetrakis(hydroxymethyl)phosphonium chloride; h, hours.

of fibroblast cells. Our data reveal the high biocompatibility of Au-pXs and their ability to scavenge reactive oxygen species (ROS) responsible for premature cellular death, thereby further enhancing their potential for biomedical applications.

Figure 1 depicts the synthetic routes for obtaining isolated and networked clusters. Both samples were produced by etching of gold nanoparticles (fig. S1) with 11-mercaptoundecanoic acid (MUA) ligands that bond to the gold atoms through their thiol end group while exposing their carboxylic functionality (*24*). Critical to the fabrication of isolated clusters is the suppression of the H-bond capability of the ligands; this can be achieved by adding tetraoctylammonium bromide (TOABr), which leads to the formation of Au_n encapsulated in $(MUA^-)(TOA^+)$ vesicles (hereafter referred to as encapsulated clusters) (*11*). In the absence of the vesicles, the hydrogen bonding between the carboxylic functionalities of MUA^- leads to the formation of Au-pXs. The size of the synthesized clusters and the composition of the ligand shell were investigated by means of electrospray ionization mass spectrometry and x-ray photoelectron spectroscopy, which indicated that both routes produce Au_8 clusters capped by four MUA units (figs. S2 and S3 and tables S1 and S2).

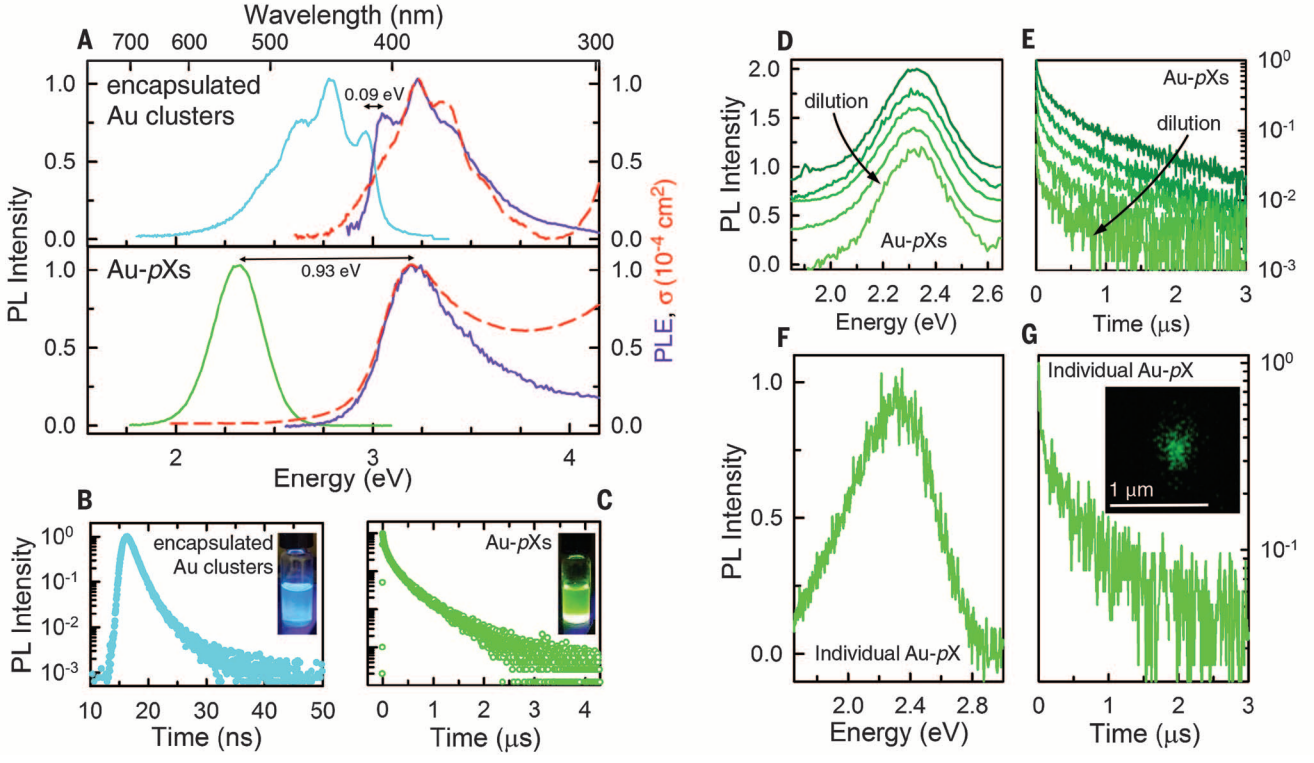

Fig. 2. Optical properties of encapsulated and networked gold quantum clusters. (**A**) Absorption cross section (σ, dashed red lines), PL (blue and green lines for encapsulated Au and Au-pXs, respectively), and PLE (purple lines) spectra recorded at the maximum of emission. The Stokes shift is indicated by the black arrows. (**B**) Time-resolved PL measurements of encapsulated clusters and (**C**) Au-pXs. The insets are photographs of the two systems under ultraviolet illumination. (**D**) Normalized PL spectra and (**E**) PL decay profiles of Au-pXs in water at increasing dilution (as indicated by the arrow): from dark to light green, 740, 148, 74, 7.4, and 0.74 μM. (**F**) PL spectrum and (**G**) respective decay curve of an individual Au-pX on glass. The inset is a confocal fluorescence image of the same particle. All measurements were performed using 3.25 eV excitation.

The optical absorption, photoluminescence (PL), and PL excitation (PLE) spectra of the synthesized materials are shown in Fig. 2A, together with the respective PL decay traces (Fig. 2, B and C). Both samples show narrow spectral features indicating monodispersity of the cluster size. The optical absorption and PLE spectra peak at 3.22 eV, corresponding to the ground-state absorption energy predicted by the jellium model for Au_8 (*25*). The essentially identical absorption profiles and cross sections for encapsulated and networked clusters confirm that the size of the gold cores is unaffected by the phase transfer with TOABr and that, in both cases, the Au_8 cores are noninteracting in the ground state.

Despite such similarity, encapsulated clusters and Au-pXs exhibit striking differences between their PL spectra and decay dynamics. Encapsulated systems show blue PL at ~2.75 eV, mirroring their absorption profile with distinct vibronic replica with an energy separation of ~175 meV, due to coupling with the C-H vibrations of the ligands. The PL quantum yield is Φ_{PL} = 12 ± 2%. The total PL lifetime of the encapsulated clusters is $\tau_{tot}^{enc} = 1.6$ ns, which yields a radiative decay time $\tau_{rad}^{enc} = \tau_{tot}^{enc}/\Phi_{PL}$ =13.3 ns, in good agreement with the radiative lifetime obtained through the Strickler-Berg analysis (12.0 ns) and with dendrimer-templated Au_8 [18.0 ns; fig. S4 and (*25*)]. This confirms the encapsulation of individual clusters into (MUA^-) (TOA^+) vesicles and the absence of LM-ET. In contrast, the PL spectrum of Au-pXs is featureless and peaks at ~2.36 eV (Φ_{PL} = 4.5 ± 0.8%), resulting in a Stokes shift of ~0.93 eV. The decay dynamics extend to the microsecond time regime, with average lifetime $\tau_{tot}^{Au-pX} = 114$ ns. In this case, the radiative lifetime extracted from the decay trace, $\tau_{rad}^{Au-pX} = 2.5$ µs, is over 200 times as long as the radiative lifetime $\tau_{rad}^{Au-pX} = 11.4$ ns obtained through the Strickler-Berg analysis. This indicates that the long-lived emission of Au-pXs does not arise from the absorbing state. Both samples feature MUA ligands, which excludes LM-ET as a possible origin of the Stokes-shifted PL of Au-pXs. The PL decay trace in Fig. 2C shows no measurable rise time, indicating that such emission does not arise from a subpopulation of larger clusters excited through energy transfer from the dominant fraction of Au_8 that is responsible for the absorption profile (supplementary materials).

The photophysical phenomenology can be comprehensively described by the behavior of a molecular excimer (*22*). Our metal-cluster excimers present a fundamental difference with respect to conventional excimers, that is, their formation is independent of the monomer density. This is confirmed by data in Fig. 2, D and E, showing that both the PL spectra and the decay dynamics of water solutions of Au-pXs are unaffected by increasing the dilution by over four orders of magnitude. This behavior is unexpected because, in contrast to ground-state aggregation, whose reaction equilibrium can be shifted in favor of dimerization regardless of the monomer concentration, the formation of excimers is a collisional bimolecular process that occurs exclusively within the monomer excited-state lifetime. Excimer formation is, therefore, strongly concentration-dependent, with probability dropping to zero at low monomer densities (*22*). As a result, with increasing dilution, the emission profile and decay dynamics of molecular excimers evolve toward the behavior of the isolated monomers (*22*). The invariance of the spectral and dynamical properties of Au-pXs with increasing dilution indicates that the Au_8 are in close proximity to each other in concentration regimes where conventional chromophores behave as isolated monomers. Despite such a coalescence state, ground-state interaction is hindered, and optical excitation is required for the formation of a bound system in which the excited-state wavefunction is delocalized over two or more Au_8 cores. To assess the persistence of Au-pXs in "infinite" dilution conditions, we performed spectroscopic measurements of individual superstructures. Single-particle data shown in Fig. 2, F and G, reveal identical PL spectra and decay dynamics to those of the aqueous solutions, which unambiguously confirms that each Au-pX behaves as a permanent excimer at the single-particle level.

Transmission electron microscopy images enabled us to visualize the Au-pXs (fig. S5), which appear as isolated spheroid structures with a radius of ~4 to 5 nm, probably resulting from the coalescence of several Au_8 clusters. To investigate the cohesive forces responsible for intercluster networking, we conducted Fourier transform infrared transmission (FT-IR) experiments on encapsulated Au_8 and Au-pXs. The data shown in fig. S6 indicate that the carboxylic hydrogen atoms are retained in Au-pXs, leading to the formation of hydrogen bonds between the carboxylic terminals of the MUA ligands. PL experiments conducted while titrating the Au-pX solution with NaOH or HCl (fig. S7) indicate that hydrogen networking between the ligands introduces strong cohesive forces that preserve the supramolecular architecture in harsh pH conditions.

To gain deeper insight into the physical mechanism underpinning the photophysics of Au-pXs, we performed ground- and excited-state density functional theory (DFT) and time-dependent DFT (TD-DFT) calculations. Building on the experimental evidence and preliminary screening calculations (figs. S8 to S10), we selected a star-shaped $[Au_8(MUA)_4]^{4-}$ cluster with C2 alkyl chains as a starting model monomer (**1** in Fig. 3A). Ground-state geometry optimizations reveal a strong propensity to form carboxylic acid dimers (**2.1**), with a formation energy exceeding 1 eV even after correcting for the translational and rotational entropic losses. A secondary configuration is characterized by strong reconstruction of the two interacting Au_8 cores (**2.2**). Given

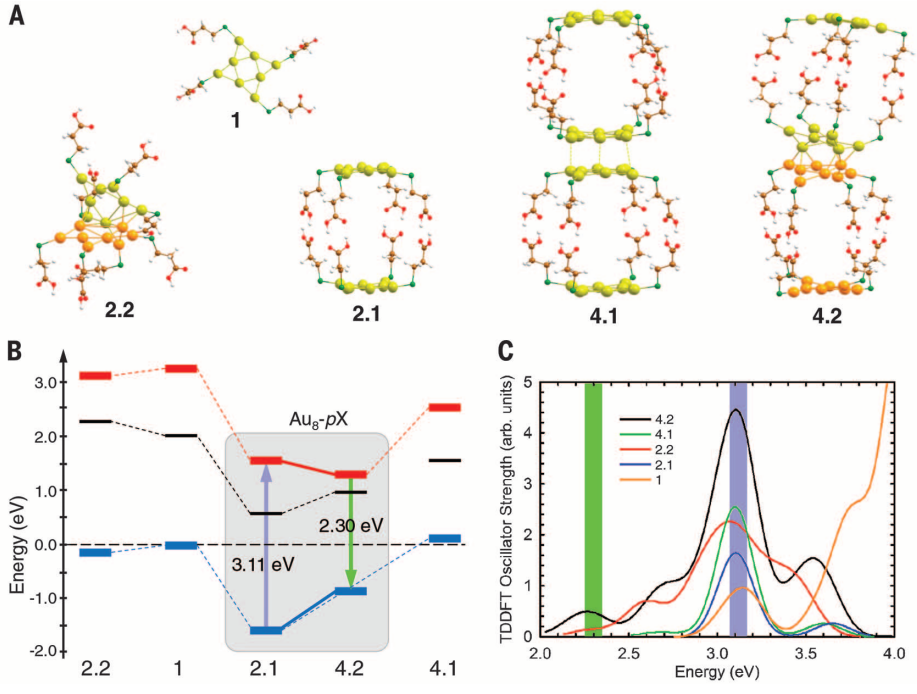

Fig. 3. DFT and TD-DFT calculations. (**A**) Optimized molecular structures of the $[Au_8(MUA)_4]^{4-}$ model monomer with C2 alkyl chains (**1**), of a dimer and tetramers linked by hydrogen bonds between their carboxylic end groups (**2.1**, **4.1**, and **4.2**), and of a dimer interacting only through the Au_8 cores (**2.2**). Au, yellow; S, green; O, red; C, brown; H, white. For **2.2** and **4.2**, yellow and orange are used for gold atoms belonging to different starting monomers. (**B**) Energy diagrams for the ground state (blue), dark excited state (black), and bright excited state (red) of the modeled species (listed on the *x* axis). An excimer formation from **2.1** to **4.2** is highlighted in the shaded area. (**C**) Absorption spectra of the various structures, calculated by TD-DFT/CAM-B3LYP (a hybrid exchange–correlation functional). The vertical bars represent the experimental absorption (purple) and emission (green) energies, corresponding to the colored arrows in (B). arb., arbitrary.

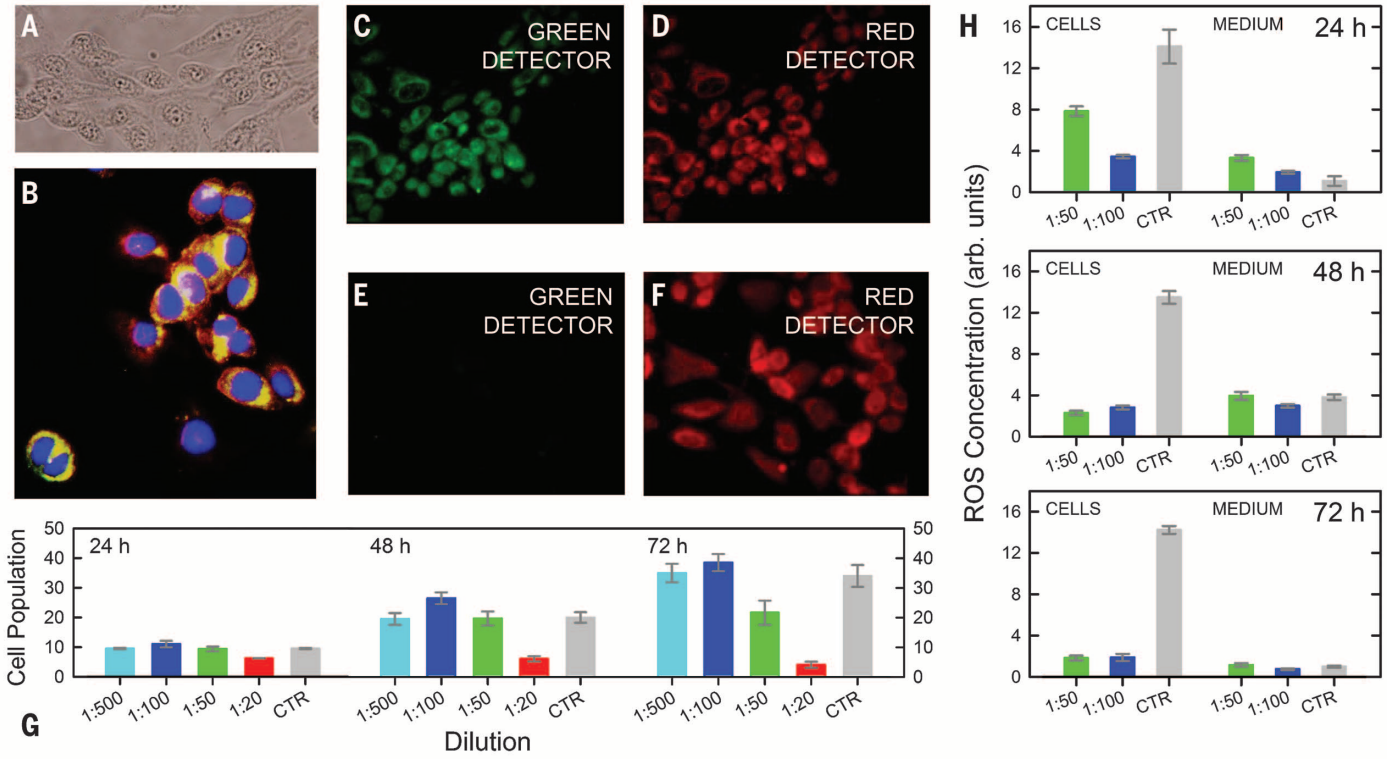

Fig. 4. Cellular imaging and radical oxygen scavenging using Au-pXs. (**A**) Bright-field image of 3T3 stem cells on glass. (**B**) Fluorescence image of fixed cells stained with DAPI (blue), Au-pXs (green), and PKH-26 (red). (**C** and **D**) Confocal fluorescence images of 3T3 cells stained with Au-pXs and PKH-26 and (**E** and **F**) only PKH-26 for direct comparison (excitation at 3.25 eV for all images). (**G**) MTT test on 3T3 cells stained with Au-pXs at increasing concentrations (from 1:500 to 1:20 dilution of the 740-μM mother solution) at three time points during cell proliferation. CTR, control. (**H**) ROS test on 3T3 cells stained with Au-pXs at 1:500 and 1:100 dilution of the mother solution. Error bars are the standard deviation of the mean values calculated for five independent experiments.

its high stability, **2.1** is probably the species that dominates the solution equilibrium (Fig. 3B). The TD-DFT–calculated absorption profiles are shown in Fig. 3C. Notably, **2.1** shows essentially the same absorption maximum and spectral shape as the monomer, in excellent agreement with the measured absorption spectra and with the jellium model. The energy stabilization of **2.1** (Fig. 3B) is thus due to the ligand interactions, with negligible electronic perturbation of the Au_8 cores. A broader and red-shifted spectrum calculated for **2.2**, reflecting the perturbation of the electronic structure caused by formation of the reconstructed Au_{8+8} aggregate. Although the high stability of **2.1** correlates with the lack of free carboxylic groups observed by means of FT-IR (fig. S6), it cannot explain the excimeric behavior, which must relate to a species that is stable exclusively in the excited state. Structure **2.2** cannot be such a species, because it shows free carboxylic groups and its ground state is lower in energy than that of structure **1** (Fig. 3A). Furthermore, when capped with C11 chains, structure **2.2** is too high in energy to be favorably formed in the excited state (fig. S10). We have thus considered two interacting aggregates, leading to larger structures involving four Au_8 cores, **4.1** and **4.2** in Fig. 3A. **4.1** has two almost intact staggered cores, whereas **4.2** shows a reconstruction of the two interacting cores, similar to **2.2**. Structure **4.1** is considerably less energetically stable than twice the energy of **2.1** (including entropic losses), whereas the formation of **4.2** is ~0.5 eV disfavored in the ground state but is favored by ~0.2 eV in the bright excited state (Fig. 3B). Neglecting further excited-state relaxation, we calculate that **4.2** should emit at 2.3 eV (2.0 eV) in the bright (lowest) excited state, and both of these values are consistent with the experimental data. A plausible excimer structure seems therefore related to a reconstructed Au_{8+8} metal core.

To validate the applicative potential of Au-pXs for cellular imaging and to assess their stability in biological media, we performed in vitro experiments on 3T3 fibroblast cells. Shown in Fig. 4, A and B, are bright-field and fluorescence images of cells stained with Au-pXs and with DAPI (4′,6-diamidino-2-phenylindole), and PKH-26 dyes, which respectively mark the nucleus and the cellular membrane. Because Au-pXs are not functionalized with target-specific ligands, they disperse in the cytoplasm. Fluorescence microscopy of cells with unstained nuclei confirmed the internalization of Au-pXs, producing excellent-quality images when using the green and red detection channels for Au-pXs and PKH-26, respectively (Fig. 4, C and D). In the absence of Au-pXs, only the red emission of PKH-26 was observed (Fig. 4, E and F).

To evaluate the cell viability and potential effects of Au-pXs on cellular biology, we performed the 3-(4,5-dimethylthiazol-2-yl)-2,5-diphenyltetrazolium bromide (MTT) assay and monitored the concentration of ROS over time. ROS are typically formed as byproducts of the oxygen metabolism. They play important roles in cell signaling and homeostasis (*26*), but they can become cytotoxic at high concentrations, causing damage to cell structures and possibly leading to cell death or apoptosis (*26*, *27*). Figure 4G shows the results of the MTT assay on cells stained with increasing concentrations of Au-pXs, showing that cell proliferation is unaffected by Au-pXs, except at the highest concentration. This staining level is orders of magnitude higher than that of standard biomarkers such as PKH-26 (~1 μM). The data shown in Fig. 4H reveal the beneficial effect of Au-pXs on the metabolisms of 3T3 cells, which, regardless of the cluster content, show a markedly lower ROS level relative to unstained cells. Furthermore, Au-pXs behave as ROS scavengers, reducing the ROS concentration by over a factor of 4 in cells incubated for 72 hours with the 1:50-diluted Au-pX solution. This effect was also observed in control experiments using a saturated aqueous solution of H_2O_2 (fig. S11). The ROS scavenging behavior of Au-pXs could be linked to the reported catalytic effect of Au_n on chemical and photochemical reactions involving oxygen (*28*, *29*), and it suggests potential applications for Au-pXs as fluorescent probes with therapeutic capability.

By using the capping ligands to control intermolecular interactions between metal quantum clusters, we have demonstrated a previously unknown aggregation state of matter that conveys the photophysics of excimers into stable self-standing

particles. This type of excited-state intermolecular aggregation adds a degree of freedom for designing colloidal metal nanostructures with electronic properties that are controllable at the supramolecular level, a property which, up until now, was exclusive to organic-based architectures. Bio imaging experiments performed on living cells highlight the biocompatibility of our structures and their ability to scavenge cytotoxic agents. The approach that we have demonstrated with Au clusters is not size- or composition-specific and could be applied to different metals or alloys, allowing the realization of permanent excimeric superstructures with predesigned optical and electronic properties.

REFERENCES AND NOTES

1. L. Zhang, E. Wang, *Nano Today* **9**, 132–157 (2014).
2. C.-A. J. Lin *et al.*, *ACS Nano* **3**, 395–401 (2009).
3. W. Qin, J. Lohrman, S. Ren, *Angew. Chem. Int. Ed.* **53**, 7316–7319 (2014).
4. L. Shang, S. Dong, G. U. Nienhaus, *Nano Today* **6**, 401–418 (2011).
5. A. Fernando, K. L. D. M. Weerawardene, N. V. Karimova, C. M. Aikens, *Chem. Rev.* **115**, 6112–6216 (2015).
6. F. Aldeek, M. A. H. Muhammed, G. Palui, N. Zhan, H. Mattoussi, *ACS Nano* **7**, 2509–2521 (2013).
7. J. Chen, Q.-F. Zhang, T. A. Bonaccorso, P. G. Williard, L.-S. Wang, *J. Am. Chem. Soc.* **136**, 92–95 (2014).
8. K. G. Stamplecoskie, P. V. Kamat, *J. Am. Chem. Soc.* **136**, 11093–11099 (2014).
9. F. Meinardi *et al.*, *Nat. Nanotechnol.* **10**, 878–885 (2015).
10. R. Jin, S. Egusa, N. F. Scherer, *J. Am. Chem. Soc.* **126**, 9900–9901 (2004).
11. Z. Wang, W. Cai, J. Sui, *ChemPhysChem* **10**, 2012–2015 (2009).
12. B. Santiago González *et al.*, *Nano Lett.* **10**, 4217–4221 (2010).
13. X. Huang *et al.*, *J. Phys. Chem. C* **116**, 448–455 (2012).
14. W. Guo, J. Yuan, E. Wang, *Chem. Commun.* **48**, 3076–3078 (2012).
15. T. A. C. Kennedy, J. L. MacLean, J. Liu, *Chem. Commun.* **48**, 6845–6847 (2012).
16. K. Pyo *et al.*, *J. Am. Chem. Soc.* **137**, 8244–8250 (2015).
17. H. Duan, S. Nie, *J. Am. Chem. Soc.* **129**, 2412–2413 (2007).
18. C.-C. Huang, Z. Yang, K.-H. Lee, H.-T. Chang, *Angew. Chem. Int. Ed.* **46**, 6824–6828 (2007).
19. X. Yang, M. Shi, R. Zhou, X. Chen, H. Chen, *Nanoscale* **3**, 2596–2601 (2011).
20. V. Venkatesh, A. Shukla, S. Sivakumar, S. Verma, *ACS Appl. Mater. Interfaces* **6**, 2185–2191 (2014).
21. J. Mei *et al.*, *Adv. Mater.* **26**, 5429–5479 (2014).
22. J. B. Birks, *Photophysics of Aromatic Molecules* (Wiley-Interscience, 1970).
23. J. R. Lakowicz, *Principles of Fluorescence Spectroscopy* (Springer, 2010).
24. J. Huang *et al.*, *Angew. Chem. Int. Ed.* **50**, 401–404 (2011).
25. J. Zheng, C. Zhang, R. M. Dickson, *Phys. Rev. Lett.* **93**, 077402 (2004).
26. J. M. Matés, J. A. Segura, F. J. Alonso, J. Márquez, *Arch. Toxicol.* **82**, 273–299 (2008).
27. W. Fiers, R. Beyaert, W. Declercq, P. Vandenabeele, *Oncogene* **18**, 7719–7730 (1999).
28. Y. Gao, N. Shao, Y. Pei, Z. Chen, X. C. Zeng, *ACS Nano* **5**, 7818–7829 (2011).
29. Z. Jiang *et al.*, *J. Phys. Chem. C* **111**, 12434–12439 (2007).

ACKNOWLEDGMENTS

This work is dedicated to the loving memory of Jon Mikel Azpiroz, colleague and friend. B.S.-G., F.M., R.L., and S.B. acknowledge support from the Cariplo Foundation (grants 2012-0844 and 2012-0920). S.B. thanks the European Commission's Seventh Framework Programme (FP7) for financial support under grant agreement no. 324603 (EDONHIST project). The data presented in this report are available upon request to S.B.

SUPPLEMENTARY MATERIALS

www.sciencemag.org/content/353/6299/571/suppl/DC1
Materials and Methods
Figs. S1 to S11
Tables S1 and S2
References (*30*–*40*)

17 February 2016; accepted 13 July 2016
10.1126/science.aaf4924

GRAPHENE

Tuning the valley and chiral quantum state of Dirac electrons in van der Waals heterostructures

J. R. Wallbank,[1,2] D. Ghazaryan,[2] A. Misra,[2] Y. Cao,[3] J. S. Tu,[3] B. A. Piot,[4] M. Potemski,[4] S. Pezzini,[5] S. Wiedmann,[5] U. Zeitler,[5] T. L. M. Lane,[1,2] S. V. Morozov,[2,6,7] M. T. Greenaway,[8] L. Eaves,[2,8] A. K. Geim,[3] V. I. Fal'ko,[1,2]* K. S. Novoselov,[1,2]* A. Mishchenko[1,2]*

Chirality is a fundamental property of electrons with the relativistic spectrum found in graphene and topological insulators. It plays a crucial role in relativistic phenomena, such as Klein tunneling, but it is difficult to visualize directly. Here, we report the direct observation and manipulation of chirality and pseudospin polarization in the tunneling of electrons between two almost perfectly aligned graphene crystals. We use a strong in-plane magnetic field as a tool to resolve the contributions of the chiral electronic states that have a phase difference between the two components of their vector wave function. Our experiments not only shed light on chirality, but also demonstrate a technique for preparing graphene's Dirac electrons in a particular quantum chiral state in a selected valley.

The chiral properties of Dirac electrons in monolayer graphene (*1*–*3*) (and the Berry phase π associated with them) have been used to explain Klein tunneling, the absence of backscattering in graphene p-n junctions (*4*–*6*), specific features in weak localization (*7*, *8*), a peculiar Landau-level spectrum (in which one level is pinned exactly at the Dirac point, leading to the "half-integer" quantum Hall effect) (*1*, *2*), and valley selection of the interband transitions excited by polarized light (*9*). Chirality is determined by the relative phase in the two-component wave function of the Dirac quasi-particles, which arises from the sublattice composition in graphene (*3*) and from spin states in topological insulators (*10*). Such a two-component wave function is typically described in terms of a specific vector—the pseudospin—which, for chiral particles, is locked to their direction of motion. However, it has proved difficult to image directly the chirality and the pseudospin polarization in electrical or optical measurements. To date, the phase shift in the sublattice composition of the electron states in graphene has been detectable only by angle-resolved photoemission spectroscopy (*11*–*13*).

Here, we report an alternative technique for pseudospin and chirality detection that is based on tunneling of electrons in van der Waals (vdW) heterostructures (*14*, *15*) in which graphene (Gr) and hexagonal boron nitride (hBN) are stacked in a multilayer structure (Fig. 1A). In these devices, it has been shown that the exceptionally high quality of graphene, provided by its encapsulation, allows the electrons to tunnel between graphene electrodes with conservation of in-plane momentum (*16*, *17*), making one graphene electrode a bias voltage (V_b)–tunable spectrometer for electrons emitted by the other. However, the usual tunneling formalism, which does not take into account the interference between the two components of the wave function of the tunneling electrons, fails in the case of chiral quasi-particles. Here, we show that the tunneling current-voltage characteristics $I(V_b,B)$, in the presence of an in-plane magnetic field B (*18*), essentially depend on the pseudospin orientation and enable detection of the valley sublattice structure determined by the relative phase between the two sublattice components of the Dirac spinor vector wave function of electrons in graphene.

A small misalignment angle between the crystalline lattices of the two graphene flakes (Fig. 1E) causes specific parts of $I(V_b,B)$ to arise from the tunneling of electrons in specific regions of momentum space. Furthermore, for the case of chiral electrons, different states in momentum space (and thus with specific pseudospin orientation) have different tunneling probability—depending on whether the interference between the two components of electron wave function is constructive (Fig. 1, B to D) or destructive (Fig. 1, F to H) as electrons tunnel out of the emitting graphene layer (*19*). A particular state can be chosen

[1]National Graphene Institute, University of Manchester, Manchester M13 9PL, UK. [2]School of Physics and Astronomy, University of Manchester, Manchester M13 9PL, UK. [3]Centre for Mesoscience and Nanotechnology, University of Manchester, Manchester M13 9PL, UK. [4]Laboratoire National des Champs Magnétiques Intenses, LNCMI-CNRS-UGA-UPS-INSA-EMFL, 25 avenue des Martyrs, 38042 Grenoble, France. [5]High Field Magnet Laboratory (HFML-EMFL) and Institute of Molecules and Materials, Radboud University, Nijmegen, 6525 ED, Netherlands. [6]Institute of Microelectronics Technology and High Purity Materials, RAS, Chernogolovka 142432, Russia. [7]National University of Science and Technology "MISiS", 119049, Leninsky pr. 4, Moscow, Russia. [8]School of Physics and Astronomy, University of Nottingham, Nottingham NG7 2RD, UK.
***Corresponding author. Email: vladimir.falko@manchester.ac.uk (V.I.F.); kostya@manchester.ac.uk (K.S.N.); artem.mishchenko@manchester.ac.uk (A.M.)**

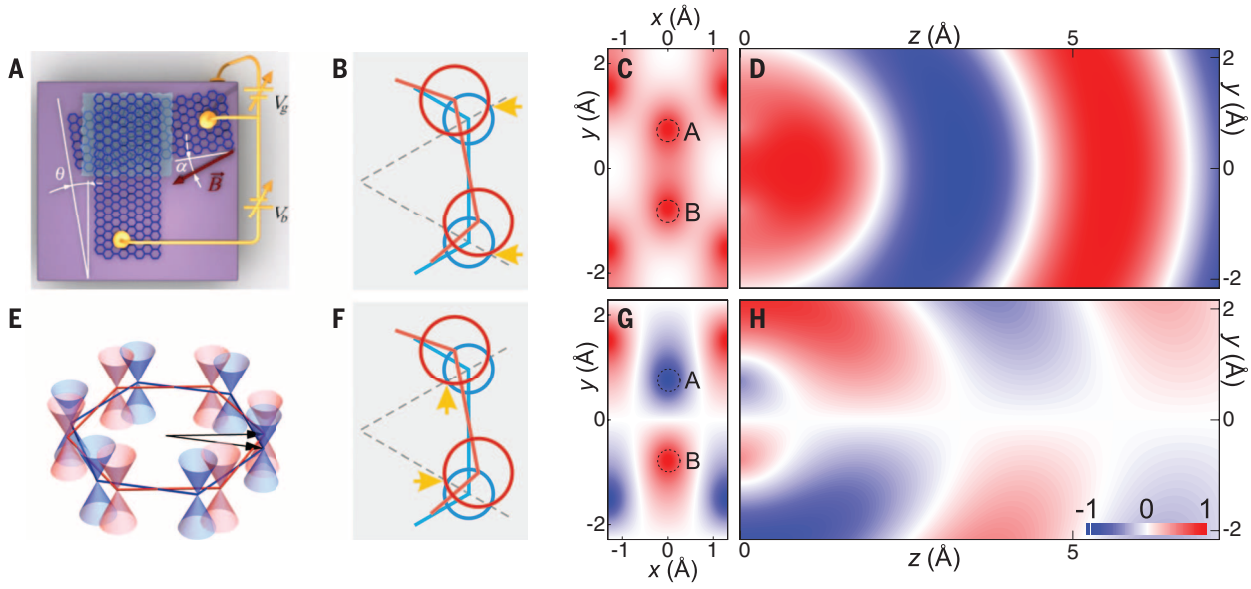

Fig. 1. Device schematics, band structure, and chiral composition of the wave function. (**A**) Schematic diagram of the Si/SiO_2/Gr/hBN/Gr device (dark blue hexagonal layers are graphene electrodes; light blue, hBN; purple, Si/SiO_2 back gate). The gate voltage V_g is applied between the bottom graphene and Si substrate. (**B**) Two corners of the BZ [the full BZ is shown in (E)] schematically demonstrating the Fermi surfaces for emitter (blue circles) and collector (red circles). Yellow arrows mark the states in the emitter when the components of the wave function on the two sublattices are in phase [shown in (C)]. (**C**) Real-space distribution of the real part of the wave function on the A and B sublattices. The two components of the wave function are in phase. (**D**) Schematic representation of the interference of the two-component wave function of graphene electron at the given distance above the graphene layer when the electron is taken away from graphene. The original electron state at $z = 0$ is as in (C). (**E**) Small-angle rotational misalignment between the two graphene crystals leads to a small momentum mismatch between the two band structures in the reciprocal space. (**F**) Same as (B). Yellow arrows mark the states in the emitter when the components of the wave function on the two sublattices are out of phase [shown in (G)]. (**G**) Real-space distribution of the real part of the wave function on the A and B sublattices. The two components of the wave function are out of phase. (**H**) Same as in (D), but when the original electron state at $z = 0$ is as in (G). Color scales for (C), (D), (G), and (H) are the same.

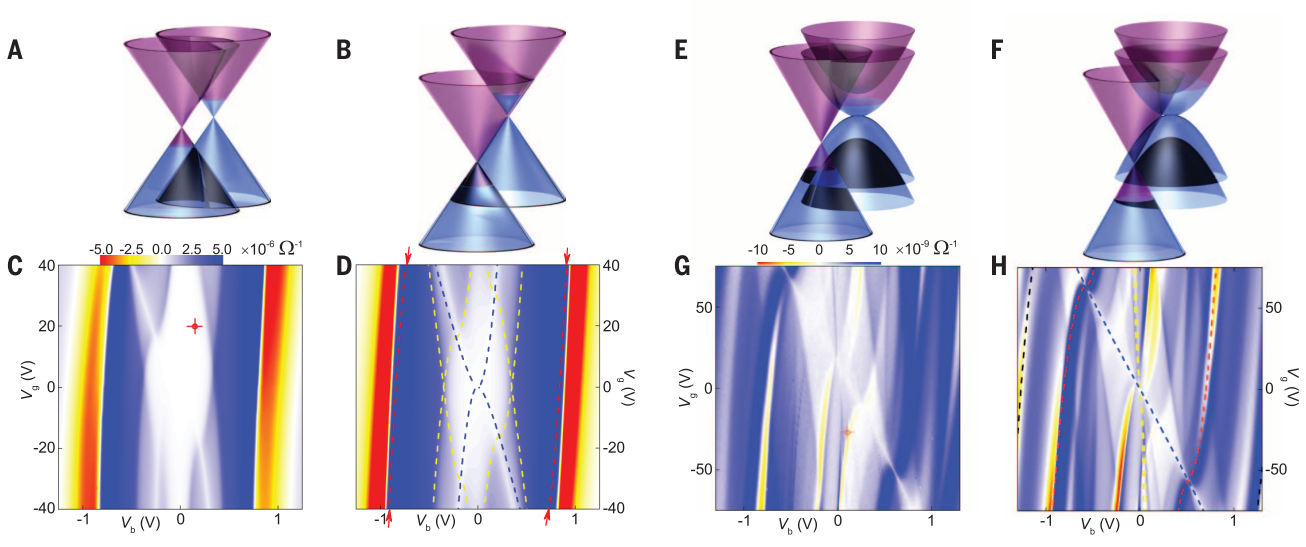

Fig. 2. Tunneling characteristics of our devices. (**A** and **B**) Relative position of the bands and the Fermi levels in the two graphene electrodes rotated by a small angle with respect to each other for conditions highlighted by yellow (A) and red (B) dashed lines in (D). Red dashed lines in (D) are also marked by red arrows for clarity. (**C** and **D**) Experimental (C) and simulated (D) tunneling characteristics for a Gr/3hBN/Gr device with the graphene electrodes misaligned by 1.8°. The red cross in (C) marks the V_b and V_g used for the calculations of chirality polarization in Fig. 4, C to I. The blue dashed lines in (D) and (H) mark the conditions when the Fermi level in one of the electrodes passes through the Dirac point where the DOS is zero, which leads to the suppression of tunneling conductance. (**E** and **F**) Relative position of the bands and the Fermi levels in the Gr and BGr electrodes rotated by a small angle with respect to each other for the resonant conditions highlighted by red (E) and black (F) dashed lines in (H). In (E), the low-energy subband in the valence band in bilayer graphene touches the graphene cone. In (F), the higher-energy subband in the valence band in bilayer graphene touches the graphene cone. (**G** and **H**) Experimental (G) and simulated (H) tunneling characteristics for a Gr/5hBN/BGr device with the graphene electrodes misaligned by 0.5° (a small part of the sample is misaligned by 3°, which explains some of the weaker features). The yellow dashed lines mark the resonance when the Fermi level in monolayer graphene touches the bottom (top) of the conduction (valence) band in the bilayer graphene. The red cross in (G) marks the V_b and V_g used for the calculations of chirality polarization in Fig. 4, M to R.

with the help of a magnetic field, applied perpendicular to the current. This provides the electrons with a tunable momentum boost as they traverse the barrier [as shown previously in studies of vertical transport in III-V semiconductor heterostructures (*20*, *21*)]. For graphene, by rotating the magnetic field in the plane of the Gr/hBN/Gr device, we can resolve the contributions to the measured differential conductance, $G = \partial I/\partial V_b$, arising from electrons with clearly identifiable momenta in a given valley of graphene's band structure, and hence detect the features related to the sublattice composition of the electronic wave functions.

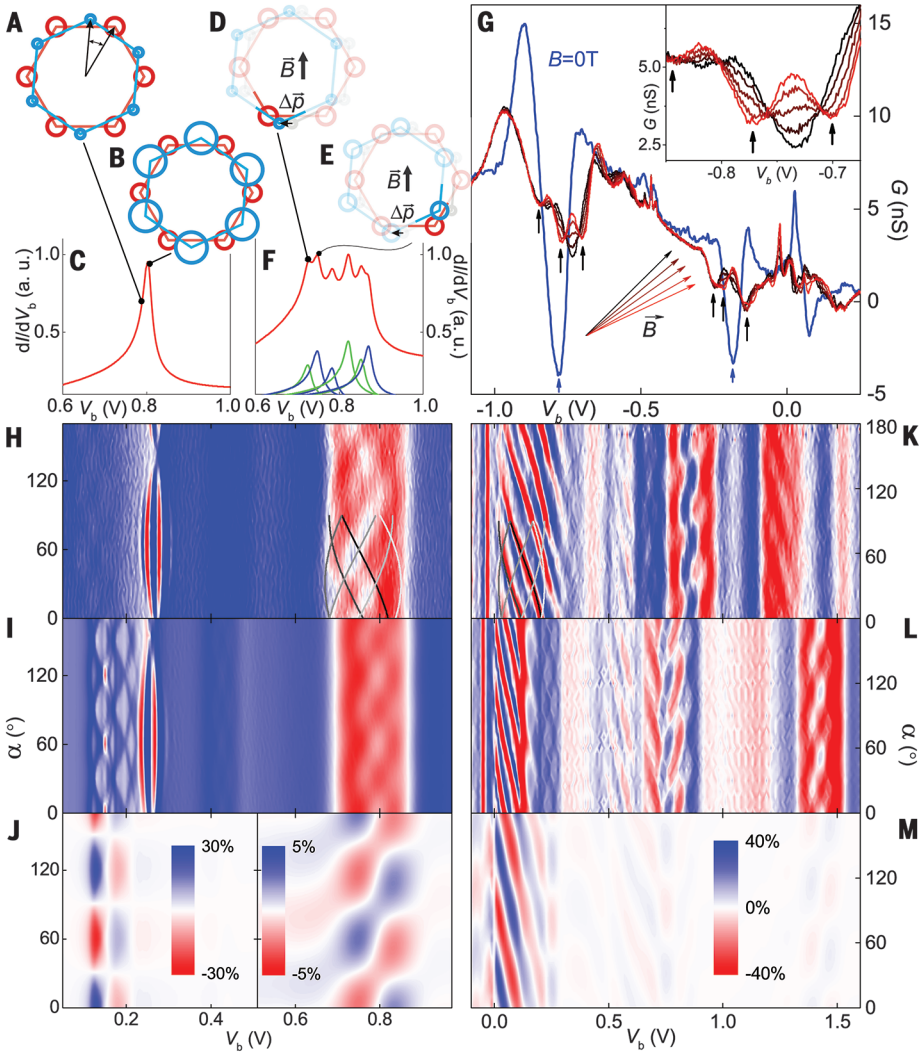

Fig. 3. Magnetotunneling characteristics of studied devices. (**A**) Schematic representation of the BZ for the emitter (blue) and collector (red) graphene electrodes rotated by a small angle with respect to each other. Circles represent the Fermi surfaces in the two graphene layers. (**B**) As in (A) but with increased Fermi level in the emitter, which induces resonant condition of the type presented in Fig. 2A for all six corners of the BZ simultaneously. (**C**) Resonance in dI/dV_b corresponding to (B). (**D**) As in (A) but with B applied parallel to graphene layers. The Lorentz force leads to an additional momentum acquired by electrons when tunneling from the emitter to the collector, which can be represented by a relative shift of the two BZs by the vector $\Delta\vec{p}$ (gray, the BZ in $B = 0$; blue, in finite B). This can bring different corners of the BZ into resonance, depending on α. (**E**) As in (D) but at different doping (increased Fermi level in the emitter), which brings a different corner of the BZ into resonance. (**F**) The resonant peak in dI/dV_b splits into six peaks in finite magnetic field (red curve), each corresponding to a resonance that occurs in each corner of the BZ (green and blue curves for K and K′ valleys, respectively). Examples for particular resonant conditions for two corners of the BZ are shown in (D) and (E). (**G**) Conductance of the Gr/5hBN/BGr device at $V_g = -45$ V for $B = 0$T (blue) and 30 T for α increasing from 0° in 5° steps (black to red). Note that some minima (marked by short blue arrows) are split by the magnetic field (black arrows); see enlarged inset. (**H** and **I**) dG/dV_b versus V_b and α for the Gr/3hBN/Gr device with $V_g = 20$ V. (**K** and **L**) dG/dV_b versus V_b and α for Gr/5hBN/BGr device with $V_g = 60$ V. (H) and (K), experimental data; (I) and (L), theory. The six black, gray, and white lines in (H) and (K) are guides to the eye and mark the position of the resonances for the six corners of the BZ. (**J** and **M**) Calculated valley polarization of tunneling current for Gr/3hBN/Gr (J) and Gr/5hBN/BGr (M) devices. Note different color scales for $V_b < 0.5$ V and $V_b > 0.5$ V in (J).

In the series of vdW heterostructures studied here, a tunnel barrier of hBN separates a graphene monolayer from either a monolayer or a bilayer of graphene. During preparation, we ensure that the crystallographic orientations of the two graphene electrodes are closely aligned (Fig. 1A), by aligning the edges of the flakes in the transfer procedure [for details, see (*19*, *22*)]. The devices are placed on the oxidized surface of a doped silicon substrate, which forms an insulated back gate electrode, as in previously reported graphene tunneling transistors (*16*, *17*, *23*). The two types of multilayer stack are thus of the form Si/SiO_2/hBN/Gr/N-hBN/(B)Gr/hBN, where (B)Gr denotes (bilayer) graphene and N-hBN denotes N layers of hBN. The typical active areas of our devices are between 10 and 100 μm^2.

Typical plots of G versus V_b, and back gate voltage, V_g, for the Gr/3hBN/Gr and Gr/5hBN/BGr devices are presented in Fig. 2 [see examples of other aligned devices in (*19*)]. In these aligned devices, a number of resonant features in the tunneling $I(V_b)$ characteristics are observed, such as when the Fermi level in one layer coincides with the lowest energy at which the band dispersion curves of the two layers intersect (Fig. 2A). Schematic representations of some of these resonant alignment conditions are shown in Fig. 2, with more details given in (*19*). These resonances are absent in the devices in which the graphene electrodes are strongly misaligned; for these devices, momentum conservation is satisfied by elastic scattering and/or phonon emission (*19*, *24*–*26*).

There are qualitative differences in the tunneling conductance plots of the Gr/hBN/Gr and Gr/hBN/BGr devices mainly due to (i) the difference in the density of states (DOS) between graphene (DOS is linear with energy) and bilayer graphene (DOS is independent of energy) and (ii) the presence of the second subband in bilayer graphene. Thus, the difference in DOS leads to most features in the conductivity plot for Gr/hBN/Gr having a square-root dependence in the V_b-V_g plane, whereas some of these features are linear for the Gr/hBN/BGr devices (compare blue dashed lines in Fig. 2, D and H). Also, the presence of the second subband in the bilayer roughly doubles the number of the observed resonances.

To gain further insight, we computed the tunnel conductance using a previously developed model of the device electrostatics (*16*, *23*) and a chiral tunneling formalism (*27*). The only free parameters in the model are the relative angle between the crystallographic directions of the graphene flakes and the energy broadening of their plane wave states. By comparing the experimental and calculated results in Fig. 2, we can extract the relative orientation angle between the two graphene flakes, which we find to cover the range 0.5° to 3° for the group of devices that we studied.

A strong magnetic field, ~30 T, applied parallel to the graphene layers gives rise to additional

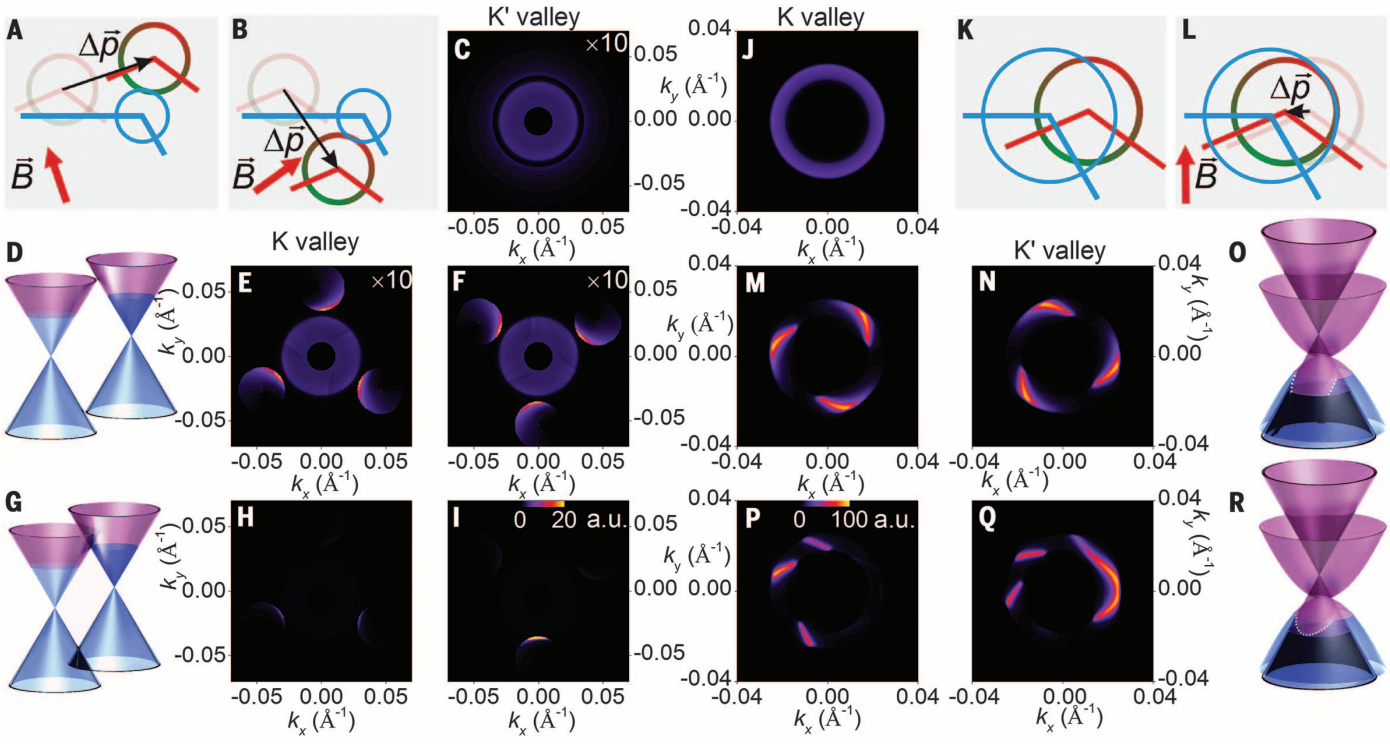

Fig. 4. Calculated tunneling of chirality-polarized electrons. (**A**) Schematic representation of a resonant condition for tunneling between two graphene electrodes in a magnetic field. The gradient coloring of the Fermi surface in the collector represents a particular phase difference φ between the wave function components (green: φ = π; red: φ = 0). Similar coloring for the emitter is omitted for simplicity. (**B**) As in (A) but for a different orientation of magnetic field. States with different φ than in (A) are now in resonance. (**C**) Contribution of different states in the K′ valley of the graphene emitter to the current for the Gr/3hBN/Gr device with V_b = 0.13 V, V_g = 20 V and B = 0 T (marked by a red cross in Fig. 2C) for the case of infinitely short elastic scattering time (inelastic tunneling). States with all orientations of momentum contribute equally to tunneling. The situation in the K valley is the same, and the color scale is enhanced by ×10 compared to (H) and (I). (**D**) Relative position of the Fermi energies in the two graphene electrodes for V_b = 0.13 V and V_g = 20 V at B = 0 T. (**E** and **F**) The contribution of different states in the K valley or K′ valley of the graphene emitter to the current for the conditions presented in (D). No resonant conditions are achieved, so the small current observed in (E) and (F) is a consequence of the energy broadening of states [color scale enhanced by ×10 compared to (H) and (I)]. (**G** to **I**) Similar to (D) to (F) except with B = 30 T. Resonant conditions are now achieved in the K′ valley only [depicted in (G)], which is reflected by the current distribution in (I). (**J** to **R**) Similar to (A) to (I) except for the Gr/5hBN/BGr device at V_b = 0.045 V and V_g = −30 V (marked by a red cross in Fig. 2G), with either B = 0 T [(J), (K), (M), (N), and (O)] or B = 30 T [(L), (P), (Q), and (R)]. There is no enhancement of the color scale between [(J), (M), and (N)] and [(P) and (Q)]. The resonant states in (O) and (R) are highlighted with dashed white lines. Only one of the two lines of resonant states in (O) produces a visible contribution to the tunneling current [(M) and (N)]. This can be traced by using the phase information in (K): For the lower intersection of the two Fermi lines, the interference between wave function components is destructive (green).

fine structure in G (Fig. 3G), which is strongly dependent on the angle between B and the principal axes of the graphene crystals. This is best revealed in the $G' \equiv \partial G/\partial V_b$ plots (Fig. 3, H and K), with further examples presented in (*19*). The angular dependence of these features corresponds to six intertwined sinusoids.

The origin of this fine structure is explained in Fig. 3, A to F. In zero magnetic field, all six corners of the Brillouin zone (BZ) experience resonance conditions simultaneously, leading to a single resonance peak (Fig. 3, A to C, where an example is given for the resonant alignment, similar to the "touch" depicted in Fig. 2A). In a finite magnetic field, the tunneling electrons experience a Lorentz force and gain an in-plane momentum boost, given by

$$\Delta\vec{p} = ed\hat{z} \times \vec{B}$$

Here, $\hat{z}$ is a unit vector in the tunneling direction, e is the electron charge, and d is the thickness of the hBN tunneling barrier. In Fig. 3, D and E, this is represented as a relative shift of the two BZs, additional to the rotation arising from the small angular misalignment of the two graphene layers. Hence, depending on the orientation of magnetic field, the resonant conditions for the six corners of the BZ are fulfilled at six slightly different voltages, leading to the splitting of the resonance peak into six individual peaks. The V_b value required for resonance at each particular corner is a sinusoidal function of the angle α between B and the "armchair" direction of the graphene lattice: $V_b(B,\alpha,j) \approx V_b(B = 0) + \Delta V(B,\alpha)\sin(\alpha + j\pi/3)$, where j = 0,1…5 is the index of a particular BZ corner (as shown by grayscale-colored lines in Fig. 3, H and K). Our theoretical model provides a very good fit to our experimental results (Fig. 3, I and L).

The intensities of these resonances also depend on α, so only half of the period of the sinusoid is visible (Fig. 3, H, I, K, and L). This is particularly obvious in Fig. 3, K and L, for the resonance between V_b = 0 and 0.25 V. This asymmetry arises from the electronic chirality of graphene. The electron wave function is a vector with two components, ψ_A and ψ_B, representing the probability of finding the electron on the two sublattices, A and B, of the honeycomb lattice. Chirality is the specific property of the relative phase φ between the wave-function components, which is locked to the direction of the electron's momentum, $\vec{p} = p(\cos\vartheta, \sin\vartheta)$, counted from the nearest BZ corner. For a monolayer $\varphi = \vartheta$; for gapless bilayer graphene, it would be $\varphi = 2\vartheta$ for A/B' sublattices supporting low-energy bands.

Electron tunneling from one graphene layer to another requires a correlation between the two components of the wave function in both layers. In effect, this projects the wave function in the graphene emitter and collector onto evanescent waves in the barrier space between two two-dimensional (2D) crystals (in case of bilayer graphene, we project only the wave functions located on the layer closest to the hBN tunneling barrier).

The projected states are composed of two sublattice components in the emitter and collector. As a result, momentum-dependent constructive ($\varphi_{e(c)} = 0$) or destructive ($\varphi_{e(c)} = \pi$) interference between sublattice components is governed by $|\psi_A + \psi_B|^2 \propto 1 + \cos\varphi_{e(c)}$, for the states both in emitter (φ_e) and collector (φ_c) and manifests itself in the tunneling characteristics $I(V_b)$. Because the magnetic field selects the pairs of particular plane wave states probed by tunneling at a particular gate or bias voltage (Fig. 4, A and B), the measured asymmetry provides a direct visualization of the pseudospin polarization of the Dirac fermions.

In the presence of the magnetic field, each resonance peak represents tunneling from a particular corner of the BZ. This allows one to inject electrons with a particular valley polarization, and from a selected corner of the BZ. We use the experimental parameters to calculate the amount of polarization achieved in our experiment (Fig. 3, J and M), and estimate that the valley polarization, $P = (I_K - I_{K'})/(I_K + I_{K'})$ [where $I_K(I_{K'})$ is the current injected into the K(K′) valley] can be as high as 30% (40%) for the particular Gr/3hBN/Gr (Gr/5hBN/BGr) devices. The main limit to the degree of polarization is the energy broadening of states at the Fermi levels caused by inelastic tunneling processes. However, even for the current level of disorder, with the resonances at around $V_b \approx 0$ V (e.g., resonances marked by yellow dashed lines on Fig. 2D at $V_g > 50$ V), which maximizes the number of states participating in tunneling and sensitive to magnetic field, a polarization close to 75% could be achieved (*19*). By using devices with smaller misalignment between the graphene electrodes [on the order of 0.2°, now within the reach of the current technology (*19*)], valley polarization close to 100% is possible (*19*).

The same mechanism can also be used to select electrons with a particular pseudospin polarization. In Fig. 4, C to R, we present results of a calculation of the contribution of different electronic states in k-space to the tunnel current for the Gr/3hBN/Gr (Fig. 4, C to I) and Gr/5hBN/BGr (Fig. 4, J to R) devices. We choose the position of the Fermi levels in the emitter and collector to be very close to a resonance at $B = 0$ T. Then, for certain directions of B, the resonant conditions are achieved only in one valley and for only a very narrow distribution in k-space (Fig. 4, G to I). Tunneling of the electrons from other parts of k-space is prohibited either because they are off-resonance or because of the pseudospin selection rule. Alternatively, for the Gr/5hBN/BGr device and exploiting the difference in curvature of monolayer and bilayer electronic bands, we can choose the overlap between the bands in such a way that the magnetic field reduces the overlap in one valley and increases it for the other (Fig. 4, M to R). In this case, momentum conservation at $B = 0$ T is fulfilled for the states marked by white dashed lines (Fig. 4O). However, only one of those lines contributes to tunneling, owing to pseudospin interference (Fig. 4, M and N).

Our technique, which enables tunneling of valley-polarized electrons in monolayer and bilayer graphene, also allows one to selectively inject carriers propagating in the same direction and to probe pseudospin-polarized quasi-particles. In principle, the technique can be extended to tunneling devices in which surface states of topological insulators are used as electrodes; then, all-electrical injection of spin-polarized current (*28*) with non-invasive tunneling contacts could reveal a number of exciting phenomena (*29*–*31*).

REFERENCES AND NOTES

1. K. S. Novoselov *et al*., *Nature* **438**, 197–200 (2005).
2. Y. Zhang, Y. W. Tan, H. L. Stormer, P. Kim, *Nature* **438**, 201–204 (2005).
3. A. H. Castro Neto, F. Guinea, N. M. R. Peres, K. S. Novoselov, A. K. Geim, *Rev. Mod. Phys.* **81**, 109–162 (2009).
4. M. I. Katsnelson, K. S. Novoselov, A. K. Geim, *Nat. Phys.* **2**, 620–625 (2006).
5. M. I. Katsnelson, *Eur. Phys. J. B* **51**, 157–160 (2006).
6. A. F. Young, P. Kim, *Nat. Phys.* **5**, 222–226 (2009).
7. F. V. Tikhonenko, D. W. Horsell, R. V. Gorbachev, A. K. Savchenko, *Phys. Rev. Lett.* **100**, 056802 (2008).
8. E. McCann *et al*., *Phys. Rev. Lett.* **97**, 146805 (2006).
9. M. L. Sadowski, G. Martinez, M. Potemski, C. Berger, W. A. de Heer, *Phys. Rev. Lett.* **97**, 266405 (2006).
10. X. L. Qi, S. C. Zhang, *Rev. Mod. Phys.* **83**, 1057–1110 (2011).
11. S. Y. Zhou *et al*., *Nat. Phys.* **2**, 595–599 (2006).
12. A. Bostwick, T. Ohta, T. Seyller, K. Horn, E. Rotenberg, *Nat. Phys.* **3**, 36–40 (2007).
13. M. Mucha-Kruczyński *et al*., *Phys. Rev. B* **77**, 195403 (2008).
14. A. K. Geim, I. V. Grigorieva, *Nature* **499**, 419–425 (2013).
15. G. H. Lee *et al*., *Appl. Phys. Lett.* **99**, 243114 (2011).
16. A. Mishchenko *et al*., *Nat. Nanotechnol.* **9**, 808–813 (2014).
17. B. Fallahazad *et al*., *Nano Lett.* **15**, 428–433 (2015).
18. L. Pratley, U. Zulicke, *Phys. Rev. B* **88**, 245412 (2013).
19. Supplementary materials are available on *Science* Online.
20. R. K. Hayden *et al*., *Phys. Rev. Lett.* **66**, 1749–1752 (1991).
21. V. I. Fal'ko, S. V. Meshkov, *Semicond. Sci. Technol.* **6**, 196–200 (1991).
22. A. V. Kretinin *et al*., *Nano Lett.* **14**, 3270–3276 (2014).
23. L. Britnell *et al*., *Science* **335**, 947–950 (2012).
24. F. Amet *et al*., *Phys. Rev. B* **85**, 073405 (2012).
25. S. Jung *et al*., *Sci. Rep.* **5**, 16642 (2015).
26. E. E. Vdovin *et al*., *Phys. Rev. Lett.* **116**, 186603 (2016).
27. T. L. M. Lane, J. R. Wallbank, V. I. Fal'ko, *Appl. Phys. Lett.* **107**, 203506 (2015).
28. C. H. Li *et al*., *Nat. Nanotechnol.* **9**, 218–224 (2014).
29. D. Culcer, E. H. Hwang, T. D. Stanescu, S. Das Sarma, *Phys. Rev. B* **82**, 155457 (2010).
30. O. V. Yazyev, J. E. Moore, S. G. Louie, *Phys. Rev. Lett.* **105**, 266806 (2010).
31. D. Pesin, A. H. MacDonald, *Nat. Mater.* **11**, 409–416 (2012).

ACKNOWLEDGMENTS

This work was supported by the European Union FP7 Graphene Flagship Project 604391, European Research Council Synergy Grant, Hetero2D, Engineering and Physical Sciences Research Council (EPSRC) (Toward Engineering Grand Challenges and Fellowship programs), the Royal Society, U.S. Army Research Office, U.S. Navy Research Office, and U.S. Air Force Office of Scientific Research. M.T.G acknowledges support from the Leverhulme Trust. A.M. acknowledges support of EPSRC Early Career Fellowship EP/N007131/1. S.V.M. was supported by NUST "MISiS" (grant K1-2015-046) and Russian Foundation for Basic Research (RFBR15-02-01221 and RFBR14-02-00792). Measurements in high magnetic field were supported by High Field Magnet Laboratory–Radboud University/Foundation for Fundamental Research on Matter (HFML-RU/FOM) and Laboratoire National des Champs Magnétiques Intenses–Centre National de la Recherche Scientifique (LNCMI-CNRS), members of the European Magnetic Field Laboratory (EMFL), and by EPSRC (UK) via its membership to the EMFL (grant no. EP/N01085X/1).

SUPPLEMENTARY MATERIALS

www.sciencemag.org/content/353/6299/575/suppl/DC1
Materials and Methods
Supplementary Text
Figs. S1 to S9
References (*32*–*49*)

11 February 2016; accepted 13 July 2016
10.1126/science.aaf4621

ARCHAEOLOGY

Outburst flood at 1920 BCE supports historicity of China's Great Flood and the Xia dynasty

Qinglong Wu,[1,2,3]*† Zhijun Zhao,[2,13] Li Liu,[4]‡ Darryl E. Granger,[5] Hui Wang,[6] David J. Cohen,[7]‡ Xiaohong Wu,[1] Maolin Ye,[6] Ofer Bar-Yosef,[8] Bin Lu,[9] Jin Zhang,[10] Peizhen Zhang,[3,14]§ Daoyang Yuan,[11] Wuyun Qi,[6] Linhai Cai,[12] Shibiao Bai[2,13]

China's historiographical traditions tell of the successful control of a Great Flood leading to the establishment of the Xia dynasty and the beginning of civilization. However, the historicity of the flood and Xia remain controversial. Here, we reconstruct an earthquake-induced landslide dam outburst flood on the Yellow River about 1920 BCE that ranks as one of the largest freshwater floods of the Holocene and could account for the Great Flood. This would place the beginning of Xia at ~1900 BCE, several centuries later than traditionally thought. This date coincides with the major transition from the Neolithic to Bronze Age in the Yellow River valley and supports hypotheses that the primary state-level society of the Erlitou culture is an archaeological manifestation of the Xia dynasty.

China's earliest historiographies, including *Shujing* (*Book of Documents*) and *Shiji* (*Records of the Grand Historian*, by Sima Qian), tell of the Great Flood, a lengthy, devastating flood of the Yellow River. The culture hero Yu eventually tamed this flood by dredging, earning him the divine mandate to establish the Xia dynasty, the first in Chinese history, and marking the beginning of Chinese civilization. Because these accounts laid

the ideological foundations for the Confucian rulership system, they had been taken as truth for more than 2500 years until challenged by the "Doubting Antiquity School" in the 1920s. Within a decade, archaeological excavations demonstrated the historicity of the second dynasty, Shang, and the search for similar evidence for Xia began (*1*, *2*). Archaeological fieldwork since the 1950s on the Early Bronze Age Erlitou culture (~1900 to 1500 BCE) has led many scholars to associate it with the Xia (*1*–*6*) because it overlaps with the spatial and temporal framework of the Xia dynasty. Traditionally, historians have dated the start of Xia to ~2200 BCE, whereas the government-sponsored Xia-Shang-Zhou Chronology Project adopted the date as 2070 BCE (*5*), leaving a chronological gap in associating Erlitou with Xia (*7*–*9*). Other scholars see Xia purely as a myth fabricated to justify political succession (*10*, *11*).

Scholars also have long sought a scientific explanation of the Great Flood (*12*–*14*), with even Lyell mentioning it (*15*), yet no evidence for it has been discovered. Here, we present geological evidence for a catastrophic flood in the early second millennium BCE and suggest that it may be the basis of the Great Flood, thereby lending support to the historicity of the Xia dynasty. The evidence found in our investigations along the Yellow River in Qinghai Province includes remains of a landslide dam, dammed lake sediments (DLS) upstream, and outburst flood sediments (OFS) downstream (Fig. 1 and figs. S1 to S5) that allow us to reconstruct the size of the lake and flood (*16*).

Field observations (fig. S2B) show that the ancient landslide dam deposits reach an elevation of 240 m above present river level (arl) and stretch for 1300 m (fig. S2A) along Jishi Gorge (Figs. 1A and 3A). We estimate that the saddle of the dam would have been 30 to 55 m lower than the highest preserved remnants, so the lake would have filled to an elevation of 185 to 210 arl [2000 to 2025 m above sea level (asl)] (fig. S2B), impounding 12 to 17 km^3 of water (*16*) (table S1). Based on typical river discharge values, the dam would have completely blocked the Yellow River for 6 to 9 months before overtopping (*16*). DLS distributed widely upstream of the dam are up to 30 m thick and have a highest elevation of ~1890 m asl (Fig. 1B and figs. S1 and S3A). We interpret this as indicating that the catastrophic breach dropped the water level 110 to 135 m (Fig. 1B), releasing ~11.3 to 16 km^3 of water (*16*) (table S1), tens of times that estimated by a previous study (*17*). After the breach, DLS infilled a residual lake behind the lowest part of the dam that remained.

Outburst flood sediments are found downstream at elevations from 7 to 50 m arl in the lower Jishi Gorge and in Guanting Basin (Fig. 1 and figs. S1 and S4). They are characterized by high-concentration suspension deposition and consist exclusively of angular clasts of greenschist and purple-brown mudrock sourced from Jishi Gorge (table S2). At the mouth of the gorge, where the Yellow River enters Guanting Basin, the sediments reach 20 m thickness and include boulders up to 2 m in diameter (Fig. 1B and figs. S1 and S4, C and D). We also identified the OFS at the earthquake-destroyed prehistoric Lajia site (fig. S5), a settlement of the Qijia culture (*18*, *19*) known for its early noodle remains (*20*), 25 km downstream from the dam. OFS at Lajia covered the settlement's last Qijia culture occupation and filled in collapsed cave dwellings (fig. S5, A and B), pottery vessels (fig. S5B), and earthquake fissures (fig. S5C), mixing with pottery sherds (fig. S5D) and other Qijia cultural materials, with heights of up to 38 m arl.

Stratigraphic relationships of the OFS, remnant dam, DLS, loess, and other deposits in Jishi Gorge and neighboring basins, along with destruction features at the Lajia site (fig. S1), allow us to reconstruct and date a sequence of events ending in the outburst flood. First, they show that the damming and outburst flood event occurred during the archaeological Qijia culture period (~2300 to 1500 BCE) after the collapse of the Lajia cave-houses. Ground fissures caused by the earthquake at the Lajia site were entirely filled with OFS (fig. S5C) before silts from surface runoff during the annual rains could enter them, indicating that the outbreak flood must have occurred less than 1 year after the earthquake and collapse of the houses. It is likely that the same earthquake that destroyed Lajia also triggered the landslide that dammed the river, along with widespread contemporaneous rock avalanches whose deposits lay directly beneath the DLS (fig. S3A).

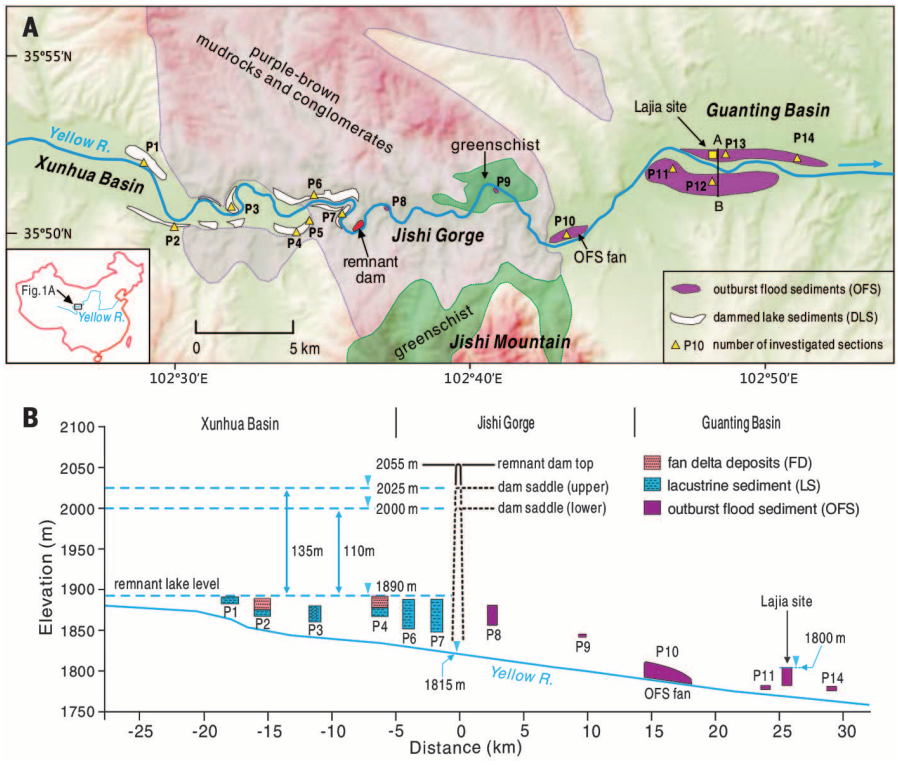

Fig. 1. Evidence of the exceptional outburst flood in the upper valley of the Yellow River. (**A**) Distributions of OFS, DLS, and landslide dam. Light purple and dark green shaded areas indicate purple-brown mudrock and greenschist, respectively. Line AB across the Lajia site shows the location of the reconstructed cross section in fig. S6C. (**B**) The vertical distribution of the OFS, landslide dam, DLS, Lajia site and reconstructed lake levels relative to the longitudinal profile of the present Yellow River. DLS are classified into lacustrine sediments (LS) and fan delta deposits (FD).

[1]School of Archaeology and Museology, Peking University, Beijing 100871, China. [2]School of Geography Science, Nanjing Normal University, Nanjing 210023, China. [3]State Key Laboratory of Earthquake Dynamics, Institute of Geology, China Earthquake Administration, Beijing 100029, China. [4]Department of East Asian Languages and Cultures, Stanford University, Stanford, CA 94305, USA. [5]Department of Earth, Atmospheric, and Planetary Sciences, Purdue University, West Lafayette, IN 47907, USA. [6]Institute of Archaeology, Chinese Academy of Social Sciences, Beijing 100710, China. [7]Department of Anthropology, National Taiwan University, Taipei 10617, Taiwan (R.O.C). [8]Department of Anthropology, Harvard University, Cambridge, MA 02138, USA. [9]CCTEG Xi'an Research Institute, Xi'an 710077, China. [10]Institute of Geology, Chinese Academy of Geological Sciences, Beijing 100037, China. [11]Lanzhou Institute of Seismology, China Earthquake Administration, Lanzhou 730000, China. [12]Qinghai Provincial Institute of Cultural Relics and Archaeology, Xining 810007, China. [13]Jiangsu Center for Collaborative Innovation in Geographical Information Resource Development and Application, Nanjing, Jiangsu 210023, China. [14]School of Earth Science and Geological Engineering, Sun Yat-sen University, Guangzhou 510275, China.

***Corresponding author. Email: wuqinglong@pku.edu.cn**

†Present address: School of Geography Science, Nanjing Normal University, Nanjing 210023, China. ‡These authors contributed equally to this work. §Present address: School of Earth Science and Geological Engineering, Sun Yat-sen University, Guangzhou 510275, China.

To date the outburst flood, we collected carbon samples for accelerator mass spectrometry (AMS) ^{14}C dating (*16*). Seventeen charcoal samples from the OFS and the only charcoal sample from a layer overlying the OFS (fig. S1) indicate that the age for the flood is between 2129 and 1770 cal. BCE [95% confidence interval (CI)] (Fig. 2A and table S5) (*16*). Charcoal samples from DLS upstream of the dam (fig. S1) yield calibrated ^{14}C results (95% CI) spanning 2020 to 1506 BCE (Fig. 2A and table S5), demonstrating that the DLS is coeval with or younger than the outburst flood and confirming that it is fill from the remnant lake. The best dating for the flood comes from the Lajia site (*16*), because it was destroyed within 1 year before the outburst flood. Radiocarbon determinations of bone samples from three human victims, aged 6 to 13 years old, in collapsed Lajia dwellings (Fig. 2B) agree to within uncertainty (Fig. 2A and table S5), consistent with that of two victims reported previously (*21*) as well. Because the radiocarbon calibration curve is linear in this region and the bones are the same age, we use the inverse variance weighted mean of the three measurements. This yields a calibrated age with a median of 1922 ± 28 BCE (1 SD) and a 95% CI of 1976 to 1882 BCE (Fig. 2C). To simplify this range, we use 1920 BCE to indicate the approximate date of the flood.

We estimate the peak discharge of the flood in two ways. Empirical formulas considering the volume of the lake and the height of the dam lead to estimates ranging from 0.08 to 0.51×10^6 m^3s^{-1}, with large uncertainties (*16*) (table S3). We also reconstruct the flood channel cross section from detailed surveys in Guanting Basin and use Manning's equation to estimate a peak discharge of 0.36 to 0.48×10^6 m^3s^{-1} (*16*) (fig. S6 and table S4), consistent with the dam break estimations (*16*) (table S3). The calculated peak discharge of ~0.4×10^6 m^3s^{-1} is more than 500 times the average discharge of the Yellow River at Jishi Gorge. This ranks globally among the largest freshwater floods of the Holocene (*22*).

We do not explicitly model the inundation and effect of this outburst flood in the lower reaches of the river, but analogous events demonstrate that outburst floods from landslide dams can propagate long distances. In 1967, an outburst flood with a volume of just ~0.64 km^3 propagated at least 1000 km along the Yalong-Yangtze Rivers (*23*), so the Jishi prehistoric outburst flood, with a volume of ~11 to 16 km^3, could have easily travelled more than 2000 km downstream. The Jishi flood would have breached the natural levees of the Yellow River, resulting in rare, extensive flooding. It is possible that this outburst flood was also the cause of a major avulsion of the lower Yellow River (Fig. 3A) inferred from archaeological data, with a previously estimated date of ~2000 BCE (*24*, *25*). Widespread destruction of levees and deposition of tributary mouth bars may have destabilized the main river channel, leading to repeated flooding until a new river channel was established. Extensive flooding on the lower Yellow River plain would have had a great effect on societies there. We argue that this event and its aftermath likely would have survived in the collective memories of these societies for generations, eventually becoming formalized in the received accounts of the Great Flood in the first millennium BCE. In fact, early texts such as the *Shujing* and *Shiji* even record that a place called Jishi (the same characters as the gorge where the outburst flood began) was where Yu began his dredging of the Yellow River; whether this is a coincidence will require further historical geographical research.

The ~1920 BCE flood shares the main characteristics of the Great Flood described in ancient texts. Apart from its huge peak discharge, the secondary flooding on the lower plains may have been long-lasting, just as the Great Flood remained uncontrolled for 22 years until it was managed by dredging (rather than by blocking breaches in natural levees). There is also the issue of whether the Great Flood could have been caused by exceptional meteorological flooding, but a speleothem record shows a generally weakened Asian summer monsoon from 8000 to 500 years before the present (*26*), and proxies from lake and loess records also indicate that a cool, dry climate regime begins 2000 BCE along the lower Yellow River (*27*), so this would be unlikely. Furthermore, the early textual records make no mention of frequent, extreme storms related to the Great Flood.

The discovery and reconstruction here of the massive outburst flood originating in Jishi Gorge provide scientific support that the ancient Chinese textual accounts of the Great Flood may well be rooted in a historic natural event. They also shed light on the potential

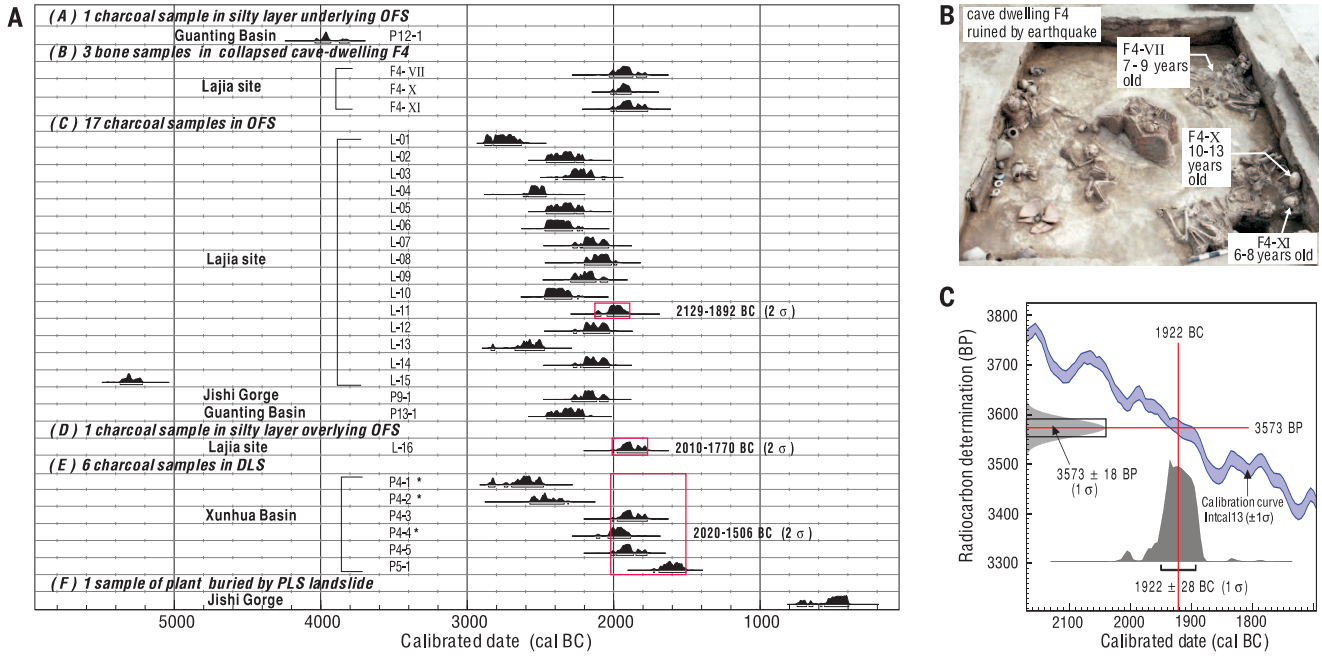

Fig. 2. Radiocarbon chronology of the prehistoric outburst flood on the Yellow River. (**A**) Calibrated age probabilistic histograms of radiocarbon data. The outliers of the ages inconsistent with stratigraphic sequences and indicating reworking are denoted with asterisks. Samples best constraining the age of the outburst flood are boxed in red. See fig. S1 for sample locations. (**B**) The radiocarbon dated skeletons in cave dwelling F4 at the Lajia site. The skeletons were identified by reference (*30*). (**C**) The calibration of the inverse variance weighted mean for three bone samples on calibration curve IntCal13 (*31*). All radiocarbon dates were calibrated individually with IntCal13 (*31*) and OxCal 4.2 (*32*).

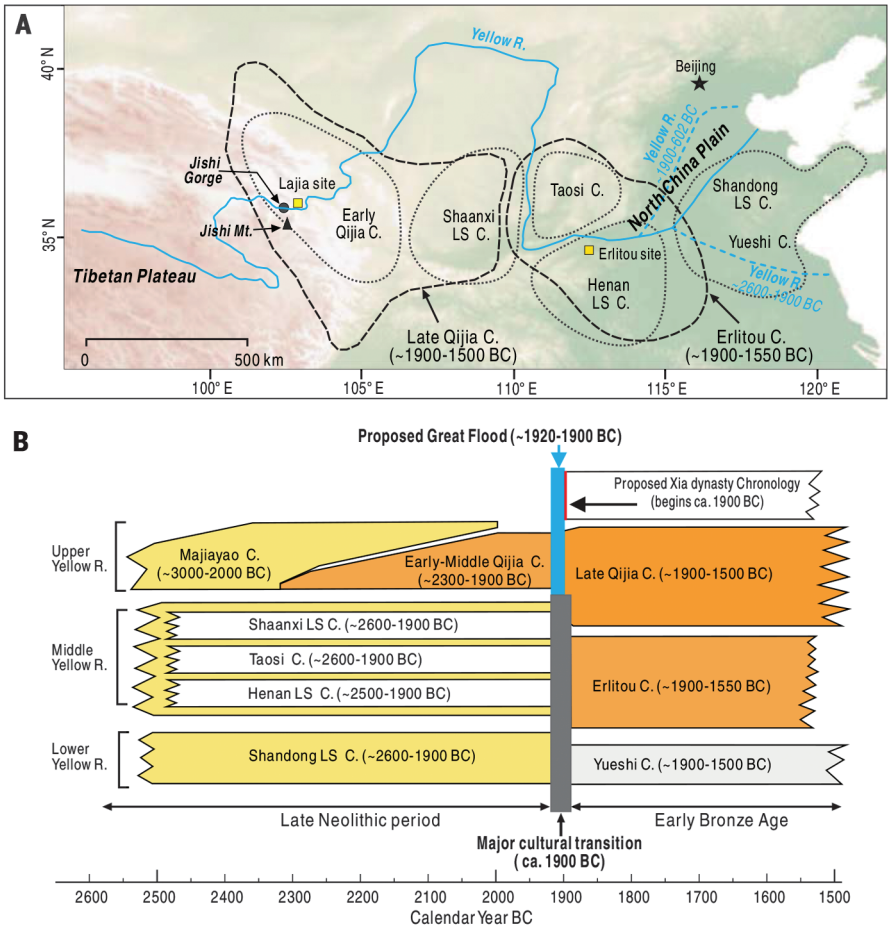

Fig. 3. Major transition of archaeological cultures in the Yellow River valley around 1900 BCE. C, culture; LS C, Longshan culture. (**A**) Distribution of the late Neolithic and early Bronze Age cultures in the Yellow River valley. Blue dashed lines show avulsion of the lower Yellow River channel ~2000 BCE (*24*). (**B**) Timeline showing ages of the archaeological cultures (*6*, *29*) and the proposed Great Flood of China.

historicity of the Xia dynasty itself, as Yu's founding of the dynasty is directly tied to his achievements in controlling the Great Flood. According to the *Shiji*, Yu's father labored unsuccessfully for 9 years to tame the flood before Yu took over for 13 more years. Yu's success led to his mandate to become founding king of the Xia 22 years after the flood started. If the Jishi Gorge outburst flood of ~1920 BCE is the natural cataclysm that came to be known as the Great Flood, then we can propose a new beginning date for the Xia dynasty, ~1900 BCE. This date, some 2 to 3 centuries later than previous reckonings (*1*, *2*, *5*), is compatible with the 1914 BCE date proposed by Nivison based on astro-historiographical evidence (*28*). This 1900 BCE date for the founding of the Xia coincides with the beginning of the Erlitou culture (*6*), so this finding also supports the arguments that the Erlitou culture is the archaeological manifestation of the Xia and that the Erlitou site was a Xia dynastic capital (*1*–*3*). This outburst flood is also coincident with the major sociopolitical transition from Neolithic to Bronze Age in the Yellow River valley (*2*, *6*, *29*) (Fig. 3, A and B), suggesting that the concurrence of these major natural and sociopolitical events known through the geological, historiographical, and archaeological records may not simply be coincidence but rather an illustration of a profound and complicated cultural response to an extreme natural disaster that connected many groups living along the Yellow River.

REFERENCES AND NOTES

1. X. P. Yuan, W. M. Yan, C. X. Zhang, Y. L. Lou, Eds., *The History of Chinese Civilization*, vol. 1 (Cambridge Univ. Press, New York, 2012).
2. K. C. Chang, *The Archaeology of Ancient China, 4th ed.* (Yale Univ. Press, New Haven and London, 1986).
3. H. Zou, *Henan Wenbo Tongxun* **1**, 34–35 (1978).
4. R. L. Thorp, *Early China* **16**, 1–33 (1991).
5. The Xia-Shang-Zhou Chronology Project Group, *The Xia-Shang-Zhou Chronology Project Report for the years 1996–2000 (abridged)* (World Book Publishing Company, Beijing, 2000).
6. L. Liu, X. C. Chen, *The Archaeology of China: From the Late Paleolithic to the Early Bronze Age* (Cambridge Univ. Press, New York, 2012).
7. A. Lawler, *Science* **325**, 934 (2009).
8. L. Liu, H. Xu, *Antiquity* **81**, 886–901 (2007).
9. Y. K. Lee, *Asian Perspect.* **41**, 15–42 (2002).
10. S. Allan, *J. R. Asiat. Soc. GB. Irel.* **116**, 242–256 (1984) (New Series).
11. M. E. Lewis, *The Flood Myths of Early China* (State Univ. of New York Press, New York, 2006).
12. D. K. Pang, *J. Hydro.* **96**, 139–155 (1987).
13. X. Q. Li, *Zhongguo Lishi Wenwu* **2002**, 4–12 (2002) (Journal of National Museum of Chinese History).
14. W. X. Wu, Q. S. Ge, *Quaternary Science* **25**, 741–749 (2005).
15. C. Lyell, *Principles of Geology*, 9th ed. (Little, Brown & Co., 1853).
16. Methods are available as supplementary materials on *Science* Online.
17. Q. L. Wu, P. Z. Zhang, H. P. Zhang, M. L. Ye, Z. Q. Zhang, *Dokl. Earth Sci.* **39**, 1148–1159 (2009).
18. IA CASS, *Chinese Archaeology* **3**, 1–6 (2003).
19. X. Y. Yang, Z. K. Xia, M. L. Ye, *Chin. Sci. Bull.* **48**, 1877–1881 (2003).
20. H. Lu *et al.*, *Nature* **437**, 967–968 (2005).
21. X. L. Zhang, M. L. Ye, S. H. Qiu, J. Zhong, *Kaogu* **11**, 91–104 (2014).
22. J. E. O'Connor, J. E. Costa, The world's largest floods, past and present: Their causes and magnitudes. U.S. Geological Survey Circular 1254 (U.S. Department of the Interior, 2004); http://pubs.usgs.gov/circ/2004/circ1254/pdf/circ1254.pdf.
23. S. G. Evans, K. B. Delaney, R. L. Hermanns, A. Strom, G. Scarascia-Mugnozza, in *Natural and Artificial Rockslide Dams*, S. G. Evans, K. B. Delaney, R. L. Hermanns, A. Strom, G. Scarascia-Mugnozza, Eds. (Springer, 2011), pp. 1–75.
24. Q. Wang, *Cultural Relics of Central China* **1993**, 63–72 (1993).
25. D. N. Keightley, in *The Cambridge History of Ancient China*, M. Loewe, E. L. Shaughnessy, Eds. (Cambridge Univ. Press, New York, 1999), pp. 30–36.
26. Y. Wang *et al.*, *Science* **308**, 854–857 (2005).
27. A. M. Rosen *et al.*, *Holocene* **25**, 1640–1650 (2015).
28. D. S. Nivison, K. D. Pang, *Early China* **15**, 87–95 (1990).
29. J. Y. Han, *The Environment and Cultural Development in Pre-Qin Northwestern China* (Wenwu Press, Beijing, 2008), pp. 40–468.
30. M. H. Wang, *Kaogu* **2002**, 1081–1084 (2002).
31. P. J. Reimer *et al.*, *Radiocarbon* **55**, 1869–1887 (2013).
32. University of Oxford, OxCal/ORAU; https://c14.arch.ox.ac.uk/oxcal/OxCal.html.

ACKNOWLEDGMENTS

This research was supported by the National Science Foundation of China (nos. 40801010 and 41271017), Fundamental Research Grant of China (no. F-IGCEA-0607-1-10), Chinese Geological Survey Project (no. 121201102000150009-16), the Priority Academic Program Development of Jiangsu Higher Education Institutions, and National Science and Technology Support Program (no. 2013BAK08B01). P. Dong, H. P. Zhang, and W. Qin partly contributed to the fieldwork; X. Su and P. M. Zhang provided important financial support; Y. Chen and J. Liu-Zeng provided partial financial support; and J. K. Lu gave suggestions on the discharge estimation. Three anonymous reviewers provided valuable comments on the manuscript. We especially thank and commemorate H. B. Wang, who passed away in an accident in November 2011, for his passionate and laborious work in reconstruction of the cross section in June 2010. All data are available in the main manuscript and supplementary materials.

SUPPLEMENTARY MATERIALS

www.sciencemag.org/content/353/6299/579/suppl/DC1
Materials and Methods
Figs. S1 to S7
Tables S1 to S5
References (*33*–*47*)

20 December 2015; accepted 14 June 2016
10.1126/science.aaf0842

BIOENGINEERING

Metabolic engineering of microbial competitive advantage for industrial fermentation processes

A. Joe Shaw,[1]* Felix H. Lam,[2] Maureen Hamilton,[1] Andrew Consiglio,[1] Kyle MacEwen,[1] Elena E. Brevnova,[1,3]† Emily Greenhagen,[1]‡ W. Greg LaTouf,[1] Colin R. South,[1]§ Hans van Dijken,[1] Gregory Stephanopoulos[1,2]

Microbial contamination is an obstacle to widespread production of advanced biofuels and chemicals. Current practices such as process sterilization or antibiotic dosage carry excess costs or encourage the development of antibiotic resistance. We engineered *Escherichia coli* to assimilate melamine, a xenobiotic compound containing nitrogen. After adaptive laboratory evolution to improve pathway efficiency, the engineered strain rapidly outcompeted a control strain when melamine was supplied as the nitrogen source. We additionally engineered the yeasts *Saccharomyces cerevisiae* and *Yarrowia lipolytica* to assimilate nitrogen from cyanamide and phosphorus from potassium phosphite, and they outcompeted contaminating strains in several low-cost feedstocks. Supplying essential growth nutrients through xenobiotic or ecologically rare chemicals provides microbial competitive advantage with minimal external risks, given that engineered biocatalysts only have improved fitness within the customized fermentation environment.

Microbial bioconversion of plant biomass is a promising route to sustainable liquid fuels and chemicals (*1*, *2*). For compatibility with society's petroleum-based infrastructure, researchers have used metabolic engineering to produce "drop-in" molecules that meet existing petrochemical standards (*3*–*5*). However, despite many technical advances enabling the production of biofuels and biochemicals, their large-scale production at competitive economic cost is lagging. One of the major obstacles for new bioprocesses is microbial contamination, which negatively affects yield, productivity, and operability. When scaling up new bioprocesses, contamination can be a major barrier to successful operation (*6*).

Conventional biofuel and biochemical fermentations use naturally occurring organisms that are highly competitive in their specific operating environment. For example, *Saccharomyces cerevisiae*, which is used to produce over 100 billion liters of ethanol per year (*7*, *8*), is well suited to exploit the environment provided by modern fruit (*9*), where it rapidly converts high concentrations of simple sugars to ethanol. Ethanol inhibits many competing microbes and allows the more tolerant *S. cerevisiae* to dominate the fermentation. By co-opting this naturally evolved competitive advantage, bioethanol producers avoid the need for feedstock refining and sterilization, enabling cost-competitive biofuel production. However, even with this natural competitive advantage, ethanol producers often resort to antibiotic treatment to halt the growth of contaminating bacteria (*10*, *11*), particularly *Lactobacilli*, that tolerate high ethanol concentrations (*12*).

A consequence of manipulating their central metabolism to produce advanced biofuels and biochemicals is that engineered microorganisms often have reduced growth rates or other competitive impairments. We sought to address this challenge by endowing biocatalysts with an engineered competitive advantage. We did this by supplying the macronutrients nitrogen and phosphorus (which are required by all microorganisms for growth) through low-cost xenobiotic or ecologically rare compounds and metabolically engineering their complementary assimilation pathways (Fig. 1). This combination creates an environment where the engineered biocatalyst becomes the dominant microorganism without solely relying on naturally evolved ecological fitness. We have termed this strategy "robust operation by utilization of substrate technology" (ROBUST).

To test the ROBUST strategy, we engineered *Escherichia coli* ATCC 10798 with a synthetic six-step pathway for the conversion of melamine, a xenobiotic compound containing 67% nitrogen by weight, to ammonia and carbon dioxide. We demonstrated the utilization of melamine's six nitrogen atoms (figs. S1 and S2) through expression of *Acidovorax avenae*, *Pseudomonas* sp., *Rhodococcus* sp., *E. coli*, and *S. cerevisiae* enzymes that had previously been characterized for the bioremediation of triazides (*13*–*16*). When transformed with a low-copy plasmid carrying the melamine utilization pathway, *E. coli* grew with melamine at a maximum rate of 0.12 ± 0.02 hour^{-1}

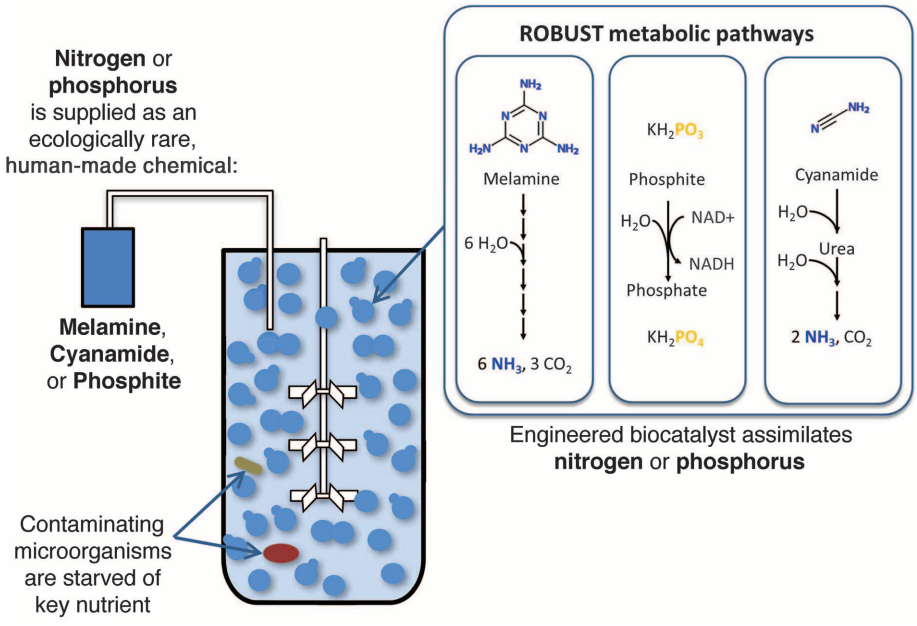

Fig. 1. The ROBUST strategy. Macronutrients essential for microbial growth are supplied in the form of xenobiotic or ecologically rare chemicals. Metabolic pathways enabling macronutrient assimilation are engineered in the desired biocatalyst (blue cells), establishing them as the dominant microorganism over nonutilizing contaminants (brown and red cells) inside the industrial bioreactor environment. NAD+, oxidized nicotinamide adenine dinucleotide; NADH; reduced nicotinamide adenine dinucleotide.

[1]Novogy, 85 Bolton Street, Cambridge, MA 02140, USA. [2]Department of Chemical Engineering, Massachusetts Institute of Technology, Cambridge, MA 02139, USA. [3]Total New Energies USA, 5858 Horton Street, Emeryville, CA 94608, USA.
*Corresponding author. Email: jshaw@novogyinc.com †Present address: Evelo Therapeutics, 620 Memorial Drive, Cambridge, MA 02139, USA. ‡Present address: Ginkgo Bioworks, 27 Drydock Avenue, Boston, MA 02210, USA. §Present address: Proterro, 66 Palmer Avenue, Bronxville, NY 10708, USA.

(n = 3). We next performed adaptive laboratory evolution spanning about 100 generations in defined medium containing 0.5 mM melamine; we subsequently isolated a colony, designated strain NS163, with a threefold increase in growth rate to 0.40 ± 0.04 hour^{-1} (n = 3).

Plasmid isolation from NS163 and reintroduction into wild-type *E. coli* resulted in an immediate growth rate on melamine of 0.4 hour^{-1} (fig. S3). Sequencing of the parental and reisolated plasmids identified a single point mutation in the evolved plasmid, resulting in an arginine-to-serine change at amino acid 352 of the *E. coli* gene *guaD*, which encodes ammeline deaminase, the second of six steps required for complete melamine degradation. That *E. coli guaD* is a target of evolutionary selection is perhaps not surprising, given that *guaD* is a "housekeeping" enzyme with primary activity for guanine deamination and is thought to catalyze ammeline deamination as a side activity (*17*).

To establish competitive advantage, the melamine utilization pathway ideally operates at a rate that makes ammonium available for rapid growth, but not so fast that free ammonium is excreted. With strain NS163, no free ammonium was detected during growth on melamine (fig. S4), although the degradation intermediate cyanuric acid did accumulate to about 13% of the total melamine fed, suggesting that further pathway optimization is possible. Growth on melamine also acted to maintain plasmid stability (fig. S5).

In coculture experiments in defined medium with melamine as the nitrogen source, *E. coli* strain NS163 rapidly outcompeted a control *E. coli* strain carrying the pACYC177 reference plasmid (Fig. 2A). The utilization pathway additionally conferred growth on melamine to the industrially relevant *E. coli* B, MG1655, and Crooks strains (fig. S6).

Next, we engineered *S. cerevisiae* to utilize cyanamide, a nitrile-containing compound, and we engineered both *S. cerevisiae* and the oleaginous yeast *Yarrowia lipolytica* to utilize phosphite, a phosphorus-containing chemical-industry intermediate. For the former, we expressed a cyanamide hydratase (*18*) gene homolog from *Aspergillus niger* to convert cyanamide to biologically accessible urea. After adaptive evolution, this strain grew with cyanamide as the sole nitrogen source. The process was repeated for the conversion of phosphite to biologically accessible phosphate by expression of bacterial phosphite dehydrogenase (*19*) and adaptive evolution (supplementary text and fig. S7). This resulted in *S. cerevisiae* strain NS586, which was able to simultaneously use cyanamide as a nitrogen source and potassium phosphite as a phosphorus source. We additionally expressed phosphite dehydrogenase in *Y. lipolytica* wild-type (strain NS324) and lipid-overproducing backgrounds (strain NS392), which enabled phosphite medium–based growth and lipid production at rates comparable to those in phosphate medium (fig. S8), without the need for adaptive evolution.

In competition with a control *S. cerevisiae* strain, NS586 demonstrated superior fitness in cyanamide-containing media (Fig. 2B), despite baseline growth of the control strain. Likewise, the *Y. lipolytica* phosphite-assimilating strain NS324 outcompeted a control strain in phosphite-containing media (Fig. 2C).

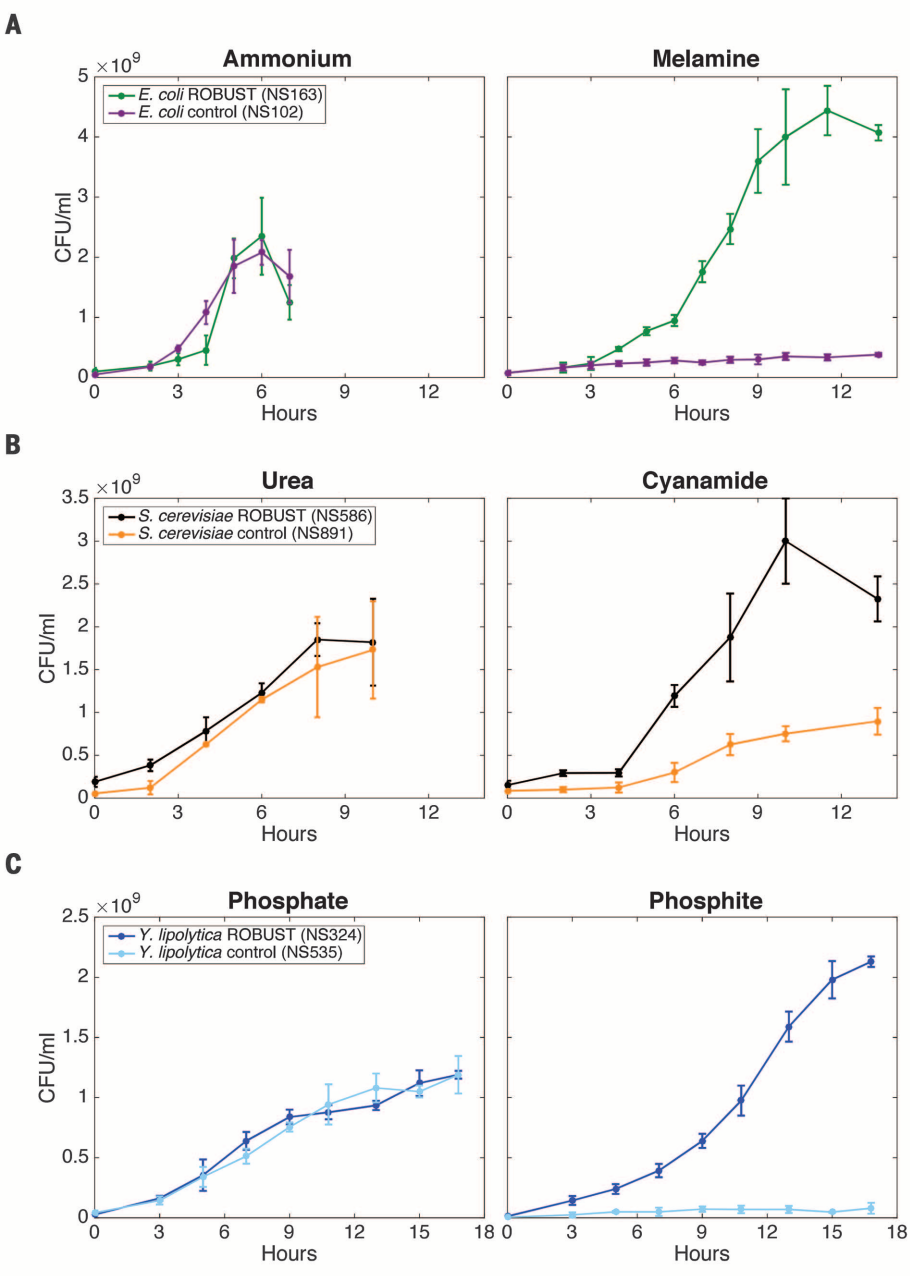

Fig. 2. Competition experiments in glucose medium. Each panel shows colony-forming unit (CFU) counts during cofermentation of ROBUST and control strains inoculated at a 1:1 ratio in defined glucose medium, with either standard or ROBUST chemicals supplying key macronutrients. (**A**) *E. coli* strains NS102 (containing the reference plasmid pACYC177) and NS163 (containing the melamine utilization plasmid pNC153), co-inoculated with ammonium chloride or melamine as the nitrogen source. (**B**) *S. cerevisiae* reference strain NS891 and cyanamide hydratase–expressing strain NS586, co-inoculated with urea or cyanamide as the nitrogen source. (**C**) *Y. lipolytica* reference strain NS535 and phosphite dehydrogenase–expressing strain NS324, co-inoculated with potassium phosphate or potassium phosphite as the phosphorus source. CFU counts are reported as means ± SD (n = 4).

For the supply of nitrogen and phosphorus through synthetic compounds to be economically viable, additional costs must be minimal and more than offset by the use of lower-cost processing methods and feedstocks. The compounds

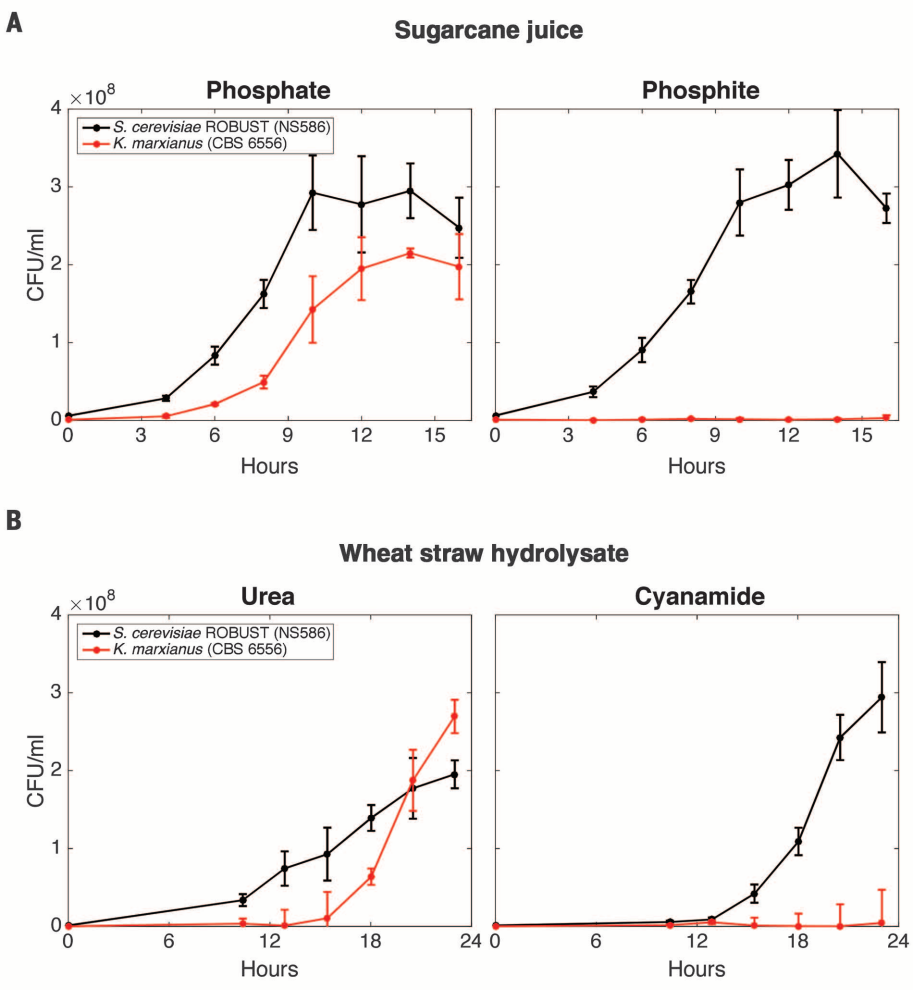

Fig. 3. Improved biocatalyst fitness with industrial feedstocks. Shown are data from aerobic fermentation with ROBUST *S. cerevisiae* NS586 and contaminant *K. marxianus* CBS 6556. (**A**) Sugarcane juice with potassium phosphate or potassium phosphite as the phosphorus source. (**B**) Wheat straw lignocellulosic hydrolysate with urea or cyanamide as the nitrogen source. CFU counts are reported as means ± SD (n = 3).

in this study are derived from bulk industrial chemical precursors and represent a cost that is comparable to that of industrial antimicrobial additives (table S1) and superior to that of sterile fermentation (table S2). We sought next to apply ROBUST to minimally refined, low-cost feedstocks.

We evaluated sugarcane juice and wheat straw lignocellulosic hydrolysate, two broadly available industrial feedstocks, for ROBUST fermentation with *S. cerevisiae* strain NS586. Sugarcane juice is composed primarily of simple sugars, but also contains some free amino acid–bound nitrogen and 0.1 to 0.6 g of phosphorus per kilogram of dry matter, or 1.7 to 12.5% of the phosphorus necessary for complete aerobic conversion of the sugars to yeast biomass (table S3). We tested batch fermentation of 2% w/v sugarcane juice supplemented with media containing 4 mM potassium phosphate or potassium phosphite. To these media, strain NS586 and *Kluyveromyces marxianus* CBS 6556, a fast-growing spoilage yeast (*20*), were co-inoculated at a 10:1 ratio. Despite the presence of a low level of naturally occurring phosphate, in the phosphite-supplemented medium, NS586 outcompeted *K. marxianus* for sugar utilization (Fig. 3A). With variability in raw feedstock supplies, ROBUST may be more or less effective at different naturally occuring phosphate concentrations. For a given set of operating conditions (e.g., biocatalyst loading, growth rate, fermentation time), a maximum natural phosphate concentration may be established for reliable operation; blending raw sugarcane juice with refined sugar could be used to keep phosphate below this level.

Wheat straw lignocellulosic hydrolysate is under evaluation for the production of bioethanol and biochemicals, and it requires nitrogen supplementation for complete growth of *S. cerevisiae* (fig. S9). We co-inoculated *S. cerevisiae* NS586 and *K. marxianus* CBS 6556 at a 10:1 initial ratio with 5 mM urea or cyanamide in 2% w/v glucan-equivalent wheat straw hydrolysate. Although the cyanamide condition has a 4- to 5-hour lag relative to the urea condition, it enables *S. cerevisiae* NS586 both to grow unhindered by *K. marxianus* (Fig. 3B) and to achieve a higher cellulosic ethanol titer (fig. S10). Other industrial feedstocks such as sugarcane bagasse, sugar beet molasses, and corn stover have comparable limiting phosphorus and nitrogen contents (table S3), making them feasible for further ROBUST processing.

Corn has the highest annual yield (in metric tons) of any cereal crop worldwide and produces the most starch per acre of cultivated crops. In general, there are two processes for producing fermentable carbohydrate from corn. The first, dry milling, is the lowest-cost route to a fermentable intermediate (*7*) but results in a heterogeneous, semi-solid mash that is challenging to sterilize. The second process, wet milling, produces a highly refined pure glucose but requires substantial capital and operating investment (*7*) (table S2). We sought to apply ROBUST to dry-milled corn, which could be complicated by the nitrogen and phosphorus present in whole corn kernels. However, by using low-capital dry-mill fractionation (*21*, *22*), 90% of the phosphorus can be readily separated from fermentable starch, with coproduction of protein and oil containing corn germ (Fig. 4A). In simultaneous saccharification and fermentation experiments co-inoculated with *Y. lipolytica* NS392 [engineered for phosphite utilization and lipid overproduction (*23*)] and *S. cerevisiae* Ethanol Red (an industrial ethanol production strain used in this study as a contaminant), the *S. cerevisiae* strain outcompeted *Y. lipolytica* even at a 10:1 initial disadvantage because of rapid ethanol accumulation, which decreases *Y. lipolytica* viability (Fig. 4B). However, when phosphorus was supplied as potassium phosphite, *Y. lipolytica* NS392 continued to grow and produce lipids, and no ethanol accumulated during fermentation (Fig. 4, C and D). Nearly identical *Y. lipolytica* performance was observed when the yeast antibiotic hygromycin was added to inhibit *S. cerevisiae* during phosphate fermentation (fig. S11). These results demonstrate the capability of ROBUST to fundamentally shift production toward a desired product in an otherwise identically configured fermentation.

Naturally selected microorganisms may emerge that are capable of assimilating almost any xenobiotic chemical (table S4), but the ability to synthesize new nitrogen- and phosphorus-containing compounds and to engineer metabolic assimilation pathways should enable the deployment of future ROBUST compound-pathway iterations. This dynamic is similar to the arms race currently underway with multidrug-resistant bacterial strains (*24*). However, with ROBUST, the competition between industrial biotechnologists and natural evolution can occur without the risk of spreading antibiotic resistance genes (*25*). Although engineered biocatalysts should be able to consume ROBUST compounds to below trace levels, we do anticipate that a full life-cycle analysis will be required for the use of any new compound in an industrial bioprocess.

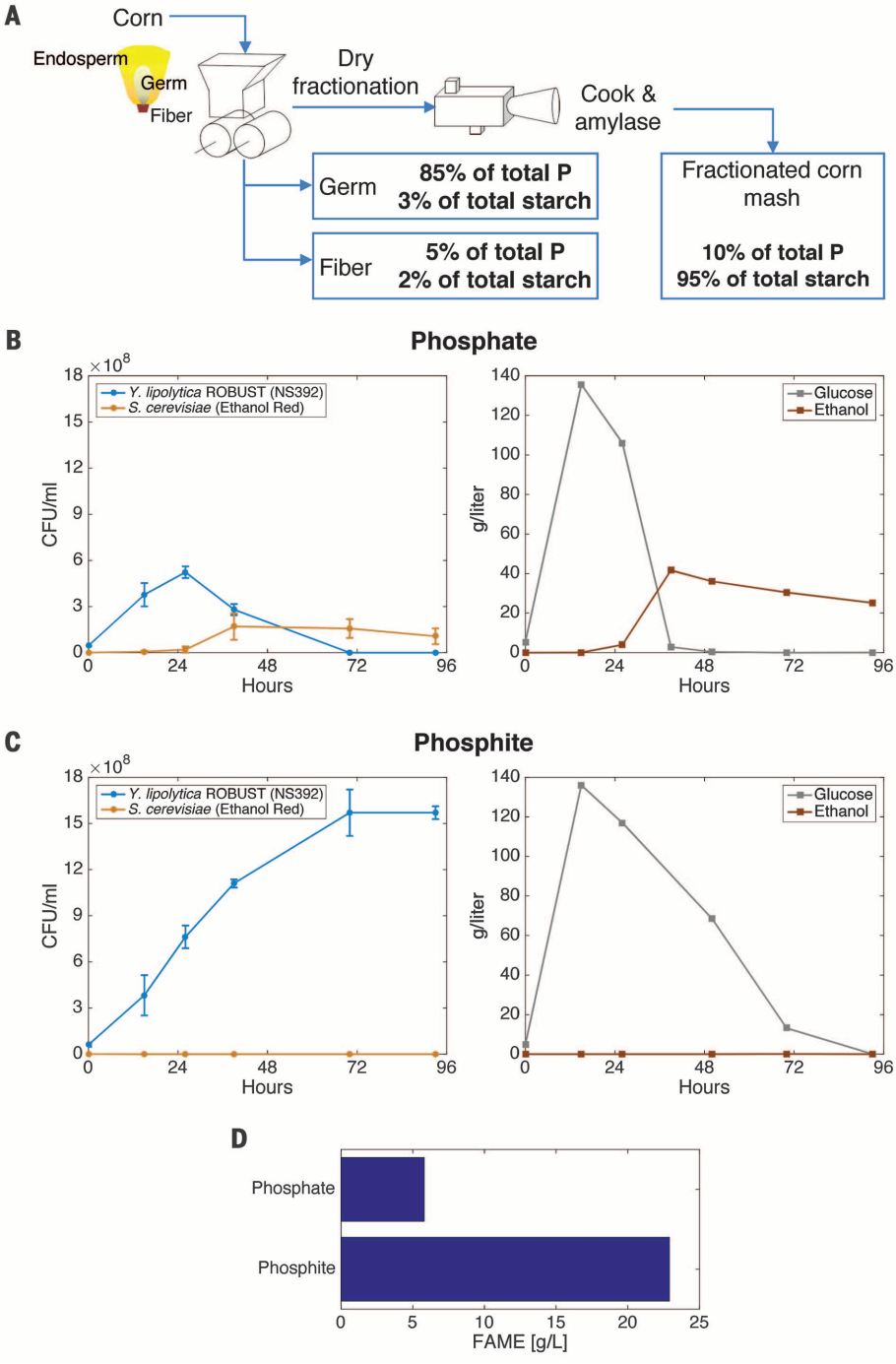

Fig. 4. ROBUST-enabled grain-to-lipid fermentation. (**A**) Dry-mill corn fractionation enables low-cost separation of food- and animal feed–quality germ and fiber from fractionated corn mash. (**B**) Simultaneous saccharification and fermentation in fractionated mash co-inoculated with lipid-overproducing *Y. lipolytica* NS392 (engineered for phosphite utilization) and contaminating *S. cerevisiae* strain Ethanol Red at a 10:1 initial ratio, with potassium phosphate supplying phosphorus. (**C**) Fermentation under identical conditions, except with potassium phosphite supplying phosphorus. In (B) and (C), CFU counts are reported as means ± SD (n = 4). (**D**) Lipid accumulation, reported as fatty acid methyl ester (FAME), at the end of fermentation.

REFERENCES AND NOTES

1. M. Grayson, *Nature* **474**, S1 (2011).
2. L. M. Fulton, L. R. Lynd, A. Körner, N. Greene, L. R. Tonachel, *Biofuels Bioprof. Biorefining* **9**, 476–483 (2015).
3. P. P. Peralta-Yahya, F. Zhang, S. B. del Cardayre, J. D. Keasling, *Nature* **488**, 320–328 (2012).
4. B. de Jong, V. Siewers, J. Nielsen, *Curr. Opin. Biotechnol.* **23**, 624–630 (2012).
5. L. S. Gronenberg, R. J. Marcheschi, J. C. Liao, *Curr. Opin. Chem. Biol.* **17**, 462–471 (2013).
6. P. J. Westfall, T. S. Gardner, *Curr. Opin. Biotechnol.* **22**, 344–350 (2011).
7. W. M. Ingledew, "Ethanol fuel production: Yeast processes," in *Encyclopedia of Industrial Biotechnology* (Wiley, 2009), pp. 1–14.
8. G. M. Walker, *J. Inst. Brew.* **117**, 3–22 (2011).
9. S. Dashko, N. Zhou, C. Compagno, J. Piškur, *FEMS Yeast Res.* **14**, 826–832 (2014).
10. S. H. Hynes, D. M. Kjarsgaard, K. C. Thomas, W. M. Ingledew, *J. Ind. Microbiol. Biotechnol.* **18**, 284–291 (1997).
11. N. V. Narendranath, S. Brey, "Bacterial contamination and control," in *The Alcohol Textbook—A Reference for the Beverage, Fuel and Industrial Alcohol Industries*, W. M. Ingledew, Ed. (Nottingham Univ. Press, ed. 5, 2009), pp. 337–356.
12. K. M. Bischoff, K. A. Skinner-Nemec, T. D. Leathers, *J. Ind. Microbiol. Biotechnol.* **34**, 739–744 (2007).
13. R. W. Eaton, J. S. Karns, *J. Bacteriol.* **173**, 1215–1222 (1991).
14. B. Martinez, J. Tomkins, L. P. Wackett, R. Wing, M. J. Sadowsky, *J. Bacteriol.* **183**, 5684–5697 (2001).
15. N. Shapir *et al.*, *J. Bacteriol.* **189**, 674–682 (2007).
16. Materials and methods are available as supplementary materials on *Science* Online.
17. J. L. Seffernick, A. G. Dodge, M. J. Sadowsky, J. A. Bumpus, L. P. Wackett, *J. Bacteriol.* **192**, 1106–1112 (2010).
18. U. H. Maier-Greiner *et al.*, *Proc. Natl. Acad. Sci. U.S.A.* **88**, 4260–4264 (1991).
19. A. M. G. Costas, A. K. White, W. W. Metcalf, *J. Biol. Chem.* **276**, 17429–17436 (2001).
20. M. M. Lane, J. P. Morrissey, *Fungal Biol. Rev.* **24**, 17–26 (2010).
21. S. Rajagopalan, E. Ponnampalam, D. McCalla, M. Stowers, *Appl. Biochem. Biotechnol.* **120**, 37–50 (2005).
22. R. J. Giguere, U.S. Patent US8113447 B1 (2012).
23. J. Friedlander *et al.*, *Biotechnol. Biofuels* **9**, 77 (2016).
24. K. Hede, *Nature* **509**, S2–S3 (2014).
25. K. Bush *et al.*, *Nat. Rev. Microbiol.* **9**, 894–896 (2011).

ACKNOWLEDGMENTS

We thank O. Vidalin and V. Rajgarhia for managerial support, D. Crabtree and J. Afshar for analytical support, H. Blitzblau and V. Tsakraklides for helpful comments, Cereal Process Technologies and the National Corn to Ethanol Research Center for materials and insight into corn fractionation processes, Beta Renewables for wheat straw hydrolysate, and Phibro for the yeast Ethanol Red. This work was supported by Novogy and Total New Energies. F.H.L. and G.S. were supported in part by the U.S. Department of Energy (grant DE-SC0008744). A.J.S., C.R.S., H.v.D., E.G., M.H., W.G.L., A.C., K.M., and Novogy have filed patent applications [WO2014107660 (A3), WO2015031441 (A3), and WO2015157431 (A3)] that relate to the use of ROBUST pathways for fermentation selective advantage. PROESA wheat straw hydrolysate is available from Biochemtex under a material transfer agreement. Data are available in the supplementary materials, and strains are available by request. A.J.S., F.H.L., E.E.B., E.G., W.G.L., C.R.S., H.v.D., and G.S. participated in the design of the experiments and/or the interpretation of the results. A.J.S., F.H.L., M.H., A.C., K.M., E.E.B., and E.G. participated in the acquisition and/or analysis of data. A.J.S., F.H.L., and G.S. participated in drafting and/or revising the manuscript.

SUPPLEMENTARY MATERIALS

www.sciencemag.org/content/353/6299/583/suppl/DC1
Materials and Methods
Supplementary Text
Figs. S1 to S11
Tables S1 to S6
References (*26*–*58*)
Database S1

20 March 2016; accepted 22 June 2016
10.1126/science.aaf6159

PLANT SCIENCE

Circadian regulation of sunflower heliotropism, floral orientation, and pollinator visits

Hagop S. Atamian,[1] Nicky M. Creux,[1] Evan A. Brown,[2] Austin G. Garner,[2] Benjamin K. Blackman,[2,3] Stacey L. Harmer[1]*

Young sunflower plants track the Sun from east to west during the day and then reorient during the night to face east in anticipation of dawn. In contrast, mature plants cease movement with their flower heads facing east. We show that circadian regulation of directional growth pathways accounts for both phenomena and leads to increased vegetative biomass and enhanced pollinator visits to flowers. Solar tracking movements are driven by antiphasic patterns of elongation on the east and west sides of the stem. Genes implicated in control of phototropic growth, but not clock genes, are differentially expressed on the opposite sides of solar tracking stems. Thus, interactions between environmental response pathways and the internal circadian oscillator coordinate physiological processes with predictable changes in the environment to influence growth and reproduction.

Most plant species display daily rhythms in organ expansion that are regulated by complex interactions between light- and temperature-sensing pathways and the circadian clock (*1*). These rhythms arise in part because the abundance of growth-related factors such as light signaling components and hormones (e.g., gibberellins and auxins) are regulated by both the circadian clock and light (*2*–*4*). A further layer of regulation is afforded by circadian gating of plant responsiveness to these stimuli, with maximal sensitivity to light during the day (*5*) and to gibberellin and auxin at night (*6*, *7*).

Because the direction and amount of solar irradiation undergo predictable daily changes, light capture might be optimized by links between the circadian clock and directional growth pathways. One such growth pathway is phototropism, in which plants align their photosynthetic organs with the direction of incoming light. Phototropism was first recognized by Charles Darwin (*8*) and is mediated by the perception of blue light by phototropin photoreceptors that then trigger asymmetric growth via the auxin signaling pathway (*9*). Heliotropism, or solar tracking, is a more dynamic form of phototropism, with aerial portions of the plant following the Sun's movement throughout the day. Some heliotropic plants such as sunflowers also reorient during the night so that their leaves and apices face east before sunrise (*10*, *11*). Here we show that heliotropism in the common sunflower, *Helianthus annuus*, is generated by the coordinate action of light-signaling pathways and the circadian clock and enhances plant performance in the natural environment.

Sunflower stems exhibit heliotropic movement such that their shoot apices shift from facing east at dawn to facing west at dusk as they track the Sun's relative position. Shoot apices then reorient at night to face east in anticipation of dawn (Fig. 1A and movie S1) (*12*, *13*). We disrupted this process in two ways, either by rotating potted plants every evening so that they faced east at nightfall (and thus faced west each morning after directional nighttime growth) or by tethering plant stems to solid supports to limit their tracking movements. In multiple trials, we detected ~10% decreases in both dry biomass and leaf area of the manipulated plants relative to controls in both types of experiments (Fig. 1B and fig. S1; significance assessed using linear mixed-effect models with treatment as fixed effect, trial and leaf number as random effects), demonstrating that solar tracking promotes growth.

The nighttime reorientation of young sunflowers in the absence of any obvious environmental signal suggests involvement of the circadian system; however, an alternative explanation would be an hourglass-like timing mechanism. To distinguish between these possibilities, we examined the kinetics of nighttime reorientation near the summer solstice and the fall equinox. The rate of apical movement at night was higher at midsummer [16 hours light: 8 hours dark (16L:8D)] than during the longer nights of autumn (12L:12D), so that in each case plant apices face fully east just before dawn (Fig. 1C). We next investigated whether plants continue rhythmic tracking movements in the absence of directional light cues. Sunflower plants grown in pots in the field in 14L:10D conditions were heliotropic (Fig. 1D). When moved to a growth chamber with constant, fixed overhead lighting, these plants maintained their directional growth rhythms for several days. Plants reoriented toward the east during the subjective night and toward the west during the subjective day, with times of maximal inclination corresponding to subjective dawn and dusk. As is true for many types of circadian outputs after withdrawal of environmental signals, rhythmic movements dampened over time (Fig. 1D).

Another way to distinguish rhythms regulated by the circadian clock from those directly induced by environmental cues is to maintain organisms in light-dark cycles with total period lengths (T-cycles) that differ from 24 hours (*14*). We examined heliotropism in a growth chamber with four directional blue LED (light-emitting diode) lights sequentially turned on and off to mimic the Sun's daily path. After several days in a 24-hour T-cycle (16L:8D), plants bent toward the light source during the day so that "westward" movement culminated at dusk. Anticipatory "eastward" movement then occurred throughout the dark period (Fig. 1E and fig. S2). Upon transfer to a 30-hour T-cycle (20L:10D), maximal "westward" inclination no longer occurred at the light-dark transition, and directionality of nighttime movement was erratic. The return to a 24-hour T-cycle reestablished anticipatory nighttime movement that began when lights were turned off (Fig. 1E and fig. S2). The complex patterns in 30-hour T-cycles suggest uncoordinated growth controlled by both environmental response pathways and the circadian clock. Thus, the circadian clock guides solar tracking in sunflowers.

Because sunflowers lack pulvini, the specialized motor organs that mediate solar tracking in some species (*15*), we hypothesized that regulated stem elongation might drive solar tracking. We observed a gradual reduction in the amplitude of heliotropic movements as plants reached maturity, correlating with cessation of stem elongation (Fig. 2, A and B, and Fig. 3A). To further investigate the involvement of stem elongation in heliotropism, we examined solar tracking and stem growth rates in *dwarf2* (*dw2*) sunflowers, which are deficient in the production of gibberellin growth hormones (*16*). In the absence of exogenous gibberellin, *dw2* plants have very short stems and no perceptible heliotropism (movie S2). Treatment with exogenous gibberellin transiently restored normal elongation (Fig. 2A) and heliotropism (Fig. 2B) in the mutant. Between days 7 and 14 after the last gibberellin application, stem elongation and the amplitude of solar tracking rhythms coordinately diminished by ~35% (Fig. 2, A and B). Thus, stem elongation is essential for heliotropism.

Many plant species show daily rhythms in nondirectional stem and leaf growth (*1*). We hypothesized that heliotropism results from differential elongation on opposite sides of stems. Indeed, the growth pattern on the east side of solar tracking sunflower stems was different from that on the west side (Fig. 2C). Growth rates on the east side were high during the day and very low at night, whereas growth rates on the west side were low during the day and higher at night. The higher growth rate on the east versus west side of the stem during the day

[1]Department of Plant Biology, University of California, One Shields Avenue, Davis, CA 95616, USA. [2]Department of Biology, University of Virginia, PO Box 400328, Charlottesville, VA 22904, USA. [3]Department of Plant and Microbial Biology, University of California, 111 Koshland Hall, Berkeley, CA 94720, USA.
*Corresponding author. Email: slharmer@ucdavis.edu

enables the shoot apex to move gradually from east to west. At night, the higher growth rate on the west side culminates in the apex facing east at dawn. We postulated that one of these growth patterns might be similar to the overall growth rhythms of sunflower plants not manifesting heliotropism. We therefore monitored plants maintained in 16L:8D cycles in a growth chamber with overhead lighting. Consistent with reports in pea and zinnia (*17*, *18*), stem elongation growth rates were higher at night than during the day under these controlled conditions (Fig.

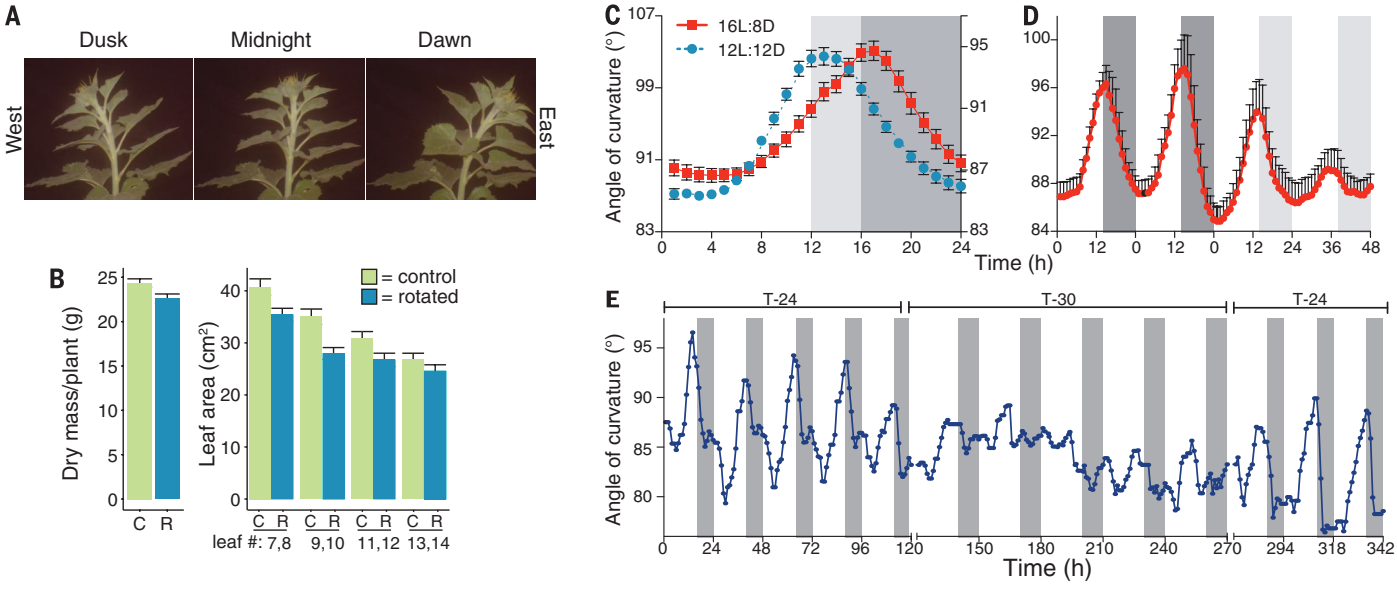

Fig. 1. The circadian clock regulates solar tracking. (**A**) Nighttime reorientation of stem and shoot apex. (**B**) Disruption of solar tracking by daily evening 180° rotation of experimental plants results in a 7.5% reduction in biomass (left) and an 11% reduction in leaf area (right) compared with 360°-rotated control plants [mean ± SEM (error bars), $n = 80$ plants, $P = 0.01$ (biomass) and 1×10^{-6} (leaf area), mixed effect linear regression models]. Numbers refer to leaf pairs. C, control; R, rotated. (**C**) Changes in orientation anticipate dawn and dusk transitions in both fall (left y axis) and summer (right y axis) [mean ± SEM, $n = 10$ plants]. (**D**) Persistence of rhythmic movements after transfer from field to continuous light and temperature conditions. In (C) and (D), white areas denote daytime; dark and light gray areas represent night and subjective night, respectively [mean ± SEM, $n = 3$ plants]. (**E**) The onset of "eastward" movement in a growth chamber equipped with four directional lights is consistently phased with lights being turned off in 24-hour T-cycles (left and right) but is erratic in 30-hour T-cycles (center). Time zero indicates dawn [(C) and (D)] or the beginning of the first T-cycle (E). Angles <90° and >90° represent inclination toward east and west, respectively. White areas, day; gray, night.

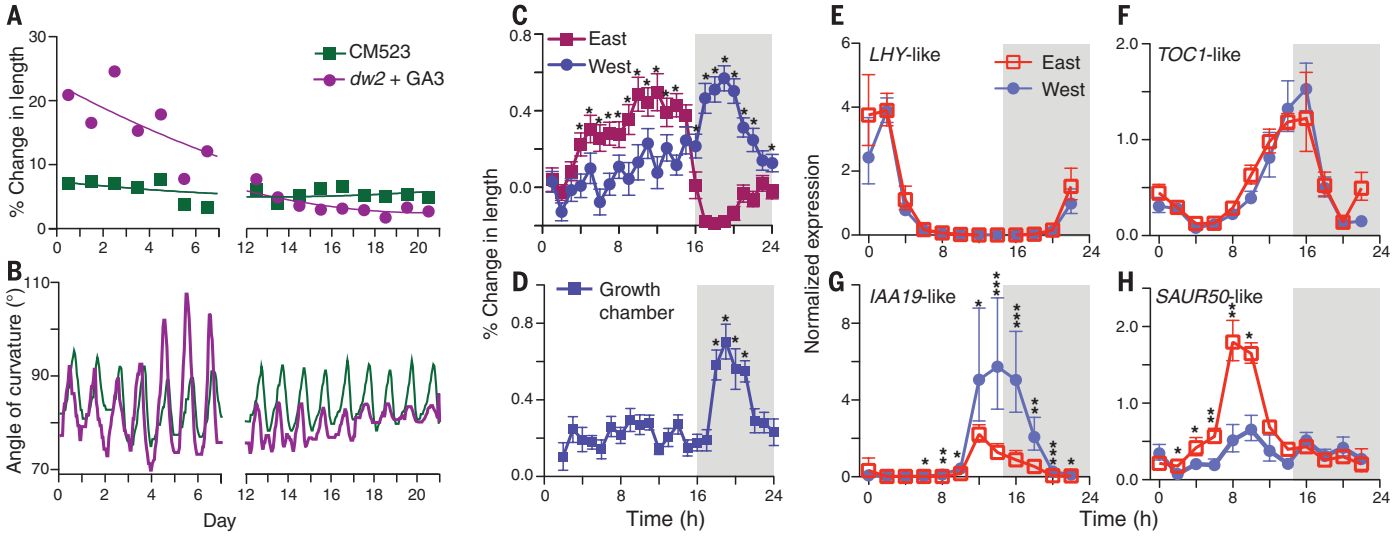

Fig. 2. Solar tracking is driven by opposing growth rhythms on the east and west sides of stems. (**A**) Changes in stem elongation and (**B**) the angle of curvature of the shoot apex relative to the horizon in control (green) and gibberellin-deficient *dw2* plants (purple). *dw2* mutants were treated twice with 2 μM of the gibberellin GA_3 (gibberellic acid), with the last treatment on day 0. Data in (A) were fitted to centered second-order polynomial equations to aid visualization. (**C**) Timing of elongation for east and west sides of stems of solar tracking field-grown plants [mean ± SEM, $n = 42$ plants]. (**D**) Timing of stem elongation of plants growing vertically in a top-lit environmental control chamber [mean ± SEM, $n = 9$ plants]. Asterisks indicate that the east and west sides of the stem (C) or the daytime and nighttime means (D) significantly differ (*$P <$ 0.05, Student's t test). (**E** to **H**) Differential gene expression on the east and west sides of solar tracking stems assessed by quantitative reverse transcription polymerase chain reaction (*$P < 0.05$, **$P < 0.01$, ***$P < 0.001$; orientation by time-point effect, single linear mixed model). Time zero indicates dawn [(C) and (E) to (H)] or when lights were turned on (D). White areas, day; gray, night.

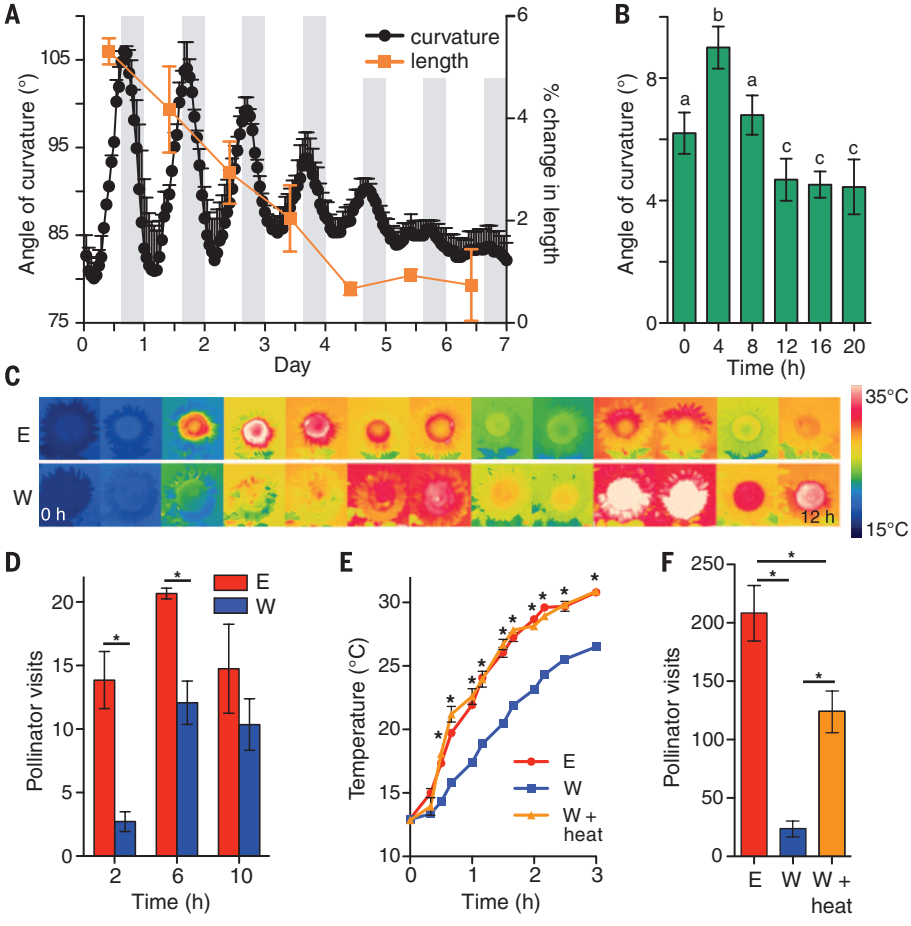

Fig. 3. Eastward orientation of sunflower heads after anthesis is due to gating of light responses by the circadian clock and enhances pollinator visits. (**A**) Amplitude of solar tracking and changes in stem growth of mature plants nearing floral anthesis. Petals were first observed during day 5 (mean ± SEM, n = 2 plants). (**B**) Stem curvature of juvenile plants entrained in 16L:8D cycles and then exposed to unidirectional blue light for 4 hours at the indicated times (mean ± SEM, n = 11 plants). Different letters indicate significantly different curvature values in pairwise comparisons ($P < 0.05$, Student's t test). (**C**) FLIR images of east-facing (E) and west-facing (W) floral disks at hourly intervals. (**D**) Pollinator visits to east- and west-facing plants (mean ± SEM, n = 4 days, eight plants per treatment) during 45-min intervals at three times of day. (**E**) Temperature (mean ± SEM, n = 6 plants per condition) of sunflower disks with east or west (with or without supplemental heat) orientations. (**F**) Pollinator visits in the morning to the inflorescences with temperatures reported in (E). In (D) to (F), *$P < 0.05$, t test with unequal variances; comparisons are for: (D) E versus W, (E) W versus W + heat, and (F) all three values. Time zero indicates dawn [(A) and (C) to (E)] or lights on (B).

2D), resembling the growth pattern of the west side of solar tracking stems. These data suggest that heliotropism is mediated by both the default pattern of growth on the west sides of stems and an environmentally imposed growth pattern on the east sides.

Because our data implicate the circadian clock in solar tracking movements, we examined the expression of sunflower homologs of central clock genes on the east and west sides of solar tracking stems. Although a *LATE ELONGATED HYPOCOTYL*–like gene and a *TIMING OF CAB EXPRESSION1*–like gene displayed the expected rhythmic patterns of daily expression, these genes were not differentially expressed on the opposite sides of stems (Fig. 2, E and F). However, expression of two homologs of genes implicated in phototropism (*19*, *20*) differed on the opposite sides of solar tracking sunflower stems, with an *INDOLE-3-ACETIC ACID19*–like gene more highly expressed on the west side at night (Fig. 2G) and a *SMALL AUXIN-UPREGULATED50 (SAUR50)*–like gene more highly expressed on the east side during the day (Fig. 2H). Homologs of these genes are induced by auxin in many species (*21*), and SAUR proteins promote cell elongation (*22*). Directional growth toward a light source is thought to be instigated by the phototropin-triggered redistribution of auxin across plant stems (*9*), whereas the circadian clock regulates both auxin levels and plant responsiveness to exogenous auxin (*4*, *7*). It is plausible that solar tracking rhythms are generated by coordinate regulation of auxin signaling by blue-light photoreceptors and the circadian clock on the opposite sides of a radially symmetrical organ, the sunflower stem.

In nature, only young sunflower plants exhibit heliotropic movements. At the final stage of floral development, or anthesis, sunflower apices stop tracking the Sun and acquire a permanent eastward orientation (*12*). Close examination of the growth dynamics over this period revealed that as stem elongation slows, likely accounting for the overall reduction in movement, the apices move less and less to the west each day, although they return to face east by morning (Fig. 3A and movie S3). This gradual cessation of westward movement might be explained by circadian gating of plant responsiveness to light, with plants responding more strongly to activation of the phototropin blue-light photoreceptors in the morning than at other times of day. We tested this possibility by entraining young plants in 16L:8D cycles and measuring their bending response after exposure to unidirectional blue light at different times of the day or night. Plants exposed to light during the first part of the day showed a stronger tropic response than those stimulated late in the day or at night (Fig. 3B), consistent with studies in potato (*23*). These data suggest that lower competence of plants to respond to directional light in the afternoons and evenings (Fig. 3B), combined with progressively reduced elongation rates as plants approach maturity, likely accounts for the progressive loss of daily stem movements toward the west and can explain the eastward orientation of sunflower disks at anthesis.

We next investigated whether this eastward orientation provides any ecological advantage. Because floral orientations that elevate floral temperature enhance pollinator visitation in alpine plants (*24*, *25*), we hypothesized that an eastward orientation may promote sunflower attractiveness to pollinators through increased morning interception of solar radiation, coincident with the daily timing of anther and stigma exsertion. Sunflowers were grown in pots in the field; just before the appearance of ray petals, half of these plants were rotated to face west. Hourly recording of disk temperature by forward-looking infrared (FLIR) imaging and more continuous monitoring with thermocouples revealed that east-facing heads warmed up more quickly in the morning than west-facing heads (Fig. 3C and fig. S3). In these early morning hours, pollinators visited east-facing heads fivefold more often than west-facing heads (Fig. 3D and movie S4). This differential was observed only when east-facing flowers were warmer than west-facing flowers. With the exception of one trial where plants flowered during a period of inclement weather, these observations were consistent across trials, years, and field sites (fig. S3). Notably, west-facing flowers warmed with portable heaters so that their morning surface temperatures matched east-facing flowers received significantly more pollinator visits than nonheated west-facing flowers (Fig. 3, E and F, and fig. S3, F and G), albeit fewer than east-facing flowers.

Thus, temperature directly contributes to, but does not solely determine, the differential attractiveness of east- and west-facing flowers to pollinators. In the future, we will investigate how temperature affects floral physiology and interactions with pollinators.

Circadian oscillators enhance fitness by coordinating physiological processes with predictable changes in the environment (*26*, *27*). Our findings demonstrate that such effects accrue in part through the coordinate regulation of directional growth by environmental response pathways and the circadian oscillator. Such coordination generates the heliotropic movement of young sunflowers, enhancing plant growth, and also leads to the eastward orientation of blooming sunflower disks, promoting a key component of reproductive performance.

REFERENCES AND NOTES

1. L. M. Müller, M. von Korff, S. J. Davis, *J. Exp. Bot.* **65**, 2915–2923 (2014).
2. K. Nozue *et al.*, *Nature* **448**, 358–361 (2007).
3. K. R. Foster, P. W. Morgan, *Plant Physiol.* **108**, 337–343 (1995).
4. L. Jouve, T. Gaspar, C. Kevers, H. Greppin, R. Degli Agosti, *Planta* **209**, 136–142 (1999).
5. A. J. Millar, S. A. Kay, *Proc. Natl. Acad. Sci. U.S.A.* **93**, 15491–15496 (1996).
6. M. V. Arana, N. Marín-de la Rosa, J. N. Maloof, M. A. Blázquez, D. Alabadí, *Proc. Natl. Acad. Sci. U.S.A.* **108**, 9292–9297 (2011).
7. M. F. Covington, S. L. Harmer, *PLOS Biol.* **5**, e222 (2007).
8. C. R. Darwin, *The Power of Movement in Plants* (John Murray, London, 1880).
9. W. R. Briggs, *Plant Physiol.* **164**, 13–23 (2014).
10. J. P. Vandenbrink, E. A. Brown, S. L. Harmer, B. K. Blackman, *Plant Sci.* **224**, 20–26 (2014).
11. U. Kutschera, W. R. Briggs, *Ann. Bot.* **117**, 1–8 (2016).
12. J. H. Schaffner, *Bot. Gaz.* **25**, 395–403 (1898).
13. H. Shibaoka, T. Yamaki, *Sci. Pap. Coll. Gen. Educ. Univ. Tokyo* **9**, 105–126 (1959).
14. M. Merrow, M. Brunner, T. Roenneberg, *Nature* **399**, 584–586 (1999).
15. D. Koller, in *Photomovement*, D.-P. Häder, M. Lebert, Eds. (Elsevier, 2001), pp. 833–896.
16. M. Fambrini *et al.*, *Plant Mol. Biol.* **75**, 431–450 (2011).
17. J. A. Stavang *et al.*, *Plant Physiol.* **138**, 2344–2353 (2005).
18. W. G. Neily, P. R. Hicklenton, D. N. Kristie, *J. Am. Soc. Hortic. Sci.* **122**, 778–783 (1997).
19. H. Ren, W. M. Gray, *Mol. Plant* **8**, 1153–1164 (2015).
20. K. Tatematsu *et al.*, *Plant Cell* **16**, 379–393 (2004).
21. G. Hagen, T. Guilfoyle, *Plant Mol. Biol.* **49**, 373–385 (2002).
22. A. K. Spartz *et al.*, *Plant Cell* **26**, 2129–2142 (2014).
23. D. Vinterhalter, B. Vinterhalter, J. Miljuš-Djukić, Ž. Jovanović, V. Orbović, *J. Plant Growth Regul.* **33**, 539–550 (2014).
24. P. G. Kevan, *Science* **189**, 723–726 (1975).
25. M. L. Stanton, C. Galen, *Oecologia* **78**, 477–485 (1989).
26. Y. Ouyang, C. R. Andersson, T. Kondo, S. S. Golden, C. H. Johnson, *Proc. Natl. Acad. Sci. U.S.A.* **95**, 8660–8664 (1998).
27. A. N. Dodd *et al.*, *Science* **309**, 630–633 (2005).

ACKNOWLEDGMENTS

We thank C. Pugliesi and the U.S. Department of Agriculture (Agricultural Research Service, North Central Regional Plant Introduction Station) for providing germplasm; the Morven Farm staff, R. Karp, J. Vandenbrink, L. Henry, and N. Infantino for assistance in the field and with video scoring; and J. Maloof for helpful discussions. This work was supported by NSF grant IOS-1238040 (to S.L.H. and B.K.B.) and a University of Virginia Harrison Undergraduate Research Award (to E.A.B.). The supplementary materials contain additional data.

SUPPLEMENTARY MATERIALS

www.sciencemag.org/content/353/6299/587/suppl/DC1
Materials and Methods
Figs. S1 to S3
Table S1
References (*28*–*35*)
Movies S1 to S4

28 April 2016; accepted 15 June 2016
10.1126/science.aaf9793

BIOMINERALIZATION

Macromolecular recognition directs calcium ions to coccolith mineralization sites

Assaf Gal,[1,2] Richard Wirth,[3] Joachim Kopka,[2] Peter Fratzl,[1] Damien Faivre,[1] André Scheffel[2]*

Many organisms form elaborate mineralized structures, constituted of highly organized arrangements of crystals and organic macromolecules. The localization of crystals within these structures is presumably determined by the interaction of nucleating macromolecules with the mineral phase. Here we show that, preceding nucleation, a specific interaction between soluble organic molecules and an organic backbone structure directs mineral components to specific sites. This strategy underlies the formation of coccoliths, which are highly ordered arrangements of calcite crystals produced by marine microalgae. On combining the insoluble organic coccolith scaffold with coccolith-associated soluble macromolecules in vitro, we found a massive accretion of calcium ions at the sites where the crystals form in vivo. The in vitro process exhibits profound similarities to the initial stages of coccolith biogenesis in vivo.

Mineralized structures formed by organisms are hybrid materials, characterized by the intimate association of organic macromolecules within and/or around the inorganic phase (*1*–*3*). The hierarchical assembly of the organic and inorganic components is accountable for the superior materials properties that biominerals exhibit (*4*). Soluble organic macromolecules control mineralization by interacting with the developing mineral. Such interactions can affect the morphology of the growing crystal, stabilize a transient amorphous precursor phase, or inhibit precipitation in solution (*5*–*7*). The insoluble organic components of biominerals, usually forming scaffold structures, also have been shown to influence crystal nucleation and growth (*8*–*10*). These observations have led to the general view that the localization of crystallization is determined by direct interactions between nucleating macromolecules and the developing mineral.

One of the prominent examples demonstrating high degree of control over crystallization are the calcitic scales produced by coccolithophores (*11*, *12*). These ubiquitous marine microalgae, which are the main calcifying phytoplankton, produce complex arrays of calcite crystals, termed coccoliths (*13*). Each coccolith is formed inside a specialized vesicle and upon completion, it is extruded to the cell surface to form an extracellular shell (Fig. 1, A and B) (*11*). Coccolith biogenesis starts with formation of an organic scale, called the base plate, inside the coccolith vesicle (*14*, *15*). Calcite crystals nucleate on the periphery of the base plate with their crystallographic orientation being precisely controlled (*13*). Ultrastructural studies on coccoliths have led to the hypothesis that crystal nucleation is mediated by specific chemical moieties at the base-plate periphery (*13*, *16*). The initial simple crystals grow and develop genus-specific, complex morphologies (*15*, *17*). Acidic polysaccharides, which become tightly associated with the mineral phase during its formation, further affect crystal nucleation and growth (*7*, *18*–*20*) (supplementary text).

We tested the proposed functions of the organic building blocks of coccoliths individually and in a holistic context in vitro. For this, we isolated coccoliths from live *Pleurochrysis carterae* cells using a mild harvesting procedure, preserving the coccolith-associated organic material as close as possible to its native state. *P. carterae* coccoliths consist of two types of morphologically distinct calcite crystals that are placed in an alternating order along the base-plate periphery. Previous characterization of the organic constituents of *Pleurochrysis* coccoliths have shown that the organic base plate is composed of cellulosic fibers and proteins, and that the soluble fraction is dominated by acidic polysaccharides (*7*, *17*, *21*–*25*) (supplementary text).

Atomic force microscopy (AFM) of isolated and dried base plates on a negatively charged mica surface showed a radial array of fibers, characteristic for the bottom side of the base plate (Fig. 1, C and D) (*15*, *17*). When the mica surface was functionalized with positively charged polylysine, however, the base plates adsorbed

[1]Max-Planck Institute of Colloids and Interfaces, Potsdam-Golm 14476, Germany. [2]Max-Planck Institute of Molecular Plant Physiology, Potsdam-Golm 14476, Germany. [3]GeoForschungsZentrum Potsdam, Potsdam 14473, Germany.
***Corresponding author. Email: scheffel@mpimp-golm.mpg.de**

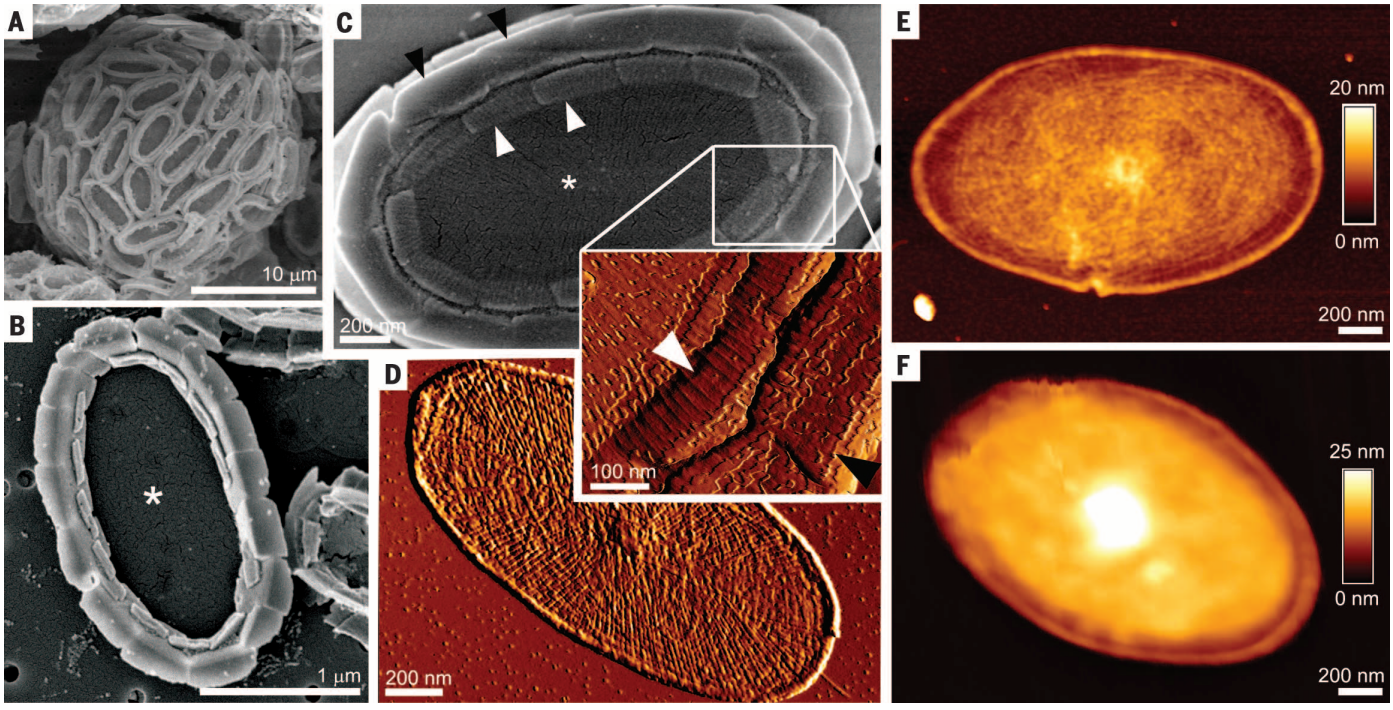

Fig. 1. Coccolith-associated organic components. (**A**) Scanning electron microscopy (SEM) image of a *P. carterae* coccolith shell. (**B** and **C**) SEM images of isolated coccoliths consisting of calcite crystals and a base plate (*). In (C), the coccolith is oriented upside down, displaying its bottom side. The base plate covers only one crystal type [inner circle of crystals indicated with white arrowheads, also known as "V-type" crystals (*13*, *16*)], whereas the second type of crystals are only in contact with the base-plate circumference (outer circle of crystals indicated with black arrowheads, also known as "R-type" crystals). The inset shows an AFM phase-contrast image of a similar sample with the base-plate fibers covering only the "V-type" crystals. (**D**) AFM phase-contrast image of the fibrous bottom side of a demineralized base plate on polylysine-functionalized mica. (**E**) AFM height-image showing the topography of the top side of a demineralized base plate. (**F**) AFM height-image of the top side of a demineralized base plate imaged in solution. Some swelling of the inner area is observed.

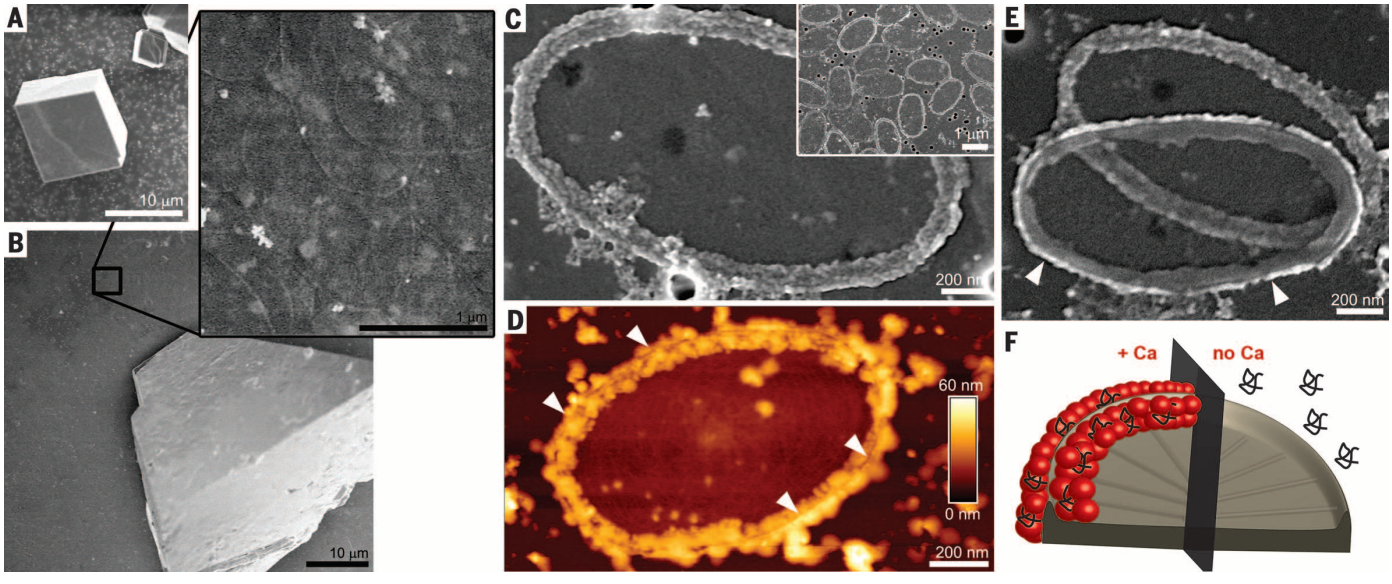

Fig. 2. Calcium-mediated formation of particle aggregates at the base-plate periphery. (**A**) SEM image of a calcite crystal growing in the absence of organic components. (**B**) SEM image showing the outcome of a mineralization experiment with purified base plates as organic additive. The inset shows base plates lying on top of each other. (**C**) SEM image of a base plate after a mineralization experiment, including also the soluble coccolith-associated macromolecules. Inset shows lower magnification. (**D**) AFM height-image of the aggregated particles on the base-plate periphery. Arrowheads indicate the boundary between the narrow outer layer and inner ring. (**E**) SEM image of two base plates after a mineralization experiment. The base plate in the upper part of the image is facing up, whereas the one in the lower part is facing down. Owing to the upside down orientation, the inner part of the aggregate ring is shaded by the base plate, whereas the uncovered outer ring (arrowheads) produces bright contrast. (**F**) A scheme showing the specific locations on the base plate where the particle aggregates (red balls) form during a mineralization experiment in the presence of the soluble macromolecules (black knots).

preferentially with their mineral-associated side facing up (Fig. 1E). This observation suggests distinct surface-charge properties of the two sides of the base plate. The most prominent feature of the mineral-associated side (top side) is a thickening at the periphery of the base plate, raising 2 to 3 nm above the ~10-nm-thick inner area. This topological feature, previously recognized as a potential crystal nucleation site (*16*), was also prominent when the base plates were imaged in solution (Fig. 1F). Amino acid and monosaccharide analyses of isolated base plates showed them to be composed of a glucose-rich polymer, which could be cellulose, additional polysaccharides, and yet unidentified proteins (table S1 and fig. S1), as previously reported (*22*, *23*). The soluble organic fraction of the coccoliths contained the three known acidic polysaccharides (*21*) as well as unidentified proteins (figs. S1 and S2).

We tested the ability of the isolated base plates to nucleate calcite in vitro using the ammonium carbonate diffusion method (*26*). A $CaCl_2$ solution, with or without the base plates, was placed in a closed desiccator. CO_2 and ammonia diffused into the solution via evaporation of the solid ammonium carbonate salt, thus slowly raising the saturation degree of the solution relative to calcium carbonate. In the absence as well as in the presence of base plates, rhombohedral calcite crystals grew (Fig. 2, A and B). Several experimental modifications, such as varying calcium and/or base-plate concentrations, varying diffusion rates, and adding inorganic additives, yielded similar results (see supplementary text). However, the addition of the coccolith-associated soluble macromolecules changed the mineralization products entirely. When the soluble macromolecules were mixed with the base plates (or if the crude organic extract was used without separating the insoluble and soluble components), no calcite precipitation was observed. Instead, each base plate was decorated by a prominent ring of aggregated particles (Fig. 2, C and D). These ~20-nm particles attach exclusively to the periphery of the base plate. Aggregation of the nanoparticles is restricted to the edge of the top side of the base plate (i.e., the side that nucleates the crystals in vivo), with a layer of particles projecting inward and a second, narrower layer projecting outward (Figs. 2, D to F, and 3A). The aggregated nanoparticles were observed at calcium concentrations >0.1 mM, while at calcium concentrations >10 mM, unspecific precipitation of particles dominated (fig. S3). Aggregate formation was pH dependent, with acidic conditions (pH <4) inhibiting the reaction (fig. S4). We tested the elemental specificity of the aggregation behavior using other cations—Sr, Mg, and Na. Only Sr ions yielded particle aggregates at the base-plate periphery but always accompanied by unspecific precipitation in the surrounding of the base plate. Mg ions showed only unspecific precipitation, and Na ions caused no precipitation (fig. S5).

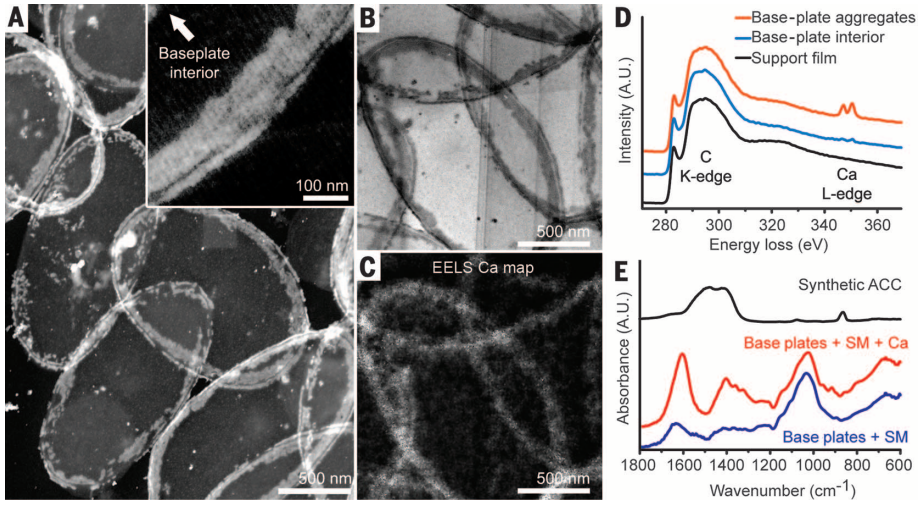

Fig. 3. Compositional analysis of the aggregates on the base-plate periphery. (**A**) HAADF-STEM image of base plates recovered from a mineralization experiment. Inset shows a higher-magnification image of the base-plate periphery with two separate rings of particle aggregates. (**B**) Bright-field TEM image of base plates from the same mineralization experiment, and (**C**) the corresponding EELS map showing calcium-rich locations with bright pixels. (**D**) Carbon K-edge EELS spectra of three different locations in the sample. (**E**) ATR-FTIR spectra of base plates and soluble macromolecule (SM) mixtures before (blue) and after (red) a mineralization experiment. The differences between the spectra are due to residual ammonium vibrations (~1400 cm^{-1}) and possibly altered conformations of the macromolecules. None of the characteristics carbonate peaks, as shown in a spectrum of amorphous calcium carbonate (ACC), are detected.

High-angle annular dark-field scanning–transmission electron microscopy (HAADF-STEM) images showed that the electron-dense particles are assembled into two rings separated by a ~5-nm gap (Fig. 3A). Electron energy-loss spectroscopy (EELS) mapping showed that the aggregate particles are indeed calcium-rich (Fig. 3, B and C). When we analyzed the EELS spectrum of the aggregates at the carbon K-edge, expecting features characteristic for carbonate, the spectrum was identical to that of organic carbon from the base plate and the supporting film (Fig. 3D). We acquired attenuated total reflectance Fourier-transformed infrared (ATR-FTIR) spectra of bulk precipitates from a mineralization experiment and again found no evidence for carbonate (Fig. 3E). The lack of involvement of carbonate ions in the precipitation of the calcium-rich aggregates on the base-plate periphery was corroborated by observing identical aggregates that formed in the absence of ammonium carbonate vapor (fig. S6).

To follow the reaction in situ, we took advantage of carboxylic residues in the soluble macromolecules (*21*) and conjugated a hydroxylamine-functionalized fluorophore to a fraction of them. The fluorescently labeled macromolecules showed a uniform fluorescence pattern when mixed with base plates or with calcium (Fig. 4, A and B). However, when base plates, fluorescently labeled macromolecules, and calcium were mixed, oval-shaped fluorescent rings with dimensions similar to those of the base plates were observed (time from mixing to image acquisition was 3 min) (Fig. 4C). After 30 min, the background fluorescence from unbound macromolecules diminished whereas the ring fluorescence did not change in intensity, suggesting the aggregation process to be completed within 3 min (Fig. 4, D to F). Colocalization of fluorescence signals from the soluble macromolecules and calcium ions was observed when calcein, a fluorescent chelator of calcium ions, was added to the reaction (fig S7). These observations show that the aggregation reaction is almost instantaneous when calcium is present and that the soluble macromolecules are a substantial component of the aggregates.

Our results suggest that templating the nucleation of calcite from a supersaturated solution is not an intrinsic feature of the *P. carterae* base plate. However, the calcium-mediated recognition between soluble macromolecules and the base-plate periphery is a highly specific process that drives large amounts of complexed calcium ions to the site where crystals ultimately nucleate. Such an additional step to the biomineralization process—i.e., localizing concentrated calcium pools by ion-binding before crystal nucleation—can provide an additional level of control over crystal nucleation. On the base plates, this process generates a geometric segregation of the concentrated calcium pool into two distinct rings. Such partitioning could facilitate the nucleation of two distinct crystal orientations, as occurs in vivo.

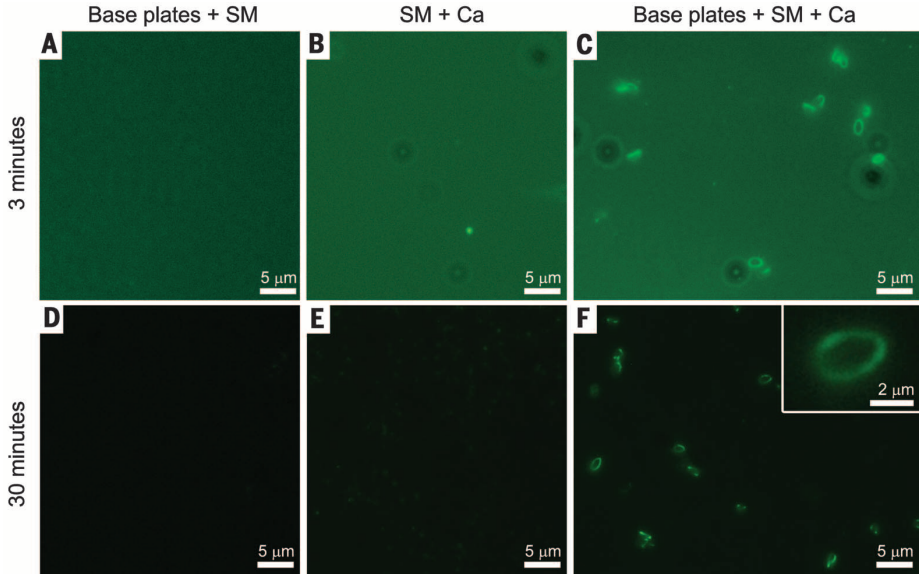

Fig. 4. In situ monitoring of the aggregation reaction with fluorescently labeled soluble macromolecules. (**A** and **D**) Fluorescence images of a mixture containing the base plates and the labeled soluble macromolecules (SM), 3 and 30 min after mixing. (**B** and **E**) Images of a mixture containing the soluble macromolecules and calcium ions. After 30 min, scattered, weakly labeled aggregates emerge, corresponding to unspecific aggregation. (**C** and **F**) Images of a mixture with all three components. The inset shows a higher magnification of a single base plate. Acquisition time was identical for all images.

The in vitro observations presented here exhibit similarities to coccolith biogenesis as observed inside of cells. First, the base plate and the soluble macromolecules were shown to colocalize inside the coccolith vesicle, where the macromolecules are associated with a concentrated, as yet unidentified, calcium phase in the form of ~20-nm particles (*16*, *17*). Second, these calcium-bearing nanoparticles have been shown to aggregate on the base-plate periphery before the onset of crystallization (*16*). Third, calcium has a longer residence time in the cell relative to carbon (*27*), supporting a distinct calcium accumulation process, which is followed by carbonate incorporation, presumably by active transport into the coccolith vesicle.

Dynamic light scattering showed that in the presence of calcium, the soluble macromolecules undergo a concentration-dependent aggregation process (fig. S8). The calcium concentration needed to saturate the aggregation potential of the macromolecules was higher (>1 mM) than the concentration needed to induce the aggregation on the base plate (<1 mM). This suggests that the higher calcium-binding affinity of the base-plate periphery facilitates the dominance of the specific aggregation pattern over nonspecific precipitation. When the polysaccharide alginate, which is rich in carboxylic acid residues, was tested as a substitute for the soluble macromolecules, no particle aggregates formed on the base-plate periphery (fig. S9). In addition, enzymatic degradation of the soluble proteins did not hinder the aggregation reaction (table S2 and fig S2). These observations suggest that neither the presence of carboxylate residues alone nor the presence of the soluble proteins can account for the macromolecular recognition reaction. On the base-plate side, we can rule out simple geometric affinity to the edges of the scale, because the very similar cellular structures called "body scales" (*15*) do not calcify in vivo and also do not show affinity for the calcium-loaded macromolecules in vitro (fig. S10). Supporting the notion of site-specific chemical interactions, AFM phase-contrast images in solution demonstrated that the surface of the base-plate periphery is chemically distinct from that of the base-plate interior (fig. S11).

The cooperative role of the organic template and soluble macromolecules in directing a calcium reservoir to the site of mineralization represents a sophisticated strategy for biological control over crystallization. It extends the role of biomolecules, which not only establish a controlled chemical environment for mineralization, but are also involved in specifying the localization of the process via specific macromolecular interactions. The paradigm of mineralization control through macromolecular recognition may be of relevance to many other biominerals, where organic templates and soluble macromolecules are well studied but the interactions between them are unclear.

REFERENCES AND NOTES

1. S. Weiner, L. Addadi, *Annu. Rev. Mater. Res.* **41**, 21–40 (2011).
2. L. Addadi, S. Weiner, *Angew. Chem. Int. Ed. Engl.* **31**, 153–169 (1992).
3. P. U. P. A. Gilbert, M. Abrecht, B. H. Frazer, *Rev. Mineral. Geochem.* **59**, 157–185 (2005).
4. P. Fratzl, R. Weinkamer, *Prog. Mater. Sci.* **52**, 1263–1334 (2007).
5. G. Falini, S. Albeck, S. Weiner, L. Addadi, *Science* **271**, 67–69 (1996).
6. Y. U. T. Gong *et al.*, *Proc. Natl. Acad. Sci. U.S.A.* **109**, 6088–6093 (2012).
7. N. Ozaki, S. Sakuda, H. Nagasawa, *Biochem. Biophys. Res. Commun.* **357**, 1172–1176 (2007).
8. A. J. Giuffre, L. M. Hamm, N. Han, J. J. De Yoreo, P. M. Dove, *Proc. Natl. Acad. Sci. U.S.A.* **110**, 9261–9266 (2013).
9. F. Nudelman *et al.*, *Nat. Mater.* **9**, 1004–1009 (2010).
10. E. Bonucci, *Biological Calcification* (Springer, Berlin, Heidelberg, 2007).
11. J. R. Young, S. A. Davis, P. R. Bown, S. Mann, *J. Struct. Biol.* **126**, 195–215 (1999).
12. J. R. Young, K. Henriksen, *Rev. Mineral. Geochem.* **54**, 189–215 (2003).
13. J. R. Young, J. M. Didymus, P. R. Brown, B. Prins, S. Mann, *Nature* **356**, 516–518 (1992).
14. K. M. Wilbur, N. Watabe, *Ann. N. Y. Acad. Sci.* **109**, 82–112 (1963).
15. I. Manton, G. F. Leedale, *J. Mar. Biol. Assoc. U. K.* **49**, 1–16 (1969).
16. M. E. Marsh, *Protoplasma* **207**, 54–66 (1999).
17. D. E. Outka, D. C. Williams, *J. Protozool.* **18**, 285–297 (1971).
18. K. Kayano, K. Saruwatari, T. Kogure, Y. Shiraiwa, *Mar. Biotechnol. (NY)* **13**, 83–92 (2011).
19. K. Henriksen, S. L. S. Stipp, J. R. Young, M. E. Marsh, *Am. Mineral.* **89**, 1709–1716 (2004).
20. M. Okazaki, T. Sato, N. Mutho, N. Wada, T. Umegaki, *J. Mar. Biotechnol.* **6**, 16–22 (1998).
21. M. E. Marsh, D. K. Chang, G. C. King, *J. Biol. Chem.* **267**, 20507–20512 (1992).
22. H. D. Isenberg, L. S. Lavine, C. Mandell, H. Weissfellner, *Nature* **206**, 1153–1154 (1965).
23. R. M. Brown Jr., W. W. Franke, H. Kleinig, H. Falk, P. Sitte, *Science* **166**, 894–896 (1969).
24. Y. Hirokawa, S. Fujiwara, M. Tsuzuki, *Mar. Biotechnol. (NY)* **7**, 634–644 (2005).
25. N. Ozaki, S. Sakuda, H. Nagasawa, *Biosci. Biotechnol. Biochem.* **65**, 2330–2333 (2001).
26. L. Addadi, S. Weiner, *Proc. Natl. Acad. Sci. U.S.A.* **82**, 4110–4114 (1985).
27. M. E. Marsh, *Protoplasma* **190**, 181–188 (1996).

ACKNOWLEDGMENTS

We are grateful to A. Skeffington, N. Kröger, and U. Armbruster for critically reading the manuscript; M. Brzezinka for help with SDS–polyacrylamide gel electrophoresis; and A. Erban for gas chromatography–mass spectrometry analysis. This research was supported by the Max-Planck Society, Deutsche Forschungsgemeinschaft (DFG) grants Sche1637/3-1 to A.S., and FA835/9-1 to D.F. A.G. is supported by an Alexander von Humboldt postdoctoral fellowship. D.F. acknowledges financial support from the European Research Council (Starting Grant MB2 No.256915). P.F. acknowledges financial support from the Gottfried Wilhelm Leibniz Preis of the DFG. All data used to support the conclusions in this manuscript are provided in the supplementary materials.

SUPPLEMENTARY MATERIALS

www.sciencemag.org/content/353/6299/590/suppl/DC1
Materials and Methods
Supplementary Text
Figs. S1 to S11
Tables S1 and S2
References (*28*–*36*)

30 March 2016; accepted 14 July 2016
10.1126/science.aaf7889

STRUCTURAL BIOLOGY

The inhibition mechanism of human 20S proteasomes enables next-generation inhibitor design

Jil Schrader,[1]* Fabian Henneberg,[1]* Ricardo A. Mata,[2] Kai Tittmann,[3] Thomas R. Schneider,[4] Holger Stark,[1] Gleb Bourenkov,[4]† Ashwin Chari[1]†

The proteasome is a validated target for anticancer therapy, and proteasome inhibition is employed in the clinic for the treatment of tumors and hematological malignancies. Here, we describe crystal structures of the native human 20S proteasome and its complexes with inhibitors, which either are drugs approved for cancer treatment or are in clinical trials. The structure of the native human 20S proteasome was determined at an unprecedented resolution of 1.8 angstroms. Additionally, six inhibitor-proteasome complex structures were elucidated at resolutions between 1.9 and 2.1 angstroms. Collectively, the high-resolution structures provide new insights into the catalytic mechanisms of inhibition and necessitate a revised description of the proteasome active site. Knowledge about inhibition mechanisms provides insights into peptide hydrolysis and can guide strategies for the development of next-generation proteasome-based cancer therapeutics.

Proteasomes play a major role in cytosolic and nuclear proteolysis and are central to cellular physiology and growth (*1*–*4*). The inhibition of proteasomes is proposed as an efficient strategy for restricting cancer growth. However, the development of new proteasome inhibitors is hampered by a lack of structural knowledge of ligand binding sites and by a lack of understanding of the biochemical mechanisms underlying proteasome inhibition. The proteasome is a large macromolecular complex (750 kD), with an overall architecture that is defined by four coaxially stacked heteroheptameric rings, the outer two consisting of α subunits (α1 to α7) and the inner two formed by β subunits (β1 to β7) (Fig. 1A) (*1*, *2*, *5*). The β1, β2, and β5 subunits contain the proteolytic active sites with caspase-like, tryptic-like, and chymotryptic-like specificities, respectively (*1*, *2*, *5*). Most of the current structural knowledge about the proteasome and its binding sites for inhibitors comes from studies of the yeast proteasome (*1*, *2*).

High-resolution structures of human 20S proteasomes are required to understand the chemical nature of proteasome inhibition at the atomic level. Although recently the first structures of the human 20S proteasome in complex with inhibitors were determined by x-ray crystallography and electron cryomicroscopy at 2.9 and 3.5 Å (*6*, *7*), respectively, direct observation of the atomic details of inhibition was not possible.

To obtain structural information at higher resolution, we established an optimized and robust pipeline for the production, purification, and crystallization of human 20S proteasomes that generates large quantities of protein and allows hundreds of crystals to be grown that routinely diffract to high resolution. A series of technical improvements were essential to establish this pipeline, which we summarize as follows: (i) A chromatography-free purification procedure at constant ionic strength, employing polyethylene glycol (PEG) fractionation of HeLa lysates and density gradients [see the supplementary materials (SM)]. Gradient fractions are then precipitated and concentrated by PEG addition, yielding the finally purified protein preparation. (ii) Buffer conditions were optimized by Proteoplex that we recently developed (*8*) and is identical to the crystallization buffer. We thus obtained highly soluble and stable complexes with specific activity higher by a factor of 10 (fig. S1) than that reported for previous human 20S proteasome preparations (*9*). (iii) Crystals belong to space group $P2_12_12_1$ and grow to typical dimensions of 150 × 150 × 200 μm^3 in size within 20 hours of incubation at 18°C (Fig. 1C). (iv) Postcrystallization treatments (see SM) yield complete, isotropic diffraction data sets to better than 2.0 Å resolution (Fig. 1D) using "top-hat" beam profiles defined by a compound refractive lens (CRL) transfocator system on beamline P14 at the PETRA III storage ring (see SM).

Employing this pipeline, we first determined the native crystal structure of the complete human 20S proteasome at 1.8 Å resolution. Second, crystal structures of four previously uncharacterized inhibitor complexes of the human 20S proteasome with clinically relevant inhibitors were elucidated in the resolution range of 1.9 to 2.1 Å (table S2), giving rise to a revised view of the inhibition chemistry.

For the native structure, final crystallographic maps revealed exceptionally clear electron densities for the entire particle and several ligands (Fig. 2A). The identity of many ions was validated by anomalous difference Fourier maps, partially in native crystals or in crystals, where the ligands in question were exchanged against anomalous scatterers (see SM). We were able to unambiguously assign 58 chloride, 15 magnesium, and 6 potassium ions, as well as several PEG molecules and more than 3500 localized water molecules. Given that the quality of electron density maps in previous studies of 20S proteasome crystals was severely affected by anisotropy in the diffraction of the respective crystals (*5*, *6*, *9*–*11*), we attribute the high quality of the electron density maps presented here to a large extent to far more isotropic diffraction.

At 1.8 Å resolution, a number of functionally important differences with respect to the previously published 20S proteasome structures become visible. Notably, a solvent molecule, previously assigned as catalytic water (NUK) (*5*, *6*, *9*, *10*), was identified as a chloride ion in all active sites (Figs. 2, B, C, and D). Soaking crystals grown in $MgCl_2$ with $Mg(OAc)_2$ leads to the replacement of chloride with water in the NUK position, which suggests that this solvent molecule acts as a vehicle for a proton shuttle rather than a nucleophile (see below). Three additional, localized water molecules (H_2O-1, -2, and -3), which were not seen in earlier structures, are visualized in the proteasome active site. All inhibitors analyzed in this manuscript are described to have specificity for the β5 subunit; we will therefore restrict the discussion to this active site.

The most prominent differences with respect to previously determined structures were observed in the β5 active site of the 1.9 Å proteasome-Oprozomib cocrystal structure. Oprozomib is an orally bioavailable epoxyketone inhibitor (*12*) that is in clinical trials for the treatment of advanced refractory or recurrent solid tumors (*13*). Epoxyketone inhibitors are characterized by a short peptide core and a terminal α,β-epoxyketone dual electrophilic reactive warhead, which is the basis of their efficacy. Based on several cocrystal structures of epoxyketone inhibitors with yeast, mouse, and human 20S proteasomes (*6*, *9*–*11*, *14*), it has been concluded that the γ-OH of the proteasome active site Thr^1 reacts with the ketone moiety, whereas the N-terminal amino group of Thr^1 reacts irreversibly with the carbon atom in the α position of the epoxide (*6*, *9*–*11*, *14*) (fig. S2), allegedly resulting in a 1,4-morpholine (six-membered) ring product.

After refinement of the Oprozomib-human 20S proteasome structure at 1.9 Å resolution (Fig. 3A), we were unable to confirm the formation

[1]Department of Structural Dynamics, Max Planck Institut für biophysikalische Chemie, Am Fassberg 11, D-37077 Göttingen, Germany. [2]Institut für Physikalische Chemie, Georg-August-Universität, Tamannstrasse 6, D-37077 Göttingen, Germany. [3]Göttinger Zentrum für Molekulare Biowissenschaften und Schwann-Schleiden-Forschungszentrum, Georg-August-Universität Göttingen, Julia-Lermontowa-Weg 3, D-37077 Göttingen, Germany. [4]European Molecular Biology Laboratory (EMBL), Hamburg Outstation c/o Deutsches Elektronen Synchrotron (DESY), Notkestrasse 85, D-22603 Hamburg, Germany.
*These authors contributed equally to this work. †Corresponding author. Email: ashwin.chari@mpibpc.mpg.de (A.C.); gleb@embl-hamburg.de (G.B.)

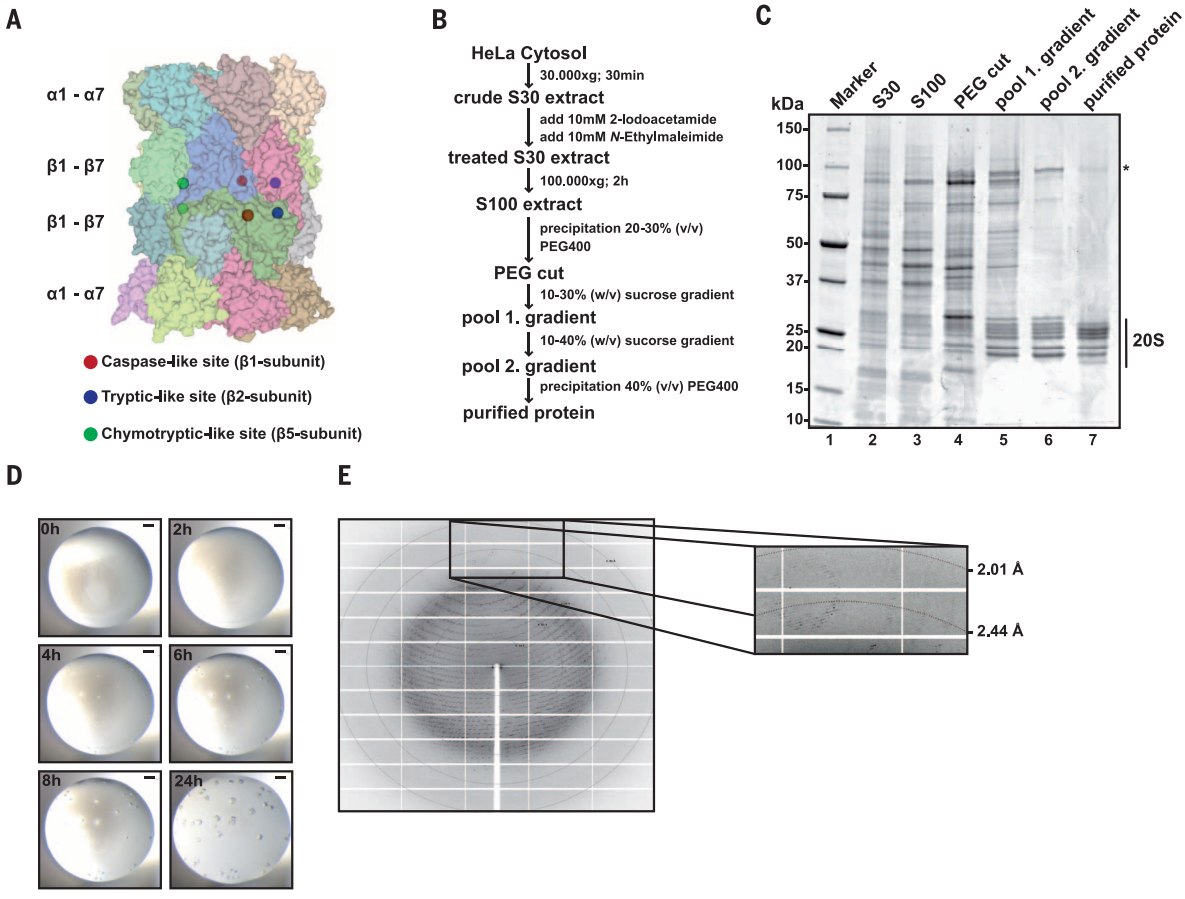

Fig. 1. A high-throughput pipeline for the structure-based discovery of human 20S proteasome inhibitors. (**A**) Space-filling representation of the human 20S proteasome. The four coaxially stacked heteroheptameric rings, the outer two consisting of α subunits (α1 to α7) and the inner two formed by β subunits (β1 to β7), are indicated in individual colors. Red dots denote the spatial positions of the β1 (caspase-like), blue dots the β2 (tryptic-like), and green dots the β5 (chymotryptic-like) active sites, respectively. (**B**) Schematic representation of the purification procedure for human 20S proteasomes (see SM for details). (**C**) SDS–polyacrylamide gel electrophoresis analysis of the purification procedure. Samples of S30 (lane 2) and S100 (lane 3) extracts, the resuspended PEG cut (lane 4), the pool of the first and second sucrose gradients (lanes 5 and 6), the final purified protein preparation (lane 7), and a molecular weight marker (lane 1) are depicted. The asterisk denotes a contamination, which is less than 10% in final protein preparation. (**D**) Time-lapse experiment of human 20S crystallogenesis at 0, 2, 4, 6, 8, and 24 hours. Crystals nucleate at 4 hours and grow to full size within 20 hours. Scale bars, 0.3 mm. (**E**) Diffraction pattern of stabilized and dehydrated human 20S proteasome crystals measured with CRLs at beamline P14-PETRA III, EMBL Hamburg. The beam size matched the crystal size (150 × 200 μm^2), exposure time is 40 ms, and the oscillation range is 0.05°. The right panel shows a zoom-in to better show the high-resolution diffraction. The diffraction limit of this crystal is 1.8 Å.

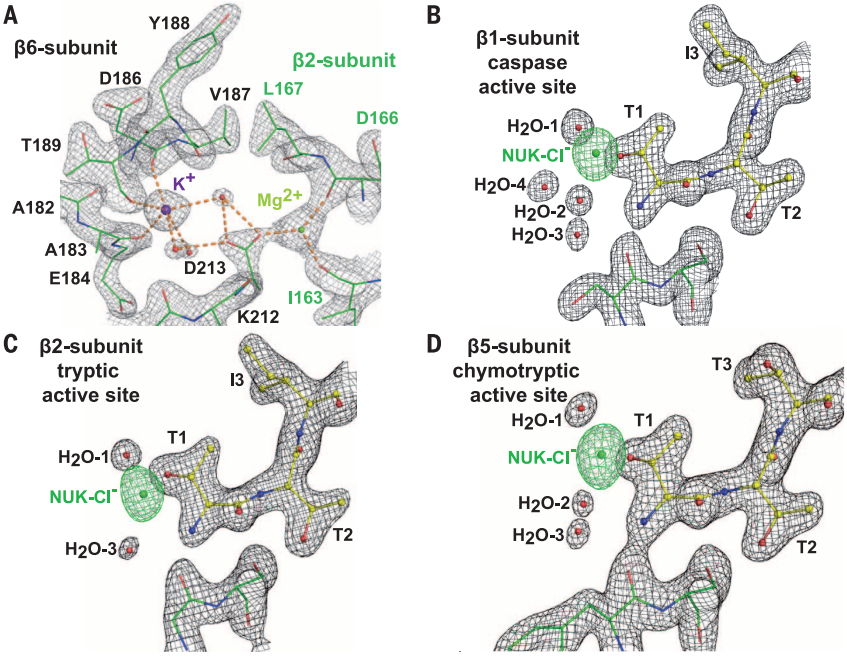

Fig. 2. Details of the high-resolution human 20S proteasome structures. (**A**) Electron density maps exemplifying the quality obtained in the high-resolution structures determined in this work. Shown is a potassium (magenta)–magnesium (green) double ion site, which stabilizes the interface between the β2 and β6 subunits. A σ_A-weighted electron density map (*24*) is shown contoured at 1.5σ. The protein main chain and side chains are labeled in the figure. (**B**) Close-up view of the caspase (β1) active site; shown are Thr^1, Thr^2, and Ile^3, along with four H_2O molecules. The NUK solvent molecule was identified to be a chloride (green sphere). The 2mFo-DFc electron density map is shown contoured at 1.5σ. (**C**) Depicted is the same as in (B), close-up of the tryptic (β2) active site along with two H_2O molecules, as well as the NUK chloride, and (**D**) for the chymotryptic (β5) active site along with three H_2O molecules and the NUK chloride. Single-letter abbreviations for the amino acid residues are as follows: A, Ala; C, Cys; D, Asp; E, Glu; F, Phe; G, Gly; H, His; I, Ile; K, Lys; L, Leu; M, Met; N, Asn; P, Pro; Q, Gln; R, Arg; S, Ser; T, Thr; V, Val; W, Trp; and Y, Tyr.

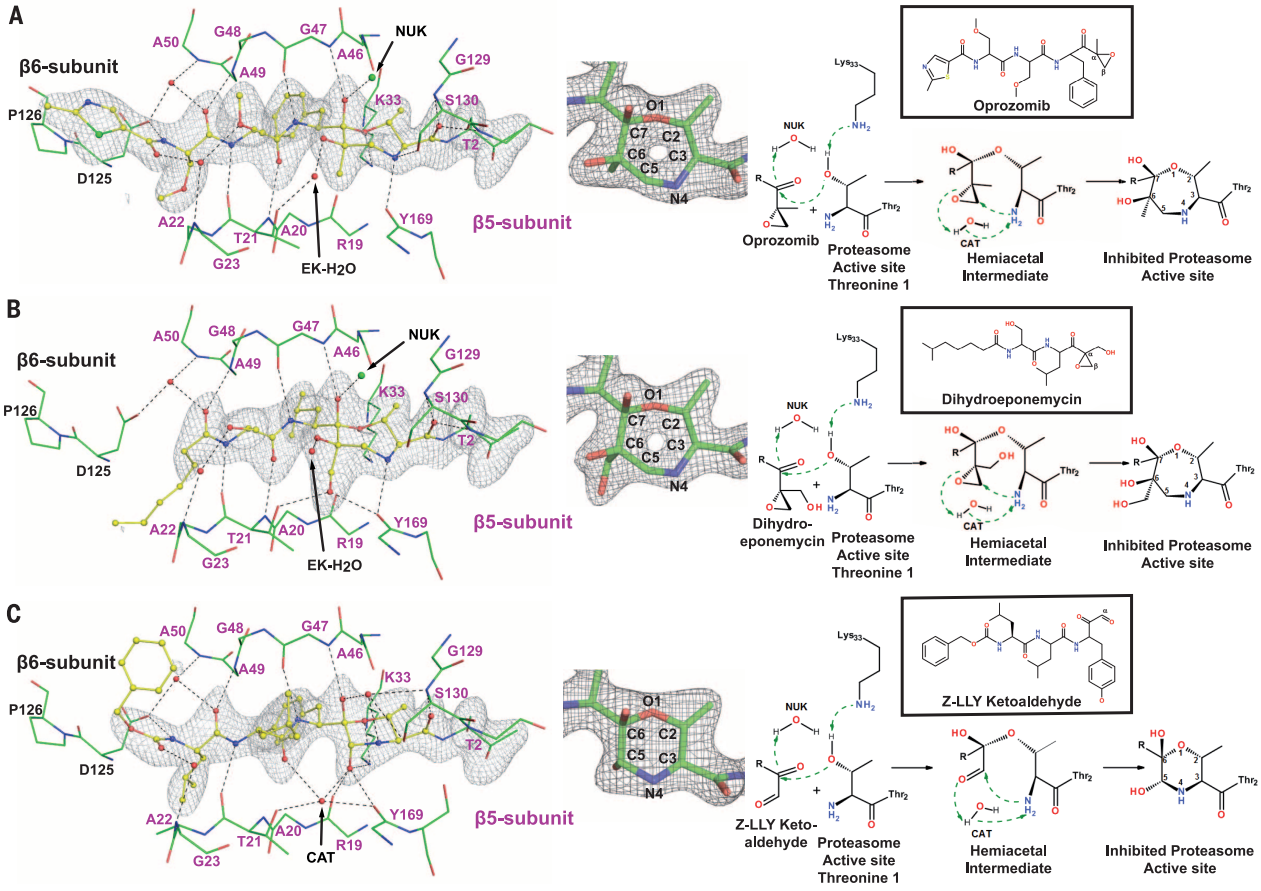

Fig. 3. High-resolution human 20*S* proteasome in complex with inhibitors reveals prominent differences to earlier structures. (**A**) Oprozomib, (**B**) Dihydroeponemycin, and (**C**) Z-LLY-Ketoaldehyde inhibitors. In all cases, the left panel illustrates the inhibited β5 active site, along with an omit map contoured at 4σ for the inhibitor, the cyclic linkage, and β5Thr[2]. The main chain segments of β5 residues 2, 19 to 21, 33, 45 to 50, 129 to 131, 169, and 170 and β6 residues 125 and 126 are indicated along with the β5 side chains of Thr[2], Thr[23], Lys[33], and Ser[130] and the side chains of β6 Asp[125] and Pro[126] as sticks (green carbon). The respective inhibitors covalently attached to Thr[1] are depicted in ball-and-stick representation (yellow carbon, red oxygen, blue nitrogen, and green sulfur). The NUK chloride is shown as a green dot. Dashed lines signify hydrogen bonds (≤3.2 Å distance). In the respective middle panels, close-up views of the inhibitor-Thr[1] linkages are shown, along with an omit map contoured at 6σ (green carbon, red oxygen, and blue nitrogen). The right panel indicates the respective proposed inhibition mechanism.

of the predicted 1,4-morpholine ring structure. Instead, electron density maps clearly revealed a larger ring-shaped electron density for the inhibitor-Thr[1] conjugate, providing space for an additional methylene group within the ring. The cyclic moiety visible in the inhibited state could be modeled as a 1,4-oxazepane (seven-membered) ring structure with the C6-methyl group oriented toward the inner, solvent-inaccessible side of the ring. The C6-OH moiety is on the solvent-exposed side overlaying the position, where the methanolic group of the 1,4-morpholine ring had been modeled previously (*6*, *9*–*11*, *14*). Waters 1 to 3 are displaced by the bound inhibitor and, instead, an epoxyketone-specific water molecule (EK-H_2O; EK designates epoxyketone) is hydrogen-bonded to the C6-OH moiety and to Thr[21] γ-OH.

This structure suggests that the inhibition reaction yielding a seven-ring product proceeds via nucleophilic attack by the N-terminal amine of the epoxide β carbon (Fig. 3A) and not the epoxide α carbon (fig. S2), as previously reported (*6*, *9*–*11*, *14*). This would have consequences not only for the mode of inhibition but also for the general reactivity of the proteasome active site. We therefore carried out a series of additional control experiments: (i) By soaking crystals with $Mg(OAc)_2$ before soaking with Oprozomib, we were able to ensure that the presence of a chloride ion in the NUK site is not responsible for seven-ring formation (fig. S3). (ii) A dose-series experiment performed with Oprozomib revealed that seven-ring formation was not caused by radiochemistry during x-ray data collection (fig. S4). (iii) Cocrystal structures of the natural product epoxyketone Epoxomicin showed electron densities perfectly matching the seven-ring model (fig. S5), albeit at a lower resolution of 2.4 Å. (iv). We determined the structure of the 20*S* proteasome in complex with another natural product epoxyketone, Dihydroeponemycin, at 2.0 Å resolution. Dihydroeponemycin differs from Oprozomib and Epoxomicin by a substitution of the epoxide α carbon methyl group by a methanolic group (Fig. 3B). If the N-terminal amino group of Thr[1] reacted with the epoxide α carbon, the reaction would yield a six-ring structure with a nonchiral center containing two methanolic groups (fig. S6). Instead, the electron density clearly shows a seven-ring structure similar to Oprozomib/Epoxomicin but with the C6-methanolic group on the inner side of the ring (Fig. 3B), thus confirming the reaction of the Thr[1] N-terminal amine with the epoxide β carbon. The C6-methanol oxygen atom forms hydrogen bonds to Thr[21] γ-OH and to Tyr[169] carbonyl, whereas the EK-H_2O remains hydrogen-bonded to the C6-OH. (v) Competitive refinement by enforcing a six-ring linkage poorly fit the electron density and led to a model with severely distorted molecular geometry (fig. S7). These findings suggest that the efficacy of epoxyketone inhibitors lies in their ability to form 1,4-oxazepane (seven-membered) ring structures with the active site Thr[1].

To explore the structural implications of a six-ring linkage, we determined the structure of the human 20*S* proteasome inhibited by Z-LLY-Ketoaldehyde (*15*) at 2.1 Å resolution (Fig. 3C). Here, the ring formation can proceed only via a carbon atom in the α position of the ketone. In these case, the electron density in the active site can indeed be unambiguously interpreted

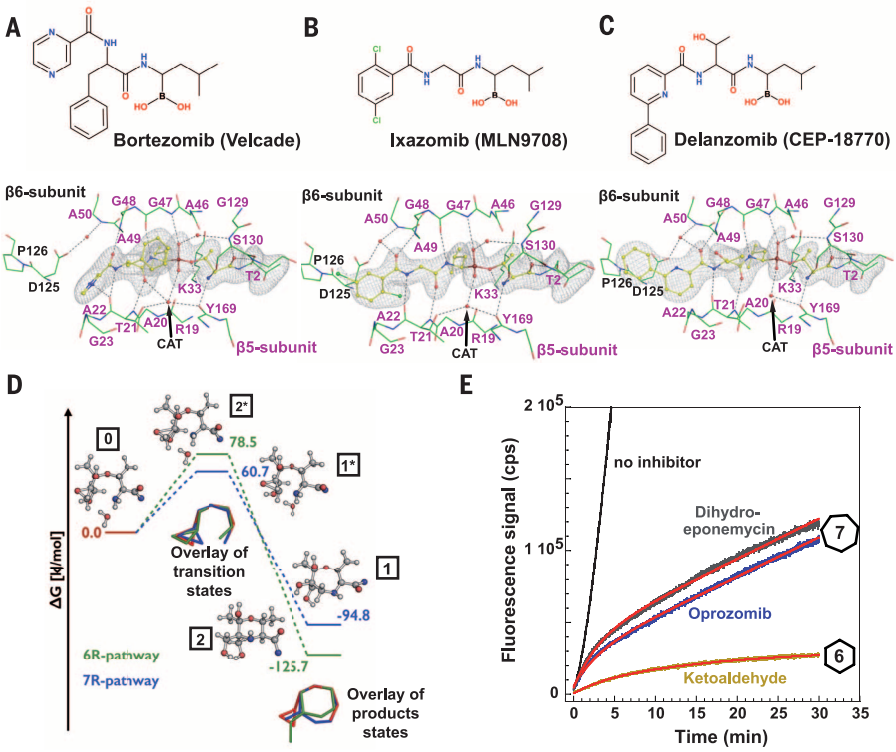

Fig. 4. Elucidation of the inhibition mechanism of epoxyketone inhibitors. (**A**) Bortezomib, (**B**) Ixazomib, and (**C**) Delanzomib. In all cases, the left panel illustrates the inhibited β5 active site, along with an omit map contoured at 4σ for the inhibitor, covalent linkage, and β5Thr^{2}. The main chain segments of β5 residues 2, 19 to 21, 33, 45 to 50, 129 to 131, 169, and 170 and β6 residues 125 and 126 are indicated along with the β5 side chains of Thr^{2}, Thr^{23}, Lys^{33}, and Ser^{130} and the side chains of β6 Asp^{125} and Pro^{126} as sticks (green carbon). The respective inhibitors attached to Thr^{1} are depicted by ball-and-sticks (yellow carbon, red oxygen, blue nitrogen, and green sulfur). The NUK chloride is exchanged by water in all three cases. Dashed lines signify hydrogen bonds (≤3.2 Å distance). The CAT (H_2O-3) molecule is ideally positioned to support the cyclization step of inhibition. (**D**) Computed reaction pathways in the Dihydroeponemycin model, including a schematic overlay of the starting state structure (red) and the stationary points. The seven-ring reaction pathway proceeds from 0 through 1* to 1, whereas the six-ring reaction pathway proceeds from 0 through 2* to 2. (**E**) Kinetic analyses of the first-order inactivation rate constants for the six-ring–forming Ketoaldehyde and for the seven-ring–forming Dihydroeponemycin and Oprozomib indicate that seven-ring formation occurs kinetically faster (fits shown in red). The residual rate of 3% of the maximum activity detected for epoxyketone inhibitors suggests that the seven-ring product is thermodynamically less stable, resulting in a reversible inhibition, which is in full agreement with the computed free reaction energy differences for the six and seven rings in (D).

by a six-membered ring and reveals clear density for a hydroxyl group at the C5 position of the linkage (Fig. 3C). We therefore conclude that inhibition by Z-LLY-Ketoaldehyde results in the formation of a 1,4-morpholine (six-membered) ring and not a 5,6-dihydro-2H-1,4-oxazine ring as reported previously (*16*). Coordination of the 1,4-morpholine ring in the active site diverges substantially from that of a seven-ring (Fig. 3C). The NUK chloride ion is absent, and a water molecule appears 1.2 Å away from the NUK site, where it hydrogen bonds to the Ser^{130}-amine and γ-OH, as well as to N4 and C6-OH of the 1,4-morpholine ring. The C5-OH moiety is stabilized through a dense hydrogen-bond network involving Arg^{19}-carbonyl, Tyr^{169}-carbonyl, Lys^{33}-Nε, and the active site H_2O-3. These findings hint that H_2O-3 might play a critical, yet undefined, role both in proteasomal catalysis of peptide cleavage and in the cyclization step of the inhibition reaction.

To address the putative role of H_2O-3 in the inhibition mechanism, we determined the high-resolution structures of human 20*S* proteasomes with boronic acid inhibitors, which mimic the first tetrahedral intermediate in protein cleavage (Fig. 4, A to C). Boronic inhibitors constitute a particularly important class since Bortezomib was the first proteasome inhibitor approved in 2004 for the treatment of multiple myeloma (*17*). Ixazomib was approved as an orally bioavailable inhibitor to treat the same disease in 2015 (*18*), and Delanzomib is presently in clinical trials for this purpose and to treat autoimmune disease (*19*). Specifically, we determined the 2.1 Å resolution structure of the Bortezomib-20*S* proteasome complex (Fig. 4A), the 2.0 Å structure of the Ixazomib(MLN9708)-20*S* proteasome complex (Fig. 4B), and the 2.0 Å structure of the Delanzomib(CEP-18770)-20*S* proteasome complex (Fig. 4C). In all these cocrystal structures, the NUK chloride is exchanged against water, and H_2O-1 and H_2O-2 are displaced from the active site upon inhibitor binding. H_2O-3, however, remains prominently hydrogen-bonded to the hydroxyl group of the boronic acid moiety, suggesting that it stabilizes the tetrahedral intermediate (Figs. 4, A, B, and C). Given these observations, two conclusions can be drawn: (i) the NUK solvent molecule resides on the opposite stereoface of the inhibitor and thus cannot support the cyclization step in the inhibition mechanism for epoxyketones and ketoaldehydes, and (ii) H_2O-3 appears well positioned to play a role in this second step.

To better understand the proteasome inhibition mechanism, we performed cluster quantum chemical calculations on the basis of the crystal structures. Our results indicate that residues Asp^{17} and Lys^{33} cooperate to activate the Thr^{1}-γOH nucleophile, whereas the NUK solvent molecule stabilizes the resulting tetrahedral oxyanion (figs. S8 and S9 and supplementary text). Second, we obtained full reaction pathways for both six- and seven-ring formation through a similar epoxide ring opening event (fig. S10 and SM). The reaction bottleneck is this cyclization step of the inhibition mechanism, where we find that the seven-ring pathway is kinetically favored (by ~18 kJ/mol) (Fig. 4D). Thermodynamically, the six-ring product is more stable (by ~30 kJ/mol) (Fig. 4D), but the strain of the transition state results in a preferential seven-ring formation (movies S1 and S2). We have found no evidence that the NUK solvent molecule could participate in this cyclization step due to its location at the opposite stereoface relative to the amine nucleophile. Instead, from the computed pathways and the boronic inhibitor cocrystal structures, H_2O-3 likely serves as a proton shuttle in this step. We propose to refer to H_2O-3 as CAT (for a catalytic water), given its likely role in the second step of the inhibition mechanism and the implicated role in peptide hydrolysis. Our kinetic measurements provide further evidence of the kinetic preference toward the seven-ring formation. The first-order inhibition rate constant for the ketoaldehyde is smaller by a factor of ~20 than for Oprozomib and Dihydroeponemycin (Fig. 4E). A residual rate of 3% of the maximum catalytic activity was only found in the case of seven-ring–forming epoxyketones, confirming that this product is thermodynamically less stable than the six-ring–forming ketoaldehyde. This is in agreement with our computed free energy differences.

The high-resolution structures of the human 20*S* proteasome described here were obtained as a result of numerous technical improvements in sample purification, crystal handling, and crystallographic data collection. Based on electron density maps at resolutions between 1.8 and 2.1 Å, we redefined the native and inhibited proteasome active site in terms of solvent molecules and covalent linkages with inhibitors. These findings were corroborated by cluster quantum chemical calculations and kinetic assays and are relevant for understanding the catalytic details of

proteasome activity and its inhibition chemistry. The insights into the atomic details of the catalytic center of the human 20*S* proteasome—an actual target of cancer therapeutics—provide important clues for the design of a new class of proteasome inhibitors. In particular, our results suggest that dual-electrophile inhibitors, where both electrophiles are in a β position to each other, would exhibit kinetically enhanced inhibition rates. Generally, with the tools described here, large numbers of such potential cancer therapeutics can be structurally analyzed at high resolution (several hundred per week could be feasible in an industrial setting), allowing for systematic exploration of ligand binding space toward improved efficacy and specificity.

REFERENCES AND NOTES

1. M. Bochtler, L. Ditzel, M. Groll, C. Hartmann, R. Huber, *Annu. Rev. Biophys. Biomol. Struct.* **28**, 295–317 (1999).
2. E. Kish-Trier, C. P. Hill, *Annu Rev Biophys* **42**, 29–49 (2013).
3. A. Ciechanover, *Cell* **79**, 13–21 (1994).
4. D. Finley, *Annu. Rev. Biochem.* **78**, 477–513 (2009).
5. M. Groll *et al.*, *Nature* **386**, 463–471 (1997).
6. W. Harshbarger, C. Miller, C. Diedrich, J. Sacchettini, *Structure* **23**, 418–424 (2015).
7. P. C. da Fonseca, E. P. Morris, *Nat. Commun.* **6**, 7573 (2015).
8. A. Chari *et al.*, *Nat. Methods* **12**, 859–865 (2015).
9. E. M. Huber *et al.*, *Cell* **148**, 727–738 (2012).
10. E. M. Huber *et al.*, *Nat. Commun.* **7**, 10900 (2016).
11. E. M. Huber, W. Heinemeyer, M. Groll, *Structure* **23**, 407–417 (2015).
12. S. D. Demo *et al.*, *Cancer Res.* **67**, 6383–6391 (2007).
13. T. A. Grigoreva, V. G. Tribulovich, A. V. Garabadzhiu, G. Melino, N. A. Barlev, *Oncotarget* **6**, 24733–24749 (2015).
14. M. Groll, K. B. Kim, N. Kairies, R. Huber, C. M. Crews, *J. Am. Chem. Soc.* **122**, 1237–1238 (2000).
15. J. F. Lynas, P. Harriott, A. Healy, M. A. McKervey, B. Walker, *Bioorg. Med. Chem. Lett.* **8**, 373–378 (1998).
16. M. A. Gräwert *et al.*, *Angew. Chem. Int. Ed. Engl.* **50**, 542–544 (2011).
17. R. C. Kane, A. T. Farrell, R. Sridhara, R. Pazdur, *Clin. Cancer Res.* **12**, 2955–2960 (2006).
18. M. Shirley, *Drugs* **76**, 405–411 (2016).
19. M. K. Bennett, C. J. Kirk, *Curr. Opin. Drug Discov. Devel.* **11**, 616–625 (2008).

ACKNOWLEDGMENTS

We thank T. Conrad and H. Kohansal for help with HeLa cell culture and extract preparation, respectively. The coordinates for the determined structures are deposited in the Protein Data Bank (PDB accession codes 5LE5, 5LEX, 5LEY, 5LEZ, 5LF0, 5LF1, 5LF3, 5LF4, 5LF6, and 5LF7; these codes are associated with the relevant structures in table S2). We thank A. N. Popov for support at beamline ID23, ESRF Grenoble, France, and M. Cianci for support at beamline P13, PETRA3@DESY, in the initial stages of this project. This work was funded by grants from the Deutsche Forschungsgemeinschaft (DFG; CH1098-1/1 to A.C., SFB860-TP A5 to H.S.). H.S. and A.C. received support from an R&D Instruct grant as part of the European Strategy Forum on Research Infrastructures (ESFRI), which is supported by national member subscriptions. The installation of the transfocator system into beamline P14 was supported by Bundesministerium für Bildung und Forschung (BMBF) grant 05K2013-624 to EMBL. A.C., J.S., F.H., and H.S. have applied for patents regarding the purification method (EP 16 17 3037.9 and USSN 62/345,913) and the next-generation proteasome inhibitor design (EP 16 17 3057.7 and USSN 62/346,203) described in this Report.

SUPPLEMENTARY MATERIALS

www.sciencemag.org/content/353/6299/594/suppl/DC1
Materials and Methods
Supplementary Text
Figs. S1 to S10
Tables S1 and S2
Movies S1 and S2
References (*20*–*33*)

16 April 2016; accepted 14 July 2016
10.1126/science.aaf8993

MOLECULAR IMAGING

Spatial organization of chromatin domains and compartments in single chromosomes

Siyuan Wang,[1] Jun-Han Su,[1] Brian J. Beliveau,[2]* Bogdan Bintu,[1] Jeffrey R. Moffitt,[1] Chao-ting Wu,[2]† Xiaowei Zhuang[1]†

The spatial organization of chromatin critically affects genome function. Recent chromosome-conformation-capture studies have revealed topologically associating domains (TADs) as a conserved feature of chromatin organization, but how TADs are spatially organized in individual chromosomes remains unknown. Here, we developed an imaging method for mapping the spatial positions of numerous genomic regions along individual chromosomes and traced the positions of TADs in human interphase autosomes and X chromosomes. We observed that chromosome folding deviates from the ideal fractal-globule model at large length scales and that TADs are largely organized into two compartments spatially arranged in a polarized manner in individual chromosomes. Active and inactive X chromosomes adopt different folding and compartmentalization configurations. These results suggest that the spatial organization of chromatin domains can change in response to regulation.

The spatial organization of chromatin, such as chromatin domains, chromatin loops, associations of chromatin with nuclear structures, and chromosome territories, plays an important role in essential genome functions (*1*–*6*). However, many gaps remain in our understanding of the three-dimensional (3D) folding of individual chromosomes in the nucleus. Recently, chromosome-conformation-capture methods such as Hi-C (*4*, *7*) have revealed a wealth of structural insights for interphase chromosomes. For example, chromatin is organized into topologically associating domains (TADs) or contact domains that are hundreds of kilobases (kb) in size (*8*–*11*). These domains tend to spatially segregate from each other (*9*, *12*, *13*) and, in *Drosophila*, correspond to the banding patterns of polytene chromosomes (*14*, *15*). At length scales from several hundred kilobases to several megabases, the power-law scaling of Hi-C contact frequency is consistent with a fractal-globule polymer model (*7*, *16*), whereas, within TADs, Hi-C contact maps are better described by a loop-extrusion model (*17*, *18*). Superresolution imaging shows that chromatin domains in different epigenetic states adopt distinct folding configurations with different power-law scaling properties (*13*). Whether the ideal fractal-globule model can describe chromatin at length scales beyond several megabases remains an open question (*19*, *20*). Hi-C analyses have also revealed two multi-TAD compartments, compartments A and B, that are enriched with active and inactive chromatin, respectively (*7*, *21*). However, because the contact maps used to identify these compartments were derived from ensemble averaging of many chromosomes, it is unclear whether the A and B compartments are structures that exist in individual chromosomes inside single cells and, if so, how the two compartments are spatially arranged with respect to each other. To answer questions regarding the spatial organization of individual chromosomes requires methods that directly visualize the conformation of single chromosomes in single cells.

Fluorescence in situ hybridization (FISH) provides a powerful means to directly image the spatial organization of chromosomes, especially when used to simultaneously target two or more genomic loci (e.g., *19*, *20*, *22*–*24*). In one effort, a three-color barcoding approach has been used to simultaneously label multiple chromatin loci to trace the conformation of a chromosome arm in *Drosophila* blastoderm embryos (*24*). Nonetheless, routine tracing of the complex 3D folding path of chromosomes has remained challenging because of the difficulties associated with simultaneously imaging and unambiguously identifying many genomic regions on interphase chromosomes. Here, we report a multiplexed FISH method that enables sequential imaging of many genomic regions for 3D tracing of individual chromosomes in the nucleus and the use of this method to study the spatial arrangements of TADs and compartments in chromosomes 20, 21, 22, and X of human diploid (XX) IMR90 cells.

[1]Howard Hughes Medical Institute, Department of Chemistry and Chemical Biology, Department of Physics, Harvard University, Cambridge, MA 02138, USA.
[2]Department of Genetics, Harvard Medical School, Boston, MA 02115, USA.
*Present address: Wyss Institute for Biologically Inspired Engineering, Harvard University, Boston, MA 02446, USA.
†Corresponding author. Email: zhuang@chemistry.harvard.edu (X.Z.); twu@genetics.med.harvard.edu (C.-t.W.)

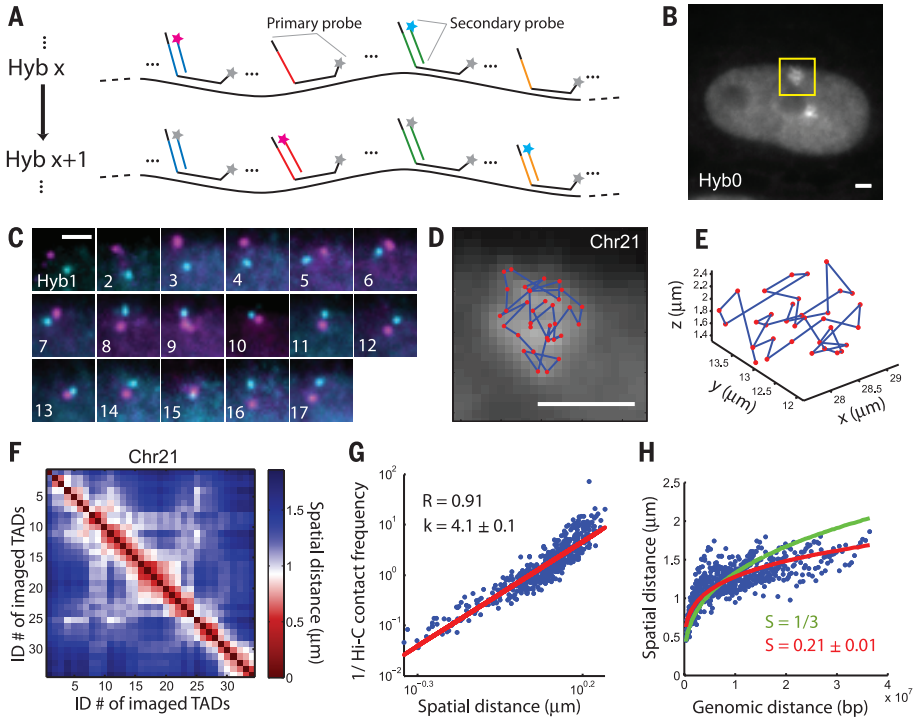

Fig. 1. Mapping the spatial organization of the central 100-kb regions of all 34 TADs in chromosome 21 (Chr21) of IMR90 cells. (**A**) A simplified scheme of the imaging approach. All primary probes are first hybridized to the targeted chromosome, after which secondary probes targeting each TAD are sequentially hybridized to the readout sequences on the primary probes, imaged, and then bleached. In each round of secondary hybridization, two different secondary probes tagged with dyes of different colors allowed simultaneous visualization of two TADs. More details are depicted in fig. S1. (**B**) Image of an IMR90 cell after the primary hybridization (Hyb 0) with primary probes targeting all TADs in Chr21. The two bright patches, one marked by a yellow box, correspond to the two copies of Chr21 in this diploid cell. (**C**) Images of the yellow-boxed region in (B) after each round of secondary hybridization (Hyb 1 to 17). (**D**) Positions of the 34 TADs of the chromosome were plotted as red dots overlaid on the Hyb 0 image. Scale bars in (B) to (D), 2 μm. (**E**) TAD positions plotted in 3D. (**F**) Mean spatial distance matrix for the 34 TADs, with each element of the matrix corresponding to the mean spatial distance between a pair of TADs. (**G**) Inverse Hi-C contact frequency between each pair of TADs versus their mean spatial distance. The correlation coefficient (*R*) and the slope of a fitted line (*k*) are shown. Contact frequency is calculated as the total Hi-C counts between two TADs normalized to their genomic lengths (*8*). (**H**) Mean spatial distance versus genomic distance for all pairs of TADs. The lines are power-law function fits with either a predefined scaling exponent (*S* = 1/3, green) or with *S* as a fitting parameter (red). Data from 120 individual chromosomes were used to generate (F) to (H).

To map the 3D spatial positions of TADs, delineated here as genomic domains based on ensemble-average Hi-C maps (*8*), along an entire chromosome, we labeled the central 100-kb regions of TADs using a dual-oligonucleotide version of Oligopaints (*25*, *26*), wherein each TAD was targeted with 1000 distinct "primary" oligonucleotide probes and a companion "secondary" probe (Fig. 1A and fig. S1). Each of the 1000 primary probes consisted of a unique targeting sequence complementary to a given sequence within the TAD and a nongenomic region, called Mainstreet, that contained a readout sequence shared by all 1000 probes but unique for each TAD. The secondary probe contained a sequence complementary to the readout sequence on Mainstreet. We used the genomic coordinates of TADs derived from Hi-C (*8*) to design the targeting sequences of primary probes and produced these probes with a high-yield enzymatic amplification method (*27*). We exploited a similar hybridization and imaging protocol as we previously described in multiplexed error-robust fluorescence in situ hybridization (MERFISH) (*27*) but with some modifications. First, we hybridized all primary probes to the chromosome of interest (fig. S1, Hyb 0), imaged the sample, and located the chromosome in the nucleus. We then photobleached the sample and performed a series of secondary hybridizations, separated by photobleaching, to sequentially label and image individual TADs (Fig. 1A and fig. S1, Hyb 1, Hyb 2, and so on). Each round of secondary hybridization employed two different secondary probes, respectively labeled with two spectrally distinct dyes, enabling us to visualize two TADs simultaneously using two-color, 3D fluorescence imaging with *z*-stepping. The centroid positions of the 3D images of individual TADs were used to approximate their positions in *x*, *y*, and *z*.

We first used this method to image chromosome 21 (Chr21) in interphase IMR90 cells. The Hyb 0 image showed that, when imaged together, the fluorescent signals from all 34 TADs of Chr21 coalesced into a continuous patch (Fig. 1B). The 17 rounds of secondary hybridization then allowed us to image each of the 34 TADs separately (Fig. 1C), determine the 3D position of each TAD, and trace the 3D path of this chromosome at the TAD level (Fig. 1, D and E). To characterize the organization of Chr21, we traced 120 copies of Chr21 in many cells, calculated the mean spatial distance between each pair of TADs (averaged over all 120 chromosomes), and constructed a pair-wise mean spatial distance matrix for the 34 TADs (Fig. 1F).

To compare our measurements with previous Hi-C data (*8*), we correlated the mean spatial distance matrix with the corresponding Hi-C contact frequency matrix of Chr21 (fig. S2). Notably, the mean spatial distance showed high correlation with the inverse contact frequency between TADs, with a Pearson correlation coefficient of 0.91 across nearly three orders of magnitude in contact frequency (Fig. 1G). Such a strong correlation between the results from two different methods provided a cross validation for both methods at the TAD-to-chromosome length scales probed in this work. The relationship between the spatial distance and contact frequency also provides a valuable measure for exploring chromosome organization. A mean-field approximation predicts that the contact frequency should be inversely proportional to the third power of the mean spatial distance, whereas the power for real chromatin is expected to be bigger than 3 (*19*). Our data showed that the Hi-C contact frequency was inversely proportional to the fourth power of the mean spatial distance [Fig. 1G, scaling exponent k = 4.1 ± 0.1, 95% confidence interval (CI), N = 120 chromosomes]. We also analyzed the distributions of the spatial distances between pairs of TADs (fig. S3) and found that the Hi-C contact frequency scaled linearly with the probability of two TADs coming into spatial proximity (fig. S4). These results suggest a calibration function to convert Hi-C contact frequencies into mean spatial distances at TAD-to-chromosome length scales, although it remains to be determined whether this calibration extends to sub-TAD scales where the correlation between the Hi-C contact frequency and spatial proximity may be weaker (*28*).

In addition, our data showed that the mean spatial distance between TADs scaled with

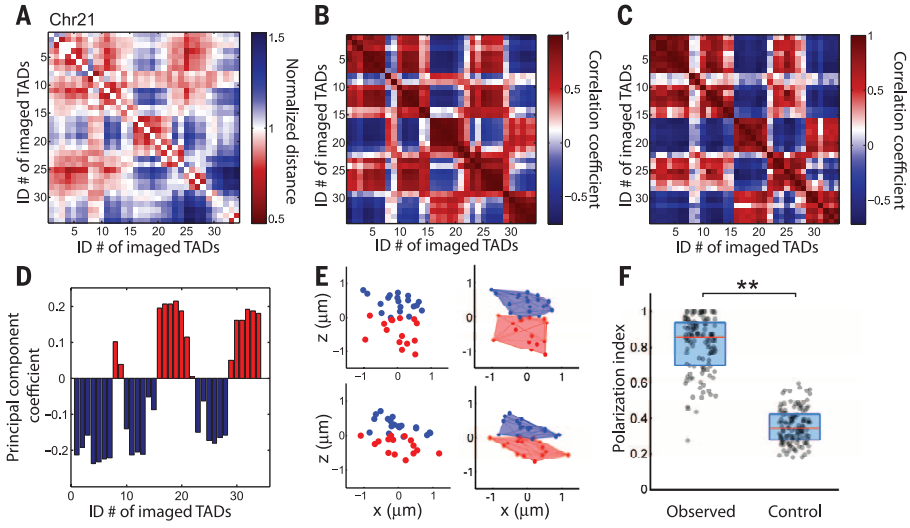

Fig. 2. Spatial organization of compartments in individual chromosomes of Chr21. (**A**) Normalized spatial distance matrix for the 34 TADs, normalized over the expected spatial distances determined by the power-law function fit in Fig. 1H (red line). (**B**) Pearson correlation matrix of the 34 TADs, determined from the normalized spatial distance matrix in (A). (**C**) Pearson correlation matrix of the 34 TADs calculated from previous Hi-C data (*8*). (**D**) Assignment of TADs to compartment A (red bars) or compartment B (blue bars) based on a principal components analysis of the Pearson correlation matrix shown in (B). (**E**) (Left panels) Spatial position maps of compartment-A TADs (red) and compartment-B TADs (blue) in two individual chromosomes. For better visualization, the chromosomes were rotated so that the polarization axis connecting the centroids of compartments A and B is aligned along the *z* axis. (Right panels) Corresponding 3D convex hull plots. (**F**) Polarization index values measured for individual chromosomes (observed) in comparison with those derived from a randomization control where the compartment assignments were randomized while maintaining the total number of TADs in each compartment. The nonzero control values arose from fluctuations associated with the finite number of TADs per chromosome, which provides a baseline for comparison. Each dot corresponds to the polarization index of a single chromosome, the red lines represent the median values, and the blue boxes represent the 25% to 75% quantiles. $^{**}P < 0.001$ (Wilcoxon test). Data from 120 individual chromosomes were used to generate (A), (B), (D), and (F).

their genomic distance to about one-fifth power (Fig. 1H, scaling exponent $S = 0.21 \pm 0.01$, 95% CI, $N = 120$ chromosomes). This value deviated from the one-third power expected from the ideal fractal-globule polymer model (*19*). The deviation was most pronounced for large genomic distances, whereas data points with genomic distances less than 7 Mb showed a scaling exponent close to one-third (fig. S5), consistent with previous results (*7*, *19*). Interestingly, a previous simulation of confined, unknotted, finite-sized polymers showed a deviation of the scaling exponent from one-third at large length scales (*29*), suggesting a possible physical model to explain our experimental observation.

Next, we determined whether the spatial positions of TADs are partitioned into distinct compartments by implementing a normalization analysis similar to that performed for the Hi-C data (*7*). First, we normalized the mean spatial distance matrix to the expected spatial distance at each genomic distance as predicted by the power-law scaling shown in Fig. 1H. The normalized spatial distance matrix showed a pattern with alternating regions of large and small values (Fig. 2A), suggesting the existence of two subgroups of TADs. Next, we calculated the Pearson correlation coefficient between each pair of columns in the normalized distance matrix, defined this coefficient as the correlation between the two corresponding TADs, and constructed a Pearson correlation matrix for all TAD pairs (Fig. 2B). This Pearson correlation matrix showed a plaid pattern, consistent with the existence of two compartments with TADs from the same compartment being positively correlated. For comparison, we used a similar approach (*7*) to analyze the Hi-C data (*8*) and obtained a nearly identical Pearson correlation matrix (Fig. 2C), suggesting that the two compartments observed in our imaging data correspond to the A and B compartments identified by Hi-C analysis (*7*, *21*). To assign each TAD to a compartment, we performed a principal components analysis on the Pearson correlation matrix derived from the normalized spatial distances and assigned TADs with positive and negative values along the first principal component to compartments A and B, respectively (Fig. 2D). Nearly identical assignment was obtained by applying the principal components analysis directly to the normalized spatial distance matrix (fig. S6). We further observed that histone modifications for active chromatin (*30*, *31*) and inactive chromatin (*32*) were enriched in compartments A and B, respectively (fig. S7), consistent with previous Hi-C analysis (*7*). We then analyzed the scaling relationship between inverse Hi-C contact frequency and mean spatial distance for pairs of TADs that are either within the same compartment or cross-compartment and found that cross-compartment TAD pairs gave a moderately higher scaling exponent (fig. S8).

The above population-averaged analyses cannot reveal whether the higher correlation observed between TADs in the same compartment represents transient proximity between these TADs or whether the two compartments are physical structures that exist in individual chromosomes, nor can they reveal how compartments are spatially arranged—e.g., whether one compartment wraps around the other to form a radial organization within a single chromosome or whether the two compartments are arranged in a side-by-side, polarized manner. To address these questions, we examined the spatial positions of the central regions of TADs in single chromosomes. Notably, most individual chromosomes in single cells showed a spatially polarized arrangement of compartment-A and compartment-B TADs (Fig. 2E). To quantify the polarized separation of the compartments in individual chromosomes, we defined a polarization index as $\sqrt{(1-V_S/V_A)(1-V_S/V_B)}$, where V_A and V_B are the convex hull volumes of the two compartments and V_S is their shared volume. If the two compartments perfectly overlap with each other, or if one compartment wraps around the other, the polarization index should equal zero; on the other hand, if the two compartments are completely separated in space in a polarized manner, the polarization index should equal 1 (fig. S9). The measured polarization index values of Chr21 were indeed close to 1, with a median value of 0.86, substantially larger than the values derived from a randomization control (Fig. 2F).

To investigate whether the above findings were chromosome-specific, we traced the positions of the central 100-kb regions of TADs in Chr22 and Chr20 by imaging all 27 TADs in Chr22 and 30 of the 60 TADs (every other one) in Chr20 and found conclusions similar to those described for Chr21. First, the Hi-C contact frequency was inversely proportional to the fourth power of the mean spatial distance between TADs (figs. S10A and S11A). Second, the mean spatial distance between TADs scaled with genomic distance to a similar, albeit slightly smaller, power than in Chr21 (Fig. 3, A and B), substantially deviating from the one-third power predicted by the

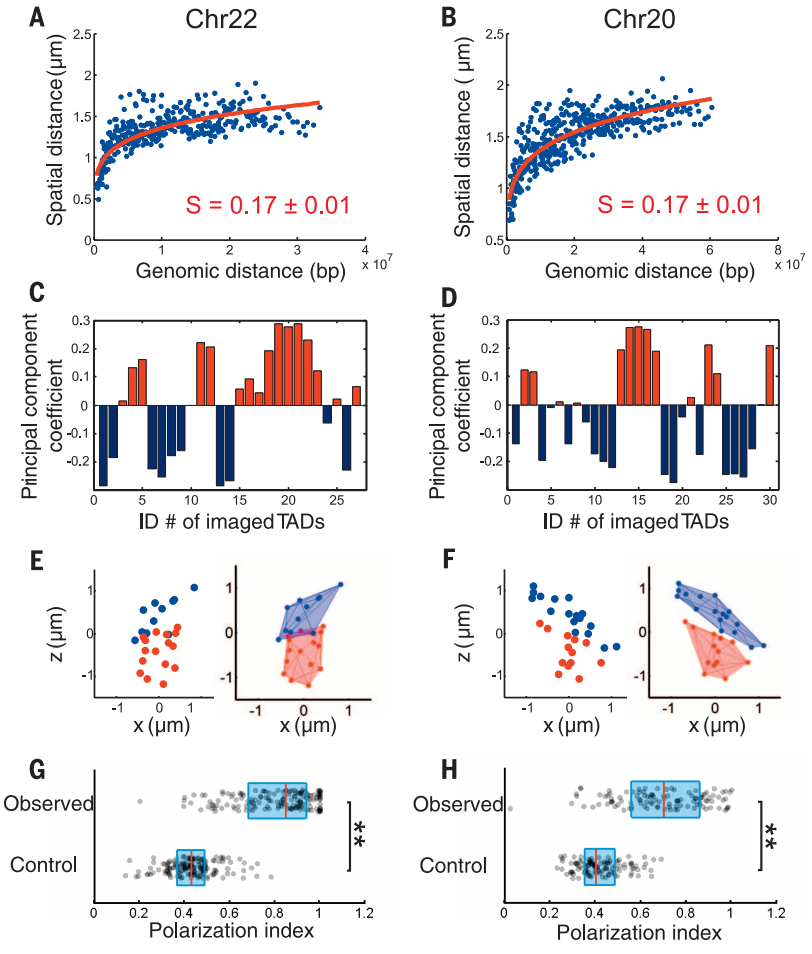

Fig. 3. Spatial organization of the central 100-kb regions of TADs in chromosome 22 (Chr22) and chromosome 20 (Chr20). (**A** and **B**) Mean spatial distance versus genomic distance for Chr22 (A) and Chr20 (B). Power-law function fits are shown as red lines, and the scaling exponents (*S*) are shown. (**C** and **D**) Compartment assignments of TADs based on principal components analyses of the Pearson correlation matrix for Chr22 (fig. S10D) and Chr20 (fig. S11D). Blue bars, compartment B. Red bars, compartment A. (**E** and **F**) Spatial position maps of compartment-A TADs (red) and compartment-B TADs (blue) in single chromosomes for Chr22 (E) and Chr20 (F), plotted without (left) or with (right) 3D convex hulls. (**G** and **H**) Polarization index values measured for individual chromosomes for Chr22 (G) and Chr20 (H) (observed) in comparison with those of the randomization control (control). The dots, red lines, and blue boxes are defined as in Fig. 2F. $^{**}P < 0.001$ (Wilcoxon test). Data from ~150 individual chromosomes were used to generate (A), (C), and (G), and data from ~110 individual chromosomes were used to generate (B), (D), and (H).

ideal fractal-globule model. Third, analysis based on spatial distances showed that TADs in Chr22 and Chr20 were partitioned into two spatial compartments (Fig. 3, C and D, and figs. S10, B to E, and S11, B to E), with assignments nearly identical to those obtained from our analysis on Hi-C data. These two compartments were again spatially organized in a polarized, side-by-side manner in individual chromosomes (Fig. 3, E to H), although the degree of polarized separation is moderately smaller in Chr20. Whether these findings extend to all other autosomes remains to be determined.

Finally, we traced the positions of the central 100-kb regions of TADs in the X chromosome (ChrX). We imaged 40 TADs (out of 86 total) spanning the whole chromosome at relatively uniform intervals. It is known that one of the two copies of ChrX in female mammalian cells undergoes X-inactivation (*33*, *34*). We used TAD coordinates obtained from the combined Hi-C data (*8*) of both active and inactive copies of ChrX (Xa and Xi) to determine labeling sites but note that the TAD structures are attenuated or absent on Xi (*9*, *35*). We distinguished Xa and Xi by immunostaining of macroH2A.1 (fig. S12), a histone variant enriched in Xi (*35*). The mean spatial distance matrices of Xi and Xa were strikingly different, with the Xi matrix elements being substantially more homogeneous and mostly having smaller values than the Xa matrix elements (fig. S13, A and B). Indeed, fitting a power-law function to the spatial versus genomic distance plot yielded a very small scaling exponent of $S = 0.074 \pm 0.003$ (95% CI, $N = 95$ chromosomes) for Xi (Fig. 4A), whereas the scaling exponent for Xa ($S = 0.22 \pm 0.01$, 95% CI, $N = 95$ chromosomes) remained similar to those of Chr20, Chr21, and Chr22 (Fig. 4B). These observations suggest that Xi not only was more compact (*36*) but also adopted a spatially more intermixed chromatin arrangement with more homogeneous interloci distances, reminiscent of the chromatin organization observed for Polycomb-repressed domains using superresolution imaging (*13*). Given the enrichment of Polycomb group proteins on Xi (*33*, *34*), these observations suggest a potentially general mechanism to induce such a compact and highly intermixed chromatin folding configuration.

Notably, ChrX also formed two compartments, but the compartmentalization schemes were different for Xi and Xa. Consistent with previous allele-specific Hi-C analyses (*21*, *35*, *37*), Xi was largely partitioned into two contiguous compartments (also called superdomains or megadomains) separated on the genomic map by the DXZ4 macrosatellite (Fig. 4C and fig. S13, C, E, and G). Such a scheme might result from the ability of the DXZ4 element to recruit the chromatin insulator CTCF to Xi but not to Xa (*38*). The Xa TADs were also partitioned into two spatial compartments, but the two compartments corresponded instead to the p and q arms of the chromosome (Fig. 4D and fig. S13, D, F, and H). Interestingly, the two compartments in both Xa and Xi were again spatially organized in a polarized, side-by-side manner in individual chromosomes (Fig. 4, E to H). However, the degree of polarized segregation was notably smaller for Xi (Fig. 4G), consistent with our observation of more intermixed chromatin in Xi. It is worth noting that within the individual arms of Xa, TADs were further partitioned into two subcompartments (fig. S14, A to C), one of which appeared to be relatively enriched with histone modifications for active chromatin (fig. S14D), implying that these subcompartments potentially correspond to the A and B compartments.

Our observation that compartments A and B are organized in a spatially polarized manner in single chromosomes in most cells suggests that these are relatively stable physical structures that are present most of the time in individual cells. The fact that we observed this spatial organization for all three examined autosomes (Chr20, 21, and 22) also supports the possibility that these structures are functionally important and maintained by specific mechanisms (*2*, *4*). Because compartments A and B consist mainly of active and inactive chromatin, respectively (*7*, *21*), their presence may serve to locally enrich for transcription

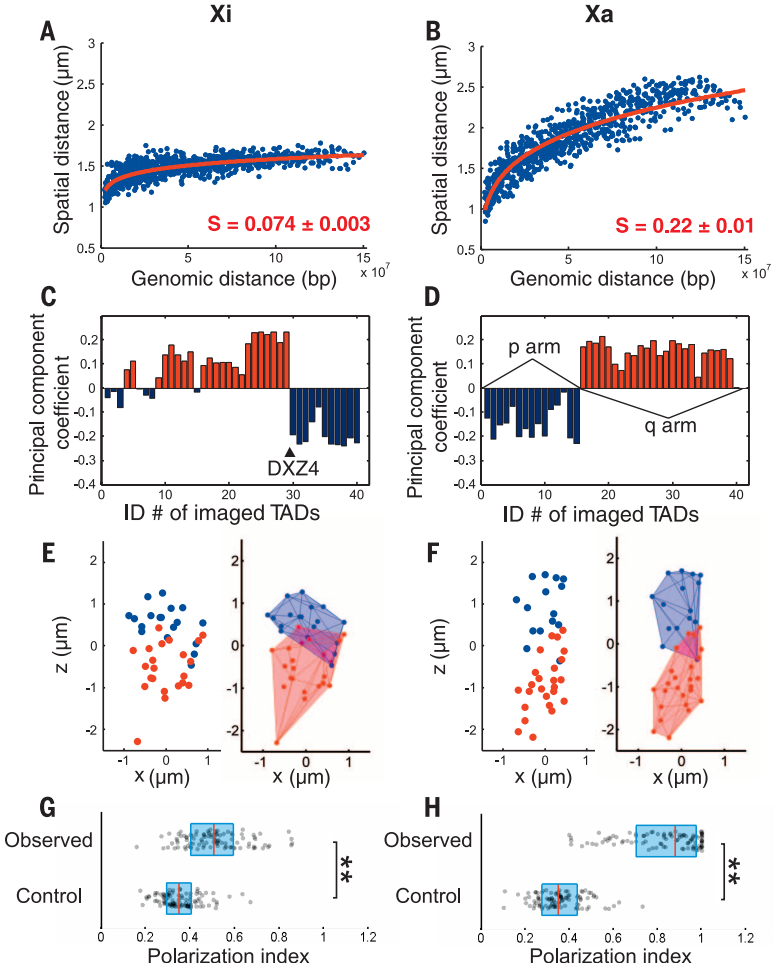

Fig. 4. Spatial organization of the central 100-kb regions of TADs in inactive and active X (Xi and Xa) chromosomes. The TAD structures are attenuated or absent on Xi (*9*, *35*) and hence, for Xi, the term "TAD" simply represents imaged genomic loci. (**A** and **B**) Mean spatial distance versus genomic distance for Xi (A) and Xa (B). Power-law function fits are shown as red lines, and the scaling exponents (*S*) are shown. (**C** and **D**) Compartment assignments for Xi (C) and Xa (D), based on principal components analyses of the Pearson correlation matrix for Xi (fig. S13C) and Xa (fig. S13D). Positions of the DXZ4 macrosatellite in Xi and the p and q arms in Xa are indicated. (**E** and **F**) Spatial position maps of TADs in single Xi (E) and Xa (F) chromosomes, without (left) or with (right) 3D convex hulls. (**G** and **H**) Polarization index measured for Xi (G) and Xa (H) (observed) in comparison with those of the randomization control (control). The dots, red lines, and blue boxes are defined as in Fig. 2F. $^{**}P < 0.001$ (Wilcoxon test). Data from 95 individual chromosomes were used to generate (A) to (D), (G), and (H).

machinery and/or epigenetic regulators and thus enhance the efficient use of these molecular resources. The interactions that maintain these compartments could be direct and/or indirect—i.e., some chromatin binding factors may directly cross-link TADs belonging to the same compartment or some factors may recruit TADs to predefined nuclear areas to form compartments. The large-scale extension of chromatin upon activation (*39*, *40*) may also contribute to the separation of inactive and active chromatin. Finally, we observed distinct compartmentalization schemes for inactive and active X chromosomes, with Xi being partitioned into two contiguous compartments separated by the DXZ4 element (*21*, *35*, *37*) and Xa being partitioned according to the p and q arms, although individual arms of Xa may be further partitioned into A and B compartments. Together, these results suggest that the spatial organization of chromatin domains may play an important role in gene regulation and that this organization could be altered to facilitate different chromosomal functions.

REFERENCES AND NOTES

1. T. Misteli, *Cell* **128**, 787–800 (2007).
2. D. U. Gorkin, D. Leung, B. Ren, *Cell Stem Cell* **14**, 762–775 (2014).
3. M. Levine, C. Cattoglio, R. Tjian, *Cell* **157**, 13–25 (2014).
4. J. Dekker, L. Mirny, *Cell* **164**, 1110–1121 (2016).
5. W. A. Bickmore, B. van Steensel, *Cell* **152**, 1270–1284 (2013).
6. T. Cremer, M. Cremer, *Cold Spring Harb. Perspect. Biol.* **2**, a003889 (2010).
7. E. Lieberman-Aiden *et al.*, *Science* **326**, 289–293 (2009).
8. J. R. Dixon *et al.*, *Nature* **485**, 376–380 (2012).
9. E. P. Nora *et al.*, *Nature* **485**, 381–385 (2012).
10. T. Sexton *et al.*, *Cell* **148**, 458–472 (2012).
11. C. Hou, L. Li, Z. S. Qin, V. G. Corces, *Mol. Cell* **48**, 471–484 (2012).
12. P. J. Fabre *et al.*, *Proc. Natl. Acad. Sci. U.S.A.* **112**, 13964–13969 (2015).
13. A. N. Boettiger *et al.*, *Nature* **529**, 418–422 (2016).
14. K. P. Eagen, T. A. Hartl, R. D. Kornberg, *Cell* **163**, 934–946 (2015).
15. S. V. Ulianov *et al.*, *Genome Res.* **26**, 70–84 (2016).
16. L. A. Mirny, *Chromosome Res.* **19**, 37–51 (2011).
17. G. Fudenberg *et al.*, *Cell Reports* **15**, 2038–2049 (2016).
18. A. L. Sanborn *et al.*, *Proc. Natl. Acad. Sci. U.S.A.* **112**, E6456–E6465 (2015).
19. J. D. Halverson, J. Smrek, K. Kremer, A. Y. Grosberg, *Rep. Prog. Phys.* **77**, 022601 (2014).
20. J. Mateos-Langerak *et al.*, *Proc. Natl. Acad. Sci. U.S.A.* **106**, 3812–3817 (2009).
21. S. S. P. S. P. Rao *et al.*, *Cell* **159**, 1665–1680 (2014).
22. H. Yokota, G. van den Engh, J. E. Hearst, R. K. Sachs, B. J. Trask, *J. Cell Biol.* **130**, 1239–1249 (1995).
23. K. Bystricky, P. Heun, L. Gehlen, J. Langowski, S. M. Gasser, *Proc. Natl. Acad. Sci. U.S.A.* **101**, 16495–16500 (2004).
24. M. G. Lowenstein, T. D. Goddard, J. W. Sedat, *Mol. Biol. Cell* **15**, 5678–5692 (2004).
25. B. J. Beliveau *et al.*, *Proc. Natl. Acad. Sci. U.S.A.* **109**, 21301–21306 (2012).
26. B. J. Beliveau *et al.*, *Nat. Commun.* **6**, 7147 (2015).
27. K. H. Chen, A. N. Boettiger, J. R. Moffitt, S. Wang, X. Zhuang, *Science* **348**, aaa6090 (2015).
28. I. Williamson *et al.*, *Genes Dev.* **28**, 2778–2791 (2014).
29. M. V. Imakaev, K. M. Tchourine, S. K. Nechaev, L. A. Mirny, *Soft Matter* **11**, 665–671 (2015).
30. R. D. Hawkins *et al.*, *Cell Stem Cell* **6**, 479–491 (2010).
31. B. E. Bernstein *et al.*, *Nat. Biotechnol.* **28**, 1045–1048 (2010).
32. T. Chandra *et al.*, *Mol. Cell* **47**, 203–214 (2012).
33. D. Lessing, M. C. Anguera, J. T. Lee, *Annu. Rev. Genomics Hum. Genet.* **14**, 85–110 (2013).
34. R. Galupa, E. Heard, *Curr. Opin. Genet. Dev.* **31**, 57–66 (2015).
35. A. Minajigi *et al.*, *Science* **349**, aab2276 (2015).
36. C. Naughton, D. Sproul, C. Hamilton, N. Gilbert, *Mol. Cell* **40**, 397–409 (2010).
37. X. Deng *et al.*, *Genome Biol.* **16**, 152 (2015).
38. A. H. Horakova, S. C. Moseley, C. R. McLaughlin, D. C. Tremblay, B. P. Chadwick, *Hum. Mol. Genet.* **21**, 4367–4377 (2012).
39. T. Tumbar, G. Sudlow, A. S. Belmont, *J. Cell Biol.* **145**, 1341–1354 (1999).
40. M. J. Levesque, A. Raj, *Nat. Methods* **10**, 246–248 (2013).

ACKNOWLEDGMENTS

We thank B. Harada, K. H. Chen, A. Boettiger, and G. Nir for helpful discussions. This work is supported in part by the National Institutes of Health (to X.Z. and C.W.). S.W. is supported in part by a Jane Coffin Childs Fellowship. X.Z. is a Howard Hughes Medical Institute Investigator.

SUPPLEMENTARY MATERIALS

www.sciencemag.org/content/353/6299/598/suppl/DC1
Materials and Methods
Figs. S1 to S15
Tables S1 to S8
References (*41*–*51*)

2 April 2016; accepted 12 July 2016
Published online 21 July 2016
10.1126/science.aaf8084

AXONAL DEGENERATION

RIPK1 mediates axonal degeneration by promoting inflammation and necroptosis in ALS

Yasushi Ito,[1] Dimitry Ofengeim,[1] Ayaz Najafov,[1] Sudeshna Das,[2] Shahram Saberi,[3,4] Ying Li,[1,5] Junichi Hitomi,[1] Hong Zhu,[1] Hongbo Chen,[1] Lior Mayo,[6] Jiefei Geng,[1] Palak Amin,[1] Judy Park DeWitt,[1] Adnan Kasim Mookhtiar,[1] Marcus Florez,[1] Amanda Tomie Ouchida,[1] Jian-bing Fan,[7] Manolis Pasparakis,[8] Michelle A. Kelliher,[9] John Ravits,[3,4] Junying Yuan[1,5]*

Mutations in the *optineurin* (*OPTN*) gene have been implicated in both familial and sporadic amyotrophic lateral sclerosis (ALS). However, the role of this protein in the central nervous system (CNS) and how it may contribute to ALS pathology are unclear. Here, we found that optineurin actively suppressed receptor-interacting kinase 1 (RIPK1)–dependent signaling by regulating its turnover. Loss of OPTN led to progressive dysmyelination and axonal degeneration through engagement of necroptotic machinery in the CNS, including RIPK1, RIPK3, and mixed lineage kinase domain–like protein (MLKL). Furthermore, RIPK1- and RIPK3-mediated axonal pathology was commonly observed in *SOD1*^{G93A} transgenic mice and pathological samples from human ALS patients. Thus, RIPK1 and RIPK3 play a critical role in mediating progressive axonal degeneration. Furthermore, inhibiting RIPK1 kinase may provide an axonal protective strategy for the treatment of ALS and other human degenerative diseases characterized by axonal degeneration.

Loss-of-function mutations in the *optineurin* (*OPTN*) gene have been implicated in both familial and sporadic cases of amyotrophic lateral sclerosis (ALS), a devastating degenerative motor neuron disease (*1*–*3*). The *Optn* gene encodes a ubiquitin-binding protein involved in tumor necrosis factor–α (TNFα) signaling but is dispensable for nuclear factor κB (NF-κB) activation (*4*, *5*). It is still unclear how the loss of function of *OPTN* leads to human ALS.

Receptor-interacting kinase 1 (RIPK1) is a critical regulator of cell death and inflammation (*6*). RIPK1 regulates necroptosis, a form of regulated necrotic cell death, by promoting the sequential activation of two downstream targets, RIPK3 and mixed lineage kinase domain–like protein (MLKL) (*7*–*9*). Application of necrostatin-1 (7-Cl-O-Nec-1) (Nec-1s), a highly specific inhibitor of RIPK1 kinase activity, blocks necroptosis and inflammation in vitro and in vivo (*10*, *11*). However, the pathophysiological significance of RIPK1 and necroptosis in the genetic context of human diseases remains to be established.

ALS belongs to axonal "dying back" neurodegenerative diseases, as the onset begins with axonal pathology. Axonal degeneration makes a substantial contribution to neurological disability in these patients (*12*). Axonal degeneration induced by direct nerve injury—known as Wallerian degeneration—is mediated through a mechanism distinct from apoptosis of neuronal cell bodies (*13*, *14*). Axonal degeneration in patients with neurodegenerative diseases such as ALS may also exhibit features similar to those of Wallerian degeneration and is referred to as "Wallerian-like" degeneration. The mechanism of Wallerian or Wallerian-like degeneration is still unclear.

To understand the mechanism by which the loss of OPTN could lead to ALS, we developed *Optn*$^{-/-}$ mice (fig. S1, A and B). We examined the impact of *Optn* loss in the spinal cord of *Optn*$^{-/-}$ mice. The number and morphology of spinal cord motor neurons in *Optn*$^{-/-}$ mice were indistinguishable from wild-type (WT) mice (fig. S1, C and D). However, from the age of 3 weeks to 2 years, we observed a marked reduction in the number of motor axons and abnormal myelination in the ventrolateral spinal cord white matter in the *Optn*$^{-/-}$ mice (Fig. 1, A to D, and fig. S1E). The axonal pathology presented as a decompaction of myelin sheaths with a decreased g-ratio (axon diameter/axon-plus-myelin diameter), an increased number of large-diameter axons, and a decreased axonal number in the ventrolateral white matter (Fig. 1, B to D), which suggested degeneration and swelling of motor neuron axons in *Optn*$^{-/-}$ mice. This finding is similar to the axonal pathology observed in the spinal cords of ALS patients in the early stages of the disease (*15*). The pathology was progressive—a reduction in axonal numbers was observed at 12 weeks or older but not at 3 weeks (fig. S1F). Similar pathology was observed in the ventral roots of motor axons in *Optn*$^{-/-}$ mice (fig. S1, G to J). In addition, denervation of neuromuscular junctions in the tibialis anterior muscle was observed in *Optn*$^{-/-}$ mice (fig. S1, K and L). Thus, OPTN deficiency leads to axonal pathology without affecting motor neuron cell bodies. Consistent with this notion, we observed a significant increase in the number of cells positive for terminal deoxynucleotidyl transferase–mediated deoxyuridine triphosphate nick end labeling (TUNEL^{+} cells) in the ventrolateral white matter of spinal cords of *Optn*$^{-/-}$ mice (Fig. 1E). Thus, Optn deficiency sensitizes cells to cell death in the spinal cord white matter of *Optn*$^{-/-}$ mice.

To determine the cell types involved in mediating Optn deficiency–induced axonal degeneration, we generated lineage-specific deletion of Optn using *Cnp-cre*, *Lyz2-cre*, *Gfap-cre*, and *Mnx1-cre* mice (*16*–*18*) (fig. S2). Loss of Optn from oligodendrocytes and myeloid cells, but not from astrocytes or motor neurons, was sufficient to reproduce axonal myelination pathology (Fig. 1, F to I). Furthermore, we induced Optn loss from the microglial lineage by dosing *Optn*$^{F/F}$;*Cx3cr1*^{Cre} mice (*19*) with tamoxifen for 1 month (fig. S3A) and also found axonal pathology like that in *Optn*$^{-/-}$ mice (fig. S3, B to E).

We found that knockdown of Optn sensitized cells to necroptosis in our genome-wide small interfering RNA screen (*20*, *21*) (Z-score = –2.07) (table S1). We further confirmed that knockdown of *Optn* sensitized L929 cells to necroptosis induced by TNFα or zVAD.fmk (fig. S4, A and B). zVAD-induced necrosis is known to involve autocrine TNFα activity (*22*). Thus, *Optn* deficiency sensitized cells to necroptosis (fig. S4C). The biochemical hallmarks of necroptosis—including the upshifts of Ripk1, Ripk3, and phospho-MLKL (p-MLKL), as well as the levels of complex IIb—were significantly higher in *Optn*$^{-/-}$ mouse embryo fibroblasts (MEFs) than in *Optn*$^{+/+}$ MEFs stimulated by TNFα, zVAD, or cycloheximide (fig. S4D). Note that *Optn*$^{-/-}$ oligodendrocytes were sensitized to die by TNFα-induced necroptosis but were protected by Nec-1s and in *Optn*$^{-/-}$;*Ripk1*$^{D138N/D138N}$ and *Optn*$^{-/-}$;*Ripk3*$^{-/-}$ double mutants (*23*, *24*) (Fig. 2A). Thus, Optn deficiency can promote necroptosis of oligodendrocytes.

The expression levels of Ripk1, Ripk3, and MLKL—the key mediators of necroptosis—were all increased in the spinal cords of *Optn*$^{-/-}$ mice (Fig. 2B). Furthermore, we detected the interaction of Optn and Ripk1 in spinal cords from WT mice (Fig. 2C). Compared with WT mice, RIPK1 lysine 48 (K48) ubiquitination levels were decreased, whereas Ripk1 mRNA was unchanged in the spinal cords of *Optn*$^{-/-}$ mice (Fig. 2, D and E). Furthermore, Ripk1 was degraded more slowly in *Optn*$^{-/-}$ MEFs than that in WT cells

[1]Department of Cell Biology, Harvard Medical School, 240 Longwood Avenue, Boston, MA 02115, USA. [2]MassGeneral Institute for Neurodegenerative Disease, Massachusetts General Hospital, Cambridge, MA 02139, USA. [3]Department of Neurology, Harvard Medical School, Boston, MA 02115, USA. [4]ALS Translational Research Program, Department of Neurosciences, University of California, San Diego, La Jolla, CA 92093, USA. [5]Interdisciplinary Research Center on Biology and Chemistry, Shanghai Institute of Organic Chemistry, Chinese Academy of Sciences, 26 QiuYue Road, PuDong District, Shanghai, 201210, China. [6]Ann Romney Center for Neurologic Diseases, Brigham and Women's Hospital, Harvard Medical School, Boston, MA 02115, USA. [7]Illumina, Inc., San Diego, CA 92122, USA. [8]Institute for Genetics, University of Cologne, 50674 Cologne, Germany. [9]Department of Cancer Biology, University of Massachusetts Medical School, Worcester, MA 01605, USA.
*Corresponding author. Email: jyuan@hms.harvard.edu

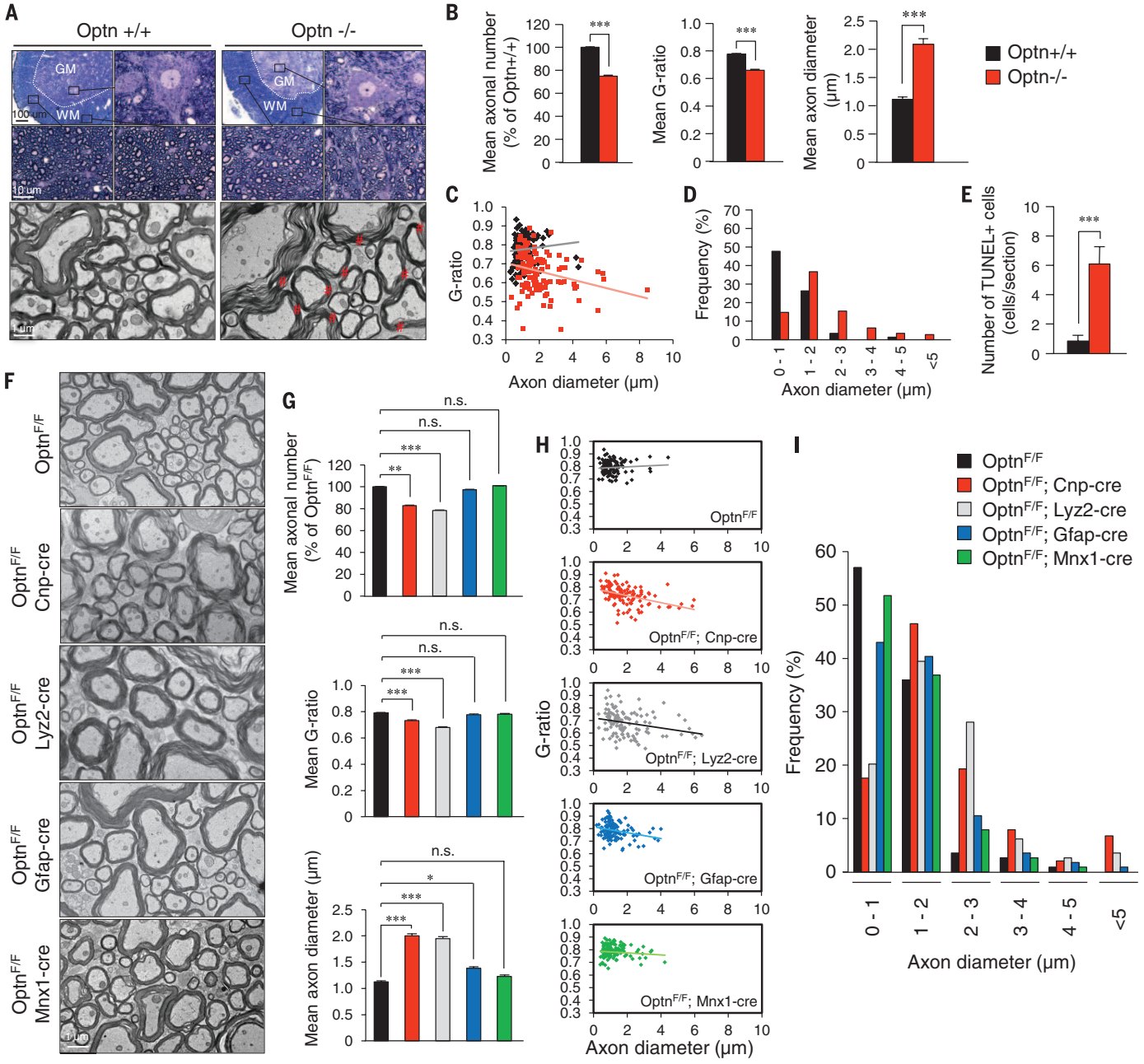

Fig. 1. Optn deficiency in oligodendrocyte and myeloid lineages promotes axonal loss and dysmyelination in the spinal cords of *Optn*$^{-/-}$ mice. (**A**) (Top) Toluidine blue–stained sections from the ventrolateral lumbar spinal cords of WT and *Optn*$^{-/-}$ mice. The boxes show axons in the ventrolateral lumbar spinal cord white matter and the motor neurons in the ventral lumbar spinal cord gray matter, respectively. (Bottom) Electron microscopic analysis of motor axonal myelination in the ventrolateral lumbar spinal cords from WT and *Optn*$^{-/-}$ mice. (**B** to **D** and **F** to **I**) The mean axonal numbers, mean g-ratios, and mean axonal diameters; individual g-ratio distribution; and distributions of axonal diameters in the ventrolateral lumbar spinal cord white matter (L1 to L4) of WT, *Optn*$^{-/-}$ mice, *Optn*$^{F/F}$ mice, *Optn*$^{F/F}$;*Cnp-cre* mice, *Optn*$^{F/F}$;*Lyz2-cre* mice, *Optn*$^{F/F}$;*Gfap-cre* mice, and *Optn*$^{F/F}$;*Mnx1-cre* mice, as indicated. (**E**) The number of TUNEL^{+} cells in the lumbar spinal cords (L1 to L4, one section each) of indicated genotype (five mice for each genotype).

(Fig. 2F). Thus, OPTN might control sensitivity to necroptosis by regulating proteasomal turnover of RIPK1.

Phospho-Ser$^{14/15}$, a marker of Ripk1 activation, was increased in *Optn*$^{-/-}$ microglia relative to WT microglia, which were inhibited by Nec-1s and *Ripk1*$^{D138N/D138N}$ mutation (Fig. 2G). Because microglia express little MLKL, we hypothesize that Ripk1 activation in microglia promotes inflammatory signaling not necroptosis. Consistent with this notion, we detected an increased production of multiple proinflammatory cytokines—including interleukins IL-1α, IL-1β, IL-2, and IL-12; interferon-γ (IFN-γ); and TNFα in the spinal cords of *Optn*$^{-/-}$ mice—which were markedly reduced in the *Optn*$^{-/-}$;*Ripk1*$^{D138N/D138N}$ mice (Fig. 2H). In addition, *Optn*$^{-/-}$ microglia had elevated TNFα, which was inhibited by Nec-1s (fig. S5A). As predicted, the levels of TNFα were also increased in the spinal cords of *Optn*$^{F/F}$;*Lyz2-cre* mice (fig. S5B).

To explore the effect of Optn deficiency on transcriptions, we performed RNA sequencing on WT, *Optn*$^{-/-}$, and *Optn*$^{-/-}$;*Ripk1*$^{D138N/D138N}$ primary microglia. Coexpression analysis (*25*) identified a module with ~1300 genes (ME1) differentially expressed between WT and *Optn*$^{-/-}$ microglia and suppressed by *Ripk1*$^{D138N/D138N}$.

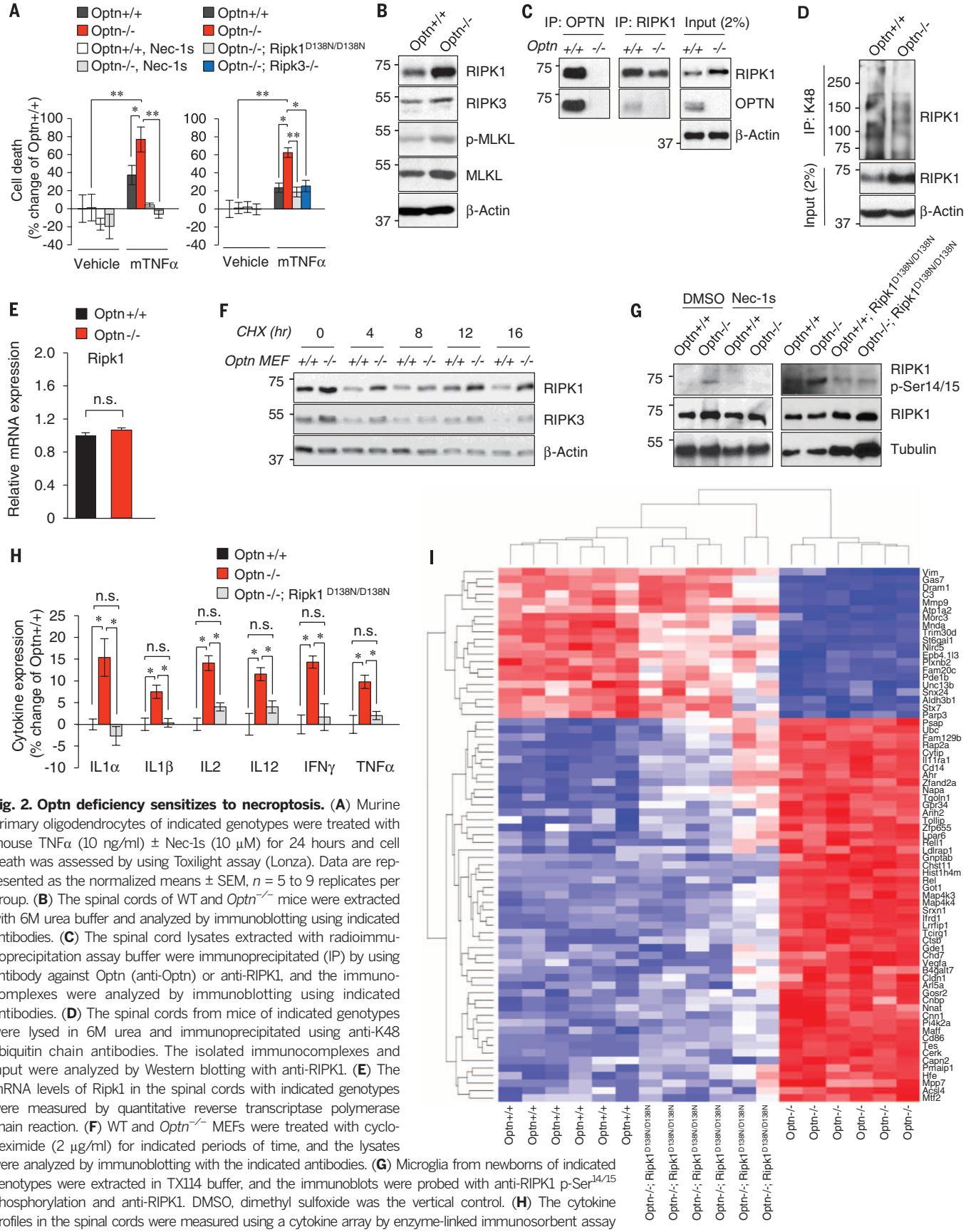

Fig. 2. Optn deficiency sensitizes to necroptosis. (**A**) Murine primary oligodendrocytes of indicated genotypes were treated with mouse TNFα (10 ng/ml) ± Nec-1s (10 μM) for 24 hours and cell death was assessed by using Toxilight assay (Lonza). Data are represented as the normalized means ± SEM, $n = 5$ to 9 replicates per group. (**B**) The spinal cords of WT and *Optn*$^{-/-}$ mice were extracted with 6M urea buffer and analyzed by immunoblotting using indicated antibodies. (**C**) The spinal cord lysates extracted with radioimmunoprecipitation assay buffer were immunoprecipitated (IP) by using antibody against Optn (anti-Optn) or anti-RIPK1, and the immunocomplexes were analyzed by immunoblotting using indicated antibodies. (**D**) The spinal cords from mice of indicated genotypes were lysed in 6M urea and immunoprecipitated using anti-K48 ubiquitin chain antibodies. The isolated immunocomplexes and input were analyzed by Western blotting with anti-RIPK1. (**E**) The mRNA levels of Ripk1 in the spinal cords with indicated genotypes were measured by quantitative reverse transcriptase polymerase chain reaction. (**F**) WT and *Optn*$^{-/-}$ MEFs were treated with cycloheximide (2 μg/ml) for indicated periods of time, and the lysates were analyzed by immunoblotting with the indicated antibodies. (**G**) Microglia from newborns of indicated genotypes were extracted in TX114 buffer, and the immunoblots were probed with anti-RIPK1 p-Ser$^{14/15}$ phosphorylation and anti-RIPK1. DMSO, dimethyl sulfoxide was the vertical control. (**H**) The cytokine profiles in the spinal cords were measured using a cytokine array by enzyme-linked immunosorbent assay (ELISA). (**I**) Heat map of the top 71 genes in the module ME1 differentially expressed in microglia of indicated genotypes. Low expression is shown in blue and high expression, in red.

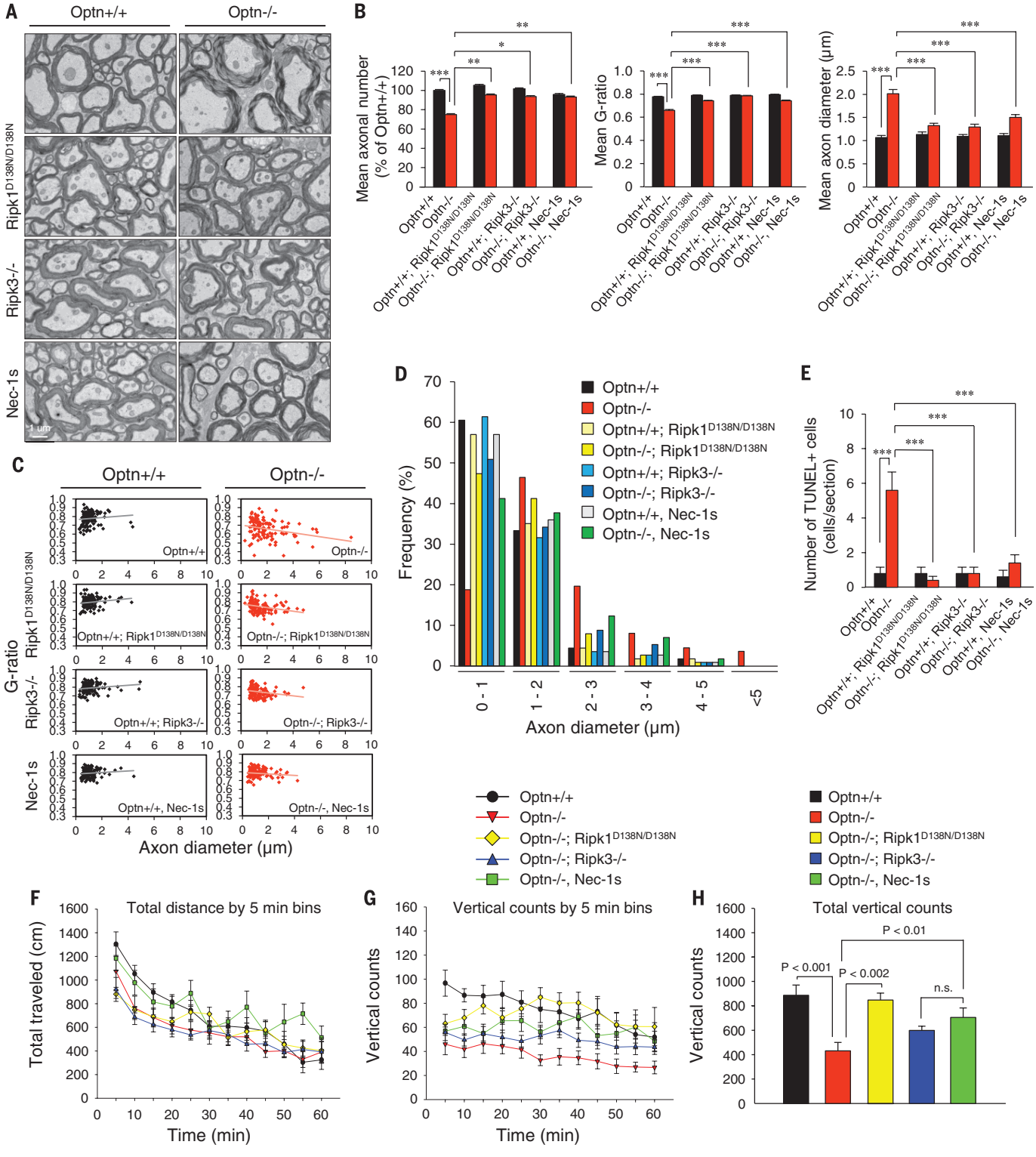

Fig. 3. Ripk1 and Ripk3 mediate axonal pathology in the spinal cords of *Optn*$^{-/-}$ mice. (**A**) Dysmyelination in the spinal cords of *Optn*$^{-/-}$ mice was blocked by genetically inhibiting Ripk1 in *Optn*$^{-/-}$;*Ripk1*$^{D138N/D138N}$ mice, pharmacologically inhibiting Ripk1 by Nec-1s (oral dosing of Nec-1s for 1 month starting from 8 weeks of age), and by loss of Ripk3 in *Optn*$^{-/-}$;*Ripk3*$^{-/-}$ mice. (**B** to **D**) Mean axonal numbers, g-ratios, and axonal diameters (B); individual g-ratio distributions (C); and axonal diameter distributions (D). (**E**) The number of TUNEL^{+} cells in the lumbar spinal cords (L1 to L4, one section each) of indicated genotypes at 3 months of age (five mice per genotype). (**F** to **H**) Mice of indicated genotypes were tested in open-field test for spontaneous motor activity. The mice were at 3 months of age and 28 to 32 g of body weight (no statistically significant difference in body weight between different groups). The total distance traveled in 1 hour showed no difference between different groups (F). *Optn*$^{-/-}$ mice showed a significant deficit on the vertical rearing activity (frequency with which the mice stood on their hind legs). This deficit was blocked after dosing with Nec-1s for 1 month starting from 8 weeks old and in *Optn*$^{-/-}$;*Ripk1*$^{D138N/D138N}$ double-mutant mice and reduced in *Optn*$^{-/-}$;*Ripk3*$^{-/-}$ double-mutant mice (G and H).

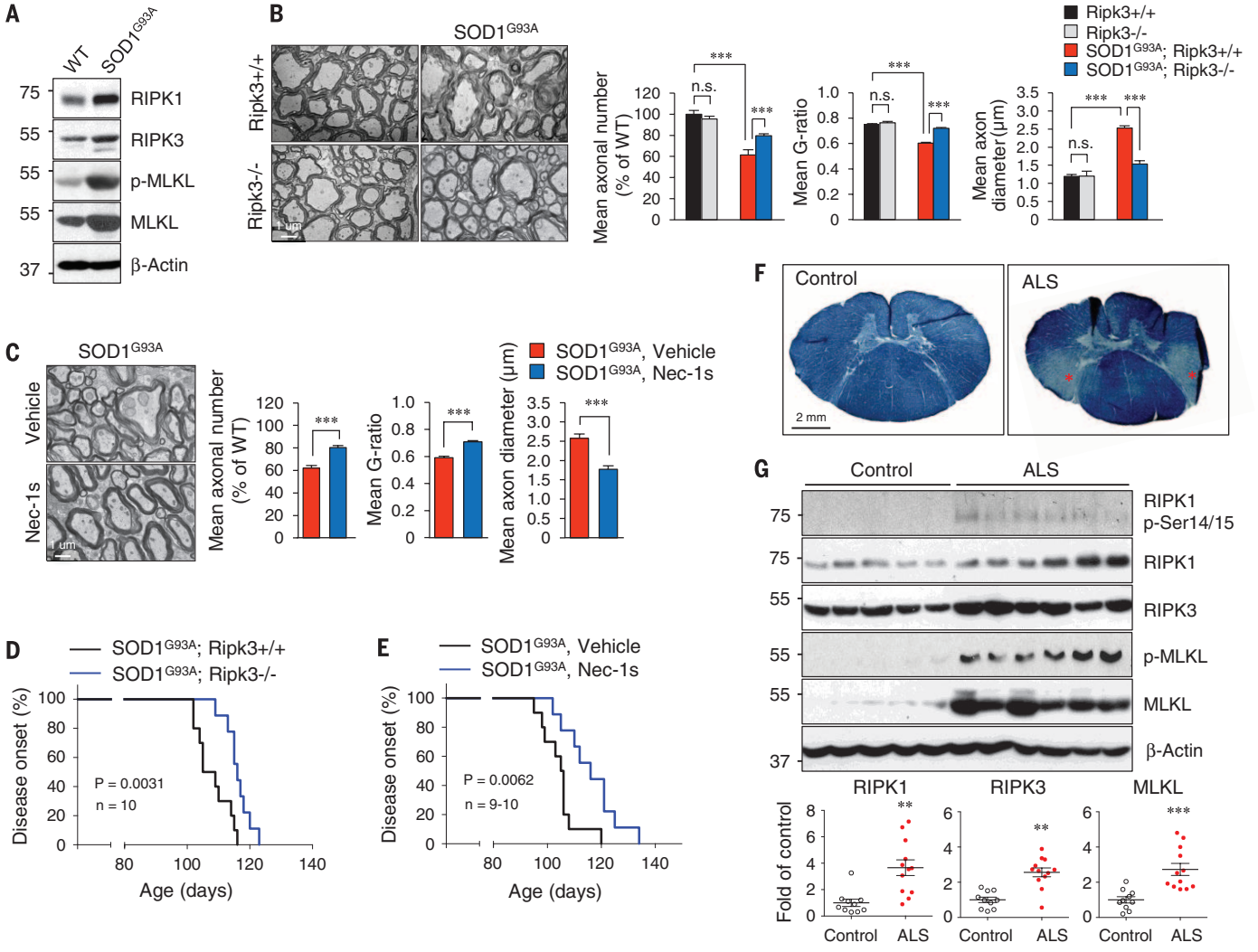

Fig. 4. RIPK1- and RIPK3-mediated axonal pathology is a common mechanism in ALS. (**A**) Urea buffer lysates of spinal cords from WT and *SOD1*^{G93A} transgenic mice (12 weeks of age) were analyzed by immunoblotting using indicated antibodies. (**B** and **C**) The myelination morphology (top), mean axonal numbers (bottom), mean g-ratios (bottom), mean axonal diameters (bottom) of the ventrolateral lumbar spinal cord white matter of *SOD1*^{G93A} mice, *SOD1*^{G93A};*Ripk3*$^{-/-}$ mice (12 weeks of age), and *SOD1*^{G93A} mice dosed with vehicle or Nec-1s for 1 month starting from 8 weeks of age. (**D** and **E**) Ripk3 deficiency (D) and inhibition of Ripk1 by Nec-1s starting from 8 weeks of age (E) delayed the onset of motor dysfunction in *SOD1*^{G93A} mice. (**F**) Sections of pathological spinal cords from a human control and an ALS patient were stained with Luxol fast blue for myelin to show reduced myelination in the lateral column of lower spinal cords of ALS patients. (**G**) Immunoblotting analysis of human control and ALS spinal cord samples using indicated antibodies (top) and the quantification of RIPK1, RIPK3, and MLKL levels from 10 controls and 13 ALS patients (bottom).

The top 71 genes in this module include CD14 and CD86, biomarkers for the proinflammatory M1-like state (*26*) (Fig. 2I and table S2). Elevated CD14 and CD86 in *Optn*$^{-/-}$ microglia were suppressed by Nec-1s and *Ripk1*$^{D138N/D138N}$ (fig. S5C). Thus, Optn deficiency promotes an M1-like inflammatory microglia.

We analyzed the genes differentially expressed in *Optn*$^{-/-}$ microglia using MSigDB (Molecular Signatures Database) (*27*) to identify transcription factors with targets that were overrepresented. We found a significant overrepresentation of the predicted Sp1 transcription factor targets in the ME1 module (table S3) with a network (*28*) of 225 Sp1 targets regulated by RIPK1 (fig. S6A). Increased production of TNFα and the death of L929 cells were blocked by knockdown of Sp1 and by Nec-1s (fig. S6, B and C). Thus, loss of Optn in the spinal cord may increase RIPK1-dependent inflammation.

We examined the involvement of necroptosis in *Optn*$^{-/-}$ mice in vivo. The increase in TUNEL^{+} cells and the axonal pathology of *Optn*$^{-/-}$ mice were all rescued in the *Optn*$^{-/-}$;*Ripk1*$^{D138N/D138N}$ double-mutant and the *Optn*$^{-/-}$;*Ripk3*$^{-/-}$ double-mutant mice and by Nec-1s (Fig. 3, A to E). Behaviorally, *Optn*$^{-/-}$ mice showed no difference in total locomotor activity, whereas the vertical rearing activity was significantly reduced compared with that of WT mice (Fig. 3, F to H). Thus, Optn deficiency leads to hindlimb weakness. Furthermore, the vertical rearing deficit in *Optn*$^{-/-}$ mice was rescued pharmacologically by Nec-1s and genetically in the *Optn*$^{-/-}$;*Ripk1*$^{D138N/D138N}$ mice and *Optn*$^{-/-}$;*Ripk3*$^{-/-}$ mice. Thus, Optn deficiency leads to the activation of necroptotic machinery to promote axonal pathology.

To explore the involvement of RIPK1-mediated axonal pathology in ALS in general, we used *SOD1*^{G93A} transgenic mice. Oligodendrocytes in *SOD1*^{G93A} mice degenerate early, but the mechanism is unclear (*29*). We found that the expression of Ripk1, Ripk3, and MLKL in the spinal cords of *SOD1*^{G93A} transgenic mice was elevated (Fig. 4A). In addition, we observed a similar axonal pathology as that of *Optn*$^{-/-}$ mice in *SOD1*^{G93A} mice before the onset of motor dysfunction (Fig. 4, B and C). Furthermore, these axonal myelination defects were blocked and motor dysfunction onset was delayed genetically by *Ripk3* knockout or by oral administration

of Nec-1s (Fig. 4, D and E). Thus, although we cannot rule out the contribution of Ripk1 or other proapoptotic factors to the degeneration of motor neuron cell bodies (*30*, *31*), the activation of necroptosis contributes to axonal pathology and motor dysfunction in the $SOD1^{G93A}$ transgenic mice.

We next characterized the role of RIPK1 and necroptosis in human ALS. We found evidence of demyelination in the lateral column white matter of lower spinal cord pathological samples from ALS patients as reported (Fig. 4F). In human ALS pathological samples, we also detected multiple biochemical hallmarks of necroptosis, including increased levels of RIPK1, RIPK3, and MLKL and increased RIPK1 p-$Ser^{14/15}$ and p-MLKL in both microglia and oligodendrocytes (Fig. 4G, fig. S7, and table S4). Note that p-MLKL was primarily localized in the white matter, where demyelination was found.

Taken together, our results provide a direct connection between Wallerian-like degeneration induced by OPTN deficiency and RIPK1-regulated necroptosis and inflammation. By promoting both inflammation and cell death, RIPK1 may be a common mediator of axonal pathology in ALS (fig. S8). Because RIPK1 is recruited specifically to the TNF receptor TNFR1 to mediate the deleterious effect of TNFα (*32*), blocking RIPK1 may provide a therapeutic option for the treatment of ALS without affecting TNFR2. Finally, given the recruitment of OPTN to intracellular protein aggregates found in pathological samples from patients with Alzheimer's disease, Parkinson's disease, Creutzfeldt-Jakob disease, multiple system atrophy, and Pick's disease (*33*, *34*), a possible role of RIPK1 in mediating the wide presence of axonal degeneration in different neurodegenerative diseases should be considered.

REFERENCES AND NOTES

1. E. Beeldman *et al.*, *Amyotroph. Lateral Scler. Frontotemporal Degener.* **16**, 410–411 (2015).
2. E. T. Cirulli *et al.*, *Science* **347**, 1436–1441 (2015).
3. H. Maruyama *et al.*, *Nature* **465**, 223–226 (2010).
4. I. Munitic *et al.*, *J. Immunol.* **191**, 6231–6240 (2013).
5. G. Zhu, C. J. Wu, Y. Zhao, J. D. Ashwell, *Curr. Biol.* **17**, 1438–1443 (2007).
6. D. Ofengeim, J. Yuan, *Nat. Rev. Mol. Cell Biol.* **14**, 727–736 (2013).
7. S. He *et al.*, *Cell* **137**, 1100–1111 (2009).
8. L. Sun *et al.*, *Cell* **148**, 213–227 (2012).
9. D. W. Zhang *et al.*, *Science* **325**, 332–336 (2009).
10. A. Degterev *et al.*, *Nat. Chem. Biol.* **4**, 313–321 (2008).
11. A. Degterev *et al.*, *Nat. Chem. Biol.* **1**, 112–119 (2005).
12. L. Conforti, J. Gilley, M. P. Coleman, *Nat. Rev. Neurosci.* **15**, 394–409 (2014).
13. M. C. Raff, A. V. Whitmore, J. T. Finn, *Science* **296**, 868–871 (2002).
14. J. T. Wang, Z. A. Medress, B. A. Barres, *J. Cell Biol.* **196**, 7–18 (2012).
15. S. Sasaki, S. Maruyama, *J. Neurol. Sci.* **110**, 114–120 (1992).
16. L. Zhuo *et al.*, *Genesis* **31**, 85–94 (2001).
17. B. E. Clausen, C. Burkhardt, W. Reith, R. Renkawitz, I. Förster, *Transgenic Res.* **8**, 265–277 (1999).
18. C. Lappe-Siefke *et al.*, *Nat. Genet.* **33**, 366–374 (2003).
19. C. N. Parkhurst *et al.*, *Cell* **155**, 1596–1609 (2013).
20. D. E. Christofferson, J. Yuan, *Curr. Opin. Cell Biol.* **22**, 263–268 (2010).
21. J. Hitomi *et al.*, *Cell* **135**, 1311–1323 (2008).
22. D. E. Christofferson *et al.*, *Cell Death Dis.* **3**, e320 (2012).
23. A. Polykratis *et al.*, *J. Immunol.* **193**, 1539–1543 (2014).
24. D. Ofengeim *et al.*, *Cell Rep.* **10**, 1836–1849 (2015).
25. P. Langfelder, S. Horvath, *BMC Bioinformatics* **9**, 559 (2008).
26. K. A. Kigerl *et al.*, *J. Neurosci.* **29**, 13435–13444 (2009).
27. A. Subramanian *et al.*, *Proc. Natl. Acad. Sci. U.S.A.* **102**, 15545–15550 (2005).
28. S. I. Berger, J. M. Posner, A. Ma'ayan, *BMC Bioinformatics* **8**, 372 (2007).
29. S. H. Kang *et al.*, *Nat. Neurosci.* **16**, 571–579 (2013).
30. D. B. Re *et al.*, *Neuron* **81**, 1001–1008 (2014).
31. T. W. Gould *et al.*, *J. Neurosci.* **26**, 8774–8786 (2006).
32. J. J. Peschon *et al.*, *J. Immunol.* **160**, 943–952 (1998).
33. T. Osawa *et al.*, *Neuropathology* **31**, 569–574 (2011).
34. H.-X. Deng *et al.*, *Arch. Neurol.* **68**, 1057–1061 (2011).

ACKNOWLEDGMENTS

We thank B. Caldarone of the NeuroBehavior Laboratory, Harvard Institute of Medicine, for conducting mouse behavior analysis; J. Walters at the Harvard Medical School Nikon microscope facility for fluorescence microscopy; and M. Ericsson of the Electron Microscopy Facility at Harvard Medical School for analysis. This work was supported in part by grants from the National Institute of Neurological Disorders and Stroke (1R01NS082257) and the National Institute on Aging (1R01AG047231), NIH; and by the National Science and Technology Major Project of China (2014ZX09102001-002) and State Key Program of National Natural Science of China (no. 31530041) (to J.Y.); National Institute of Allergy and Infectious Diseases (2RO1AI075118) (to M.A.K.); European Research Council Advanced Grants (grant agreement no. 323040) (to M.P.) and Target ALS (to J.R.). Y.I. was supported in part by postdoctoral fellowships from Japan (Daiichi Sankyo Foundation of Life Science, The Nakatomi Foundation, the Mochida Memorial Foundation for Medical and Pharmaceutical Research, and Japan Society for the Promotion of Science). D.O. was supported by a postdoctoral fellowship from the National Multiple Sclerosis Society and a National Multiple Sclerosis Society Career Transition Award. H.C. was supported by a grant from Huazhong University of Science and Technology, Wuhan, China. $Ripk3^{-/-}$ mice and K48 ubiquitin antibodies are available from V. Dixit under a material transfer agreement with Genentech. $Ripk1^{D138N}$ mice are available from M. Pasparakis of University of Cologne, Germany, under a material transfer agreement with University of Cologne. J.Y. is an inventor on U.S. patent 7,491,743 B2 held by Harvard University that covers 7-Cl-O-Nec-1.

SUPPLEMENTARY MATERIALS

www.sciencemag.org/content/353/6299/603/suppl/DC1
Materials and Methods
Figs. S1 to S8
Tables S1 to S4
References (*35*–*40*)

13 March 2016; accepted 7 July 2016
10.1126/science.aaf6803

ECACC
European Collection of Cell Cultures
Operated by Public Health England

A CULTURE TO RELY ON

For over 30 years, we have provided the research community with a complete and innovative range of cell culture products. We continue to develop strategic partnerships with key organizations like the European Collection of Authenticated Cell Cultures (ECACC®), and remain committed to providing the outstanding quality and service you need to make your research successful.

Dependability

- Consistency you require and expect

Quality

- Application-tested products provide superb performance

Selection

- Widest offering of sera, media, supplements, cell lines, and labware

Service

- Easy online ordering, fast delivery worldwide and world-class technical support

Find out more at
sigma-aldrich.com/cellculture

SIGMA-ALDRICH®

Mirus | The Transfection Experts

Are your CHO cells this happy?

NEW! CHOgro® Expression System

At Mirus Bio, we know it's all about great expression. Introducing the new CHOgro® Expression System, a transient transfection platform that supports high protein titers with robust cell growth in the most relevant CHO cells.

- **Efficient** – Enables high protein titers with simple workflow
- **Convenient** – Quick adaptation to CHO cell line lineages
- **Optimized** – High density growth with minimal clumping post-transfection
- **Worry-free** – No commercial license required; animal origin free

Available as a complete system or components sold separately.

To get the latest white paper or order, visit: www.mirusbio.com/chogro.

PASSION VISION INSPIRATION Celebrating 20 YEARS

mirusbio.com

Providing gene delivery expertise since 1995

myIDP: A career plan customized for you, by you.

For your career in science, there's only one Science

my IDP
ScienceCareers

Recommended by leading professional societies and the NIH

Features in myIDP include:

- Exercises to help you examine your skills, interests, and values.
- A list of 20 scientific career paths with a prediction of which ones best fit your skills and interests.
- A tool for setting strategic goals for the coming year, with optional reminders to keep you on track.
- Articles and resources to guide you through the process.
- Options to save materials online and print them for further review and discussion.
- Ability to select which portion of your IDP you wish to share with advisors, mentors, or others.
- A certificate of completion for users that finish myIDP.

Visit the website and start planning today!
myIDP.sciencecareers.org

ScienceCareers In partnership with:

advancing the life sciences 1912-2012 FASEB Federation of American Societies for Experimental Biology

UCSF University of California San Francisco

Medical College of Wisconsin

Burroughs Wellcome Fund

CHO Cell Media

BalanCD CHO Feed 4 is a chemically defined, animal component-free powder feed for large-scale bioproduction in a variety of high-performing Chinese hamster ovary (CHO) cells. When paired with BalanCD CHO Growth A in fed-batch culture systems, BalanCD CHO Feed 4 can achieve cell density of up to 20 million viable cells/mL and antibody titers of up to 6 g/L. Recent developments in cell-line engineering have resulted in cell lines capable of reaching high cell densities and productivity rates. To achieve their full production potential, these cell lines need nutrient-rich media; however, these feeds can be difficult to dissolve and require complicated, time-consuming preparation protocols. BalanCD CHO Feed 4 is designed and formulated to prepare easily using a simplified hydration procedure that does not require pH adjustments. It maintains pH stability in culture and is designed to support growth while minimizing the production of metabolites that adversely affect titer levels, resulting in process consistency and high protein production and protein quality.

Irvine Scientific
For info: 800-577-6097
www.irvinesci.com

Flow Slides and Channels

The µ-Slide Membrane ibiPore Flow—a product designed for migration and transport studies on cells—enables researchers to culture single or multiple cell types on a porous glass membrane, and then analyze the cells using high-resolution microscopy—something that is not currently possible when using typical polymer cell-culture inserts. This special microscopy chamber contains a cross-channel structure with a thin, porous, optical glass membrane located in between. Cells can be cultured on both sides of the glass membrane and then visualized using phase contrast or fluorescence microscopy. The special construction of the slide allows full fluidic access to the apical and basal sides of adherent cells for cell studies under static or flow conditions. Typical applications include coculture of smooth muscle cells with endothelial cells under perfusion, transmigration of leukocytes with dynamic shear stress, and invasion assays using cancer cells.

ibidi
For info: 844-276-6363
www.ibidi.de

Cell Culture System

The Avatar system enables a new generation of cell-based assays by allowing for complete control of key physiological conditions found in cell microenvironments, including settings for pressure, oxygen, temperature, and carbon dioxide levels. Mimicking the physiological conditions of a sample's native environment is critical to obtaining accurate and actionable experimental results in important fields such as cancer research, biomarker discovery, lead candidate selection and optimization, stem cell research and regenerative medicine, and immunotherapy drug development. Avatar provides a new platform for culturing and propagating tumor samples, circulating tumor cells from liquid biopsies, stem cells, and primary samples. In addition to enabling the culturing of difficult samples such as tumor biopsies and primary samples, the system overcomes the limitations of traditional cell cultures to generate results that exhibit the phenotypic, genomic, and proteomic characteristics of the native sample.

Xcell Biosciences
For info: 415-937-0321
www.xcellbio.com

Kinetic Cytometry Imaging

Livecyte enables cell biology researchers to achieve a deeper understanding of the phenotypic and kinetic behaviors of both individual live cells and live-cell populations in a label-free environment, and uniquely allows users to interleave fluorescence measurements during different drug treatments or across cell types within a single experiment. With the ability to image multiple regions of interest within wells and across well plates, this intuitive system delivers multiparametric, quantitative data and high-contrast, high-fidelity images and videos. Perfectly focused cells and powerful cell-tracking software (patent pending) enable enhanced lineage tracking. The system's ability to image continuously ensures that large (mm) fields of view can be captured without stitching, so highly motile cells are not lost during long time courses. Cell perturbation is minimized because cells are imaged in their growth media. This technique is particularly useful for fragile cells such as primary cells and stem cells.

Phasefocus
For info: +44-(0)-114-286-6377
www.phasefocus.com

Automated Cell Counter

The Countstar Automated Cell Counter is a cell-counting and analysis instrument based on the classic trypan blue staining method. The system integrates advanced optical imaging technology with intelligent image recognition technology to give outstanding results. At its heart is a powerful software system that integrates basic cell counting and cell morphology analysis with analysis charts and data management capabilities. The Countstar offers accurate and rapid counting, innovative cell aggregation correction, and rigorous manual impurity correction. One-stop statistical analysis capability combined with flexible data output and advanced data security features make the Countstar one of the most advanced systems of its type on the market. The Countstar IC1000 measures not only cell concentration and viability, but also gives the average diameter range and aggregation of cells in the form of histograms.

Eikonix
For info: +44-(0)-1223-515440
www.eikonix.com

Electronically submit your new product description or product literature information! Go to www.sciencemag.org/about/new-products-section for more information.

Newly offered instrumentation, apparatus, and laboratory materials of interest to researchers in all disciplines in academic, industrial, and governmental organizations are featured in this space. Emphasis is given to purpose, chief characteristics, and availability of products and materials. Endorsement by *Science* or AAAS of any products or materials mentioned is not implied. Additional information may be obtained from the manufacturer or supplier.

want new technologies?

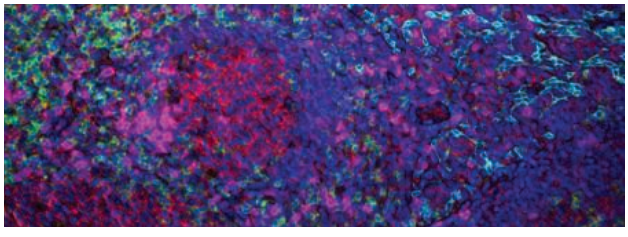

antibodies
apoptosis
biomarkers
cancer
cytometry
data
diseases
DNA
epigenetics
genomics
immunotherapies
medicine
microbiomics
microfluidics
microscopy
neuroscience
proteomics
sequencing
toxicology
transcriptomics

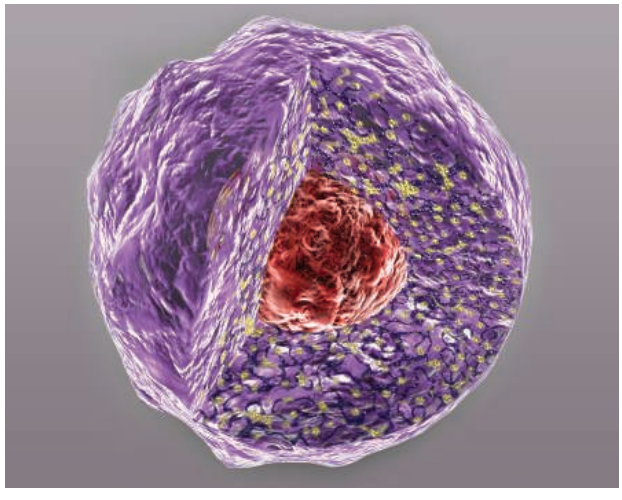

watch our webinars

Learn about the latest break-throughs, new technologies, and ground-breaking research in a variety of fields. Our expert speakers explain their quality research to you and answer questions submitted by live viewers.

VIEW NOW!
webinar.sciencemag.org

Science
AAAS

Brought to you by the *Science*/AAAS Custom Publishing Office

@SciMagWebinars

R&D Systems is Your New Trusted Source for Luminex® Instrumentation!

Direct access to Luminex staff for world-class on-site and 24x7x365 remote support

Unlimited emergency equipment repair

Discounts and special acquisition programs tailored to any lab's budget

Learn more about Luminex® instruments | rndystems.com/luminexinstruments

bio-techne®

Global info@bio-techne.com bio-techne.com/find-us/distributors TEL +1 612 379 2956
North America TEL 800 343 7475 **Europe | Middle East | Africa** TEL +44 (0)1235 529449
China info.cn@bio-techne.com TEL +86 (21) 52380373

bio-techne.com

By **Jason Cantley**

Working my way out

Less than 24 hours after the mass murders that took place at a gay nightclub in Orlando, Florida, in June, I posted an emotionally raw message on social media. I usually avoid posting about potentially divisive issues, but I made an exception because, as a gay man, I wanted to reach out to the LGBTQ community to provide comfort, and to encourage us to come together in this time of pain. I was acutely aware that all of my "friends" would be able to see my post, including a few new coworkers whose positions on LGBTQ issues I was not certain about. But, after years of being hesitant to tell other scientists that I was gay, I no longer cared. Something changed for me that day. I decided that it was no longer useful for me to worry about how others judge me based on my sexual orientation.

The next day, I was taken aback when a white male faculty member in the department where I work as a postdoc went out of his way to stop me in the hall to thank me for sharing my thoughts and to offer his support. Later, my boss—another white male—checked on me. All day, I felt support from my colleagues that was only possible because I was out as gay at work.

I've been out for more than a decade, having first come out as a sophomore in high school—a liberating but grim experience, which brought death threats from students and had my parents worrying that I'd be killed in a dark alley or contract HIV. But professionally, I came out much later. As an undergrad biology major, I was hesitant to come out to people in positions of authority, especially white male faculty members. And there seemed to be good reason to worry. Early on, for example, a faculty member implied that female scientists' work was less important than that done by men. In my head, I extended this judgment to LGBTQ individuals, including myself, and I thought that other scientists would not take me or my work seriously if they knew that I was gay. "Am I good enough?" I frequently asked myself. I also avoided seeking out professors when I needed help, which made it harder to do well in my classes and hindered my development of networking skills.

Graduate school was the first time that I felt I could come out professionally, but it still wasn't easy. I knew that my adviser would be supportive—I had chosen to work with her partly because I felt that I would be safe under her supervision—but every time I had an opportunity to tell her, I couldn't find the words. My heart would leap into my throat, my face would flush, and I'd panic. It took a few years before I succeeded. And I never officially came out to any other faculty members while I was a student, mostly because of nagging fears that it would negatively affect their views of my research.

"I feel no reason to hide or be ashamed of being gay while doing science."

Coming out as a postdoc was easier because I had already met my current boss and become friends with him via social media, where I'm open about my sexual orientation. These days, I'm out to most of my professional colleagues, which has greatly improved my mental health and helped me develop strong professional relationships. For instance, I'm out to many members of an incredibly inclusive professional botanical organization. They have helped me understand that my research stands on its own, independent of my sexuality.

But now, at a pivotal point in my career when I'm searching for a permanent position as a tenure-track faculty member, I find myself again worrying about how and when to come out. What should I do if, during the interview process, I'm asked whether I have a wife? Will being gay hurt my chances of getting the job? How will I settle in with new colleagues as an openly gay scientist?

Despite my concerns, after the tragedy in Orlando I resolved to stop this unhealthy worrying. Life is too precious for that. I feel no reason to hide or be ashamed of being gay while doing science. I'm still thinking about how to manage coming out as I move forward in my career, but I am confident that my science speaks for itself. ■

Jason Cantley is a postdoc at Bucknell University in Lewisburg, Pennsylvania. Send your career story to SciCareerEditor@aaas.org.

ILLUSTRATION: ROBERT NEUBECKER

Science Careers Advertising

For full advertising details, go to ScienceCareers.org and click For Employers, or call one of our representatives.

Tracy Holmes
Worldwide Associate Director
Science Careers
Phone: +44 (0) 1223 326525

THE AMERICAS

E-mail: advertise@sciencecareers.org
Fax: +1 (202) 289 6742

Tina Burks
Phone: +1 (202) 326 6577

Nancy Toema
Phone: +1 (202) 326 6578

Online Job Posting Questions
Phone: +1 (202) 312 6375

EUROPE / INDIA / AUSTRALIA / NEW ZEALAND / REST OF WORLD

E-mail: ads@science-int.co.uk
Fax: +44 (0) 1223 326532

Sarah Lelarge
Phone: +44 (0) 1223 326527

Kelly Grace
Phone: +44 (0) 1223 326528

Online Job Posting Questions
Phone: +44 (0) 1223 326528

JAPAN

Katsuyoshi Fukamizu (Tokyo)
E-mail: kfukamizu@aaas.org
Phone: +81 3 3219 5777

Hiroyuki Mashiki (Kyoto)
E-mail: hmashiki@aaas.org
Phone: +81 75 823 1109

CHINA / KOREA / SINGAPORE / TAIWAN / THAILAND

Ruolei Wu
E-mail: rwu@aaas.org
Phone: +86 186 0082 9345

Danny Zhao
E-mail: dzhao@aaas.org
Phone: +86 131 4114 0012

ScienceCareers
FROM THE JOURNAL SCIENCE AAAS

ScienceCareers.org

BIOMOLECULAR NMR SPECTROSCOPIST

Florida State University Department of Chemistry & Biochemistry and the National High Magnetic Field Laboratory are searching for a **mid-career faculty member with research interests in biochemistry and solution NMR spectroscopy**. Preference will be given to candidates whose research represents strong arguments for spectroscopy at high magnetic fields including, but not limited to, work in intrinsically disordered proteins or macromolecular dynamics. The successful candidate will be expected to maintain an extramurally funded research program, teach both graduate and undergraduate classes, and to actively participate in the Magnet Lab's efforts to take solution NMR spectroscopy to much higher magnetic fields and to help drive the development of high frequency probes for NMR science.

Persons interested in the position can contact **Professor Timothy A. Cross** for more information. Applicants should email all application materials, including cover letter, CV, statement of research plans and teaching interests, and the names and contact information for three professional references to **nmr_search@chem.fsu.edu**. Review of applications will begin on **October 1, 2016**, and continue until the position is filled.

FSU is an Equal Opportunity/Access/Affirmative Action/Pro Disabled & Veteran Employer. FSU's Equal Opportunity Statement can be viewed at: http://www.hr.fsu.edu/PDF/Publications/diversity/EEO_Statement.pdf

Postdoc Positions
Rigas Lab
Division of Cancer Prevention

Stony Brook Medicine

We seek highly motivated candidates for two Postdoctoral Associate positions to study the molecular mechanisms of action of novel anti-cancer agents working predominantly through redox-sensitive pathways. Work will include efficacy studies in tumor animal models and correlation of in vitro and in vivo data.

Our lab has expertise in drug metabolism, PK/PD studies, drug formulation in nanocarriers, advanced molecular methods; morphological and imaging studies; high-throughput in vivo methods; and various tumor animal models including patient-derived xenografts (of which we have our own annotated tissue bank from various human cancers).

For details regarding the required and preferred qualifications, a description of job duties, instructions for submitting an application, and to learn more about Stony Brook University, please visit **http://www.stonybrook.edu/jobs** and view Postdoctoral Associate position numbers: **1503792** and **1503794**. The application deadline for these jobs is **08/31/2016**, but you'll find other opportunities for well-qualified postdoctoral candidates at stonybrookedu/jobs..

Visit the Division of Cancer Prevention at: **https://medicine.stonybrookmedicine.edu/medicine/cancer_prevention**

Equal Opportunity Employer, females, minorities, disabled, veterans

Bring your job search in for a smooth landing.

Target your job search using relevant resources on **ScienceCareers.org**.

ScienceCareers
FROM THE JOURNAL SCIENCE AAAS

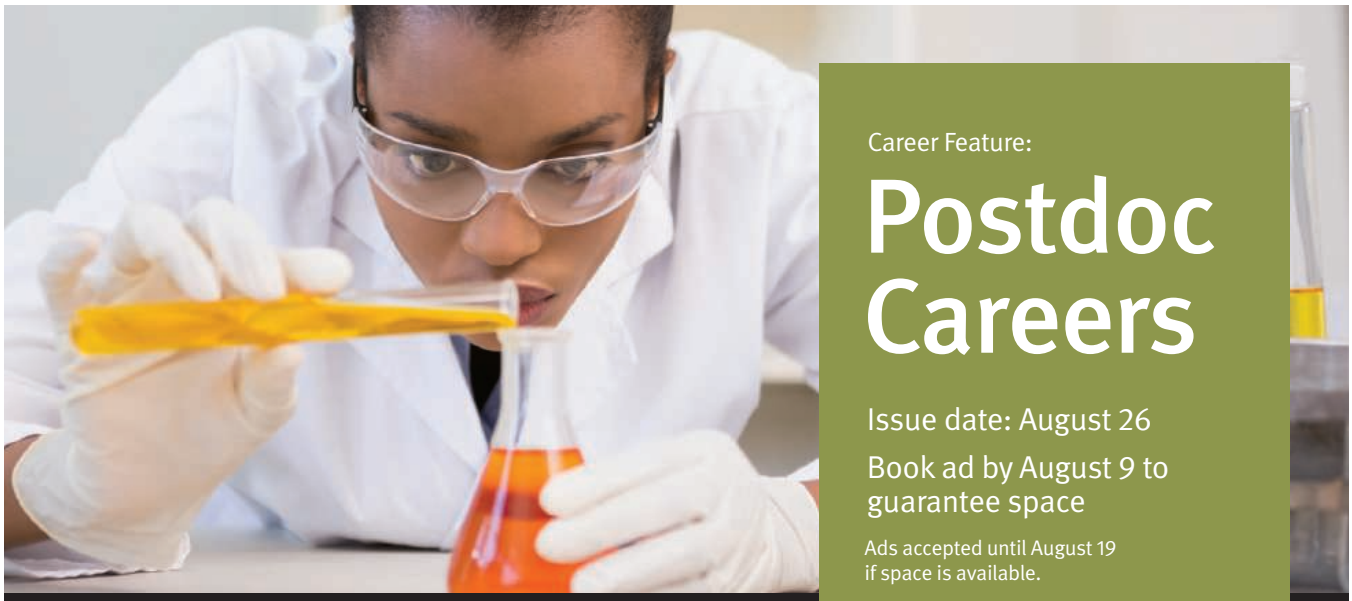

For recruitment in science, there's only one *Science*.

Career Feature:

Postdoc Careers

Issue date: August 26

Book ad by August 9 to guarantee space

Ads accepted until August 19 if space is available.

Looking to fill your postdoc positions?

Scientists will be eager to learn about non-faculty career options in academia in STEM. What do these jobs involve and how can scientists prepare for them? What are the entry points and skills needed for success? Postdocs who have moved into these types of careers will share their success stories. Reach these readers and share opportunities at your university or company.

What makes *Science* the best choice for recruiting?

- Read and respected by 400,000 readers around the globe
- 78% of readers read *Science* more often than any other journal
- Your ad dollars support AAAS and its programs, which strengthens the global scientific community.

Why choose this Postdoc Feature for your advertisement?

- Relevant ads lead off the career section with a special "Postdoc" banner.

Expand your exposure by posting your print ad online:

- Link on the job board homepage directly to postdoc positions
- Dedicated landing page for postdoc positions.

Produced by the *Science*/AAAS Custom Publishing Office.

Deliver your message to a global audience of targeted, qualified scientists.

129,574
subscribers in print every week

352,966
monthly unique browsers on ScienceCareers.org

65%
of our weekly readers are Ph.D.s

SCIENCECAREERS.ORG

ScienceCareers
FROM THE JOURNAL SCIENCE AAAS

To book your ad: **advertise@sciencecareers.org**

The Americas
+202 326 6582
Japan
+81 3 3219 5777
Europe/RoW
+44(0)1223 326500
China/Korea/Singapore/Taiwan
+86 186 0082 9345

Perelman School of Medicine
University of Pennsylvania
The Children's Hospital of Philadelphia

Pediatric Hematologist, University of Pennsylvania
Perelman School of Medicine
Department of Pediatrics
Associate/Full Professor - Bone Marrow Failure

The Children's Hospital of Philadelphia and the Division of Hematology in the Department of Pediatrics at the Perelman School of Medicine at the University of Pennsylvania seek candidates for an Associate or Full Professor position in either the tenure track or the non-tenure clinician-educator track. Applicants must have an M.D. or Ph.D. or M.D./Ph.D. degree. M.D. or M.D./Ph.D. candidates must have board certification in pediatric hematology/oncology (preferred) or medical hematology.

Applicants must have demonstrated excellence in education, research, and (for physicians) clinical care.

The CHOP Bone Marrow Failure Center provides comprehensive care for patients with acquired or inherited non-malignant bone marrow failure syndromes and basic, translational and clinical research into these disorders.

The successful applicant will have a national reputation in research involving patients with aplastic anemia or related bone marrow failure syndromes, program administration skills, and commitment to direct and grow a clinical program, including interaction with patient advocacy groups. Significant research and clinical resources, space for the research and clinical programs and protected time will be provided to the successful candidate.

We seek candidates who embrace and reflect diversity in the broadest sense.

The University of Pennsylvania and The Children's Hospital of Philadelphia are EOEs. Minorities/Women/Individuals with disabilities/Protected Veterans are encouraged to apply.

Apply for this position online at:
https://www.med.upenn.edu/apps/faculty_ad/index.php/g331/d4377

University of Iowa Carver College of Medicine
University of Iowa Health Care

Department of Pharmacology Faculty Position in Neuroscience

The Department of Pharmacology seeks exceptional applicants at the Assistant, Associate or Professor level to conduct innovative state-of-the-art research in Neuroscience. Applicants should have an outstanding record of innovative research and academic excellence and demonstrated expertise in any area of neuroscience including systems, molecular/cellular, behavioral, neurodegenerative disorders, and pain, employing cutting edge methodologies. The candidate will join a strong and growing community of neuroscientists in the Carver College of Medicine which has designated neuroscience as a strategic priority for growth and investment. Newly remodeled research space with state-of-the-art shared instrumentation is available.

This position includes a 12-month salary, benefits and a highly competitive start up package. All applicants must have a relevant doctoral degree and a record of accomplishment commensurate with appointment as Assistant Professor in the Tenure Track, Associate Professor with Tenure, or Professor with Tenure. The successful candidate will maintain a vigorous, independent, extramurally funded research program, have a desire to train students and postdoctoral fellows, and participate in departmental teaching.

To apply for this position, visit The University of Iowa website at: **http://jobs.uiowa.edu**, requisition **#69412**.

The University of Iowa is an Equal Opportunity/Affirmative Action Employer. All qualified applicants are encouraged to apply and will receive consideration for employment free from discrimination on the basis of race, creed, color, national origin, age, sex, pregnancy, sexual orientation, gender identity, genetic information, religion, associational preference, status as a qualified individual with a disability, or status as a protected veteran.

FRED HUTCH
CURES START HERE™

Senior Faculty Leadership Position in Global Oncology at Fred Hutchinson Cancer Research Center

Fred Hutchinson Cancer Research Center seeks exceptional applicants for a full-time senior faculty leadership position in the Global Oncology Program at the Full Member level (comparable to Professor). The primary responsibility of this position will be to lead the development and execution of Fred Hutch's global oncology research agenda, encompassing basic and translational research, innovative prevention and treatment, and implementation science. The leader will be expected to conduct groundbreaking scientific research with global impact and to foster scientific collaborations involving multiple investigators across Fred Hutch and external, international partners. The ideal candidate will have a well-established and funded research portfolio with international recognition for scientific excellence and have a demonstrated record in mentoring faculty and partners to pursue an international research portfolio.

The Fred Hutch has established a broad international footprint to enable the conduct of innovative basic and clinical research in cancer, and particularly in infectious disease-related cancers. In May 2015, the Fred Hutch and the Uganda Cancer Institute (UCI) opened the world-class UCI-Fred Hutch Cancer Centre in Kampala, Uganda. This 25,000 square-foot facility supports research, outpatient care and training, as well as clinical laboratory and specialized laboratories for molecular diagnostics, biorepository, histopathology and immunology. This first comprehensive cancer center holds promise for accelerating groundbreaking scientific cancer and infectious research. Additional opportunities for global oncology pathogen-associated research are afforded with in-country partners at our state-of-the-art 10,000 square-foot freestanding immunology laboratory in Cape Town, South Africa. Through our long-term China collaborative research initiative, the FH has joint research and training partnerships for clinical and epidemiologic studies linked to pathogen-associated and environmentally-linked cancer development.

The Global Oncology Leader will guide the collaboration with the Uganda Cancer Institute, lead the Global Oncology program staff and will oversee Fred Hutch's international operations. Applicants must have an MD and/or PhD (or foreign equivalent) and board eligibility in clinical oncology is preferred. Expertise in cancer biology and pathogen-mediated cancers are also desirable characteristics. Selection criteria include excellence in clinical care, scholarship, creativity in research, success in developing and advancing collaborations, and demonstrated leadership in the profession. Ideal candidates will have experience working in international settings.

The Global Oncology leader will be based in Seattle, Washington, at Fred Hutch in the Vaccine and Infectious Disease Division (VIDD) and have opportunities for cross-divisional appointments based on research expertise. Fred Hutch offers a vibrant intellectual environment within a beautiful, lakeside campus in Seattle's South Lake Union biotech hub. VIDD occupies a new building that is connected by walking trails to Seattle Cancer Care Alliance and the other four Fred Hutch Divisions and by trolley to major partners such as the University of Washington School of Medicine, Seattle Children's Research Institute, Center for Infectious Disease Research, and the Infectious Disease Research Institute.
Salary DOE + excellent benefits.

Interested candidates should submit a CV, a concise statement of their research interests, and the names and contact information for three (3) references to **fredhutch.org/job/7959**. Specific inquiries can be directed to **Dr. Julie McElrath** at **206-667-1858**.

Applications should be received by **September 1, 2016** to assure consideration and will be evaluated as received.

The Fred Hutchinson Cancer Research Center is an Affirmative Action, Equal Opportunity Employer. All qualified applicants will receive consideration for employment without regard to, among other things, race, religion, color, national origin, sex, age, status as protected veterans, or status as qualified individuals with disabilities. We strongly encourage applications from women, minorities, individuals with disabilities and covered veterans.

10 ways that *Science* Careers can help advance your career

1. Register for a free online account on **ScienceCareers.org**.
2. Search thousands of job postings and find your perfect job.
3. Sign up to receive e-mail alerts about job postings that match your criteria.
4. Upload your resume into our database and connect with employers.
5. Watch one of our many webinars on different career topics such as job searching, networking, and more.
6. Download our career booklets, including Career Basics, Careers Beyond the Bench, and Developing Your Skills.
7. Complete an interactive, personalized career plan at "my IDP."
8. Visit our Career Forum and get advice from career experts and your peers.
9. Research graduate program information and find a program right for you.
10. Read relevant career advice articles from our library of thousands.

Visit **ScienceCareers.org** today — all resources are free

ScienceCareers

FROM THE JOURNAL SCIENCE AAAS

SCIENCECAREERS.ORG

WASHINGTON STATE UNIVERSITY

Behavioral Ecology - Assistant Professor
School of Biological Sciences, College of Arts and Sciences

The School of Biological Sciences at Washington State University, Pullman, Washington, invites applications for a full-time, permanent, tenure-track faculty position in behavioral ecology. This position is to be filled at the Assistant Professor level and will begin in August of 2017.

Required qualifications: (1) Earned doctorate in an appropriate biological discipline at the time of application. (2) Record of research accomplishment in behavioral ecology. (3) Evidence of commitment to teaching excellence and potential for outstanding teaching. (4) Effective communication skills.

Preferred qualifications:
Expertise in genomic, molecular, neurobiological, physiological, and/or use of quantitative approaches to study behavior. Research areas of interest include proximate mechanisms of behavior, behavioral responses to the environment, complex social systems, communication, or ultimate causes of behavior. Ability to complement our faculty's strengths in organismal and evolutionary biology, population, genetics, ecology, and animal physiology.

Job Duties: The successful candidate will be expected to develop and maintain an internationally recognized, extramurally funded research program in behavioral ecology, train graduate and undergraduate students, participate in graduate and undergraduate teaching, participate in service needs, and advance the university's commitment to diversity and multiculturalism.

To apply visit **www.wsujobs.com** and upload application materials. Applications must include a letter of application addressing qualifications, a curriculum vitae, separate teaching and research statements, and up to three selected reprints of published or in press papers. Three letters of recommendation that address the applicant's history of and potential for research, teaching and communication excellence are required. The reference letters will be automatically requested and obtained from the reference provider through our online application system. Review of applications with reference letters begins **September 30, 2016**. For information on the position or the status of your application, candidates may contact Dr. Hubert Schwabl (huschwabl@wsu.edu). Full notice of vacancy can be viewed at https://www.wsujobs.com

EEO/AA/AD

Jefferson Science Fellowship

USAID
FROM THE AMERICAN PEOPLE

The National Academies of Science, Engineering, and Medicine is pleased to announce a call for nominations and applications for the 2017 Jefferson Science Fellowship (JSF) program. Initiated by the Secretary of State in 2003, this fellowship program engages the American academic science, technology, engineering and medical communities in the design and implementation of U.S. foreign policy and international development objectives.

Fellows spend one year at the U.S. Department of State or the U.S. Agency for International Development (USAID) for an on-site assignment in Washington, D.C. As part of their assignments, Fellows may also have the opportunity to travel to U.S. embassies and missions overseas.

The fellowship is open to tenured, or similarly ranked, academic scientists, engineers, and physicians from U.S. institutions of higher learning. Nominees/applicants must hold U.S. citizenship and will be required to obtain a security clearance.

The deadline for 2017-2018 program year applications/nominations is **October 31, 2016.** To learn more about the Jefferson Science Fellowship and to apply, visit the website at:

www.national-academies.org/jsf

The National Academies of
SCIENCES · ENGINEERING · MEDICINE

Assistant Professor of Food Microbiology

PennState

The Department of Food Science at The Pennsylvania State University is seeking an Assistant Professor to work in the area of food microbiology. The Department, housed in the Food Science Building completed in 2006, boasts state-of-the art research and teaching labs, three specialized and dedicated pilot plants, and the Berkey Creamery. The successful candidate will join a dynamic, productive and collaborative faculty in a vibrant and growing Department. For more information on the department, visit http://foodscience.psu.edu. The successful candidate will be expected to establish a strong, externally-funded research program in an area of food microbiology with an emphasis on food safety. This position will be responsible for developing and teaching undergraduate- and graduate-level food microbiology lecture and/or laboratory courses, as well as a course in their area of study/interest and contribute to other courses as needed; advise undergraduate students; and supervise graduate students in thesis research projects. The candidate is also expected to participate in the outreach activities and programs of the department, college and university, as appropriate. Requires a Ph.D. in food science or a closely related field, with experience in food microbiology, and a strong record of publication. Postdoctoral or industrial experience is highly desirable. The ability to work professionally with faculty, staff, and students from diverse populations required. Visit **http://apptrkr.com/840722** for details and to apply. Review of applications will begin on October 1, 2016 and will continue until a suitable candidate is found. Anticipated start date is January 2017 or as negotiated.

CAMPUS SECURITY CRIME STATISTICS: For more about safety at Penn State, and to review the Annual Security Report which contains information about crime statistics and other safety and security matters, please go to http://www.police.psu.edu/clery/, which will also provide you with detail on how to request a hard copy of the Annual Security Report.

Penn State is an equal opportunity, affirmative action employer, and is committed to providing employment opportunities to all qualified applicants without regard to race, color, religion, age, sex, sexual orientation, gender identity, national origin, disability or protected veteran status.

NIMS

Research Position at ICYS, NIMS, Japan

The International Center for Young Scientists (ICYS) of the National Institute for Materials Science (NIMS) is now seeking a few researchers. Successful applicants are expected to pursue innovative research on broad aspects of materials science using most advanced facilities in NIMS (**http://www.nims.go.jp/eng/index.html**).

In the ICYS, we offer a special environment that enables young scientists to work independently based on their own idea and initiatives. All management and scientific discussions will be conducted in English. An annual salary approximately 5.35 million yen (level of 2015) will be offered depending on qualification and experience. Additional research grant of 2 million yen per year will be supplied to each ICYS researcher. The initial contract term is two years and may be extended by one more year depending on the person's performance.

All applicants must have obtained a PhD degree within the last ten years. Applicants should submit an **application form** including a research proposal to be conducted during the ICYS tenure, **CV Header**, CV with list of publications and patents (Be sure to attach the header), list of DOI of journal publications following our instruction, reprints of three significant publications to ICYS Recruitment Desk by **SEPTEMBER 29, 2016 JST**. The **application form** and **CV header** can be downloaded from our website. Please visit **our website** for more details.

ICYS Recruitment Desk,
National Institute for Materials Science
http://www.nims.go.jp/icys/recruitment/index.html